UNIVERSITEIT GENT

FACULTEIT **WETENSCHAPPEN**
Vakgroep **Geologie-Bodemkunde**
Onderzoekseenheid **Renard Centre of Marine Geology**

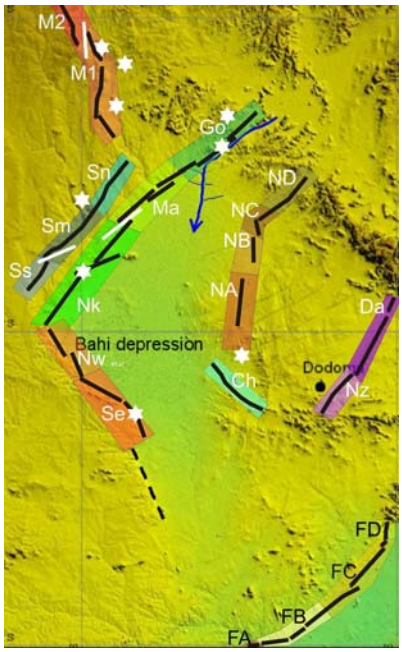

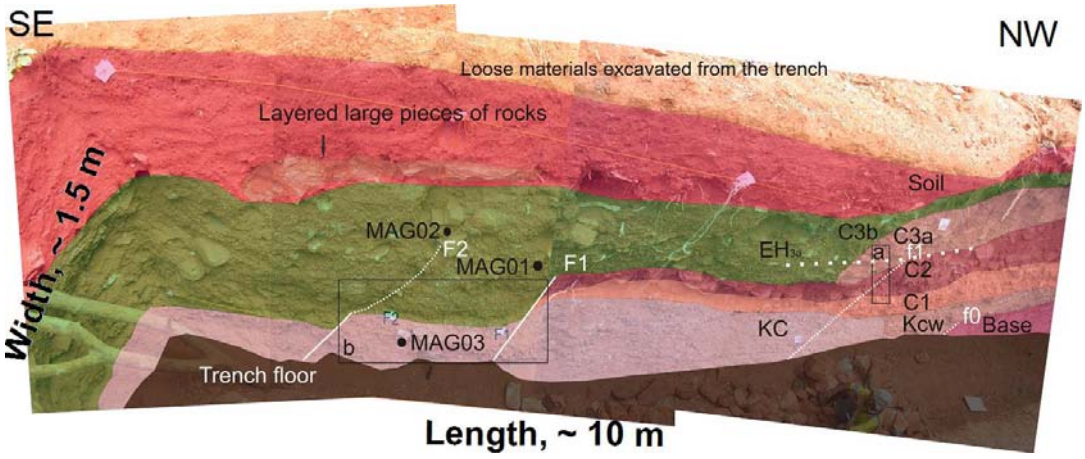

Fault Segmentation, Paleostress and Paleoseismic Investigation in the Dodoma Area, Tanzania: Implications for Seismic Hazard Evaluation

Athanas Simon MACHEYEKI

Academiejaar 2007-2008

Frontpage figures:
Top left = fault segments in the study area, as determined in this study (Chapter 5)
Top right = conjugate fault system observed on the Hombolo fault. The principal stresses σ_1, σ_2 and σ_3 are also shown (Chapter 6)
Bottom = The Magungu trench along the Gonga segment of the Bubu fault (Chapter 7).

Fault Segmentation, Paleostress and Paleoseismic Investigation in the Dodoma Area, Tanzania: Implications for Seismic Hazard Evaluation

Athanas Simon MACHEYEKI
Student registration number: 20045573

A thesis submitted in fulfillment of the requirements for the degree of
Doctor of Science in Geology

Universiteit Gent
Academiejaar 2007-2008

Promotor: Prof. Dr. Marc De Batist, Universiteit Gent, Belgium
Co-Promotors: Prof. Dr. Abdulkarim Mruma, University of Dar Es Salaam, Tanzania.
Dr. Damien Delvaux, Royal Museum for Central Africa, Belgium

Key words: Central Tanzania, Eastern branch, Active Faults, Fault segments, Paleostress, Slip Tendecy Analysis, Thermal springs, Paleoseismic investigations, Manyara-Dodoma rift segment, Chenene surface fractures, Seismic Hazard Evaluation.

Declaration

I, Athanas Simon Macheyeki (37 yr), hereby declare that this Ph.D. thesis, titled "Fault Segmentation, Paleostress and Paleoseismic Investigation in the Dodoma Area, Tanzania: Implications for Seismic Hazard Evaluation", contains data and results of my own work and has never been submitted in any other University in the world for similar award, and that all sources that I have used or quoted throughout the thesis have been indicated and acknowledged by complete references at the end of the thesis.

---------- ----------
Signature of Candidate Date

---------- ----------
Signature of Promoter Date

Dedication

To the memory of my lovely mother Lusiya Sayi Petro Sambusa Matula Hima (1950-1995) and to my father, Malimi Simon Macheyeki Shija Magengeledi Shidūka Makūngū (1936-) for bringing me up and sending me to school.

Acknowledgements

I foremost mention the most forgotten name in science – "the Creator, Jehovah, God" for His marvelous mercy in this work. Through Him, though I was alone most of the time, I never felt lonely. I deeply thank Him in all dimensions for without Him my work would be dimensionless.

My thesis supervisor, Professor Marc De Batist, has been giving me guidance to my work and has been available for me at any time. Through him, I have gained a tremendous confidence in my field! His input in my work (design, comments and suggestions) was so great that I regard him as one of my greatest teachers of science! Professor De Batist has been so kind, keeping on encouraging me. As if that is not enough, when my laptop collapsed, he bought a new one for me instantly – thank you so much, Marc.

I am indebted to Professor Abdul Mruma, my Professor at the University of Dar Es Salaam and currently the Chief Executive Officer of the Geological Survey of Tanzania. His role as a Tanzania-based supervisor cannot go unnoticed. Professor Mruma assisted me to get all geological data I needed from the Survey and he was an important link between the Universiteit Gent, my sponsors and my employer – thank you so much, Abdul.

Dr. Damien Delvaux, my co-supervisor, worked tirelessly with me. He is a person who shared a lot of good times with me. He provided me with a lot of logistics and technical assistance both in the field (Tanzania) and in the office, particularly at the Royal Museum for Central Africa (RMCA). Damien has worked extensively in Tanzania and I feel honored to have known and worked with him. Let me say, I appreciate your enormous

contribution to my career. Thank you, Damien, and thanks to your family for their hospitality!

I am also indebted to Dr. Kris Vanneste of the Royal Observatory of Belgium (ROB) for his great technical and scientific input in this thesis, particularly for Chapter 7. Dear Kris, I count on your contribution.

The Kingdom of Belgium, through the Belgian Technical Cooperation (BTC), and the Government of the United Republic of Tanzania, through the Ministry of Energy and Minerals (MEM), are both highly appreciated for their financial supports. I mention Daphnée Windey, Victor Ndiyezeye, Sylvia Kimpe, Joachim Defraye, Liesbet Vastenavondt and Janet Lindoya from BTC, and Mrs. Lukindo, Mr. A.L. Msigwa and S.A.S. Msambachi from MEM for their dedicated cooperation at their capacity before and during my studies.

Lieven Naudts, Marc Faure Didelle, Wim Versteeg, Dr. Jeffrey Poort, Prof. Jean-Pierre Henriet, Jeroen Vercruysse, Koen De Rycker, Els Verfaillie, Kristien Schelfhaut, Hans Pirlet, Dr. David Van Rooij and my fellow students from the Renard Centre of Marine Geology, Universiteit Gent. Also Prof. E. Mbede of the University of Dar Es Salaam, currently working for the Ministry of Education, are collectively thanked very much for their technical cooperation and their encouragements.

I am giving a special "thank you" to all Tanzanian students in Belgium for their moral support throughout my studies. Thanks also go to all students who were staying with me at *Ontmoeting Buitenlandse Studenten Gent* (OBSG) for their general support.

I am indebted to Dr. François Kervyn who took a lot of time teaching me how to process various data using various softwares, which in turn enabled me to work independently – I would be very unfair if I do not say to him "*nashukuru sana"*.

This chapter, however, remains far unclosed if I do not mention Dr. Luc Tack and Dr. Karel Theunissen from RMCA for their useful comments on the geological setting of Tanzania. I must also thank Dr. Max Fernandez Alonso for his technical and social support in RMCA. Similarly, I thank Christelle Wauthier and Benoît Smets. Christelle and Benoît worked with me for a month in northern Tanzania following the July 2007 seismic crisis. From RMCA, I also mention Suzane for her kindness and preparedness to help throughout my stay in the laboratories of the RMCA at Tervuren. As I cannot mention all people from the RMCA, let me just thank all of them in the African language: "*asanteni"*.

Others in this list are Koen Verbeeck and Toon Petermans from the Royal Observatory of Belgium, who are highly thanked for their constructive comments. Dr. Shukrani Manya from the University of Dar Es Salaam, who provided me with the information about a project that was related to this study, is thanked as well. I also thank Prof. Sospeter Muhongo, the Regional Director of ICSU-Regional Office for Africa, and Dr. Ibrahim Chikira, Dr. Martin Kimanya, Ms. Annelies De Craene and Mr. Charles Bakundukize

from the Universiteit Gent for their encouragements. My students at Madini (Mineral Resources) Institute and my work mates Mr. Placid Kabyemera, Mrs. Halima Kikoti, Mr. Florian Asenga, Mr. E.B. Temu, Mr. Faustin Petro Nyanda, Mr. Sadiki Kipaya, Mr. Alphonce Bushi, Mr. Charles Baasha, Mr. Gumbo, Bi Suzy Kiweru and others are similarly thanked for their moral support and readiness to support me. My immediate boss, Mr. Kandidus P. Lupindu is thanked in the similar accord. I thank all public leaders in Dodoma and Singida regions (Hombolo, Kwamtoro, Chenene, Bahi, Sanzawa, Fufu, Gonga, Kilimatinde, Mponde, Musuhaa and Saranda) for their support during my field work. I also thank Mr. J.S. Rweyemamu of Bukoba Tanzania for his moral support – thank you.

A special thank goes to Mr. Linus Salamba of Geita Gold Mine. He freely accepted to assist me twice in the field and rejected any payments from me for his assistance! I also thank his entire family in Dodoma for accommodating me for weeks during the difficult task of drafting this thesis – thank you for food, drinks and moral support. Equally so are the families of Mr. Joseph Manhyakenda and Jerenimo Mhande in Dar es Salaam for their supports.

I dedicatedly thank my lovely wife Paulina Awasi, our dear children Juliana, Mathias, Faith, and their nurse Aifa, for their tireless prayers and good wishes to my success and dedicated support. Similarly, I must mention Mr. David Kitundu, Philbert Christopher, Mr. Mdongo's family of Shinyanga Tanzania and Rehema Kalawa of Iringa Tanzania for intervening with my family during my absence. I love you all.

I would not be fair if I did not mention my lovely father Mr. Simon Malimi Macheyeki and the whole dear extended family for their prayers at all times of my studies and for the encouragements that "*usichoke mwanetu* (i.e. our son, never give up)".

As I close these pages, I would like to thank all people who, from ages, took the lead in making sure that I am who I am now. This is a long list beginning with my lovely late mother, "*Ng'wana Sambusa*", my dear standard one teachers at Igunya Primary School, fellow pupils and students at all levels through which I have passed, to many others whose names requires a separate volume to list in full. Please, wherever you are, and in whichever form you are, kindly accept my words that I deeply recognize your role and contributions towards this special dream of my life – *"mkabejano"*!

Finally, I thank all members of the Jury for their constructive comments. Your comments have shaped my final work, thank you all, and thank you so much.

Table of Contents

English Abstract

The Dodoma area (Tanzania) lies within the Tanzanian craton, in a region where the eastern branch of the East African Rift System seems to die out (or propagate?) into the craton. The area is characterized by low- to moderate-magnitude seismic activity, sometimes concentrated into so-called "earthquake swarms", but also by rare large earthquakes (up to $M_w = 6.2$). On 4 November 2002, an earthquake of $M_w \sim 5.5$ struck the region during a session of the Tanzanian Parliament in Dodoma, causing cracks in the Parliament building. This seismic event raised the awareness of a large proportion of the Tanzanian society on geo-hazards. This research is a response to that awareness.

This works intends i) to identify the faults that are potentially active in the area, ii) to study their orientation and geometry and their degree of segmentation, iii) to conduct a detailed paleostress analysis and analyse the stress-field responsible for the present-day seismic activity, iv) to evaluate the history of fault-slip activity throughout the Holocene, and v) to make an attempt in quantifying the future potential earthquakes in the area.

At least seven active faults were identified in the area and were studied in detail: i.e., the Mponde, Saranda, Bubu, Makanda, Hombolo, Bahi and Fufu faults. The Mponde and the Bahi faults trend NW-SE to N-S, whereas the other five faults generally trend NE-SW. Displacement profiles of these faults and their geometric pattern show that the faults are segmented. The fault segments obtained are: Segment 1 (31 km) and Segment 2 (28 km) for the Mponde fault; Saranda south segment (11 km), Saranda mid segment (29 km) and Saranda north segment (24 km) for the Saranda fault; Nkambala segment (33 km), Makutupora segment (30 km) and Gonga segment (42 km) for the Bubu fault; Segment A ($\leq$ 31 km), Segment B (18 km), Segment C (15 km) and Segment D (22 km) for the Makanda fault; Nzuguni segment ($>$ 19 km) and Dam segment ($\geq$ 18 km) for the Hombolo fault; Northwestern segment ($\leq$ 29 km) and Southeastern segment ($\geq$ 25 km) for the Bahi fault, Segment A (6 km), Segment B (25 km), Segment C (31 km) and Segment D ($\geq$ 5) for the Fufu fault. The length of each segment reflects the earthquake potential for that given segment. Studies of fault segments deduced from displacement profiles show that the segments in the Dodoma area can generate relatively large earthquakes in the order of $M_w = 6.3$ to 7.

The reduced stress tensor for the stress regimes computed from (Late Cenozoic) fault-slip data for distinct segments of the Saranda, Bubu, Nkambala, Bahi, Fufu and Hombolo faults in the Dodoma area show comparable S_{hmin} values that are nearly E-W. The present-day stress regime that was computed from focal-mechanism data in the larger region of the "Manyara-Dodoma rift" also shows a S_{hmin} direction that is approximately E-W. In addition, newly formed surface fractures also reflect this E-W extensional stress field.

Limited paleoseismic data obtained from a trench across the Bubu fault, indicates that the most recent large earthquake event along the Bubu fault in the Dodoma area took place in

the Middle Holocene (i.e., more recently than 6807-6999 cal. yr BP) and had a vertical offset of about 30 cm, corresponding to a possible magnitude of M_w = 6.3-6.4. The time interval between this Middle Holocene event and the preceding large seismic event is about 2200 yr, equivalent to an average slip rate of about 0.15 mm/yr.

All these results imply that the Dodoma area is indeed seismically active and prone to large earthquakes. The risk can be diminished by building structures that take into account earthquake resistant design and by educating people about earthquake safety. However, more paleoseismological researches integrated with other related studies, such as seismology, archeology and geophysics, need to be undertaken in order to better assess and evaluate the seismic risk of the Dodoma area, which is where the fast-growing capital city of Tanzania is located.

Nederlandse samenvatting

De streek rond Dodoma (Tanzania) bevindt zich pal op het Tanzaniaanse craton, maar wel in een gebied waar de oostelijke tak van de Oost-Afrikaanse Riftzone zuidwaarts lijkt te verdwijnen in (of te propageren in?) het craton. De streek wordt vooral gekenmerkt door aardbevingen met geringe tot matige magnitude, die soms geconcentreerd voorkomen in zogenaamde "aardbevingszwermen", maar ook door sporadische zware aardbevingen met magnitudes tot M_w = 6.2. Op 4 november 2002 werd het gebied getroffen door een aardbeving met magnitude M_w ~ 5.5, en dit gedurende een bijeenkomst van het Tanzaniaanse parlement in Dodoma. De aardbeving veroorzaakte barsten in het parlementsgebouw en ernstige schade in verschillende dorpen rondom Dodoma. Deze aardbeving maakte dan een groot deel van de Tanzaniaanse bevolking bewust van de natuurlijke risico's in hun land. Dit onderzoek is in eerste instantie een antwoord op deze bewustwording…

Deze studie heeft tot doel om i) de breuken die mogelijk actief zijn in de streek rond Dodoma op te sporen en te identificeren, ii) hun oriëntatie en geometrie, en hun graad van segmentatie te bestuderen, iii) een gedetailleerde paleostress-analyse uit te voeren, en een analyse van het huidige spanningsveld dat verantwoordelijk is voor de actuele seismische activiteit, iv) de geschiedenis van de bewegingen langsheen de breuken doorheen het Holoceen te reconstrueren, en v) een poging te ondernemen om de mogelijke toekomstige aardbevingen in de regio te quantificeren.

Minstens zeven actieve breuken konden worden geïdentificeerd in het studiegebied rond Dodoma: i.e., de Mponde, Saranda, Bubu, Makanda, Hombolo, Bahi en Fufu breuken. Ze werden alle in detail bestudeerd. De Mpondo en Bahi breuken hebben een NW-SE tot N-S strekking, terwijl de vijf andere breuken over het algemeen een NE-SW strekking vertonen. Een gedetaileerde analyse van de laterale variaties in breukverplaatsing en -geometrie toont aan dat al deze breuken gesegmenteerd zijn. De verschillende geïdentificeerde breuksegmenten zijn: Segment 1 (31 km) en Segment 2 (28 km) voor de Mponde breuk; Saranda zuid segment (11 km), Saranda midden segment (29 km) en Saranda noord segment (24 km) voor de Saranda breuk; Nkambala segment (33 km), Makutupora segment (30 km) en Gonga segment (42 km) voor de Bubu breuk; Segment A (≤ 31 km), Segment B (18 km), Segment C (15 km) en Segment D (22 km) voor de Makanda breuk; Nzuguni segment (> 19 km) en Dam segment (≥ 18 km) voor de Hombolo breuk; Noordwestelijk segment (≤ 29 km) en Zuidoostelijk segment (≥ 25 km) voor de Bahi breuk, Segment A (6 km), Segment B (25 km), Segment C (31 km) en Segment D (≥ 5) voor de Fufu breuk. De lengte van elk segment is een maat voor de potentiële magnitude van aardbevingen die kunnen veroorzaakt worden door breukbeweging langsheen dat segment. De breuksegmenten in de streek van Dodoma kunnen aldus relatief zware aardbevingen veroorzaken met magnitudes van M_w = 6.3 to 7.

Teneinde het paleo-spanningsveld in de streek rond Dodoma te reconstrueren werd een gereduceerde stress tensor berekend aan de hand van (Laat-Cenozoïsche)

breukbewegingsindicatoren, die werden geobserveerd op een aantal segmenten van de Saranda, Bubu, Nkambala, Bahi, Fufu en Hombolo breuken. Dit leverde vrij homogene S_{hmin} waarden op die duiden op een E-W extensierichting. Het huidige regionale spanningsveld, dat werd berekend aan de hand van de studie van haardmechanismen uit een ruimer gebied (i.e., de "Manyara-Dodoma rift", waar het studiegebied deel van uitmaakt), wordt ook gekenmerkt door een E-W-georiënteerde S_{hmin} richting. Ook een aantal recent gevormde oppervlakkige barsten in het Chenene gebergte bevestigen de aanwezigheid van een spanningsveld gekenmerkt door een E-W-gerichte extensie.

Een onderzoekssleuf, die werd gegraven vlakbij de Bubu breuk, levert beperkte paleoseismische informatie op over het studiegebied rond Dodoma. De laatste sterke aardbeving langsheen de Bubu breuk vond plaats tijdens het Midden Holoceen (i.e., recenter dan 6807-6999 cal. yr BP) en vertegenwoordigde een vertikale breukverplaatsing van 30 cm, op basis waarvan een mogelijke magnitude van M_w = 6.3-6.4 kan afgeleid worden. Het tijdsinterval tussen deze Midden-Holocene aardbeving en de vorige zware aardbeving bedraagt ongeveer 2200 yr, hetgeen overeenkomt met een gemiddelde breukbeweging van ong. 0.15 mm/yr.

We can expect that rocks RECORD the large seismic activities; our main task as geologists is to PRINT and INTERPRET these record(s); the quality of the printout is partly a function of the quality of the record!

Chapter 1

General Introduction

1. General introduction

1.1. General framework of this study

Natural disasters include a.o. earthquakes, volcanic eruptions, landslides, floods, hurricanes, tsunamis and meteoric impacts. Efforts have been made by humankind to eliminate or lessen their impacts in various ways in order to make our planet a good and safe place for living. In geosciences, especially earthquakes and volcanic eruptions are a main concern.

Earthquakes and volcanic eruptions are interrelated phenomena in that volcanic eruptions are always associated with earthquakes; the reverse is not the case. By definition, an earthquake is the trembling or vibration of the Earth due to sudden release of stored energy in rocks. As the energy is released, the Earth vibrates at frequencies and amplitudes that are a function of the amount of energy released by the quake, depth to the hypocenter and distance to the epicenter. The energy stored in rocks comes from movement of tectonic plates (a) against each other (collision), (b) away from each other (extension) or (c) parallel to each other. While the processes of collision (compression), extension and movement of plates past each other are well observed at plate boundaries, these processes are also manifested away from these boundaries at different magnitudes.

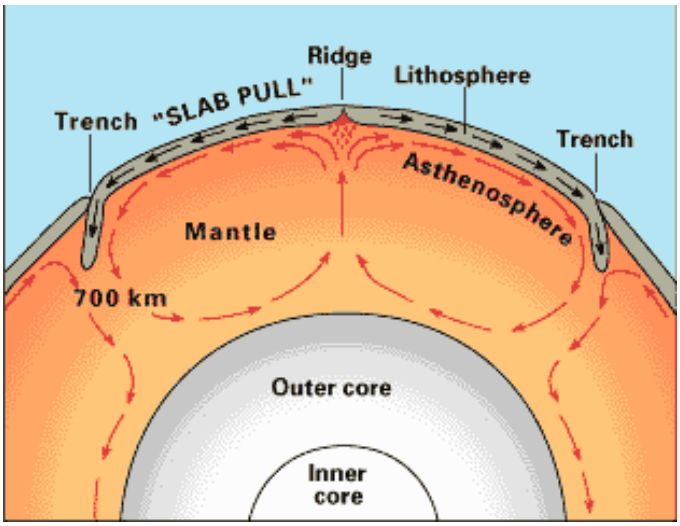

Fig. 1 - Convective cells in the mantle.
(http://geology.er.usgs.gov/eastern/plates.html).

The movement of tectonic plates is possible because the lithosphere is composed of a number of coherent rheological plates (Allen and Allen, 2005) and is geared by convective cells located below the lithosphere. Convective cells are made up of rocks themselves, which are considered to have the behaviour of a fluid over geologic time

scales. Alfred Wegener states "*All that can be said with certainty is that the earth behaves as a solid, elastic body when acted upon by short-period forces such as seismic waves, and there is no question of plastic flow here. However, under forces applied over geological time scales, the earth must behave as a fluid"*. As the convective cells move, they carry the lithosphere (i.e., the crust plus part of the upper mantle) on top of them (Fig. 1). Because there are several convective cells that move in different directions and magnitudes, the lithospheric plates are also many (i.e., the Eurasian, Philippine, Australian, Pacific, Juan de Fuca, Cocos, Caribean, Nazca, North America, South America, Scotia, Arabian, African, Antarctic and Indian plates) and they move in different directions and with different speeds (Fig. 1.2).

Tectonic plates represent a manifestation of regional tectonic activities. This means that at local scales, such processes are also observed. An important thing to note also is that within a given tectonic plate, compressional, transcurrent and extensional movements can be observed. Intermediate tectonic settings combining two of these processes are also possible.

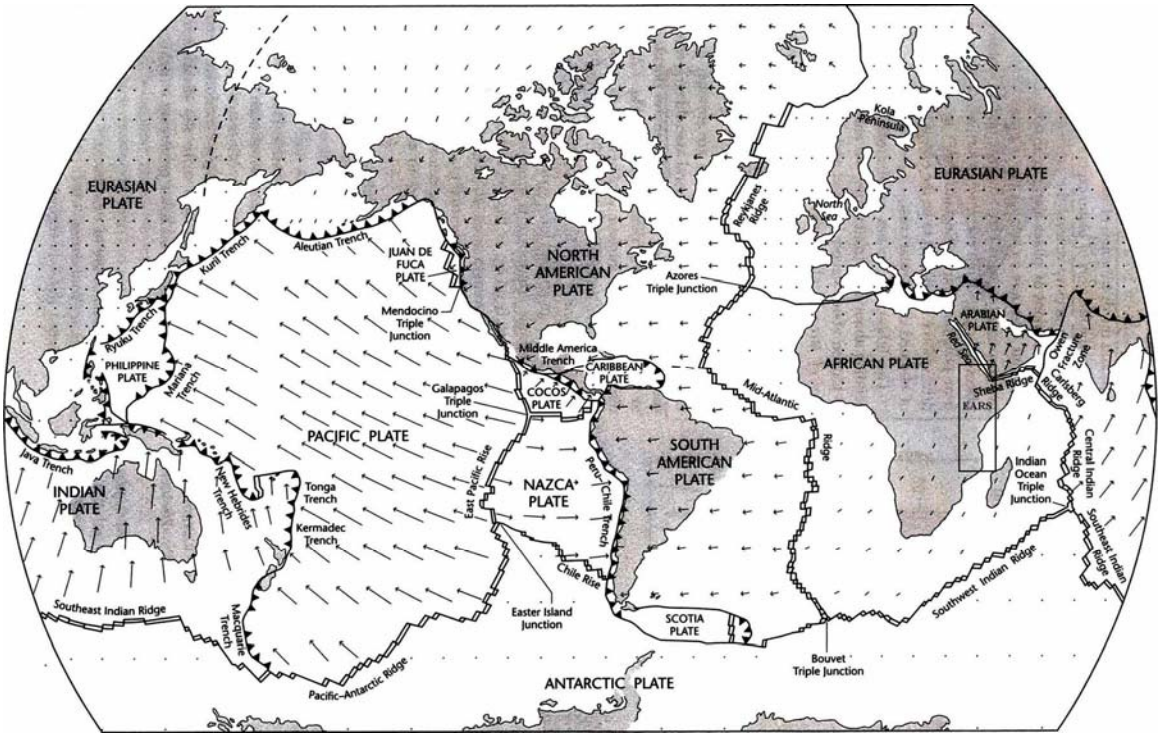

Fig. 1.2 - The lithospheric plates, showing plate boundaries (Le Pichon et al., 1973) and absolute motion vectors (Minster and Jordan, 1978). Length of arrows is proportional to the plate velocity. The fastest plate motion is in the western Pacific and Indian oceans, whereas Africa, Antarctica, and Eurasia are almost stationary with respect to the mantle reference frame (after Allen and Allen, 2005).
EARS in a rectangular box stands for the EARS and the Afar.

The East African Rift System (EARS) (Fig. 1.3) is considered as an analog to the initial stage of mid-oceanic ridge development (Morley, 1999). The EARS, like other plate boundaries is characterized by earthquakes and volcanic eruptions. Earthquakes can be studied either directly using instrumental techniques (seismology) or indirectly using the

information recorded in geological materials that can act as archives, as used in paleoseismology and paleostress analysis.

This study is mainly concerned with the paleoseismic investigations and paleostress analysis, but also utilizes data from seismological studies at some stages for reasons to be stated later in this Introduction and in Chapter 4.

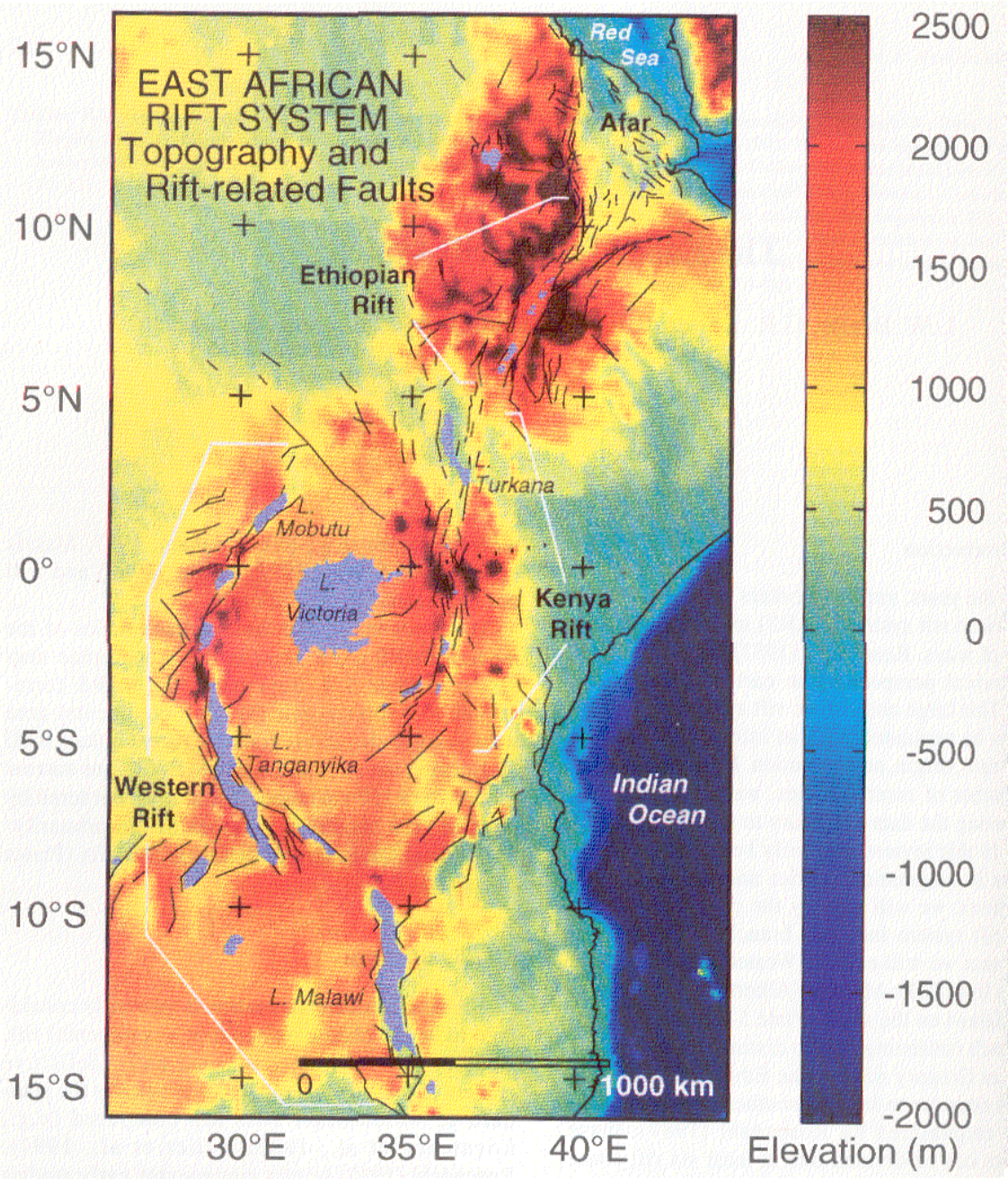

Fig. 1.3 - Topographic map of EARS (After Braile et al., 1995).
Approximate location of the EARS is shown in Fig. 1.2.

1.2. Location and background of the area

The Dodoma area, which has been chosen as study area for this thesis, is about 28,749 km^2, i.e. covering an area between 5°00'-7°00'S and 34°50'-36°00'E (Fig. 1.4). This area is within the eastern branch of the EARS and characterized by low- to moderate-magnitude seismic activity, sometimes concentrated into so-called "earthquake swarms" (Macheyeki et al., 2008a; 2008b), but also by rare large earthquakes (up to M_w = 6.2).

On 4 November 2002, an earthquake of M_w ~ 5.5 struck the area during a session of the Tanzanian Parliament in Dodoma, causing cracks in the Parliament building. The quake was also felt in many parts of the country such as Morogoro, Singida, Iringa, Mbeya and Arusha regions (Fig. 1.4). Near Dodoma and in the Chenene mountain area, in particular, several village buildings, schools and houses collapsed. The 4 November 2002 seismic event raised the awareness of a relatively large proportion of the Tanzanian society on geo-hazards. This research is a response to that awareness.

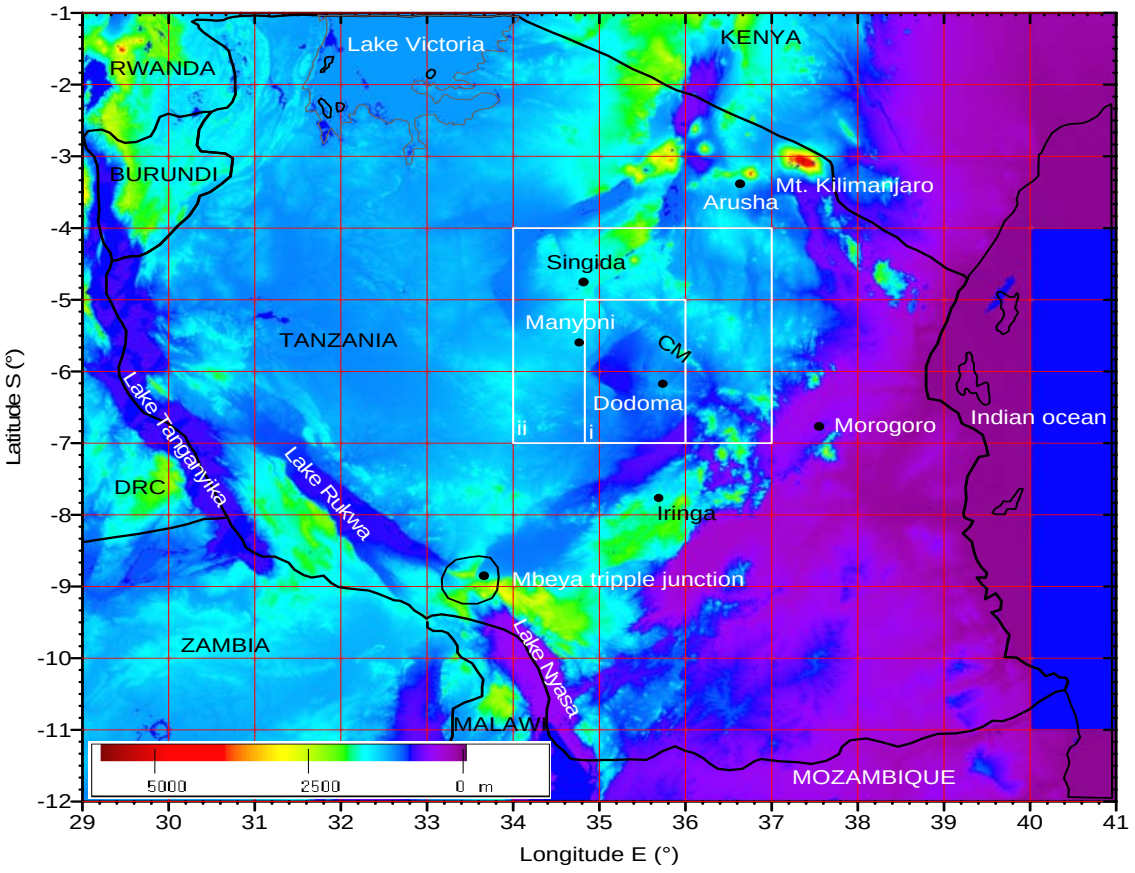

Fig. 1.4 - The 90 m resolution SRTM-DEM map for Tanzania. The study area is defined by coordinates 5°00' to 7°S and 34°50' to 36°00'E (i). Further in this study, a slighly larger area, defined by coordinates 4°00' to 7°00'S and 34°00' to 37°00'E, shall commonly be presented as a base map (ii). Note the area without data between 40°00'E to 41°00'E and 4°00'S to 11°00'S. CM = Chenene Mountains.

1.3. Previous work in the area

Little work on active tectonics (i.e., active fault segmentation, paleoseismic investigations) has been undertaken in the Dodoma area so far. This is, among other reasons, partly due to the fact that the eastern branch of the EARS fades away or is poorly developed in this area (Macheyeki et al., 2008b). Much more emphasis has been put on the Kenya (Gregory) Rift north of the Dodoma area, which is relatively better developed in terms of rift morphology. However, researchers who worked on the Gregory Rift area and south of it, such as Sykes (1970), Fairhead and Girdler (1971), Fairhead and Stuart (1982), Shudofsky (1985), Shah (1986), Wagner and Langston (1988), Kebede (1989), Iranga (1992), Nyblade et al. (1996), Langston, et al. (1998) and Brazier et al. (2005), focused on seismological studies and showed that the Dodoma area, like many parts of the EARS, is seismically active. Details of this will be presented in Chapter 3.

1.4. Objectives

This problem-solving work intends to answer a number of questions related to active tectonics in the Dodoma area:

(1) What are the faults that are potentially active from a seismic point of view?
(2) What are their orientations, total lengths and vertical offsets?
(3) Are they segmented or continuous?
(4) How was/were the paleostress regime(s) oriented before present and how can the paleostress regime(s) have controlled the present-day tectonic stress regime(s) and earthquakes?
(5) Is it possible to quantify the future potential earthquakes in the area?

These five questions have been answered using seven major approaches:

- active fault mapping,
- determination of fault segments,
- paleostress analysis,
- present-day tectonic stress (focal mechanisms) analysis,
- fault-slip tendency analysis,
- study of thermal springs, and
- paleoseismic investigation.

Present-day tectonic stress (focal mechanisms) and fault slip tendency analyses have been carried out in an area that is larger than the Dodoma area *sensu stricto*, in order to obtain a regional framework and reliable data about the present-day stress regime. A multidisciplinary approach has been used here in order to properly understand the seismic potential of this region, and to assess the associated geo-hazards (e.g., Michetti et al. 2005).

Seismological data in Tanzania, as it is the case for large parts of Africa, are only available for the last 100 years. In fact, instrumental catalogues span at most 70 years world-wide, which is not long enough to provide an estimate of recurrence intervals for the largest events (Goes, 1996). Historic catalogues, however, may span several recurrence intervals of Ms $\geq$ 7 earthquakes but suffer from incompleteness and inhomogeneity. In other words, wherever seismological and/or historical earthquake data are available, they are not homogeneous. For example, in Tanzania, patches of complete seismic records existed from 1953 to 1957 and from 1963 to 1990, but with a decrease of data recording in 1970-1988 (Iranga, 1992). Thereafter, from 1992 to 1999, seismic data were collected by ESARSWG & ISC. Also, in the years 1994 and 1995, seismic recordings were undertaken by the Tanzania Broadband Seismic Experiment (Brazier et al., 2005). Therefore, such a non-continuous monitoring of earthquakes in Tanzania provides a heterogeneous record of data that has most likely not recorded a significant number of earthquakes in many parts of Tanzania, which could aid in the better understanding of the spatial and temporal characteristics of the seismic events. The latter are two important components in seismic hazard evaluation (e.g. Keller and Pinter 2002).

Although this study is in principle mostly concerned with the documentation, characterization and analysis of relatively large earthquakes ($M_w \geq 5.5$), which could also have been recorded internationally by seismic networks, these large earthquake-related data are not immediately accessible and, whenever they are available, they face the same time-limit problem (i.e., seismographs came into existence world-wide a little over a century ago). Earthquakes of societal concern can be traced through the Holocene (e.g., Sibson, 1986b), though records of individual earthquakes may extend well back into the Late Pleistocene in regions with long recurrence intervals (e.g., Crone et al., 1992). As such, it is only through paleoseismic investigation that large earthquakes that occurred in that span of time, i.e. over the whole Quaternary period, can be recorded and interpreted. McCalpin (1996) reported that *"…it is difficult to reconstruct quantitatively the amplitude of shaking in pre-historic earthquakes but only by paleoseismological means…"*. Therefore, for better characterization of fault activities (and paleo-earthquakes associated with them), paleoseismological investigations are necessary (e.g., Philip et al., 2001; Keller and Pinter, 2002; Michetti et al., 2005). Because of that, the results of this work should contribute to the understanding of pre-historic earthquakes in Tanzania and provide a base for future similar studies in the area and its surroundings for the purpose of improving our understanding and our capacity in seismic hazard evaluations.

For a complete seismic hazard evaluation, an assessment of the likelihood of an earthquake(s) to occur in a given area is required (Burbank and Anderson, 2001). In other words, in order to know how often earthquakes have occurred in the past, and when and how large the last event was (e.g., Pavlides et al. 1999), more questions than those highlighted above need to be answered. Additional questions include:

(6) Have the faults moved aseismically or in discrete events that generated earthquakes?
(7) Is there regularity to the timing of events?
(8) Is there a pattern to the rupture that is repeated from event to event?

(9) Can the fault or given faults be divided into independent segments that rupture in characteristic events?
(10) Does an earthquake on one fault increase the likelihood of rupture on other nearby faults, and how do those changes depend on the orientation of the fault ?
(11) Can we estimate the likelihood of a fault to produce an earthquake of a given magnitude within a specified period of time?

These six questions are not answered in this work but can form future assignments for paleoseismologists and/or geologists!

1.5. This thesis

This thesis has ten chapters:

Chapter 1. General Introduction,
Chapter 2. Introduction: active continental extension,
Chapter 3. Geological setting of the study area,
Chapter 4. Methods of investigation,
Chapter 5. Active faults and fault segmentation,
Chapter 6. Fault kinematics and tectonic stress,
Chapter 7. Paleoseismic investigations,
Chapter 8. Chenene surface fractures,
Chapter 9. Discussion,
Chapter 10. Conclusions and recommendations.

Four appendices are provided at the end of the thesis:

Appendix 1. The SRTM-derived profiles in the Dodoma area,
Appendix 2. Thermal springs in the Dodoma area,
Appendix 3. Fault-slip data in the Dodoma area,
Appendix 4. Reports on earthquakes/tremors in the area of Dodoma.

In Chapter 1, reasons for selecting the Dodoma area as a study area are given. Chapter 2 elaborates the relevant literature review that was at the basis of this research work. Thereafter, a chapter (Chapter 3) on the East African Rift System (i.e., the regional geodynamic setting) and the tectonic and geologic setting of the Dodoma area is provided. The subsequent Chapter 4 presents the means, methods and procedures that were taken to undertake this research (i.e., collection of data, processing and evaluation, etc). The chapters on the results of the research work and the interpretation follow (i.e., Chapters 5-8): they provide a detailed description of results obtained and give the possible interpretation of the data, together with some comments on data quality control in which the possible sources of error in the respective results are assessed. These chapters are Chapter 5 “Active faults and fault segmentation”, Chapter 6 “Fault kinematics and tectonic stress”, Chapter 7 “Paleoseismic investigations” and Chapter 8 “Chenene surface fractures”. Chapter 9 discusses the results obtained and the interpretations made and puts the findings in a broader perspective. In this chapter, a comparison of the results with other results obtained elsewhere in the EARS and in the world on similar investigations is undertaken. It is followed by Chapter 10 with conclusions and recommendations.

The appendices contain SRTM-derived profiles (x-y-z coordinates provided), description of the characteristics of the thermal springs, raw data of geological fault-data, and archived historic reports of the effects of earthquakes or earth tremors in the region in 1964 and 1965.

Chapter 2

Introduction: Active Continental Extension

2. Introduction: active continental extension

By definition, "active continental extension" refers to extension of the continental lithosphere due to various natural processes that are largely related to plate tectonics. It results in the formation of rift systems. These processes manifest themselves at the surface by "active normal faults" (i.e., faults that have moved in the last 10,000 years), either as discrete, singular faults, or as multiple faults (i.e., in the case of rift systems).

In the first part of this chapter, a general description of various aspects of active continental extension will be given. The definition of a "continental rift" will be given, and the role of rifting in active continental extension will be discussed. Finally, various published models of continental extension will be presented in a general way.

The second part of the chapter deals with the fault sytems that constitute the architecture of the rift.

2.1. Rift systems

2.1.1 Rifts

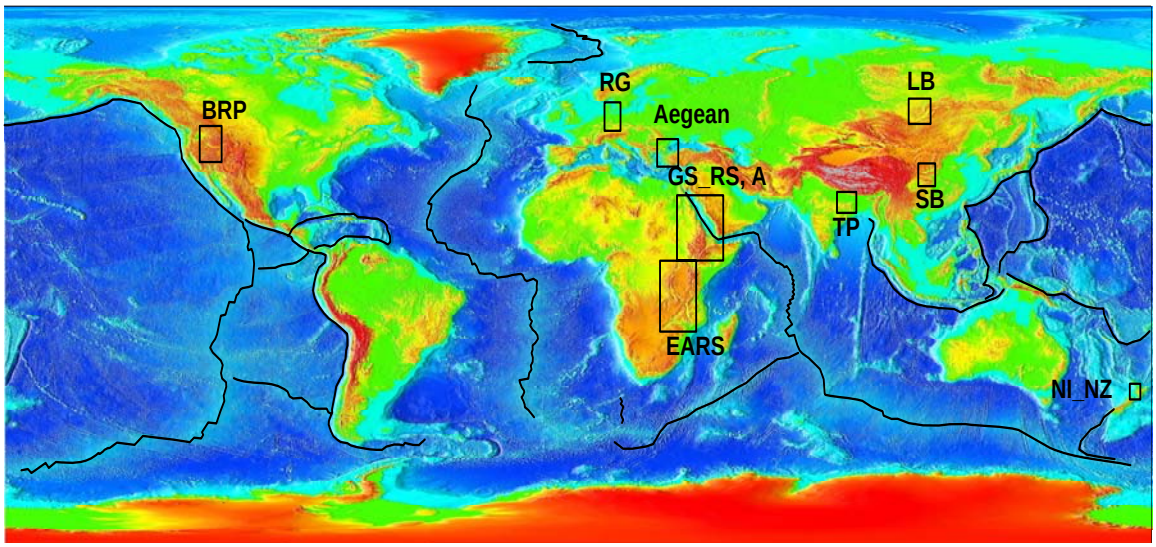

Fig. 2.1 - World map with plate boundaries (solid lines) to show main areas of active continental extension. BRP = Basin and Range Province, Rio Grande; RG = Rhine Graben; GS_RS, A = Gulf of Suez, Red Sea, Afar; EARS = East African Rift; TP = Tibetan Bohai; SB = Shaanxi Bohai; LB = Lake Baikal; NI_NZ = North Island New Zealand.

"Rifts" can be defined as areas that overlie crust that has been thinned due to crustal extension (Allen and Allen, 2005). They occur as narrow (50-100 km wide), elongated (up to 1000 km long) structures and are often segmented (Leeder, 1995). Geomorphologically, rifts are well defined as elongated depressions, bounded by normal faults (Olsen, 1995). The major areas in the world that are currently undergoing continental rifting are shown in Fig. 2.1.

The common association of rifts with volcanism, high heat flow, anomalous crust (e.g., negative Bouguer gravity anomalies) and upper mantle structure, and seismicity provides strong evidence that rifts are essentially confined to upper crustal levels, but they are linked to dynamic processes that involve the lithosphere and asthenosphere (Olsen, 1995; Allen and Allen, 2005; Fig. 2.2).

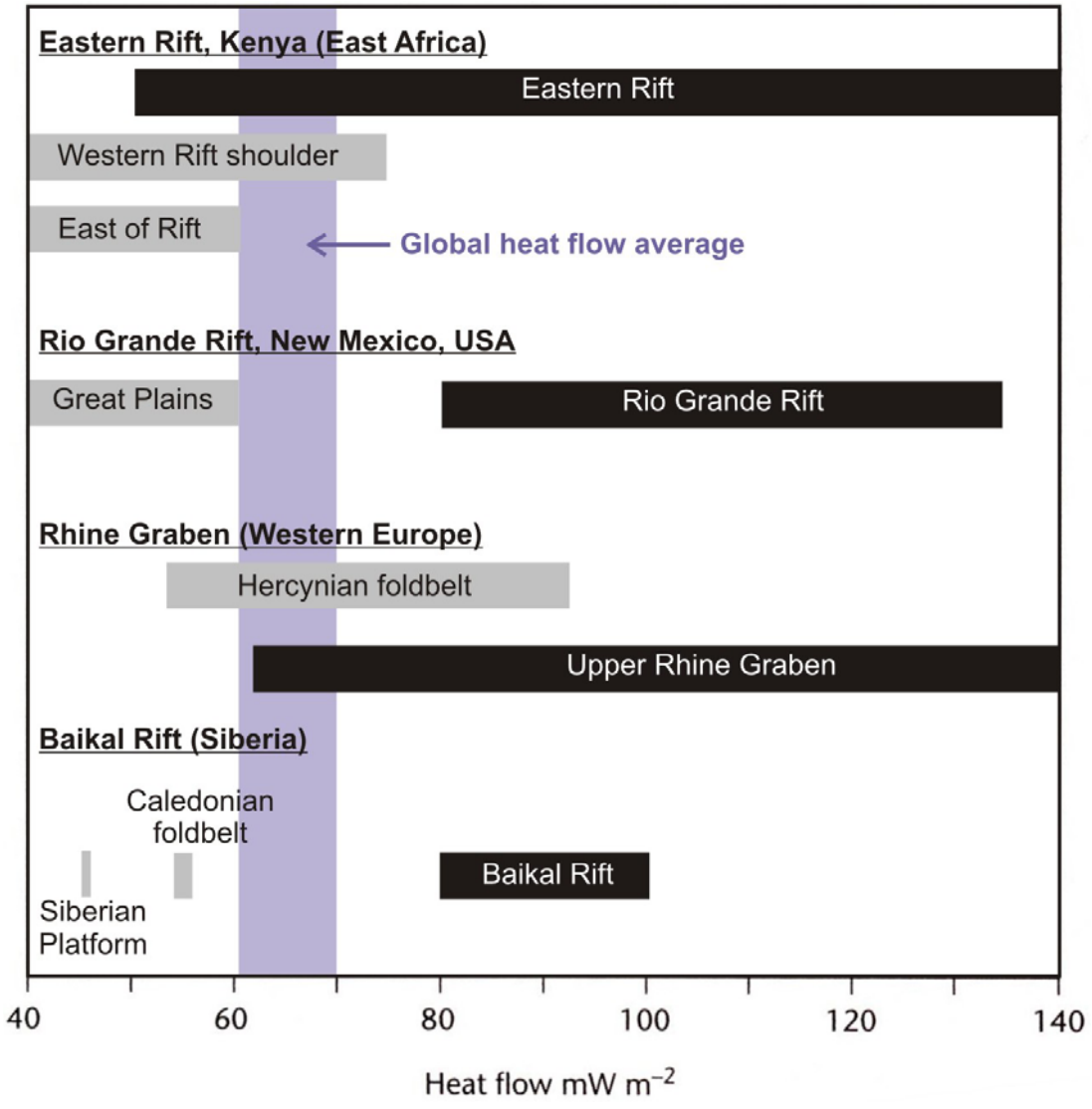

Fig. 2.2 - Heat flow values in some continental rifts and surrounding regions, compared to the global heat flow average. Dark boxes are rift zones; light boxes are rift flanks or adjacent unstretched regions (after Allen and Allen, 2005).

2.1.2 Continental rifts

A continental rift is an elongate tectonic depression along which the entire lithosphere has been modified in extension (Olsen, 1995). As there are often different stages in the process of rift development, it may sometimes be difficult to differentiate between the separate stages, such as simple grabens, true continental rifts, highly extended terranes and passive margins. Olsen and Morgan (1995) term these structures as "closely related structures" (Fig. 2.3) and differentiate them based on strain percentage.

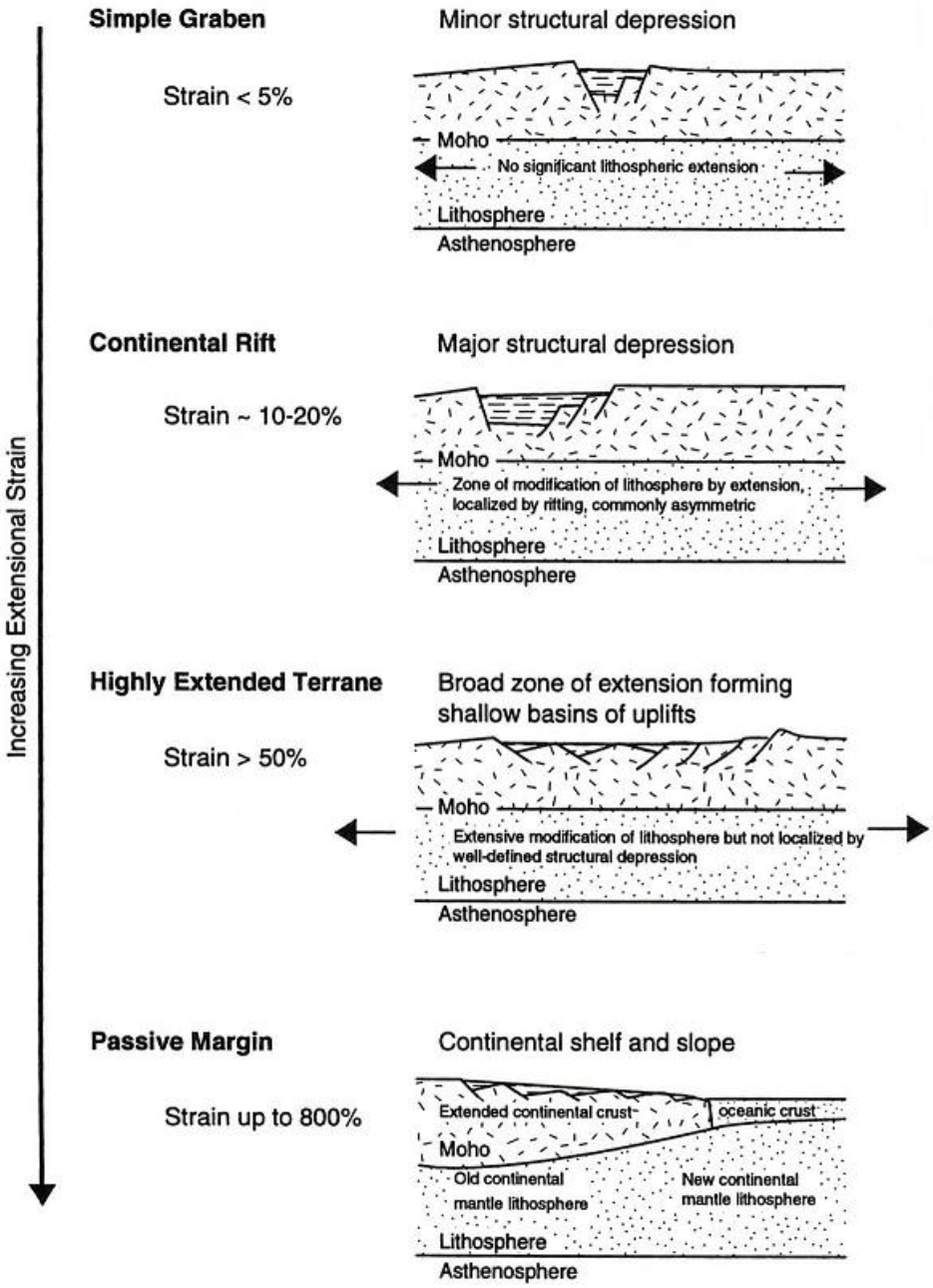

Fig. 2.3 - Major terrane styles associated with continental extension (Olsen and Morgan, 1995).

Continental rifts may represent the initial stage of continental break-up and the start of a Wilson cycle of plate tectonics (ocean opening and closing, Fig. 2.4). Plate tectonics has placed new emphasis on continental rifts as possible sites of incipient lithospheric separation and formation of new oceanic basins because continental lithosphere is weaker than oceanic lithosphere with a similar geothermal gradient (e.g., Vink et al., 1984).

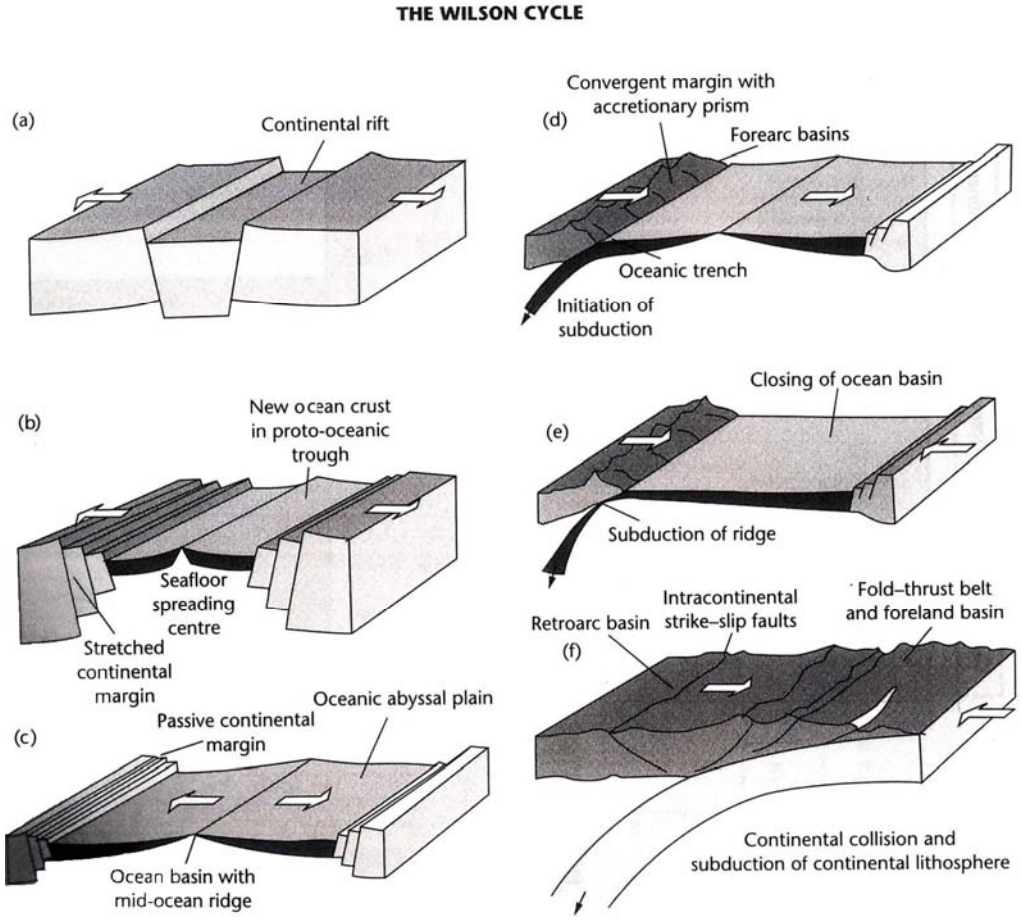

Fig. 2.4 - The Wilson cycle of ocean formation and ocean closure. Continental extension (a) is followed by creation of new oceanic spreading centre (b) and oceanic enlargement (c). Subduction of ocean floor (d) leads to closure of the ocean basin. Subduction of the oceanic ridge (e) takes place before continental-continental collision (f). (Allen and Allen, 2005).

2.1.3 Mechanisms of continental rifting

There are two mechanisms that can explain continental rifting initiation: “active” and “passive” rifting (Fig. 2.5). In the passive hypothesis, lithospheric tension of distant origin causes failure of the continental lithosphere and subsequent development of the anomalous underlying upper mantle. In contrast, in the active rifting model, the anomalous upper mantle develops first by convective upwelling and doming; volcanism and extension are the consequence (Bott, 1995).

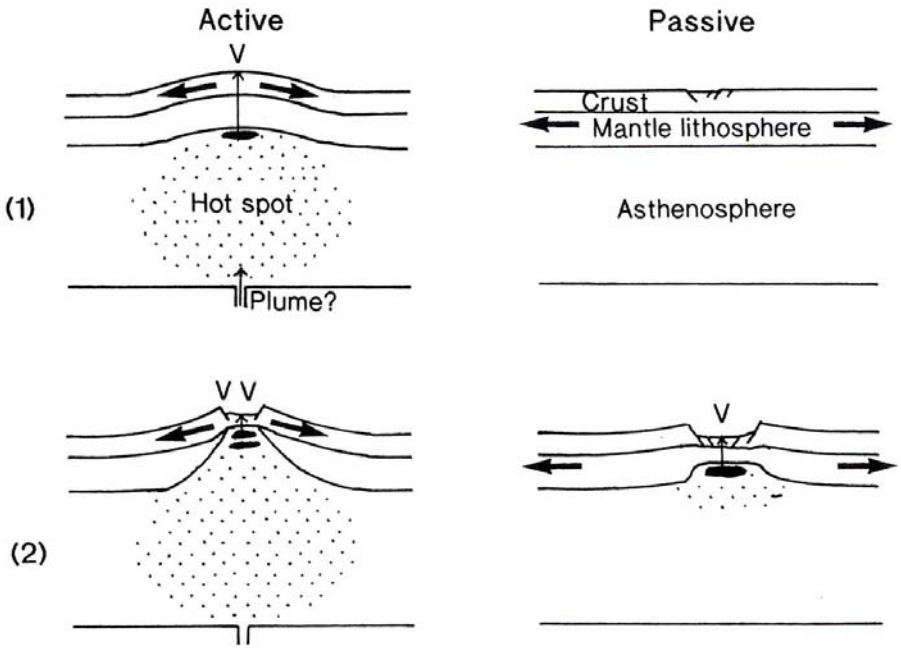

Fig. 2.5. - Idealized diagram comparing the active and passive hypotheses for initiation of continental rifting. (1) shows the initial stage of both hypotheses, and (2) shows subsequent stages of development. The shading indicates hot, low-density regions of the sub-lithospheric upper mantle; V denotes volcanism (Bott, 1995).

2.1.4 Modes of continental extension and influence of magmatism

There are three types or modes of continental extension/rifting; (1) narrow rifting, (2) wide rifting and (3) core complex mode (e.g., England, 1983; Buck, 1991; Olsen and Morgan, 1995; Fig. 2.6).

2.1.4.1 Narrow rifting

It is the type of rifting that concentrates on crustal and mantle lithospheres (Fig. 2.6) and gives rise to narrow regions (generally up to 100-150 km wide) of intense normal faulting (Buck, 1991; Corti et al., 2003). Such rifts include the East African Rift System, Rio Grande Rift, Baikal Rift, northern Red Sea, West Antarctic rift and the European Cenozoic Rift System (Rosendahl, 1987; Corti et al., 2003).

Narrow rifts are characterized by large lateral gradients in crustal thickness, topography and presence of a hot (possibly asthenospheric) upper mantle beneath the rift (e.g., Prodehl et al., 1997).

In terms of initial crustal thickness and thermal conditions, narrow rifts will form if the lithosphere is initially cold (Hopper and Buck, 1996).

2.1.4.2 Wide rifting

Wide rifts such as the Basin and Range Province, the Aegean Rift and the Tibetan Plateau (Fig. 2.6) result from a uniform crustal and lithospheric mantle thinning over a width greater than the lithospheric thickness. This distributed deformation gives rise to a typical surface expression characterized by a large number of separated basins extending over a region of up to 1000 km wide.

In terms of initial crustal thickness and thermal conditions, wide rifts will form if the lithosphere is initially warmer (Hopper and Buck, 1996).

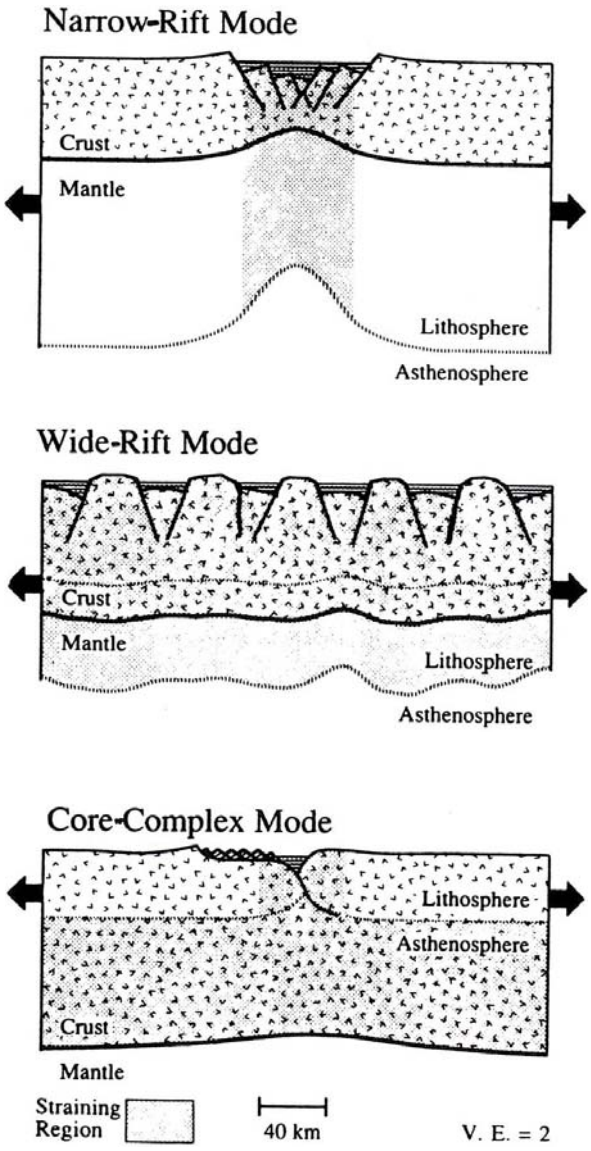

Fig. 2.6 - Sketch of the lithosphere in three modes of continental extension, emphasizing regions undergoing greatest amount of extensional strain. "Lithosphere" connonates areas with effective viscosities greater than 10^{21} Pa.s. Hatched lines show base of lithosphere. (After Buck, 1991).

2.1.4.3 Core complex mode of extension

According to Buck (1991), core complex mode of extension is the type of extension that consists of high-grade metamorphic rocks originating in the middle-lower crust and which are exposed at the surface, exhumed by low-angle normal faults, uplift and erosion (e.g., Coney, 1980; Brun et al., 1994).

Core complexes (Fig. 2.6) are normally associated with wide rifts (e.g., in the Basin and Range Province and the Aegean Rift), and this close correspondence has been interpreted as related to successive rifting phases characterized by different styles of extension (e.g., Sokoutis et al., 1993). Such a close association of core complex structures with wide rifts may suggest that core complex structures are local anomalies within wide rifts (Brun, 1999).

The above classification of rifts is based on dynamics/genesis of rifts, i.e. based on the origin of forces that lead to rifting (Busby and Ingersoll, 1995). Rifts can also be classified based on their structure (Block and Royden, 1990; Wernicke, 1991), geometry (Şengör, 1987a) and kinematics (i.e., according to the environment of the overall displacement and strain field in which they form) (Kampunzu and Popoff, 1991; Busby and Ingersoll, 1995).

The length of fault segments in rifts has been found to be inversely proportional to the degree of obliquity of the rift (e.g., McClay et al., 2002). Lateral propagation of these segments, results in the merging of the different rift basins in one single rift, in which the initial *en échelon* geometry remains visible (McClay and White, 1995; Mart and Dauteuil, 2000). McClay and White (1995) consider rifts to fall into two types or modes (based on geometry and kinematics): “orthogonal rift models” and “oblique models”.

Rifts that form in accordance to orthogonal rift model are characterized by long, relatively straight rift-border faults and shorter intra-rift faults. Both the rift border and intra-rift faults form perpendicular to the direction of extension (Fig. 2.7). For orthogonal rifts $\alpha = 90°$ (α is the angle between the rift axis and the extension direction).

During orthogonal rifting, magma is passively squeezed from an axial position towards the footwall of the major normal faults, resulting in major magma accumulations occurring in a lateral position (off-axis emplacement) with a rift-parallel trend. Lateral transfer and off-axis emplacement of magma can provide an explanation for the occurrence of flank or off-axis volcanoes in continental rifts, such as the Main Ethiopian and Kenya rifts in the East African Rift System, the Limagne Graben in the Cenozoic European Rift System, and the Red Sea (Corti et al., 2003; Fig. 2.8).

In oblique rift models, the direction of extension is not orthogonal to the rift axis (Fig. 2.7). In this case, the rift border faults are highly segmented and form *en échelon* arrays parallel to the zone of rifting. The intra-rift faults in this type of model form orthogonal to, or at high angles to, the extension vector.

During oblique rifting, the occurrence of magma at depth influences the fault pattern, localizing strain in the overlying crust. In turn, deformation favors magma to emplace within the main rift depression, giving rise to elongated intrusions with an oblique, and in some cases, *en échelon* pattern. In nature, this pattern may be representative of the *en échelon* faults and volcanic alignments, oblique to the axial valley trend, characterizing continental rifts such as the Main Ethiopian Rift (Fig. 2.8).

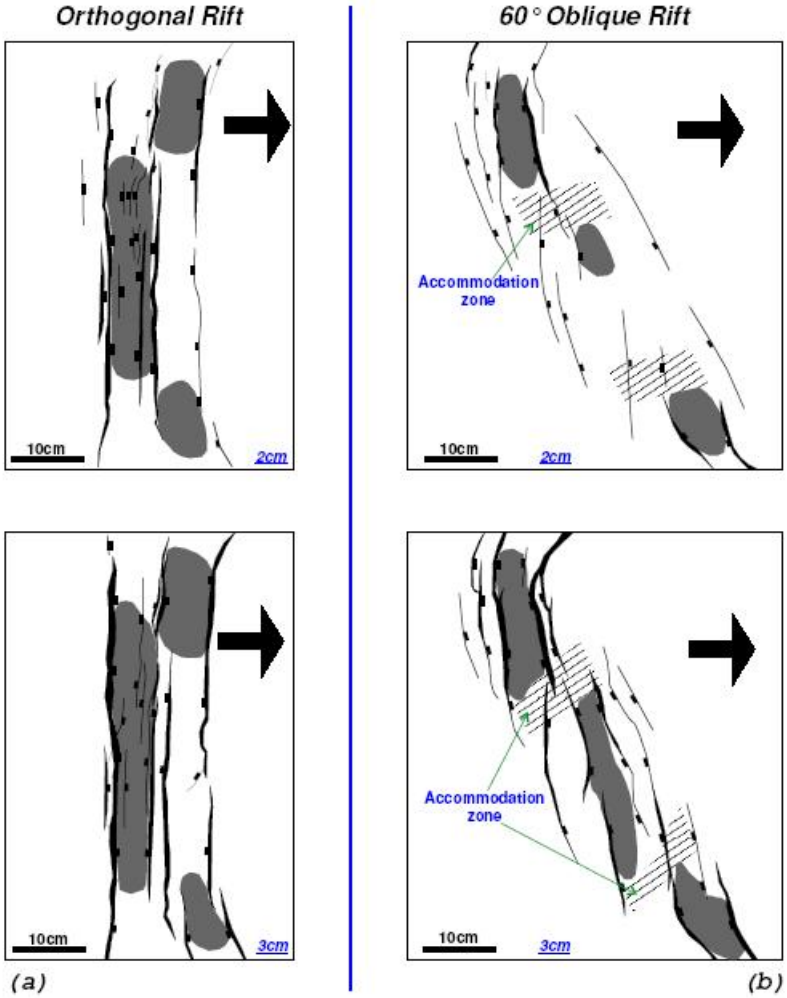

Fig. 2.7 - Interpretations of horizontally sliced models of three-dimensional rift experiments; (a) orthogonal extension, α = 90° and (b) oblique extension, α = 60°. In the orthogonal rift long linear faults develop that are oriented perpendicular to the direction of extension, whereas in the oblique model, different smaller faults form in *en échelon* geometry. Grey shadings in the figure represent local depocentres. Arrows point to the extension direction (McClay and White, 1995; Hus, 2004).

At times, and at a given rift, oblique rifting may be preceded by orthogonal rifting. This type of rifts results from so-called polyphase rifting. In this case, the rift kinematics strongly affect the modalities of magma emplacement. During the orthogonal rifting phase, magma is squeezed laterally, causing an off-axis emplacement, while during the successive oblique rifting phase, emplacement occurs in oblique (or *en échelon*) intrusions. This evolution matches the tectonomagmatic history of the Main Ethiopian

Rift where important off-axis volcanoes formed on the rift shoulders during the Miocene-Pliocene orthogonal rifting.

It should be noted that increased extension in the oblique and moderately oblique rift systems ($\alpha = 45°$ and $60°$) cause the intra-rift faults to rotate towards parallelism with the rift border faults (Morley et al., 1992; McClay and White, 1995).

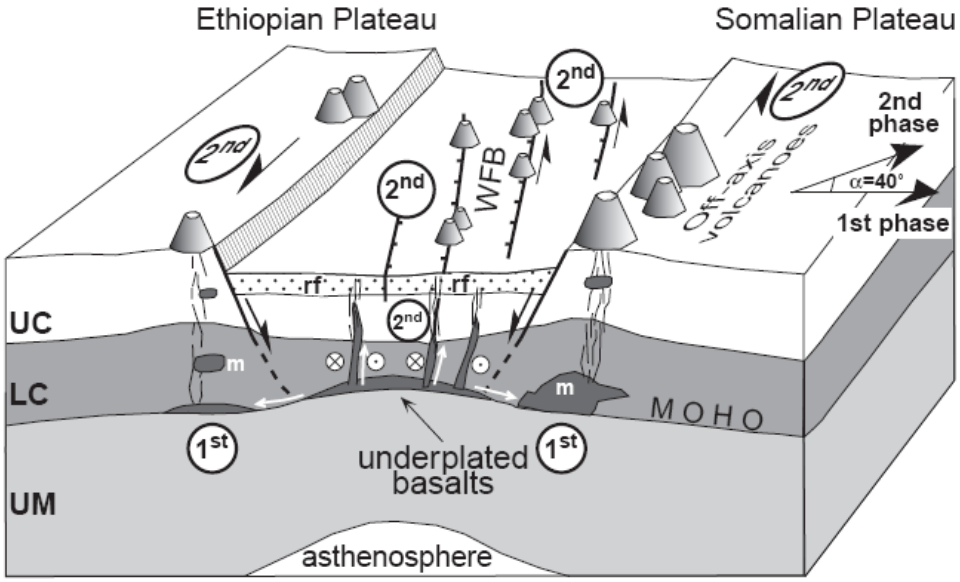

Fig. 2.8 - Interpretative schematic 3D block diagram of the Main Ethiopian Rift evolution based on the modelling results, relating (1) off-axis volcanism to lateral flow of the lower crust and magma during the first orthogonal rifting phase (denoted by 1st) and (2) oblique faulting and magmatism to the second oblique rifting phase (denoted by 2nd). Note that this interpretation includes both the effect of isostatic compensation provided by the asthenosphere and the thermal thinning of the crust, which were not considered in the current models. UC: upper crust; LC: lower crust; m: magma; rf: rift fill. WFB stands for Wonji fault belt (Corti et al., 2003).

2.1.5 Continental lithospheric strength versus magmatism in extension processes

There is a close relationship between lithospheric strength and the presence of magmatic bodies in or beneath a lithosphere. When a large volume of melt is emplaced in the continental lithosphere, the thermal and mechanical properties of the lithosphere are modified; this weakens the lithosphere and enhances deformation and strain localization (e.g., Lynch and Morgan, 1987; Chèry et al., 1989; Geoffroy, 1998; Morley, 1999a).

As the continental lithosphere undergoes extension, major magma intrusions concentrate in a relatively narrow area. This process may lead to a shift of deformation from major boundary faults to minor fault swarms concentrated in narrow regions within the rift depression (e.g., Mohr, 1987; Morley, 1994; 1999a; 1999b; Ebinger and Casey, 2001).

2.1.5.1 Magmatism versus faulting and stress regime

The fault pattern can be locally influenced in several ways by intruding magmatic bodies beneath the upper crust (e.g., Morley, 1999a; 1999b). For instance, low-angle normal faults can be initiated. Inflation of overpressured magma in the middle-upper crust may create local compressional stresses, causing σ_1 (the maximum principal stress axis) direction to rotate from a vertical orientation near the surface to horizontal near the intrusion. Furthermore, heating caused by the magma may allow the lower crust to flow, creating a basal shear stress between the flowing and the stable crust with a subsequent reorientation of the principal stress axes (Yin, 1989). In both cases, the process of faulting is influenced in a way that causes a variation in the normal fault dip from 45-70°, as predicted by the Andersonian theory, to < 30-45°. Furthermore, as new magmatic material is added within the crust, the stress regime of extending regions may significantly be affected because such an added magma can potentially absorb extension (e.g., Parsons and Thompson, 1991; 1993).

2.1.5.2 Dynamics of rifting versus the geometry of the resulting structures

The dynamics of the rifting process (steady and episodic rifting) has a major influence on the geometry and mechanics of the resulting structures (Mulugeta and Ghebreab, 2001) in brittle-ductile extension.

For steady or constant, progressive rifting, extension is accommodated by rapid subsidence and flexure of the brittle crust, with formation of a central rift zone characterised by a complex array of domino-style faults and bounded marginal grabens. In this type of extension, forces that drive extension are larger than buoyancy forces generated by the differential pressure between the rift depression and the rift margins. These drive an outward flow of ductile material that promote thinning and subsidence of the central rift zone.

For episodic rifting, spaced grabens and horsts characterized by less-pronounced subsidence are formed. This pattern is produced by a counter-flow of ductile materials from the margins and the regions of higher topography to the central rift zone. This is a dynamic consequence of heterogeneous stretching. The counter-flow of ductile materials from the regions of higher topography towards the rift depression tries to remove the differential pressure between the rift margins and the rift depression and to restore isostatic equilibrium (Shudofsky, 1985; Mulugeta and Ghebreab, 2001).

2.1.6 Forces on the continental lithosphere

Stresses may be transmitted through the continental lithosphere over large lateral distances (Allen and Allen, 2005). These deviatoric stresses are termed in-plane stresses (e.g., Zoback, 1992; Allen and Allen, 2005) or far-field stresses (e.g., Delvaux, 1991; Zoback, 1992) since they are in the plane of the plate (that means they are stresses that have a resultant horizontal component). Details on how these far-field stresses are propagated are given in Allen and Allen (2005).

2.1.7 Models of strain geometry in rifts

There are models that have been developed to explain how strain occurs in rifts. These models are (a) pure shear, and (b) simple shear (e.g., Kusznir et al., 1991; Buck, 1998; Allen and Allen, 2005). Kusznir et al., (1991) use the model of pure and simple shear to explain strain geometry in the lithospheric mantle and crust respectively.

2.1.7.1 Pure shear model

In the pure shear model, the lithosphere extends symmetrically with the initial fault-controlled subsidence spatially superimposed on the thermal subsidence. The ductile stretching may be accompanied by dilation due to the intrusion of melts (Royden et al., 1980; Fig. 2.9a).

2.1.7.2 Simple shear model

In the simple shear model the lithosphere may extend asymmetrically, the zone of ductile subcrustal stretching being relayed laterally from the zone of brittle crustal stretching (e.g., Buck, 1998; Allen and Allen, 2005). It is proposed that the entire lithosphere can be traversed by a gently dipping shear zone on a large scale that brings about lithospheric extension (Wernicke, 1981). Such a shear zone transfers or relays extension from the upper crust in one region to the lower crust and mantle lithosphere in another region (Fig. 2.9b).

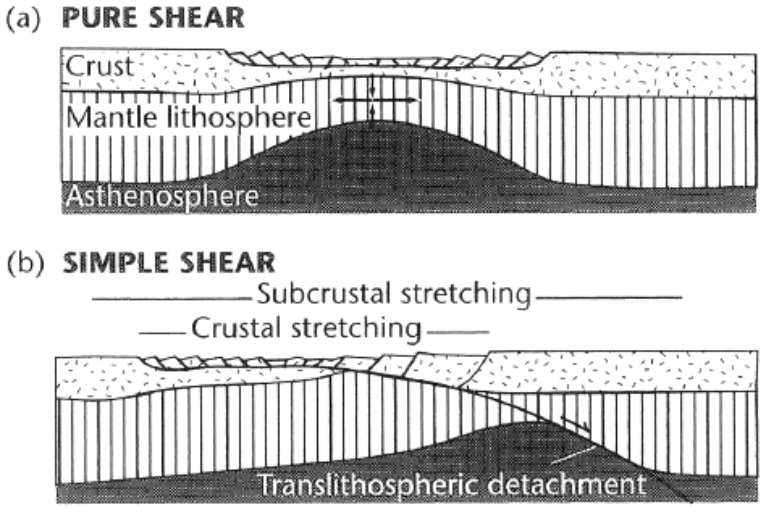

Fig. 2.9 - Models of strain geometry in rifts (Coward, 1986; Buck, 1998). (a) Pure shear geometry with an upper brittle layer overlying a lower ductile layer, producing a symmetrical lithospheric cross-section with the initial fault-controlled subsidence spatially superimposed on the thermal subsidence. The ductile stretching may be accompanied by dilation due to the intrusion of melts (Royden et al., 1980); (b) Simple shear geometry with a through-going low-angle detachment dividing the lithosphere into an upper plate or hanging, and lower plate or footwall. Thinning of the lower lithosphere is relayed along the detachment plane, producing a highly asymmetrical lithospheric cross-section (after Wernicke, 1981; 1985). Initial fault controlled (synrift) subsidence is spatially separated from the thermal subsidence (Allen and Allen, 2005).

2.2. Faults: types of faults and fault architecture

In this part, the focus is on faults, the definition of faults, their classification and their relationship with active tectonics. Relay ramps are briefly discussed too.

2.2.1 Faults

A fault is a surface or narrow zone across which there has been relative displacement of the two sides of the surface, and parallel to it (e.g., Bates and Jackson 1987; Angelier, 1989). The term displacement is the general term for the relative movement of two fault blocks along a fault plane, with a slip vector that lies in the fault plane (Fig. 2.10).

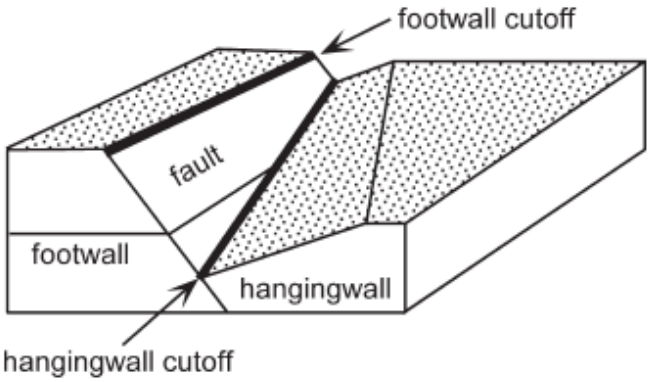

Fig. 2.10 - General terminology for a surface (patterned) offset by a fault. Heavy lines are hanging-wall and footwall cutoff lines (Groshong, 2006).

Displacement variation along faults is a rule, as displacement is null at the fault tips and reaches a maximum in between. Displacement gradients are typically steeper near fault terminations (tips) than on the fault as a whole. The presence of a displacement gradient requires that either one or both of the hanging-wall and footwall cut-off lines must differ in length from their original, pre-faulting, lengths. The magnitude and partitioning of strain between footwall and hanging-wall cutoffs depend on five factors: (1) dip of fault, (2) shape of fault (curved versus planar), (3) displacement gradient on fault, (4) degree of footwall uplift versus hanging-wall subsidence, and (5) orientation of fault slip vector (Ferrill and Morris, 2001).

2.2.2 Classification of faults

2.2.2.1 Normal faults

Normal faults are dip-slip faults. They generally form in the upper 10-15 km (McClay, 1987). As the continued stretching of the Earth's crust during its uplift does not end with

the formation of fractures, the tension fractures pass into faults, most commonly into normal faults. Normal faults rarely occur separately; they are usually combined in one way or another to form grabens and horsts or step faults (Beloussov, 1962).

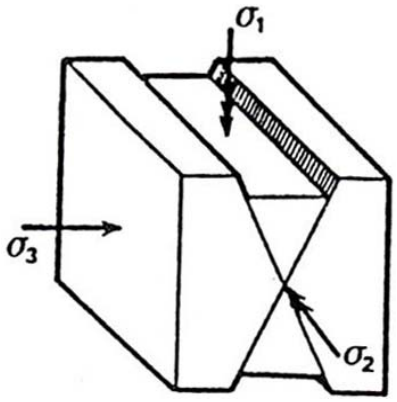

Fig. 2.11a - Normal dip slip faults (conjugate system). (Angelier, 1989).

Normal faults or fault planes typically dip about 60° from the horizontal. The principal stresses σ_1, σ_2 and σ_3 are arranged in such a way that σ_1 is subvertical and the others, σ_2 and σ_3 are subhorizontal (Anderson, 1951; Angelier, 1989; Fig. 2.11a).

2.2.2.2 Strike-slip faults

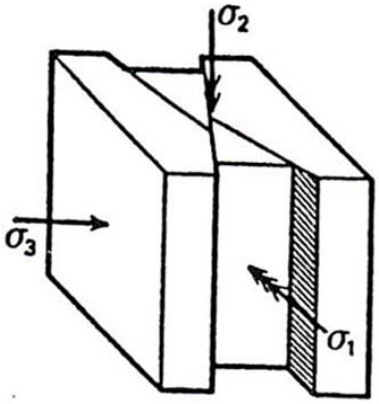

Fig. 2.11b - Strike slip faults (conjugate system). (Angelier, 1989).

Strike-slip faults are faults whose surface is typically vertical or nearly so. The motion along a strike-slip fault is parallel to the strike of the fault surface, and the fault blocks move sideways past each other. A strike-slip fault in which the block across a given fault moves to the right is described as a dextral strike-slip fault. If it moves left, the relative motion is described as sinistral. Local deformation near bends in strike-slip faults can produce pull-apart basins and grabens. Bends and step-overs give rise to compressional and extensional stresses, resulting in push-up structures and pull-apart basins. The

intermediate stress axis σ_2 is subvertical, whereas σ_1 and σ_3 are both subhorizontal (Anderson, 1951; McClay, 1987; Angelier, 1989; Fig. 2.11b).

2.2.2.3 Reverse faults

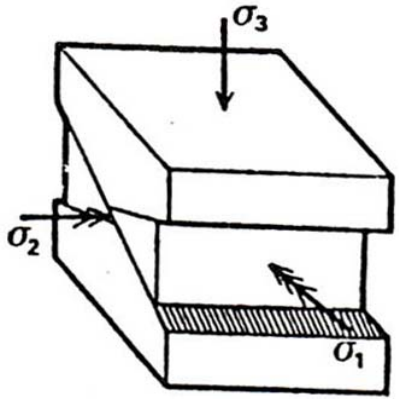

Fig. 2.11c - Reverse slip faults (conjugate system). (Angelier, 1989).

Reverse faults are characterized by low-angle fault planes, typically about 30° from the horizontal and σ_3 is subvertical, whereas σ_1 and σ_2 are subhorizontal (Anderson, 1951, McClay, 1987; Angelier, 1989; Fig. 2.11c).

2.2.2.4 Active faults

An active fault is defined as a fault that is currently moving or has moved in the past, over a certain period of years. The length of this period may vary following the authors and the context. According to a restricted definition, this period is fixed as 10,000 years (McCalpin, 1996), which is generally used in the USA by insurance companies because of the obvious risk for the society. However, longer periods are also used e.g. in the world map of active faults (McCalpin, 1996; Skobelev et al., 2004). The most obvious manifestation of active extension is normal faulting associated with earthquakes (Jackson and White, 1989).

2.2.3 Fault segments and fault segmentation

Fault segments are discrete portions of given faults. They should not be confused with earthquake segments (or rupture segments) which are discrete portions of faults that have demonstrably ruptured to the surface two times or more (McCalpin, 1996).

In their early stages of formation fault segments occur as individual fault strands with displacement profiles that decrease from maximum in or near the center to zero at either tips (Burbank and Anderson, 2001; Young et al., 2001). Faults can grow by radial propagation (Cartwright et al., 1995; Burbank and Anderson, 2001), i.e. the individual fault segment simply lengthens and accumulates more displacement, while maintaining the standard displacement profiles (Fig. 2.12). Faults can also grow by segment linkage

(Burbank and Anderson, 2001), when different individual fault segments become connected as they grow laterally, overlap and become hooked to each other on tips (Burbank and Anderson, 2001; Young et al., 2001) in a process which is referred to as fault interaction (Fig. 2.12). Such interactions may promote or inhibit fault nucleation and growth, distort fault slip profiles, produce fault linkage and coalescence, and collectively result in populations of faults with distinctive characteristics (Peacock and Sanderson, 1991).

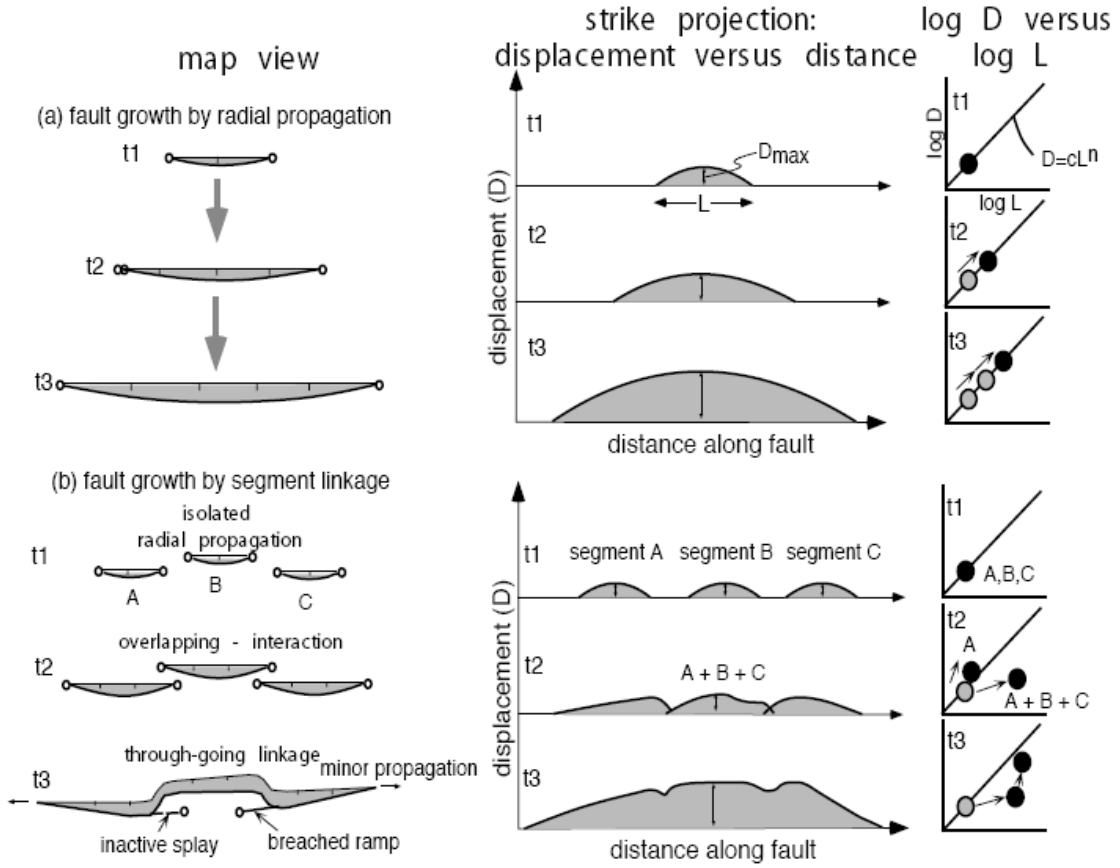

Fig. 2.12 - Two models of fault growth. (a) Radial propagation. In this model, an individual fault simply lengthens and accumulates more displacement through time t. Plots of displacement versus fault length (right column) show a steady increase in displacement as the fault grows. (b) Segment linkage. In this model, different small individual faults gradually link up to create one large, through-going fault. Whereas the accumulation of displacement follows a predictable path for individual segments, when they link up, displacement becomes considerably less than that predicted for a fault of this length (see right-hand column). Through time, the slip deficiencies near the point of segment linkage are reduced. Ultimately, the only indication that the large fault resulted from fault linkage of smaller ones may be the presence of perturbations to the smooth, bow-shaped displacement near the former zones of overlap and linkage (Burbank and Anderson, 2001; Cartwright et al., 1995).

According to Burbank and Anderson (2001), the maximum displacement of a resulting fault (from linkage) is 9 % larger than that of a similar isolated fault, of length *a* when spaced 0.05*a* from each other. Details on fault displacements are provided by Pollard and

Segall (1987); Walsh and Watterson (1987); Cowie and Scholtz (1992a; 1992b); Bürgmann et al. (1994) and Peacock and Sanderson (1996).

Large normal faults develop through the interaction and linkage of individual segments. Evolving faults follow a distinct growth path, as segments progressively link and transfer zones (e.g., relay ramps) break down (Peacock and Sanderson, 1991; Cartwright et al., 1995). Consequently, a number of transient geological structures are believed to characterize specific conceptual stages in the evolution of faults (Table 2.1), Young et al., 2001, Tentler and Mazzoli, (2005).

Table 2.1 - A summary of geological structures that characterize specific stages in the evolution of normal faults (Young et al., 2001).

Fault growth stage	Characteristics of structures
1. Isolated strands	(i) Individual fault strands with displacement profiles that decrease from a maximum in the centre to zero at the fault tips (ii) Local depocentres in the hanging walls of isolated fault strands are filled by the early syn-rift sequences that have a limited area extend and are thickest towards the centre of isolated fault strands (iii) Fault strands and associated hanging-wall depocentres are separated by relative highs; regions that experience displacement deficit rather than displacement transfer. These highs are onlapped by the early syn- rift sequences.
2. Soft linkage	(i) Formation of "ductile structures" such as relay ramps, which transfer displacement between echelon stepping, soft linked fault strands or segments. (ii) Fault displacement profiles exhibit steep displacement gradients towards transfer zones.
3. Break-down	(i) Strain accumulation in ductile structures reaches critical levels and the structures begin to deform in a brittle manner. Faults begin to cut across relay structures.
4. Hard linkage	(i) Transfer faults cut through relay zones linking previously discontinuous fault traces. This results in a single through-going fault that has distinct bends or jogs disrupting the along-strike trend of the fault trace. (ii) The latest syn-rift sequences are thickest towards the centre of hard-linked faults.

The phenomenon of fault segmentation has been recognized for over 20 years (Keller and Pinter, 2002). Although the processes by which segments form are still poorly understood (Vermilye and Scholz, 1999), seismotectonic studies show that it is commonly one or two fault segments that are involved in rupturing during large seismic events, each fault segment rupturing independently of the other, each with its own rupture history (Zhang et al., 1998). Ruptures that occur along entire lengths of long faults are much rarer (Keller and Pinter, 2002). Large earthquakes, commonly of a characteristic size, repeatedly rupture the same part of segment of a fault, less commonly extending into adjacent segments (Schwartz and Coppersmith, 1984). Therefore, for evaluation of both past and future earthquakes, the study of fault segments using geologic data from

paleoseismological sites (from both stratigraphic and geomorphic evidence) is essential (Piccardi, 2005). The study of fault segmentation is thus commonly used as an approach to estimate the potential earthquake size. Segment boundaries play an important role in arresting earthquake ruptures from event to event (Zang et al., 1998).

Segment boundaries are commonly characterized by complex fault-zone geometry consisting of step-overs, jogs, bifurcations, bends, gaps, and other patterns that create both "geometric discontinuities" and "structural discontinuities" within a fault zone (Zhang et al., 1998). The structural discontinuities of a fault zone may potentially act as structural barriers that influence earthquake rupture initiation and termination, and may impede or stop earthquake rupture propagation (Zhang et al., 1998). Small-scale structural discontinuities (< 1 km) are, however, probably not capable to stop an earthquake rupture with a length of more than 30 km or magnitude 7 or larger (Crone and Haller, 1991). Therefore, the size of a structural discontinuity with respect to the rupture length or displacement may play an important role in controlling rupture termination.

Table 2.2 - Types of fault segments and the characteristics that are used to define them (McCalpin, 1996)

Type of segment	Characteristics used to define the segment	Likelihood of being an EQ segment*
Earthquake	Historic rupture limits	Very high (by definition, 100 %)
Behavioral	(i) Prehistoric rupture limits defined by multiple, well-dated paleoearthquakes	High
	(ii) Segment bounded by changes in slip rates, recurrence intervals, elapsed times, sense of displacement, creeping versus locked behavior, fault complexity	Moderate, 26 %
Structural	Segment bounded by fault branches, or intersections with other faults, folds, or cross-structures	Moderate-High, 31 %
Geologic	(i) Bounded by Quaternary basins or volcanic fields (ii) Restricted to a single basement or rheologic terrain (iii) Bounded by geophysical anomalies (iv) Geomorphic indicators such as range-front morphology, crest elevation	Variable, 39 %
Geometric	Segments defined by changes in fault orientation, step-overs, separation, or gaps in faulting	Moderate-High, 18 %

* An EQ segment (an earthquake segment) means a discrete portion of a fault that has demonstrably ruptured to the surface two times or more (McCalpin, 1996).

Earthquakes may be termed "characteristic earthquakes" when they show repetition, break segments, rupturing the full width of the seismic zone and relieving the bulk stress on the fault segment they break (Kelleher et al., 1973; Schwartz and Coppersmith, 1984).

Characteristic earthquakes should have comparable rupture extent, magnitude, and total slip. In otherwords, such earthquakes should have some regularity to their occurrence (Goes, 1996; McCalpin, 1996). According to McCalpin 1996, there is a relationship between the type of fault segment, its characteristics and the likelihood of that given fault segment being an earthquake segment (Table 2.2).

2.2.4 Relay ramps

Relay ramps are areas that are tilted between two overlapping synthetic normal faults (Larsen, 1988; Peacock and Sanderson, 1991; Peacock et al., 2000a; Peacock and Parfitt, 2001). Relay ramps are common features in extensional environments that can also demonstrate fault interaction (fault segment linkage, Fig. 2.13a,b). The surface of relay ramps usually tilts towards the hanging-wall fault segment (Figs. 2.13; 2.14), and this tilt often causes a decrease in the total fault displacement in the overlap zone. According to Ferrill and Morris (2001), relay ramps in brittle rocks transfer displacement between overlapping normal faults by vertical axis rotation (accommodating horizontal heave gradients on faults) and tilting (accommodating vertical throw gradients on the faults). An additional note is that relay ramps can be good sites for hydrocarbon migration (as quoted by Peacock and Parfitt, 2001).

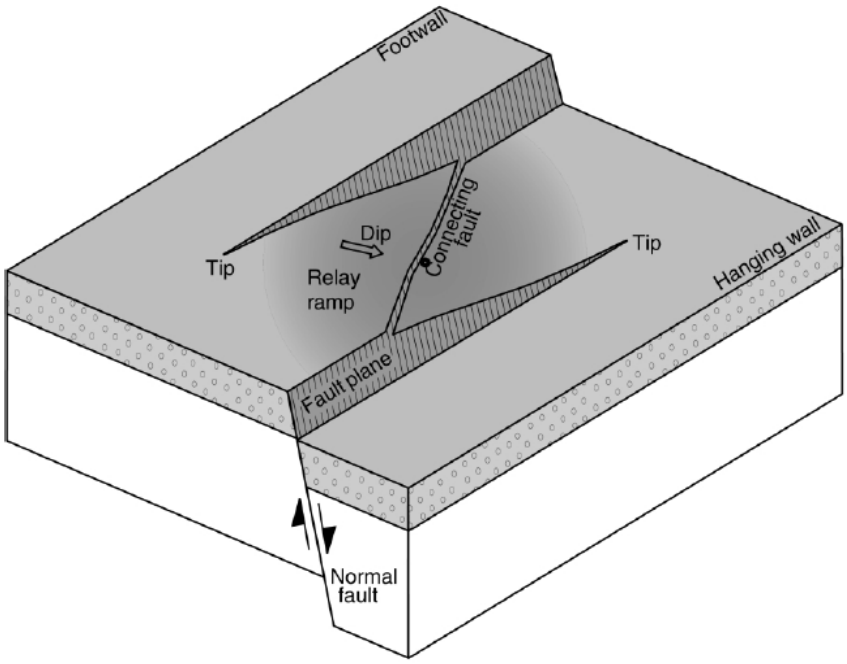

Fig. 2.13a - Block diagram of a relay ramp between two normal faults that overstep in map view and that dip in the same direction. Displacement between the faults is transferred as blocks tilt within the relay ramp (Peacock and Partfitt, 2001).

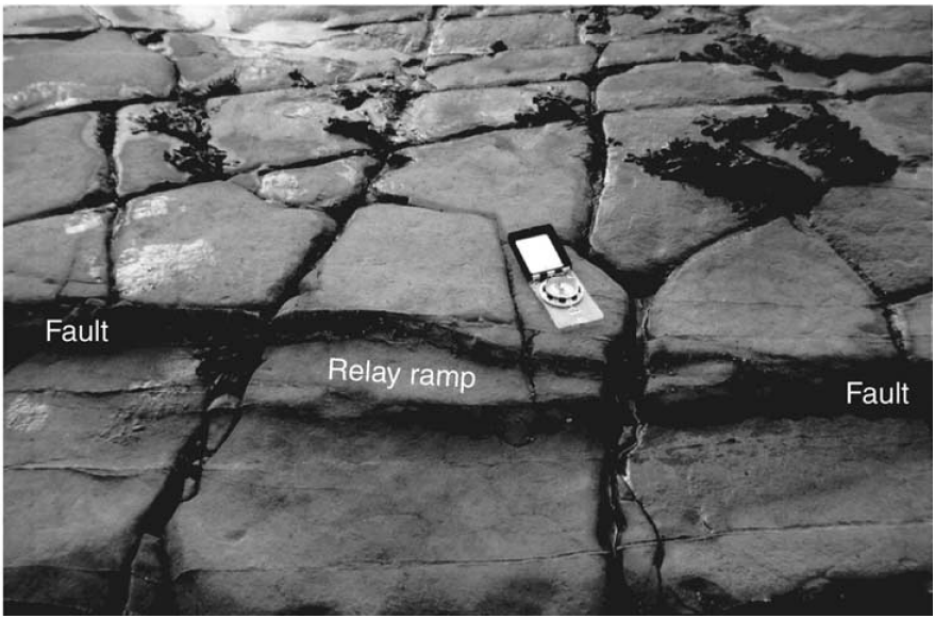

Fig. 2.13b - A relay ramp in the field (Peacock, 2001).

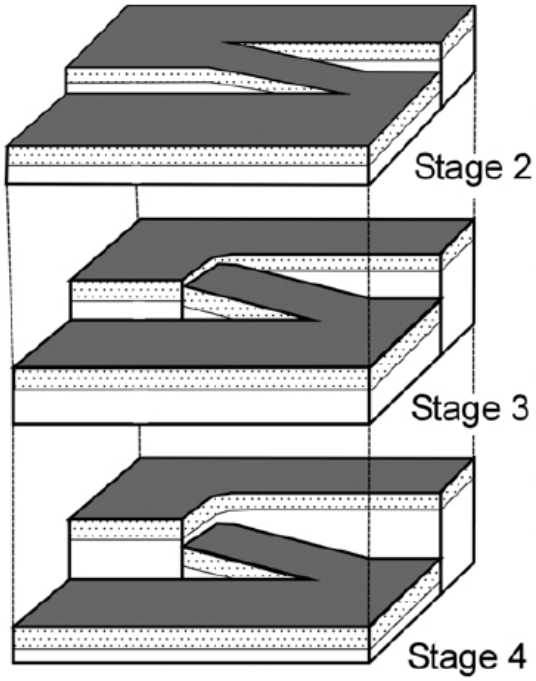

Fig. 2.14 - Schematic block diagram showing the stages of relay ramp growth and breaching inferred from geometric analysis of outcrop-scale (adapted from Peacock and Sanderson, 1994). Stage 1, which is when the fault segments are isolated and non-interacting, is not always required (Walsh et al., 2003) and is not shown here; Stage 2 is when the fault segments interact and a relay ramp develops; Stage 3 is when a breaching fault propagates across the base or, as shown here, the top of the relay ramp; Stage 4 is when the fault segments are fully hard-linked. Peacock and Sanderson (1994) have pointed out that different levels within the same relay zone may have different displacements and hence be at different stages of development (Imber et al., 2004).

2.2.5 Transfer faults

Transfer faults are cross-faults that accommodate differences in strain or structural styles along the strike of the extensional system (e.g., Bosworth, 1985; Lister et al., 1986; Chorowicz, 1989; Salah and Alsharhan, 1996; Hus, 2004). They have a rather small horizontal dimension of up to 50 km, less than the thickness of the continental lithosphere. Because of that, they have to be considered as upper crustal features with no deep ductile continuation. Further more, they do not extend beyond the rift system and they trend parallel to ancient faults, selectively reactivating some of the older faults (Chorowicz, 1989).

Rift transfer faults are portrayed in the literature as pure strike-slip faults, when parallel to the extension direction, or as oblique-slip faults, with variable amount of dip displacement, when oblique to the extension direction (Gibbs, 1984; Lister et al., 1986; Destro et al., 2002). Transfer faults usually connect major normal faults with similar or opposite polarities and their sense of slip is contrary to the apparent offset of the related normal faults (Gibbs, 1984).

2.3. Faults, tectonic stress and paleostress analysis

Paleostress is a term compounded from the terms *paleo* that means before present and *stress* that means force acting on a given surface area. It hence refers to the study of forces that acted on a given volume of rock in the past.

The key task in tectonic stress field analysis of geological fault-slip data and earthquake focal-mechanism data entails reconstruction of a reduced stress tensor which best models the state of stress of the given volume of rock sampled at outcrop scale for fault-slip data or regional scale for focal mechanisms (Angelier, 1989; Angelier, 1994; Delvaux and Sperner, 2003).

The complete stress tensor has six independent variables: the orientation of the three orthogonal principal axes and the magnitude of the principal stresses σ_1, σ_2 and σ_3, where $\sigma_1 \geq \sigma_2 \geq \sigma_3$, as can be represented in a stress ellipsoid (Fig. 2.15). The last three variables can also be expressed in terms of the ratio of the principal stress differences $R = \sigma_2 - \sigma_3 / \sigma_1 - \sigma_3$, ratio of extreme principal stresses σ_3/σ_1 and isotropic stress σ_i. The ratio R ("stress ratio") expresses the magnitude of σ_2 relative to the magnitudes of σ_1 and σ_3. Using geological fault-slip data alone, only the first four variables of the stress tensor (σ_1, σ_2, σ_3 and R) can be obtained as the modeled shear direction on a plane under a given state depends only on these four parameters (the "reduced stress tensor"). The extreme principal stress ratio σ_3/σ_1 can be constrained only using the rupture and friction laws, given that the physical properties of the fractured rock are known.

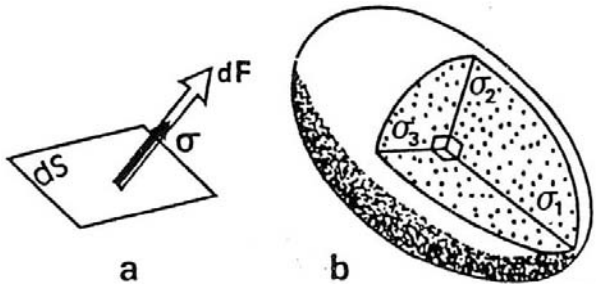

Fig. 2.15 - (a) Stress vector, (b) Stress ellipsoid. Surface element dS, force dF and stress vector σ ($\sigma = dF/dS$). Principal axes of the stress ellipsoid shown as σ_1, σ_2 and σ_3 ($\sigma_1 > \sigma_2 > \sigma_3$): σ_1 is the maximum compressional stress, σ_2 the intermediate stress and σ_3 the minimum stress (Angelier, 1989).

The basis of the stress inversion lies in the principle that, knowing the stress state acting on a rock mass (the 4 parameters of the reduced stress tensor) and given their orientation, one can determine the shear stress and hence the expected slip orientation on any plane (Wallace, 1951; Bott, 1959; Angelier, 1989). Inversely, knowing the orientation of a variety of fault planes of different orientations in a rock mass and the orientation and sense of movement associated with slip lines contained in these planes, is it theoretically possible to model the state of stress that (re)activated these faults by the four parameters of the reduced stress tensor. This presupposes that slip on a plane occurs on the direction of resolved shear stress on the plane and that this direction can be approximated by the orientation and slip sense of the slip lines that are commonly observed on the fault planes.

2.3.1 The relationship between normal stress and shear stress

The relationship between normal stress σ and shear stress τ can be well illustrated by the Mohr circle (e.g., Ragan, 1973; Fig. 2.16). It has been observed that the amount of shear and normal stresses necessary to move an intact rock is higher than that needed to move a similar rock that is having pre-existing weakness zones oriented in various directions, (e.g., Angelier, 1994). The frictional strength of existing faults is less than the stress necessary to form new ones. Once formed, faults constitute planes of weakness that may be reactivated in stress fields that are optimally oriented.

For renewed sliding, as in the case of fault reactivation, sliding will take place when the ratio of shear stress to normal stress on the plane is equal to the coefficient of friction:

$$\tau/\sigma = \tan \phi \qquad \text{or} \qquad \tau = \sigma \tan \phi$$

where ϕ is the angle of internal friction.

Thus the first possibility of renewed faulting occurs when the circle in the Mohr diagram is tangent to the evelope (Ragan, 1973). This can only occur on a plane whose normal measured from the σ_1 direction (Fig. 2.16a-iii) is given by

$$2\theta = 90 + \phi \qquad \text{or} \qquad \theta = 45 + \phi/2.$$

For a plane that is oriented differently, a further increase in shear stress is required to produce sliding (Ragan, 1973; Angelier, 1994; Fig. 2.16a-iv,v).

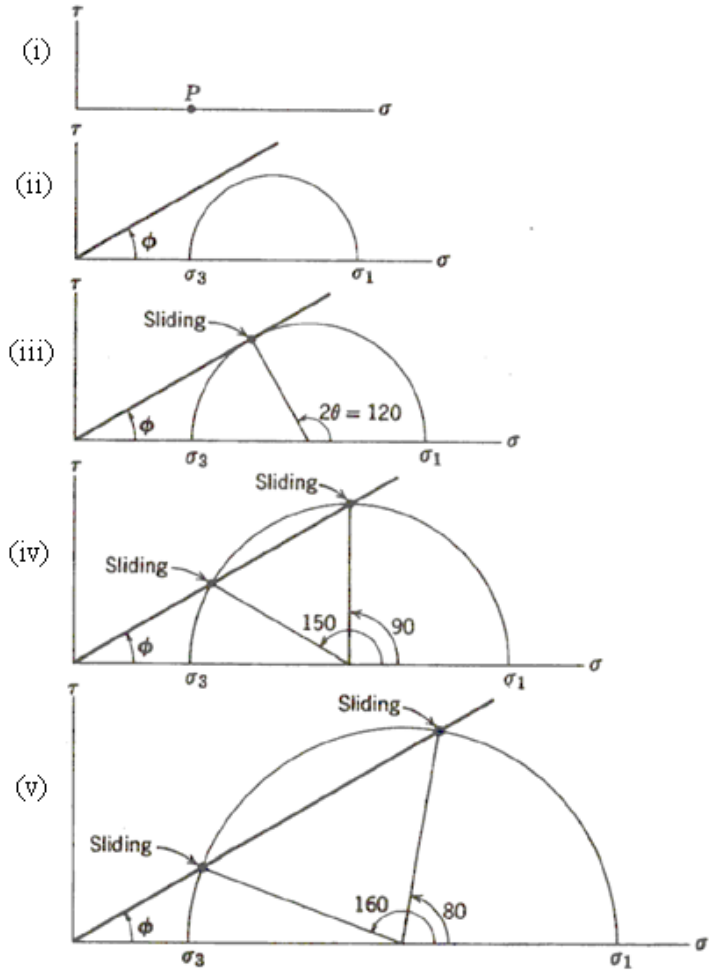

Fig. 2.16a - Conditions required for renewed sliding on variously oriented planes of no cohesion, assuming an angle of friction $\phi = 30°$ (Ragan, 1973).

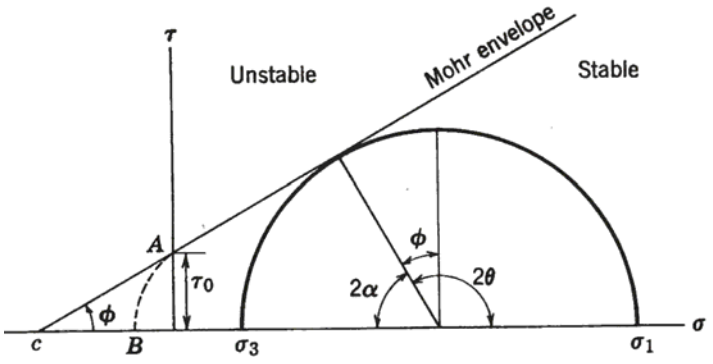

Fig. 2.16b - The Mohr envelope representing the Coulomb criterion failure. Mohr's circle illustrates the stresses of failure (Ragan, 1973).

However, with newly formed faults, the situation is different since an added component τ_0 is put into consideration. This is a shear strength or cohesive strength. Thus, as per Coulomb criteria, the shear stress which tends to cause failure is restricted in two ways: (1) by the normal stress across the potential shear plane, and (2) by the cohesive shear strength of the material, expressed as

$$\tau = \tau_0 + \sigma \tan \phi \qquad \text{or} \qquad \tau = \tau_0 + \mu \sigma$$

At zero normal stress, ϕ is, by analogy with sliding friction, the angle of internal friction, and μ is the coefficient of internal friction (Ragan, 1973). According to Ragan (1973), the cohesive strength of sedimentary and crystalline rocks is respectively 100-200 bars and 500 bars and the average frictional angle is ~ 30°. Presentation of the Coulomb criteria is as in Fig. 2.16b, where the Mohr diagram that obeys the Coulomb criteria has its boundary separating stable and unstable stress conditions not passing through the origin.

In most situations, faults related to a given tectonic event occur in rocks which are much older than the faults and have undergone earlier brittle deformation, so that numerous pre-existing planes of weakness were reactivated as faults during the event under consideration (Angelier, 1994).

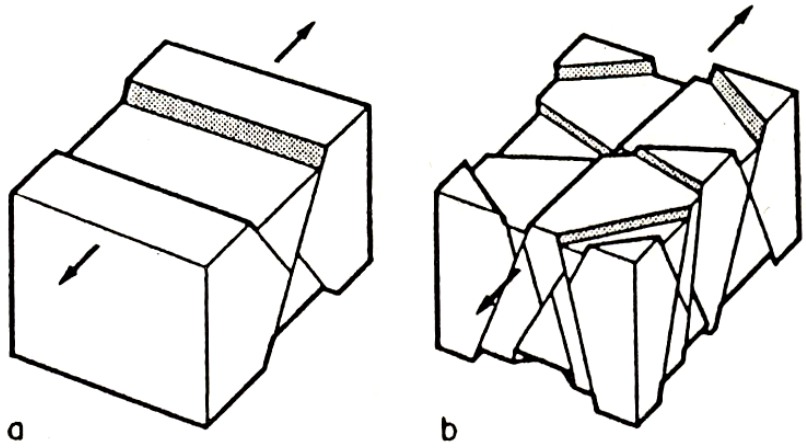

Fig. 2.17 - (a) Newly formed faults (b) Inherited faults.
Arrows indicate direction of extension (Angelier, 1994).

Planes of weakness may be present in rocks even when there has not been brittle tectonic deformation. This is typically the case for cooling joints in plutons, and bedding joints. Neo-formed fault systems are geometrically simple (Fig. 2.17a) so that determination of principal paleostress axes is easy. Inherited faults, on the contrary, have various attitudes (Fig. 2.17 b) and determination of the orientation of stress axes may be difficult.

2.3.2 Tectonic stress regime

The tectonic regime is expressed by the "stress regime index" (R'), defined from a combination of the stress ratio (R), and the nature of the most vertical stress axis

(Delvaux et al., 1997; Delvaux and Sperner, 2003). From the most extensional (radial extension) to the most compressional (constriction) stress regime, R ranges from 0 to 1 for normal faulting regimes (σ_1 sub-vertical), from 1 to 0 for strike-slip regimes (σ_2 sub-vertical) and again from 0 to 1 for thrust faulting regimes (σ_3 sub-vertical). R' is defined in order to express a continuous scale from 0 (radial extension) to 3 (constriction):

R' = R for normal faulting regime,
R' = 2 - R for strike-slip regimes, and
R' = 2 + R for thrust faulting regimes.

In its simplest form, the relationship between stress ratio and stress regime index can be illustrated as in Fig. 2.18. The use of sub-vertical axes as reference is based on the assumption that one of the principal stress axes should be close to the vertical as no shear stress can exist on the Earth's free surface on a regional scale and in normal conditions (Angelier, 1994).

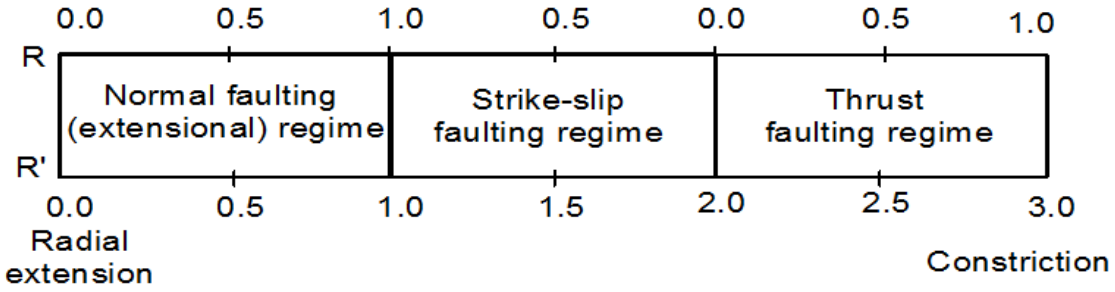

Fig. 2.18 - The relationships between stress ratio R, stress regime index R' and the resulting stress regimes.

Stress permutations involve the variation over time of one or more of the principal stress axes, as illustrated in Fig. 2.19. Stress permutations (variations) at local and regional scale are possible at any given place (e.g., Angelier and Bergerat, 1983). For example, where extensional faulting (normal faulting) occurs, stress permutation can result in perpendicular systems of conjugate normal faults (σ_2/σ_3 permutation, Fig. 2.19A) or in mixed conjugate sets of normal and strike-slip faults (σ_1/σ_2 permutation, Fig. 2.19B). Permutation of σ_1/σ_2 from strike-slip to normal fault extension is also possible (Fig. 2.19C).

2.3.3 Age constraints of stress tensors

The relative age of a stress tensor is estimated from crosscutting relationships of striations and fault planes. Also, age can be indirectly inferred from faulting depth as can be estimated by mineralization on the fault plane and its consolidation state. Epidote-chlorite minerals can be indicators for deep brittle faulting. Haematite can be formed at shallower levels. Consolidated breccia and fault gauges on the fault surface are used as indicators

for older faulting, while non-consolidated breccia and gauge indicate very superficial faulting (Eldeen et al., 2002).

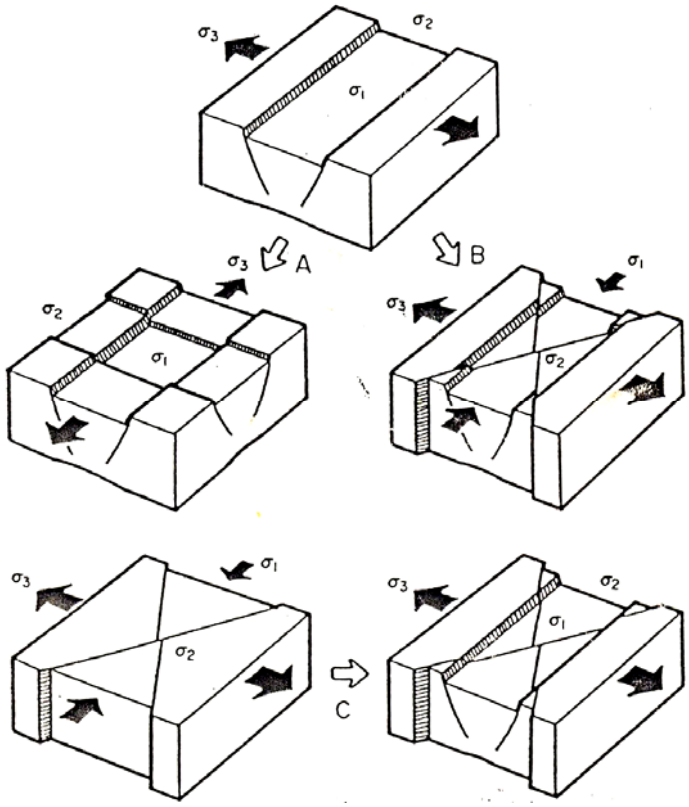

Fig. 2.19 - Permutations between stress axes and rift opening. (A) σ_2/σ_3 permutation (perpendicular extension). (B) σ_1/σ_2 permutation (from normal fault extension to strike-slip regime). (C) σ_1/σ_2 permutation (from strike-slip regime to normal fault extension regime). (Angelier, 1994; Hu and Angelier, 2004).

2.3.4 Fault-slip data and sense of shear

Fault planes with slip lines (slickensides) with their sense of shear are the best type of data that can be used in stress inversion. They can be neo-formed or reactivated. Neo-formed faults constrain the orientation of the stress axes and, the stress ratio R better than reactivated faults. The sense of shear along the fault plane is constrained using variety of asymmetric features encountered on the fault plane. They can be among others, accretion mineral steps, Riedel shears, conjugate shear structures, lunate fractures and pressure shadows against small asperities, (e.g., Petit, 1987; Angelier, 1989).

2.3.5 Criteria for identifying sense of slip

The criteria used to identify sense of slip are called “positive” or “negative” (Angelier, 1979a; 1989; 1994); positive when a hand motion over the fault surface in the direction of

the presumed movement of the absent block is easy, and negative when the resistance against this hand motion is greater (Fig. 2.20, part 1-8):

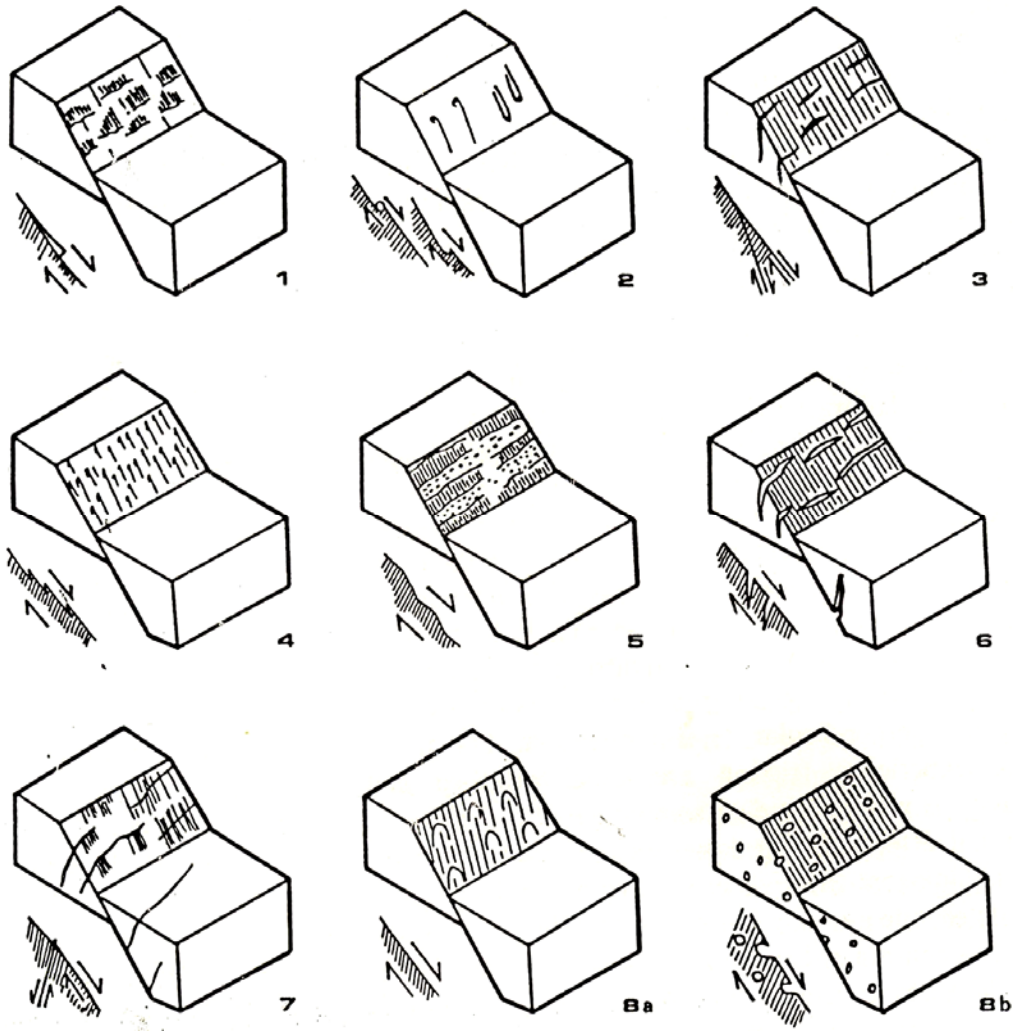

Fig. 2.20 - Criteria for determining the sense of motion on a fault surface. The examples shown are dip slip normal faults, but the criteria are valid regardless of fault slip orientation. Numbers between parentheses refer to description in the text. (1) Mineral steps. (2) Tectonic tool marks. (3) Riedel shears. (4) Stylolitic peakes. (5) Alternating polished (or crushed, and/or striated) and rough facets. (6) Tension gashes. (7) Conjugate shear fractures. (8) Miscellaneous criteria: (a) parabolic marks, and (b) deformed bubbles in lava (After Angelier, 1979a; 1989; 1994).

(1) Accretionary mineral steps: They develop due to crystal (e.g., calcite or quartz or gypsum) growth fibres or other grains being crystallized during fault slip. Fibrous minerals (e.g., asbestos in sheared serpentinites) developing along slickenside lineations form steps that indicate the sense of motion in the same way. This criterion is positive and 100 % reliable.
(2) Tectonic tool markers (pebbles and other clasts): The tool can be a small quartz grain or a larger boulder, and be present or absent at the distal end of the tool mark. When the tool is not destroyed, this criterion (a negative one) is reliable.

(3) Riedel shears: Commonly intersect fault surfaces. These structures form an angle of 5-25° with the fault plane. Their sense of motion is the same as that on the main plane. This criterion is negative.
(4) Stylolitic peaks (lineations): They are produced by solution phenomena on frictional facets. Facets tend to open during fault motion. This criterion (a negative one), like accretionary mineral steps, has 100 % reliability.
(5) Polished and rough facets: Polished facets experience friction during fault motion while rough facets tend to open. The criterion is useful in non-calcitic rocks especially where pressure-solution phenomena cannot occur so that criteria (1) or (4) are absent. It is 80 % reliable.
(6) Tension gashes: Tension gashes intersect with a fault surface approximately perpendicular to the slickenside lineation making acute angle of 30-50° with the surface so that the corresponding crest has "negative" polarity, as with Riedel shears. This criterion is 70 % reliable.
(7) Conjugate shear fractures or small faults at an angle of 40-70° to the main fault form a "negative" criterion which is 70 % reliable. As with Riedel shears and tension gashes, the intersection of such features on the main fault plane is approximately perpendicular to the slickenside lineation.
(8) Other criteria: These include for instance shear lenses or a rotated block along a fault plane. It also includes parabolic marks that are commonly found on polished faults, which define a "positive" criterion despite the sense of relief. Others are deformed bubbles in lavas that are strained close to the fault surface and thus indicate the sense of motion, as a "positive" criterion, etc.

In the field, the quality of slip sense determination is evaluated as "certain", "probable", "supposed" or "unknown".

Joints and fractures are also used in paleostress reconstruction as kinematic indicators, taking into account their mechanical significance (e.g., Dunne and Hancock, 1994, Delvaux and Sperner, 2003). Dunne and Hancock (1994) show that in stable areas such as platform covers over cratonic areas, where uniformly oriented sets of structures are related to remote (far-field) stresses, small-scale brittle microstructures such as joints prove to be valuable stress indicators. Similarly, as for faults, the type of joint (tension, shear or unknown) is defined and the quality of determination evaluated as "certain", "probable" or "supposed".

2.3.6 Fracture(s)

Fractures are cracks across which the cohesion of the material is lost, and may be regarded as planes or surfaces of discontinuity (Park, 1997). According to Blés and Feuga (1986), a fracture is a discontinuity of mechanical and tectonic origin, within the upper and middle crustal levels. The term therefore includes joints, tension fractures, stylolites, and faults of various sizes. A fracture is the most common geologic feature to encounter in the field.

2.3.7 Joint(s)

The term "joint" has been used since the 18th century (Hancock, 1985; Dunne and Hancock, 1994) in order to express the idea that the parts of a rock mass are joined together across fractures and that joint could as well be called a crack (Dunne and Hancock, 1994). Joints are the most commonly developed brittle structures (McClay, 1987) and can be defined as discontinuities whose sides are contiguous and show no relative movement between the two portions (Blés and Feuga, 1986) at the field scale (Hancock, 1985). So, when there is no displacement, or where the displacement is too small to be easily visible, the fracture (crack) is called a joint (Hancock, 1985; Park, 1997). According to Blés and Feuga (1986), the word joint is used for discontinuities perpendicular or at an angle to the stratification or schistosity.

However, others consider a joint to be a fracture with field evidence for dominantly opening displacements, thus a joint is an extension fracture (Pollard and Aydin, 1988). Dunne and Hancock (1994) argue that both definitions have their shortcomings. Since classifying a fracture as a joint in the field means that with additional evidence(s) for instance from thin sections, it might be renamed a fault (shear fracture), vein or solution seam. Conversely, deciding the origin of a structure in order to describe it is an unsound practice and they therefore propose the use of the term joint to be restricted for use in the field.

The thickness of a joint is in principle zero when it is formed, but as a result of movements subsequent to its formation it can open up by a few millimeters and can then be lined with quartz or calcite. The spacing between joints generally is in the order of a decimeter to a meter (Blés and Feuga 1986). Joints may occur in sets, parallel and regularly spaced, or they can be much less regular and much less systematic (Park, 1997). Where a recognizable joint set exists, it can usually be related in some way to both regional tectonic control and to the geometry of the rock body containing the joints (Dunne and Hancock, 1994; Park, 1997).

Genetically, joints can fall into at least four categories (Dunne and Hancock, 1994):

(1) "tectonic joints" that form deep in the Earth's crust due to combined action of abnormally high pore-fluid pressures generated during the tectonic compaction of sediments and stresses of tectonic origin. The joints are subsequently exposed at the surface by uplift and denudation of the rocks that carry the joints.
(2) "hydraulic joints" also form at depth before uplift and as a consequence of the influence of high fluid pressure, but the cause of the high fluid pressures is sedimentary compaction.
(3) "unloading joints" are formed close to the Earth's surface and after uplift. The attitudes of unloading joints are controlled by the orientation of either tectonic or residual stresses at the time of their formation.
(4) "release joints" are formed after uplift but their orientations and locations are determined by pre-existing structures such as cleavage planes (Dunne and Hancock, 1994; also Park, 1997). Many joints are due to the release of stored pressure (Park, 1997).

Geometrically, several basic types of joints are proposed by McClay (1987):
(1) "dilational joints" are extensional joints with the fracture plane normal to the least principal stress σ_3 during joint formation (Fig. 2.21a).
(2) "shear joints" are often conjugate, enclosing angles of 60° or more (Fig. 2.21b). The joint planes may show small amounts of shear displacements.
(3) "hybrid joints" (combined shear and extension joints) show components of both extension and shear displacement (Fig. 2.21c).

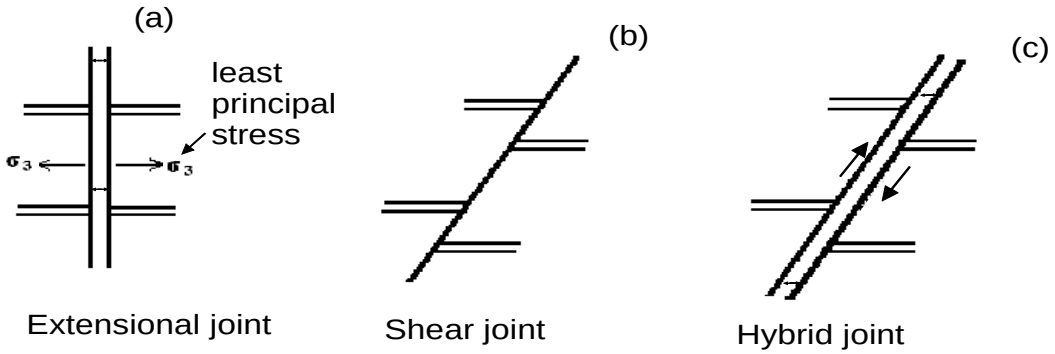

Fig. 2.21 - Joint types: (a) dilational (extensional) joints, (b) shear joints and (c) hybrid joints (McClay, 1987).

According to Blés and Feuga (1986), joints often seem to be related to deformation, such as folds or "large faults" (i.e., faults whose dimensions are sufficient to cut the entire seismogenic layer; the part of the crust that responds to stress by brittle failure (Roberts and Yielding, 1994)). If the number of joints increases towards a fault, and especially if one of these joint sets has the same orientation as the fault, it is reasonable to assume that these discontinuities replicate the fault and that they were caused by the same tectonic forces. Again, even in such a case one cannot be certain that one or more joint sets did not exist before the fault because a large fault can develop along pre-existing planes of discontinuity (Hancock, 1985; Angelier, 1989; Dunne and Hancock, 1994).

Planar or approximately planar joints belong to a regularly oriented set(s) and are called systematic joints. They reflect deep-seated tectonic or non-tectonic activities (Dunne and Hancock, 1994). When such joints can be traced over tens or even hundreds of meters, they are termed master joints. Joints that are an order of magnitude smaller but still well-defined are called major joints (McClay, 1987). Conversely, non-systematic joints characterized by irregular surfaces are superficial in origin (Dunne and Hancock, 1994).

The way in which joints are related in the field can be of use in relative age determination of the joints (Hancock, 1985; Dunne and Hancock, 1994). For instance, as illustrated by Fig. 2.22:
(a) when a joint is offset across a fault, vein or stylolite, the joint is the older structure (e.g., McClay, 1987; Dunne and Hancock, 1994);
(b) when a joint segment abuts another joint, then the trace of the joint segment that abuts the other is the younger;

(c) when the short traces of small sealed joints terminating in intact rock are cut by the longer trace of a large joint, the shorted joints are the older joints (Dunne and Hancock, 1994).

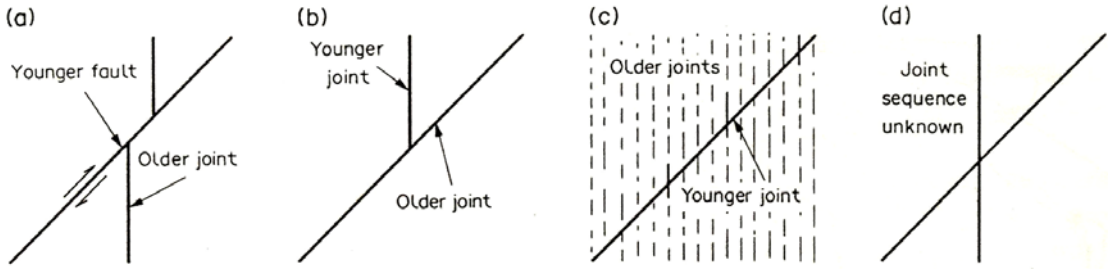

Fig. 22 - (a) An older joint trace offset by younger fault. (b) A younger joint trace abutting an older joint trace. (c) Short traces of older sealed joints cut by the long trace of younger joints. (d) Crossing traces of joints, the order of formation of which is not determinable (After Dunne and Hancock, 1994)

2.3.8 Slip data separation

In order to separate the slip data into different sets, other important observations can be made in the field:
(a) type and degree of mineralization or material found on the fault planes,
(b) the presence or absence of fault gauges,
(c) cross-cutting relationships.
The significance of the stress tensors determined on these sets are interpreted in terms of tectonic stages and assigned preliminary relative age estimation.

2.4. Earthquakes

2.4.1 Types of earthquakes

There are two types of earthquakes based on their genesis: natural and artificial earthquakes. Natural earthquakes are those earthquakes that occur in response to natural processes, such as plate tectonics, and terrestrial impacts, such as meteorites. Artifical earthquakes are caused by human activities such as blasting, moving trucks, etc. Artifitial earthquakes are not discussed here.

Earthquakes caused by plate tectonics can be classified into two main types: tectonic and volcanic (or magma-related). However, an intermediate classification exists as shall be briefly discussed below.

Magma intrusion in an area causes earthquakes. Magma-induced seismicity commonly exhibits spatial migration, focal mechanisms, and wave-form characteristics that differ

from those of non-volcanic sources. Volcanic earthquakes (B-type) usually originate in and adjacent to active craters at extremely shallow depths. They are typically of low to moderate magnitudes, low frequency (1 to 5 Hz), commonly occur without a main shock, and sometimes have non-double-couple moment tensors (Minakami, 1974). The earthquake motions consist mainly of vibrations with periods in the range of 0.2 to 1.0 s.

Tectonic earthquakes differ from volcanic earthquakes in that they are characterized by high frequency, and they include a discrete "main shock" - "aftershock" sequence, and have double-couple focal mechanisms.

A third type of earthquakes is called volcano-tectonic earthquakes. They are characterized by a frequency of 5 to 15 Hz. Volcano-tectonic earthquakes are the most common type of earthquakes.

2.4.2 Faulting and earthquakes

As a rock is compressed, it deforms initially in an elastic way but when the shear stress reaches about half the shear strength of a given rock, it starts to deform permanently due to opening and propagation of small cracks in the zone of greatest strain within which the fault movement eventually occurs (Park, 1997). According to Park (1997), the intensity of micro-fracturing increases as the shear strength is approached. The rate of propagation of the microfractures is the critical factor in determining the strain rate and hence the time taken for fracturing (and the resulting earthquake) to occur. Experiments show that large and potentially destructive earthquakes can be prevented by generating artificial smaller fractures and by pumping water into them, and hereby releasing the stress more safely (Keller and Pinter, 2002).

2.4.3 Scales of magnitude of earthquakes

Earthquake magnitudes are currently reported as "moment magnitudes" (M_w),

$$M_w = \log(M_0/1.5)-10.73$$

where M_0 is the seismic moment given by the equation

$$M_0 = \mu\ d\ a$$

where μ is the rigidity of a rock mass, i.e. the shear modulus of the crustal material involved in the rupture. It is taken as 3×10^{11} dyn/cm^2 (30 GPa) for the crust and 7×10^{11} dyn/cm^2 (70 GPa) for the upper mantle. The symbols d and a stand for average displacement and rupture area, respectively. The seismic moment is expressed either in dyn.cm (cgs) or in N.m (SI). The moment magnitude scale is related to the physical properties of the source. This scale does not saturate with large earthquakes (Shearer, 1999).

Other earthquake magnitude scales saturate as earthquake magnitude increases. These scales are the "local magnitude" (M_L) scale, the "body-wave magnitude" (m_b) scale and the "surface-wave magnitude" (Ms) scale. The "local magnitude" (M_L) scale was developed by Charles Richter in 1930; it is the so-called Richter scale (Bullen and Bolt, 1985; McCalpin, 1996; Shearer, 1999). It employs the amplitude of the earthquake-generated S-waves (Shearer, 1999), which means that the scale is a function of amplitude and distance. Mathematically, it is expressed as

$$M_L = \log A(\Delta) - \log A0(\Delta),$$

where A0 is the pre-defined maximum displacement for a zero-magnitude earthquake at distance Δ (depending on the region). Earthquake events below about $M_L = 3.0$ are generally not felt and saturation begins to occur at about $M_L = 5.5$.

The "body-wave magnitude" (m_b) scale is a more general magnitude scale that is used for global seismology. It is expressed as

$$m_b = \log_{10}(A/T) + Q(h,\Delta)$$

where T is the dominant period of the measured waves and Q is an empirical function of distance (Δ) and event depth (h). The measurement is normally made on the first few cycles of the P-wave arrival on short-period vertical component instruments, for which the dominant wave period is usually about 1 s.

The "surface-wave magnitude" (Ms) scale is used globally (Shearer, 1999). It is expressed as

$$Ms = \log_{10}(A/T) + 1.66 \log_{10}(\Delta) + 33.$$

2.4.4 Focal mechanisms

The most commonly used stress indicators employed to image the present tectonic stress in the world (e.g., on the World Stress Map) are the earthquake focal mechanisms (Zoback, 1992; Sperner et al., 2003). In order to conserve angular momentum earthquake sources must (usually) consist, in effect, of two opposing couples, i.e. the double couple, comprising the stress couple (Fig. 2.23) and the reaction of the surrounding material to it (Doyle, 1995). Seismograms, which record arrival times and amplitudes of earthquake-generated waves, can also be used to infer the type and direction of fault motions (Fig. 2.23). The type and direction of fault motions is called focal mechanism or direction of motion study (Herrmann, 1975; Das et al., 1986).

If the ground moves up during the first motion (which should be up on the seismogram record), the first P-wave arrival is one of compression, pushing away from the focus. This is because rays always propagate down into the earth and reflect back up to the recording station. If the first motion is downward, then first P-wave arrival is one of rarefaction (or

dilatation), pulling back towards the focus. Thus, the rays for each station are traced back to the source, and polarity is plotted at the intersection of these rays with a sphere around the source (Doyle, 1995). Focal plane studies show the direction of movement of plate boundaries and have been very important in confirming plate tectonic models (Das et al., 1986; Doyle, 1995).

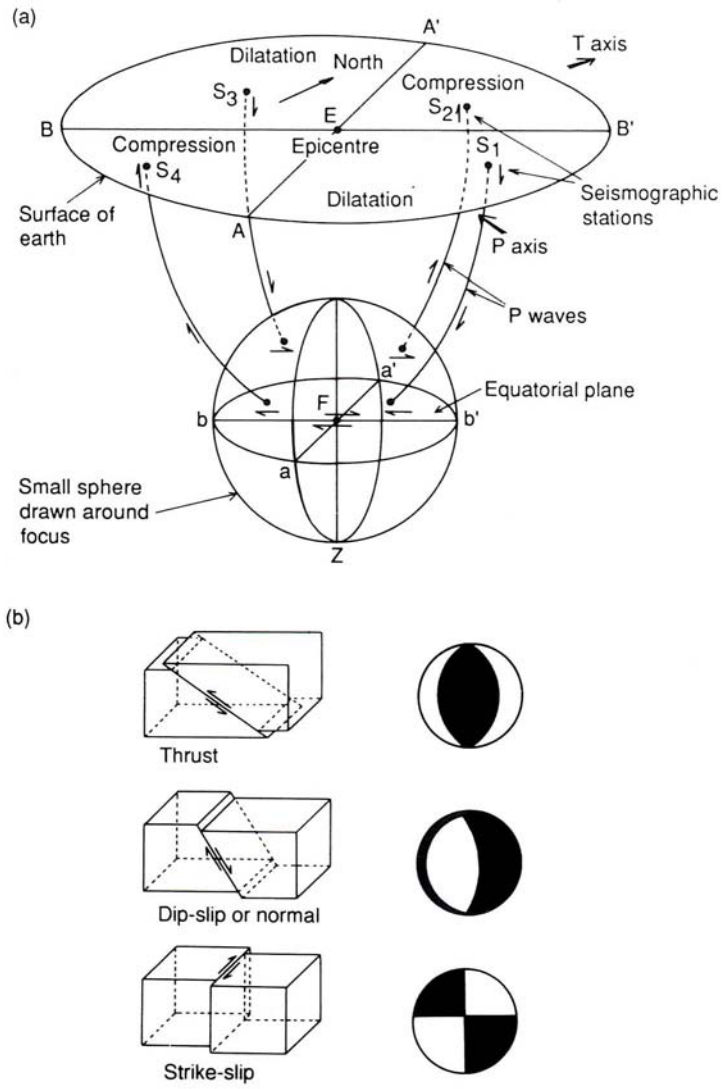

Fig.2.23 - (a) The patterns of first motion recorded at stations around the epicentre, plotted on the sphere around the focus F by projection. (b) The three main types of focal mechanisms (thrust, normal and strike-slip) and their projections on the lower hemisphere (black for compression). (Doyle, 1995).

The double-couple mechanism is represented by two perpendicular planes: i.e., an auxiliary plane and a virtual (real) plane. Both planes are called *nodal planes* by seismologists (Angelier, 1989). This means that there are always two possible fault-plane solutions for every single earthquake focal mechanism. The choice of a fault-plane solution for an earthquake might have significant consequences in terms of stress relationship. Addtional data (e.g., aftershock distribution, observed ground deformation,

trend of known faults,...) may help determining the actual fault plane. This problem does not exist for field geologists, because they can tell (based on fault-slip data on given faults) which fault moved, and they can choose the right plane between the two nodal planes (Angelier, 1989).

For the focal mechanisms in the World Stress Map, the kinematic p-axes, b-axes and t-axes are used to infer the orientations of the horizontal principal stress axes, S_{Hmax} and S_{hmin} (Zoback, 1992). Strictly speaking, the kinematic p-, b- and t-axes represent strain axes, and not stress directions. However, statistically, by averaging a great number of data (e.g., focal-mechanism data, that can represent 2/3 of the data in the World Stress Map), the stress trajectories are considered to be accurately determined by the kinematic axes.

2.4.5 Slip-tendency analysis

The potential activity of given active faults can be estimated using the principle of slip-tendency (Ts) analysis, which allows a quick assessment of the stress state on given faults (Morris et al., 1996). The likelihood that slip will occur on a given surface under a given stress field depends on its frictional characteristics and the ratio of shear to normal stress acting on this surface. Slip will occur if the resolved shear stress exceeds the frictional resistance to sliding, which is proportional to the normal stress acting across that surface. In other words, slip will be favored on faults whose orientations are in such a way that they have the highest shear stress τ and the lowest normal stress σ_n. The magnitude of these resolved stresses depends solely on the stress field and the orientation of the faulted surface. The slip tendency (τ/σ_n) is proportional to the estimated reactivation likelihood. The slip-tendency analysis considers implicitly that new fault movements are reactivating existing planes of weakness and are not newly formed faults.

2.4.6 Hot springs

Hot springs can be good indicators of active tectonics particularly when they appear to assume a particular trend, usually a linear one along fault zones (e.g., Walker, 1967; Minissale, 1991; Macheyeki et al., 2008a; 2008b). They reveal the lines or zones of weakness through which thermal water of meteoric and juvenile origin rapidly reaches the surface along active fault systems (Minissale, 1991).

2.5. Paleoseismology

Paleoseismology is the study of occurrence, size, timing and frequency of pre-historical (ancient) earthquakes of which no instrumental seismic records exist (Keller and Pinter, 2002; Michetti et al., 2005). The lower boundary of the time window usually encompassed by paleoseismology studies is Holocene, but records of individual

earthquakes may extend well back into the Late Pleistocene in regions of long recurrence (e.g., Crone et al., 1992) or unusually well-preserved evidence (e.g., Ota et al., 1992). Therefore, paleoseismology involves the geologic study of the past behavior of active faults (McCalpin, 1996).

Paleoseismology relies on two main types of geologic evidence of earthquake activity; geomorphological evidence and stratigraphic evidence (McCalpin, 1996; Keller and Pinter, 2002; Piccardi, 2005). Each earthquake source creates a signature on the geology and the geomorphology of an area that is unambiguously related to the order of magnitude of its earthquake potential (Burbank and Anderson, 2001; Michetti et al., 2005).

2.5.1 Geomorphologic evidence in extensional environment (normal faults)

Fault scarps are the primary geomorphologic indicator of paleoearthquakes in situations involving normal faults (McCalpin, 1996). A fault scarp is the direct manifestation of surface-rupturing earthquakes (Keller and Pinter, 2002). Both normal and reverse faulting can create a fault scarp, the initial angle of which will reflect the dip of the fault plane. Also strike-slip faulting may create a fault scarp. With time, a normal fault scarp degrades and forms a suite of geomorphologic components, such as a scarp crest, free face, debris slope, wash slope and scarp toe (Fig. 2.24; Table 2.3).

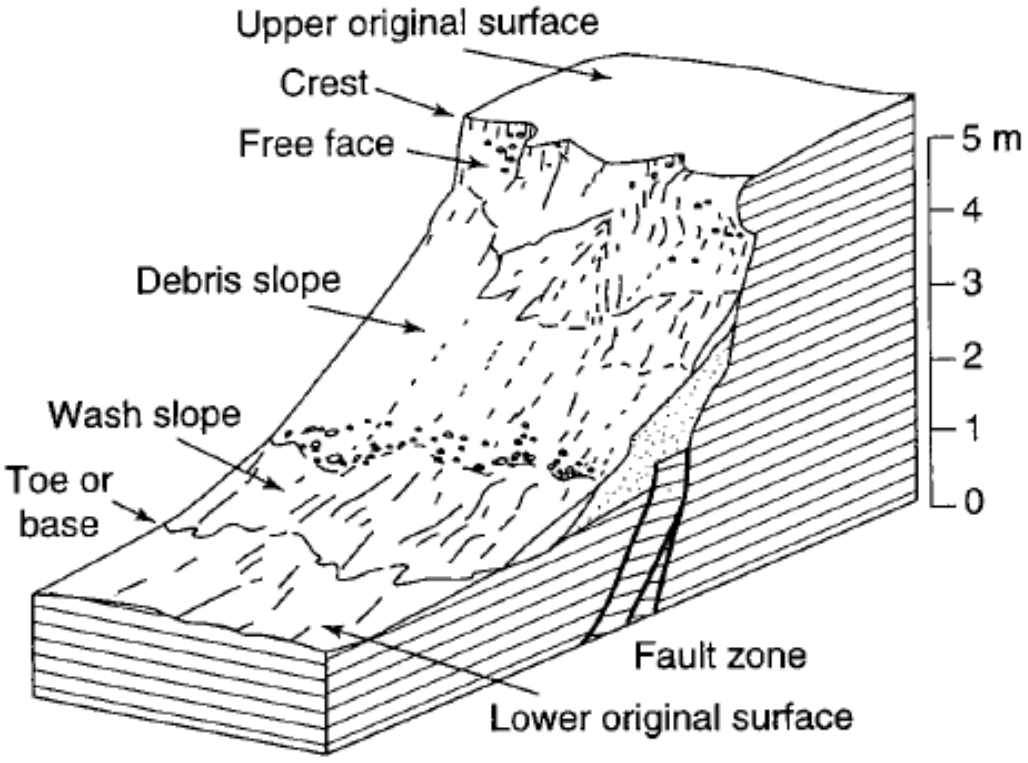

Fig. 2.24 - Basic slope elements that may be present on a simple scarp (Wallace, 1970).

Table 2.3 - Geomorphic components or fault scarp-slope morphology for simple scarps (Wallace, 1977)

Slope element	Morphology	Process (formation and/or modification)	Comments and general chronology
Crest	Top of fault scarp (break in slope) initially sharp becomes rounded with time	Produced by faulting; modified by weathering, mass wasting	Becomes rounded after free face disappears
Free face	Straight segment; initially 45° vertical to overhanging	Produced by faulting; modified by weathering, gullying, mass wasting; eventually buried from below by accumulation of debris	Dominant element for 100 years or so
Debris slope	Straight segment; angle of repose of material usually 30° to 35°	Accumulation of material that has fallen down from the free face	Is dominant element after about 100 years
Wash slope	Straight to gently concave segment; overlaps the debris slope; slope angle generally 3° to 15°	Erosion and deposition by water; deposition of wedge or fan of alluvium near toe of slope; some gullying	Is developed by 100 years, significant by 1000 years
Toe	Base of fault scarp (break is slope); may be initially sharp, but with time may become indeterminate as grades into original slope	Erosion and deposition by water; owing to change in process/form from up slope element (free face, debris slope or wash slope) to original surface below the fault scarp slope	More prominent in young fault scarps or where wash slope is not present

2.5.2 Stratigraphic evidence

The study of stratigraphic evidence of paleoearthquakes is one type of event stratigraphy. Stratigraphic evidence of paleoseismicity includes displaced strata, colluvial wedges, sand boils and fissures, displaced strata being the clearest indicator of paleoearthquakes (e.g., Bolt, 1993; McCalpin, 1996; Keller and Pinter, 2002) and colluvial wedges being the most common one. They are discussed in detail in the following sections.

2.5.2.1 Displaced strata and seismites

Displaced strata form one of the clearest types of evidence of past earthquakes (Bolt, 1993; McCalpin, 1996; Keller and Pinter, 2002). When a large earthquake occurs, some strata are displaced due to faulting associated with that earthquake. The displacement of these strata can provide information about the history of tectonic activity in a given area (Fig. 2.25).

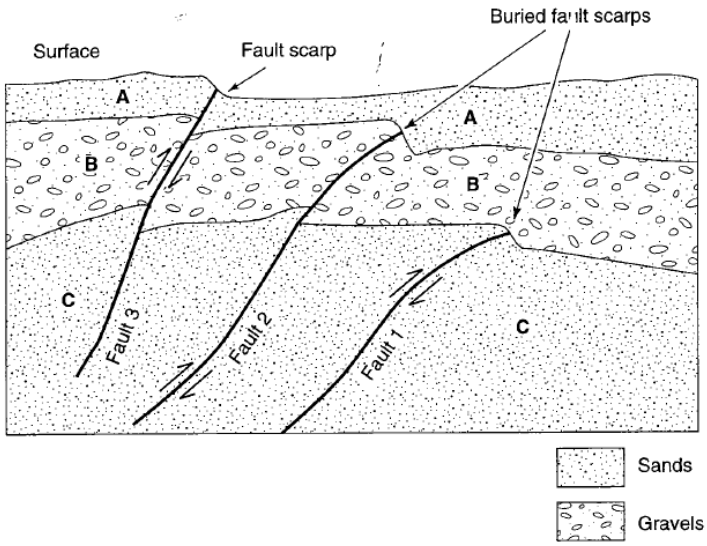

Fig. 2.25 - Trench exposure showing displacement of sand and gravel deposists, buried fault scarps, and surface fault scarp. Faul 1 displaces only unit C. Fault 2 displaces B and C, and Fault 3 displaces A, B and C. This stratigraphy, along with buried fault scarps and the surface fault scarp, suggests that three discrete faulting events occurred. The oldest faulting event occurred on Fault 1 and the youngest on Fault 3 (After Bolt, 1993).

2.5.2.2 Colluvial wedges

Colluvial wedges are formed by unconsolidated material that accumulates at the base of steep slopes. When an earthquake creates a fault scarp, colluvial wedges may form. Their size is function of fault displacement, which is related to seismic moment. Sometimes, the colluvial wedges may be buried and preserved in the stratigraphic record as evidence of past earthquakes (Fig. 2.26).

2.5.2.3 Trenching

Typical methods used to evaluate paleoearthquakes include excavating trenches across active faults (marked by fault scarps in the morphology) to study and date the sediments that have been disrupted and displaced by prehistoric earthquakes (McCalpin, 1996; Piccardi, 2005). The trench gives key insights on past displacements in a given area. However, paleoearthquakes with $M_w \leq$ 5-6 are seldomly detected by paleoseismic evaluation (McCalpin, 1996; Keller and Pinter 2002).

The basic objectives for trenching are i) to identify and date layers within a stratigraphic succession that either have been disrupted and displaced by faulting or that overlie fault traces without disruption, and ii) to document the amount of displacement in past faulting events. It is impossible to know in advance what will be found in the subsurface as a trench is being excavated. Thus, good judgment and selection of the trench location are important and may be crucial to create data-rich excavations. Even the interpretation of the stratigraphy and structures found in trenching sites is often not straightforward (McCalpin, 1996). In some fortunate circumstances, clear cross-cutting relationships and abundant materials for dating are present. So, commonly, low-energy environments are

preferred as trenching sites since they can provide rich stratigraphic records (a function of carbon-rich materials, suitable for dating). In addition, linear stratigraphic markers across which offsets are measured are most likely found well preserved in these types of environments (McCalpin, 1996; Keller and Pinter, 2002). However, each trench is relevant only to those segments of the fault directly adjacent to it (McCalpin, 1996).

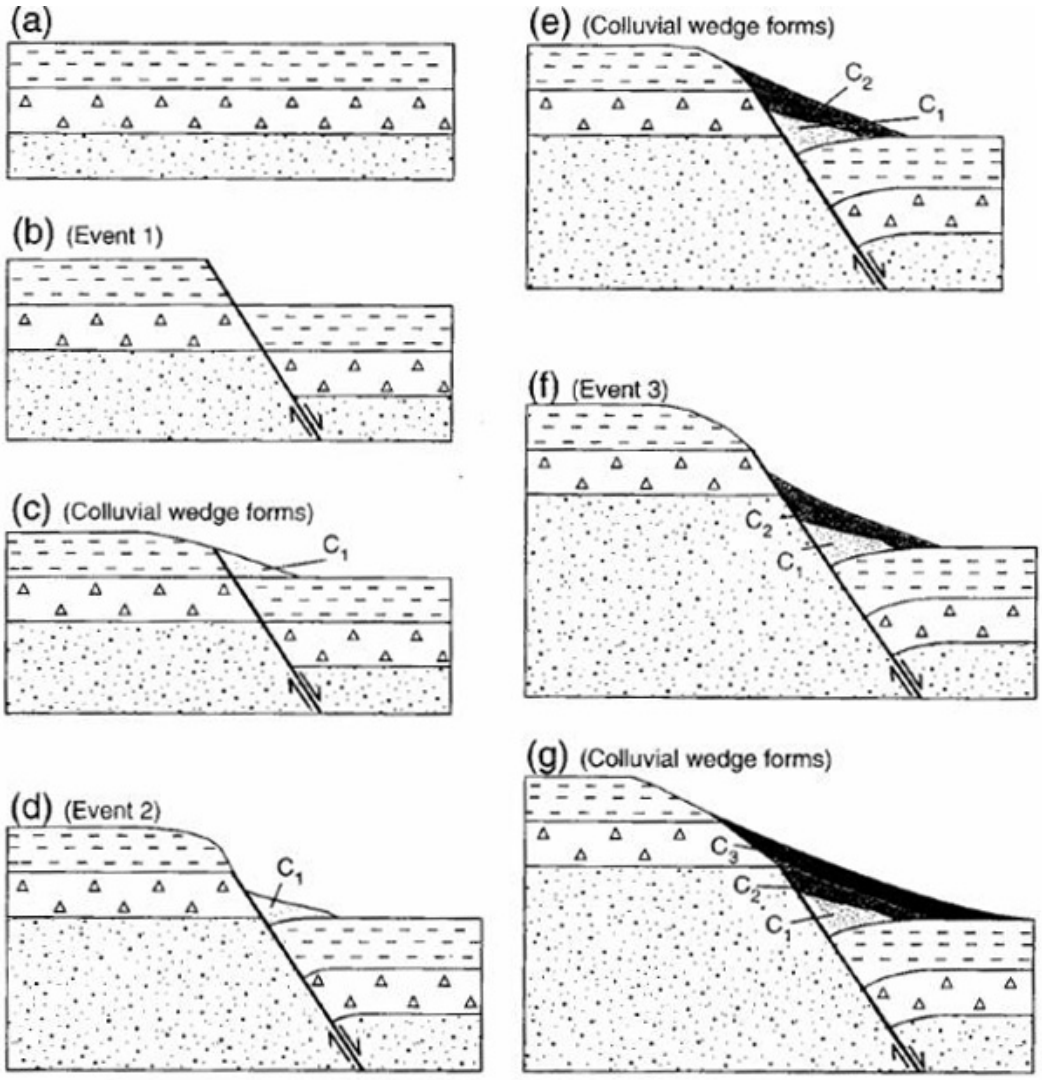

Fig. 2.26 - Development of three-event fault scarp. Each faulting event is followed by the generation of a fault-scarp colluvial wedge, C_1, C_2 or C_3. (McCalpin, 1987).

Two different strategies are commonly used to orient trenches with respect to faults. In the case of a normal fault, the trench is oriented perpendicular to the fault, while trenches are oriented parallel to the fault in strike-slip sytems (McCalpin, 1996; Michetti et al., 2005).

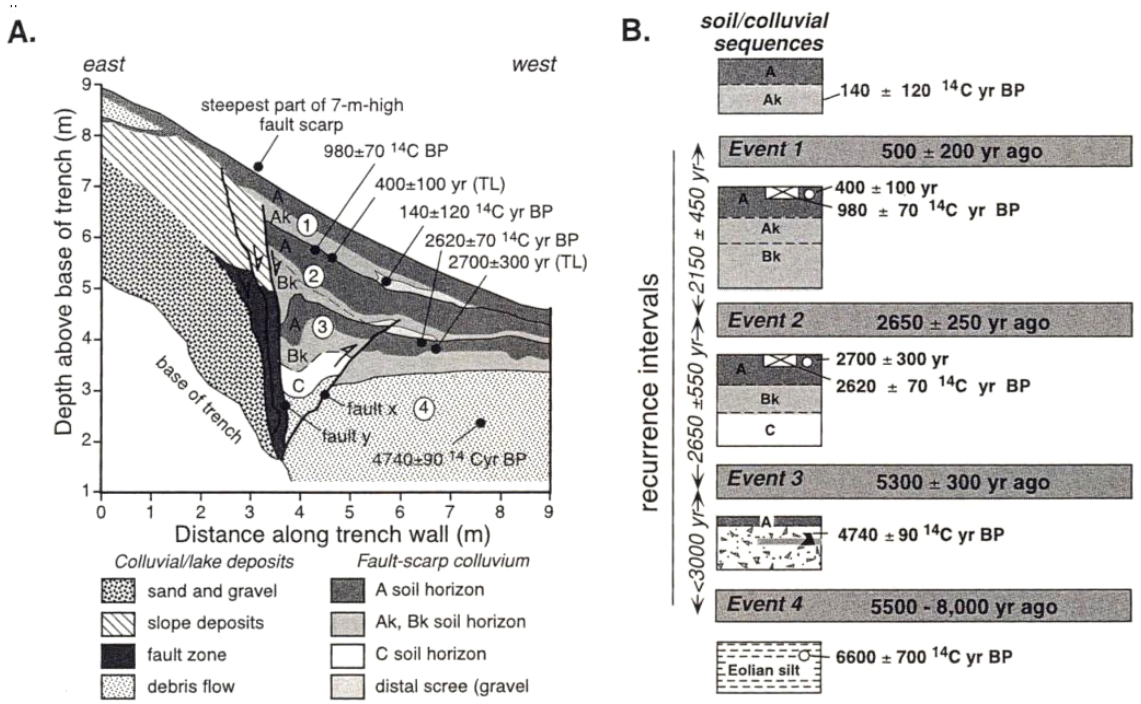

Fig. 2.27A - Evidence for three faulting events is revealed in this trench. The excavation is > 8 m deep, and yet, because markers typically show 1-3 m offset per earthquake, only three rupture events are recorded here. A repetitive soil zonation (A-AK±BK) delineates the top of each of the three-colluvial wedges (labeled 1 through 3). The magnitude of offset for each wedge can be estimated by restoring the top surface of the wedge back to the ground surface such that the 'A' soil horizon is continuous onto the upthrown block. Radiocarbon and thermoluminescence dates are used to constrain the timing of faulting events. Cross-cutting relationships with faults and soils define rupture events. Fault 'x' cuts soil sequence 3 and is overlain by sequence 2. Fault 'y' cuts soil sequence 2 and 3, but is overlain by sequence 1. Note that with the exception of the lowest and topmost stratigraphic units on the downthrown strata are represented on the upthrown block. B. Interpretation of the rupture history based on the trench stratigraphy. Evidence for the oldest faulting event is based on the nearby trench. Note that on the trenched segment of the fault, the ruptures appear to be evenly spaced in time, but the magnitude of rupture varies, with the latest offset (~ 1 m) being about half as large as the offsets during the previous two events (Machette et al., 1991; McCalpin, 1996).

For the reconstruction of the history of offsets recorded by strata within a trench, stratigraphic and structural relationships revealed in the walls of the trench have to be interpreted (McCalpin, 1996; Keller and Pinter, 2002). It is always wise to generate as many reliable age determinations as possible for a given stratigraphy, particularly if it will underpin key interpretations of the paleoseismic record. In most trenches, the strata that contain dateable materials do not consistently coincide with the strata that record rupture events. In such cases, age deteminations on strata above and below the "event horizon" are used to bracket its age (Fig. 2.27). For minimization of uncertainties in timing, dateable materials should be sought as close as possible to the rupture horizon, and the highest achievable laboratory precision should be used to reduce the analytical uncertainty on the individual ages (Sieh et al., 1989).

2.5.3 Paleoseismology in volcanic, magma- and dike-intrusion environments: a special case

In some geological settings, shallow and low-magnitude earthquakes are associated with magma intrusion and not directly related to tectonic activities.

Table 2.4 - Maximum magnitudes and focal depths of earthquakes associated with dike injection (After McCalpin, 1996).

Location	Rifting event[b] (Year)	Maximum magnitude[c]	Focal depth(s)[d] (km)	References
Iceland				
Krafla	1975-76	5.0[e]	0-4	Bjornsson et al., 1977; Einarson and Bjornsson, 1979
Krafla	1977	3.8[e]	0-6	Brandsdottir and Einarson, 1979
Krafla	1978	4.1[e]	1-4	Einarson and Brandsdottir, 1980
Hawaii, USA				
Kilauea rift zones				
East	1965	4.4 (M_L)	0-8	Bosher and Duennebier, 1985
East	1968, August	3.3	< 5	Jackson et al., 1975
East	1968, October	3.1	< 6	Jackson et al., 1975
East	1969	4.7	< 7	Swanson et al., 1976a
Southeast	1975	3.0	nd	Dzurisin et al., 1980
East	1976-77	4.0	< 10	Dzurisin et al., 1980
East	1980, August	3.0 (M_c)[f]	0.5-3	Karpin and Thurber, 1987
East	1980, November	3.1 (M_c)[f]	0.7-4	Karpin and Thurber, 1987
Southwest	1981	3.4 (M_c)[f]	1-2	Karpin and Thurber, 1987
East	1982	3.0 (M_c)[f]	0.5-3	Karpin and Thurber, 1987
Japan				
Izu Peninsula[g]	1989	5.5 (M_{JMA})	< 8	e.g. Okada and Yomamato, 1991
Africa				
Asal, Afar	1978	5.3 (Mb)	0-6	e.g. Abdallah et al., 1979
New Zealand				
Taupo volcanic zone[h]	1964-65	4.6	4-8	Grindley and Hull, 1986
Taupo volcanic zone[h]	1983	4.3	6-10	Grindley and Hull, 1986
Califonia, USA				
Mono Craters[i]	1325 ± 20	> 6.5 (M_s)	nd	Sieh and Bursik, 1986
Italy				
Mt. Etna	1989	3.3 (M_L)	< 4	e.g. Bonaccorso and Davis, 1993
Mt. Etna	1991	3.3 (M_L)	< 6	Ferrucci and Patané, 1993
Mean ± 1σ, n=19[j].		3.9 ± 0.8		McCalpin, 1996

[a] Worldwide dike-injection events associated with mafic magma except for Mono Craters which is associated with silicic magma and Mt. Etna, which is associated with intermediate magma Composition of magma for New Zealand episodes is unknown.
[b] An episode of dike injection and associated seismicity having a known beginning and end.
[c] Maximum magnitude reported for the dike-injection event. Magnitudes: M_L, Local or Richter, M_c Coda; M_{JMA}, Japan Meteorological Agency; M_b, body-wave; M_s, Surface-wave,. No definition of magnitude scale was reported for the values without magnitude designation.
[d] Depth range of volcanic seismicity and maximum magnitude earthquake associated with the dike-injection event.
[e] Einarsson (1991) reports earthquakes of magnitude ≥ 5.0 are usually associated with caldera deflation events and magnitude < 4.0 with dike injection at Krafla.
[f] Coda magnitudes greater than amplitude magnitudes for these events.
[g] This earthquake is interpreted to have triggered magma movement, but part of an earthquake swarm that began 10 days prior to a dike-fed submarine eruption.
[h] Possibly associated with tectonic subsidence of the basin or triggered by dike injection.
[i] Minimum estimate of the largest five historic earthquakes based on liquefaction deposits. These earthquakes may be associated with movements along tectonic faults.
[j] Mean and one standard deviation computed based on magnitudes as presented. Mono Craters not used because it was a minimum estimate.
[nd] No data obtained.

On the surface, however, shallow and low-magnitude earthquakes may show similar structures (such as faults, tensile cracks and related extensional features) to those generated by earthquakes due to tectonic activity.

If traditional methods of slip-rate and maximum magnitude determinations are applied without considering the volcanic record or the mechanics of magma intrusion, then the estimated frequencies and magnitudes of paleoseismic events may be erroneous (McCalpin, 1996). Geodetic and seismic patterns show a strong interaction between magmatic and regional-tectonic processes (e.g., Bursik, 1992). Therefore, although magma-induced earthquakes pose a relatively minor threat to humankind, the structures produced by these earthquakes can be mistakenly considered as being the products of single, large earthquakes of tectonic origin (McCalpin, 1996).

Dikes can form normal faults and fissures as they migrate upwards at typical rates of the order of 0.1 to 6 km/hr (e.g., Klein et al., 1987). This can result in small shallow earthquakes, which rarely exceed $M_w = 5.5$ (Table 2.5) and mostly have $M_w = 4.5$ (McCalpin, 1996). Most dike-induced fault scarps are < 1 m high, but emplacement of wide dikes or reactivation of pre-existing structures by multiple dike intrusions may produce fault scarps of > 10 m in height (McCalpin, 1996).

2.5.4 Dating methods in paleoseismic research

The age of a paleoearthquake is usually quoted as the outer bracket of the ranges of 1-sigma or 2-sigma confidence levels of the event-bounding layers. If the age ranges of the event-bounding layers overlap, Bayesian refinement may be applied to narrow down the event probability density distribution (e.g., Steier et al., 2001). Two types of dating methods are used in paleoseismic research: absolute and relative dating. Absolute dating

has an advantage over relative dating in paleoseismic investigation, particularly for seismic-hazard estimations. Keller and Pinter (2002) point out that when there are no dates, there are no slip rates, and slip rates are a very important parameter for the estimation of seismic hazard(s).

In Table 2.5, several absolute dating methods are presented, each of which can be used only for specific time windows and each of which requires specific materials and types of samples. These methods are: radio-isotopic, cosmogenic, chemical, paleomagnetic and biological dating. The details for each method can be found in the references cited for each method.

Two absolute dating methods will be discussed in more detail: radiocarbon (^{14}C) dating, which was fully applied in this study, and thermoluminescence (TL) dating, which was partly used in the study.

2.5.4.1 Radiocarbon dating

Radiocarbon dating is the most popular dating technique in the world (Björck and Wohlfarth, 2004; Fairbanks et al., 2005). It was the earliest radiometric method available (Björck and Wohlfarth, 2004) and it is used for various applications (McCalpin, 1996). By definition, it is a dating technique that takes into account the decay behaviour of radiogenic carbon isotopes present in a given sample. According to Kutchera (1999), nearly 90 % of all measurements made at the more than 50 active accelerator mass-spectrometry (AMS) laboratories are radiocarbon analyses. The useful range of radiocarbon dating technique is up to 35,000 years (Libby, 1955; Stuiver, 1970); sometimes up to 50,000 years (Fairbanks et al., 2005).

The records of the ^{14}C content (radiogenic carbon isotope) of the atmosphere and oceans contain a remarkable array of information about the Earth history (Arnold and Libby, 1949; Libby, 1955). As it is produced by cosmic rays in the upper atmosphere, $^{14}CO_2$ rapidly mixes throughout the troposphere and exchanges with the reactive carbon reservoirs of the oceans and biosphere, where it decays (Fairbanks et al., 2005).

The production of ^{14}C in the atmosphere varies both through time, due to changes in the intensity of Earth's geomagnetic field, and in its concentration, which is regulated by the carbon cycle. As a result of these two variables, a radiocarbon age is not equivalent to a calendar age. Four decades of joint research by the dendrochronology and radiocarbon communities have produced a radiocarbon calibration data set of remarkable precision and accuracy extending from the present to approximately 12,000 calendar years before present (Fairbanks et al., 2005).

The procedures to be followed in sample preparation to sample analysis are summarized in Fig. 2.28.

Table 2.5 - Absolute dating (after Burbank and Anderson, 2001).

Method	Useful range	Material needed	References
Radio isotopic			
(1) ^{14}C	35 ka	Wood, shell	(Libby, 1955; Stuiver, 1970)
(2) ^{14}C	50 ka	Wood, shell	(Fairbanks et al., 2005)
(3) U/Th	10-350 ka	Carbonate (corals, speleothems)	(Ku, 1976)
(4) Thermoluminescent (TL)	30-300 ka	Quartz silt	(Berger, 1987)
(5) Optically stimulated Luminescent	0-300 ka	Quartz silt	(Aitken, 1998)
Cosmogenic			
(1) In situ ^{10}Be, $^{2}6Al$	3-4 Ma	Quartz	(Lal, 1991; Nishiizumi et al., 1991)
(2) He, Ne	Unlimited	Olivine, quartz	(Cerling and Craig, 1994)
Chemical			
(1) Tephrochronology	0-several Ma	Volcanic ash	(Westgate and Gorton, 1981; Sarna-Wojicki et al., 1981)
(2) Amino Acid recemization	0-300 ka; rage is temperature dependent	Carbonate shell	(Bada et al., 1970; Wehmiller et al., 1988)
Paleomagnetic			
(1) Identification of reversals	> 700 ka	Fine sediments, volcanic flows	(Cox et al., 1964)
(2) Secular variations	0-700 ka	Fine sediments	(Creer, 1962)
Biological			
(1) Dendrochronology	10 ka, depending upon existence of a local master chronology	Wood	(Fritts, 1976; Yamaguchi and Hoblitt, 1995)

2.5.4.2 Thermoluminescence

Thermoluminescence (TL) dating is a geochronometric technique used for sediments, such as loess and silt deposits, sand dunes or sheets, A and C soil horizons (rarely B horizons), fissure fills, volcanic ash and glass, colluvial and alluvial materials, fluvial, deltaic, lacustrine, coastal and paleodischarge deposits, tufa mounds with windblown eolian additions, rock shelters, cave floors, bogs and peat, and marsh deposits.

The technique has an age range of 1000 to 500,000 years, intermediate between the ranges covered by the radiocarbon and the Ar-Ar dating techniques. The TL dating method is used on sediment grains with defects and impurities, which function as natural radiation dosimeters when buried. Part of the radioactive decay from radiogenic K, U, Th, and Rb isotopes in the soil, as well as contributions from cosmic rays, are trapped over

time in sediments. The longer the burial, the more absorbed dose is stored in the sediment. Greater light doses indicate an older age.

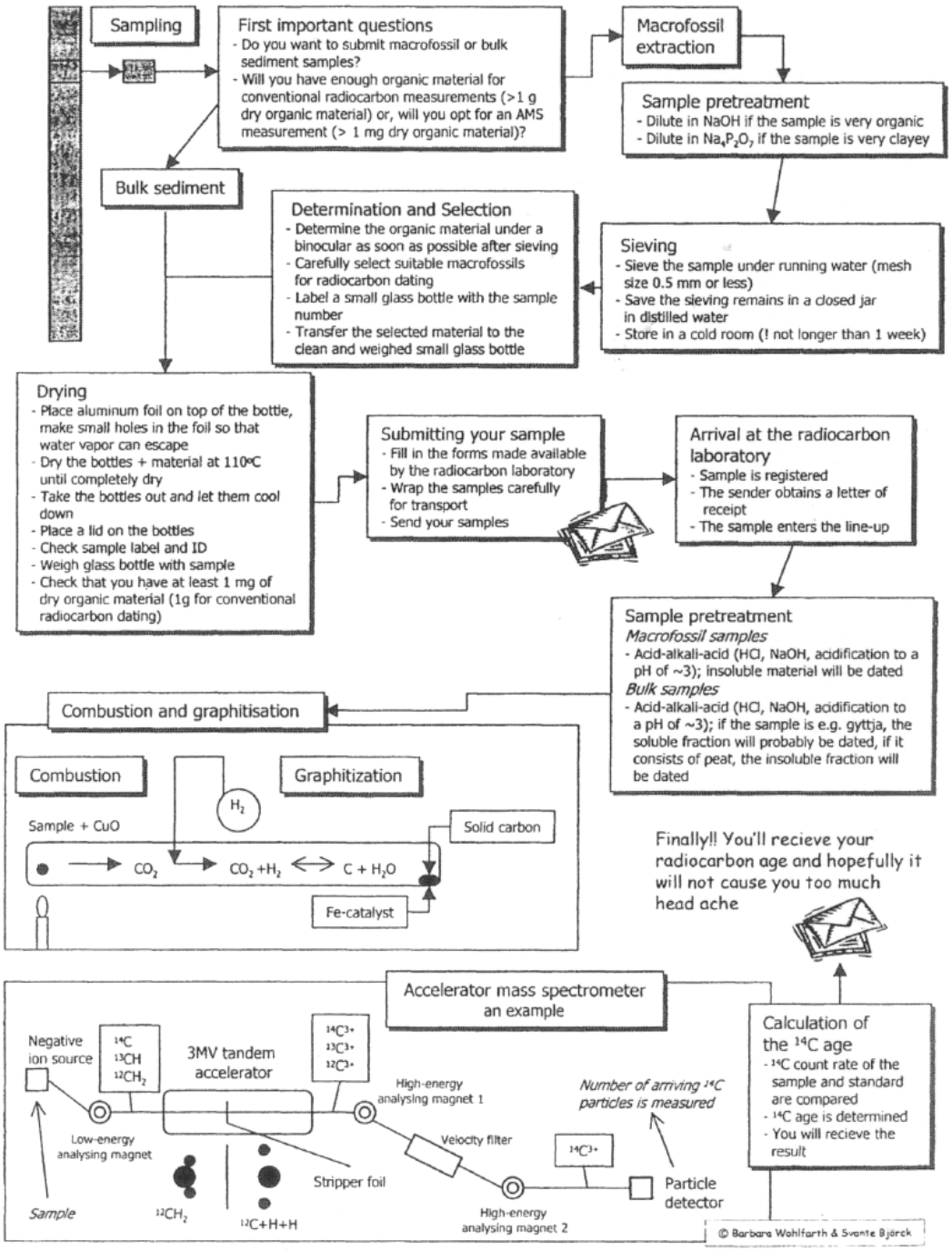

Fig. 2.28 - Sketch, illustrating the long way from sediment sample to radiocarbon date. The extraction of plant macrofossils from sediment samples and their separation is according to the technique employed at the Department of Quartenary Geology, Lund University. The shown schematic pictures, which exemplify the combustion/graphitization process and one type of accelerator mass spectrometer is based upon the techniques used at the Lund University AMS facility (Björck and Wohlfarth, 2004).

Table 2.6 - Classification of Quaternary geochronology methods. Double-dashed line indicates the type of result commonly produced by the methods below it; single-dashed line indicates the type of result less commonly produced by the methods below it (Noller et al., 2000).

Type of result					
========== Numerical-age ========== ……..					
…… .========== Calibrated-age ==……...					
…… ========== Relative-age ====..……					
……= Correlated-age =					
Type of method					
Sidereal Dendro-chronology Sclero-chronology and annual growth in other organisms (e.g., mollusks) Valve chronology Historical records	Isotopic Radiocarbon Cosmogenic isotopes ^{36}Cl, ^{10}Be, ^{26}Al, ^{14}C, ^{3}He, and others K-Ar and ^{39}Ar-^{40}Ar Uranium-series ^{210}Ph U-Pb, Th-Pb	Radiogenic Fission track Thermo-luminescence Optically stimulated luminescence Infrared stimulated luminescence Electron-spin resonance	Chemical and Biologic Amino-acid racemization Obsidian hydration and tephra hydration Rock-vanish cation ratio Lichenometry Soil chemistry ^{10}Be acumula-tion in soils	Geomorphic Soil-profile development Rock and mineral weathering Scarp morphology and other progressive landform modification Rock-vanish development Rate of deposition Rate of deformation Geomorphic position Stone coatings ($CaCO_3$)	Correlation Stratigraphy Paleomagnetism Tephrochronology Paleontology Archeology Climatic correlation Stable isotopes Astronomical correlation Tektites and microtectites

Sample grain zeroing is usually obtained by exposure to sunlight, so analyses are carried out in a darkroom. Each soil naturally has its own particular dose rate, so the in-situ dose rate is obtained with a portable gamma-ray spectrometer. Material for analysis is collected in light-tight conditions. Common grain size used is fine silt (4-11 μm). The sample is treated with various acids to remove carbonate and organics. The sample is irradiated with a β-source to artificially age the sample. The sample is then preheated and finally heated to 500°C in a vacuum oven with a N atmosphere under a photomultiplier tube. The tube measures light emitted by the sample, hereby providing an equivalent dose calculation:

Age = equivalent dose / dose rate

Thermoluminescence is used in conjunction with U-series, ^{14}C, stratigraphy and associated biological processes, whenever possible (http://geology.cr.usgs.gov/capabilities/gronemtrac/geochron/thermo/tech.html).

Noller et al. (2000) propose two ways to classify the commonly used geochronological methods: i.e., "classification by method" or "classification by result" (Table 2.6).

2.5.5 Paleoseismic slip rates, recurrence and seismic hazard

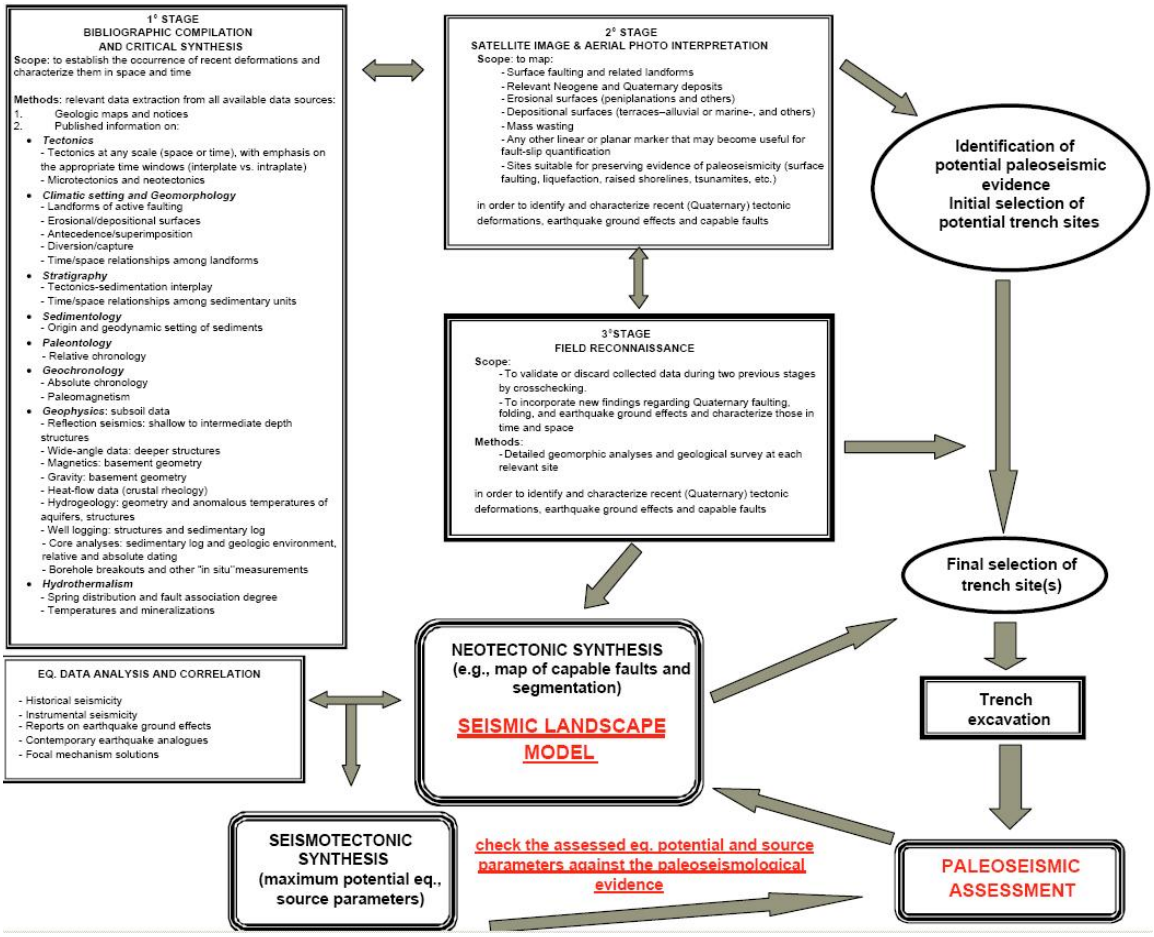

Fig. 2.29 - Proposed methodology flow-chart for the use of paleoseismology in seismic-hazard assessment (From Michetti et al., 2005).

Some models envisage that large earthquakes of relatively constant size occur repeatedly on faults at relatively regular intervals of time. These models have proved fruitful for estimating seismic hazards in certain regions. However, there is often little uniformity in the earthquake processes, particularly for what concerns recurrence intervals of prehistoric events (Sieh et al., 1989; Biasi et al., 2002). On the rare occasions that these variations have been documented, they are typically clustered in space and time (e.g., Sieh et al., 1989; Marco et al., 1996; Marco and Agnon, 2005). This can be explained by the fact that the data that can be used to study earthquake recurrence times are quite

limited, as recording seismometers have been in existence for only a little more than a century and as recurrence times are generally larger than that (i.e., hundred years or more) (McCalpin, 1996). There is a general consensus that clustering reflects the complex stress-dependent behavior of active fault systems (e.g., Harris, 1998). In these circumstances, individual faults are components of an interacting fault array. Quantitative assessment of the principal factors controlling the behavior of interacting faults requires definition of the interdependence of their displacement and earthquake histories.

Earthquake slip rates and recurrence intervals are two fundamental descriptors of paleoseismicity and both are critical components of any seismic-hazard assessment (McCalpin, 1996), because average earthquake recurrence intervals tend to decrease as slip rates increase (e.g., Roberts et al., 2004). Slip rates can be calculated from the cumulative displacement of dated landforms and deposits, even if the individual paleoearthquakes cannot be identified. Slip rates can also be calculated by dividing measured displacement per event by recurrence interval. Figure 2.29 summarizes the main steps required to produce a reliable database for seismic-hazard analyses (see also IAEA, 2002; Gürpinar, 2005).

Slip rate can also be calculated from:

$$RI = D / (S-C)$$

where RI is the mean recurrence interval, D is the displacement during a single, typical faulting event, S is the coseismic slip rate, and C is the creep slip rate (assumed to be zero for most faults unless historic creep has been documented). Recurrence intervals can be estimated by averaging slip rates, divided into assumed slip per event (Wallace, 1970).

2.5.6 Models of fault behavior

Fault behavior models are intended to show the characteristics of the coseismic displacement and how such characteristics vary with time both at a single location and along the trace of the fault. They also provide the pattern in which slip may occur on faults (Schwartz and Coppersmith, 1984). Fault behavior has both temporal and spatial aspects.

2.5.6.1 One-dimensional models

There is one very simple (one-dimensional) model that was conceived by Reid (1910): i.e., the "perfectly periodic model". It is the earliest model that describes how fault displacement varies through time at a single location of a given fault (Schwartz and Coppersmith, 1984; McCalpin, 1996). In this model, earthquakes occur whenever stress builds up to a certain level τ_1. The stress drop (to a certain level τ_2) and magnitude of each earthquake are also identical. With the additional assumption of constant stress build-up through time, the earthquake becomes perfectly periodic (Fig. 2.30; Reid, 1910). The perfectly periodic model was further subdivided into a "time-predictable model" and a "slip-predictable model" (Shimazaki and Nakata, 1980).

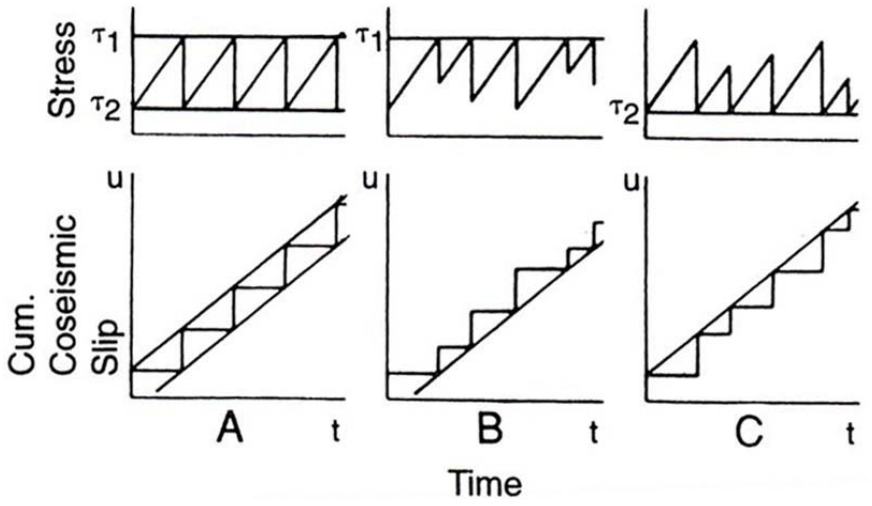

Fig. 2.30 - Diagram contrasting (A) the perfectly periodic model, (B) the time-predictable model, and (C) the slip-predicted model of earthquake recurrence. Upper figures show patters of stress drop with time, lower figures show patterns of fault slip through time (McCalpin, 1996).

Time-predictable model
Earthquakes occur at a constant critical stress level τ_1, but the stress drop and magnitude vary. Thus the time of the next earthquake in the series can be predicted based on the slip in the previous earthquake, assuming a constant slip rate through time (McCalpin, 1996).

Slip-predictable-model
In this model, earthquakes stress drop τ_2 is fixed, and thus slip in the next earthquake can be predicted from the time since the previous earthquake.

2.5.6.2 Two-dimensional models
The two-dimensional models came in existence after paleoseismologists discovered that slip varies along strike during earthquakes. According to Schwartz and Coppersmith (1984), two-dimensional models can be classified into two groups namely the "variable-slip models" and the "uniform-slip models".

Variable-slip models
The variable slip models predict that slip rate along strike is constant, but that displacement per event at a point is variable. The pattern of cumulative displacements along strike is not regular, and rupture in individual events is not limited to fault segments. The relation between displacement per event and time between events can be either time- or slip-predictable (Fig. 2.30).

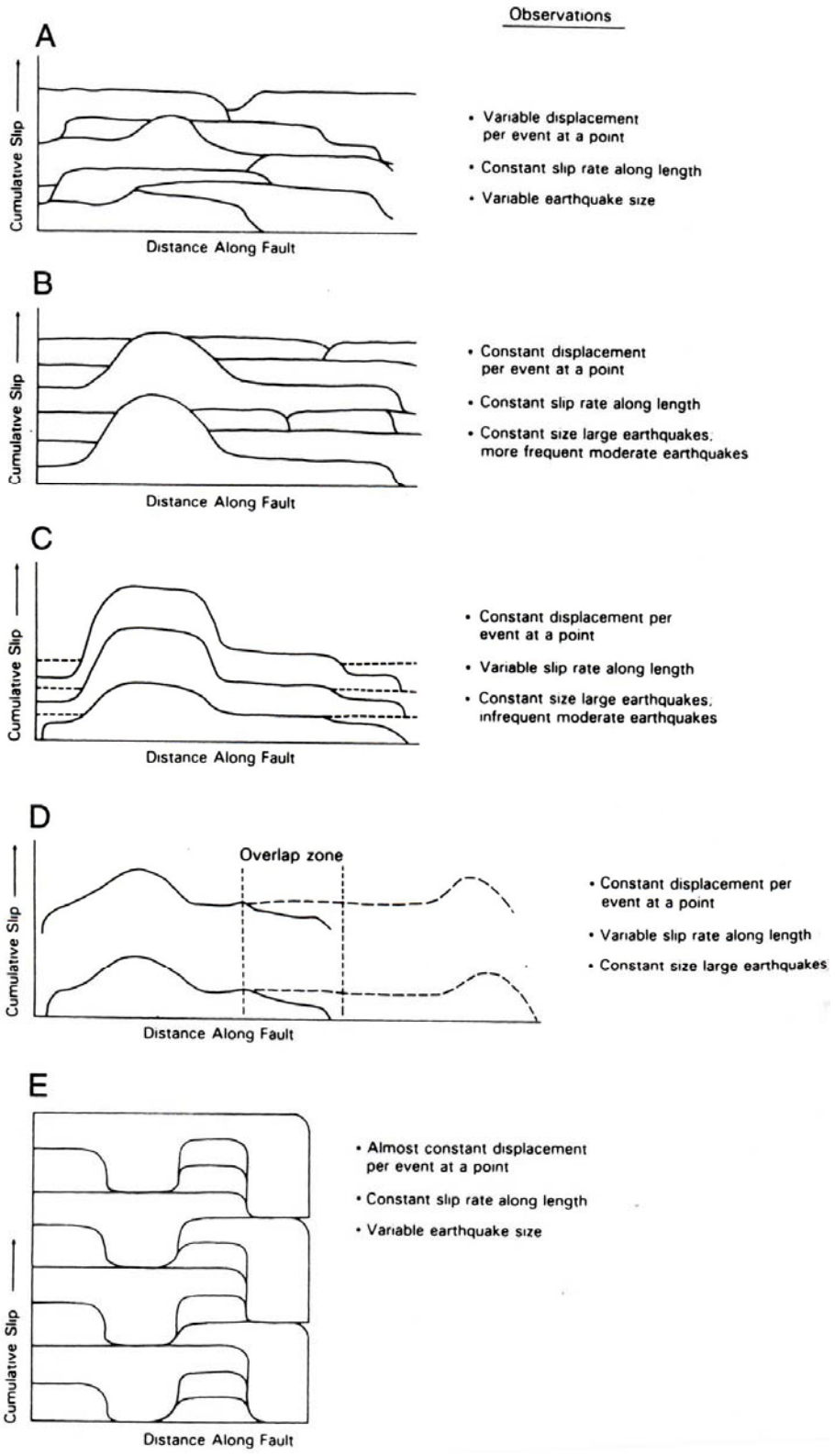

Fig. 2.31 - Diagrams showing patters of along-strike slip for various models of fault behaviour. (A) Variable slip model. (B) Uniform slip model. (C) Characteristic earthquake model. (D) Overlap model. (E) Coupled model (McCalpin, 1996).

Uniform-slip models
In the uniform-slip models, displacement per event at a point on the fault is constant but slip rate along strike may be constant or variable (Fig. 2.31B,C,D,E). Of the four uniform-slip models in Fig. 2.31, three implicitly assume that fault segments exist that are reasonably persistent.

The simplest uniform-slip model assumes that displacement per event at a point is constant, slip rate along strike is constant, and strain is released by both rare large earthquakes and more frequent smaller earthquakes (Fig. 2.31B). If moderate earthquakes are near the thresholds of recognition for surface rupture, or ground shaking, they may not be recognized in the paleoseismic record. Few paleoseismic studies have inferred a simple uniform model, possibly due to the difficulty in detecting small rupture events associated with moderate magnitude earthquakes.

The "coupled model" is similar to the uniform slip model, but it recognizes that individual rupture events are restricted to persistent fault segments (Fig. 2.31E). In the idealized drawing, segment boundaries are very narrow, and slip in a single event decreases from a constant intrasegment value to zero in a short span. Such rapid decreases in slip at rupture ends are not typical of historic ruptures. Although long-term slip rates along strike are constant, at any given moment, the cumulative amount of slip along strike may show considerable variation. In this respect, the pattern can be very similar to that of the characteristic earthquake model.

The "characteristic earthquake model" (Fig. 2.31C) assumes that most strain is released in large earthquakes within a narrow "characteristic" magnitude range (Schwartz and Coppersmith, 1984). Moderate earthquakes within a one-magnitude range below the characteristic earthquake may be rare, if not entirely absent. In this model, unlike in the other models, slip deficits at the end of ruptures are never filled in by slip from smaller earthquakes. Schwartz and Coppersmith (1984) state that *"rupture segments, barriers to fault rupture, and the distribution of slip appears to persist through repeated earthquakes…it can be argued that the constitution and strength of fault zone materials as well as the style of stress application can be considered essentially constant through several seismic cycles. Given that these set of conditions remain relatively constant, we would expect generally uniform behavior of the fault with respect to the size of characteristic earthquake that it produces"*.

The "overlap model" is a refinement model. It assumes that rupture is limited to segments. The model conceives a segment boundary as a zone of some finite along-strike length. Ruptures originating in adjacent segments extend into the segment boundary with diminished displacement, and "overlap" so that their sum is similar to the single-event displacement just outside the segment boundary. It has been suggested that trenching in segment boundaries can distinguish ruptures that propagated completely through a segment boundary, and thus involved two segments, and ruptures that died out within a segment boundary. This matter of rupture length is critical for estimating paleoearthquake magnitude.

2.5.6.3 Recurrence interval of magma-related faults

Magma-induced faults may lack sufficient displacement or suitable materials for the development of a colluvial wedge, and many are monogenic features unlikely to have undergone recurrent movement. Earthquake recurrence in volcanic-rift-zone faults can be estimated by establishing the recurrence interval of volcanic cycles. Volcanism, like recurrent faulting, is often episodic and not continuous, and therefore a viable approach is to estimate volcanic recurrence using relative and absolute chronology and to use that interval in estimation of magma-induced seismic recurrence (Hackett and Smith, 1992).

Chapter 3

Geological Setting of the Study Area

3. Geological setting of the study area

This chapter provides an overview of the regional setting of the East African Rift System (EARS) by describing its morphology, structure and modes of origin and evolution. A similar description format is adopted for the study area (i.e., the Dodoma area), which is part of the EARS.

3.1. The East African Rift System

3.1.1 Geographic context: location and morphology

The EARS (Fig. 1.2) is located between 5°00'N, 10°00'S and 25°00'E and 40°00'E (Simiyu and Keller, 1997; Zeyen et al., 1997). The EARS extends from the Ethiopian dome (Simiyu and Keller, 1997) or from the Afar triangle in the north (Chorowicz, 2005) and runs southwards (Zeyen et al., 1997) in a narrow zone of about 50-150 km (Morley et al., 1999; Atmaoui and Hollnack, 2003) before it bifurcates into two main branches: the eastern and western branch (Fig. 3.1) (a.o., Morley et al., 1999; Rogers et al., 2000; Atmaoui and Hollnack, 2003; Chorowicz, 2005; Calais et al., 2006; Casey et al., 2006; Corti, 2008). The branches have total lengths of about 2200 km (Chorowicz, 2005) and 2100 km (Chorowicz, 2005) or 2500 km (Nyblade and Brazier, 2002), respectively, whereas the total length of the EARS is about 3500 km in a sub-meridian direction (Morley et al., 1999).

The eastern branch, as it enters NE Tanzania, departs from a well developed narrow (50-80 km-wide) graben structure to the north in Kenya and splays in a 300 km wide zone of block faulting, extending from Lake Eyasi to Pangani (Chorowicz, 2005). This wide zone continues into the Tanzanian craton for up to 400 km (Tesha et al. 1997).

Generally, the EARS manifests itself as a series of adjacent individual tectonic basins (rift valleys) (Chorowicz and Sorlien, 1992; Chorowicz, 2005). Some of the basins are now filled by lakes and sediments. For instance, the eastern branch hosts Lakes Turkana, Natron, Eyasi and Manyara. Lakes Albert, Tanganyika, Rukwa, Mweru and Nyasa characterize the western branch (Fig. 3.1).

Generally, the EARS encloses the East African plateau (Simiyu and Keller, 1997). The plateau is a broad topographic high that extends from the Congo basin in the west to eastern Kenya and from the NW-SE trending Sudan-Anza rift zone in the north to the Tanganyika-Malawi (Nyasa) rift zone in the south (Simiyu and Keller, 1997; Le Gall et al., 2004). The average topographic elevation of the plateau is about 1000 m above its surroundings (Zeyen et al., 1997).

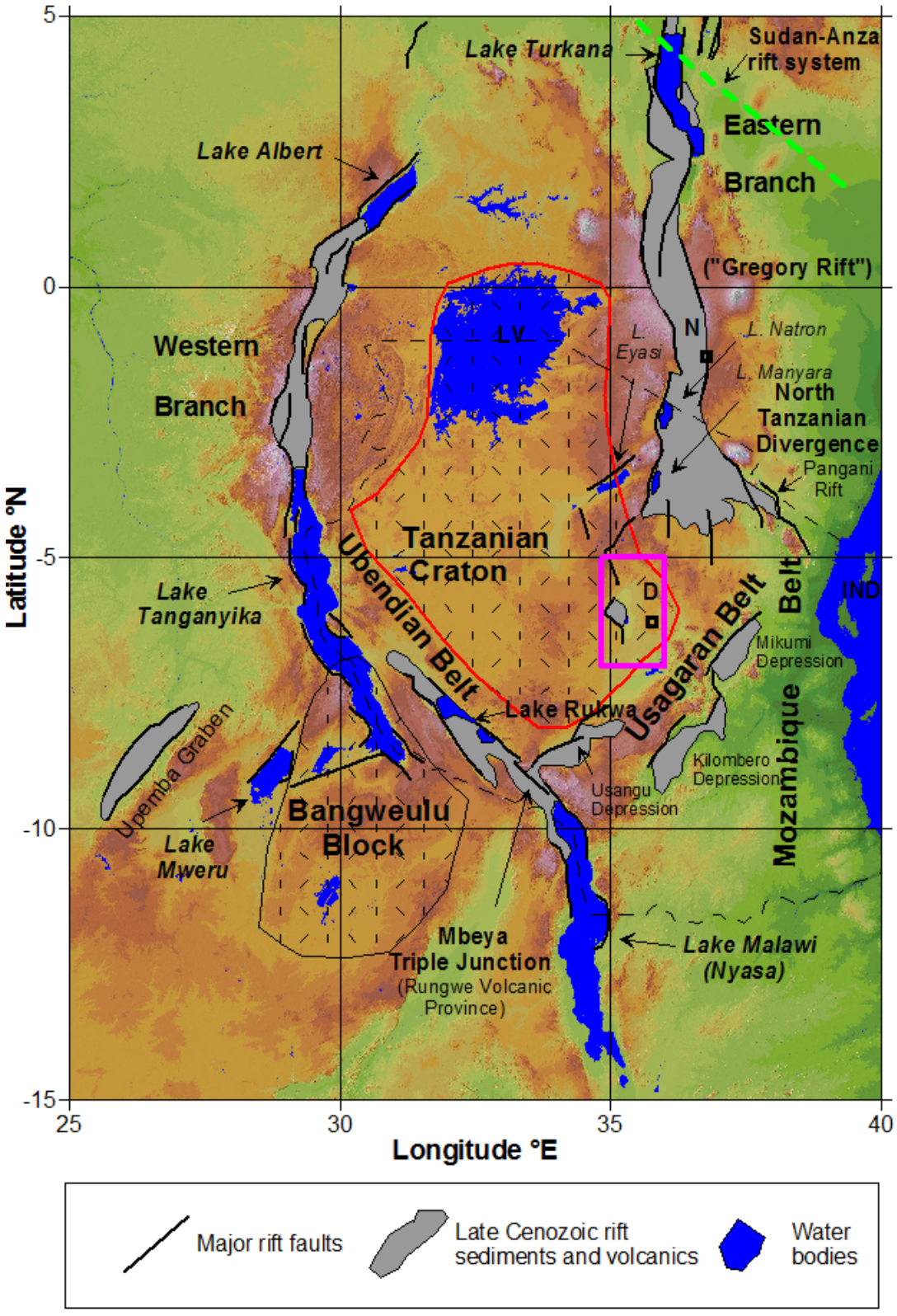

Fig. 3.1 - Schematic map of the EARS area. LV = Lake Victoria; IND = Indian Ocean; D = Dodoma; N = Nairobi. The study area is shown by a pink rectangle. A red line represents the Tanzanian craton boundary. (adapted from Delvaux, 1991; Morley, 1999; Macheyeki et al., 2008b).

3.1.2 Geological context

3.1.2.1 Structure

The Cenozoic EARS is the classic example of continental rifting (Gregory, 1921; Tesha et al., 1997), and the most extensive currently active continental rift on Earth (McConnell, 1972; Ebinger, 1989a; Delvaux, 1991; Morley, 1999a; Calais et al., 2006). It formed mainly within Proterozoic orogenic belts: i.e., the Ubendian-Usagaran (2.2-1.8 Ga), the Kibaran (Karagwe-Ankolean) belt (1.4-0.9 Ga) and the Mozambique belt of the Pan-African or Katangian Orogeny (0.6 Ga) (Holmes, 1952; Spooner et al., 1970; McConnell, 1972; Kroner, 1977; Brewer et al., 1979; Smith and Mosley, 1993; Daly, 1998). These belts surround the Archean cratons of Central and Eastern Africa (Simiyu and Keller, 1997), which are mainly the Tanzanian and Congo cratons (e.g. Morley et al., 1999). In other words, the rift avoids the central part of the cratons, which probably reflects pre-existing heterogeneity in lithospheric strength (e.g., Simiyu and Keller, 1997; Tesha et al., 1997; Morley et al., 1999; Le Gall et al., 2004) across the 1300 km wide plateau (Simiyu and Keller, 1997). While Morley et al. (1999), Atmaoui and Hollnack (2003), Ebinger (2005), Le Gall et al (2004), Macheyeki et al. (2008b) and many others show that the rift on the eastern branch does affect a part of the Archean Tanzanian craton, the western branch is purely within mobile belts (Simiyu and Keller, 1997).

In the eastern branch, evidence exists that the EARS crosses the NW-SE trending older (Cretaceous-Paleocene) Sudan-Anza rift system (e.g. Morley, 1999).

Recent structures (such as rift faults) associated with the EARS have generally inherited the fabrics of Precambrian structures (Fairhead and Stuart, 1982; Lenoir et al., 1994; Theunissen et al., 1996), since the latter acted as preferential locus for the brittle faults of the rift (Lenoir et al., 1994; Theunissen et al., 1996; Modisi et al., 2000).

According to Koehn et al. (2007), Bahat and Mohr (1987) show that the EARS contains about 12 large-scale horst structures. The most extreme example of risen horst within the EARS is the > 5000 m high, non-volcanic Ruwenzori Mountain.

3.1.2.2 Basins

There are two main types of basins in the EARS and outside:
(1) the Karoo basins (Johnson et al., 1996; Wescott and Diggens, 1998; Nyambe, 1999) (Fig. 3.2). Catuneanu et al. (2005) state: *"The Karoo basins in Africa preserve a record of a special time in Earth's history, when the Pangea supercontinent reached its maximum extent during the Late Paleozoic to Early Mesozoic interval. The term "Karoo" was extrapolated from the main Karoo Basin of South Africa, to describe the sedimentary fill of all other basins of similar age across Gondwana. The onset of sedimentation of this Karoo first-order depositional sequence is generally placed in the Late Carboniferous, around 300 Ma, following a major inversion of tectonic event along the southern margin of the supercontinent that led to the assembly of Pangea"*.

(2) the Cenozoic rift basins that are located within the EARS. The main ones are those hosting Lakes Nyasa, Tanganyika and Rukwa, all of which are located in the western branch of the EARS (Scholz et al., 1998). They are characterized by a half-graben structure, each half-graben having a size of the order of 70 x 130 km, and by alternating dip polarity along the rift-axis (Rosendahl, 1987; Scholz et al., 1998), except for the Rukwa basin (Kilembe and Rosendahl, 1992). The Cenozoic basins related to the EARS seem to be located within an area occupied by the Karoo basins, crossing almost the same parts of the countries (i.e., Kenya, Tanzania, DR Congo, Zambia, Malawi, Zimbabwe and Botswana), which seems to indicate that the Cenozoic EARS has reactivated these Karoo basins. In northern Kenya, Ebinger and Ibrahim (1994) report repeated evolution characterized by three distinct phases of rifting within almost the same area since Late Jurassic: i.e., the Anza rift and Blue and White Nile areas in southern Sudan were formed from Jurassic to Cretaceous; the same Anza rift (and western and central Turkana) were rifted during the Paleogene; the eastern Turkana, Kenya and Ethiopian rifts were formed in Miocene to Recent times.

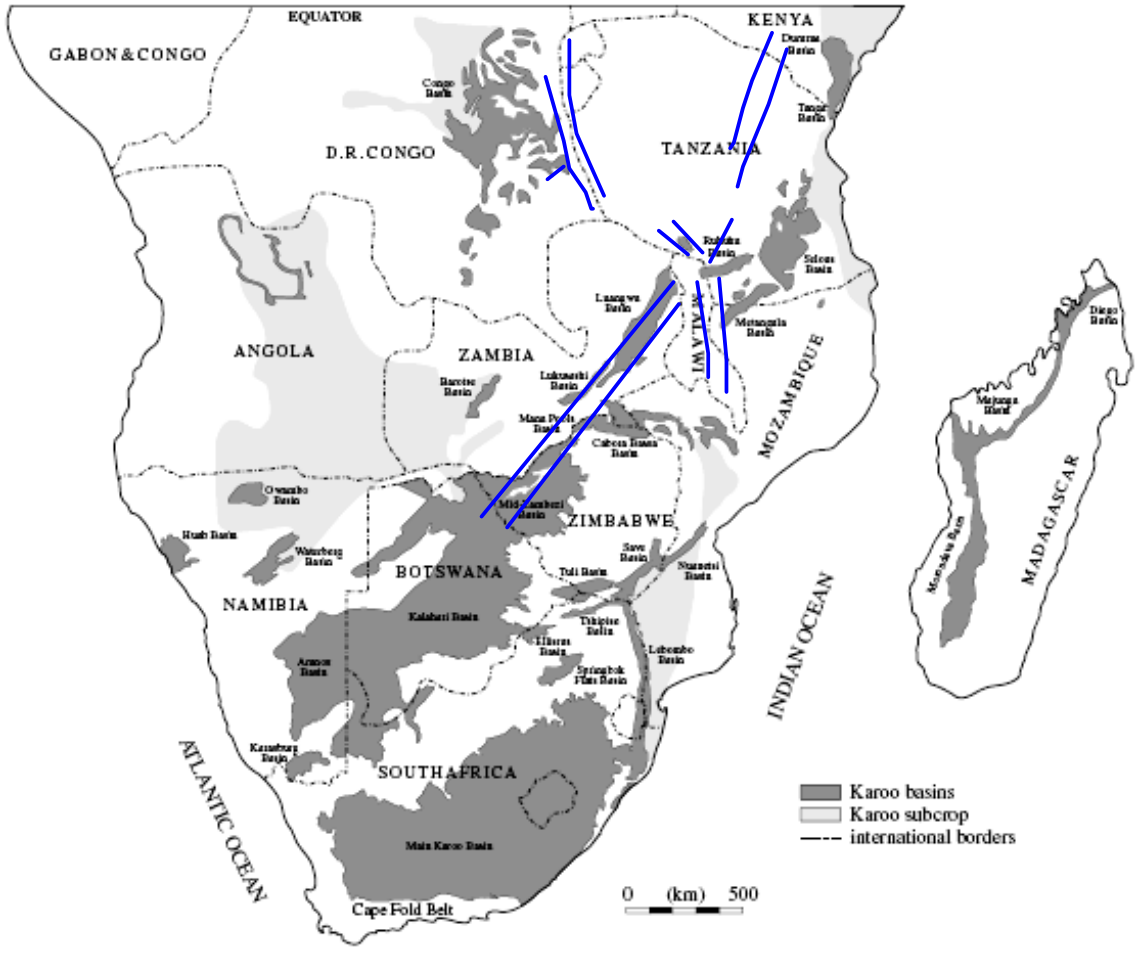

Fig. 3.2 - A sketch showing the distribution of Karoo basins in south-central Africa. The blue lines are rough approximations of the trace of the EARS (After Scholz et al., 1998).

Continental rift basins are commonly asymmetric and at early stages of development they are flanked by broad uplifts and rise 1 km or more above regional topography (Ebinger et al., 1993). Many of the current structural and stratigraphic models of lacustrine rift basins rely on data from the Tanganyika-Rukwa-Malawi (Nyasa) rifts, where the process of sedimentation and faulting continues (e.g. Scholz et al., 1990; Morley et al., 2000).

Subsidence in the Cenozoic rift basins is accommodated by slip on border faults, and the basins have the appearance of half-grabens with limited internal deformation. Based on observations in Lake Tanganyika, and assuming that subsidence continues sufficiently long, then faulting will inevitably be initiated on the flexural or hanging-wall margins of the rift basin, and the system may eventually evolve into tilted or asymmetric full graben, as is observed in parts of the lake (Rosendahl, 1987; Morley, 1998; Scholz et al., 1998).

3.1.2.3 Large faults

Major boundary faults in the EARS tend to transfer displacement between overlapping fault segments along which displacement gradually dies out on one segment and increases on one or more others (Smith, 1994; Mariita and Keller, 2007). When viewed on a large scale, transfer zones mark changes in basin geometry between contemporaneous fault systems whereas minor faults are commonly synthetic to the major boundary faults, switching polarity where major faults switch polarity (Morley, 1999b; Mariita and Keller, 2007).

3.1.2.4 Volcanism

Cenozoic volcanism in the EARS occupies a much wider area in the north, especially in the eastern branch, than in the south (Chorowicz, 2005) (Fig. 3.3). Onset of volcanism in the EARS is attributed to rifting (Nyblade and Brazier, 2002). The oldest volcanics associated with the EARS have been emplaced between 45 and 35 Ma (Ebinger et al., 1993) or at ca. 45-37 Ma (Nyblade and Brazier, 2002) in southern Ethiopia. Around 35-30 Ma, the onset volcanism reached northern Kenya, at ca. 15 Ma it reached central Kenya and at about 8 Ma (Nyblade and Brazier, 2002), or 8-5 Ma (Ebinger, 1989; Tesha et al., 1997; Morley et al., 1999) volcanism commenced in northern Tanzania.

The rift zone in NE Tanzania is characterized by large volcanic provinces comprising numerous volcanoes with some minor faulting (Tesha et al., 1997). Essimingor volcano in Kenya is the oldest dated volcano at 8.1 Ma. It produced mainly alkali basalts, trachytes and phonolites (Fairhead et al., 1972; MacIntyre et al., 1974; Tesha et al., 1997). The sequence of volcanism in the eastern branch of the EARS reveals a clear southward propagation of rifting (e.g., Ebinger, 1989; Nyblade and Brazier, 2002; Chorowciz, 2005).

To the contrary, there is no apparent southward age progression in the western branch (Nyblade and Brazier, 2002). Volcanism in the western branch began ca. 12 Ma in the Virunga Province, ca. 8 Ma in the Kivu and Rungwe Provinces, ca. 6 Ma in the Mwenga-Kamituga Province, and ca. 2-1 Ma in the Toro-Ankolean Province (Ebinger, 1989; Kampunzu et al., 1998; Nyblade and Brazier, 2002). These data show that volcanics (and hence rifting) in the western branch began at about the same time that volcanism and

rifting in the eastern branch reached southern Kenya (12-10 Ma) (Nyblade and Brazier, 2002) (Fig. 3. 4).

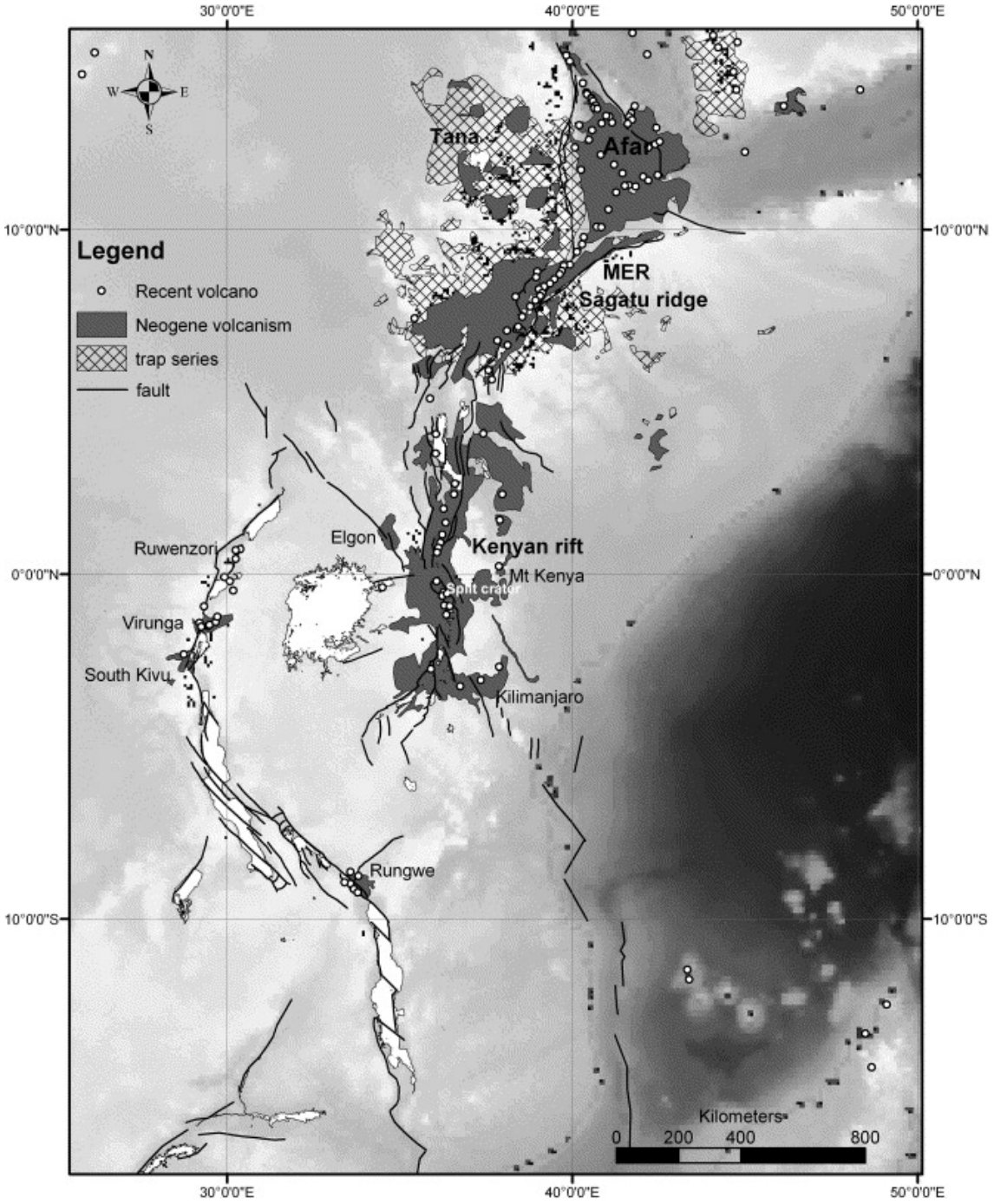

Fig. 3.3 - Time and spatial distribution of volcanism in the EARS (From Chorowicz, 2005).

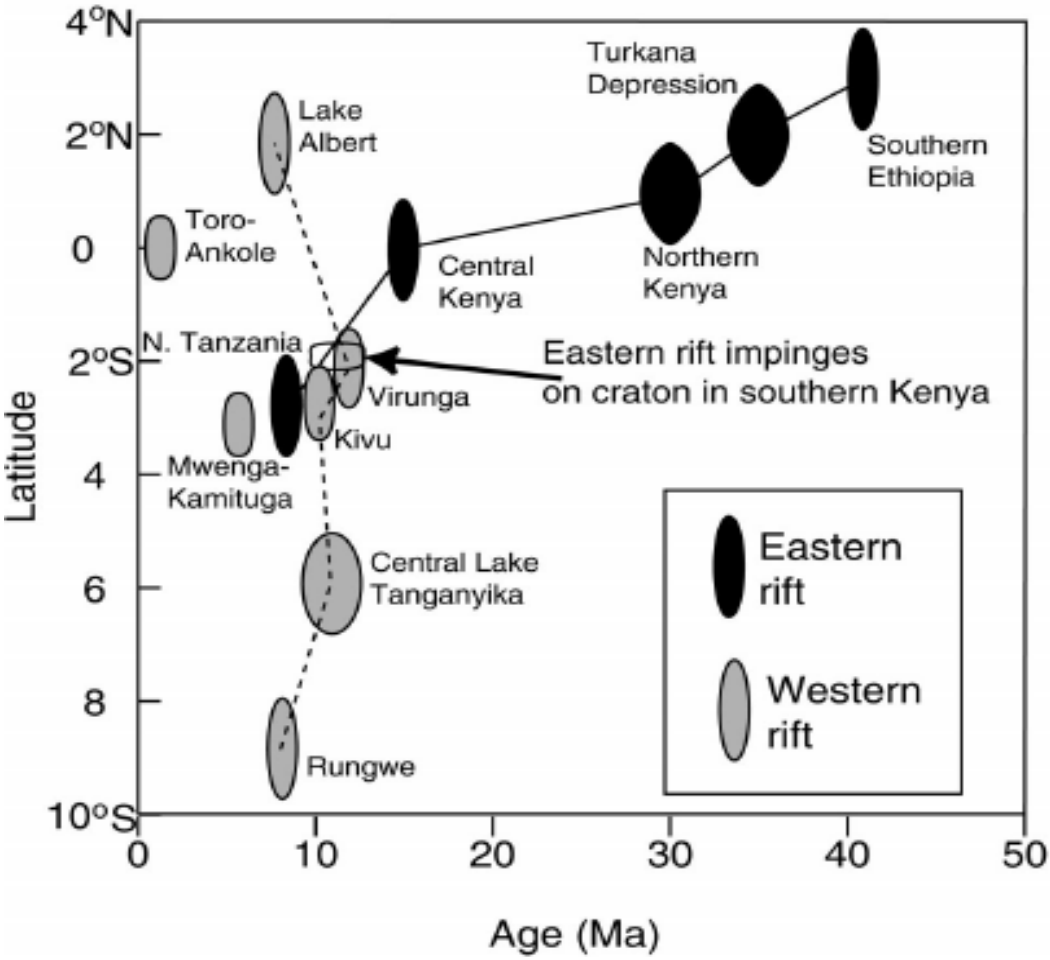

Fig. 3.4 - Age-versus-latitude diagram, showing onset age of volcanism in major volcanic provinces in East Africa (From Nyblade and Brazier, 2002).

A major faulting episode at ~ 1.2 Ma created the present-day rift escarpments and was followed by a major phase of nephelinite-phonolite-carbonatite-volcanism (Fairhead et al., 1972; MacIntyre et al., 1974; Tesha et al., 1997).

3.1.3 Seismicity

The western branch is seismically more active than the eastern branch (Fairhead and Girdler, 1971). Strong seismic activity occurs from Lake Albert (Mobutu) in the north to Lake Nyasa (Malawi) in the south (Fig. 3.5). Most earthquakes in the western branch are of larger magnitude and have deeper hypocenters (Camelbeeck and Iranga, 1996) than those from the eastern branch (Shudofsky, 1985; Foster et al., 1995). Although the eastern branch is relatively quiet in terms of large-magnitude earthquakes, yet, numerous small earthquakes characterize it (e.g., Nusbaum et al., 1993; Tongue et al., 1994).

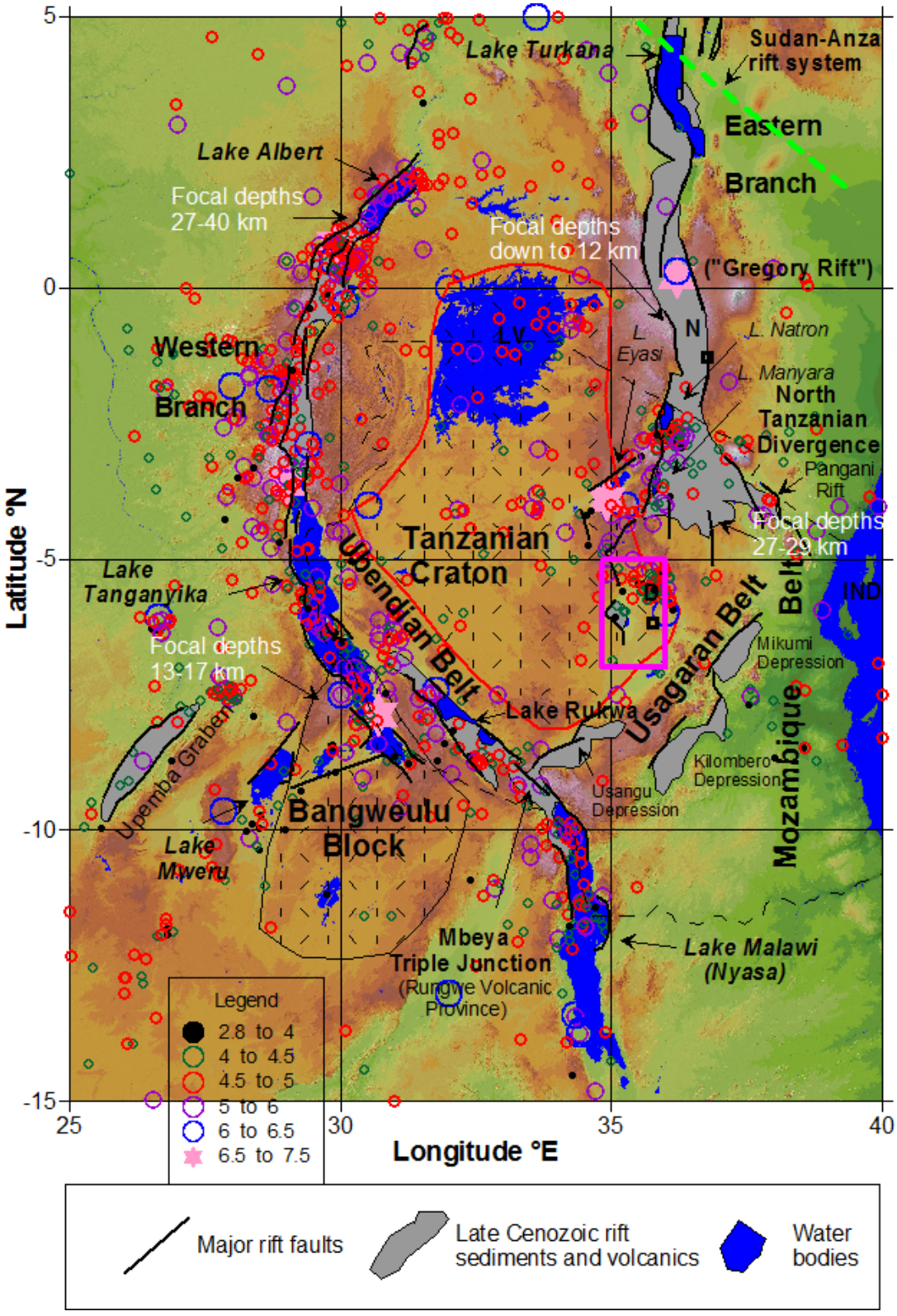

Fig. 3.5 - Seismicity map of the EARS from events recorded from 1921 to Present. Focal depths are shown in white (from Morley, 1999 and Nusbaun et al., 1993). Other details as in Fig. 3.1 (adapted from Delvaux, 1991; Macheyeki et al., 2008b). Circle and star symbols represent earthquake magnitudes (m_b).

3.1.4 Deep structures

Geophysical data show that the thickness of the crust beneath the EARS decreases from south to north (e.g., Petit and Ebinger, 2000; Tessema and Antoine, 2004; Mariita and Keller, 2007). The maximum crustal attenuation occurs beneath the Afar depression (Tessema and Antoine, 2004) where the crust is only ~ 15 km thick (Makris and Ginzburg, 1987; Tessema and Antoine, 2004). Another significant decrease in crustal thickness is reported by Mariita and Keller (2007), who show that the crustal thickness decreases from 35 km to 22 km within 700 km between the northern (around Turkana) and the southern (Naivasha) parts of Kenya (Fig. 3.6).

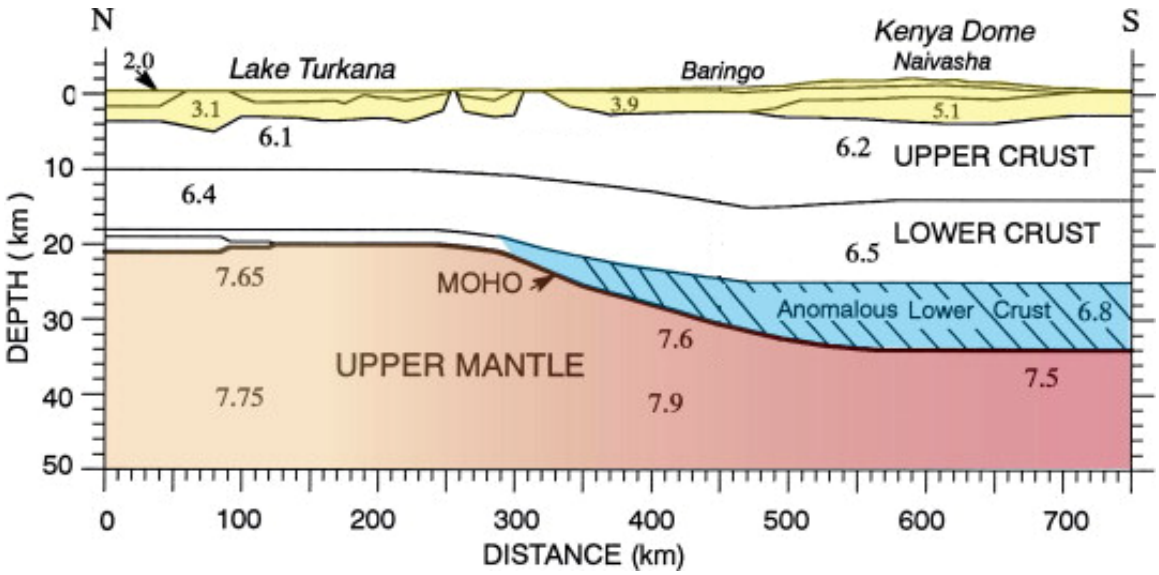

Fig. 3.6 - Kenya Rift Seismic Project (KRISP) seismic velocity model along the axial seismic line. The supracrustal sediments and volcanics are in yellow. The high-velocity lower crust associated with the Kenya dome is in blue. The uppermost mantle is in red with the gradient approximating the north to south decrease in velocity (After Mariita and Keller, 2007).

Teleseismic data indicate that the western and eastern branches of the EARS between 1°00'S and 10°00'N are overlying a crust of 35 km and 40 km thick, respectively. Below the western branch, there is a diapiric intrusion of material with high pyroxene content and possibly with some low-density eclogite, coming from the mesosphere. It has stalled at about 55 km below the surface and is cooling. The diapirism in the eastern branch has broken through to the surface (Nolet and Mueller, 1982). Generally, there is a significant lithospheric thinning beneath the EARS and geophysical data suggest an existence of deep mantle anomaly centered beneath the East African plateau and the Tanzanian craton (Simiyu and Keller, 1997; Mariita and Keller, 2007). The anomalous region widens northwards (Mariita and Keller, 2007) and is believed to be a plume characterized by a 600 km wide head (Simiyu and Keller, 1997).

3.1.5 Modes of origin and evolution of the EARS

The mode of origin and evolution of the EARS is considered to be both active and passive (e.g., Morley, 1999a; Nyblade and Brazier, 2002). The proposed bi-modal origin is based on a number of arguments:

(1) The degree of crustal extension observed in the EARS is large. This cannot be explained by active rifting alone. According to Mulugeta (1985), the active rifting mechanism is not able to produce significant crustal extension unless it is associated with favorable plate kinematics (i.e., with a passive rifting component). This is confirmed by Morley et al. (1999) who report that combined data from seismic refraction, seismic reflection, seismological, and geological studies show that the asthenosphere rises underneath the EARS by both active and passive mechanisms triggering partial melting of the upper mantle, and that consequently magma bodies are emplaced in the crust (Morley et al., 1999) (Fig. 3.7).

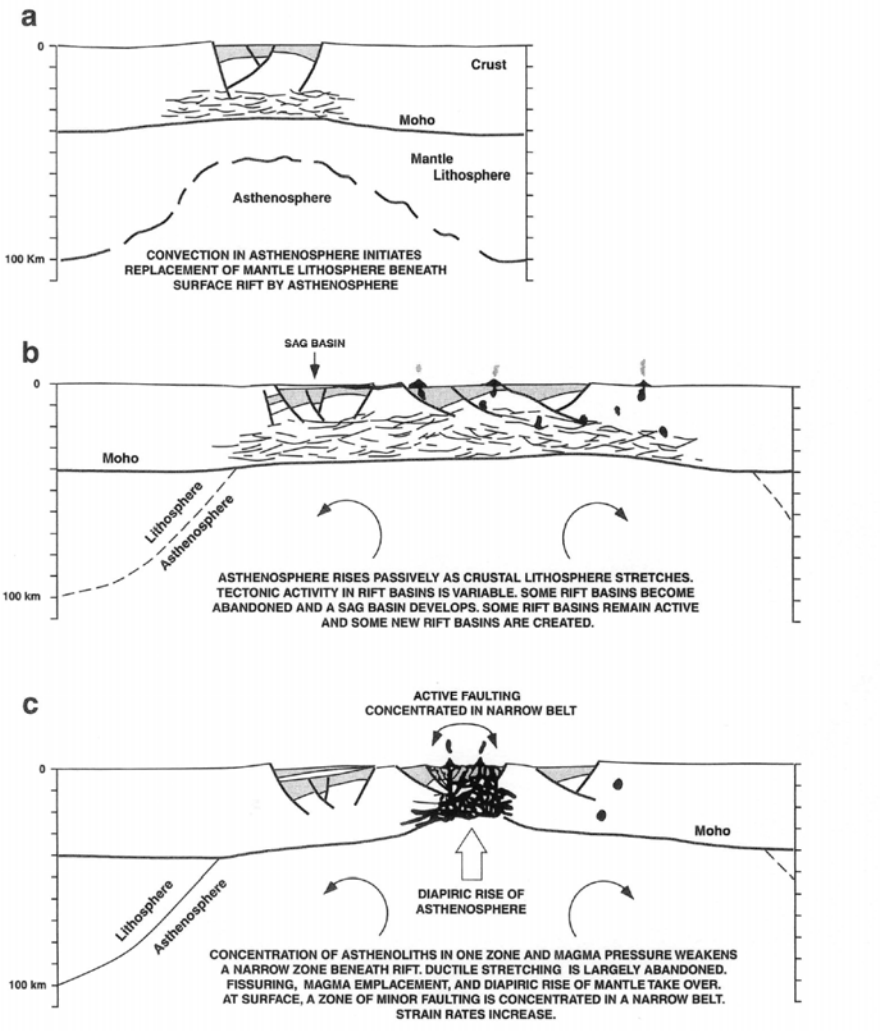

Fig. 3.7 - Schematic cross-sections illustrating the tectonic development of a continental rift system based upon the EARS (From Morley, 1994).

(2) Based on an average topographic elevation of the EARS of about 1000 m over 1000 x 1000 km^2 between its two branches (Ebinger, 1989), then an important mass deficit of at least 15 kg/m^3 (equivalent to a temperature increase of about 100-150 K) over a depth of about 200 km is needed to support such a topographic load in the case of static equilibrium (Zeyen et al., 1997).
(3) Rapid rotation of the near-surface stress field in the EARS can easily be explained by considering the effect of far-field stresses (Strecker et al., 1990; Bosworth et al., 1992). Bosworth et al. (1992) point out that it is unlikely that large-scale mantle circulation patterns can fluctuate at such rapid rates. Therefore, intraplate forces (ridge-push forces and local stresses due to rifting) are expected to significantly contribute to configuring the continental crustal stress regime. These regional stresses from ridge-push forces around Africa may be responsible for the rotation of the extension from E-W to NW-SE during the Quaternary (Bosworth et al., 1992; Ring et al., 1992; Chapola, 2005). However, the mantle plume remains the principal source of the forces which lead to rift formation (Zeyen et al., 1997; Ebinger, 2005) as expressed on the surface by the presence of flood basalts north of the EARS (Zeyen et al., 1997).

The evolution and propagation of the EARS is said to have been episodic (i.e. non continuous) (Girdler, 1983; Dawson, 1992; Zeyen et al., 1997; Nyblade and Brazier, 2002; Keranen and Klemperer, 2008) and to have been continuing over the last 45 Ma (Girdler, 1983; Ghebreab, 1998). Using radiometric dating of igneous rocks associated with the EARS, the oldest branch (the eastern branch) started to evolve ca. 44-38 Ma (Girdler, 1983). More recent work show that rifting started ca. 30-15 Ma and propagated southwards from Ethiopia into northern and central Kenya (Nyblade and Brazier, 2002). However, using (U-Th)/He thermochronometry, Pik et al. (2008) re-adjust the timing of the first phase of rifting to ca. 20-15 Ma. In the subsequent phase (ca. 12-10 Ma), the rift propagated further southwards. As it impinged on the rigid Tanzanian craton it did not substantially affect the region south of the North Tanzanian Divergence (south of 4°00'S) (Nyblade and Brazier, 2002; Macheyeki, et al., 2008b). Finally, as proposed by Fairhead et al. (1972) and MacIntyre et al. (1974), another rift propagation phase started ca. 1.2–1.3 Ma. This phase did affect the area south of the North Tanzanian Divergence zone and formed the Manyara-Dodoma rift, where rifting is still ongoing (Macheyeki et al., 2008b).

Based on the assumption that the lithosphere is stationary above the rising plume (Ebinger et al., 1989), Zeyen et al. (1997) summarize the evolution of the EARS by considering both concepts of active (due to rising plume) and passive (due to far-field stresses) rifting as follows (Fig. 3.8):
(A) A plume rises off-center beneath the Tanzanian craton due to the presence of compressional far-field stresses that affect the lithosphere before ca. 30 Ma.
(B) As the plume approaches the lithosphere, the eastern part of the Tanzanian craton and the surrounding area start to be uplifted. At this stage, compressional far-field stresses are superposed by extensional stresses due to bending and topography. This took place ca. 30-25 Ma.

(C) As the plume continuous to extend laterally, beneath the craton, it reaches the thinner lithosphere of the Pan-African realm. Extensional stresses increase and volcanism and subsequently rifting starts (25-10 Ma).

(D) The plume extends further to both sides. It has reached the western edge of the craton, forcing extension in the area of the western rift. This took place ca. 10 Ma and thus both the eastern and the western branches of the rift are born (e.g. Mariita and Keller, 2007). East of the craton the rift matures and new volcanic centers evolve east of the rift.

Zeyen et al. (1997) pinpoint further that their model can be applied to a scenario in which Africa is moving northeastward with respect to the plume (Bonavia et al., 1995).

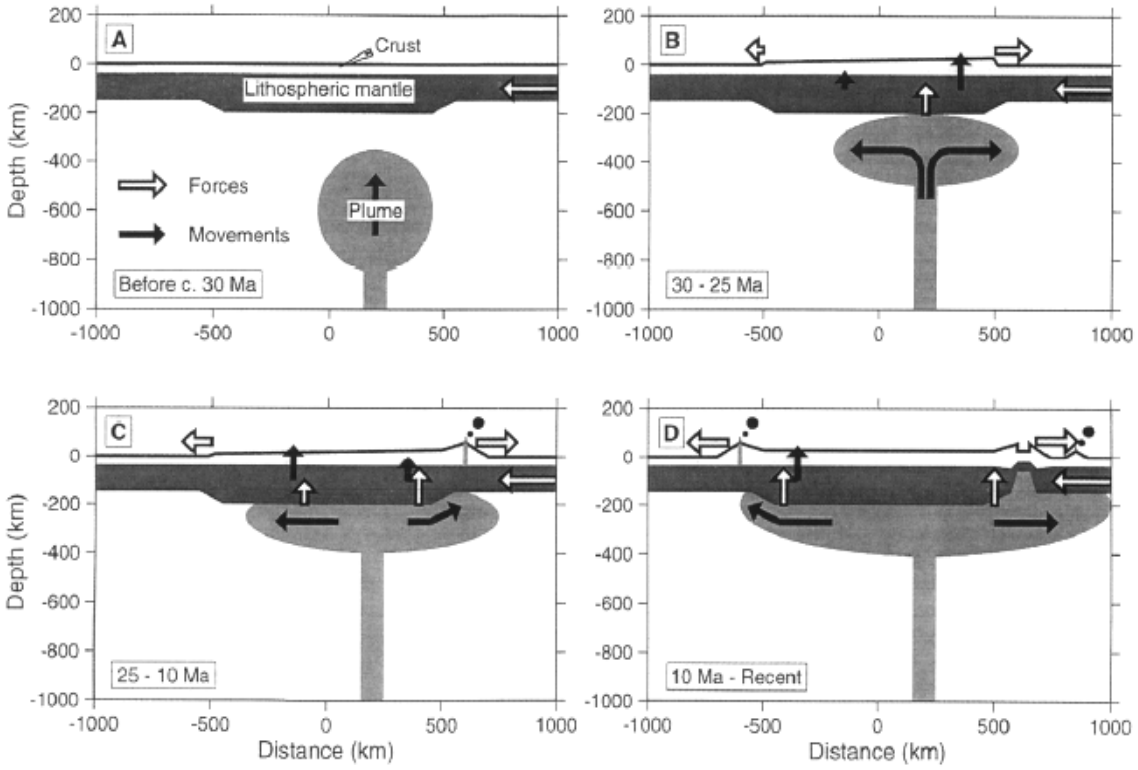

Fig. 3.8 - Sketch of plume and rift evolution in East Africa.
Different stages as discussed in the text. (From Zeyen et al., 1997).

In the kinematics framework, Nyblade and Brazier (2002) propose a model of rift development as shown in Fig. 3.9.

Finally, Tesha et al. (1997) state that the development of the EARS into the Tanzanian craton is favoured by the suture-thickened crust and that rifting in the eastern branch may have been localized by the presence of this suture-thinkened crust.

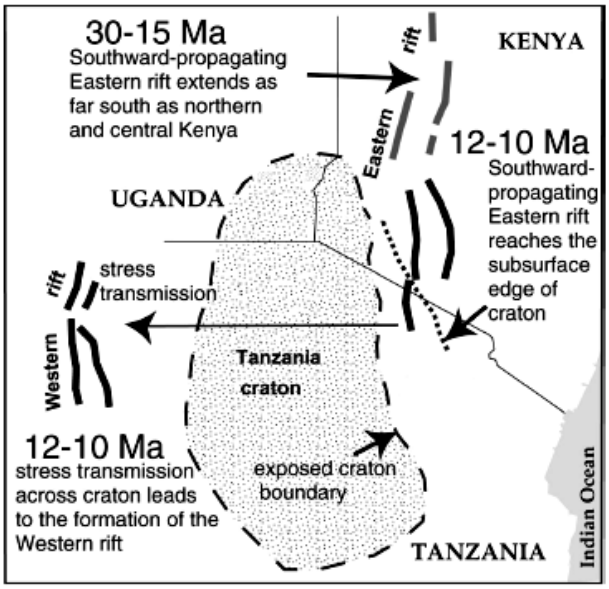

Fig. 3.9 - Kinematic framework for rift development in East Africa. Rift faulting in Eastern rift propagated southward from Ethiopia into northern and central Kenya ca. 30–15 Ma; ca. 12–10 Ma, the southward-propagating Eastern rift impinged on subsurface edge of rigid Tanzanian craton (bold dotted line), leading to extensional stress transmission across cratonic lithosphere and opening of Western rift. Subsurface edge of craton is shown only where known (From Nyblade and Brazier, 2002).

3.2. Geological setting of the Dodoma area

3.2.1 Geographic context of the Dodoma area: location and morpholoy

The study area (i.e., the area around Dodoma) is located within the eastern branch of the EARS between 5°00'-7°00'S and 34°50'-36°00'E (Fig. 1.4; 3.10a,b), i.e. south of the North Tanzania Divergence (NTD) Zone. The area can be easily reached from the Capital city of Tanzania (Dodoma). Cenozoic rifting in this part of the Tanzanian craton has not brought up spectacular reliefs (e.g., Macheyeki et al., 2008a). The highest Cenozoic-related relief is in the order of 200-300 m from the undisturbed surface. A unique morphological characteristic of the Dodoma area is a lozenge/rhombic pattern of normal faults (Fig. 3.10b) bounding wide, depressed areas (Macheyeki et al., 2008a; 2008b).

3.2.2 Basement geology in the Dodoma area

3.2.2.1 Lithology, structure and basement control

The Dodoma area is located within the Dodoman metamorphic-granitoid belt (the Dodoman tectonic domain), which is part of the granitoid Tanzanian shield (Fig. 3.10a) and was formed by migmatization and stabilization by granitic intrusions (Wades and

Oates, 1938; Fozzard, 1962; Barth, 1996). It comprises high-grade metamorphic rocks, such as granulites and charnockites, with steeply dipping E-W trending foliation (Coolen, 1980).

Whole-rock radiometric dating of the Tanzanian craton indicates that the ages of the migmatites and granitic complexes of the Dodoman tectonic domain range from 2.5 Ga to 1.87 Ga (Wendt et al, 1972; Gabert, 1973; Gabert and Wendt, 1974; Bell and Dodson, 1981). The Tanzanian craton (Fig. 3.10a) is surrounded on its southern and eastern sides by the Paleoproterozoic Usagaran tectonic domain (Mruma, 1995; Fritz et al., 2005). The eastern extension of the Usagaran tectonic domain is poorly defined as it was reworked into the Pan-African Mozambique belt (Pinna et al., 2004). Recent zircon age and Sm-Nd whole-rock data indicate that Archean and Paleoproterozoic gneisses dominate in the Mozambique belt. The gneisses (para- and orthogneisses associated with basic and ultrabasic rocks) were reworked during the Pan-African orogeny (Vogt et al., 2006). The role of the Paleoproterozoic Usagaran tectonic domain as to whether it affected or rejuvenated the craton is still under debate (Fritz et al., 2005). The Usagaran tectonic domain is thought to have formed by accretion onto the Tanzanian craton between 2.0 and 1.8 Ga. Deformation occurred in a strike-slip regime (Fig. 3.10a,b), in an island-arc setting. The Mozambique belt was formed by oblique collision between East and West Gondwana with westward thrust propagation during the Pan-African orogeny (0.65-0.58 Ga). Within the Usagaran tectonic domain, the Pan-African overprint occurred in semi-ductile to brittle facies, while in the East Gondwana block (eastern granulites) deformation is of lower crustal level, very high grade. North of Dodoma, the presence of Usagaran remnants between the Tanzanian craton and the Mozambique belt is not clear.

The basement in the Dodoma area is characterized by folds with consistent ESE-WNW fold axes. These structures are thought to have developed during the Early Archean Dodoman and Nyanzian orogenies (Holmes, 1952; Shackleton, 1986). A recent map by Pinna et al. (2004) shows E-W-trending thrust faults (dipping towards the north) south of the study area and NNE-SSW- to NNW-SSE-trending thrust faults (dipping towards the east) along the eastern and northeastern margins of the craton. These structures seem to be affected by the rift-related structures (e.g., Fig. 3.10b) and they are thought to represent remnants of Precambrian structures that controlled the Cenozoic structures. However, to date, there are no detailed published works regarding the Precambrian fabrics of the rocks in the Dodoma area. Internal reports by the Geological Survey of Tanzania show that the Dodoma area is characterized by a complex array of Precambrian structures.

Most Cenozoic rift structures are located along the boundary between the two main crustal blocks (i.e., the Usagaran tectonic domain and the Mozambique belt), in the reworked Archean Dodoman tectonic domain (Fig. 3.10b). Although there is only limited literature on Cenozoic related structures, structural geology suggests that the Precambrian structural control is important in the area. Precambrian structures, such as shear zones and faults, have a broad range of orientations due to the fact that the Dodoman tectonic domain has experienced several episodes of compressional and extensional tectonism over its ~ 3 Ga history. These include subduction and collision during the formation of

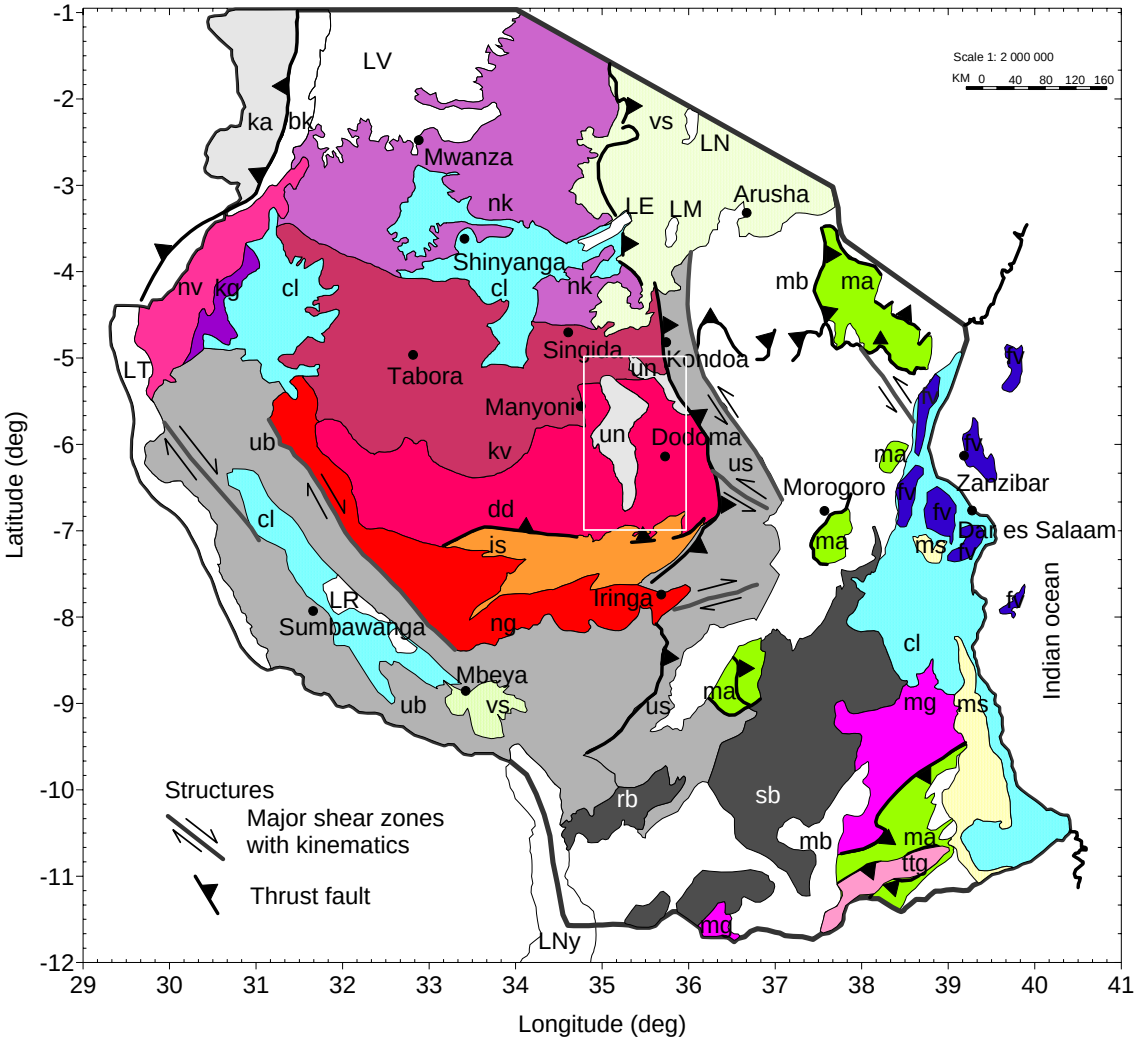

Fig. 3.10a - CENOZOIC FORMATION: un = undifferentiated Neogene to Quaternary continental sedimentary formations; cl = continental and lacustrine sedimentary formations; vs = Neogene-Quaternary volcanic formations; fv = Paleogene-Neogene sediments: marine, lacustrine and fluvio-marine formations. PALEOZOIC and MESOZOIC BASINS: ms = cretaceous sediments: marine and continental formations (sandstone, conglomerate); rb = Karoo formations in the Ruhuhu basin; sb = Karoo formations in the Selous basins. NEOPROTEROZOIC DOMAINS: bk = Neoproterozoic to Cambrian detrital sediments: Manyovu Red Beds, Ikorongo group; nv = Neoproterozoic volcano-sedimentary formations: Uha group, Nyamori Supergroup; kg = Neoproterozoic sedimentary formations (Kigonero Flags Group, Nyamori Supergroup, formerly known as Bukoban Sandstone); mb = Mozambique belt; ma = Neoproterozoic high-grade mafic and felsic granulite, gneiss and migmatite granulite-facies metamorphism, interlayered with amphibolite, marble, quartzite, schist and mylonite. MESOPROTEROZOIC DOMAINS: ttg = Mesoproterozoic-Neoproterozoic Tonolite Trondjemite Granitoids and migmatites; mg = Mesoproterozoic orthogneiss (ca. 1.19-0.0945 Ga) affected by Neoproterozoic high-grade metamorphism (Songea and Kimambi groups); ka = Mesoproterozoic Karagwe-Ankolean detrital metasediments (≥ 1.37 Ga). PALEOPROTEROZOIC DOMAINS: ub = Ubendian belt; us = Usagaran belt. ARCHEAN BASEMENT: ng = Neoarchean granitoid; nk = Neoarchean TTG granitoid and sediments (Nyanzian and Kavirodian Supergroups); kv = Neoarchean-Undifferentiated granitoid, migmatite, mafic and ultramafic rock: sediments of the Kavirondian Supergroup; dd = Dodoman Group (ca. 2.90-2.50 Ga); is = Isangan group (ca. 3.0-2.85 Ga). BODIES: LV = Lake Victoria; LT = Lake Tanganyika; LR = Lake Rukwa; LNy = Lake Nyasa; LE = Lake Eyasi; LM = Lake Manyara; LN = Lake Natron (modified after Pinna et al., 2004).

the ~ 2 Ga Usagaran belt, another episode of subduction and collision during the Pan-African orogeny at ~ 700 Ma, and, finally, development of the East African rift during the Cenozoic (Chesley, 1999). The recent structures have inherited the Precambrian structural fabric (Fairhead and Stuart, 1982; Macheyeki et al., 2008b).

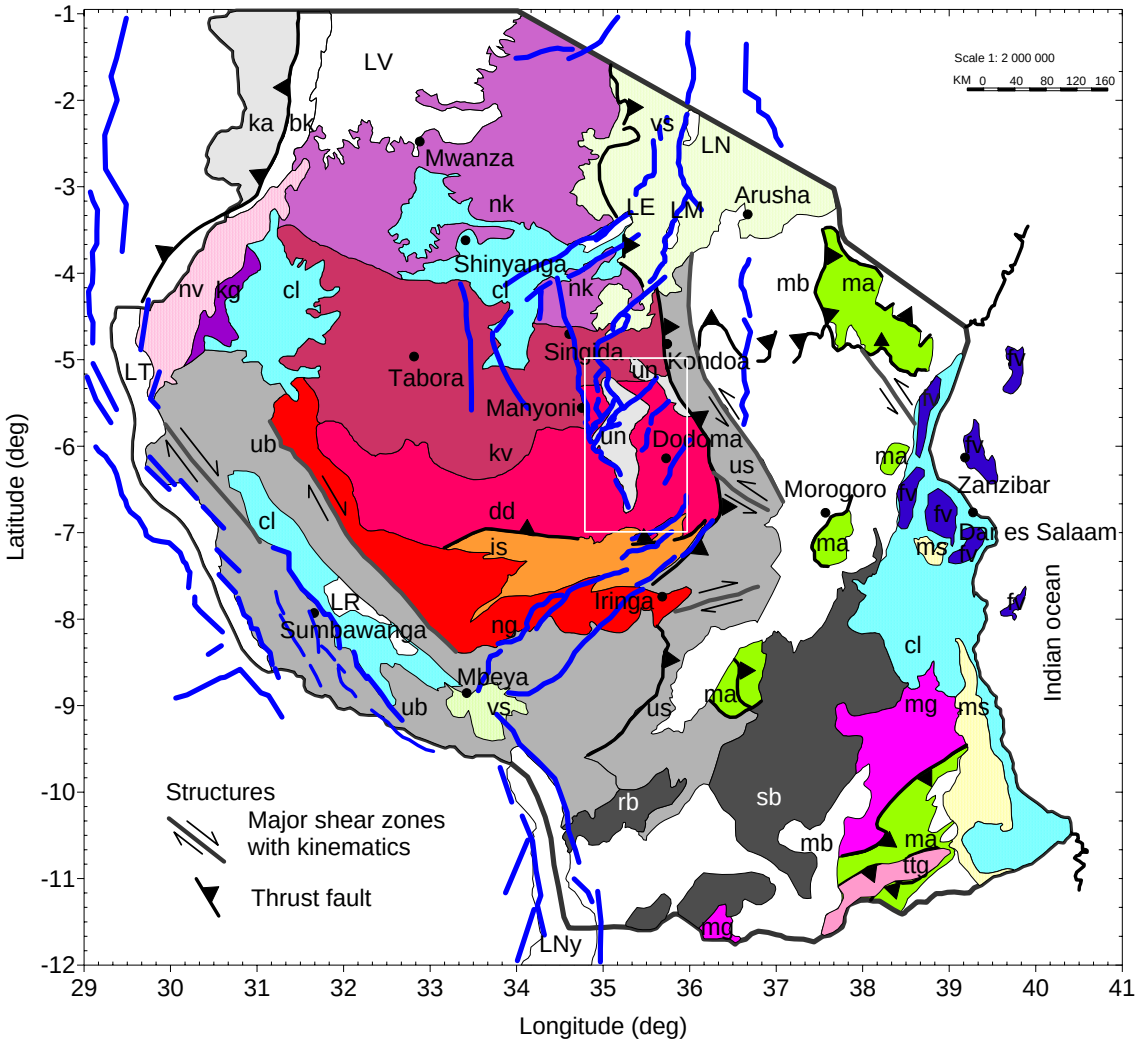

Fig. 3.10b - Cenozoic EARS (in blue) in Tanzania versus the geology of Tanzania. Thin blue lines represent most recent active faults characterized by fault scarps ≤ 50 - 60 m. Not the lozenge/rhombic pattern of Cenozoic rifts in the study area, defined by NW-SE, NE-SW and N-S faults. Other details are as in Fig. 3.10a. (modified after Pinna et al., 2004).

3.2.2.2 Basins

There exists only one relatively significant basin in the study area: i.e., the Bahi depression, located about 40 km west of Dodoma town (Fig. 3.10a,b). This basin has a width of ~ 50 km and total length of ~ 150 km. It is filled by predominantly silcrete-rich sediments (i.e., the so-called the Kilimatinde Cement) and other continental sedimentary formations of undifferentiated Neogene to Quaternary age (Pinna et al., 2004). The basin

separates two NE-SW trending antithetic faults; the southeasterly dipping Bubu fault and the northwesterly dipping Hombolo fault. Details about the faults are given in Chapter 5.

3.2.3 Deep structures in the Dodoma area

The Dodoma area is underlain by the Archean Tanzanian craton, which is considered to be a riding block characterized by a relatively deep cold root (e.g. Simiyu and Keller, 1997; Nyblade and Keller, 2002; Mariita and Keller, 2007). There is evidence that the Cenozoic EARS has avoided this rigid cold block (e.g. Ebinger, 1989; Tesha et al., 1997; Nyblade and Keller, 2002; Zeyen et al., 1997), but to what extent exactly remains debatable.

Studies that integrate the new map of P-wave velocities for the uppermost mantle beneath the Tanzanian craton with results from other geophysical data (Nyblade and Brazier, 2002) show that the mantle lithosphere beneath the Tanzanian craton occurs at a depth of about 150-200 km (Nyblade and Brazier, 2002); this can be taken to be the depth of the mantle lithosphere in the study area. The mantle lithosphere is thick and depleted of minerals (Chesley et al., 1999; Nyblade and Brazier, 2002) as revealed by Re-Os studies of mantle xenoliths (Chesley et al., 1999). To the contrary, the mantle lithosphere in Kenya is at a much shallower depth and the crust is much thinner there (e.g., Petit and Ebinger, 2000; Tessema and Antoine, 2004; Mariita and Keller, 2007).

3.2.4 Origin and evolution of rifting in the Dodoma area

As expressed in both volcanic and tectonic activities of the rift faults (timing constrained by dated volcanics and lacustrine sediments), Late Cenozoic rifting in the Dodoma area occurred in two different stages (legends of the published 1:125000 geological maps of Tanzania; Dawson, 1992), corresponding to changes in stress field (Strecker et al., 1990; Bosworth et al., 1992; Mugisha et al., 1997). In northern Tanzania, the first rifting stage started in the Late Miocene, with faulting followed by volcanism. The oldest dated volcanic rock is 8.1 Ma old (Dawson, 1992). At this stage, wide tectonic depressions developed and large amounts of basic magma formed large shield volcanoes.

A second important phase of faulting is dated between 1.3-1.2 and 0.9 Ma (Fairhead et al., 1972; MacIntyre et al., 1974) and was followed by a period of relatively minor but predominantly explosive volcanic activity, involving nephelinite, phonolite and carbonatite. In Central Kenya, the stratigraphy of the Miocene volcanic deposits has been refined by Mugisha et al. (1997), based on the new Ar-Ar dating of Deino et al. (1990). No recent radiometric ages on the rift-related volcanism in the NTD are available from the literature.

The eastern branch of the Cenozoic EARS in Kenya and northern Tanzania developed mainly within the Mozambique belt, 50-150 km east of the exposed margin of the Tanzanian Craton. It is characterized by a positive long-wavelength Bouguer anomaly (Nyblade and Pollack, 1992; Tesha et al., 1997). This anomaly has a first component with

a signature derived from shallow rift basins and a second component with a short-wavelength gravity low attributed to a discrete crustal thickening (2-5 km). The latter is interpreted as forming a crustal root along the suture between the Tanzanian craton and the Mozambique belt and this suture-thickened crust is proposed to have localized the rifting (Tesha et al., 1997).

3.2.5 Seismicity in the Dodoma area

The distribution of seismic epicenters in the Dodoma area is examined on the basis of two different sources of data: (i) an international seismic catalogue recorded during the instrumental period (for Africa) between early 1921 and late 2006, and (ii) the catalogue of earthquakes recorded during 1994-1995 by the Tanzania Broadband Seismic Experiment. The international seismic catalogue is compiled from USGS data and contains 122 teleseismic earthquakes with magnitudes ranging from m_b = 3.5 to 6.2. The strongest of these events occurred on 16 April 1922 (Fig. 3.11).

In October 1997, R.A. Brazier compiled a regional catalogue using data from the 1994-1995 Tanzania Broadband Seismic Experiment Project (Nyblade et al., 1996). For the region between 3-7°00'S and 34-37°00'E, this catalogue contains 1,395 earthquakes with epicenter locations and magnitudes (when determined) ranging from m_b = 0.8 to 5.9. These were recorded between May 1994 and May 1995, with the strongest earthquake on 12 December 1994.

The compiled international catalogue from teleseismic earthquakes (1921-2006) contains less numerous data but with higher magnitudes (m_b = 3.5-6.2) compared to those from the Tanzania Broadband Seismic Experiment catalogue. These are mainly teleseismic earthquakes recorded by the world regional seismic network. They are distributed along a broad N-S belt, mainly between 35°00'E and 36°00'E, between the Ngorongoro crater, Arusha, Singida and Dodoma. This seismically active zone corresponds to the region characterized by the highest concentration of young fault scarps.

For the Tanzania Broadband Seismic Experiment catalogue (1994-1995), the configuration of this temporary network ensures a homogeneous spatial coverage within the studied area. The distribution of epicenters from this catalogue reinforces the trend shown by the data of the international catalogue. Several areas with high concentration of epicenters can be observed.

Earthquake shaking has regularly been reported by local people, sometimes with significant macroseismic effects. In addition to the m_b = 5.5 earthquake of 4 November 2002 in the Chenene Mountains, the m_b = 6.1 earthquake of 7 May 1964, which occurred along the southern border of the Eyasi basin, was also strongly felt. No other details are available so far. Surface dislocations in the form of fractures are also reported by local villagers in their fields, in the Chenene Mountains close to the Great North Road and near Chenene village (Macheyeki et al., 2008b).

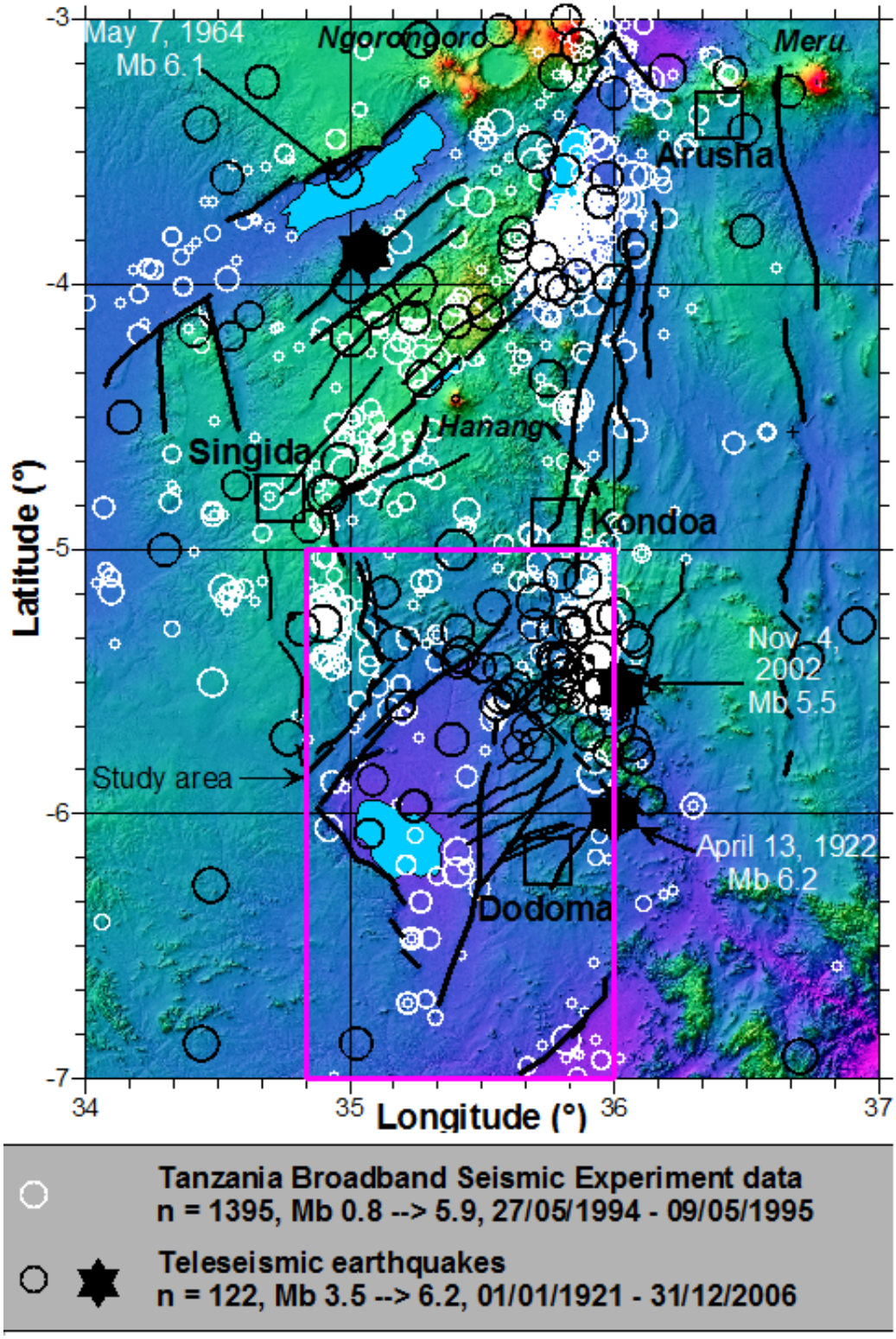

Fig. 3.11 - Seismicity map of the Dodoma area (After Macheyeki et al., 2008b)

3.2.6 Thermal springs in the Dodoma area

Thermal springs are known to be frequent in the EARS. They are also known since long times by local people. The most important ones are reported on the geological maps and even on the topographic maps. They have attracted particular attention as they can be the source for commercial salt deposits and noble gases. In Tanzania and in the study area in particular, a lot of thermal springs are known and some of them have been studied in relative detail between 1950 and 1962 by the Geological Survey of Tanganyika. After the discovery in 1947 of helium, argon and nitrogen in the gas emitted by the Nyanza cold brine spring at Uvinza (West Tanzania), intensive investigations were carried out by the East African Office of the U.K. Atomic Energy Authority in 1957 and 1958 for evaluating the potential of some springs as a source of helium. The main localities explored were the Maji Moto field (near Musoma, Lake Victoria in North Tanzania) and the Manyeghi helium springs along the Mponde fault within the study area (James, 1967a). They belong to a group of thermal springs with Na- and K-dominated salts in brines and He-, Ar- and N_2-bearing gases (Macheyeki, et al., 2008b).

Table 3.1 gives a synthesis of the available physical and chemical data compiled from the work of James (1957; 1958; 1967a), Harris (1958; 1959) and Walker (1967). Since then, no major additional important analytical work has been done on these springs. Isotopic data outside the study area (e.g., Maji moto springs) show that the $^{40}Ar/^{36}Ar$ ratio amounts to about 800/1 in the spring gases while it is about 300/1 in the air (Morgan in James, 1967b) for the Maji Moto springs outside the study area. Conversely, the measured $^{14}N/^{15}N$ ratio in the spring gas (270/1) is similar as for atmospheric nitrogen. Morgan concluded that as nitrogen in the spring gases is of atmospheric origin, the argon and helium have been added in a substantial way from a juvenile source, probably of radiogenic origin. He suggests that argon and helium have their source deep in the crust, channeled to the surface by old shear zones. Similarly, Arad and Morton (1969) also consider that in the thermal springs of the western rift branch in Uganda, most of the solutes are from a juvenile source while the water is probably meteoric.

In the Manyara-Dodoma area (Fig. 3.12), many of the springs with nitrogen/helium occur in an arid environment, and are situated in crystalline-basement rocks with little or no sedimentary cover, relatively far from centers of volcanic activity. Most of them are also connected with major fault lines, sometimes indirectly by means of antithetical faults as in the Manyeghi helium spring field (geology detailed by Fozzard, 1959). These major rift faults are inferred to penetrate deeply in the crust. In conclusion of his review, James (1967a) favors a mixed meteoric and juvenile source for the thermal springs. He further suggests that the juvenile source could be volatile components emanating from the mantle, rather than from magmatic bodies.

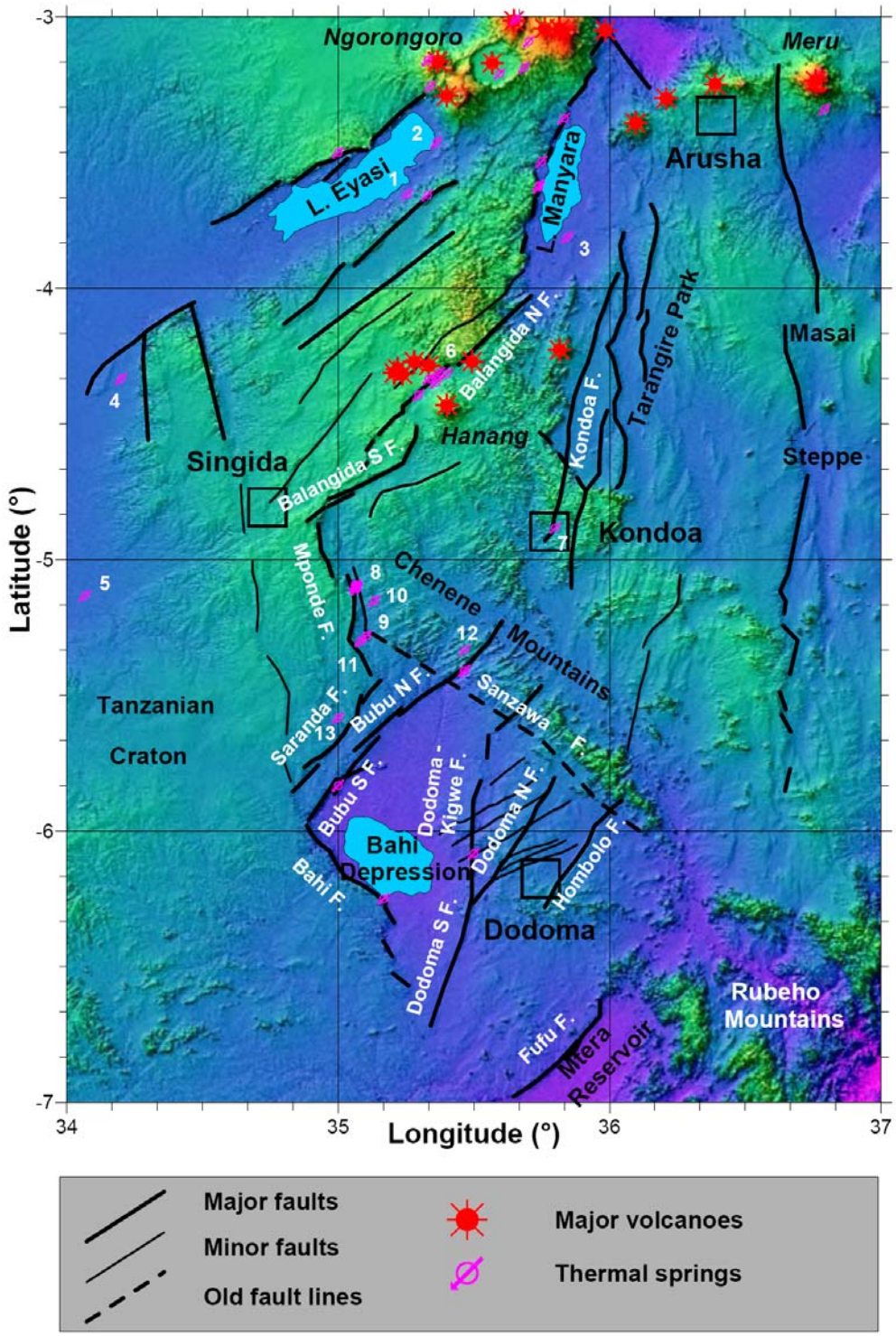

Fig. 3.12 - Neotectonic structure of the Manyara-Dodoma rift segment in Central Tanzania, shown on the SRTM topography. In addition to the major towns (in black) and the main physiographic names (in white), the name of the major faults discussed are given (from Macheyeki et al., 2008a; some faults renamed in Fig. 5.1). All features displayed (faults, volcanic centres and thermal springs) belong to the most recent rift stage that initiated 1.2-1.3 Ma ago and that is still active. The physical and chemical data from the thermal springs numbered 1 to 13 are listed in Table 3.1 (from Macheyeki et al., 2008b).

Table 3.1 - Physical parameters and chemical composition of gas and water from the major thermal sites. Compilation from James (1957; 1958; 1967a), Harris (1958; 1959) and Walker (1967). The springs are located on Fig. 3.5 using their spring number

Springs													
Spring name	Eyasi	Eyasi	Kinyoo	Itebu	Isanza	Golai	Kondoa	Manyeghi	Sumbaru	Takwa	Mponde	Gonga	Hika
Spring number	1	2	3	4	5	6	7	8	9	10	11	12	13
Fault structure	Eyasi	Eyasi	Manyara			Balangida	Kondoa	Mponde	Mponde	Mponde	Mponde	Bubu	Saranda
Location													
Latitude (°)	-3.654	-3.4637	-3.812	-4.333	-5.133	-4.312	-4.883	-5.100	-5.282	-5.152	-5.300	-5.333	-5.583
Longitude (°)	35.255	35.361	35.845	34.200	34.067	35.372	35.800	35.064	35.103	35.134	35.083	35.467	35.000
Physical Properties													
Temp (°C)	---	35	25	22		30	31	33.1 ± 4.9		38	42	47	28
Water flow (l/hr)	---	small	small	3300		110	90800	227000				6800	8200
Gas flow (l/hr)	---	small	small			small	100	3650		100	200	15	5
Gas analysis, vol.%													
CO_2	0.2	8.2	0.7	4.2		3.8	3.9	1.1 ± 0.4		1.6	0.2	1.4	0.6
H_2S	< 0.1	1.0	0.2	0.4		0.8		0.1 ± 0.2		0.9	trace	0.5	trace
CO	< 0.1	0.2	1.1	0.1								0.4	0.2
O_2	0.8	0.3	0.4	0.4		0.4	2.7	0.1 ± 0.1		0.1	0.2	n.d.	n.d.
H_2	0.2							0.2 ± 0.3		0.5		n.d.	n.d.
CH_4	< 0.1	80.3	88.5	1.6				0.2 ± 0.1		1.1	0.4	1.4	2.9
He	5.7		0.07	0.74		3.7	0.3	5.4 ± 0.7		7.0	10.2	7.7	7.1
Ar				1.02			1.0	1.5 ± 0.1		1.3	1.5		
N_2	93.1	10.0	9.0	91.6		91.3	91.6	91.5 ± 1.2		87.5	87.5	88.8	89.2
Water analysis (ppm)													
NaCl	8490		2965	26	643	4320	193	1434 ± 152	1250	1010	1,189	211	89
Na_2CO_3	1730		8510			1900		76 ± 50		27	48		
$NaHCO_3$	4630			396	215	2450		764 ± 79	328	277	264	160	150
Na_2SO_4	1000			30	231	1690	58	643 ± 151	544	649	530	220	49
NaF	150			2	17	78	2	24 ± 3	19	9	24	11	11
KCl						142		18 ± 2		15	11		
$Ca(HCO_3)_2$				89	32		248	39 ± 8	24	88	20	218	52

Chapter 4

Methods of Investigation

4. Methods of investigation

For this study, the main goal was to identify and map active faults in the area to the north of Dodoma, characterize those faults and investigate their geometry versus the Precambrian and Quaternary geology and morphology and finally submit a selection of these faults to a detailed paleostress and paleoseismic analysis.

The identification and characterization of active faults involved an interactive office work from 2005 to 2007 and two main field missions from 2006 to 2007. The methods that were used during the office work and the field missions will be described in this chapter.

4.1. Identification of active faults

One of the first steps in this investigation was the identification of the potentially active faults in the study area, bearing in mind that the region is characterized by a complex network of faults, some dating back as far as the Precambrian (e.g., Wades and Oates, 1938; Fozzard, 1962; Barth, 1996; Fairhead et al., 1972; MacIntyre et al., 1974; Fritz et al., 2005). This entailed the use of available published 1:125,000 (Fozzard 1961) and 1:2,000,000 (Pinna et al., 20004) geological maps and unpublished maps at various scales, archived both at the Geological Survey of Tanzania (in Dodoma, Tanzania) and at the Royal Museum for Central Africa (Tervuren, Belgium). Corresponding 1:50,000 topographic maps for the area were also used.

Faults cutting across Cenozoic deposits, such as the ones across the Bahi depression, which is mainly filled by Neogene to Quaternary deposits, were of particular interest (see also Fig. 3.10 for a regional geological map).

Having marked possibly active faults using the available maps, the next step was to fine-tune their geometry and position and to identify and map additional, previously unmapped, potentially active faults using the 90 m resolution Shuttle Radar Topography Mission (SRTM) data. This analysis was conducted by working interactively within a Geographic Information System (GIS), in which both geologic and topographic maps were overlain in order to decipher faults affecting Quaternary deposits from those which do not. The analysis of 90 m resolution SRTM data was made after geo-referencing and processing them into digital elevation models (DEMs) using ENVI (i.e., a commercial software package for handling geospatial imagery) and representing them in map form with colour scale in function of elevation. These DEMs were integrated with other geo-referenced documents (e.g., geological and topographical maps) using MapInfo (i.e., a commercial GIS).

4.1.1 A brief historical background of SRTM-DEM data

The SRTM-DEM at 90 m resolution is an important tool for mapping active faults, especially in remote and relatively poorly known areas, as well as for the computation of vertical offsets and for the analysis of the segmentation of given faults. These data (in raw form) were downloaded from site http://www.seamless.usgs.gov.

The SRTM project generated the first, detailed, global digital elevation model of the Earth using radar interferometry. The data were produced/released in 2002-2004. It was the result of a collaborative effort by the National Aeronautics and Space Agency (NASA) and National Imagery and Mapping Agencies (NIMA) of the USA, and the German and Italian Space Agencies (Rabus et al., 2003).

The base model of the SRTM data consists of one arc-second (30 m resolution) elevation data. The currently available 90 m resolution data are generated by selecting the centre sample of the 3 x 3 array of one arc-second points surrounding the post location. In other words, for three arc-second data, each point is the average of the nine one arc-second samples surrounding the post location. By doing so, a superior product is produced in which the high frequency "noise", which is characteristic of radar-derived elevation data, is reduced. This is similar to averaging pixels in radar images to decrease the effects of speckle and increase radiometric accuracy, although at the cost of horizontal resolution. Details regarding the acquisition, processing, interpretation, and limitations of SRTM data are found in Farr and Kobrick (2000) and Rosen et al. (2000).

The 90 m resolution SRTM data were released in spring 2004 for the African continent. Before that, the only available digital relief data for Africa were from the ETOPO 30 DEM, of 30 arc-second (900 m) resolution. The present work is the first of this kind using the high resolution SRTM-DEM at 90 m resolution, at least in Africa…

4.2. Characterization of active faults

Having identified and mapped the potentially active faults using the combined techniques discussed above, the next step was to characterize their morphology (see Table 4.1 for detailed definition of scarp morphology parameters). The aim of such characterization was mainly to determine if the studied faults are segmented. This was done using the 90 m resolution SRTM-DEM by extracting digital topographic data (Table 4.2) along selected profiles drawn perpendicular to the fault strike. These topographic profiles were further studied in order to define the approximate topographic offset associated with the related faults.

Table 4.1 - Definition of fault scarp parameters (McCalpin, 1996).

		Parts of the profile
Head	H	Edge of the uneroded original upthrown block surface
Crest	C	Point of maximum slope curvature (convex-up) between the scarp head and the steepest part of the scarp face
Face	F	Point of the scarp profile between the crest and the base
Base	B	Point of maximum slope curvature (concave-up) between the steepest part of the scarp face and the scarp toe
Toe	T	Edge of the uncolluviated original down thrown geomorphic surface
		Angular measurements
Far-field slope	A	Gradient of the faulted geomorphic surface
Maximum scarp slope	Θ	Gradient of the steepest part of the scarp face
Fault dip	B	Dip angle of the fault plane underlying the scarp face
		Height measurements
Leveled height	L	Vertical separation between the scarp toe and head, usually obtained by simple leveling. This measurement is typically used in rapid reconnaissance investigations (Baljinnyam et al., 1993; McCalpin, 1996)
Scarp height	H2	As defined by Bucknam and Anderson (1979), the vertical separation between intersections of the plane formed by the displaced original geomorphic surface
Surface (vertical) offset	SO	Vertical separation between the projection of original upthrown and downthrown geomorphic surfaces
Vertical fault displacement (throw)	H1	Vertical distance between intersections of the fault plane, and planes formed by the displaced original geomorphic surfaces
Net fault slip	*Ns*	Distance, measured on the fault plane, between two points that were originally in contact at the fault plane before faulting. For pure dip-slip motion, equals the distance measured along the fault plane, between the intersections of the fault plane with the planes formed by the displaced original geomorphic surfaces
Throw on main fault	T_m	Vertical component of fault displacement of the main fault
Throw caused by back tilting	T_t	Vertical component of fault displacement on a main or antithetic fault induced by back-tilting of the downthrown block
Throw on antithetic fault	T_a	Vertical component of fault displacement on an antithetic fault
Net throw	T_{net}	Vertical component of fault displacement across the entire deformation zone, calculated a difference between synthetic throws (H1, T_m) and antithetic throws (Tt, Ta), or calculated from the surface offset between projected upthrown and downthrown surfaces.

4.2.1 Extraction and processing of topographic profiles

Topographic profiles were extracted from the SRTM-DEM data across each fault using the Fledermaus software, at an average spacing of 5 km; the length of each profile was such that it covered both the hanging and the footwalls fully. The Fledermaus software allows an interactive 3D display of the DEM, but when sampling data for topographic cross sections, it generates intermediate points, so the data spacing along the profile is dependent on the length of the profile.

Table 4.2 - Example of format of digital topographic data extracted from SRTM-DEM. D stands for distance from origin of a profile. This is part of data in one of the topographic profiles from the Mponde fault, NW Dodoma.

D (m)	UTME	UTMN	Elevation (m)
0	750869.68	9495831.25	1821.08
20	750884.14	9495817.43	1821.59
40	750898.60	9495803.61	1822.09
60	750913.05	9495789.79	1822.52
80	750927.51	9495775.97	1822.98
100	750941.96	9495762.15	1823.41
120	750956.42	9495748.33	1823.81
140	750970.87	9495734.50	1824.22
160	750985.33	9495720.68	1824.65
180	750999.79	9495706.86	1825.05
200	751014.24	9495693.04	1825.40
220	751028.70	9495679.22	1825.84
240	751043.15	9495665.40	1825.51
260	751057.61	9495651.58	1824.98
280	751072.06	9495637.75	1824.25
300	751086.52	9495623.93	1823.33
320	751100.98	9495610.11	1822.06
340	751115.43	9495596.29	1820.65
360	751129.89	9495582.47	1818.76
380	751144.34	9495568.65	1815.77
400	751158.80	9495554.83	1812.55
420	751173.25	9495541.00	1809.1
440	751187.71	9495527.18	1805.32
460	751202.17	9495513.36	1801.24

The topographic profiles extracted from SRTM-DEM were processed in order to estimate the vertical offset associated with the morphological fault scarps using the following assumptions and procedures (as in Macheyeki et al., 2008a).

1. The undisturbed pre-Late Cenozoic flat (but inclined) morphological surface covered by the Kilimatinde Cement is taken as a reference on both sides of the fault line to evaluate the vertical offset of the hanging-wall relative to the footwall blocks. Where eroded down to the weathered basement, the Kilimatinde Cement has a thickness of 15 to 30 m. In the Bahi depression, the Kilimatinde Cement is overlain by about 75 m thick Lake Beds of possible Plio-Pleistocene age. An assumption was made that the age of the sediments on the Bahi depression (hanging wall) is the same as that of sediments covering the footwall. *The Kilimatinde Cement is the oldest sedimentary formation in the Dodoma area, dominantly silcrete composed of silicified sandstone, but locally it can be also a calcrete or a ferricrete, formed in shallow evaporative basins developed on a quasi-planar land surface, between residual hills (Fozzard, 1961)*;
2. the profile is taken long enough so that the reference surfaces on both faulted blocks can be determined far enough from the fault scarp to minimise the erosion effects on the footwall block and the colluvial sedimentation at the foot of the scarp on the hanging-wall block;

3. the topographic profile is plotted with elevation against distance along the profile, and lines are fitted on the supposed remnants of the original morphological surface on the hanging-wall and footwall blocks (synonymous to far-field slopes in Fig. 4.1) respectively;
4. knowing the equations of these two lines, the vertical distance (vertical offset, SO in Fig. 4.1) between them is computed for the distance along the profile corresponding to the expected outcropping trace of the fault, at the base of the morphological scarp;

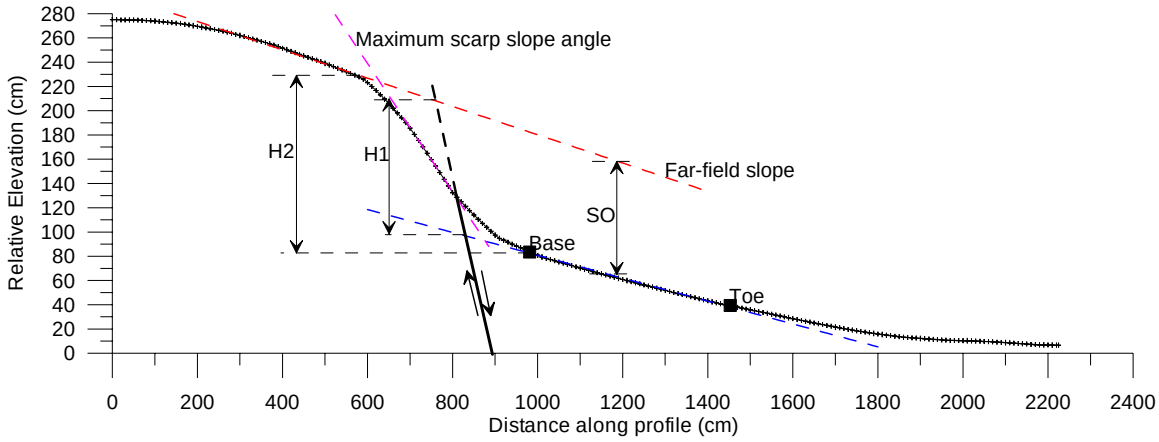

Fig. 4.1- A simplified diagram showing selected fault parameters. For definition and other details see Table 4.1 (After McCalpin, 1996).

Thereafter, these vertical offsets for each fault were plotted along the length of a given fault in order to obtain the "displacement profiles"; the latter are used to define fault segments as discussed in Chapter 5.

4.3. Determination of paleostress from active faults

When the active faults were identified and characterized, some of them were selected for detailed paleostress investigation (fault-slip data analysis).

4.3.1 Fault-slip data collection

Fault-slip data were collected during several field campaigns in March-September 2006, February 2007, May-June 2007 and November 2007, in a series of study areas selected on basis of analysis of the DEM and field verification (Fig. 6.1). These areas are northern part of Mponde fault (1a), southern part of Mponde fault (1b), middle part of Saranda fault (2), Gonga hot-spring field on the northern part of Bubu fault (3a), Magungu area along Bubu fault (3b), Makutupora area along the Bubu fault (3c), northern part of the

Makanda fault (4a), Hombolo area along the Hombolo fault (5), the Bahi fault (7), the Fufu fault (8) and Chenene village area (9). No paleostress data were taken from Maziwa fault (4b) and Chikola fault (6). Fault-slip data were collected on fault surfaces taking into account the presence or absence of slip on the fault surface, activation type (non activated, neo-formed, reactivated, or unknown), the presence or absence of striae in the format shown in Table 4.3.

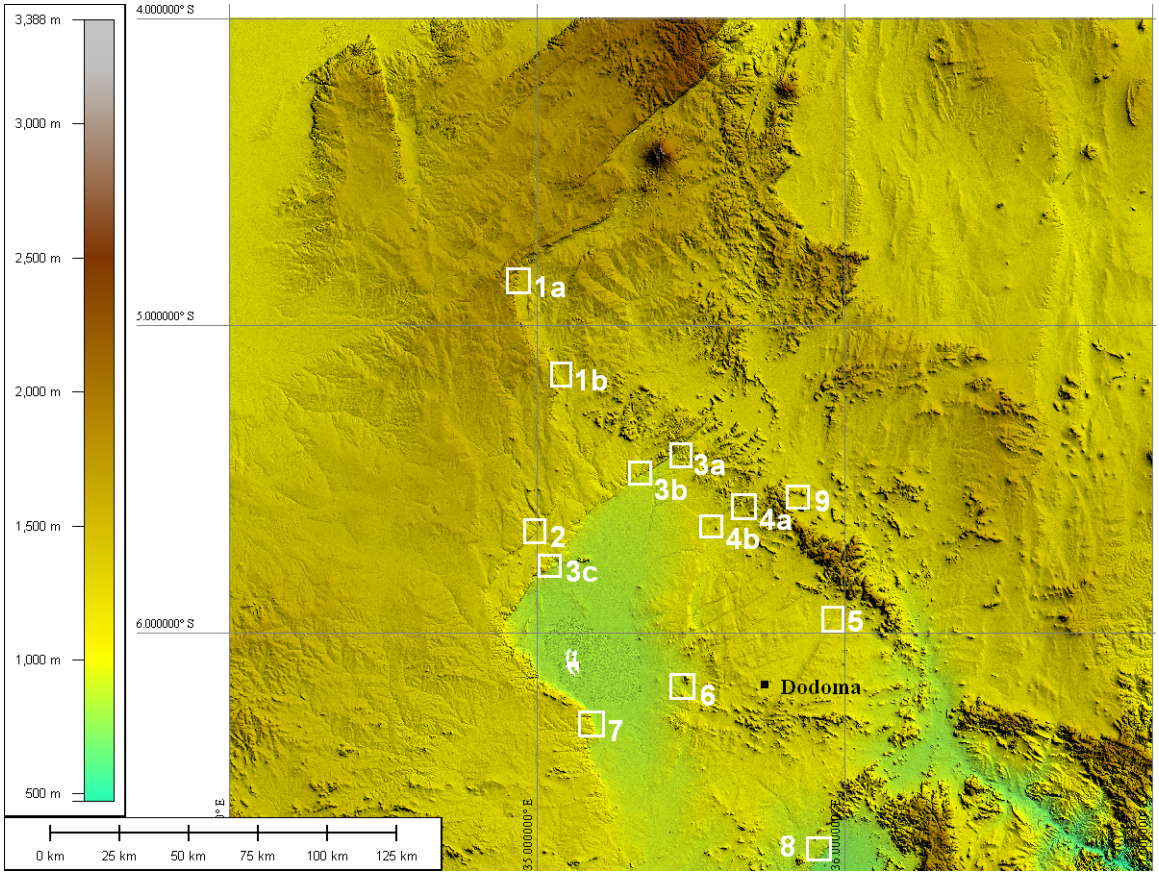

Fig. 4.2 - The SRTM-DEM of the Dodoma area showing the sample points. The dominant fault directions (i.e. NE-SW, NW-SE, NNW-SSE and N-S trending faults) can also be identified.

4.3.2 Fault slip data processing

Data processing for paleostress inversion was done using the new Win-Tensor program, developed by D. Delvaux, according to the procedure described in Delvaux and Sperner (2003) and using quality ranking scheme as in the World Stress Map project (Sperner et al., 2003; Fig. 4.3). The data were processed interactively, first using the "Right Dihedron Method", a graphical method for determination of the range of possible orientations of σ_1 and σ_3, and then using the "Rotation Optimization Method" (e.g., Fig. 4.4) of Delvaux and Sperner (2003). The "Rotation Optimization Method" is an iterative process, which involves successive rotations around the 3 principal stress axes and examination of the possible range of R values in order to find the stress tensor which minimizes a misfit

function. In this work, the misfit function F5 of the Win-Tensor program has been used (equivalent to function f3 of Delvaux and Sperner (2003)). It primarily minimizes the angular deviation between the observed slip lines and the modeled shear on every plane using the stress tensor that is being tested. In addition, this function also favours slip on the plane by reducing the resolved normal stress and enhancing the associated shear stress on the plane. This is performed in the following way: for each stress axis, the stress tensor is rotated by intervals of 5° anticlockwise (-5°) until -45° and clockwise (+5°) until 45°. For each step, the stress tensor is applied on the data selected and the value of the optimisation function is calculated. A regression curve is then fitted to the data (stability plots). The results are plotted graphically with the rotation angle on the horizontal axis and the value of the function on the vertical axis (e.g., Fig 4.4a). For the R value, the whole range of possible values (0 to 1) is checked (e.g., Fig. 4.4b). The stability of the 4 parameters of the reduced stress tensor can be estimated on the basis of these curves. The total range of the function variability is defined as the difference between the minimum and maximum values of the function F5 in the stability plots, expressed in percent of the total range of function values (from 0 to the maximum). The rotation stability corresponds to the amount of rotation needed to be performed in both clockwise and anticlockwise senses along the regression curve in order that the function F5 reaches a value which is 5 % higher than its minimum value. When computed this way, the clockwise and anticlockwise values for the axes stability are not necessarily identical. The same principle has been adapted for the stability of the stress ratio R.

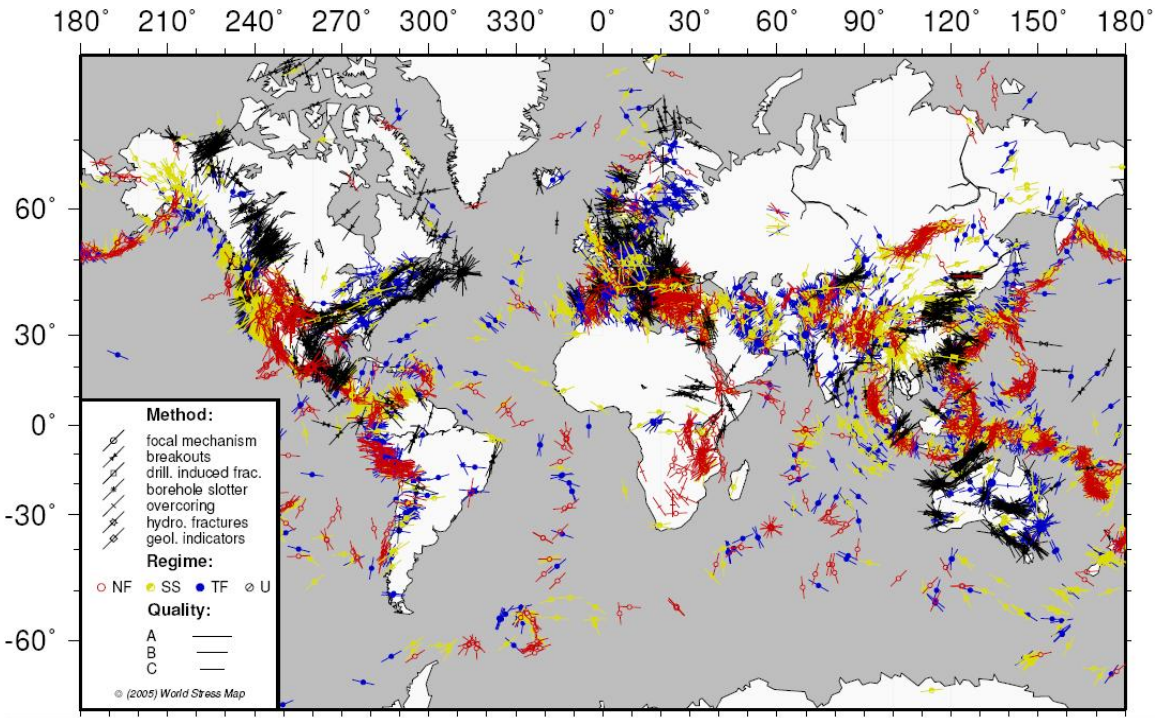

Fig. 4.3 - World Stress Map, release 2005. Shown are maximum horizontal stress orientations for qualities A, B, C. Symbols indicate type of stress measurement. Colours correspond to tectonic regimes for stress indicators deduced from focal mechanism solutions: red indicates normal, yellow strike-slip and blue thrust faulting regimes (From Barth, 2007).

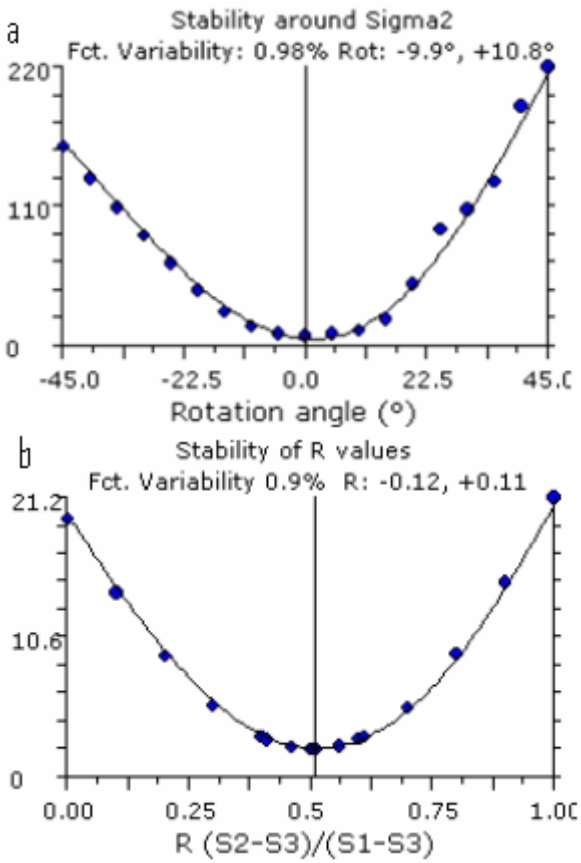

Fig. 4.4 - (a) Rotational optimization curve around sigma 2 (σ_2), (b) Rotational optimization curve around R. S1, S2 and S3 stand for σ_1, σ_2 and σ_3, respectively. In these diagrams (stability plots) the value of the misfit function F5 is plotted against the rotation angle for the stress axes and agains the R values for the stress ratio. The function variability corresponds to the ratio of the difference between the maximum and minimum values of F5, relative to the maximum possible range of the function (from 0 to its maximum), expressed in percent. The rotation stability corresponds to the amount of rotation needed to be performed in both clockwise and anticlockwise senses (or the amount of R values to be substracted or added) along the regression curve in order that the function F5 reaches a value which is 5% higher than its minimum value.

The quality ranking (QR: QRw for World Stress Map and QRt for Stress Tensor) can range from A to E: i.e., A = excellent; B = good; C = medium; D = poor; E = to be rejected. Quality ranking was obtained based on a series of parameters including (1) the number of fault data used in the stress determination (n), (2) the proportion of data used relative to the total data set (n/nt), (3) the confidence level in determination of the slip sense (CL) for faults (or fracture type for fractures), (4) the type of fault data used (DT: See Table 4.3 for definition), (5) the distribution of fault planes used (*Plen*), and (6) the distribution of slip lines (*Slen*). The overall quality of the tensor depends on these 6 parameters. Each of these parameters is assigned a quality factor according to threshold values defined in Table 4.4. Therefore, the parameter with the lowest rank is the limiting factor for the overall quality. In the World Stress Map, the quality factor (QRw) uses only the first 4 parameters. In the Win-Tensor program, the dispersion of the plane and line orientations has been added, defining a more restrictive quality factor (QRt).

Table 4.3 - An example of a field notebook on which fault-slip data were recorded. This format is in accordance to the TENSOR program (Delvaux and Sperner, 2003). These are parts of a data set from the Fufu fault, south Dodoma.

Project Code	Dodoma
Outcrop Code	A160507-7
Area Name	Fufu
Geologist	A.S. Macheyeki
Field Date	16/05/2007
Encoding date	14/06/2007
Magnetic North	+3
Latitude	06°38'34.5"S
Longitude	35°57'41.1"E
Outcrop Quality	
Outcrop Stratigraphy	Precambrian
Outcrop Lithology	Gneisses
Outcrop Structure	
Probable age of movement	Multiple
Default Input Mode	11

Fault-slip data	Input row data (User format)											
	Properties		Fault plane		Slip line							
Data Id	Format [a]	Type [b]	Dip angle	Dip direction	Dip angle	Dip direction	Slip Sense [c]	Confidence Level [d]	Activation Type [e]	Striae Intensity [f]	Subset Index [g]	Comments
A160507-7-001	11	4	82	334			X	X	2	0	1,0	Fault zone?
A160507-7-002	11	1	81	338	57	262	X	X	2	1	1,0	Fault zone?, reactivated
A160507-7-003	11	4	89	239			X	X	2	0	1,0	Fracture
A160507-7-004	11	1	81	143	24	229	X	X	2	0	2,0	Reactivation in soils, PHOTO1189 facing 300°
A160507-7-005	11	1	69	159	47	225	S	P	2	1	2,0	On soils
A160507-7-006	11	4	61	347			X	X	2	0	2,0	Fracture
A160507-7-008	11	1	47	39	43	8	S	C	2	3	2,0	Normal faulting
A160507-7-009	11	1	42	264	26	322	S	C	2	3	2,0	PHOTO 1190/1 taken facing 265° showing

[a] A format whereby attitude of fault plane or slip line presentation begins with amount of dip followed by dip direction i.e. 00/000
[b] Fault slip data type: 1 for fault plane with slip lines, 2 for conjugated shear planes, 3 for shear plane with tension fractures, 4 for fault plane without slip line (e.g. fracture, bedding plane, foliation).
[c] D for dextral, S for sinistral, X for unknown sense of movement.
[d] C for certain, P for probable, and X for unknown (see text on Chapter 2 for further explanation of these relative terms).
[e] 0 for non activated, 1 for neo-formed, 2 for reactivated and 3 for unknown faults.
[f] 0 for non striated, 1 for weakly striated, 2 for well marked striated, 3 for profoundly striated and 4 for extremely striated (corrugated) fault surface.
[g] This can be represented by any numbers, e.g. 1 for old faulting events, 2 for recent faulting events, etc. These are also relative terms (e.g. sec. 2.3.3) explanations).

Table 4.4 - Threshold values for the individual criteria used in the quality ranking of the tensor (after Delvaux and Sperner, 2003).

QR	n	n/nt	CL	DT†	*Plen*	*Slen*
A	≥25	≥0.60	≥0.70	≥0.90	≤0.80	≤0.80
B	≥15	≥0.40	≥0.55	≥0.75	≤0.85	≤0.85
C	≥10	≥0.30	≥0.40	≥0.50	≤0.92	≤0.92
D	≥6	≥0.15	≥0.25	≥0.25	≤0.95	≤0.95
E	<6	<0.15	<0.25	<0.25	>0.95	>0.95

DT†=Type of data used as in Table 4.3 is further qualified as:
Slickenside = 1.00,
Focal mechanism = 0.75,
Tension or compression fracture = 0.50,
Two conjugate planes = 0.50,
Stylolite column = 0.50,
Movement planes + tension fracture = 0.50, and
Shear frature = 0.25.

4.4. Determination of focal mechanisms: collection and processing of data

Focal mechanisms from the area between 3°00'-6°00'S and 34°00'-37°00'E, which is larger than the study area (i.e., 5°00'-7°00'S and 34°50'-36°00'E), were determined after paleostress regimes from geological (fault-slip) data were established. The analysis of focal mechanisms in this area was not a substitute of fault-slip data analysis but an integral part of tectonic stress analysis. In other words, the results from the analysis of fault-slip data obtained from recent tectonic activity were counter-checked by results from focal-mechanism analysis, whereas the latter was interpreted based on the framework of the former.

4.4.1 Focal-mechanism data collection

The present-day stress conditions were determined using data from earthquake focal mechanisms obtained from three different sources: (i) data from Kebede and Kulhanek (1991), (ii) data from the Harvard Centroid Moment Tensor catalogue (CMT), and (iii) data from Brazier et al. (2005) (Table 4.5).

4.4.2 Focal-mechanism data processing

The procedures to process focal mechanisms are similar to those described for paleostress analysis. However, there some differences: here, the kinematic p-, b- and t-axes are considered. They are used to infer the orientations of the horizontal principal stress axes, S_{Hmax} and S_{hmin} (Zoback, 1992). The kinematic p-, b- and t-axes represent strain axes, and not stress directions as is the case for fault-slip data.

Table 4.5 - Coordinates of focal mechanisms and source of data

	Date	Time	Lat (°)	Long (°)	Mb	Source
1	19720213	10:02:00	-4.50	34.10	5.0	Kebede
2	19771215	23:20:04	-4.80	34.92	5.6	Harvard
3	19771215	23:20:04	-4.80	34.90	12.0	Kebede
4	19900405	19:20:48	-3.05	36.05	5.1	Harvard
5	19900515	15:21:28	-3.43	35.77	4.7	Harvard
6	19900515	16:24:25	-3.12	35.40	5.2	Harvard
7	19910222	22:06:01	-3.94	35.94	4.4	Harvard
8	19940129	00:23:33	-5.03	35.92	4.1	Brazier
9	19940212	16:37:33	-3.88	35.67	4.5	Brazier
10	19940720	11:32:03	-4.25	35.58	4.5	Brazier
11	19941127	04:20:53	-4.08	35.83	4.0	Brazier
12	19961220	03:53:02	-5.18	35.96	4.6	Harvard
13	20030614	03:10:02	-5.71	35.97	4.6	Harvard

During the initial data processing stages (Right Dihedron method), both nodal planes of an incompatible focal mechanism are eliminated simultaneously as they both have the same counting deviation value (Delvaux and Sperner, 2003). In the subsequent stage (Rotation Optimization), all the nodal planes, which have slip deviations greater than the threshold value α, are considered as auxiliary planes and are eliminated in the data set. If both α values (i.e., slip daviations of nodal planes) are greater than the threshold value, then the entire focal mechanism is eliminated. Alternatively, in case α is lower than the threshold value, the two nodal planes are kept for further processing. This results in the progressive selection of the probable fault plane for each focal mechanism. In this study, α was kept to be 30°.

4.4.3 Slip-tendency analysis

The present-day stress regime, as computed from focal mechanisms, has subsequently been applied to the entire study area. According to Morris et al. (1996), the potential activity of faults can be estimated using the principle of slip-tendency analysis, which permits to rapidly assess the stress state on a fault. In order to do this, the strikes of all active normal faults were measured on the SRTM-DEM map (Fig. 4.2) using a protractor. The fault dips were assumed to be 60° and the overall dip directions were taken to be the ones observed in the field. They were presented as dip / dip direction (Table 4.6).

All faults were assigned a dip angle of 60° because all the observed faults are normal faults. At suitable conditions, normal faults dip 60° (see also top right figure on the cover page of this thesis).

The resulting data were entered in the Win-Tensor program for computation of a modelled stress tensor.

Table 4.6 - Orientations of faults in the study area: Dip assumed to be 60° for all faults. The format used is dip/dip direction. * refers to faults located outside the study area.

Name of fault	Orientation of fault
Mponde	60/087
Saranda	60/129
Bubu (Gonga)	60/150
Bubu (Makutupora)	60/136
Bubu (Nkambala)	60/125
Makanda	60/096
Hombolo	60/304
Bahi	60/038
Fufu Main	60/134
Fufu North	60/105
Sanzawa	60/215
*Balangida South**	*60/154*
*Balangida North**	*60/144*

4.5. Paleoseismic investigation

After the active faults were identified, characterized (in terms of morphology, fault segments) and after the establishment of the paleo- and present-day stress fields as stated above, the evolution of fault activity over time was investigated by means of trenching (paleoseismic investigation). In the following paragraphs, a description will be given of the procedures followed for this paleoseismic investigation, starting from trench location, trenching *per se*, gridding, mapping (and logging), sampling and sample analysis.

4.5.1 Trench location

The trenching site was chosen based on six main criteria (i) seismo-tectonic activity of the area, (ii) morphostructural expression of the fault across which the trench was to be established (e.g., Dost and Evers, 2000), including presence of good reference surfaces, (iii) likelihood of getting datable materials, (iv) level of water table, (v) legal aspects pertaining to the area to be trenched, and (vi) accessibility to the site with reference to camp site.

Focus was given to those faults that are considered to present a medium to high likelihood for being reactivated under the present-day stress field by Macheyeki, et al. (2008b). As additional criteria, we selected those faults which host an important number of thermal springs (e.g., James, 1967; Walker, 1969; Macheyeki, et al., 2008a; 2008b). Finally, together with other logistics on the ground, the Bubu fault was selected for trenching. This site is on point 3b in Fig. 4.2 and its panoramic view is shown in Fig. 4.5. A topographic profile corresponding to the trench area is shown in Fig. 4.6.

Integration of the six criteria above together with other logistics was necessary to make a good judgment for trench location. This was based on what McCalpin (1996) reports: "*…It is impossible to know in advance what will be found in the subsurface as a trench is being excavated… Thus, good judgment and selection of trench location are important and may be crucial to create data-rich excavation…*"

Fig. 4.5 - Panoramic view of the trench site at Magungu village.
Arrow points at the point on which the Magungu trench was established. Picture taken facing NW.

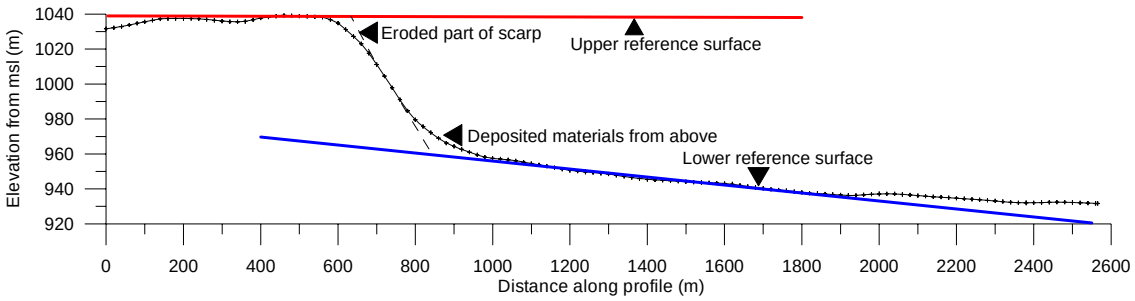

Fig. 4.6 - Topography of the Gonga segment at Magungu area.

4.5.2 Trenching

The following procedures were taken into account when preparing the trench:

(a) The trench extended on either side of scarp base of slope inflexion point (In this context, it is the point between the base of slope and the toe) (Table 4.1; Fig. 4.1) in order to ensure that datable materials from both the hanging wall and basement from the footwall would be intersected.

(b) It was perpendicular to the fault in order to avoid apparent measurements on and in the trench.
(c) It was wide and long enough to allow easy trenching, logging and sampling at depth.
(d) It retained its initial dimensions of width and length throughout its depth and had to be as smooth as possible to avoid ambiguities in measurement reading as protruding boulders and tree roots for instance may lead to apparent readings.
(e) At final or target depth, the trench floor was leveled by excavating from the bottom of trench on the hanging-wall side (as a reference level) towards the footwall side.

Fig. 4.7 - The Magungu trench as seen from the hanging-wall side. The trench is 1.5 m wide and oriented N140°E. The white line represents approximate inflexion point.
For orientation purposes, the arrow in Fig. 4.5 points approximately at the mid part of this line.

4.5.3 Gridding

A local grid was established on the southwestern wall, which was the most suitable, as it contained the best preserved deposits or layers and structures or faults. This wall was gridded in 2 x 2 m grid cells using a flexible pipe of 10 m long and 0.5’ (1.3 cm) diameter. The height of water was used as an accurate horizontal level (hereby referred to as the x-axis). The y-axes (vertical lines), were then established perpendicular to the x-axes using a tape measure and counter-checked by a protractor. The intersection points were nailed and labeled based on one local reference point (Fig. 4.8).

Fig. 4.8 - Gridded footwall side (southwestern wall) of the Magungu trench.
Congl = clastic conglomeratic layer; *Unsort. ab* = unsorted angular pebbles and boulders plus pisoliths layer; *rbparx* = reddish brown pisoliths plus weathered fewer angular pebbles and boulders layer. Below the conglomeratic layer is the basement.

4.5.4 Mapping and logging

Once the grid was established, the trench was drawn on graphing paper (with millimeter scaling). Mapped items include the topographic section of the trench. Then, deposits (layers), displaced strata and the planes along which displacement(s) of strata occurs were carefully mapped. The latter were carefully investigated in order to see if they represent real faults or not. Other information was noted in the field notebook.

4.5.5 Sampling

After description of the trench walls, samples were taken for ^{14}C-dating. A knife was used to snatch fine materials into small labelled plastic bags which were then air freed and prepared for submission to a laboratory for analysis. Samples contained visible organic materials, such as charcoal and dead organisms within disrupted or displaced layers.

4.5.6 Analysis

Sample analysis (radiocarbon dating) was done using ^{14}C AMS radiocarbon dating on organic carbon residue from the sediment at the University of Utrecht (R.J. Van de Graaff laboratorium). This technique uses the Calibration Calendar age (cal BP) of intervals 1σ-probability. The program Calib5 (Stuiver and Reimer, 1993) for the atmospheric environment is employed.

Chapter 5

Active Faults and Fault Segmentation

5. Active faults and fault segmentation

Two important results will be presented in this chapter: (a) a map of active faults in the study area, as obtained from the analysis of 90 m resolution SRTM-DEM (Fig. 5.1), and (b) a compilation of vertical offset data along each mapped active fault in order to obtain displacement profiles. The latter are used to define fault segments. Wherever possible, topographic and displacement profiles have been plotted together with thermal spring locations in order to highlight possible relationships between processes controlling deep-seated tectonic activities and active faulting.

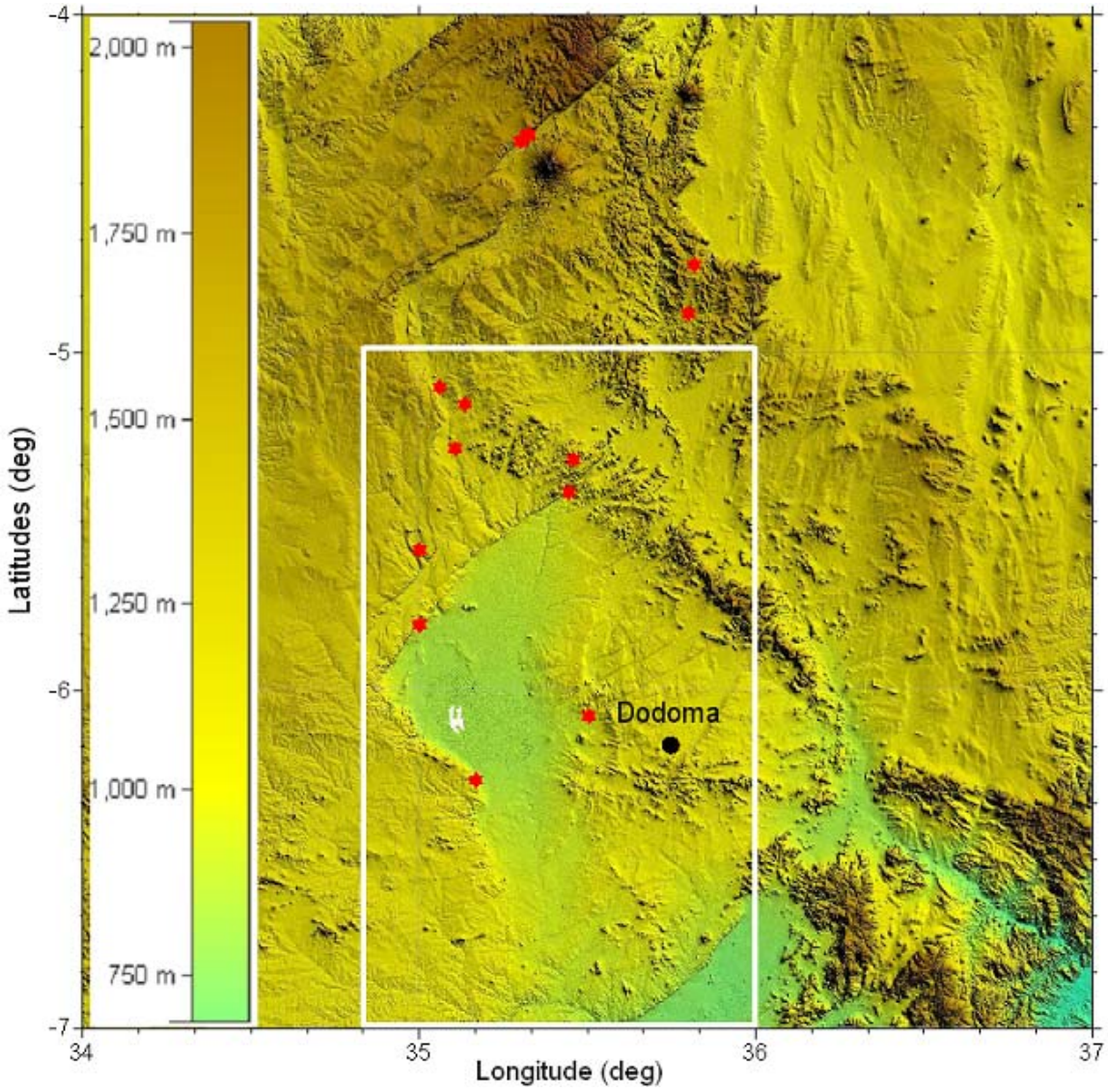

Fig. 5.1 - The SRTM-DEM base map of the region, showing the study area (white rectangular box). Red stars are locations of thermal springs (After Macheyeki et al., 2008b). The November 2002 earthquake swarm was centered on the NW-SE trending Chenene Mountains (north of Dodoma).

5.1. Active faults

Within the study area, the SRTM-DEM reveals many sets of lineaments. These can be grouped into three main sets: the NE-SW-, the NW-SE- and the N-S-trending lineaments. They appear clearly in Fig. 5.2, a "zoom" of the base map to show the study area only. In Fig. 5.2, a series of lineaments can be observed around and north of Dodoma. It is crucial to determine which ones represent (potentially) active faults and which ones do not.

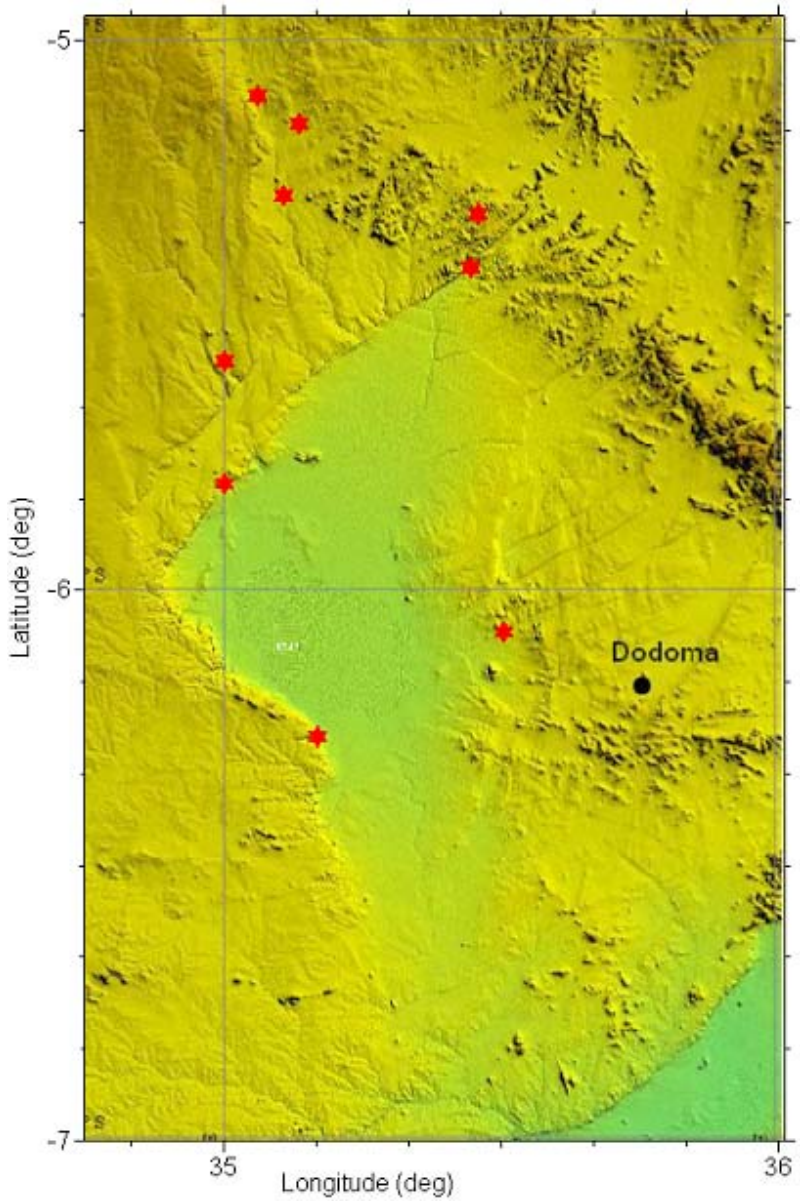

Fig. 5.2 – "Zoom" of the topographic map of the study area. Red stars represent thermal spring locations. Note the complex structures and lineaments with different orientations around Dodoma.

5.1.1 Identification of active faults

Potentially active faults were identified based on the interpretation of morphological lineaments on the SRTM-DEM, in combination with information from geological maps. They were subsequently verified by field observations. Potentially active faults were defined as faults that offset superficial deposits and Quaternary sediments (both on the maps and in the field). Such faults generally present a relatively discrete but sharp and rectilinear morphological scarp that is easily distinguished from other morphological elements.

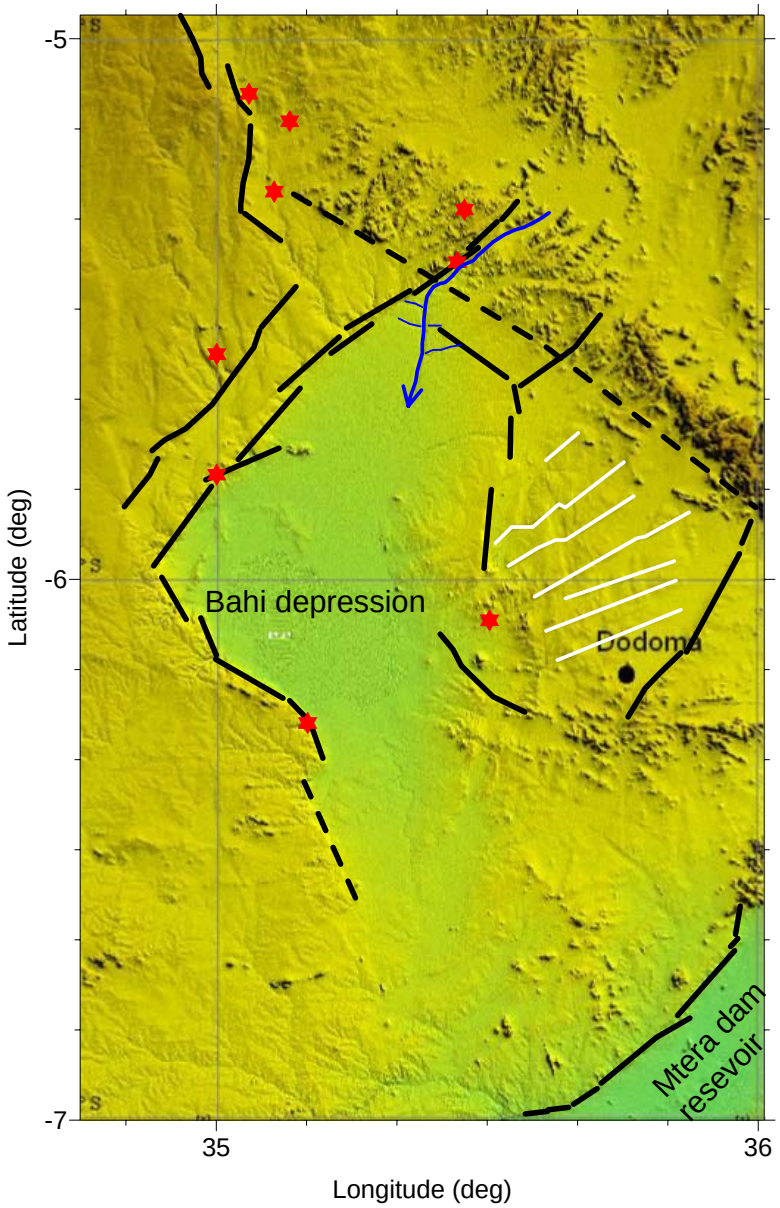

Fig. 5.3 - Various lineaments in the study area as seen on the 90 m resolution SRTM-DEM. Red stars represent thermal spring locations. The blue thick line is the Bubu river, with the arrow pointing to the direction of water flow.Black lines represent lineaments that are interpreted as active faults. White lines represent lineaments that are thought to be old (Precambrian) structures.

There is a high degree of complexity in structures in the study area. The NE-SW-trending lineaments can be further subdivided into two sets:
(a) those which trend between ~ N40°E and N50°E, and
(b) those which trend between ~ N65°E and N70°E.
The former and the latter are marked on Fig. 5.3 and indicated by black and white lines, respectively.

Closer investigation of both lineaments clearly show that the lineaments that trend between ~ N40°E and N50°E are generally associated with thermal springs (Fig. 5.3) of various chemical compositions (e.g., Macheyeki et al. 2008b), whereas the ~ N65°E-N70°E trending lineaments do not host any thermal springs. Furthermore, the morphological contrasts on the DEM maps of both sets of lineaments differ significantly. The ~ N40°E-N50°E trending lineaments are clearly expressed in the topography as opposed to the other set which are relatively faint. The ~ N65°E-N70°E trending lineaments are truncated by the ~ N40°E-N50°E trending lineaments, an evidence that the latter are younger. All these observations highlight that the ~ N40°E-N50°E trending lineaments are most likely recent (hence active) faults that deserve closer investigations, whereas the other set belongs to the Precambrian tectonic fabric, and are most likely not active at the moment. It should be pointed out, however, that the active faults are not neo-formed faults but considered to be reactivated Precambrian structures as well.

The NW-SE and the N-S trending lineaments have similar characteristics as the ~ N40°E-N50°E trending faults. They are clearly expressed in the topography. Therefore, they are considered to be active faults as well.

5.1.2 Detailed investigation of active faults in the Dodoma area

In this section, faults that were interpreted to be active are presented and described. We begin the investigation from NW of the study area to the SE of it.

5.1.2.1 The Mponde fault

The first fault on the extreme NW of the study area is the Mponde fault (Fig. 5.4). This fault is about 60 km long and characterized by an impressive, rocky scarp (Fig. 5.5). Generally, it trends N-S. To the north, it joins the NE-SW trending Balangida fault (outside the study area); to the south, it seems to join the NE-SW trending Saranda fault.

Although the general trend of the Mponde fault is N-S, its detailed orientation is complicated, because in some parts it trends NW-SE to NNW-SSE, in some other parts it trends N-S and in some other parts it curves (Fig. 5.4).

This fault hosts a number of hot/thermal springs (Fig. 5.4). Field visits conducted in March-May 2006 in this area showed that the thermal springs on the northern part of the fault are located at least 2 km to the east of the base of the Mponde scarp and they extend over a distance of at least 2 km parallel to the fault. Detailed synthesis about the thermal springs in the Dodoma area is found in Macheyeki et al. (2008b).

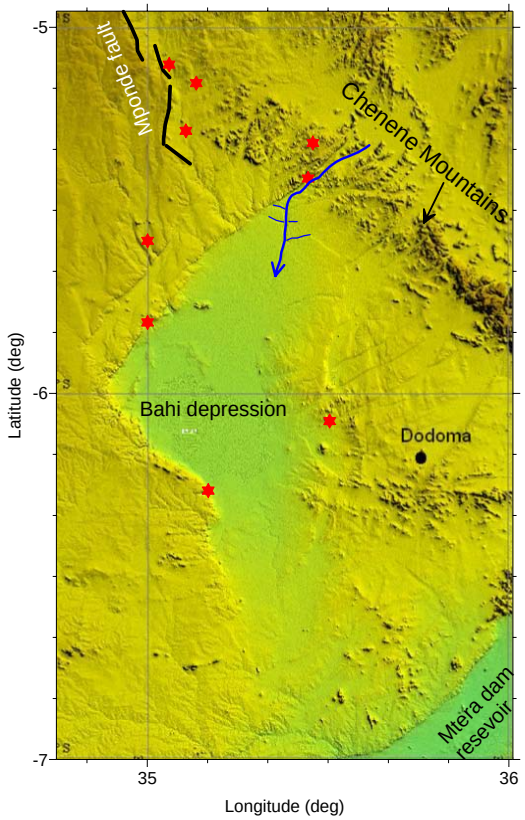

Fig. 5.4 - The Mponde fault. Red stars represent thermal spring locations.
The blue thick line is the Bubu river, with the arrow pointing to the direction of water flow.

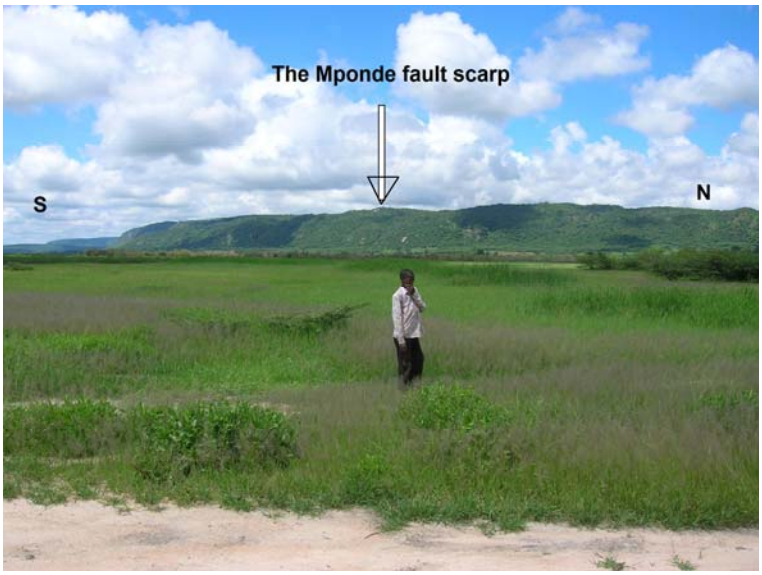

Fig. 5.5 - Overview of the Mponde fault scarp.

5.1.2.2 The Saranda fault

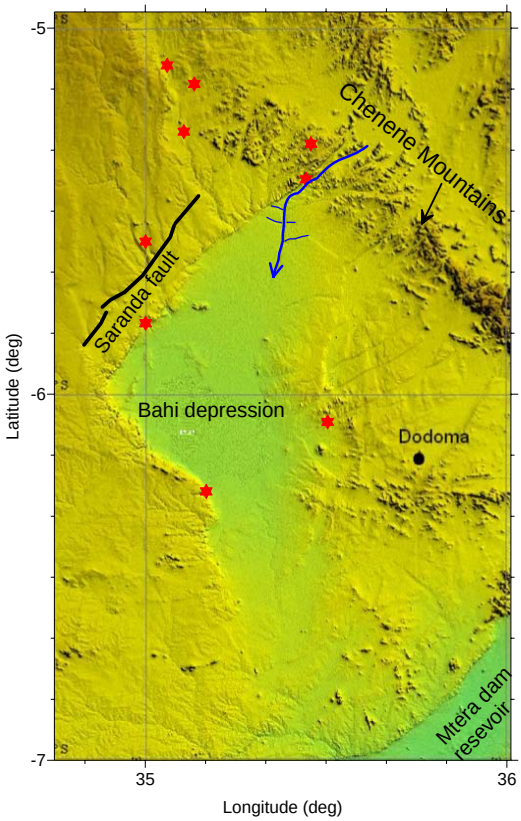

Fig. 5.6 - The Saranda fault. Red stars represent thermal spring locations.
The blue thick line is the Bubu river, with the arrow pointing to the direction of water flow.

Fig. 5.7 - The Saranda fault scarp near Saranda railway station.

South of the Mponde fault is the Saranda fault (Fig. 5.6). This fault is about 55 km long, also with an impressive scarp (Fig. 5.7). In the SRTM-DEM map, it is easy to see the sharp contact between the fault line and the rest of the area. However, the northern end of the Saranda fault is somewhat diffuse.

Around the central part of the Saranda fault, there is a thermal spring. It is located 6-7 km away from the fault scarp within the footwall (Fig. 5.6). About 25 km south of this thermal spring, there is another thermal spring. The latter is located on the hanging wall of another NE-SW trending fault called the Bubu fault.

5.1.2.3 The Bubu fault

The Bubu fault (Fig. 5.8) is parallel to the Saranda fault. Like the Mponde and the Saranda faults, it has an impressive fault scarp (Fig. 5.9); its size is comparable to that of the Mponde fault (Fig. 5.5). The total length of the fault is nearly 110 km. Generally the fault is made up of at least eight smaller faults as can be seen on Fig. 5.8. The importance of these smaller fault traces will be discussed later.

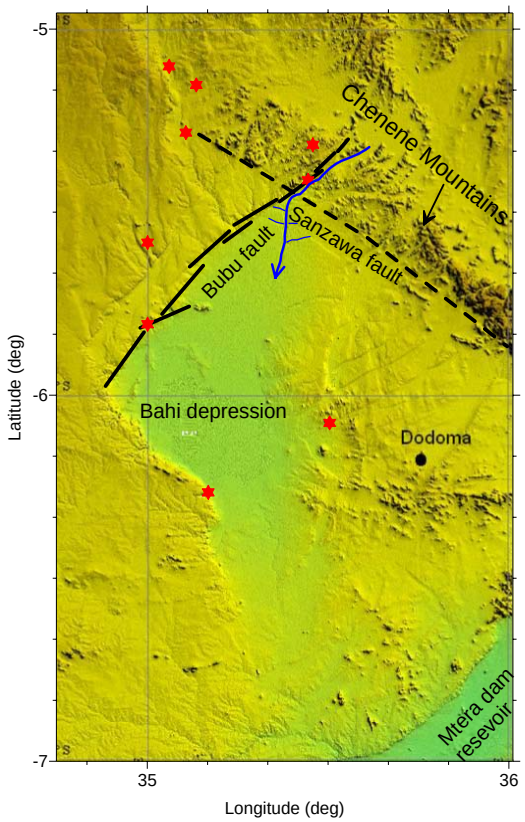

Fig. 5.8 - The Bubu fault. It is made up of about eight smaller faults. The Bubu fault crosses the inferred W-SE trending Sanzawa fault. The latter marks the southwestern limit of the Chenene Mountains. Red stars represent thermal spring locations; one of the stars on the northern end of the fault is the famous Gonga hot (thermal) spring. The blue thick line is the Bubu river, with the arrow pointing to the direction of water flow.

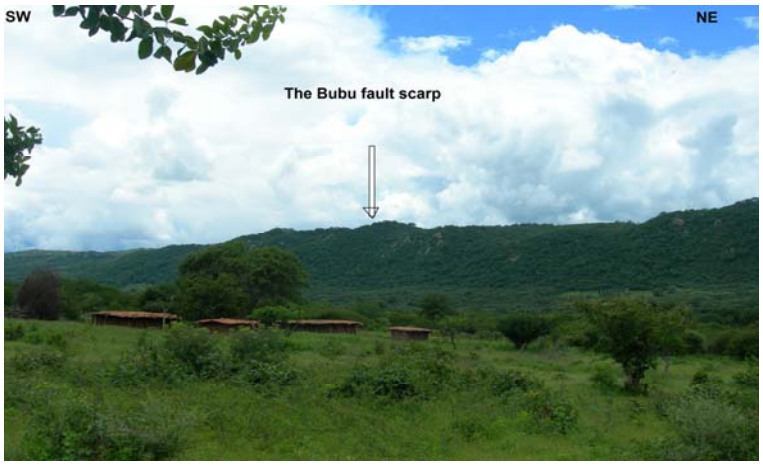

Fig. 5.9 - The Bubu fault scarp. This photo was taken about 15-21 km NE of the thermal spring located to the northern end of the Bubu fault.

The northern part of the Bubu fault cuts through the NW-SE trending Chenene mountains. In this part, an important thermal spring field is found: i.e., the "Gonga thermal spring field". It is located within the hanging-wall side of the Bubu fault in a valley that hosts the Bubu river (Fig. 5.8).

5.1.2.4 The Bahi fault

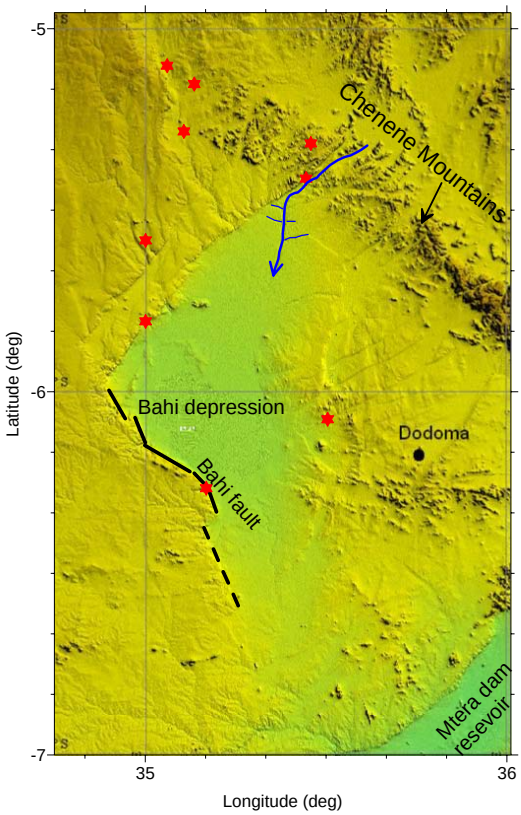

Fig. 5.10 – The Bahi fault. Red stars represent thermal spring locations.
The blue thick line is the Bubu river, with the arrow pointing to the direction of water flow.

The Bahi fault is also about 55 long (Fig. 5.10). It has an impressive scarp as seen from the hanging-wall side. The Bahi fault hosts one thermal spring on its southern part. The southern extension of the Bahi fault, from a few km south of the thermal spring onwards, is not very clear (Fig. 5.10). Both the Bahi fault and the Bubu fault define the southern and the western margins of the Bahi depression. Both faults offset recent deposits in this depression.

5.1.2.5 The Makanda fault

The Makanda fault, ~86 km long, is characterized by a series of individual fault traces that trend in two main directions: N-S and NE-SW (Fig. 5.11). Over half of the fault traces trend nearly N-S, whereas the other part trends NE-SW. The morphological expression of the entire fault shows that it cuts through the ~ N65°E-N70°E lineaments. Like the Bubu fault, it also cuts through the NW-SE trending Chenene Mountains. However, its scarp is generally small compared to that of the Bubu, Saranda and Bahi faults. A few kilometers south of the fault lies a thermal spring, the origin of which is probably related to the fault.

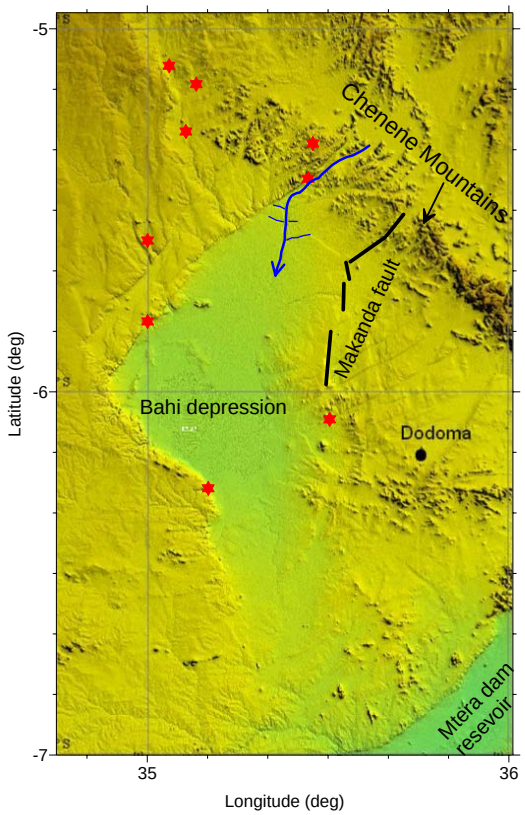

Fig. 5.11 - The Makanda fault. Red stars represent thermal spring locations.
The blue thick line is the Bubu river, with the arrow pointing to the direction of water flow.

5.1.2.6 The Hombolo fault

The Hombolo fault, also a NE-SW trending fault, is a unique fault in the study area, as it is the only fault with a westerly facing scarp. It is an antithetic fault characterized by a

scarp which is not as sharp as other faults in the study area. However, its topographic expression is similar to that of the Makanda fault. A relatively clear morphological contrast exists between this fault and the ~ N65°E-N70°E trending lineaments, whereby the Hombolo scarp seems to postdate the lineaments.

The Hombolo fault is about 40 km long and it is very close to Dodoma (Fig. 5.12). Its northern and southern extremities are not well established.

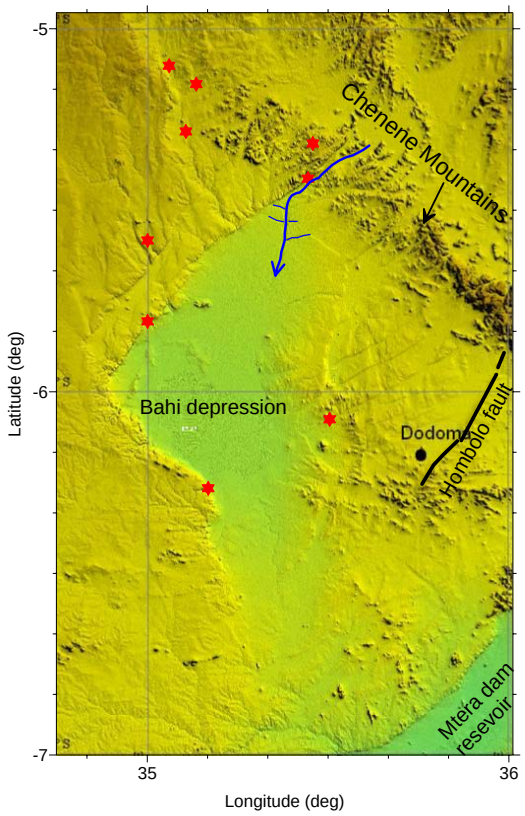

Fig. 5.12 – The Hombolo fault. Red stars represent thermal spring locations.
The blue thick line is the Bubu river, with the arrow pointing to the direction of water flow.

5.1.2.7 The Fufu fault

The Fufu fault is also a NE-SW trending fault, although its northern part trends almost N-S (Fig. 5.13). It is the second longest fault in the study area after the Bubu fault, with a total length of about 95 km. The fault is characterized by an impressive scarp (Sec. 5.2.2.7); its maximum height exceeds 100 m. Like the Bubu fault, the Fufu fault can be easily distinguished as there is a big difference in elevation between the hanging wall and footwall of the fault.

While the hanging wall of the Bubu fault is the Bahi depression, the hanging wall of the Fufu fault is the Mtera dam reservoir.

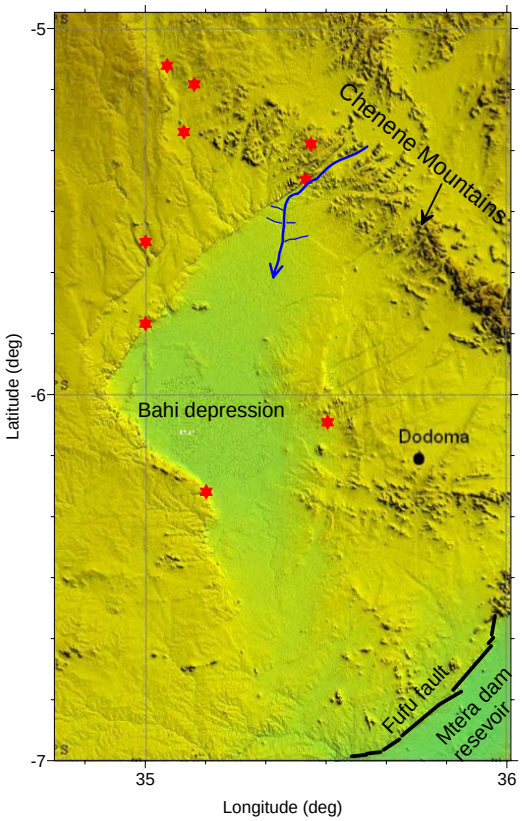

Fig. 5.13 – The Fufu fault. Red stars represent thermal spring locations.
The blue thick line is the Bubu river, with the arrow pointing to the direction of water flow.

5.1.2.8 The Chikola fault

The Chikola fault (Fig. 5.14) is one of the smallest faults in the study area. It is only about 15 km long, and characterized by a small, but clear scarp. The fault trace, arc-like in shape, trends generally parallel with the Bahi fault. The Chikola fault is near the Makanda fault and both faults are thought to be connected around the centre of the Chikola fault.

5.1.2.9 The Maziwa fault

The Maziwa fault is also a small fault (Fig. 5.15). Morphologically, it does not have any clear scarp (e.g. Macheyeki et al., 2008a). Based on the 1:50,000 topographic maps and the 1:125,000 geological maps, the fault seems to dextrally offset the deposits occupying the Bahi depression (i.e., the Kilimatinde Cement) (Fig. 5.16). However, a field visit in May 2007 did not reveal any lateral movements in or associated with the deposits.

The northwestern end of the Maziwa fault seems to terminate in the Bubu fault, whereas the southeastern end does not seem to go past the Makanda fault. In Macheyeki et al. (2008a), the Maziwa fault is considered to be a structure that probably buffers the seismic activities between the two faults and transfers deformation between them.

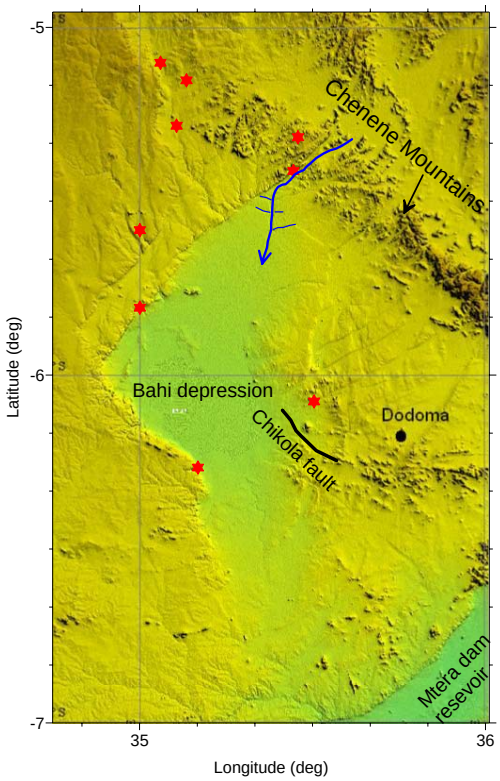

Fig. 5.14 – The Chikola fault. Red stars represent thermal spring locations.
The blue thick line is the Bubu river, with the arrow pointing to the direction of water flow.

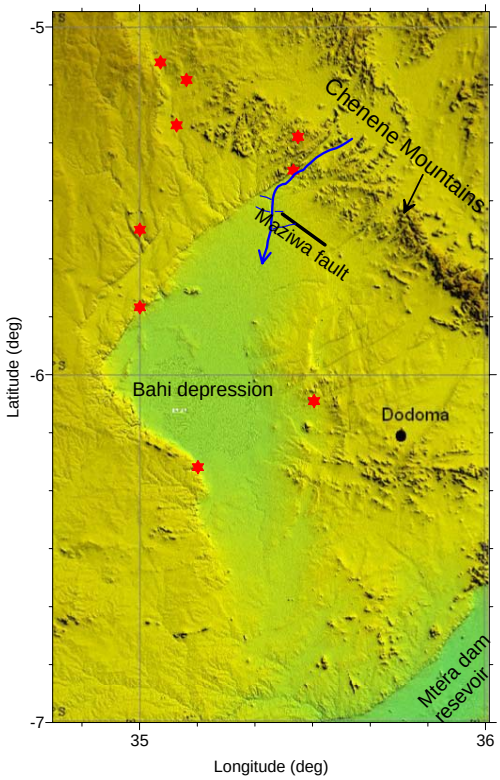

Fig. 5.15 - The Maziwa fault. Red stars represent thermal spring locations.
The blue thick line is the Bubu river, with the arrow pointing to the direction of water flow.

Fig. 5.16 - The Kilimatinde cement within a river channel located within the Maziwa fault around Maziwa village. Picture taken facing north, in May 2006.

5.1.3 Limitations

This approach of identifying and mapping active faults using SRTM-DEM at 90 m resolution can be used to map small faults characterized by fault scarps in the order of 10 m or more (i.e., personal experience on the Kanda fault system in the Ufipa Plateau, SW Tanzania). Nevertheless, the approach has limitations that are determined by the basic resolution of the DEM. Furthermore, it is unable to map concealed faults.

5.2. Displacement profiles and fault segmentation

In this subchapter, the displacement profiles of all above-listed active faults in the study area are described in detail. The Sanzawa and Maziwa faults are not further described because the former is an inferred fault and the latter does not show a sufficiently clear morphological scarp to characterize it.

Selected relay ramps that occur in the study area are also described in terms of their topographic trends and slopes. Finally, also a description of the Bahi depression is given. This depression is a basin whose limits are clearly delimited by the Bubu, Makanda and Bahi faults. The formation of the Bahi depression is thought to be tectonically related to the formation of the faults.

5.2.1 Fault parameters

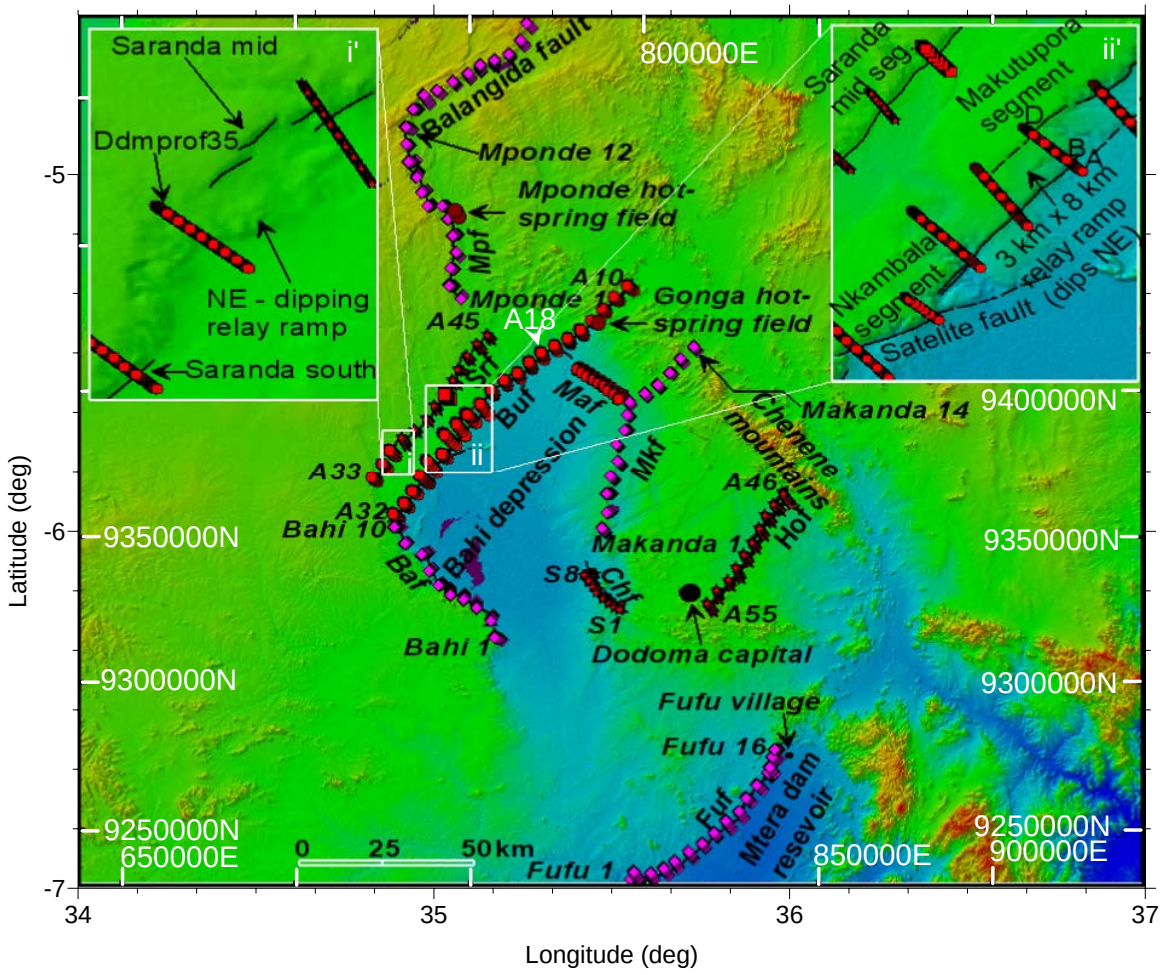

Fig. 5.17 - Color-coded view with artificial shading (sun elevation 45°from NW) of the 90 m resolution SRTM-DEM showing the main structures of the Dodoma area and the location of topographic profiles in relation to active faults in the study area. The topographic profiles, displayed as red and pink dots are set at an average spacing of 5 km. Mpf = Mponde fault; Srf = Saranda fault; Buf = Bubu fault; Maf = Maziwa fault; Chf = Chikola fault; Mkf = Makanda fault; Hof = Hombolo fault; Fuf = Fufu fault. Thermal spring fields that were also investigated in the field are indicated in brown. Topographic profile nomenclature is given in the following way: those reported in Macheyeki et al. (2008a) are preceded by a letter A or S, whereas new topographic profiles are not preceded by A or S, but instead carry the fault name (e.g., Fufu1 in this map represents Fufuprof1 in Table 5.1). Relay ramps at the Saranda and Bubu faults (details in text) are represented by boxes i and ii and are zoomed in as i' and ii', respectively. A18 in white is an abbreviation for Ddmprof18, a topographic profile where significant rotation was noted (Table 5.1).

The following quantitative fault parameters were determined for each of the faults:

(i) UTM 36 (Latitude and Longitude) coordinates (ARC 1960) of start and end points of each topographic profile,
(ii) slope difference between upper and lower reference surfaces of the profiles,
(iii) vertical offsets, and
(iv) distance of the profile along the fault from a selected point of origin (Table 5.1).

All active faults and topographic profiles across those active faults are shown in Fig. 5.17. Additional details of fault configurations shown in the figure shall be discussed later in this section.

Table 5.2 and Fig. 5.18a,b give a summary of the measured mean values of vertical offsets and slope differences. The maximum vertical offsets of the faults decrease in the following order: Bubu (nearly 200 m) → Mponde (~190 m) → Bahi (~170 m) → Fufu (~120 m) → Saranda (~90 m) → Makanda (~55 m) → Hombolo (~45 m) → Chikola (~ 25 m). Trends of mean vertical offsets (Fig. 5.18b) are somewhat different in the following order: Bubu (90 m) → Mponde (84 m) → Bahi (83 m) → Saranda (57 m) → Fufu (45 m) → Hombolo (30 m) → Makanda (18 m) → Chikola (17 m). These trends give an impression that the fault scarps decrease in height from the northwestern part to the southeastern part.

Table 5.1 - Summary of fault parameters: UTM coordinates (Arc 1960) of both ends of profiles, slope difference between upper and lower reference surfaces, vertical offset (VO) and distance of profile along the fault with reference to the start point (origin). Note that profiles which were not involved in the computations of these parameters are not included in the table. ** imply significant rotation between the reference surfaces.

The Mponde fault

Profile	UTM 36 start		UTM 36 end		Slope Difference (°)	Vertical Offset (m)	Distance (km) from origin
	UTM_E	UTM_N	UTM_E	UTM_N			
Mpodeprof1	730052	9409093	730743	9410372	-0.86	37.79	0
Mpodeprof2_upper	726236	9413468	728170	9413311	0.07	16.79	5.3
Mpodeprof2_lower	726236	9413468	728170	9413311	-0.19	31.39	5.3
Mpodeprof3	726710	9418986	728345	9418349	2.11	87.38	10.6
Mpodeprof4	728468	9423873	729964	9422094	-2.05	140.23	15.7
Mpodeprof5	727387	9429056	729499	9429283	3.76	191.77	21.9
Mpodeprof6	725882	9434080	728087	9435093	0.36	158.32	27.4
Mpodeprof7a	719637	9438413	721791	9438603	1.67	46.7	31.9
Mpodeprof7b	724168	9438402	726210	9438402	0.14	64.89	31.9
Mpodeprof8	717760	9442562	719766	9443164	3.53	35.49	36.7
Mpodeprof9	716158	9447172	716158	9447172	4.6	33.73	42.3
Mpodeprof10	713619	9452104	716425	9452427	1.45	138.23	47.5
Mpodeprof11	712997	9457666	714517	9457376	-4.26	138.98	53.1
Mpodeprof12_fait	712591	9463262	715338	9462246	-0.27	12.02	59
Mpodeprof13	715157	9468616	717261	9468649	4.82	36.97	70.3
Mpodeprof14_upper	718441	9473345	720720	9470200	-2.32	93.06	74.7
Mpodeprof14_lside	718441	9473345	720720	9470200	-1.93	37.75	74.7
Mpodeprof15	722663	9474613	724387	9473262	-1.93	37.75	Nil
Mpodeprof16	727591	9477512	729166	9476030	3.12	108.69	84.7
Mpodeprof17	732400	9479892	733481	9477948	1.27	103.41	89.9
Mpodeprof18	736319	9482680	736694	9480132	0.78	76.34	94.4
Mpodeprof19	740898	9484119	740951	9481808	3.46	43.86	99
Mpodeprof20	745362	9486069	746233	9484409	-2.18	178.74	104
Mpodeprof21	748816	9490297	750484	9488431	-0.81	155.11	110

Mpodeprof22_upper	750870	9495831	752971	9493822	-0.98	86.83	116
Mpodeprof22_lslide?	750870	9495831	752971	9493822	-2.96	84.25	116

The Saranda fault

Profile	UTM 36 start		UTM 36 end		Slope Difference (°)	Vertical Offset (m)	Distance (km) from origin
	UTM_E	UTM_N	UTM_E	UTM_N			
Ddmprof33	701748	9353381	703910	9351681	0.45	52.19	0
Ddmprof34	704919	9357753	707097	9355888	-0.81	55.54	5.23
Ddmprof35	707106	9362116	709743	9359989	0.04	28.79	10.3
Ddmprof36	711273	9366312	713276	9362852	0.8	66.48	15.3
Ddmprof37	715187	9368469	716723	9366903	0.69	66.48	20.2
Ddmprof38	718671	9372090	720287	9370357	-0.26	88.91	25.2
Ddmprof39	721388	9376358	723083	9374068	0.63	45.54	30
Ddmprof40	724719	9379736	726558	9377683	1.16	70.04	34.8
Ddmprof41	727023	9383953	729390	9382014	0.43	72.8	39.8
Ddmprof42	728880	9387336	730802	9386533	1.48	51.88	44.3
Ddmprof44	734765	9395460	736665	9393083	0.49	24.62	53.8

The Bubu fault

Profile	UTM 36 start		UTM 36 end		Slope Difference (°)	Vertical Offset (m)	Distance (km) from origin
	UTM_E	UTM_N	UTM_E	UTM_N			
Ddmprof10	782065	9413312	784318	9411507	1.15	103.13	102
Ddmprof11	777969	9409727	779742	9408150	0.46	121.51	97.7
Ddmprof12	774172	9406125	775962	9404398	1.63	126.69	92.8
Ddmprof13	770750	9402446	772562	9401245	-1.06	198.61	88.3
Ddmprof14	767092	9399553	768661	9397574	0.19	134.67	83.2
Ddmprof15	763362	9396886	764520	9394827	1.51	115.72	72.6
Ddmprof16	759248	9394757	760454	9392493	-1.28	78.07	68.2
Ddmprof17	754939	9392544	756224	9389980	1.01	32.02	63.1
Ddmprof18	751214	9389658	752691	9386932	2.00**	43.97	57.7
Ddmprof20	747504	9386124	748809	9384014	-0.63	77.44	52.4
Ddmprof21	743240	9383962	744767	9381978	-0.58	40.24	47.8
Ddmprof22	739100	9380735	740610	9378842	0.42	101.13	42.5
Ddmprof23	735570	9376777	738840	9372684	-0.38	50.71	37.9
Ddmprof24W	731137	9373559	734847	9370204	0.8	22.93	33.3
Ddmprof24E	731137	9373559	734847	9370204	0.69	58.04	33.3
Ddmprof25	728111	9370587	731393	9366119	-0.19	47.17	28.3
Ddmprof27	723627	9360918	725768	9359132	-1.32	57.28	23.6
Ddmprof28	718727	9358987	722616	9354783	-0.24	124.9	18.6
Ddmprof29	716668	9353991	720251	9350939	0.37	137.56	13.9
Ddmprof30	714384	9349055	716496	9347694	1.67	95.16	8.62
Ddmprof31	711739	9345275	713746	9343318	0.62	132.22	3.2

The Makanda fault

Profile	UTM 36 start		UTM 36 end		Slope Difference (°)	Vertical Offset (m)	Distance (km) from origin
	UTM_E	UTM_N	UTM_E	UTM_N			
Makandaprof1	774040	9337039	775385	9335272	3.46	49.65	15
Makandaprof2	775325	9341626	777266	9342262	2	21.94	21.3
Makandaprof3_upper	775301	9347750	777283	9347595	-0.74	5.13	27.3
Makandaprof3_lower	775301	9347750	777283	9347595	0	14.03	27.3
Makandaprof4	776567	9353368	778319	9351956	-0.5	14.47	33.2
Makandaprof5	778795	9358241	780556	9356746	-0.5	34.94	37.7
Makandaprof6	778479	9363545	779678	9362521	-0.36	20.19	43.2
Makandaprof7	781170	9367945	782571	9367869	1.07	3.94	49.4
Makandaprof8	781889	9372690	783286	9372011	0.46	8.47	54.3
Makandaprof9	782671	9377069	783356	9375564	-0.69	11.95	58.3
Makandaprof10	787666	9379590	788643	9378212	1.25	4.46	64.2
Makandaprof11	791545	9382206	792845	9380753	1.36	15.77	68.9
Makandaprof12	795321	9385681	796750	9385444	4.72	53.69	74.7
Makandaprof13_upper	798721	9390239	800009	9388576	0.76	20.96	79.8
Makandaprof13_lower	798721	9390239	800009	9388576	0.94	5.7	79.8
Makandaprof14	802932	9394163	804249	9392234	1.13	6.82	85.4

The Hombolo fault

Profile	UTM 36 start		UTM 36 end		Slope Difference (°)	Vertical Offset (m)	Distance (km) from origin
	UTM_E	UTM_N	UTM_E	UTM_N			
Ddmprof48	825002	9340968	827603	9338028	0.01	35.84	8.62
Ddmprof49	823067	9336944	825112	9333969	0.49	28.79	13.1
Ddmprof50	820677	9332577	822546	9329994	-0.82	16.26	18.1
Ddmprof51	818107	9328926	820272	9325687	0.11	30.62	22.6
Ddmprof52	815793	9324626	817644	9320602	0.19	45.08	28.3
Ddmprof53	813170	9320750	814491	9318200	0.58	27.57	33.1
Ddmprof54	809647	9317753	810776	9314115	-0.07	28.97	37.4

The Bahi fault

Profile	UTM 36 start		UTM 36 end		Slope Difference (°)	Vertical Offset (m)	Distance (km) from origin
	UTM	UTM	UTM	UTM			
Bahiprof1	740027	9302891	742951	9301933	2.76	109.47	53
Bahiprof2	739008	9307692	739818	9309773	5.98	117.51	46
Bahiprof3	734614	9311718	734789	9314091	3.01	167.4	40
Bahiprof4	730678	9314295	730937	9316332	2.97	161.94	35
Bahiprof5	796062	9232498	797455	9229982	1.82	42.15	30
Bahiprof6	722679	9318981	724258	9320007	0.04	38.42	27
Bahiprof7	719680	9323538	721230	9324440	0.64	84.71	21
Bahiprof8	717232	9328614	720194	9329578	1.17	44.8	16
Bahiprof9	711967	9332315	713481	9332588	1.33	19.69	9
Bahiprof10	708511	9337330	711590	9337338	0.45	38.92	3.2

The Fufu fault

Profile	UTM 36 start		UTM 36 end		Slope Difference (°)	Vertical Offset (m)	Distance (km) from origin
	UTM_E	UTM_N	UTM_E	UTM_N			
Fufuprof1	782326	9226462	784113	9226041	0.57	13.99	25.5
Fufuprof2	783274	9229077	785493	9225829	0.34	36.98	26.6
Fufuprof3	788669	9228632	789797	9225964	0.02	13.88	31.1
Fufuprof4_upper	792653	9230140	794381	9227467	0.28	9.68	35.9
Fufuprof4_lower	792653	9230140	794381	9227467	-0.99	49.27	35.9
Fufuprof5	796062	9232498	797455	9229982	-1.1	66.77	40.1
Fufuprof6	800405	9235422	802218	9232710	0.4	38.42	45.6
Fufuprof7	804817	9237870	806141	9235995	1.83	39.79	50.7
Fufuprof8	808482	9241175	809817	9239465	0.72	32.59	55.6
Fufuprof9_upper	812175	9245026	814059	9242126	-0.15	17.15	60.8
Fufuprof9_lower	812175	9245026	814059	9242126	-0.33	28.81	60.8
Fufuprof10	816072	9247819	818028	9245482	-0.82	52.43	65.9
Fufuprof11	818391	9252138	820461	9250461	-2.28	121.49	71.2
Fufuprof12	821827	9256248	823890	9254463	2.31	98.56	76.6
Fufuprof13	825385	9259925	826915	9258306	2.31	98.56	76.6
Fufuprof14	825860	9261734	827709	9259575	2.72	63.01	83.2
Fufuprof15	826702	9264766	829217	9263858	1.35	20.55	87.3
Fufuprof16_upper	827415	9267127	829208	9266855	3.4	33.9	90
Fufuprof16_lower	827415	9267127	829208	9266855	-0.2	16.89	90

The Chikola fault

Profile	UTM 36 start		UTM 36 end		Slope Difference (°)	Vertical Offset (m)	Distance (km) from origin
	UTM_E	UTM_N	UTM_E	UTM_N			
Ddmprofilesouth2	769565	9320195	771577	9321180	0.08	11.12	2.08
Ddmprofilesouth3	770739	9318581	771999	9319279	-0.3	23.62	4.01
Ddmprofilesouth4	771947	9316671	773257	9317972	-0.24	15.53	6.03
Ddmprofilesouth5	774043	9314741	774900	9316000	0.32	19.4	8.76
Ddmprofilesouth6	775867	9313295	776793	9314546	-0.14	12.36	11.1
Ddmprofilesouth7	777621	9311828	778066	9313445	0.77	21.66	14.9
Ddmprofilesouth8	779282	9311187	779799	9312759	0.44	16.61	17.8

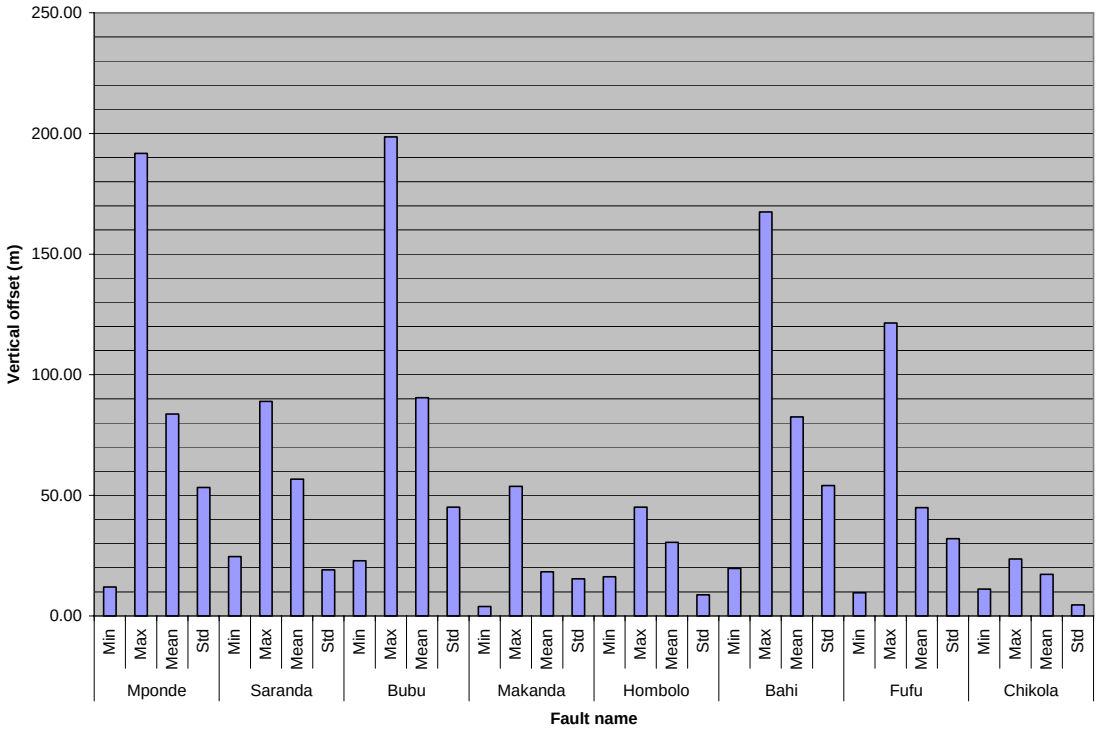

Fig. 5.18a - Histograms showing vertical offset values of faults in the Dodoma area.
Min = minimum; Max = maximum; Mean = mean; Std = standard deviation. Data from Table 5.2.

Table 5.2 - Statistical data for fault parameters (mean values); vertical offsets, VO (m), and slope differences, Sdiff (°), for the studied faults in the Dodoma area. N stands for the total data used in the computation.

	Mponde, N = 26				**Saranda**, N = 11				**Bubu**, N = 21			
	Min	Max	Mean	Std	Min	Max	Mean	Std	Min	Max	Mean	Std
Sdiff. (°)	-4.26	4.82	0.40	2.46	-0.81	1.48	0.46	0.64	-1.32	2.00	0.33	0.98
VO (m)	12.02	191.77	83.71	53.21	24.62	88.91	56.66	19.09	22.93	198.61	90.44	45.05

	Makanda, N = 16				**Hombolo**, N =7				**Bahi**, N = 10			
	Min	Max	Mean	Std	Min	Max	Mean	Std	Min	Max	Mean	Std
Sdiff. (°)	-0.74	4.72	0.90	1.52	-0.82	0.58	0.07	0.46	0.04	5.98	2.02	1.75
VO (m)	3.94	53.69	18.26	15.44	16.26	45.08	30.45	8.73	19.69	167.40	82.50	54.07

	Fufu, N = 19				**Chikola**, N =7			
	Min	Max	Mean	Std	Min	Max	Mean	Std
Sdiff. (°)	-2.28	3.40	0.55	1.46	-0.30	0.77	0.13	0.40
VO (m)	9.68	121.49	44.88	32.04	11.12	23.62	17.19	4.65

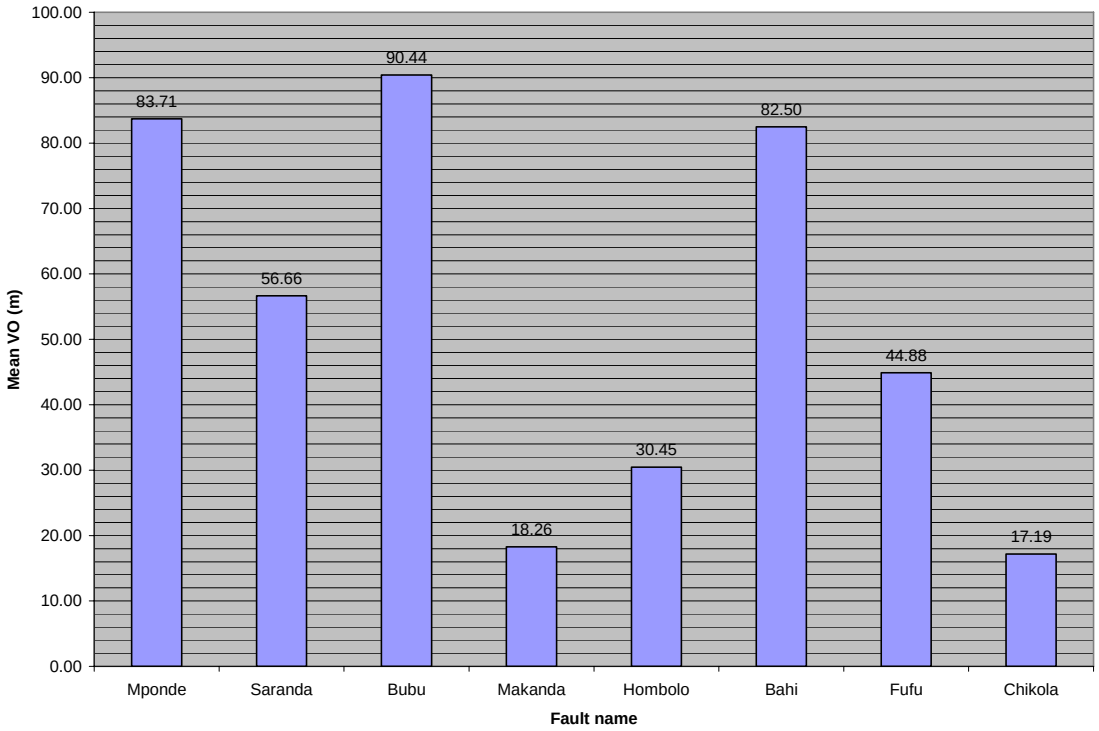

Fig. 5.18b - Mean vertical offset values (VO) of faults in the Dodoma area. Data from Table 5.2.

5.2.2 Displacement profiles

The displacement profiles presented in this section are derived from topographic profiles in Table 5.1. They are 2D profiles constructed by plotting vertical offsets values as y-axis and distance along fault as x-axis. As stated earlier, vertical offsets are a measure of vertical displacements of a given fault. However, by using SRTM-DEM data it is not possible to distinguish the amount of discrete vertical displacements corresponding to various co- or post-seismic activities of a given fault across a given topographic profile. Therefore, the vertical offsets that were calculated and presented in Table 5.1 should be regarded as cumulative displacements.

Because the displacement values are not the same along the entire fault, vertical offsets at different points along a given fault will be different as well. The along-fault vertical offset variation is used to depict or define segments and their boundaries. Segment boundaries are crudely considered to be areas of minimum vertical offset values. Likewise, areas of maximum offset values are considered to be the center of given fault segments.

Based on the empirical relationship of fault length versus vertical displacement or offset (Wells & Coppersmith, 1994), the measured offset values and fault segment lengths have also been used to determine the potential earthquake magnitude for the given segments.

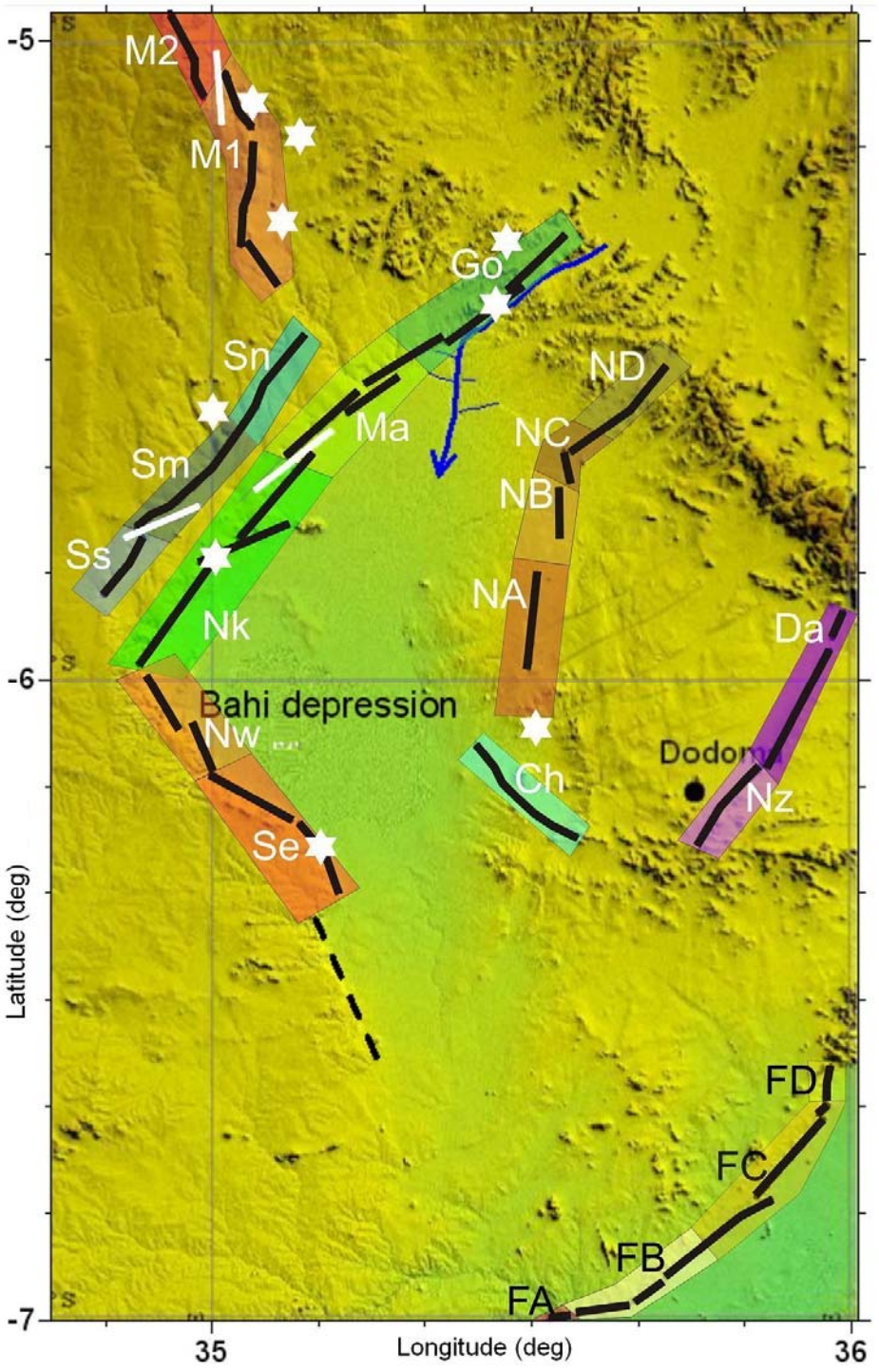

Fig. 5.19 - Fault segments as computed from data extracted from 90 m resolution SRTM-DEM. Mponde fault: M1 = Segment 1, M2 = Segment 2. Saranda fault: Ss = Saranda south segment, Sm = Saranda mid segment, Sn = Saranda north segment. Bubu fault: Nk = Nkambala segment, Ma = Makutupora segment, Go = Gonga segment. Bahi fault: Nw = Northwestern segment, Se = Southeastern segment. Makanda fault: NA = Segment A, NB = Segment B, NC = Segment C, ND = Segment D. Hombolo fault: Nz = Nzuguni segment, Da = Dam segment. Fufu fault: FA = Segment A, FB, Segment B, FC = Segment C, FD = Segment D. Chikola fault: Ch = Chikola. White stars represent locations of thermal springs and white lines represent relay ramps that were studied in detail. Black lines are faults (fault traces).

Sometimes, as shown in Fig. 5.8 for the Bubu fault (as an example), fault segments interact at different stages of fault growth: i.e., they approach or overlap each other forming relay ramps. Although this section is not focused on relay ramps, they will be discussed briefly after the analysis of the fault segments for each fault. Three important relay ramps in the area are the Mponde, the Saranda and the Bubu relay ramps.

In this section, two terminologies shall be used: i.e., "positive rotations" and "negative rotations". They simply imply block rotations that are defined by individual slope differences of ≥ +2° and ≤ -2°, respectively (Table 5.1). *Note*: Slope deference = Slope of hanging wall – slope of footwall. Throughout this section, Fig. 5.19 shall be used as a main reference figure. It represents the summary of all fault segments identified in the study area.

5.2.2.1 The Mponde fault

The Mponde fault is 60 km long. Based on the displacement profile (Fig. 5.20), the Mponde fault comprises two fault segments (Segment 1 and Segment 2). Segment 1 defines the southern part of the fault. It is 31 km long and has a maximum offset of 190 m. Segment 2 in the north is 28 km long and has a maximum vertical offset of 140 m. It has to be noted that a small part of Segment 2 is outside the study area (Fig. 5.19).

Assuming full reactivation of individual fault segments, each fault segment has the potential of generating earthquakes of magnitudes $M_w = 6.7 \pm 0.3$ and $M_w = 6.8 \pm 0.3$ (Fig. 5.20).

Both segments of the Mponde fault have fault tips that are overlapping but not fully connected. They define a relay ramp. It is defined by a 5.3 km wide zone in Fig. 5.20 and by a white line in Fig. 5.19.

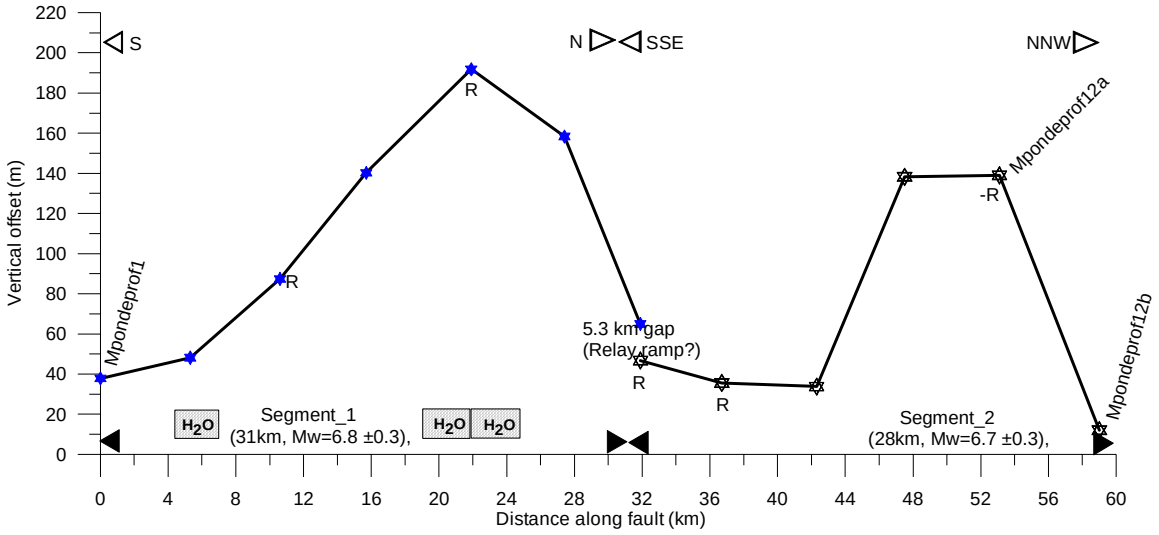

Fig. 5.20 - Displacement profile for the Mponde fault. This fault shows two fault segments (Segment 1 and 2) and the corresponding maximum possible earthquake magnitudes are $M_w = 6.8 \pm 0.3$ and 6.7 ± 0.3, respectively. Segment 1 hosts several thermal springs. They are denoted by rectangular boxes with "H_2O".

The Mponde fault: segment 1

Segment 1 is a ~ N-S trending segment (Figs. 5.20; 5.21). Parallel to it, are several thermal springs (Fig. 5.19). The northern thermal spring is close to the fault scarp (within a distance of 2 km), making large part of the hanging wall wet throughout the year (Fig. 5.22). Other thermal springs are 5 km further to the east but parallel to this segment (Fig. 5.19). In Fig. 5.20, the approximate locations of these thermal springs along the fault segment are indicated. The chemical compositions of the springs are detailed in Appendix 2. Segment 1 is characterized by positive rotations, R.

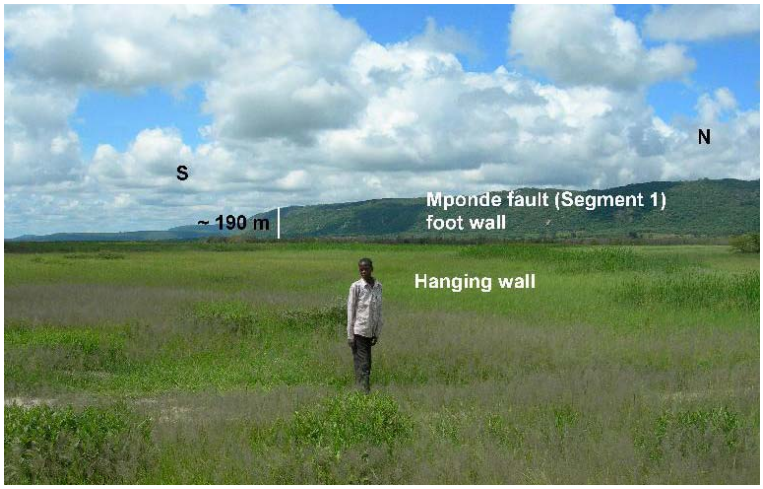

Fig. 5.21 - View of the Mponde fault scarp showing the maximum vertical offset of Segment 1. Picture taken facing westerly of the Mponde fault.

Fig. 5.22 - Picture of a thermal spring along the Mponde fault segment (Segment 1). The picture was taken by D. Delvaux in March 2006.

The Mponde fault: segment 2

Segment 2 of the Mponde fault is characterized by both positive and negative rotations. Unlike Segment 1, Segment 2 does not host any thermal springs.

5.2.2.2 The Saranda fault

The NE-SW trending Saranda fault is 55 km long. It is defined by three fault segments: i.e., the Saranda south segment, the Saranda mid segment and the Saranda north segment (Figs. 5.19; 5.23). The Saranda south segment is ≥ 11 km long and has a maximum vertical offset of 55 m; the Saranda mid segment is 29 km long and has a maximum vertical offset of 90 m (Fig. 5.24); the Saranda north segment is 24 km long and has a maximum vertical offset of 72 m. The entire Saranda fault is characterized by a series of small and large fault steps that constitute the main fault scarp (Fig. 5.23). The Hika thermal springs occur in the footwall of the Saranda mid segment (Fig. 5.19). See also Appendix 2).

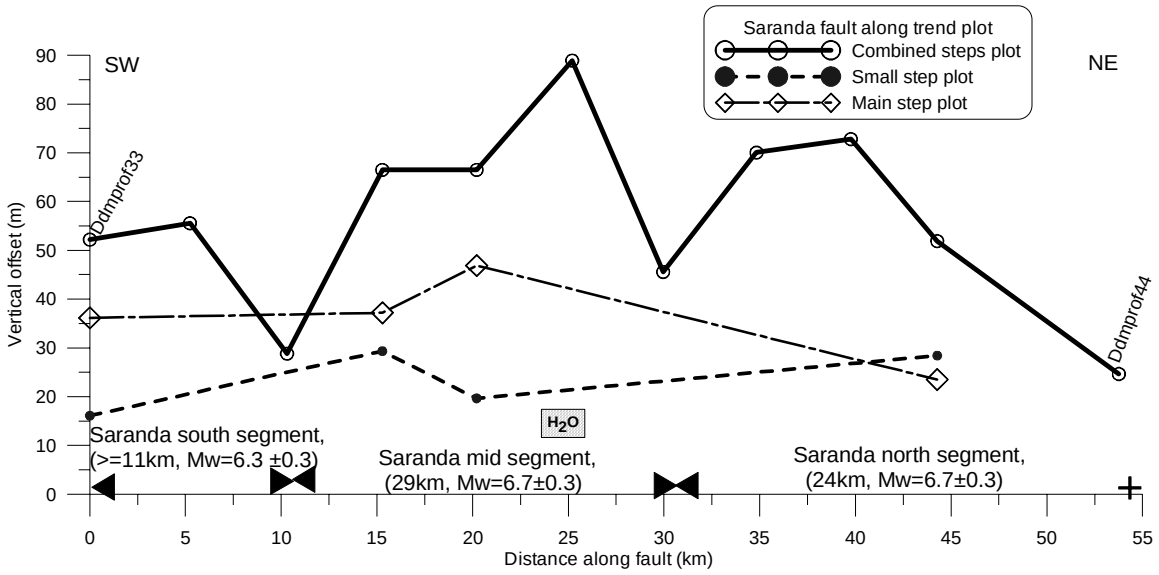

Fig. 5.23 - Displacement profile for the Saranda fault revealing the three fault segments: i.e., the Saranda south, Saranda mid and Saranda north segments. The corresponding maximum possible earthquake magnitudes are 6.3 ± 0.3, 6.7 ± 0.3 and 6.7 ± 0.3, respectively. The Saranda mid segment hosts a thermal spring field.

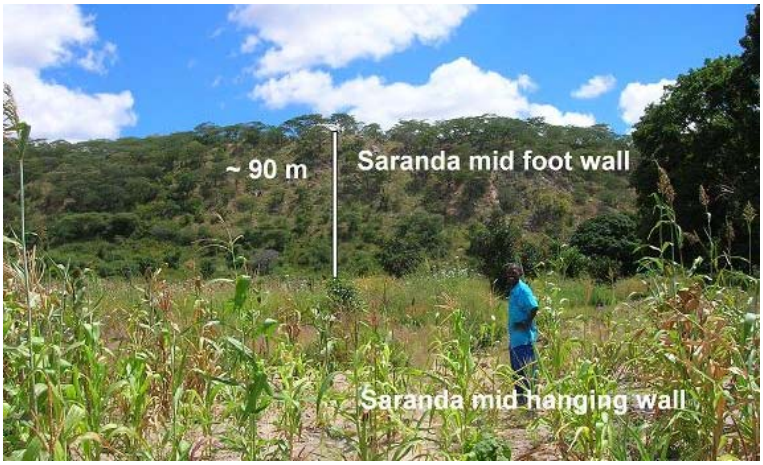

Fig. 5.24 - Picture of the Saranda mid fault segment.
The picture was taken facing west in May 2007.

5.2.2.3 The Bubu fault

The Bubu fault runs almost parallel to the Saranda fault (Figs. 5.19; 5.25). With a length of 105 km, it is the longest fault in the study area. Like the Saranda fault, it is composed of three segments: i.e., the Nkambala (33 km), the Makutupora (30 km) and the Gonga segment (42 km).

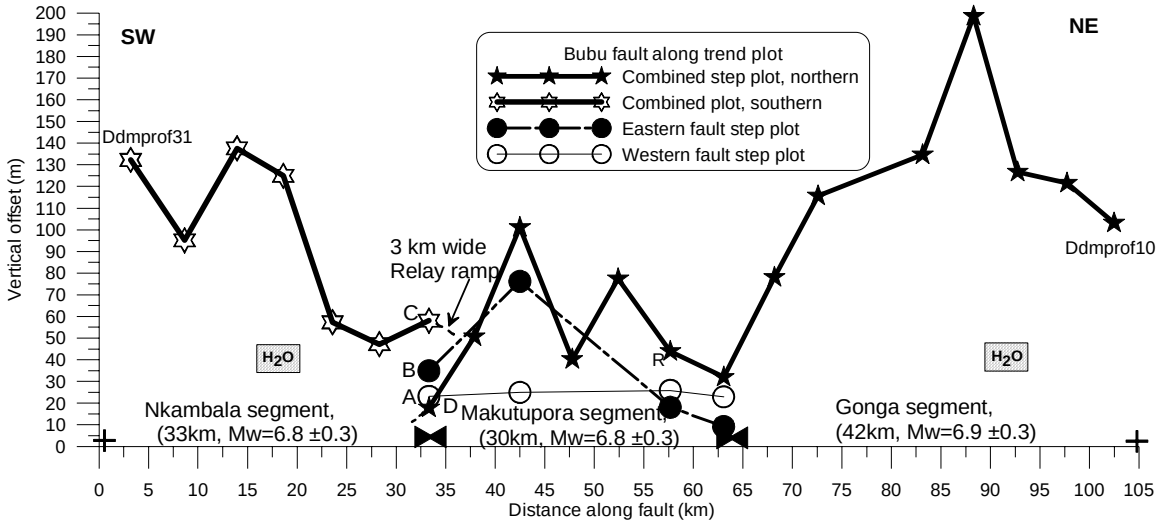

Fig. 5.25a - Displacement profile for the Bubu fault. The fault is slightly longer than 105 km. The sum of A and B equals C, see Fig. 5.25b for details. This figure shows the three fault segments: i.e., Nkambala, Makutupora and Gonga. Both the Nkambala and Gonga segments host thermal spring fields. The corresponding maximum possible earthquake magnitudes of the segments are 6.8 ± 0.3, 6.8 ± 0.3 and 6.9 ± 0.3, respectively.

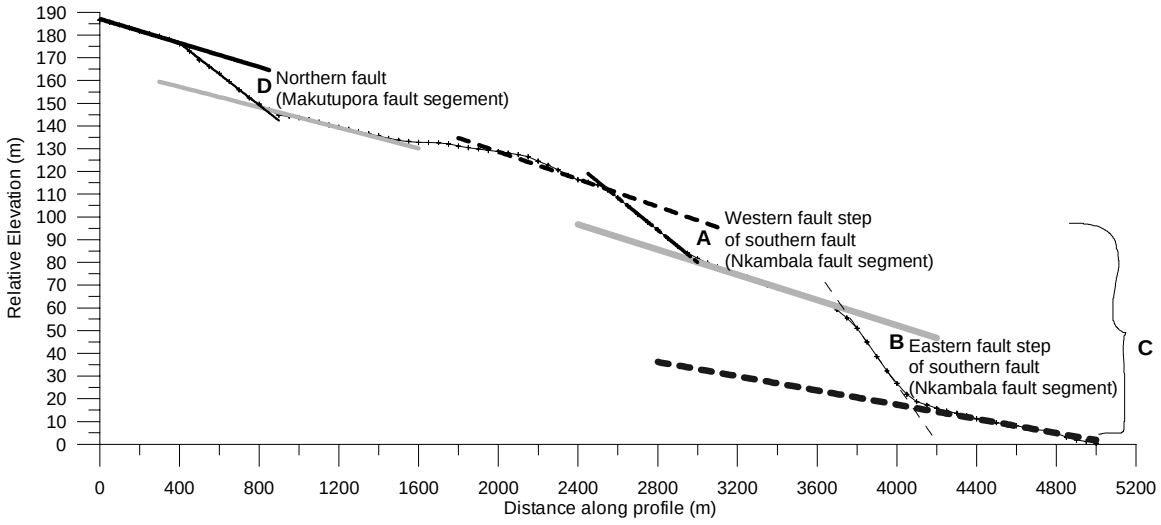

Fig. 5.25b - A profile of elevation versus distance across the Nkambala and the Makutupora fault segments (Bubu fault). Three fault steps D, A and B (naming from west), can be clearly seen. The solid dashed lines at D, A and B represent upper and lower reference surfaces. D represents the Makutupora fault segment; the fault steps A and B combine and produce the vertical offset C of the Nkambala fault segment (see on the zoom side of Bubu fault in Fig. 5.17 and Fig. 5.25a for location of A, B, C and D).

The Bubu fault: the Nkambala segment

The Nkambala segment of the Bubu fault has a length of 33 km and a maximum vertical offset of 137.6 m. It is cut across by a nearly 15 km long, ENE-trending satellite fault that bifurcates from the general trend of the Bubu fault (see a zoom on the right in Figs. 5.17; 5.19). Beyond the intersection, the Nkambala segment continues further to the NE for about 13 km and dies away. At about 15-16 km from the SW termination of the Nkambala segment, a thermal spring field (35°00'E, 5°50'S) is located (Figs. 5.19; 5.25a; Appendix 2).

The Bubu fault: the Makutupora segment

The Makutupora segment has a length of 30 km, comparable to that of the Nkambala segment. There are no thermal springs along this segment. On the other hand, it is characterized by fault steps that are marked as A and B in Fig. 5.25a,b. The vertical offset of the Makutupora segment is in the order of 100 m (Fig. 5.26).

Fig. 5.26 - The Makutupora fault segment.
The picture was taken at about 800 m west of the Bubu fault (Makutupora segment).

The Bubu fault: the Gonga segment

Further to the NE, the Makutupora segment gives way to the Gonga segment, which has a length of 42 km. This segment is also characterized by at least 3 satellite faults, all of which are sub-parallel to each other. The boundary at which the last two satellite faults form is marked by at least half a dozen thermal springs, forming the "Gonga thermal spring field" (Fig. 5.19). The presence of the thermal spring field was also reported in geological maps of Tanzania by the then Geological Survey of Tanganyika (e.g., QDS 123; Kwamtoro; Fozzard (1961). The thermal springs are aligned parallel to the general trend of the fault for about 300 m. They are located within the Bubu river, approximately 5°20'S, 35°28'E (See also Appendix 2).

The Bubu fault: the Nkambala-Makutupora transition

The transition between the Nkambala and Makutupora fault segments forms a relay ramp (Fig. 5.19). The topographic profile across this transition zone is presented in Fig. 5.25b. This configuration could be interpreted as an advanced stage of interaction and linkage between both fault segments. As seen in Fig. 5.17 on zoom ii', the fault segment tips from both the Gonga and the Makutupora fault segments have advanced towards each other and overlapped over a considerable area (3 x 8 km). This could be interpreted as a hard linkage stage.

5.2.2.4 The Makanda fault

The Makanda fault, with a length of 86 km, is located east of the Bubu fault. It trends in two directions; N10°E for 49 km, which accounts for over 50 % of the total length of the fault, and nearly N45°E for the remaining length of the fault (Fig. 5.19).

The displacement profile of the Makanda fault reveals that the fault is composed of four fault segments: i.e., segment A, segment B, segment C and segment D (Figs. 5.19; 5.27).

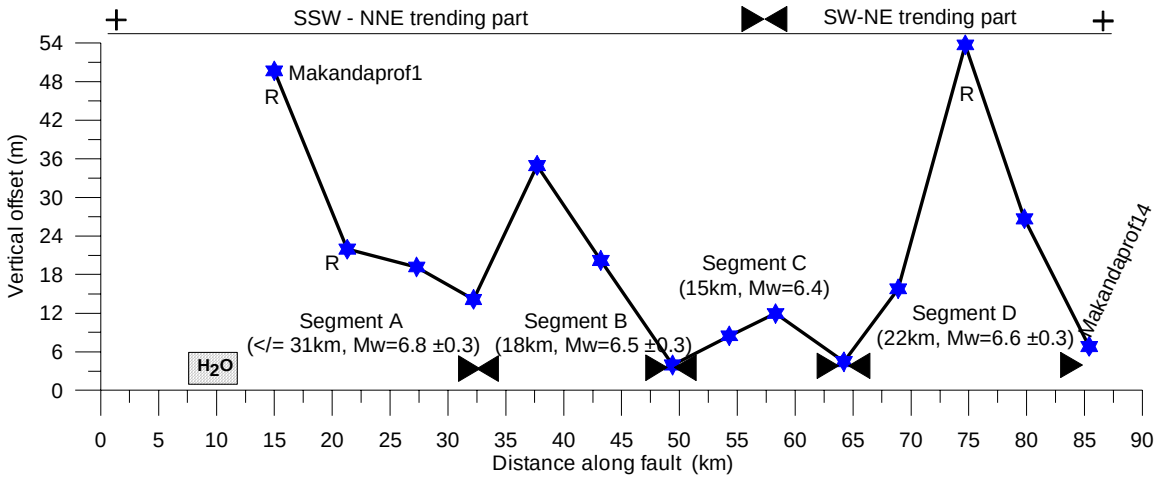

Fig. 5.27 - Displacement profile for the Makanda fault. This profile reveals four fault segments: segments A, B, C and D. Segment A hosts thermal spring fields. The corresponding maximum possible earthquake magnitudes are 6.8 ± 0.3, 6.5 ± 0.3, 6.4 ± 0.3 and 6.6 ± 0.3, respectively.

The Makanda fault: segment A

Based on Fig. 5.27, Segment A is 31 km long and has 50 m of maximum vertical offset. The segment is characterized by rotated blocks. Near its southern end, there exists a thermal spring located at 35°30'E, 6°05'S, just east of the Bahi depression (Fig. 5.19). The concentration of NaCl in some of the waters is suggestive of a deep-seated origin (Appendix 2).

The Makanda fault: segment B
Segment B is 18 km long and has a maximum vertical offset of 35 m. Unlike Segment A, it does not host thermal springs and no evidence for block rotation was recorded.

The Makanda fault: segment C
Segment C is the shortest segment of the Makanda fault, with a length of only 15 km, and it has 12 m maximum vertical offset. It does not host thermal springs and there is no evidence of block rotation. Two important observations are evident here: (i) the Makanda fault starts to turn its direction from NNE to NE, and (ii) it is within this segment that the Maziwa fault passes, which, according to Macheyeki et al. (2008a), is most likely of oblique-slip or strike-slip origin.

The Makanda fault: segment D
Segment D of the Makanda fault is also characterized by block rotations. It is the second longest fault segment (22 km long) and the only fault segment that fully trends NE (about N45°E). A large part of this segment is located within the Chenene mountains (Figs. 5.17; 5.19). The segment has a maximum vertical offset of 53.7 m. Part of this segment is shown in Fig. 5.28.

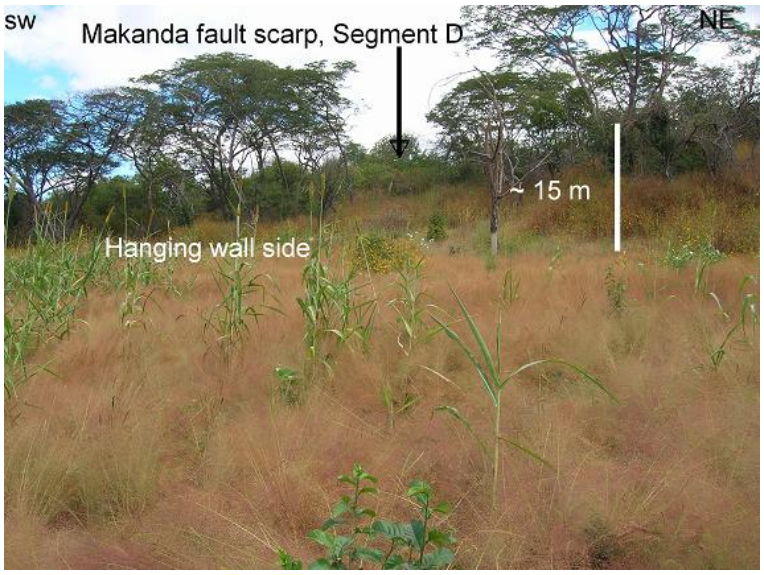

Fig. 5.28 - The Makanda fault (Segment D).

5.2.2.5 The Hombolo fault
The Hombolo fault is 40 km long (Figs. 5.19; 5.29). The fault has two fault segments: i.e., the Dam fault segment (≥ 18 km long) and the Nzuguni fault segment (> 19 km). The Dam fault segment locally shows 2-3 fault steps (not shown due to scale limitations). The Hombolo fault is a NW-dipping fault, i.e. antithetic to all other normal faults in the study area. It is not as clearly expressed in the landscape as other faults in the study area, as it is characterized by only a gentle slope. It runs through the Hombolo town center (Fig. 5.30). The fault scarp has been affected by erosion in two opposite directions (i.e., NW and SE). This erosion seems to be accelerated by both the NW slope of the fault scarp and the

slope due to easterly tilt of the entire area (Fig. 5.31). This tilt is considered to be regional since an SRTM profile drawn from north of the Mponde fault to east of the Hombolo fault (Fig. 5.32) clearly reveals a tilt in the order of 2°.

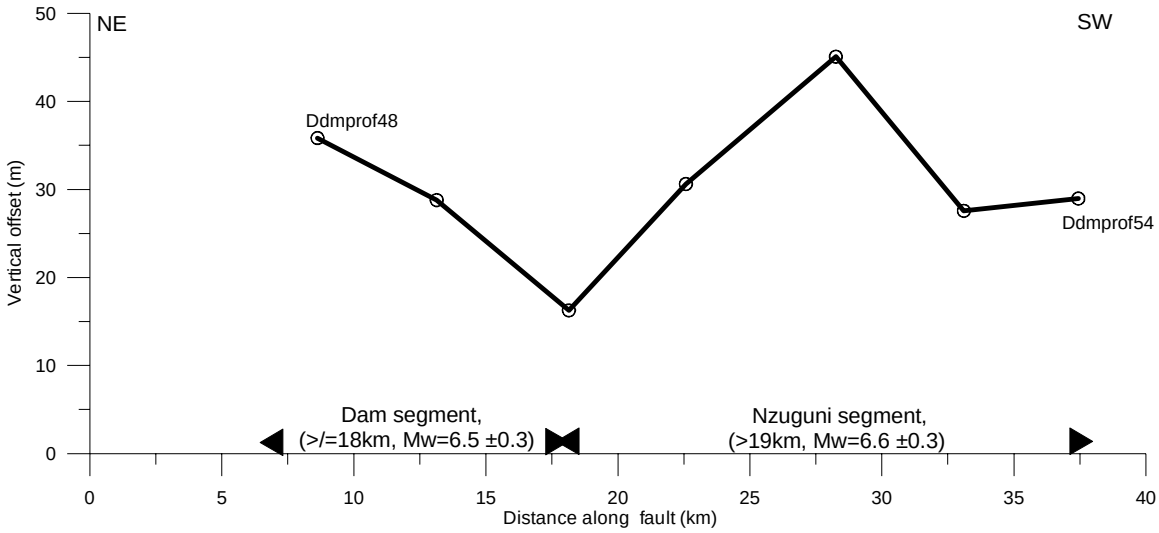

Fig. 5.29 - Displacement profile for the Hombolo fault.
Two fault segments are revealed: i.e., Dam segment and Nzuguni segment.

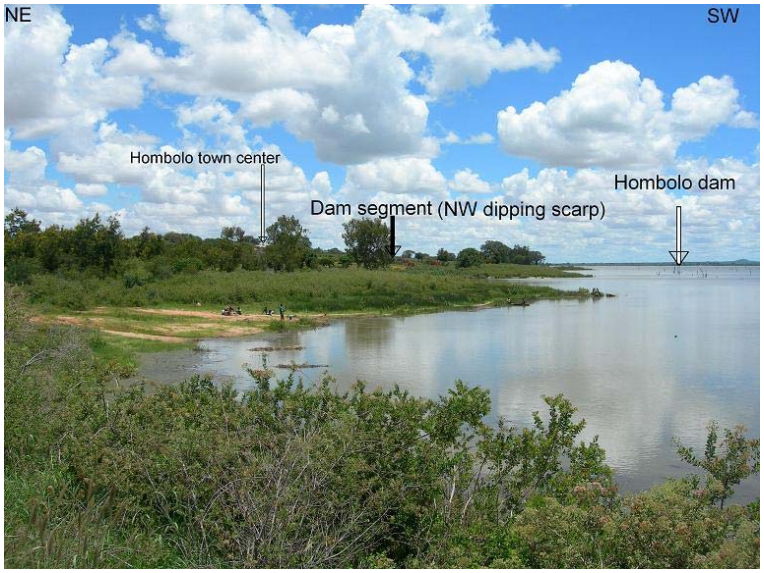

Fig. 5.30 - The Hombolo segment.
The picture was taken by D. Delvaux in March 2006.

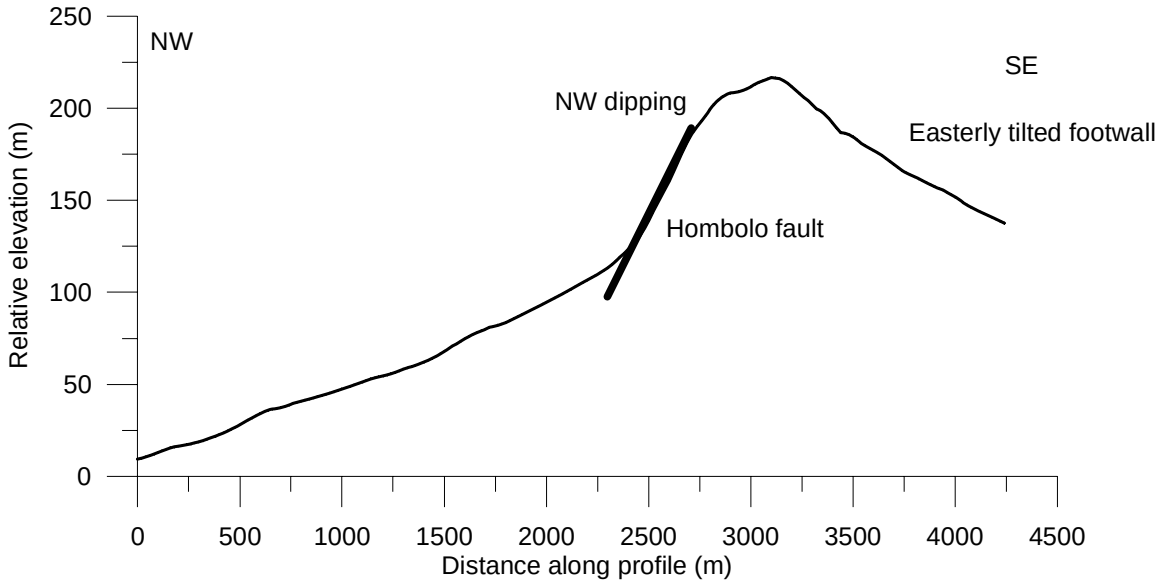

Fig. 5.31 - A 90 m resolution SRTM-DEM topographic profile across the Hombolo fault. Note the dipping direction of the fault and the tilting direction of the topography.

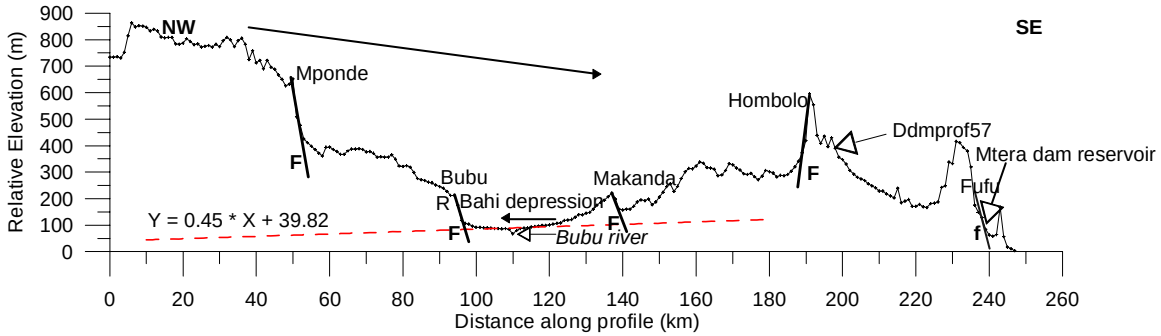

Fig. 5.32 - Detailed regional topographic profile for the Dodoma area using profile Ddmprof57 that crosses most of the studied faults in the study area. The letters 'F' and 'f' represent certain and inferred fault locations, respectively. 'R' symbolizes a significant block rotation. Arrows with filled heads show direction of tilt. Long arrows show regional tilt (Neogene or younger), whereas short arrows show local tilt (recent?). The two directions are opposite to each other. Unfilled arrows are used for locating a particular feature.

5.2.2.6 The Bahi fault

The Bahi fault is a largely NW-SE trending normal fault that dips to the NE. It is 54 km long, and is composed of two fault segments: i.e., the Southeastern segment (≥ 25 km long) and the Northwestern segment (≤ 29 km long).

The Bahi fault: Southeastern segment

The Southeastern segment of the Bahi fault is characterized by block rotation (positive rotation) and hosts a field of saline or thermal springs located in the southernmost part of

the segment (Fig. 5.19) at about 35°10'E, 6°15'S (see also Appendix 2). The maximum vertical offset of the segment is 170 m. Part of this segment is shown in Fig. 5.34.

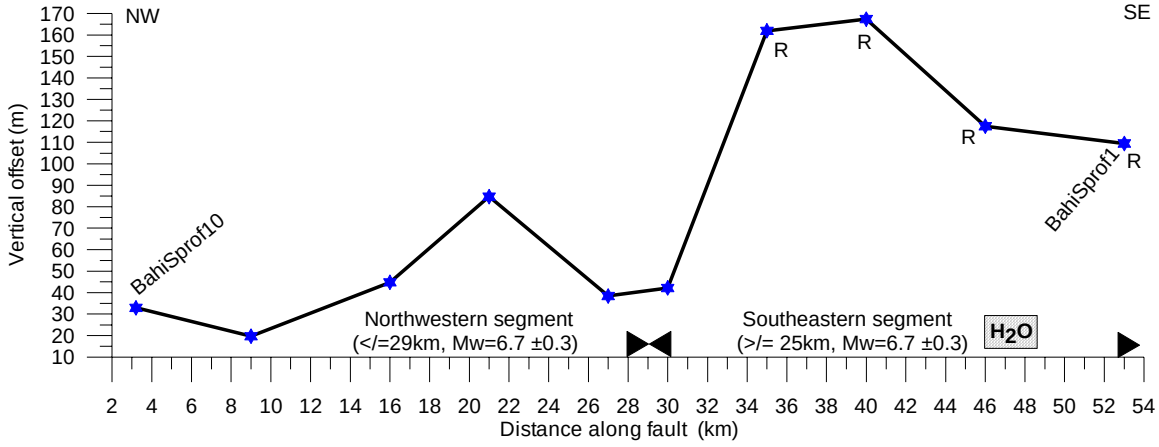

Fig. 5.33 - Displacement profile of the Bahi fault.
Two fault segments are revealed: i.e., the Northwestern segment and the Southeastern segment.

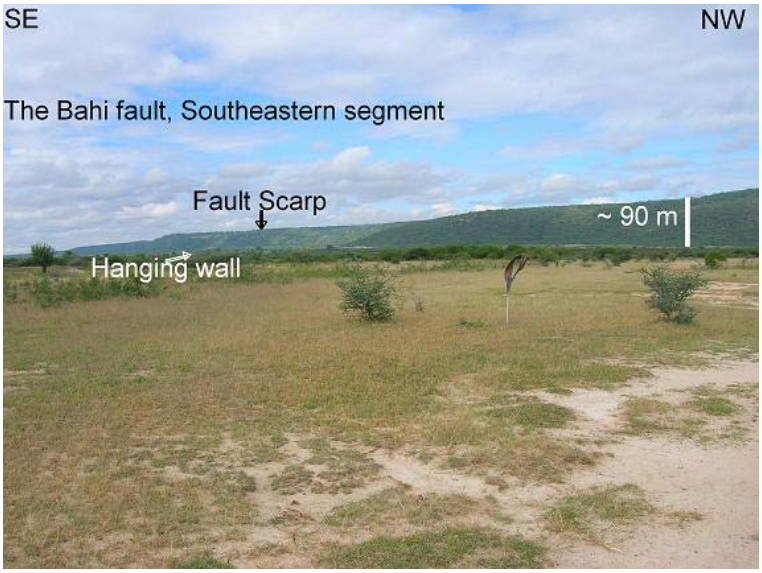

Fig. 5.34 - The Southeastern fault segment of the Bahi fault.

The Bahi fault: Northwestern segment

Unlike the Southeastern segment, the Northwestern segment does not host thermal springs and it does not show block rotation. Its maximum vertical offset is 85 m.

5.2.2.7 The Fufu fault

The Fufu fault defines the southeastern boundary of the study area. It is located about 50-60 km south of Dodoma. It is the second-longest fault in the study area, after the Bubu fault, having a total length of at least 92 km (Fig. 5.35). Like the Makanda fault, the Fufu fault has four segments: i.e., segment A, segment B, segment C and segment D (Figs. 5.19; 5.35). It also dips easterly. Generally, the fault has an impressive scarp and locally it has some fault steps particularly on Segment C close to Fufu village (Fig. 5.36).

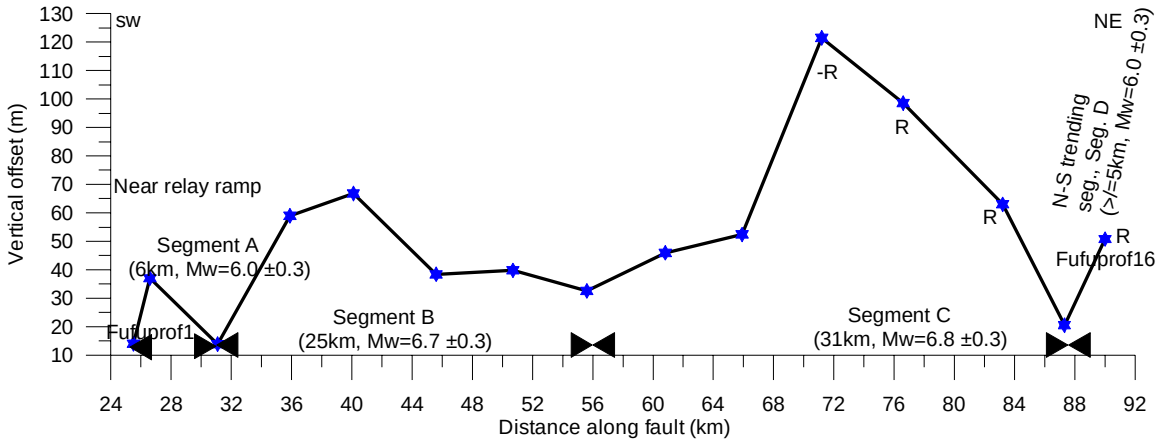

Fig. 5.35 - Displacement profile for the Fufu fault. It is interpreted as a fault with four fault segments: i.e., segment A, segment B, segment C and segment D. Corresponding maximum possible earthquake magnitude that can be generated by each segment being M_w = 6.0 ± 0.3, 6.7 ± 0.3, 6.8 ± 0.3 and 6.0 ± 0.3 respectively.

The Fufu fault: segment A

Segment A defines the southwestern part of the fault. It is only 6 km long and has a maximum vertical offset of 37 m. This fault segment links with another segment, further to the south (outside the study area), but both segments are not yet fully liked.

The Fufu fault: segment B

Segment B is 25 km long and has a maximum vertical offset of about 67 m.

The Fufu fault: segment C

Segment C is the main fault segment of the Fufu fault. The segment is characterized by both negative and positive rotations of blocks. Segment C is 31 km long and has 121.5 m maximum vertical offset. Part of Segment C is shown in Fig. 5.36.

The Fufu fault: segment D

Like Segment A, this is also a small fault segment (≥ 5 km). It trends nearly N-S (Fig. 5.19). Slope changes across this segment indicate positive block rotations.

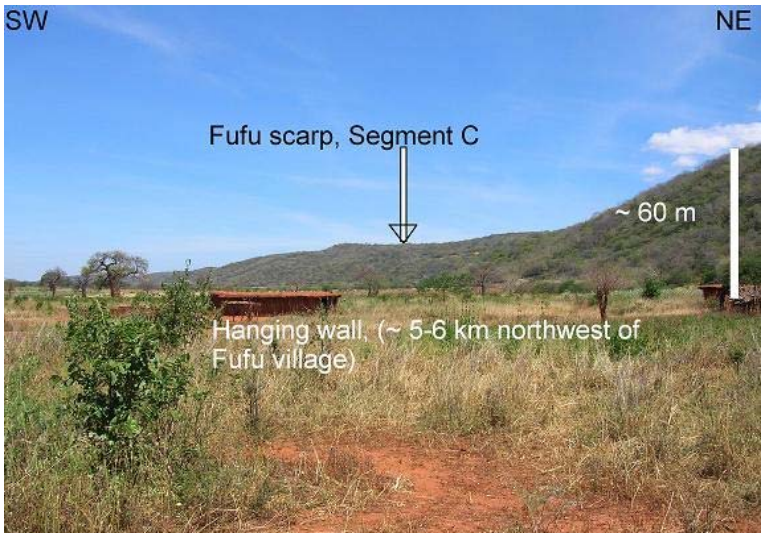

Fig. 5.36 - The Fufu scarp.
The picture was taken in May 2006, facing northwest.

5.2.2.8 The Chikola fault

The Chikola fault is located about 33 km NE of the Bahi fault, to which it runs nearly parallel. The fault is considered to be composed of a single segment (Fig. 5.37a). Unlike all other faults in this area, its vertical offset decreases from over 25 m on its ends to about 15 m towards its center. In the field, it is less impressive (Fig. 5.38).

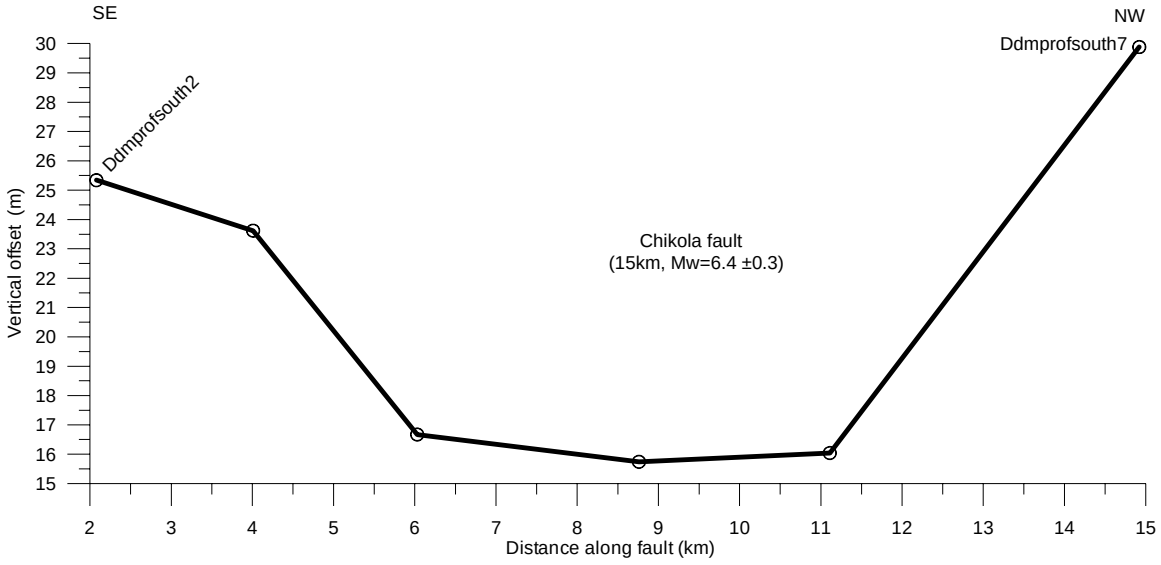

Fig. 5.37a - Displacement profile for the Chikola fault. It is a single segment fault (See also Fig. 5.19).

The decrease of vertical offset towards its center is in contradiction to observations on all other active faults discussed above. This pattern of displacement profile is thought to be a result of fault interactions: i.e., part of the stress responsible for the growth of the Chikola fault is most likely taken up by nearby faults such as the Nkambala fault (e.g., Jackson

and White, 1989). Alternatively, the Chikola fault could also be considered to consist of two segments: i.e., Chikola A and Chikola B (Fig. 5.37b). In the latter interpretation, the center of maximum vertical offsets of Chikola A and Chikola B and their subsequent minimum values (i.e., lateral and vertical limits of either segment) could not be observed nor confirmed in the field. They may have been eroded or disturbed, which could indicate that the Chikola fault is no longer active.

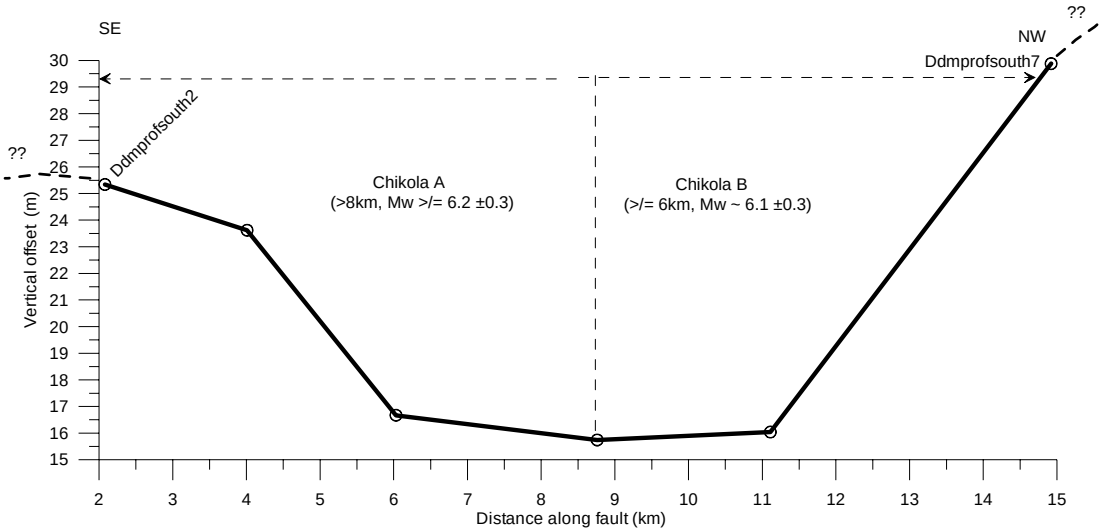

Fig. 5.37b- Displacement profile for the Chikola fault as a two-segment fault. The dashed vertical line represents the locus of the intersection between Chikola A segment and Chikola B segment. The lateral and vertical limits of either segment are uncertain (See also Fig. 5.17 and Fig. 5.19 for orientation).

Fig. 5.38 - View of the Chikola scarp.
The picture was taken in May 2006, facing southwest.

5.2.2.9 The Maziwa fault

Like the Mponde, Bahi and Chikola faults, the Maziwa fault is a NW-SE trending linear structure that occurs mainly between the Bubu and the Hombolo fault (Figs. 5.15; 5.17). It is weakly expressed on the surface and shows no particular slip pattern. Results from SRTM-DEM data show that the structure cuts through recent sediments within the Bahi depression and it joins or intersects both the Bubu fault, at the Gonga fault segment, and the Makanda fault, at its Segment C (Fig. 5.19).

Some SRTM profiles across the structure indicate a dip-slip sense but river or streams that cross it tend to be deflected dextrally. However, field checks at two points located about 3 km apart along the structure around the Maziwa village revealed no evidence to support the arguments above. This is probably due to the fact that there are no outcrops visible around both points due to a thick siliceous cover (i.e., the Kilimatinde cement, a silicate weathering product composed of kaolinite and silica; Fig. 5.16). Due to the aforesaid reasons, neither vertical offsets were calculated nor were displacement profiles established across this fault.

5.2.2.10 Relay ramps in the Dodoma area: the Mponde, Saranda and Bubu faults

Mponde relay ramp

The overlapping fault tips between Segment 1 and Segment 2 of the Mponde fault are about 5.3 km across them. They form a tilted block (indicated by a white line in Figs. 5.19; 5.39) towards the north. In other words, the relay ramp block tilts towards the hanging wall side. The start and end coordinates of the relay ramp profile are 35°01'E, 5°10'S and 35°00'E, 5°02'S.

A nearly 12 km long topographic profile along the relay ramp corresponds to a change of slightly more than 200 m of elevation (Fig. 5.39).

Saranda relay ramp

The Saranda relay ramp occurs between the Saranda south and the Saranda mid segments (Figs. 5.17; 5.19; 5.39). Its approximate end coordinates are 34°50'E, 5°46'S and 34°58'E, 5°44'S. It is around this point that both fault segments have minimum values of vertical offsets. From the topographic profile drawn parallel to the relay ramp (Fig. 5.39), it is clear that the value of vertical change (100 m) over horizontal change (11.1 km) is about half that of the Mponde relay ramp (Fig. 5.39).

Bubu relay ramp

Like the Saranda relay ramp, the Bubu relay ramp dips NE (Fig. 5.39). The approximate coordinates for the relay ramp are 35°05'E, 5°41'S and 35°11'E, 5°37'S. This relay ramp has similar dimensions to that of the Saranda fault relay ramp, and displays a vertical change of about 100 m over nearly 12 km (Fig. 3.39).

The amount of slopes for these three relay ramps show that the degree of fault growth interaction increases both towards the east but much more towards the north.

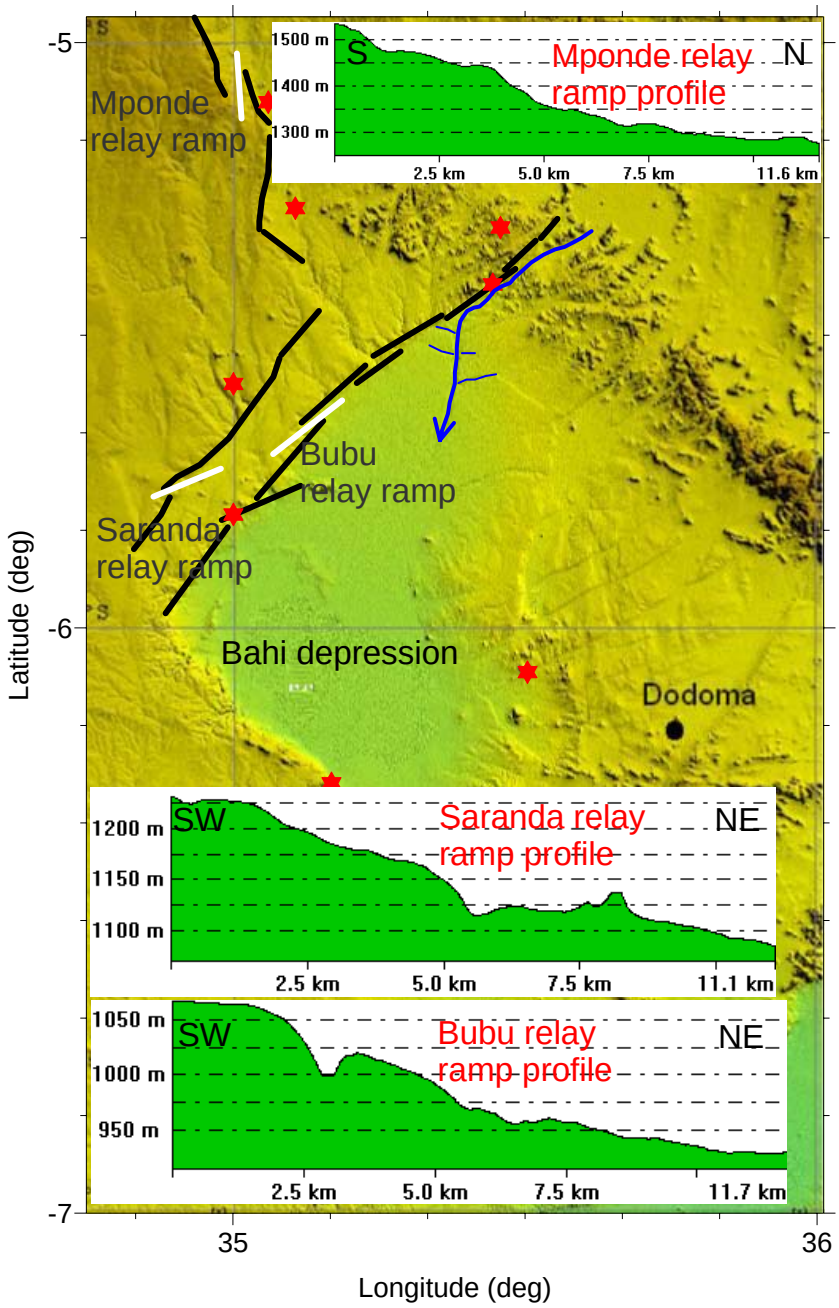

Fig. 5.39 - Relay ramps; Mponde, Saranda and Bubu.

5.2.3 The Bahi depression

The Bahi depression is a relatively large depression within the study area (40-50 km wide and 80-90 km long). It is about 40-50 km west of Dodoma. In this depression there are relatively recent, mainly siliceous (e.g., Fig. 5.16) deposits, ranging from Neogene to Present. Furthermore, thermal springs mark its margins that are defined by the Bahi, Bubu and Makanda faults. The Bubu river (Fig. 5.43) runs from north of the study area into this depression. Since rivers are sensitive features that can change their course and

shape in function of uplift, tilt or faulting (e.g., McCalpin, 1996), we believe that by studying the Bahi depression, we can obtain information related to active tectonics. Although this section does not give detailed tectonic activities related to the depression, it highlights the role of the depression in recording recent tectonic activities in the study area. Here we briefly analyze the topography of the depression relative to the entire study area.

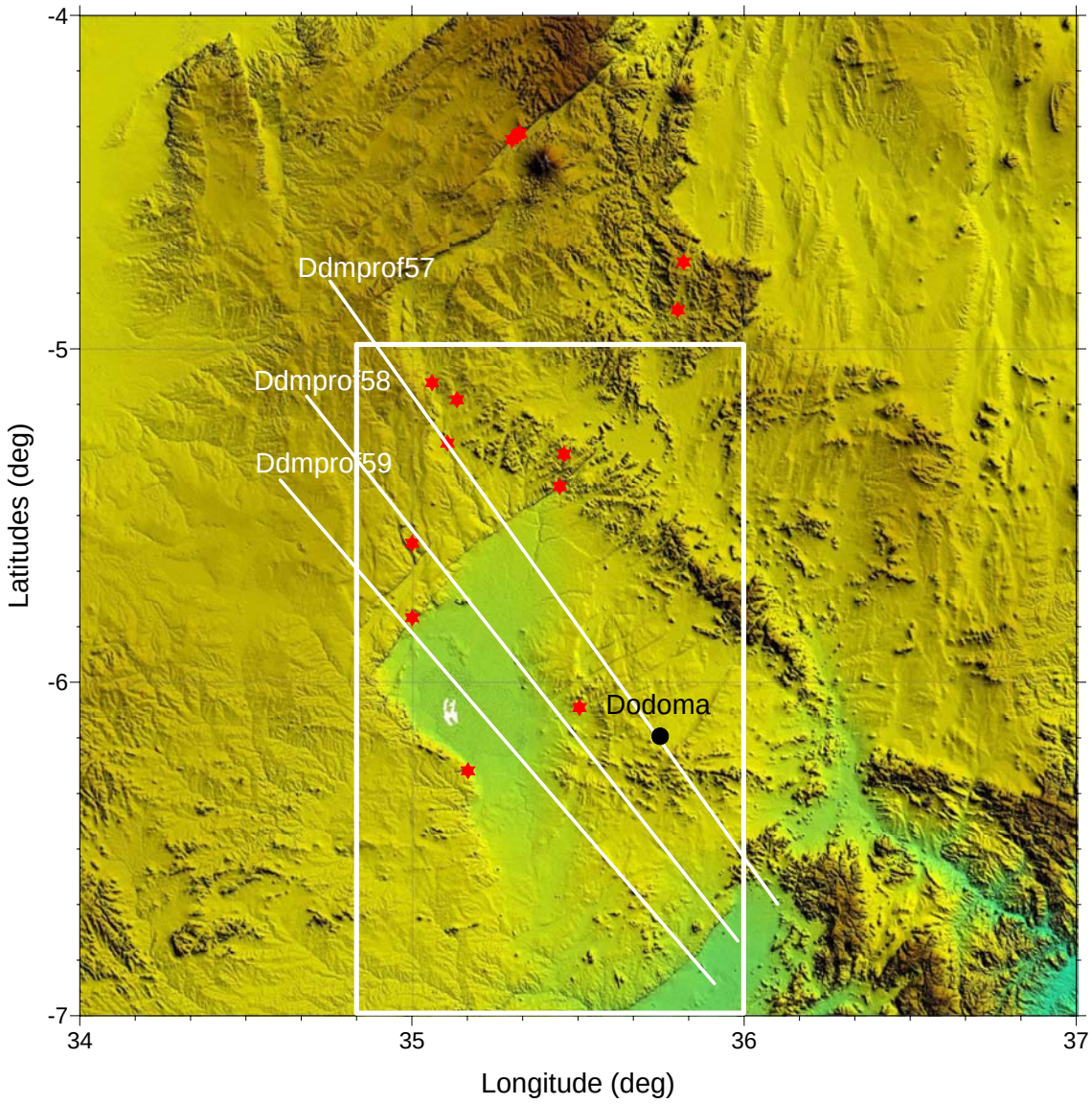

Fig. 5.40 - SRTM-DEM map showing locations of three long topographic profiles Ddmprof57-59. Corresponding plots in Fig. 5.41.

The Bahi depression is located on the hanging wall of the Bubu fault; which is the longest NW-SE trending fault in the study area. A topographic profile across the northern part of the Bubu fault at Gonga segment (Figs. 5.32; 5.40), shows that the Bahi depression is characterized by a gentle westward dip towards its northern end, which is in contrast to the general easterly dip of the entire study area (e.g., Figs. 5.41; 5.42). A 3.4 km long

profile, Ddmprof18, that crosses within the same area where Ddmprof57 passes on the Bubu fault (see Ddmprof18 marked as A18 in Fig. 5.17) has shown the biggest slope difference (of about 2.0°) between the upper and lower reference surfaces in the entire study area (Table 5.1), indicating that this place has experienced a significant block rotation.

Towards the south, the overall dip direction of the depression changes from westward to eastward. Further south the dip direction remains eastward (Fig. 5.41) but the gradient is about 6 times lower.

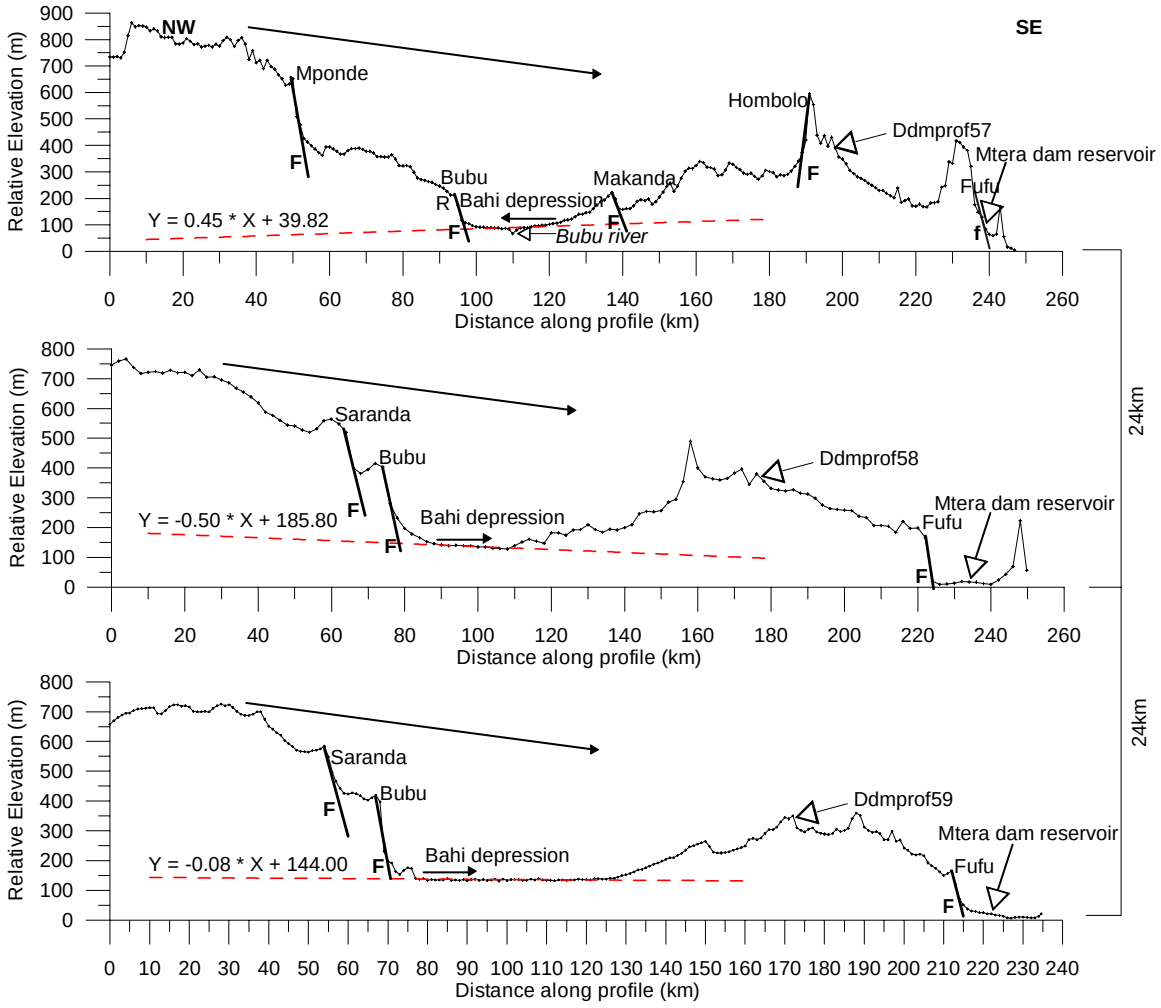

Fig. 5.41 - Topographic profiles (Ddmprof57-59) crossing a large part of the Bahi depression. The profile Ddmprof57 is set as a reference profile. Other profiles were set at roughly 24 km intervals parallel to Ddmprof57 (as in Figs. 5.32; 5.40). Although regionally (as indicated by long filled arrows) the tilt is easterly, locally, (as indicated by short filled arrows), the Bahi depression tilts westerly towards the northern end and easterly in the southern part. The profiles show change of tilt direction; i.e. from westerly to easterly. Letters and symbols as in Fig. 5.32.

5.3. Summary and conclusions

At least 7 active faults have been identified in the area north of Dodoma, based on the identification of morphological lineaments on the SRTM-DEM, combined with information from geological maps and from field observations: i.e., the Mponde, Saranda, Bubu, Makanda, Hombolo, Chikola, Bahi and Fufu faults.

Table 5.3 - List of faults in the Dodoma area along with their associated segments versus estimated possible maximum earthquake magnitudes (M_w), which can be generated by the fault segments. These estimates are only possible for each segment if and only if fully reactivation of each individual fault segment is attained (Wells & Coppersmith, 1994). Fault segments on the Maziwa fault, not revealed. The Balangida fault segments are in italics to show that they are outside the study area even if the Balangida fault is connected to the Mponde fault (no more details are given for this fault). The symbol * represents estimated earthquake magnitude from paleoseimic investigation (trenching) on one of the satellite faults in the Gonga fault segment. ♀ implies that there is an alternative interpretation (see 5.2.2.8 and the Figures 5.37a,b).

Fault / Fault segment	Fault length (km)	Maximum fault displacement (m)	Maximum magnitude of potential earthquake (M_w)
Mponde (Segment1)	31	1.41	6.8 ± 0.3
Mponde (Segment2)	28	1.03	6.7 ± 0.3
Saranda (Saranda south)	11	0.30	6.3 ± 0.3
Saranda (Saranda mid)	29	1.41	6.8 ± 0.3
Saranda (Saranda north)	24	1.03	6.7 ± 0.3
Bubu (Nkambala)	33	1.41	6.8 ± 0.3
Bubu (Makutupora)	30	~ 1.41	~ 6.8 ± 0.3
Bubu (Gonga)	42	~ 2.62	~ 7.0 ± 0.3 (6.3-6.4*)
Makanda (Segment A)	≤ 31	≤ 1.41	6.8 ± 0.3
Makanda (Segment B)	18	~ 0.55	6.5 ± 0.3
Makanda (Segment C)	15	~ 0.41	6.4 ± 0.3
Makanda (Segment D)	22	~ 0.76	6.6 ± 0.3
Hombolo / Dam	≥ 18	0.55 - 0.76	(6.5 - 6.6) ± 0.3
Hombolo / Nzuguni	> 19	0.55 - 0.76	(6.5 - 6.6) ± 0.3
Bahi (Northwestern)	≤ 29	~ 1.03	6.7 ± 0.3
Bahi (Southeastern)	≥ 25	1.03	6.7 ± 0.3
Fufu (Segment A)	6	0.12	6.0 ± 0.3
Fufu (Segment B)	25	1.03	6.7 ± 0.3
Fufu (Segment C)	31	1.41	6.8 ± 0.3
Fufu (Segment D)	≥ 5	0.09	6.0 ± 0.3
Chikola	15	~ 0.41	6.4 ± 0.3♀
Maziwa	Nil	Nil	Nil
Balangida (South)	*40*	*~ 1.92*	*6.9 ± 0.3*
Balangida (North)	*≥ 25*	*1.03*	*6.7 ± 0.3*

About 110 topographic profiles were constructed across these faults, and the following parameters were determined: (i) UTM coordinates of start and end points of each topographic profile, (ii) slope difference between upper and lower reference surfaces of the profiles, (iii) vertical offset, and (iv) distance of the profile along the faults from a

selected point of origin. These data allowed to establish that the 7 faults consist of 20 separate fault segments: i.e., 2 segments for the Mponde fault, 3 segments for the Saranda fault, 3 segments for the Bubu fault, 4 segments for the Makanda fault, 2 segments for the Hombolo fault, 1 segment for the Chikola fault, 2 segments for the Bahi fault and 4 segments for the Fufu fault.

The topographic profiles also reveal discrete changes in local and regional tilt direction of the Bahi depression, in the hanging wall of the Bubu fault. All observations highlight ongoing tectonic activity in the area.

Based on the empirical relationship of Wells and Coppersmith (1994), which gives the relationship between fault or fault-segment length, vertical displacement (or offset) and possible earthquake magnitude, it has been possible to estimate the earthquake magnitudes that the identified faults or fault segments are capable to generate (Table 5.3). Except for the Gonga segment of the Bubu fault, all fault segments in the Dodoma area can generate earthquakes of magnitudes ranging between $M_w = 6.0 \pm 0.3$ to 6.8 ± 0.3, assuming full reactivation of the given fault segment.

5.3.1 Main conclusions

Three important results can be highlighted:

1. although the thermal springs are found in the NE-SW-, NW-SE- and N-S-trending faults, the overall or regional pattern of these thermal springs also seem to be aligned N-S, probably suggesting a N-S structural control (Fig. 5.42);
2. the Maziwa fault offsets the Bubu river tributaries and possibly the satellite faults in the Bubu fault (where it is believed to intersect), in a right-lateral direction (Fig. 5.43), suggesting that the Maziwa fault is most likely a dextral strike-slip fault or a dextral oblique-slip fault;
3. some sets of old structures have not been reactivated or do not appear to be active faults, which suggests that the presence and orientation of active faults in the region is controlled by old structures that were oriented favourably to the recent stress field.

We propose that the Maziwa fault is transferring deformations between the Makanda fault and the Bubu fault. By doing so, it is acting as shock-absorber of seismic activities between both faults; more specifically, between the Gonga segment of the Bubu fault and Segment C of the Makanda fault (Fig. 5.43).

Although previous results by Macheyeki et al. (2008a), based on a first assessment of the seismic hazard in the area, suggest that the Gonga segment can generate the biggest earthquake in the area, with magnitudes of up to $M_w = 7.0 \pm 0.3$, it is possible that this magnitude cannot be attained due to the buffering influence exerted by the Maziwa fault. Determinations of earthquake magnitudes were based on empirical relationships of displacement versus fault length in accordance to Wells and Coppersmith (1994).

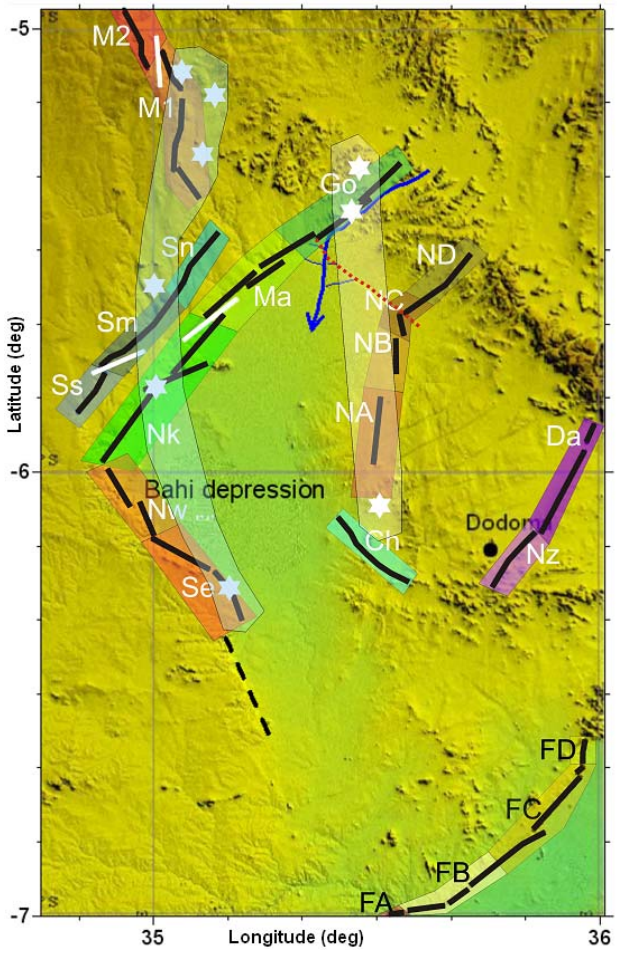

Fig. 5.42 - Map of the study area showing fault segments, relay ramps and thermal springs. The thermal springs show a N-S trend. The Maziwa fault is shown in red. All other names are as in Figs. 5.19 and 5.39.

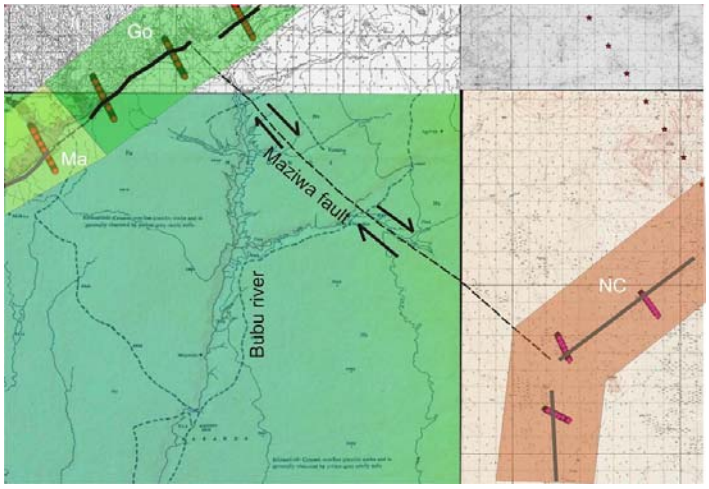

Fig. 5.43 - A zoom in of the Maziwa fault overlayed with 1:125,000 geological map, 1:50,000 topographic map and 90 m resolution SRTM-DEM. Geological and topographic maps indicate, though fairly, a right-lateral movement as shown on the map. The fault connects the Bubu fault at the Gonga segment and the Makanda fault at Segment C. For orientation see Figs. 5.19; 5.42.

5.4. Assessment of accuracy and limitations of used methods

The precision of the topographic profiles obtained from the SRTM-DEM data depends on the minimum resolution of the SRTM-DEM data itself (i.e., 90 m). Furthermore, the quality of fault-scarp slopes computed from these data varies in the function of sampling interval (i.e. the distance between sampling points along the profile). Results show that the smaller the sampling interval the higher the resolution of sampled data hence the closer is the data-fit to the reality and vice versa.

As this application (i.e., the use of SRTM-DEM data to compute fault parameters) is being used for the first time (at least in Africa?), it is important to evaluate its reliability in comparison with other high-precision field techniques, such as determination of vertical offsets using differential global position systems (DGPS) that renders few centimetres-errors.

Both approaches were compared in a study of the Kanda fault system in the Ufipa plateau in SW Tanzania by Macheyeki et al. (2008a). Fault parameters were first extracted from displacement profiles derived from the 90 m resolution SRTM-DEM and compared with high precision DGPS data collected along the same profiles. Results show that there is a good correlation between the two data sources. Vertical offsets obtained from both SRTM and DGPS for profiles which are ≤ 700 m apart, give correlation coefficients of R = 0.968 (Fig. 5.44). The faults scarps in the Kanda fault system are, however, on average only ca. 30 m in height.

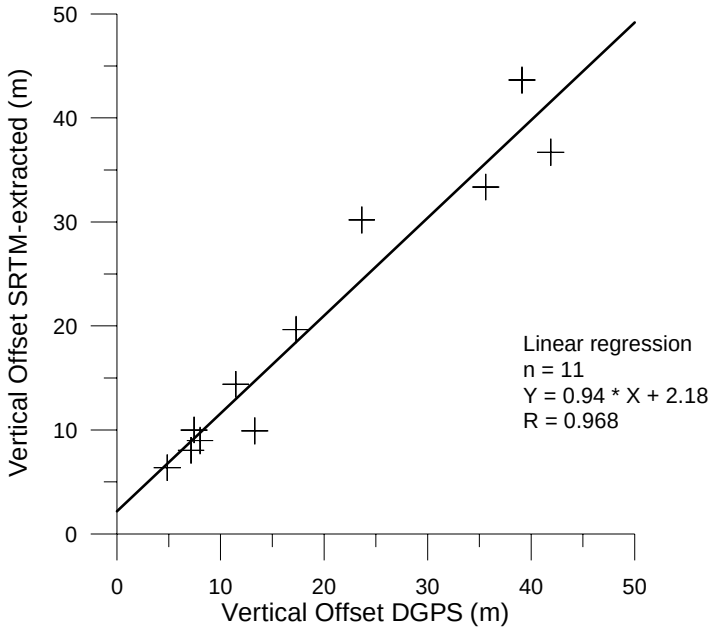

Fig. 5.44 - Comparison between vertical offsets obtained from SRTM and DGPS data for profiles which are ≤ 700 m apart. Regression line, as indicated by correlation coefficient R = 0.968, shows a good correlation between the two types of profiles (Macheyeki et al., 2008a).

It therefore follows that for the Dodoma area, where most faults have vertical offsets in excess of 100 m, the vertical offset values obtained from 90 m resolution SRTM data can be considered to be reliable and suitable for fault-parameter computations.

Chapter 6

Fault Kinematics and Tectonic Stress

A summarized version of this chapter was published as:
Macheyeki, A.S., Delvaux, D., De Batist, M., Mruma, M., 2008b. Fault kinematics and tectonic stress in the seismically active Manyara-Dodoma rift segment in Central Tanzania - Implications for the East African Rift. *Journal of African Earth Sciences,* **51**, 163-188.

6. Fault kinematics and tectonic stress

6.1. Paleostress analysis from fault-slip data

After having identified potentially active faults on the available maps and on the SRTM-DEM, after having verified in the field that these faults can indeed be considered as active, and after having computed displacement profiles and established the degree of segmentation of these faults, the next step in our approach was to analyze indications of past fault movements and to compute paleostress regimes for each of the investigated faults or fault segments.

Fault-slip data were collected during several field campaigns in March-September 2006, February 2007, May-June 2007 and November 2007, in a series of study areas selected on basis of analysis of the DEM and field verification (Fig. 6.1). These areas are northern part of Mponde fault (1a), southern part of Mponde fault (1b), middle part of Saranda fault (2), Gonga hot-spring field on the northern part of Bubu fault (3a), Magungu area along Bubu fault (3b), Makutupora area along the Bubu fault (3c), northern part of the Makanda fault (4a), Hombolo area along the Hombolo fault (5), the Bahi fault (7), the Fufu fault (8) and Chenene village area (9). No paleostress data were taken from Maziwa fault (4b) and Chikola fault (6) mainly due to lack of good/representative outcrops. Fault-slip data were collected on fault surfaces taking into account the presence or absence of slip on the fault surface, activation type (non activated, neo-formed, reactivated, or unknown), the presence or absence of striae in the format shown in Table 4.3 (Chapter 4).

In this chapter, the results of paleostress analysis of these field data will be presented. For each site, the old stress regime(s) will be discussed first, followed by the younger stress regime(s). Reduced paleostress tensors will be presented, along with corresponding rotational optimization curves.

It shall be noted that from these results, most reduced stress tensors are obtained from fracture planes that do not show evidence of slip movement. They were therefore treated as shear fractures (movement joints) associated with Precambrian rocks for constraining the stress tensor. Fracture planes without sense of movement are mainly related to recent tectonic activities. While the latter planes are generally barren, older planes that are related to strike-slip or thrust faulting are typically associated with ferruginization, kaolinization or alteration minerals.

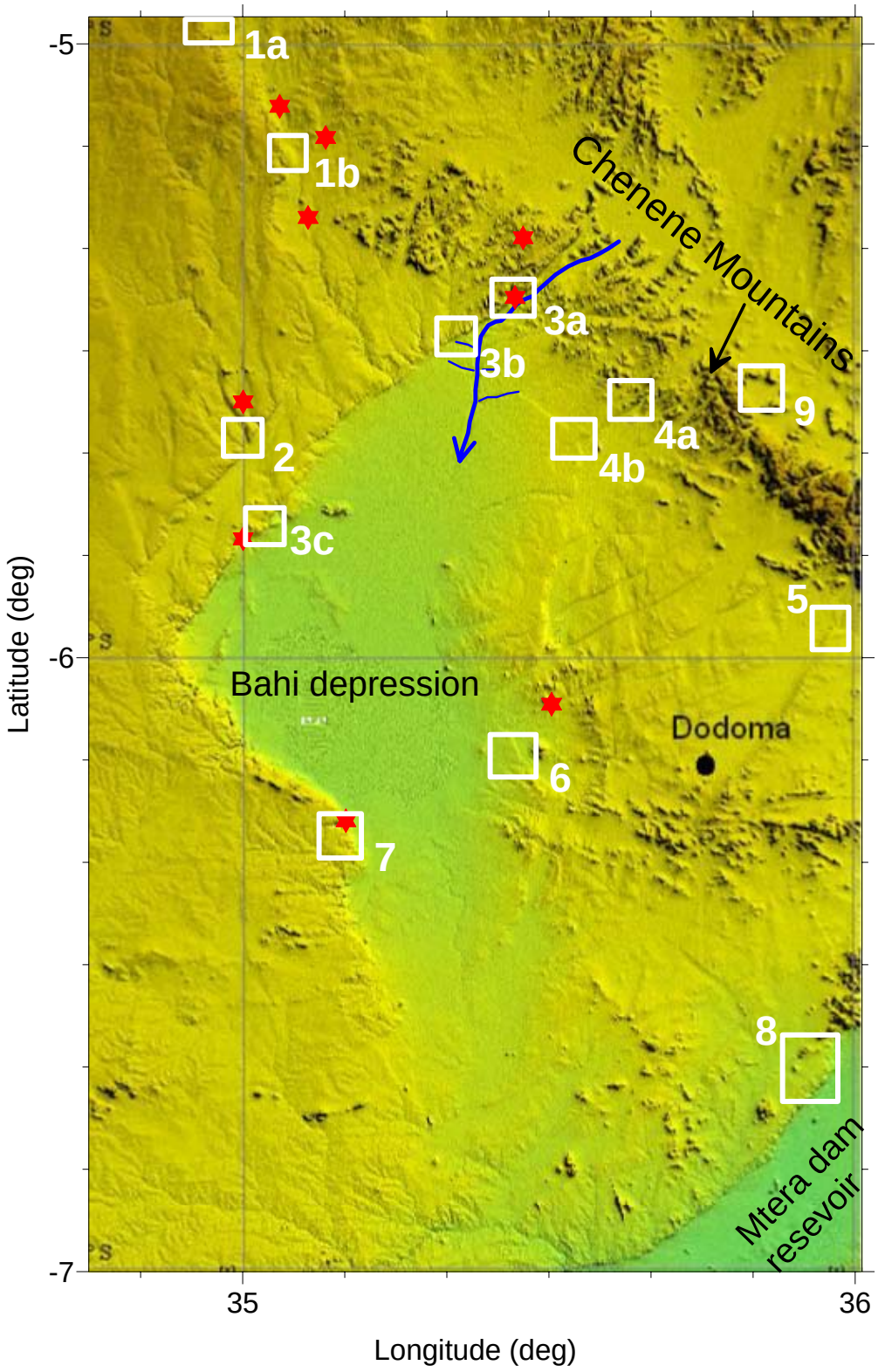

Fig. 6.1 - The SRTM-DEM map of the Dodoma area showing location of study areas where measurements were made for paleostress analysis. The dominant fault directions (i.e. NE-SW, NW-SE, NNW-SSE and N-S trending faults) can also be identified on the map. Red stars are thermal spring locations (After Macheyeki et al., 2008b).

6.1.1 Fault-slip data and interpretation

Throughout this chapter, the symbol R' is used instead of R (i.e. stress ratio) on the figures. It should not be confused with stress regime index. Principal stresses will be labeled either by symbols S1-2-3, $\sigma_{1\text{-}2\text{-}3}$ or sigma1-2-3. These annotation irregularities are imposed by the use of the Win-Tensor program for paleostress inversion.

The directions of maximum and minimum horizontal principal stress axes represented by S_{Hmax} and S_{hmin} are in a format shown in Table 6.1b. (i.e., they are measured in degrees from north clockwise).

6.1.1.1 The Mponde fault, segment 1

From this segment (location 1b; Fig. 6.1), only recent related fault kinematic data were obtained, most of which are from movement joints.

The corresponding stress tensor shows a purely extensional regime characterized by a NE-SW extensional direction that is defined by S_{Hmax} = 136, S_{hmin} = 046, stress ratio R = 0.70 and stress regime index R' = 0.70 (Fig. 6.2a; Table 6.1a,b). Based on the Mohr circles, about 90 % of the slip-data fall within the unstable field (Fig. 6.2b), suggesting that the fault (fault segment) has been formed from pre-existing structures or that the fault segment can be reactivated.

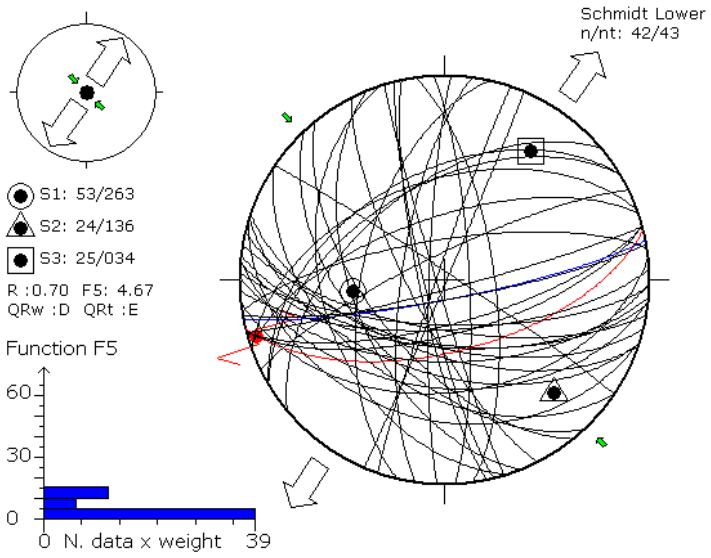

Fig. 6.2(a) - Stress tensor for recent stress regime for the Mponde fault, Segment 1 (Location: 1b on Fig. 6.1). Red and blue lines represent slikensides and old movement joints, respectively.

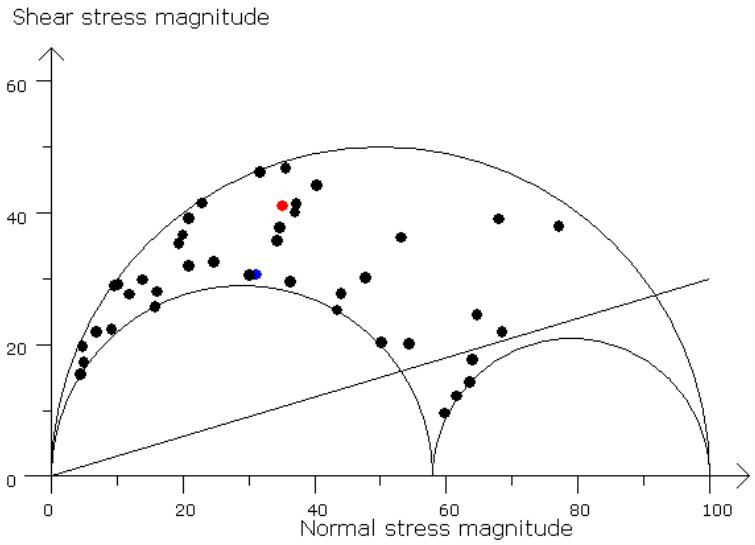

Fig. 6.2(b) - Mohr circles for the faults / movement joints plotted in (a). Red and blue points represent slikensides and old movement joints, respectively.

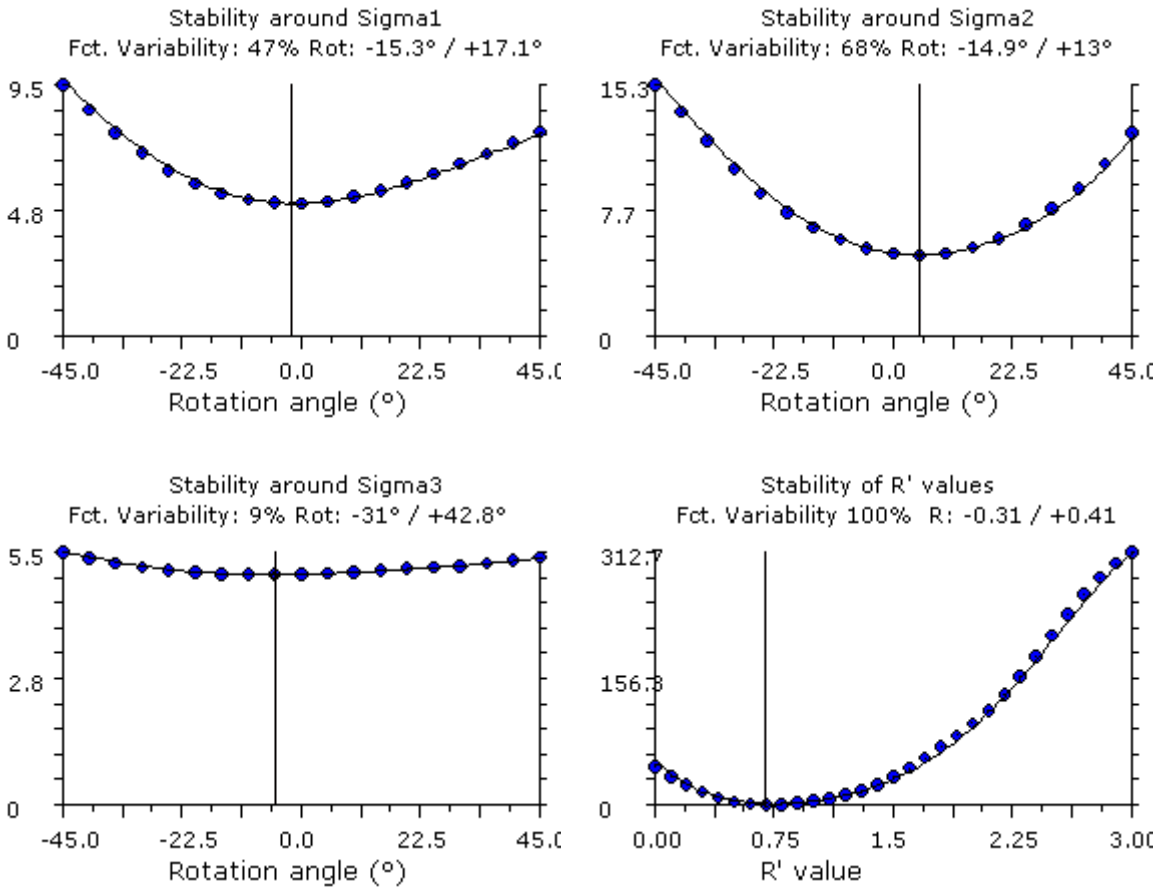

Fig. 6.2(c-f) - Rotational optimization curves of σ_1, σ_2, σ_3 and R for the Mponde fault, Segment 1.

This stress tensor is interpreted to be related to the recent/current stress regime in that particular locality because most data come from barren movements joints. Additionally, it is defined by σ_1 = 53/263, σ_2 = 24/136 and σ_3 = 25/034, where the first two digits represent the amount of dip (plunge) and the last three digits, the dip direction (azimuth). Rotational optimization curves for segment 1 show that σ_1 and σ_2 are relatively stable (Fig. 6.2c-d), while σ_3 (Fig. 6.2e) and R (Fig. 6.2f) are relatively unstable. This is most likely due to the lack of sufficient slikensides as revealed in the tensor (Fig. 6.2a).

6.1.1.2 The Mponde fault, segment 2

Like in segment 1 of the Mponde fault, only recent fault kinematic data were obtained in segment 2 (location 1a; Fig. 6.1).

It is characterized by pure extension in a N-S direction, defined by S_{Hmax} = 093, S_{hmin} = 003 and stress regime index R' = 0.50 (Fig. 6.3a; Table 6.1a,b). Additionally, it is defined by R = 0.50, σ_1 = 74/185, σ_2 = 01/096 and σ_3 = 18/003. All movement joints fall within the fault reactivation field (Fig. 6.3b). Corresponding rotational optimization curves show that σ_1 and σ_2 are stable (Fig. 6.3c-d), whereas σ_3 (Fig. 6.3e) is not stable. As a result, rotation optimization for the stress ratio R was not possible (Fig. 6.3e). This is mainly due to lack of slip lines on fault planes and limited number of data collected (Table 6.1b).

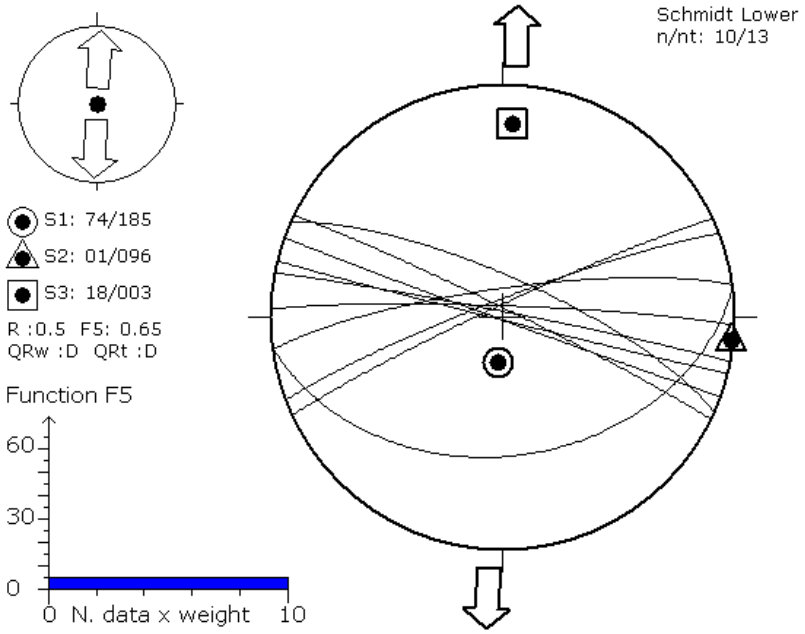

Fig. 6.3(a) - Stress tensor for recent stress regime for the Mponde fault, Segment 2 (Location: 1a on Fig. 6.1).

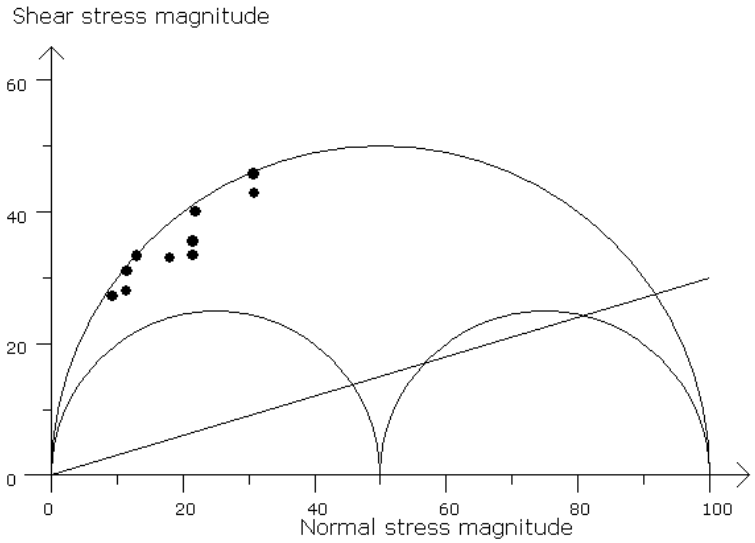

Fig. 6.3(b) - Mohr circles for the faults / movement joints plotted in (a).

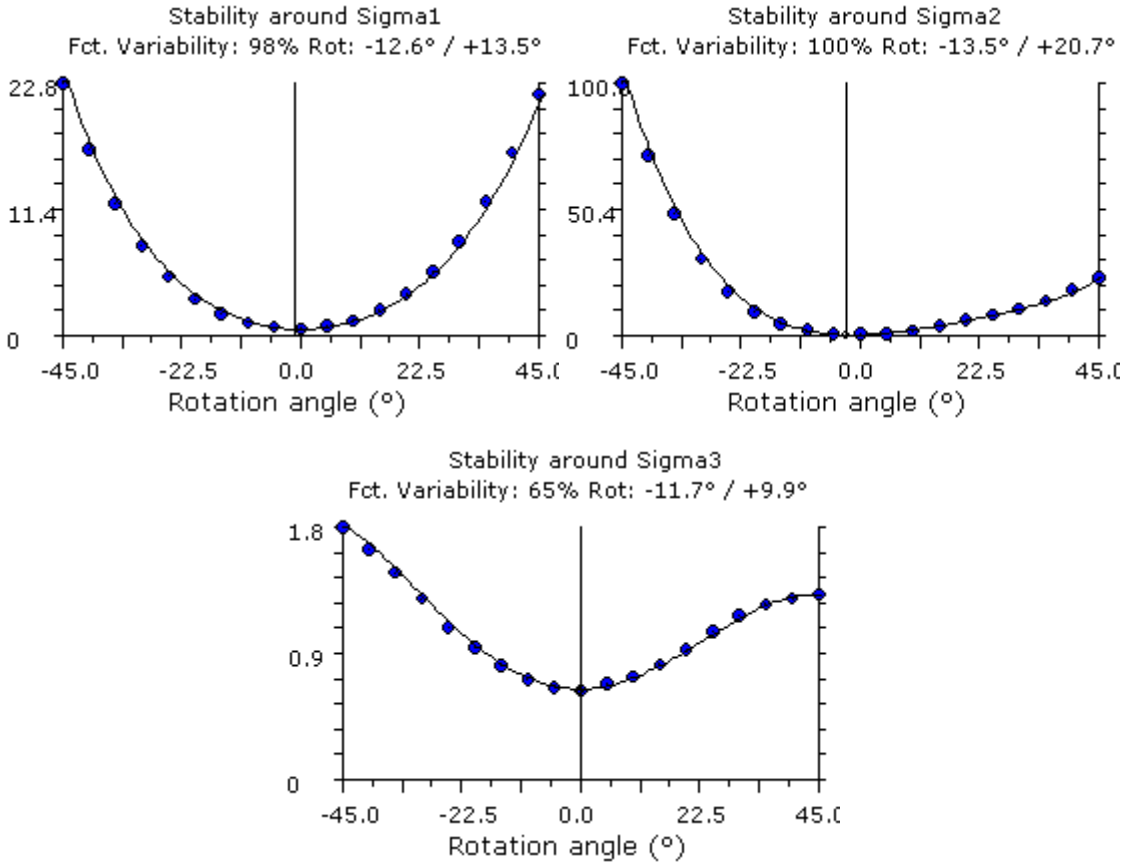

Fig. 6.3(c-e) - Rotational optimization curves of σ_1, σ_2 and σ_3 for the Mponde fault, segment 2.

6.1.1.3 The Saranda fault, Saranda mid segment

Fault kinematic data were also collected from the Saranda mid segment (location 2; Fig. 6.1).

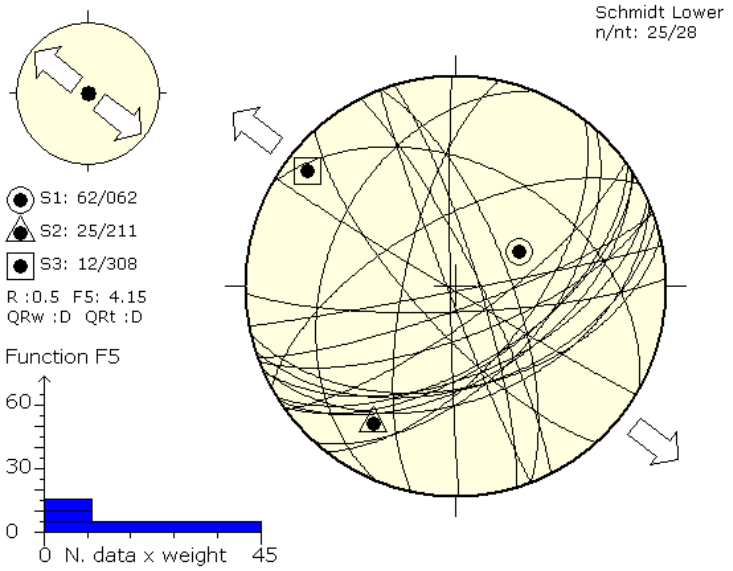

Fig. 6.4(a) - Stress tensor for recent stress regime for the Saranda fault, Saranda mid segment (Location: 2 on Fig. 6.1).

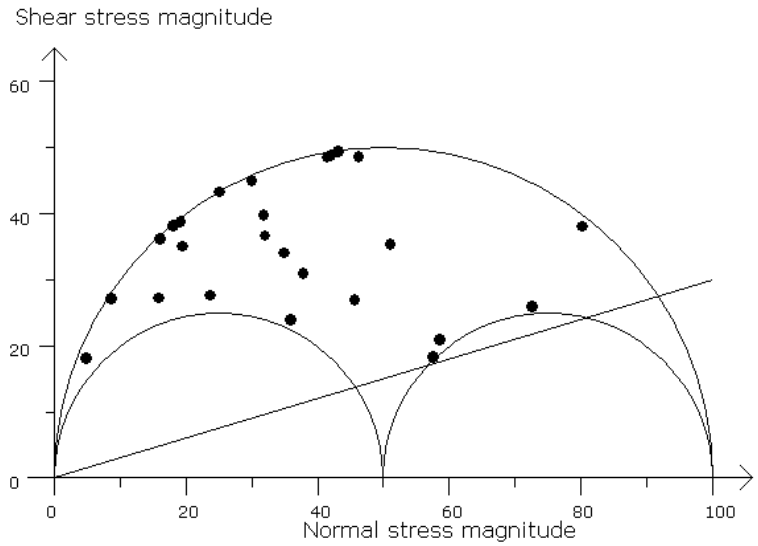

Fig. 6.4(b) - Mohr circles for the faults / movement joints plotted in (a).

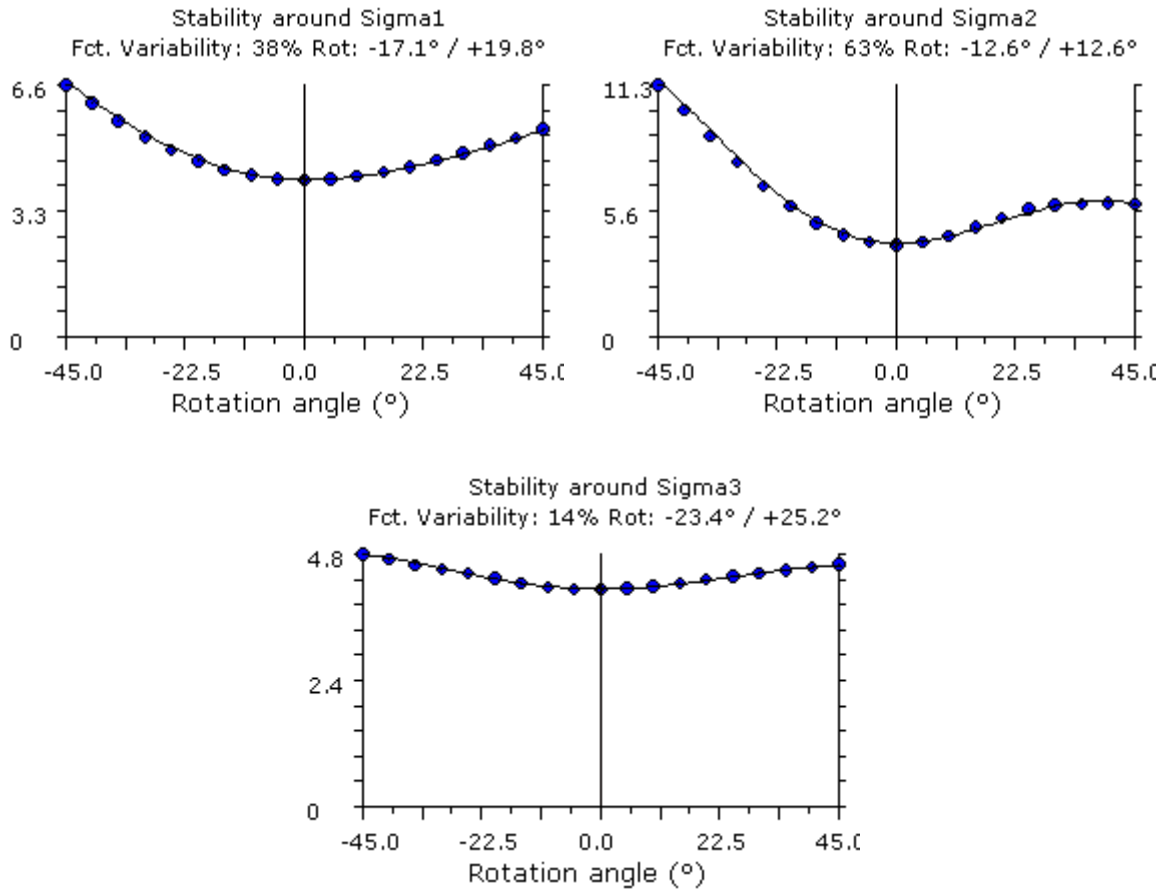

Fig. 6.4(c-e) - Rotational optimization curves of σ_1, σ_2 and σ_3 for the Saranda fault, Saranda mid segment.

Fig. 6.4a shows that, like the reduced stress tensors for the Mponde fault, the reduced stress tensor for the Saranda fault results from fault kinematic data that lack significant slip components. Only recent fault kinematic data were obtained. The stress tensor shows pure extension in a NW-SE direction, defined by S_{Hmax} = 031, S_{hmin} = 121 and stress regime index R' = 0.50 (Fig. 6.4a; Table 1a,b). This tensor is characterized by R = 0.50, σ_1 = 62/062, σ_2 = 25/211 and σ_3 = 12/308.

It is interpreted that, as for the Mponde fault, nearly all fault planes/movement joints are oriented in such a way that they can be easily reactivated (Fig. 6.4b) because all the slip-data plot within the field of reactivation (unstable field).

All the principal stresses obtained are fairly stable (Fig. 6.4c-e). However, the value of stress ratio R was not obtained due to lack of slickensides. In such case, the value of the stress ratio R was set to '0.5' (a typical value for pure extension) prior to computation of σ_1, σ_2 and σ_3.

6.1.1.4 The Bubu fault, Makutupora segment

In this fault segment (location 3c, Fig. 6.1), no recent fault-slip data were recorded. The only data recorded are related to old tectonic regimes and are subdivided in two groups: Makutupora NW-SE and Makutupora E-W. The Makutupora NW-SE and E-W tensors are from the same area. While both stress tensors correspond to old compressive regimes, the latter is interpreted to be younger than the former based on the fact that the former is characterized by relatively high degree of ferruginization and deep-seated striae (slip lines) on fault surfaces. Deep-seated striae here refer to highly marked slip lines on the fault surface. Such slip lines are formed at high confining pressures, typically indicating deep-seated environments in the crust-hence the term deep-seated striae.

Makutupora, NW-SE

The reduced stress tensor for the oldest Makutupora NW-SE (NW-SE here represents a stress tensor with compressional principal stress axes in a NW-SE direction) reveals a strike-slip regime with S_{Hmax} = 126 and S_{hmin} = 036. Additional parameters are R = 0.03, R' = 1.97, σ_1 = 08/129, σ_2 = 70/240 and σ_3 = 18/036 (Fig. 6.5a; Table 6.1a,b). The quality of the tensor (D, Table 6.1b) is restricted by the low degree of scatter fault planes (only NW-SE) faults dominate the tensor. This is also reflected by the confined size of σ_1 on the Mohr circle (Fig. 6.5b). The rotation optimization of fault parameters σ_1, σ_2, σ_3 and R show moderate stability (Fig. 6.5c-f). Epidotization, ferruginization and chloritization characterize the fault planes corresponding to this regime, indicating that the stress tensor obtained from these fault planes correspond to old tectonic regime.

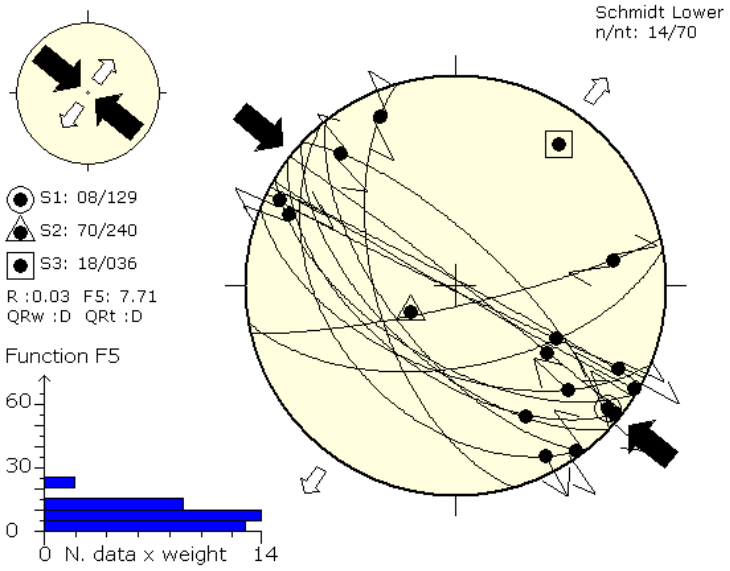

Fig. 6.5(a) - Stress tensor for old NW-SE compressive stress regime for the Bubu fault, Makutupora segment (Location: 3c on Fig. 6.1).

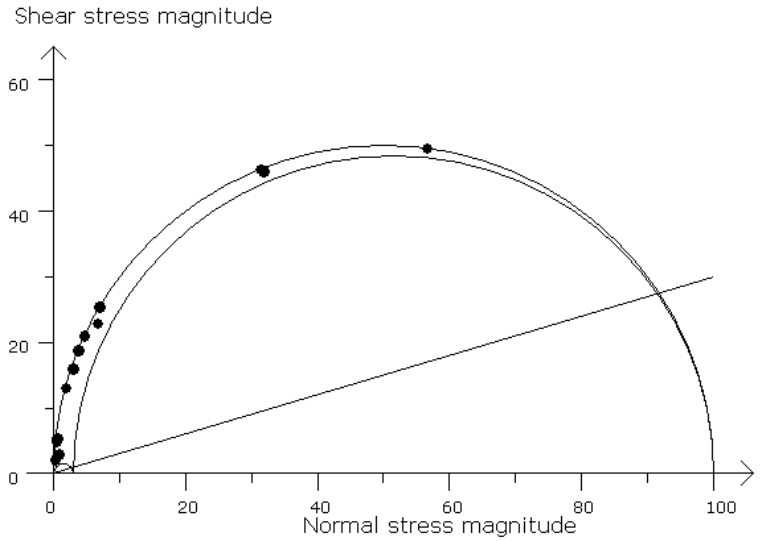

Fig. 6.5(b) - Mohr circles for the faults plotted in (a).

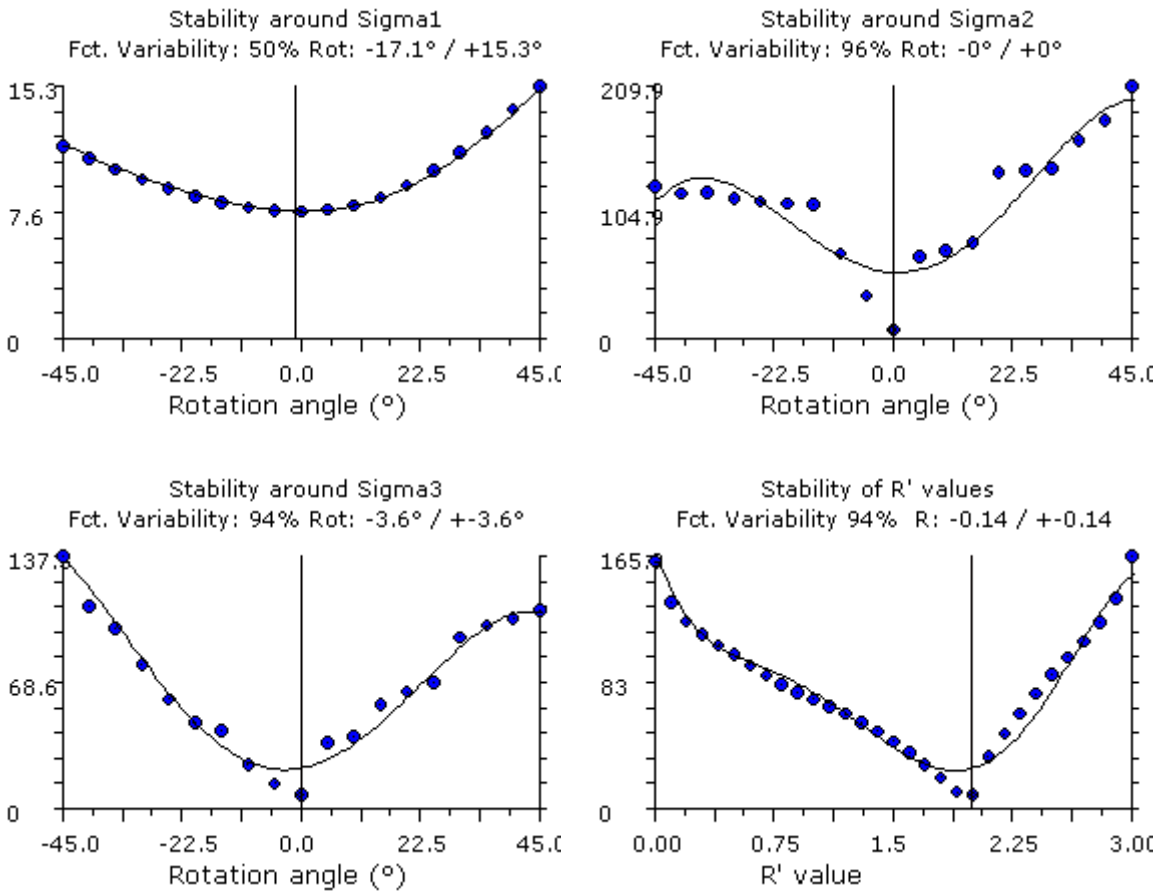

Fig. 6.5(c-f) - Rotational optimization curves of σ_1, σ_2, σ_3 and R corresponding to data in (a) for the Bubu fault at Makutupora.

Makutupora, E-W

The principal stress tensor corresponding to the Makutupora E-W is characterized by σ_1 = 04/270, σ_2 = 16/360 and σ_3 = 72/159 (Fig. 6.5g). Stress inversion reveals a compressional regime with a marked strike-slip component (R' = 2.27), a compression (S_{Hmax} = 90) and C quality (Table 6.1b). This good quality rank is mainly attributed to the fact that the faults involved in the calculation of the tensor have a wide range of directions (Fig. 6.5g). Such a good distribution of faults is also reflected in the Mohr circle (Fig. 6.5h).

In the Mohr diagram, few fault planes (up to 6 %) seem to plot below the friction line, which means that they are outside the field of reactivation. This is a minor set of faults and was ignored. The fault planes that correspond to this compressional regime are covered by epidote, chlorite and Fe-oxides. No recent tectonic activity was documented at this site. The stress ratio R is 0.27. The rotational optimization curves for σ_1, σ_2, σ_3 and R' are fairly stable (Fig. 6.5i-l).

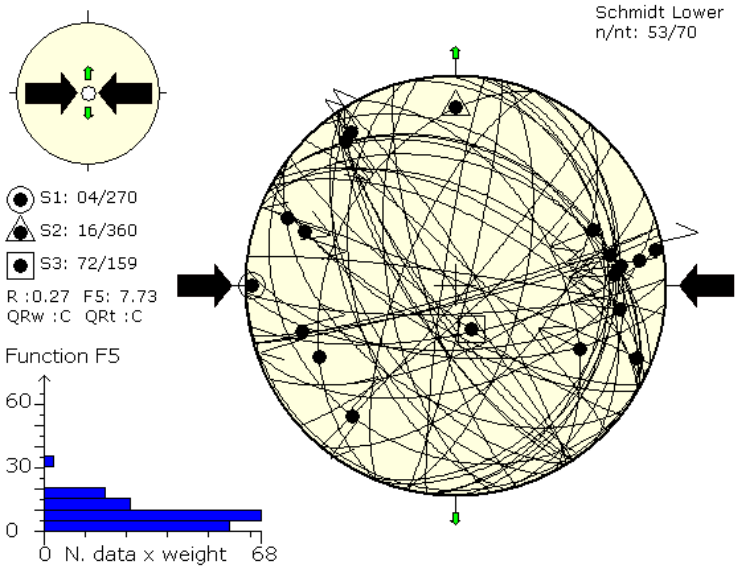

Fig. 6.5(g) - Stress tensor for old E-W compressive stress regime for the Bubu fault, Makutupora segment (Location: 3c on Fig. 6.1).

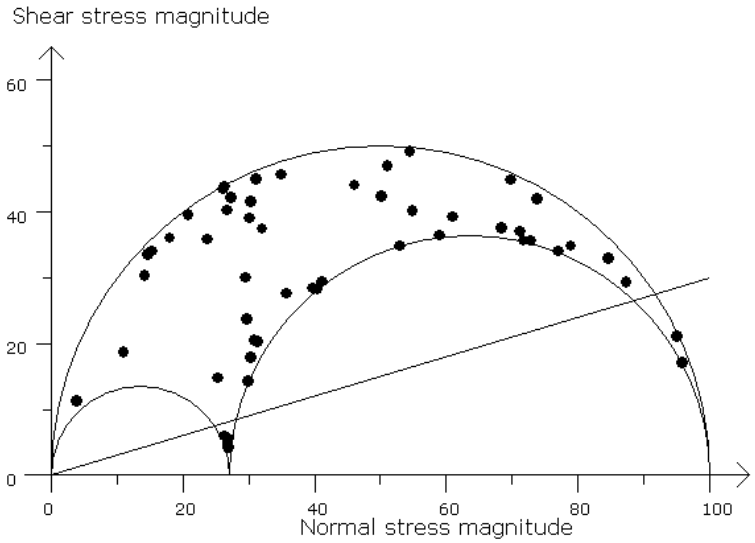

Fig. 6.4(h) - Mohr circles for the faults plotted in (g).

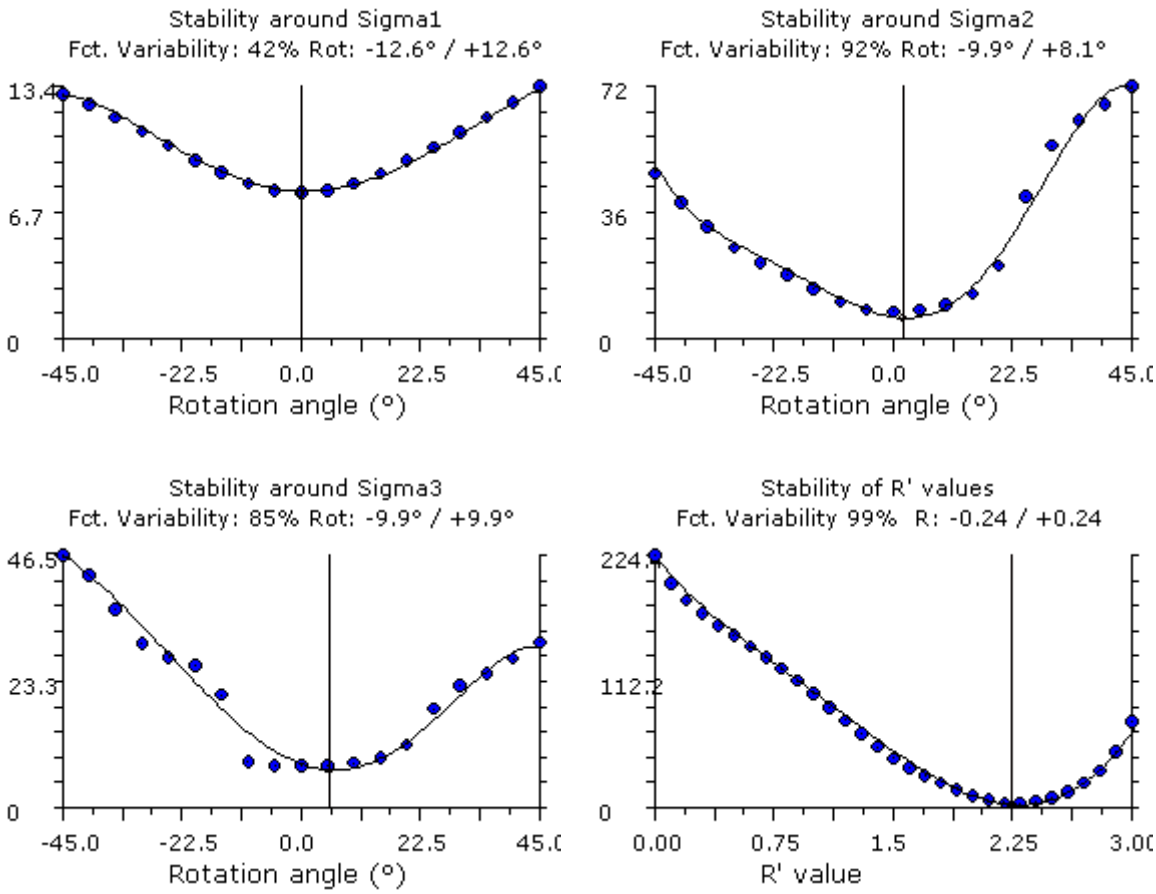

Fig. 6.5(i-l) - Rotational optimization curves of σ_1, σ_2, σ_3 and R for the Bubu fault at Makutupora. These curves belong to old stress tensor in the area, but relatively younger than that of the Makutupora, NW-SE (a-f).

6.1.1.5 The Bubu fault, Gonga segment (at Magungu village)

Only a few recent fault kinematic data were obtained at Magungu village, in the Gonga segment of the Bubu fault (location 3b; Fig. 6.1).

The corresponding stress tensor for the Gonga segment at Magungu is an extensional one with a strike-slip component (oblique extensional regime), defined by S_{Hmax} = 008, S_{hmin} = 098 and stress regime index R' = 1.50 (Fig. 6.6a; Tables 6.1a,b). The major limiting factors include lack of slip lines, lack of enough data, and lack of well distributed planes of movement joints/faults. The directions of movements shown in Fig. 6.6a are modeled shear movements. Figure 6.6b shows that all movement joints in this locality are within the field of reactivation.

R = 0.50, σ_1 = 42/026, σ_2 = 43/170 and σ_3 = 19/278. Corresponding rotational optimization curves show that only σ_1 is stable (Fig. 6.6c-e). For reasons stated above, rotation optimization of R' was not possible. This means that the amount and type of fault-slip data are the limiting factors for the quality of the tensor.

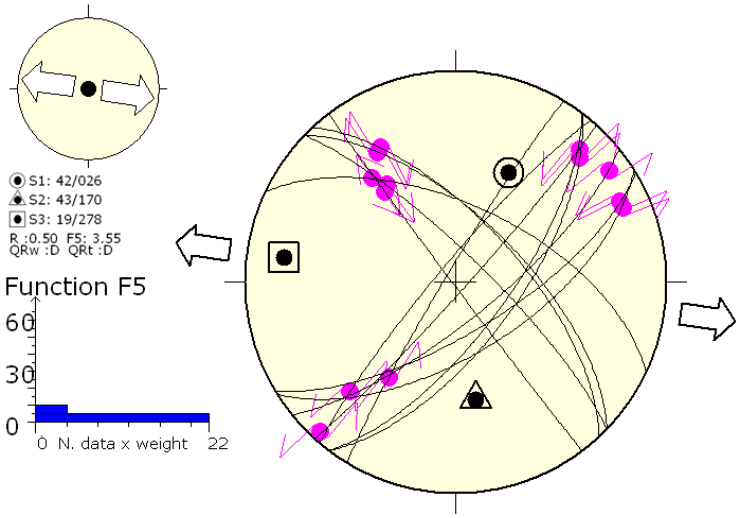

Fig. 6.6(a) - Stress tensor for recent stress regime for the Bubu fault, Gonga segment at Magungu village (Location: 3b on Fig. 6.1).

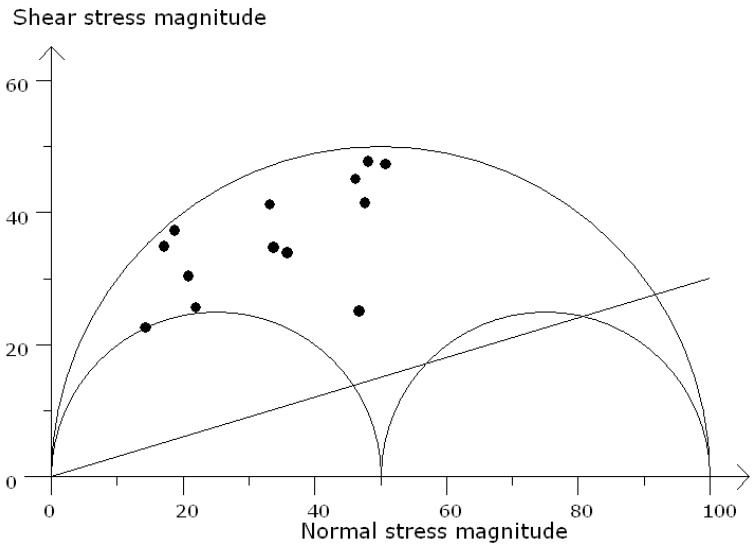

Fig. 6.6(b) - Mohr circles for the faults / movement joints plotted in (a).

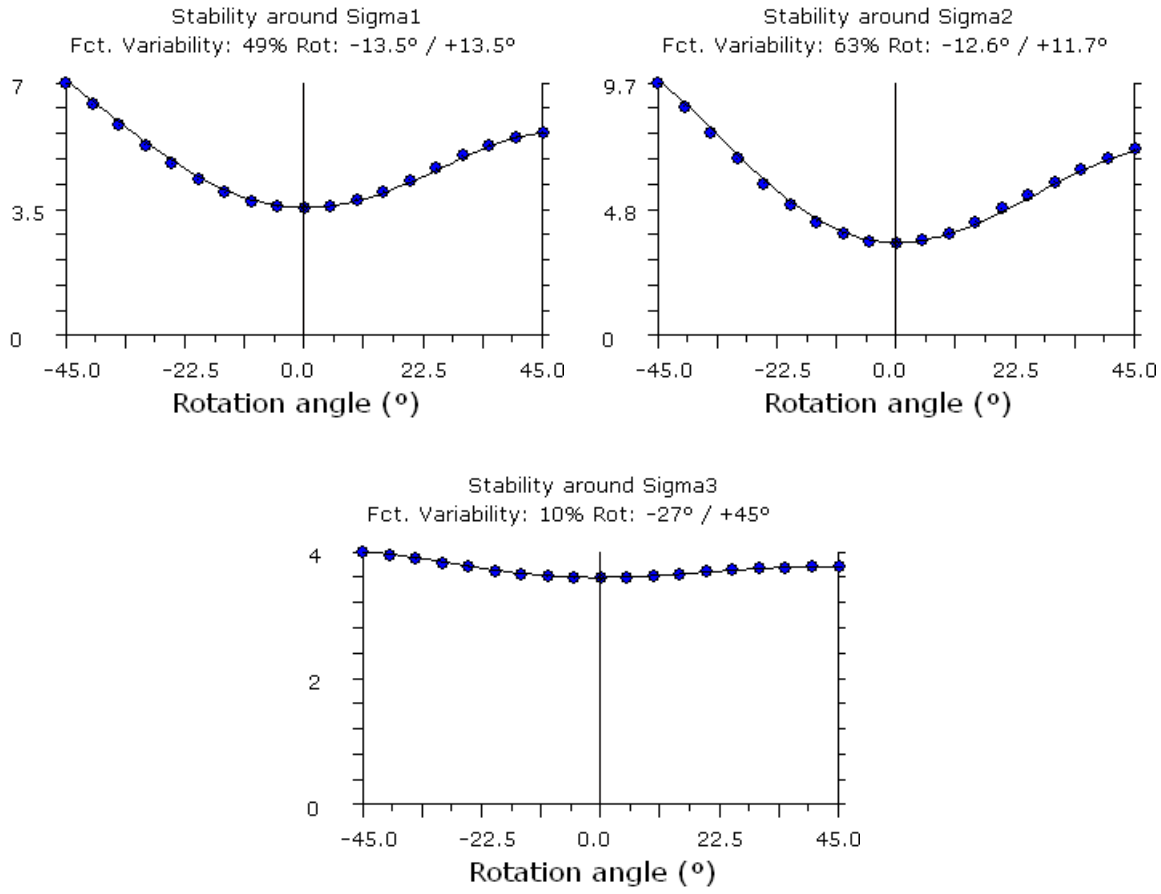

Fig. 6.6(c-e) - Rotational optimization curves of σ_1, σ_2, σ_3 and R for the Bubu fault at Magungu village.

6.1.1.6 The Bubu fault, Gonga segment (hot spring field)

The Bubu fault, at the Gonga hot spring field area (location 3a; Fig. 6.1), is characterized by high-angle fractures. Only a few fault planes have slip lines that seem to reactivate some of the sub-vertical fractures. The stress ratio was fixed to 0.5 prior to the inversion because most fault-slip data are related to faults that do not show clear slip lines, hence slip sense. Two groups were distinguished: old set and young set.

Old set

A strike-slip tensor was obtained (Fig. 6.7a) that is defined by a NW-SE horizontal compression, S_{Hmax} = 142 and a NE-SW horizontal extension, S_{hmin} = 052 (Table 6.1a, b). The tensor is stable around its vertical axis (σ_1 = 03/321), which means that the S_{Hmax} and S_{hmin} directions are well constrained, but it is less stable around the σ_3 (86/098) axis. σ_2= 04/232. R is fixed to 0.50 and R'= 1.50.

The Mohr circle shows that the reactivation of these fault/movement planes is limited to a narrow range (Fig. 6.7b), though about 90 % of the slip-data indicate that they come from unstable field (See Fig. 2.16b in Chapter 2 for reference), which implies that large part of these old set of faults can be re-activated in the computed stress regime. σ_2 and R are not well constrained (in terms of rotational optimization of their axes) owing to the type of data (Fig. 6.7c-f), which means that overall; the computed stress regime is unstable. In addition, this tensor is based solely on the inversion of shear joints; the overall rank is limited to a D quality (Table 6.1b).

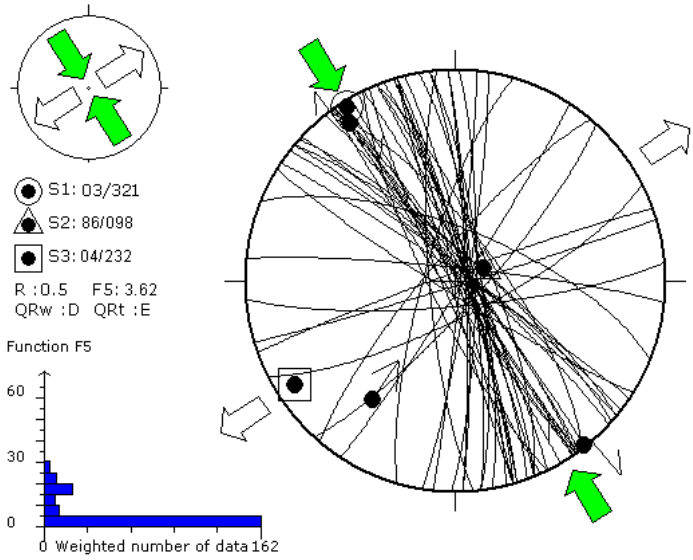

Fig. 6.7(a) - Stress tensor for old stress regime for the Bubu fault, Gonga (hot spring field), old set (Location: 3a on Fig. 6.1).

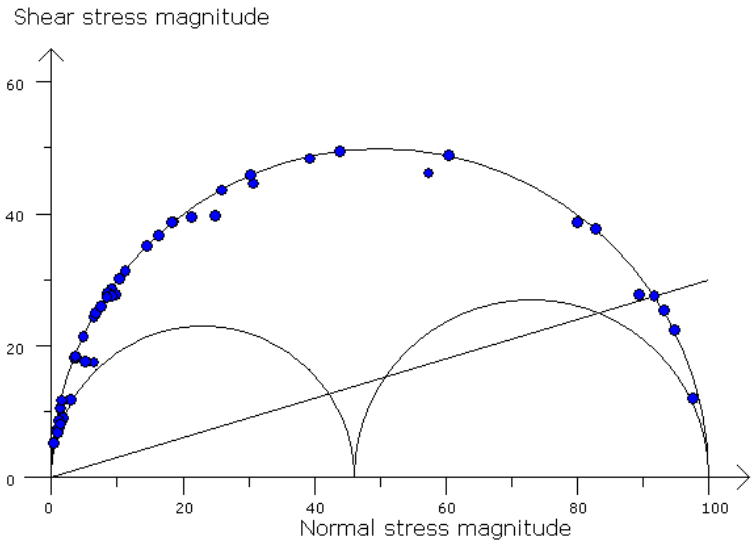

Fig. 6.7(b) - Mohr circles for the faults plotted in (a).

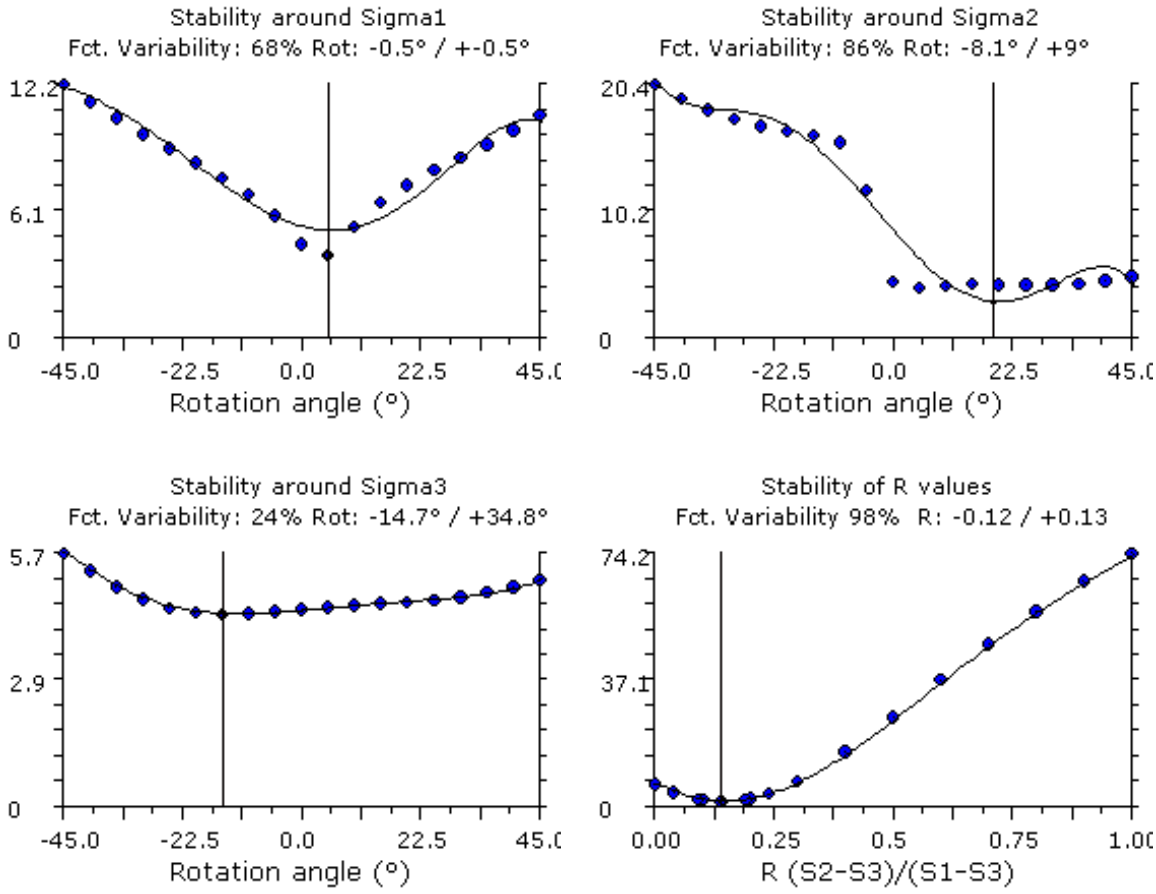

Fig. 6.7(c-f) - Rotational optimization curves of σ_1, σ_2, σ_3 and R for the Bubu fault at the Gonga hot spring field, old set.

Young set

The second set from the Gonga hot spring field area contains a few fault planes with slip lines (Fig. 6.7g).

It is characterized by a nearly E-W compression and N-S extension, defined by S_{Hmax} = 088, S_{hmin} = 178, R = 0.72 and R' = 1.26 (Table 6.8a, b). The tensor has a D quality due to the small number of data available. It is likely that it represents a minor tectonic event. About 63 % of the fault-slip data fall within the reactivation field of the Mohr circles, and about 37 % plots outside the reactivation field. The latter are interpreted to represent low-angle faults that are most likely reverse faults implying that they are not oriented suitably for being re-activated.

The σ_1 and σ_3 (Fig. 6.7i,j) axes are fairly stable upon rotations owing to presence of fault-slip data used in the stress tensor computations. Rotational optimization of σ_2 and R' shows significant instability (Fig. 6.7k,l). It is interpreted that this paleostress tensor and the one for the old set are attributed to pre-rift (strike-slip) tectonic regimes.

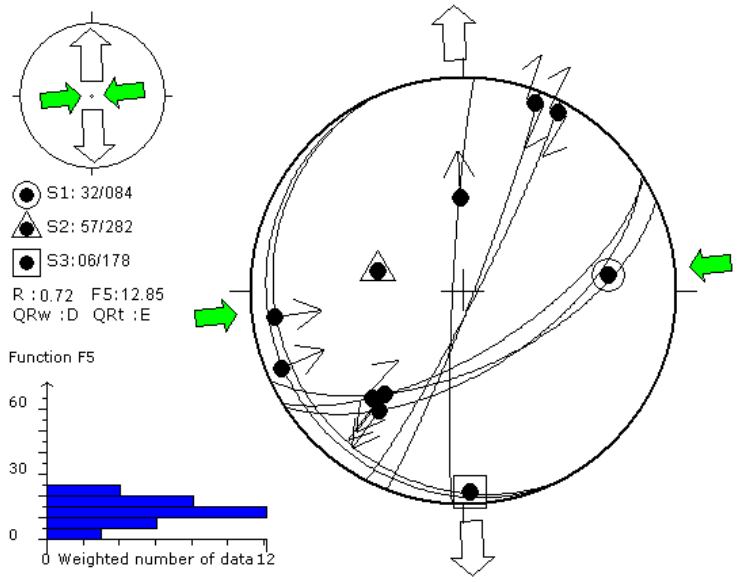

Fig. 6.7(g) - Stress tensor for old stress regime for the Bubu fault, Gonga (hot spring field), young set (Location: 3a on Fig. 6.1).

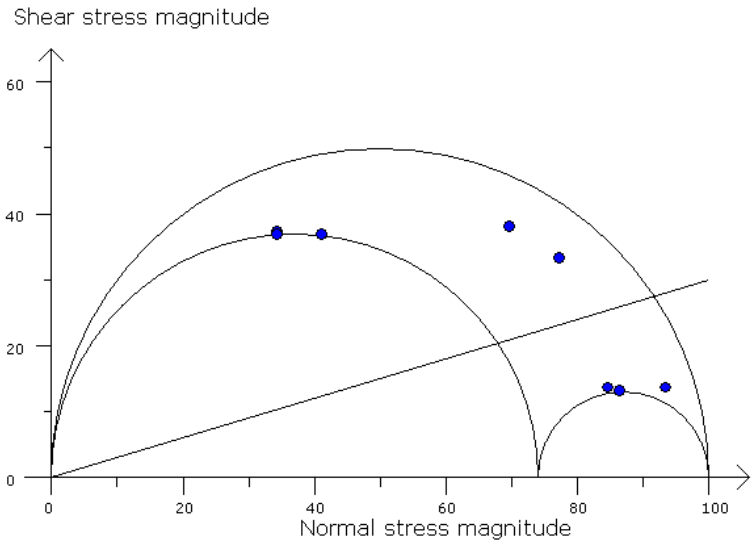

Fig. 6.7(h) - Mohr circles for the faults plotted in (g).

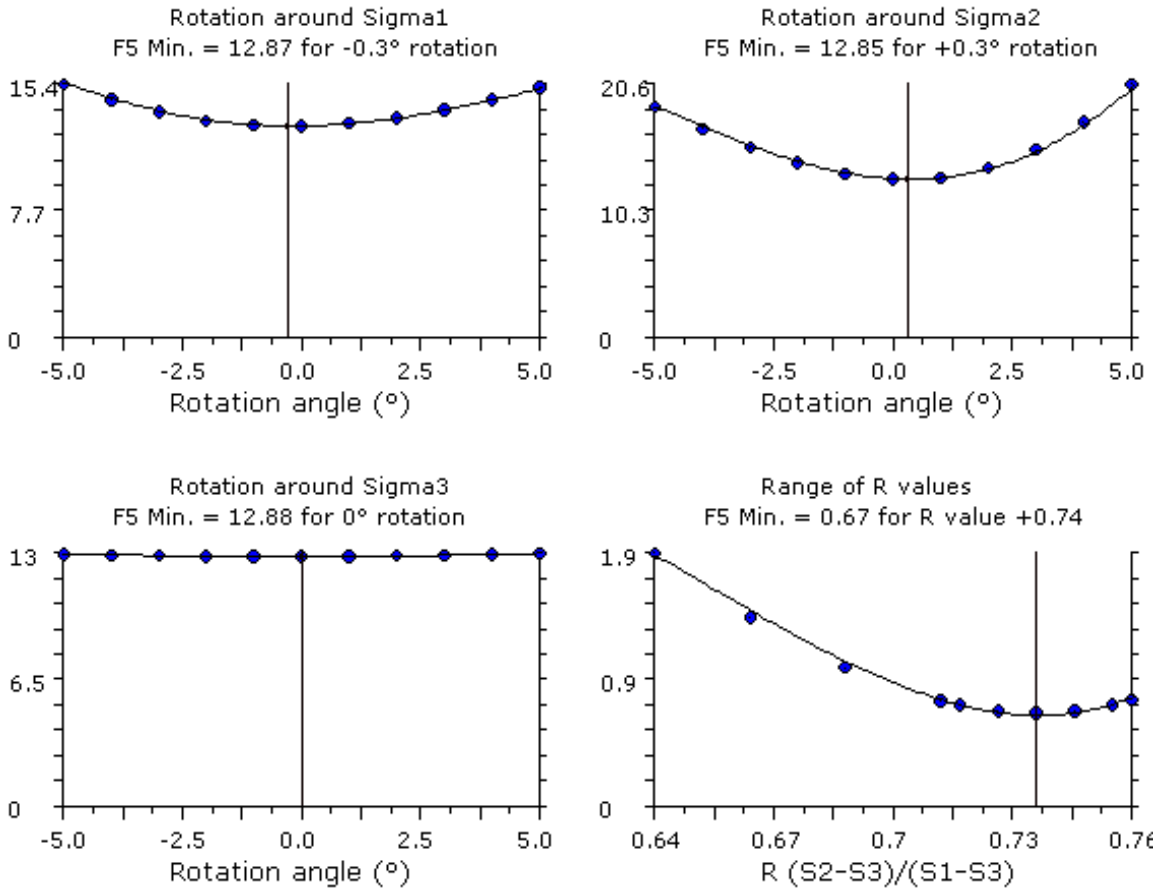

Fig. 6.7(i-l) - Rotational optimization curves of σ_1, σ_2, σ_3 and R' for the Bubu fault at the Gonga hot spring field, old set.

6.1.1.7 The Makanda fault, segment D

Like for segment 2 of the Mponde fault and the Bubu fault at Magungu, the reduced stress tensor of segment D of the Makanda fault (location 4a; Fig. 6.1) is characterized by a few movement joints that are attributed to recent fault kinematic data and one slickenside. It typically reveals an extensional regime defined by S_{Hmax} = 012, S_{hmin} = 102 and stress regime index R' = 0.49 (Fig. 6.8a; Table 6.1a,b).

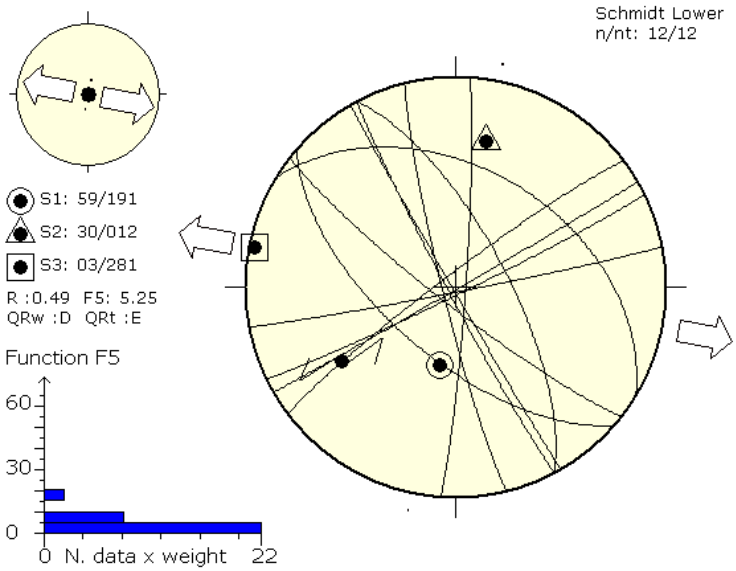

Fig. 6.8(a) - Stress tensor for recent stress regime for the Makanda fault, Segment D (location: 4a on Fig. 6.1).

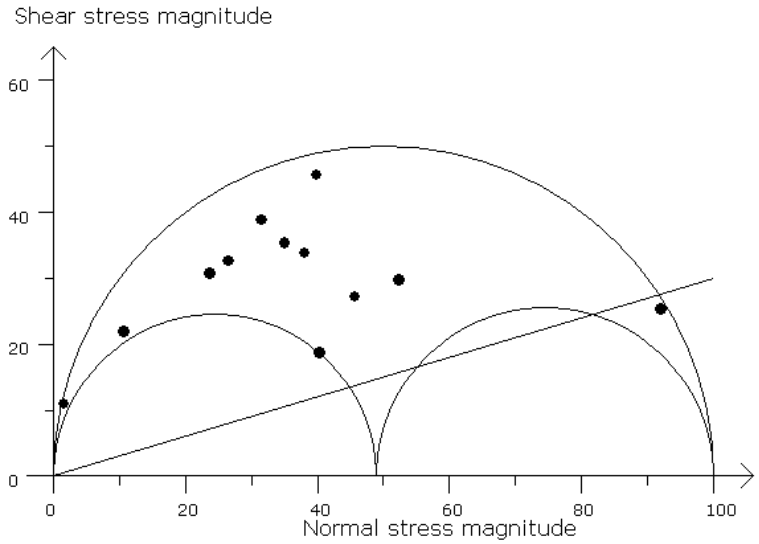

Fig. 6.8(b) - Mohr circles for the faults plotted in (a).

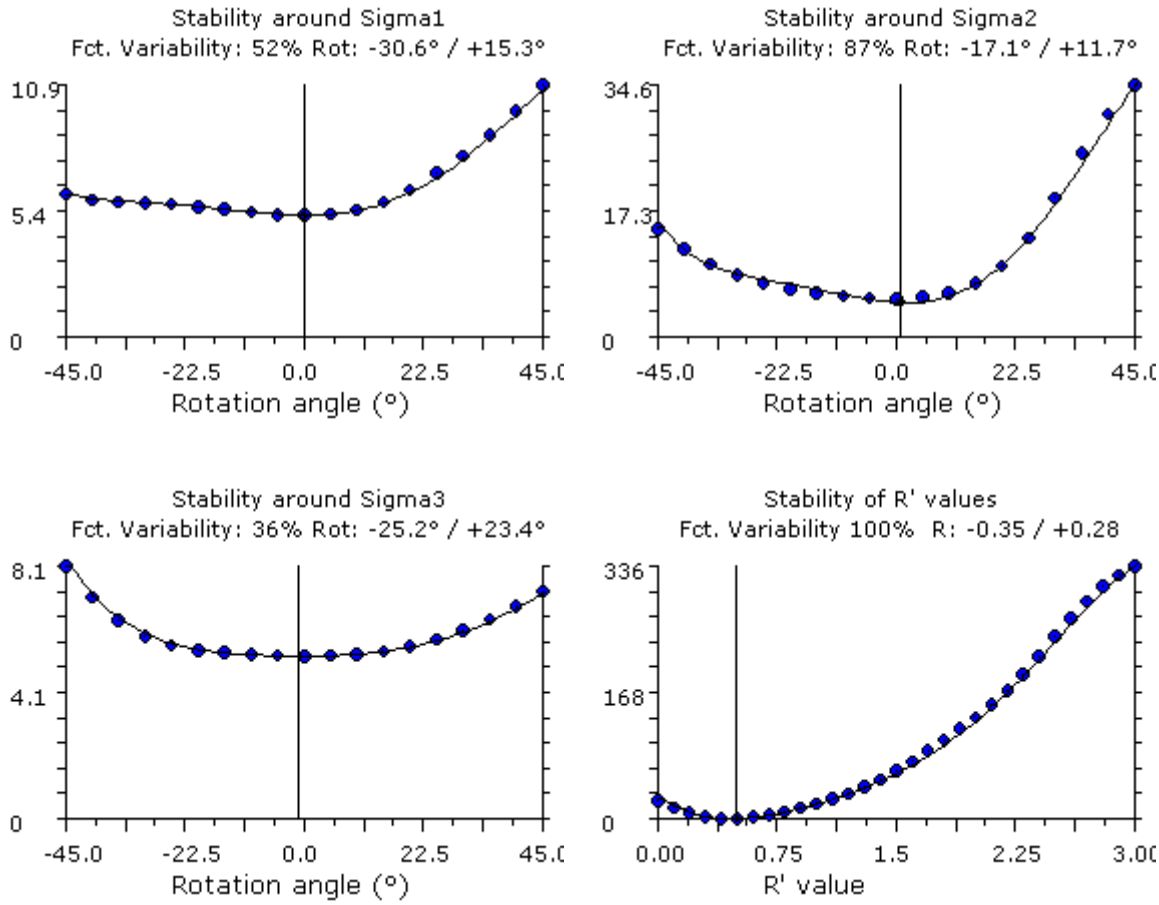

Fig. 6.8(c-f) - Rotational optimization curves of σ_1, σ_2, σ_3 and R for the Makanda fault at segment D.

The tensor has a D quality. The major limiting factors include lack of slip lines, insufficient amount of data, and lack of well-distributed planes of movement joints/faults. Figure 6.8b shows that nearly all movement joints are within the field of reactivation.

R = 0.49, σ_1 = 59/191, σ_2 = 30/012 and σ_3 = 03/281. Corresponding rotational optimization curves show that only σ_2 and σ_3 are stable (Fig. 6.8c-f).

6.1.1.8 The Hombolo fault, Dam segment

The Dam segment of the Hombolo fault (location 5; Fig. 6.1) reveals two generations of structures: an older and a younger set. Detailed field investigation on Precambrian basement rocks at the segment revealed one ductile (shearing) event and about three faulting events. The structures related to the shearing event are not presented here. However, these structures are interpreted to be the oldest in the area.

We further interpret that these structures have been responsible for the known gold mineralization in the Nzuguni segment (part of the Hombolo fault); this is not further discussed as it is out of scope of this study.

Structures related to faulting events differ in terms of dip magnitudes. Presence and absence of slip lines and mineralization on fault surfaces has been used in conjunction with dip magnitudes to characterize these fault generations at this site. They have been grouped into two: the old set and the young set.

Old set

The older structures are characterized by low-angle compressional faulting, associated with Riedel shears and lunate fractures (Fig. 6.9a). The obtained paleostress tensor (Fig. 6.9b) is similar to the one obtained for the oldest, NW-SE compressional regime at the Bubu fault at Makutupora (Fig. 6.5b). It is characterized by both low- and high-angle faults. The former are considered to be related to old reverse faults, whereas the latter are attributed to old strike-slip faults.

A reduced stress tensor modeled for the fault-slip data gives a compressional strike-slip stress tensor characterized by S_{Hmax} = 127 and an R' value of 1.95, i.e. transition between strike-slip and compressional regimes (Table 6.1a, b). σ_1 = 00/126, σ_2 = 89/216 and σ_3 = 01/037.

Mohr circles (Fig. 6.9c) show that $\sigma_2 \approx \sigma_3$, which is also why R tends to be small (R = 0.05, see Table 6.1a). At least 5 % of the old set faults may not be reactivated in a strike-slip regime, probably owing to exceedingly low-angles of some of these faults (e.g., Fig. 6.9a). Rotational optimization of σ_1, σ_2, σ_3 and R show that σ_1 and σ_2 are relatively stable, whereas σ_3 and R' are not (Fig. 6.9d-g).

Fig. 6.9a - Riedel shears at the Dam segment of the Hombolo fault. They are found on low-angle faults. They intersect the fault plane at nearly 25°. They are associated with green minerals (possibly chlorite). Because of that, they are interpreted to be old features.

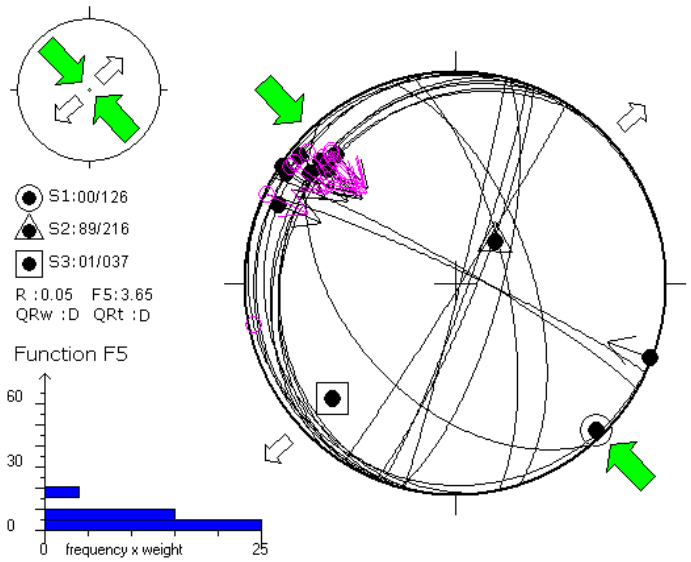

Fig. 6.9(b) - Stress tensor for old stress regime for the Hombolo fault, Dam segment (location: 5 on Fig. 6.1).

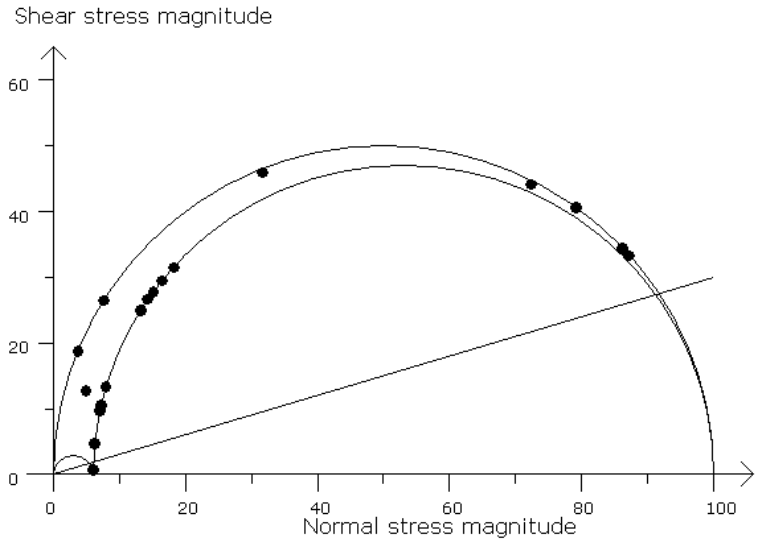

Fig. 6.9(c) - Mohr circles for the faults plotted in (b).

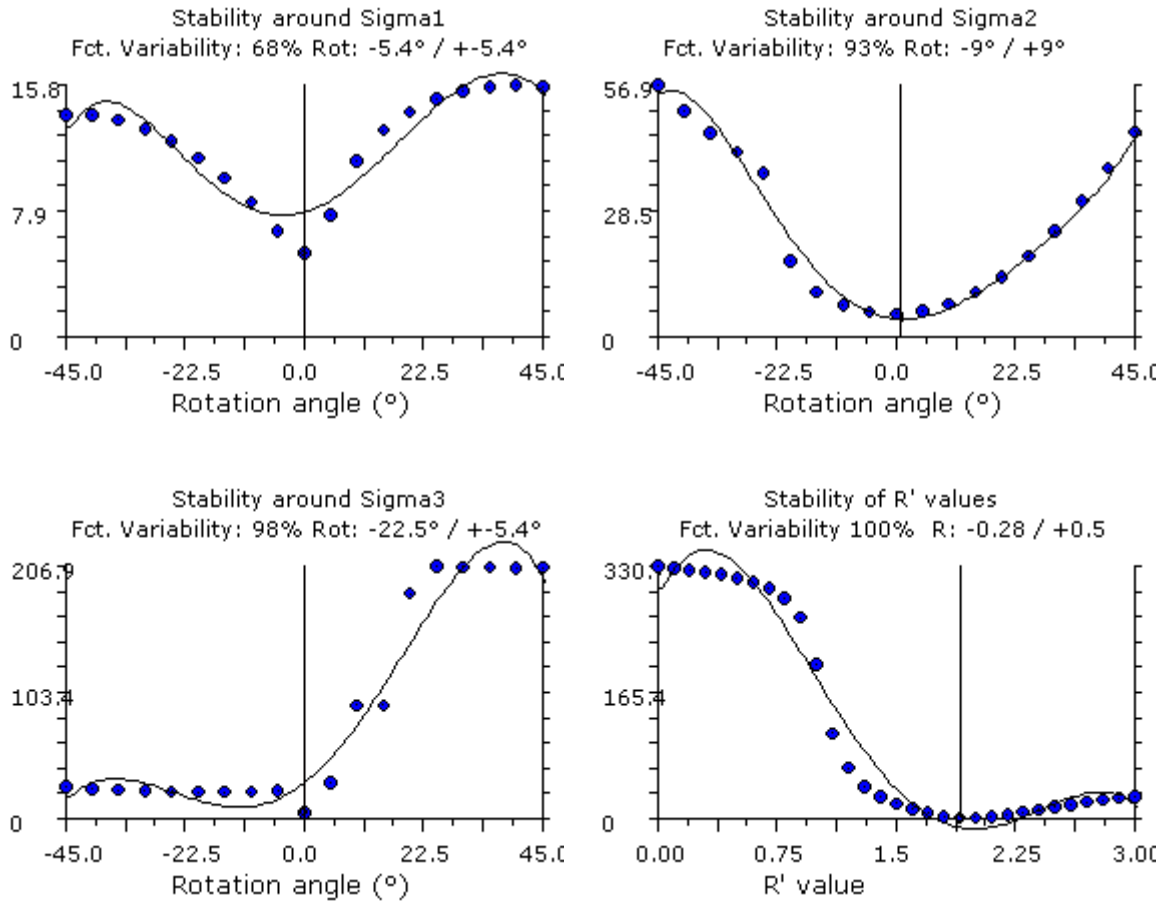

Fig. 6.9(d-g) - Rotational optimization curves of the corresponding σ_1, σ_2, σ_3 and R.

Young set

This tensor is characterized by a set of conjugated faults. Slip lines could hardly be observed, but, using the law of conjugated fractures (and considering only the intersecting fractures with a dihedral angle close to 60°), the slip directions and senses of movements were reconstructed (Fig. 6.9h,i). The corresponding stress inversion gives a σ_1 = 59/185, σ_2 = 30/014, σ_3 = 03/282, R=0.49 (compare these modeled principal axes σ_1, σ_2 and σ_3 with the observed σ_1, σ_2 and σ_3 in Fig. 6.9h). The quality of the tensor is ranked 'C'. The young set at Hombolo is also characterized by a nearly E-W sub-horizontal extension (S_{hmin} = 104) and S_{Hmax} = 014. The C quality is imposed by the type of data used (mainly conjugated shear fractures), which is here the limiting factor for the quality of the tensor (Table 6.1, b).

The Mohr circles show that 100 % of the faults can be reactivated (Fig. 6.9j). The plots of τ/σ does not only show that the fault planes plot above the friction line but also that the fault planes plot much more above the friction line, something which could imply that the degree of reactivation is most likely much higher on this fault. All the principal stress axes are stable, except R (Fig. 6.9k-n).

Fig. 6.9h - Conjugate normal fault system at the Dam segment of the Hombolo fault. The fault planes intersect at nearly 60°. This conjugate system is considered to be related to recent tectonic activity because the fault planes are barren and fresh.

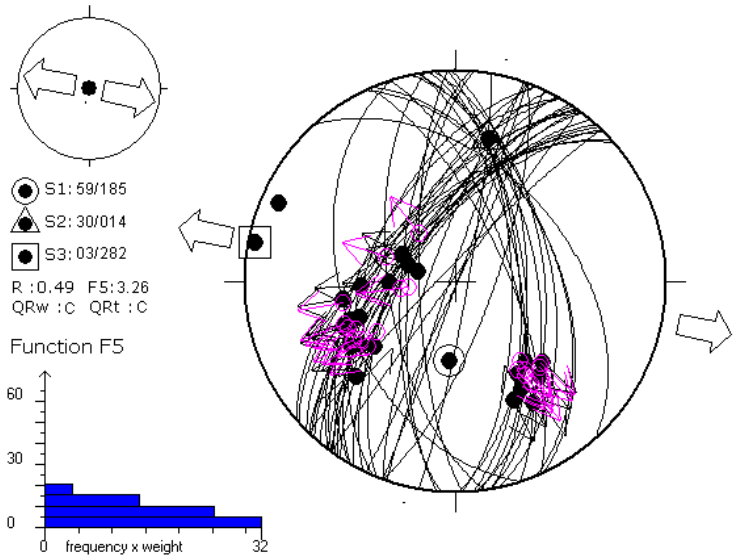

Fig. 6.9(i) - Stress tensor for old stress regime for the Hombolo fault, Dam segment (location: 5 on Fig. 6.1). The black and pink arrows on the tensor represent observed and modeled shear directions on given fault planes respectively.

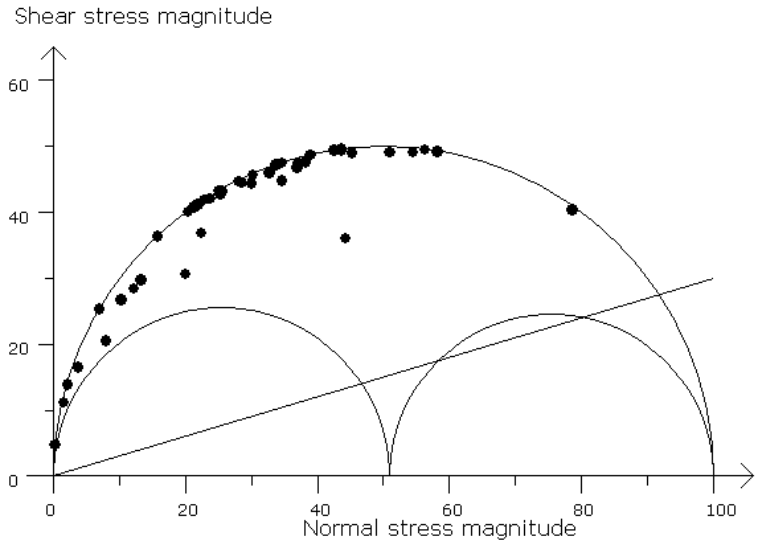

Fig. 6.9(j) - Mohr circles for the faults plotted in (i).

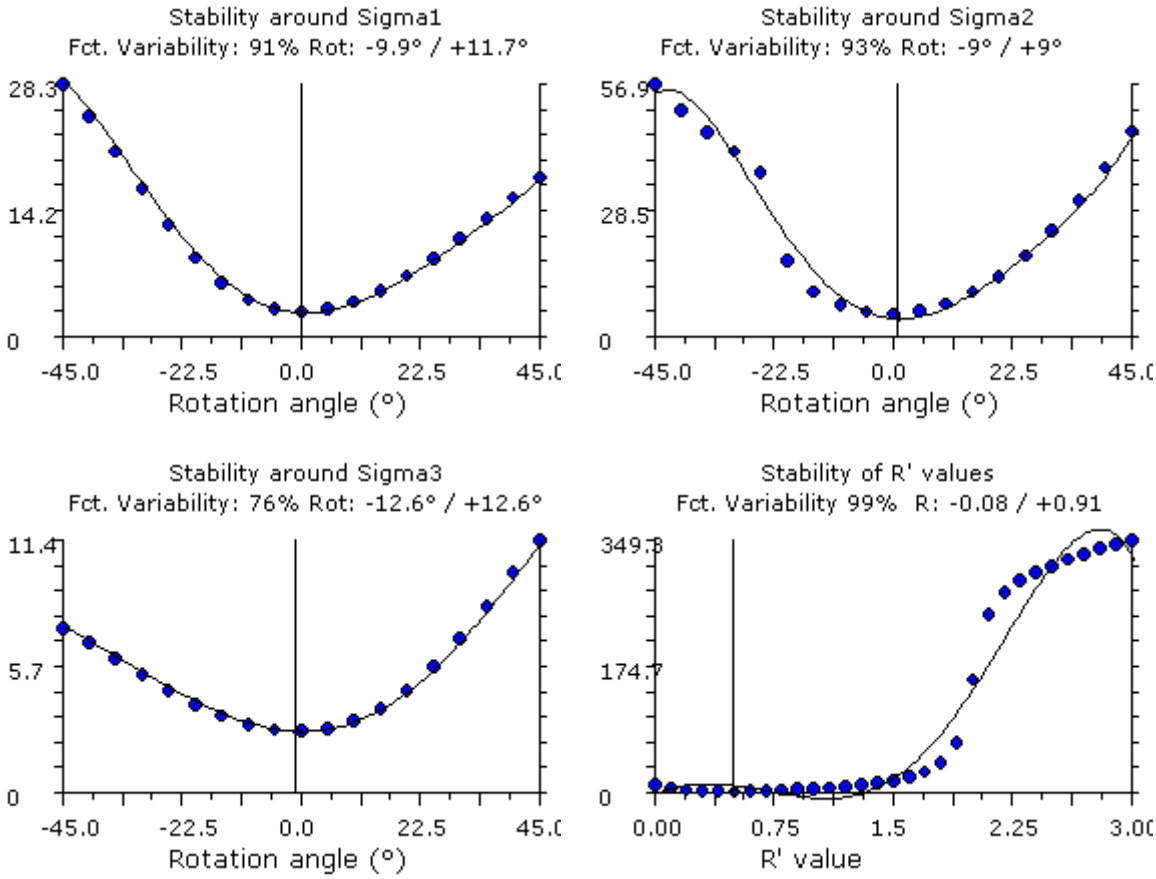

Fig. 6.9(k-n) - Rotational optimization curves of the corresponding σ_1, σ_2, σ_3 and R.

6.1.1.9 The Bahi fault, southeastern segment

The southeastern segment of the Bahi fault (location 7; Fig. 6.1) also reveals a recent stress regime that is characterized by ENE-WSW (nearly E-W) extension, defined by σ_1 = 66/318, σ_2 = 20/177, σ_3 = 15/079 and R = 0.64 (Fig. 6.10a). R' = 0.64, S_{Hmax} = 177 and S_{hmin} = 087.

Figure 6.10b shows that about 95 % of the faults/movement joints in the southwestern segment of the Bahi fault can be reactivated in the present, nearly E-W extensional regime. Except for σ_2, the other two principal stress axes, together with R' are not stable when rotational optimization is performed (Fig. 6.10c-f), mainly due to lack of sufficient fault-slip data.

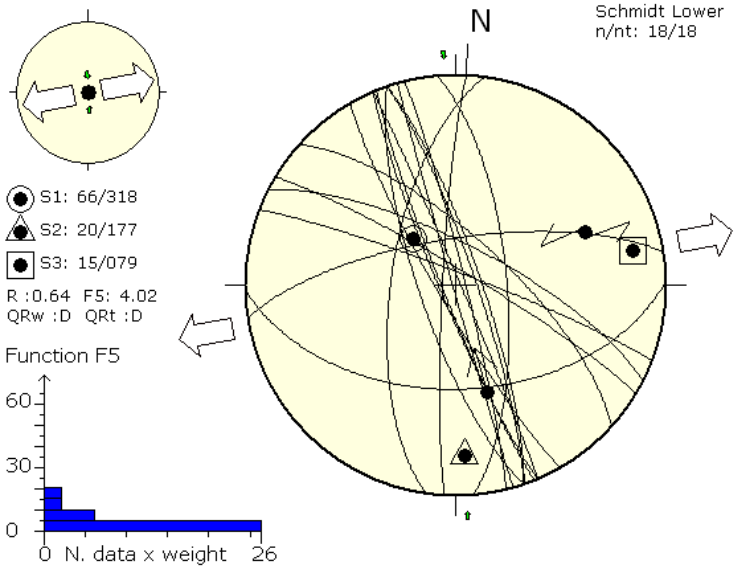

Fig. 6.10(a) - Stress tensor for recent stress regime for the Bahi fault, southeastern segment (location: 7 on Fig. 6.1).

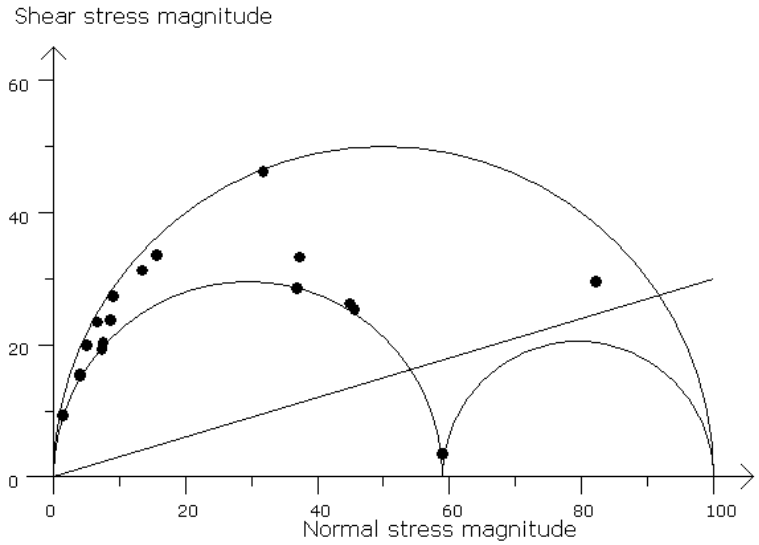

Fig. 6.10(b) - Mohr circles for the faults plotted in (a).

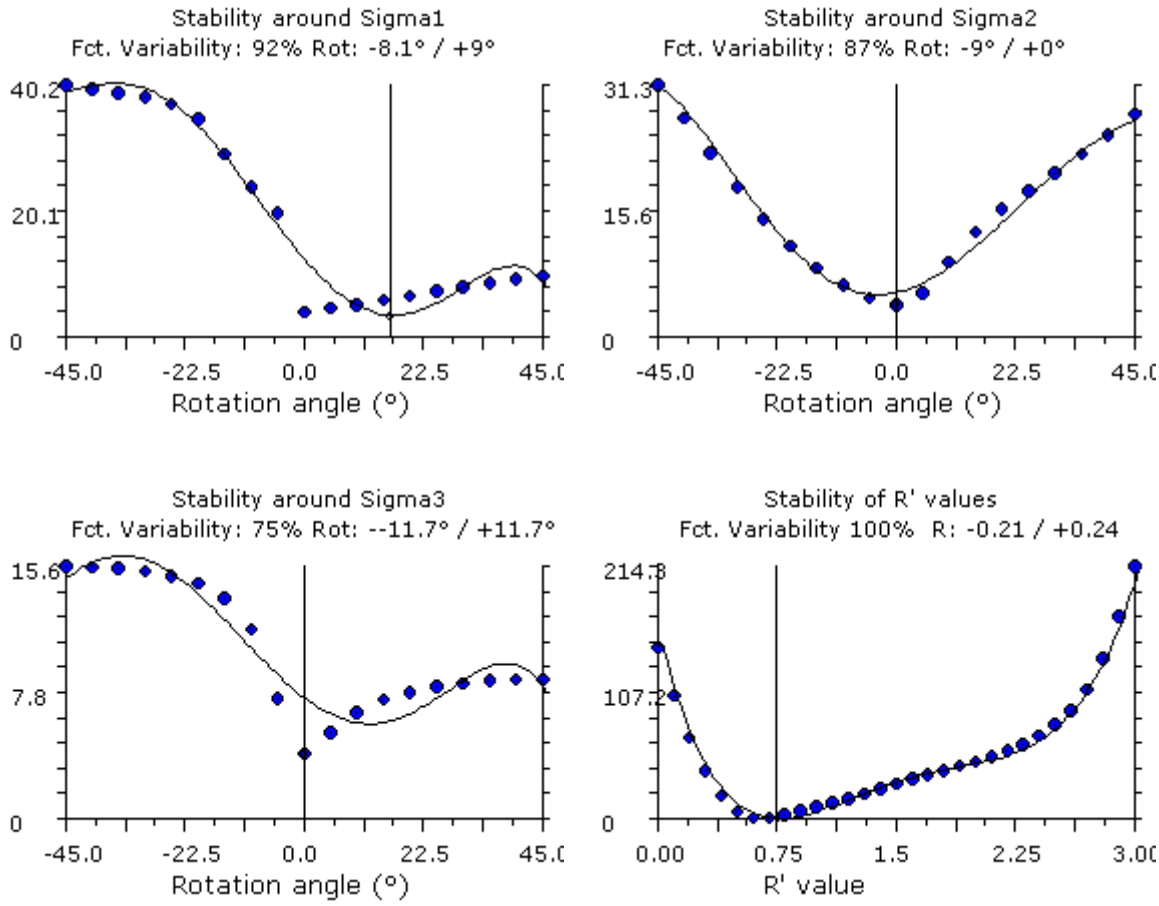

Fig. 6.10(c-f) - Rotational optimization curves of the corresponding σ_1, σ_2, σ_3 and R.

6.1.1.10 The Fufu fault, segment C

For the segment C of the Fufu fault (location 8; Fig. 6.1), the total measured data set contains 103 fault and fracture data. The data were first separated into two sets: i.e., a first set ("old set"), containing 56 sub-vertical and conjugated fractures without observed slip lines (Fig. 6.11a), and a second set ("recent set") with 34 faults and fractures of a wider variety of orientations (Fig. 6.11f). Since segment C is the main segment of the Fufu fault (Figs. 5.19; 5.35), then the fault-slip data from this segment are called data from Fufu Main (Table 6.1a,b).

Old set

Segment C of the Fufu fault ("old set") is characterized by a strike-slip stress tensor with E-W horizontal compression (S_{Hmax} = 079) and a D quality (limited by the data type) (Fig. 6.11a; Table 6.1a,b). The tensor was first fixed to R = 0.5, due to lack of slip lines. All conjugated fractures can be reactivated (Fig. 6.11b). Rotational optimization shows that only the σ_1 axis is relatively stable (Fig. 6.11c-e).

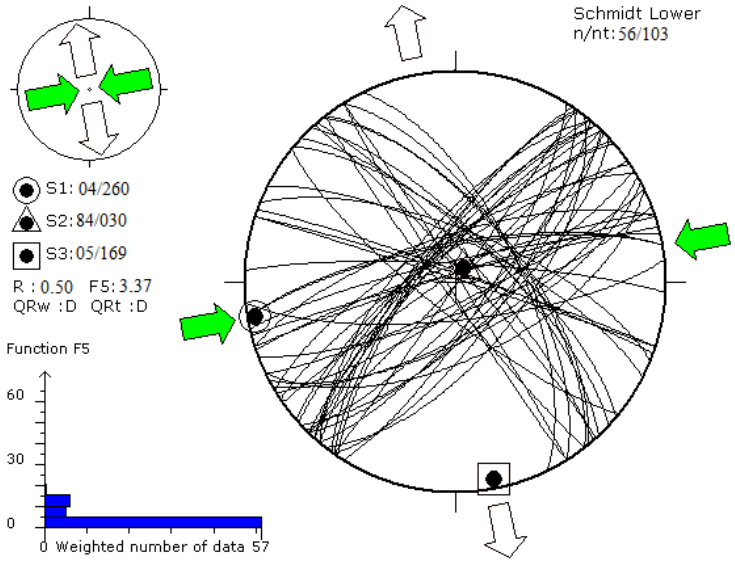

Fig. 6.11(a) - Stress tensor for old stress regime for the Fufu fault, segment C (location: 8 on Fig. 6.1).

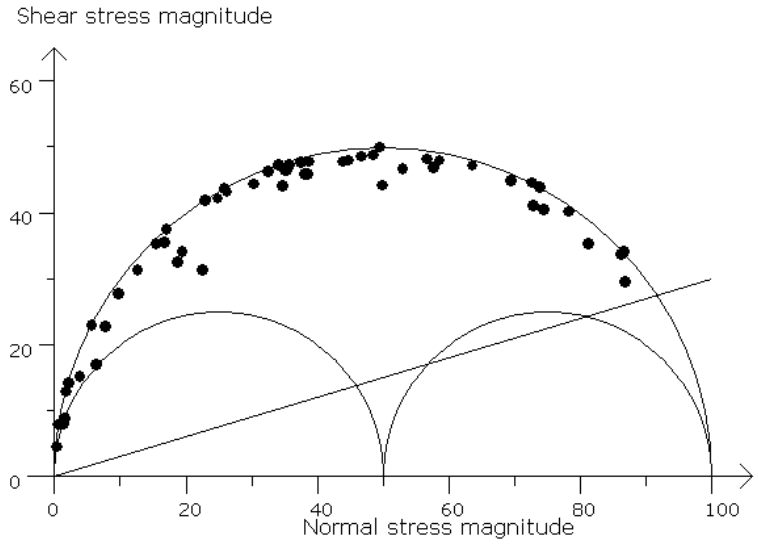

Fig. 6.11(b) - Mohr circles for the faults plotted in (a).

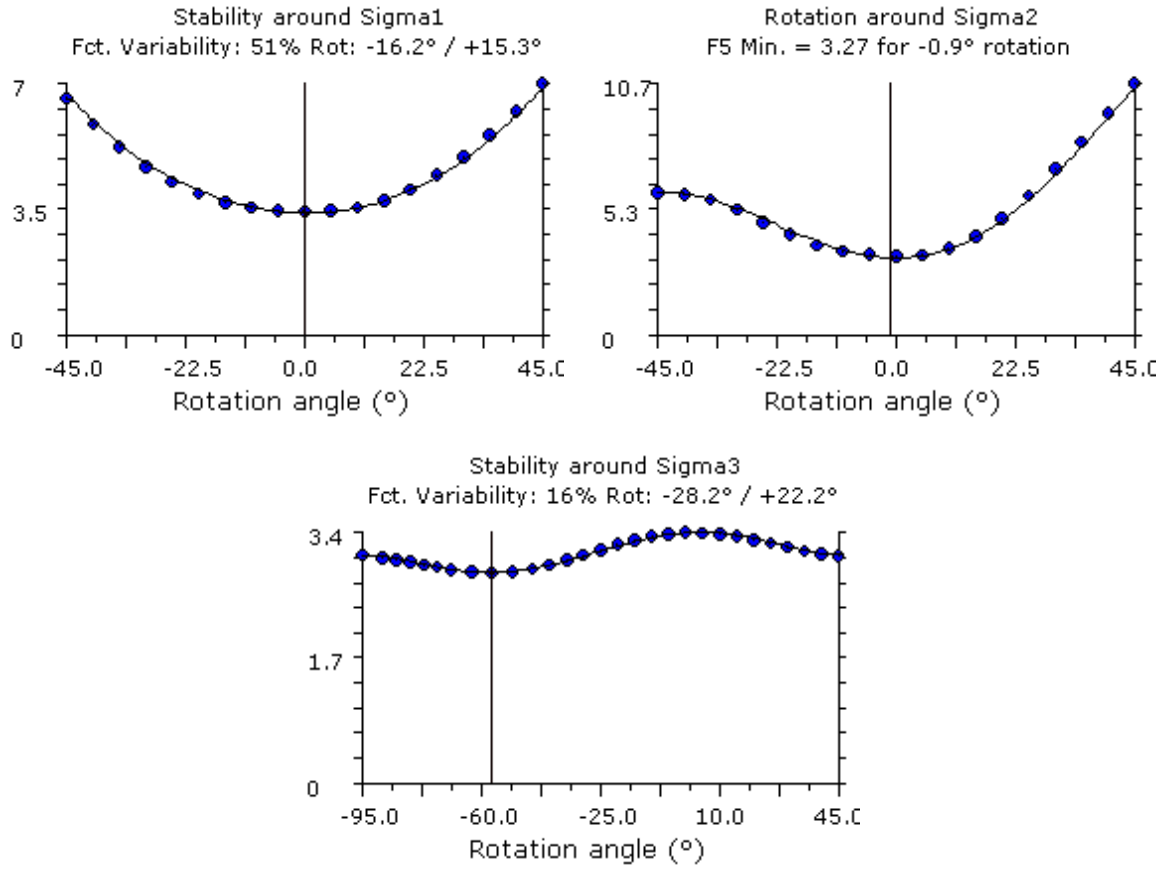

Fig. 6.11(c-e) - Rotational optimization curves of the corresponding σ_1, σ_2 and σ_3. Rotational optimization for R' could not be possible due to lack of slip-lines.

Recent set

Segment C of the Fufu fault ("recent set") gives a well-constrained normal faulting regime characterized by S_{hmin} = 040, σ_1 = 71/294, σ_2 = 18/131, σ_3 = 05/039 and R = 0.35 (Fig.6.11f; Table 6.1a,b). The quality is limited to D owing to the small proportion of the data used (n = 34, out of 103).

The orientations of most faults/movement joints (~ 95 %) plot within the unstable field area of the Mohr circle (Fig. 6.11g) implying the highest chances of being reactivated. Rotational optimization shows that only the σ_1 axis is relatively stable (Fig. 6.11h-k).

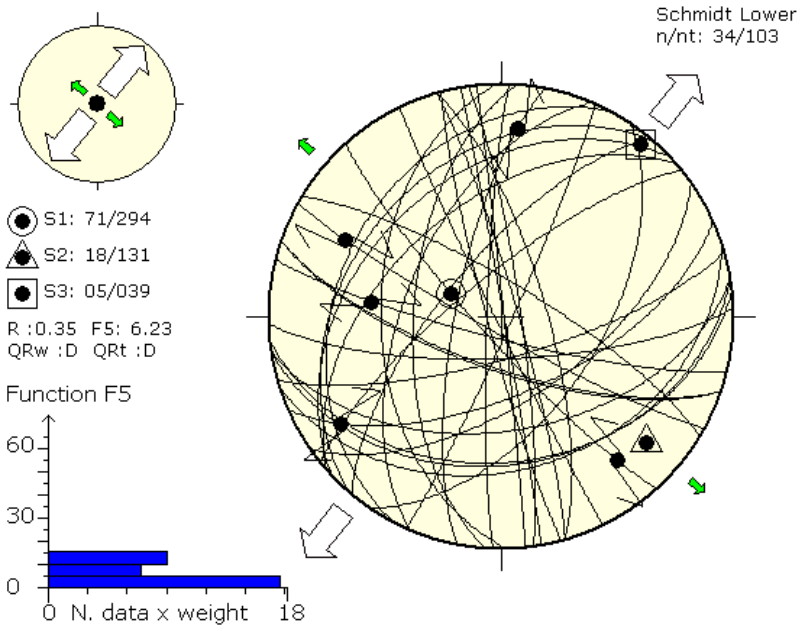

Fig. 6.11(f) - Stress tensor for recent stress regime for the Fufu fault, segment C (location: 8 on Fig. 6.1).

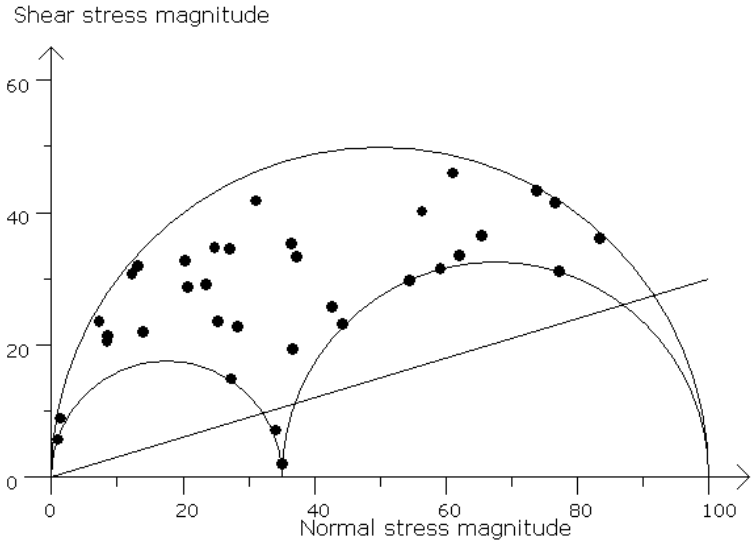

Fig. 6.11(g) - Mohr circles for the faults plotted in (a).

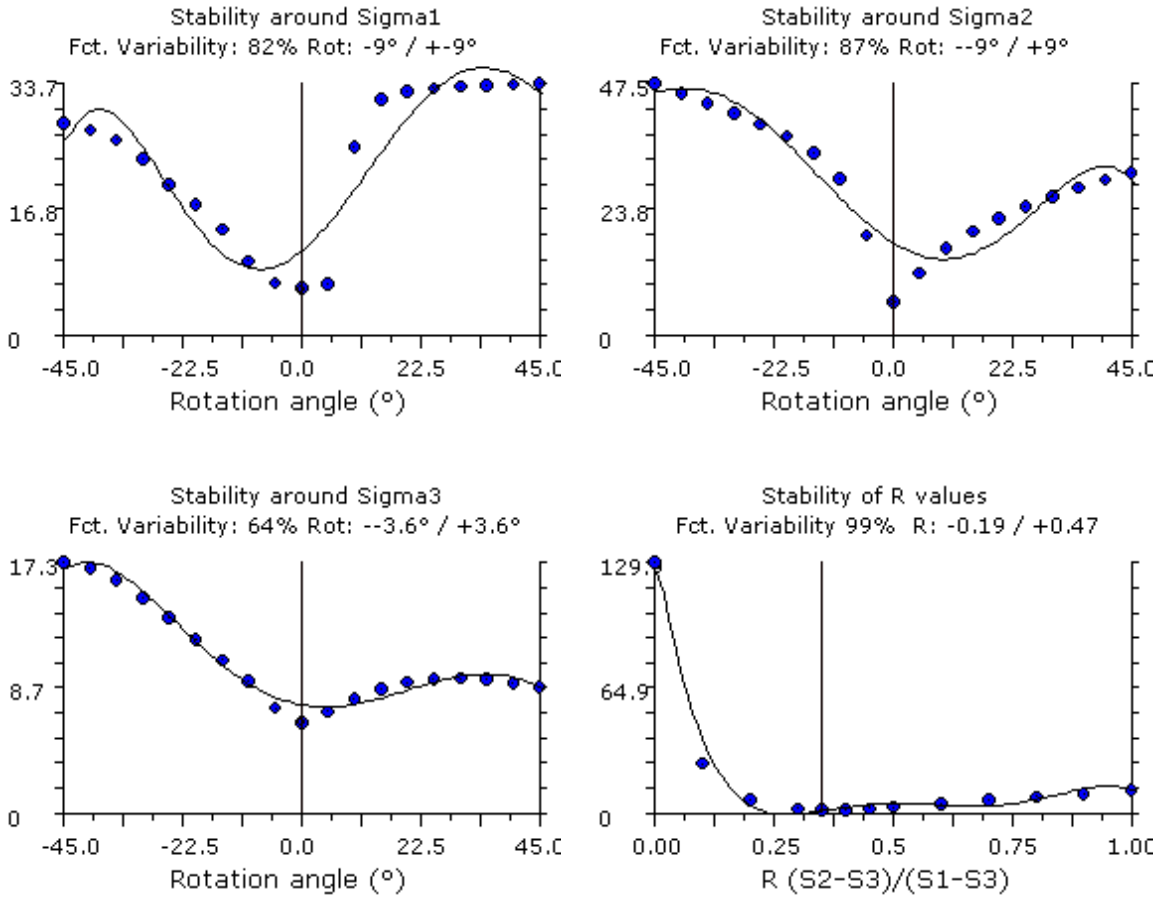

Fig. 6.11(h-k) - Rotational optimization curves of the corresponding σ_1, σ_2, σ_3 and R.

6.1.1.11 The Fufu fault, segment D

Segment D of the Fufu fault (location just north of 8; Fig. 6.1) trends nearly N-S (Hence the name Fufu north; Table 6.1a, b) and is characterized by a set of normal to oblique faults of various orientations defined by σ_1 = 74/266, σ_2 = 05/160, σ_3 = 14/072 (Fig. 6.12a) and a low R value (0.08).

The low R value implies that the position of the sub-vertical σ_1 axis is well constrained implying that the tensor obtained is of normal fault or extensional regime (σ_1 is near vertical for extensional regime; σ_2 and σ_3 being horizontal, ref. sec. 2.3.2). Both the horizontal stress axes (σ_2 and σ_3) are not well constrained. Nevertheless, an ENE-WSW direction of horizontal extension (S_{hmin} = 067) is well established. The quality of this last tensor is estimated at a C rank, owing to the number of data used (n = 17), their high proportion relative to the measured data (16/18), the good spatial distribution of the fault planes and slip lines. Only the data type, which is a combination of faults and fractures, prevents it from being ranked as a B quality. These brittle structures are often associated with traces of kaolinization, but they consist to a large extent of non-mineralized joints and barren fracture planes.

Fault planes in this area are in the field of being reactivated (Fig. 6.12b). Rotational optimization around σ_2 shows that the axis remains mostly stable (Fig. 6.12c-f).

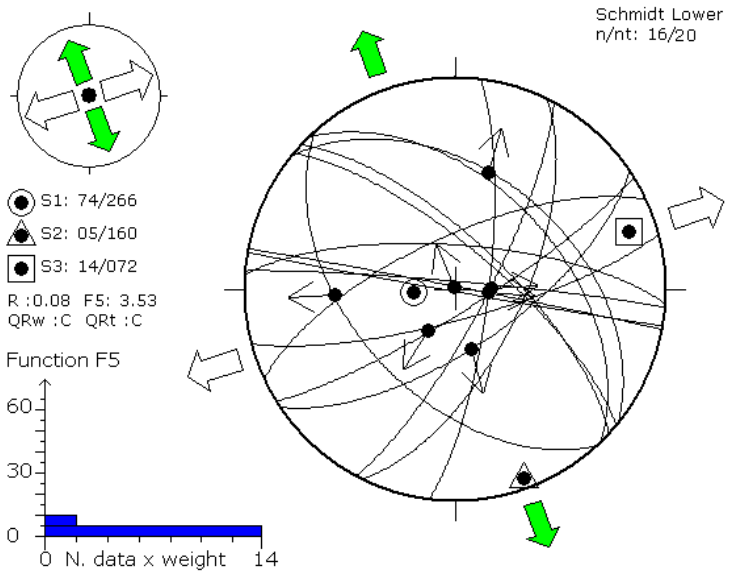

Fig. 6.12(a) - Stress tensor for recent stress regime for the Fufu fault, Segment D (location: just north of 8 on Fig. 6.1).

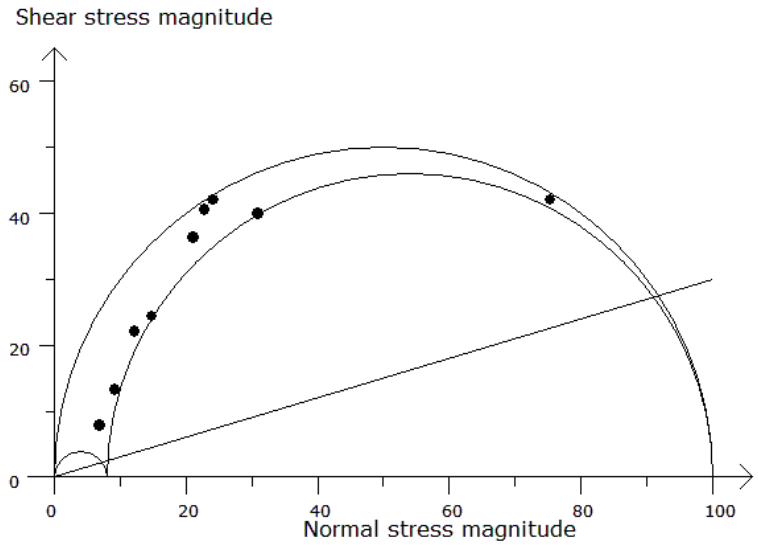

Fig. 6.12(b) - Mohr circles for the faults plotted in (a).

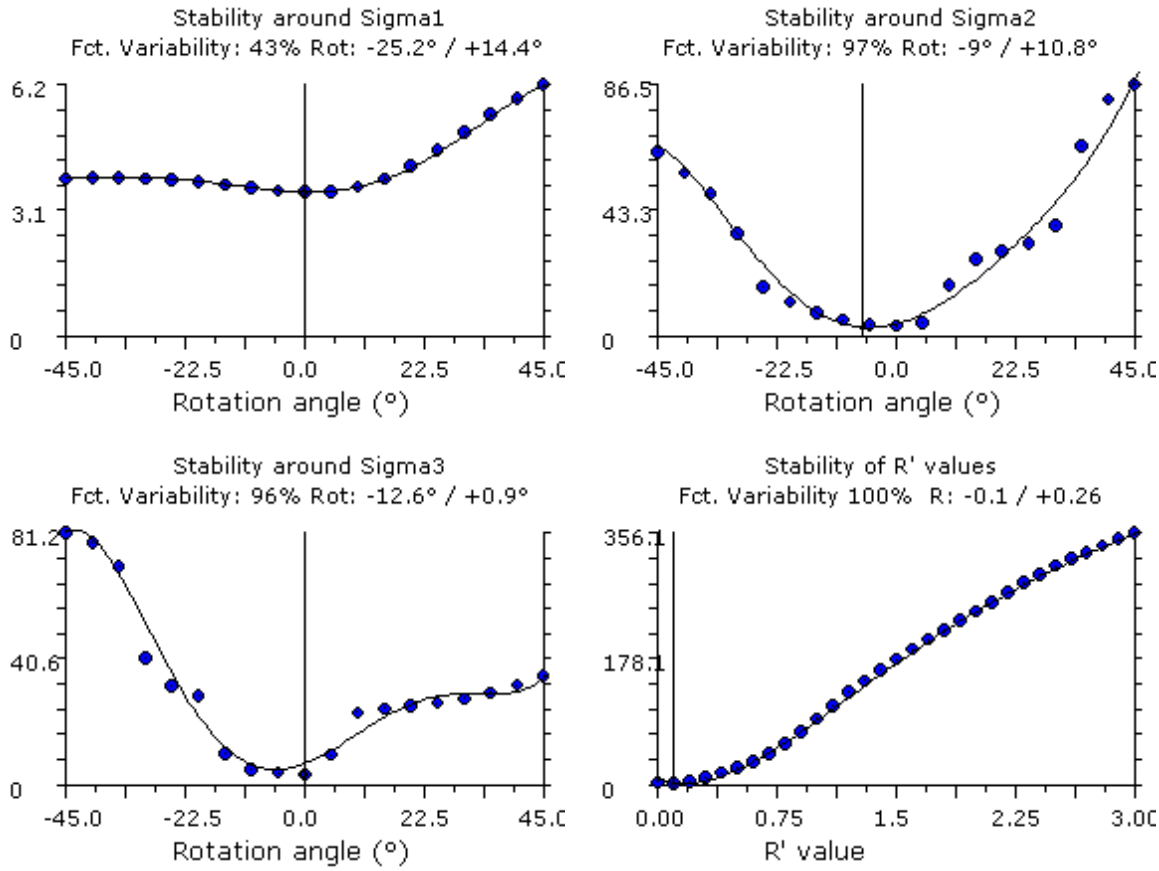

Fig. 6.12(c-f) - Rotational optimization curves of the corresponding σ_1, σ_2, σ_3 and R.

6.2. Present-day stress regime analysis from earthquake focal mechanisms

When slip occurs along an active fault (consequently causing an earthquake), the movement is in accordance with the present-day stress regime. Earthquake focal mechanisms, which define the direction of the movement along a fault that caused the earthquake, represent the most commonly used indicator to image the present-day tectonic stress regime in a region.

6.2.1 Focal mechanisms available

Earthquake focal mechanisms from the area between Arusha and Dodoma (Fig. 6.13) were compiled from Kebede and Kulhanek (1991), the Harvard Centroid Moment Tensor catalogue (CMT) and Brazier et al. (2005). The data are also listed in Table 6.2a. The focal mechanisms are presented as beach balls with their S_{hmin} directions and stress regimes on the map. The dominant regime is normal faulting under E-W extension, but strike-slip faulting also exists (Fig. 6.13).

Table 6.1a - Parameters of the paleostress tensors inverted from fault-slip data on various sites. (n): number of data used in the stress inversion, (nt): total number of data measured in the outcrop, (σ_1, σ_2, σ_3): orientation of the principal stress axes in plunge/azimuth format, (R): stress ratios, (SD): average slip deviation, (F5): misfit function.

Site	**Stage**	**n**	**nt**	**σ_1**	**σ_2**	**σ_3**	**R**	**SD**	**F5**
Mponde (segment 1)	Recent	42	43	53/263	24/136	25/034	0.70	0.27	4.67
Mponde (segment 2)	Recent	10	13	74/185	01/096	18/003	0.50	0	0.65
Saranda (Mid segment)	Recent	25	28	62/062	25/211	12/308	Fixed to 0.50	0	2.77
Bubu (Gonga - Magungu village)	Recent	12	12	42/026	43/170	19/278	Fixed to 0.50	0	3.55
Bubu (Gonga - Hot spring field)	Old	48	55	03/321	86/098	04/232	Fixed to 0.50		3.62
Bubu (Gonga - Hot spring field)	Young	8	10	32/084	57/282	06/178	0.72	4.4	12.87
Bubu (Makutupora - NW-SE)	Old	14	70	08/129	70/240	18/036	0.03	11.14	7.71
Bubu (Makutupora - E-W)	Old	53	70	04/270	16/360	72/159	0.27	4.33	7.73
Makanda	Recent	13	13	72/171	18/347	01/078	0.50		
Hombolo (Old)	Old	18	71	00/126	89/216	01/037	0.05	4.3	3.65
Hombolo (Recent)	Recent	52	71	59/185	30/014	03/282	0.49	6.6	3.26
Bahi (Southeastern segment)	Recent	18	18	66/318	20/177	15/079	0.64	0.28	4.02
Fufu (Main)	Old	56	103	04/260	84/030	05/169	Fixed to 0.50		3.37
Fufu (Main)	Recent	34	103	71/291	18/130	05/039	0.35	1.2	3.29
Fufu (North Recent)	Recent	16	20	74/266	05/160	14/072	0.08	10.42	3.53
Chikola	No paleostress data taken								
Maziwa	Limited paleostress data								

Table 6.1b - (QR): quality rank, (Reg): stress regime according to the World Stress Map, (S_{Hmax}, S_{hmin}): maximum and minimum horizontal principal stress directions, (R'): stress regime index, (limiting factor): the factor that is limiting the quality of the result, (Site ID): outcrop number. These parameters are described in more details in Delvaux and Sperner (2003). Shear sense: NF-pure normal fault, NS - normal with a sinistral component, ND-normal with a dextral component, SS-strike slip with sinistral component, TF, Compression.

Site	**Stage**	**QR**	**Reg**	**S_{Hmax}**	**S_{hmin}**	**R'**	**Limiting factor**	**Site ID**
Mponde (segment 1)	Recent	D	NF	136	046	0.70	Lack of slip lines	
Mponde (segment 2)	Recent	D	NF	093	003	0.50	Lack of slip lines	
Saranda (Mid segment)	Recent	D	NF	031	121	0.50	Lack of slip lines	
Bubu (Gonga- Magungu village)	Recent	D	NS	008	098	1.50	Lack of slip lines	
Bubu (Gonga-Hot spring field)	Old	D	SS	142	052	1.50		
Bubu (Gonga-Hot spring field)	Young	D	SS	088	178	1.26		
Bubu (Makutupora-NW-SE)	Old	D	SS	126	036	1.97		
Bubu (Makutupora-E-W)	Old	C	TF	90	000	2.27		
Makanda	Recent	D	NF	167	077	0.50		
Hombolo (Old)	Old	D	TS	127	037	1.95	Slip lines dispersion	DD824d
Hombolo (Recent)	Recent	C	NF	014	104	0.49	Data type	DD824a-c
Bahi (Southeastern segment)	Recent	D	NF	177	087	0.64	Data type + number of data	
Fufu (Main)	Old	D	SS	079	169	1.50	Data type	DD864a
Fufu (Main)	Recent	D	NF	130	040	0.35	Number of data	DD833
Fufu (North Recent)	Recent	D	NF	067	166	0.36		

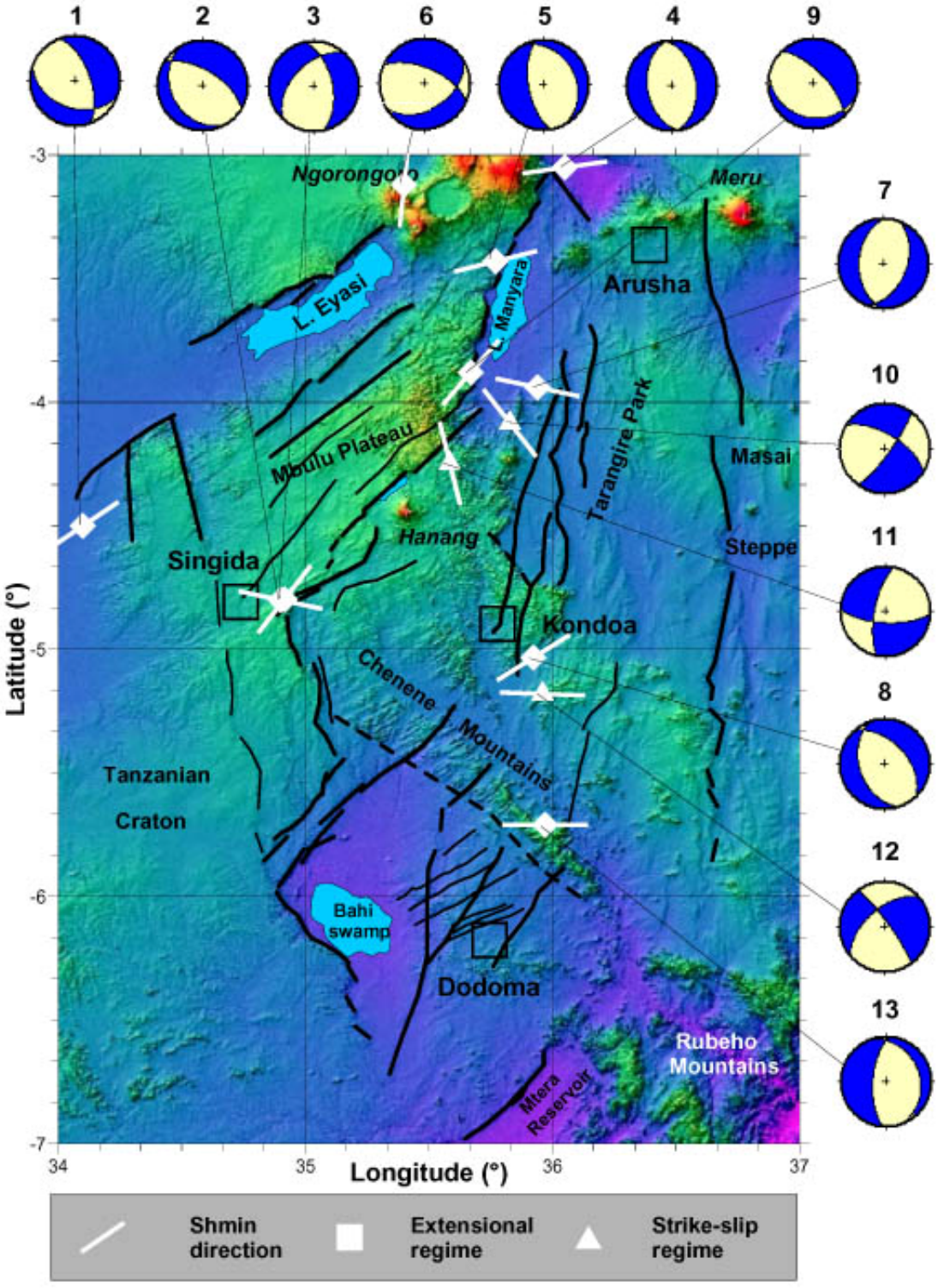

Fig. 6.13 - Earthquake focal-mechanism map of the Manyara-Dodoma rift segment in Central Tanzania shown on the SRTM topography. Data are from Table 6.2a. The horizontal principal extension direction (S_{hmin}) and the stress regimes are shown according to the principle of the World Stress Map. The dominant regime is normal faulting under E-W extension, but strike-slip faulting also exists (after Macheyeki et al., 2008b).

6.2.2 Computation of stress tensor from focal-mechanism data

Stress inversion of a pure normal faulting stress tensor (Fig. 6.14) was obtained from 10 focal-mechanism data (Table 6.3a). Only 10 of the 13 data sets were selected (i.e., nrs 1, 2, 3, 4, 5, 7, 8, 9, 12 and 13), as 3 data sets were rejected by the TENSOR program during processing due to their incompatibility with the main data set. The tensor obtained is characterized by an ENE-WSW horizontal principal extension (S_{hmin} = 080), a stress ratio R = 0.5 and a C (medium) quality (Table 6.2b).

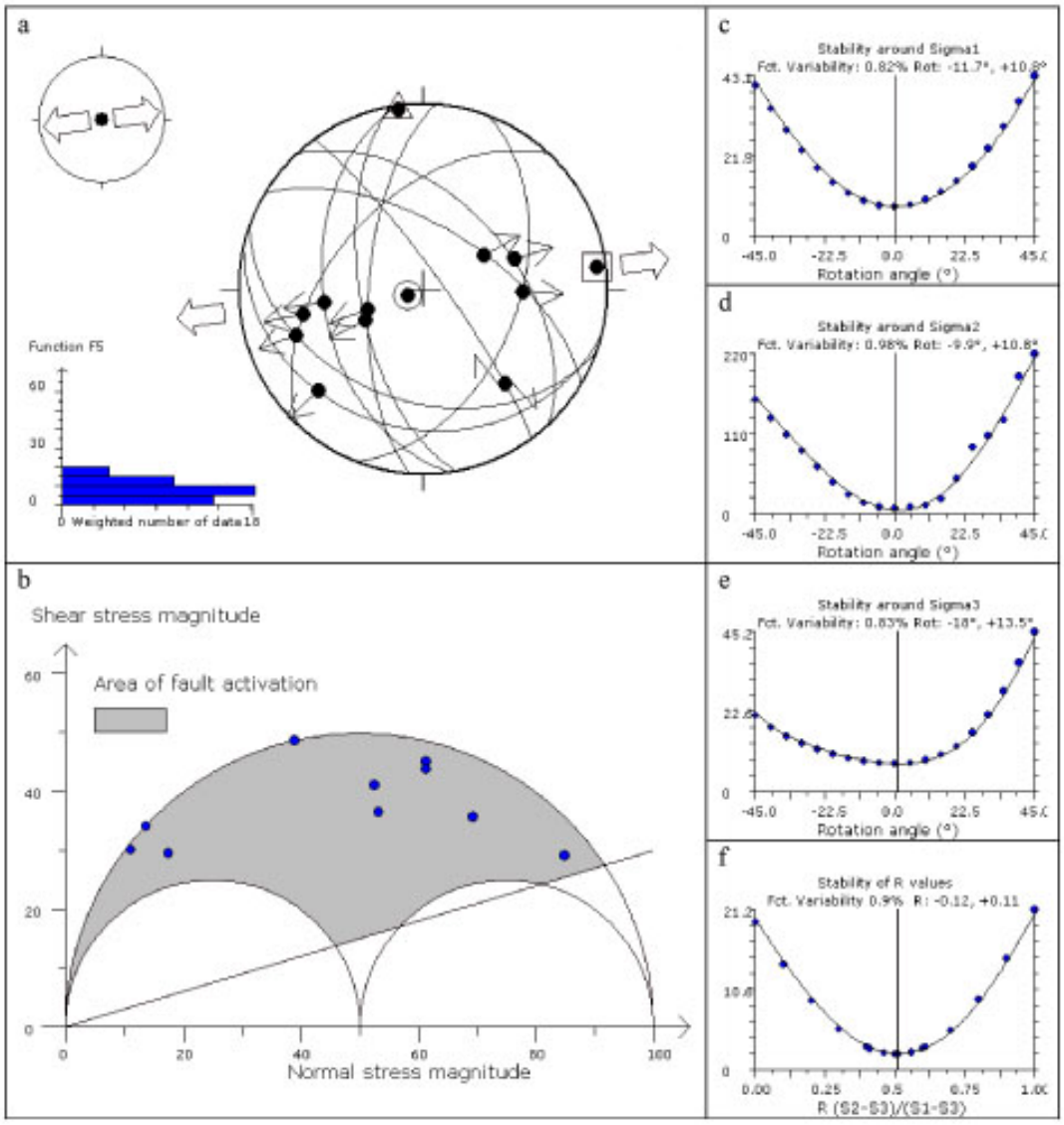

Fig. 6.14 - Stress inversion of the focal-mechanism data. (a) Lower-hemisphere Schmidt stereoplot of the selected focal planes and associated slip lines after the inversion-separation procedure. The histogram represents the distribution of the misfit function F5, weighted arithmetically according to the magnitudes. (b) Mohr diagram for the stress solution. The area of possible fault activation is constrained by the three circles and the line of initial friction corresponding to an angle of 16.7=ϕ (ref. Fig. 2.16b in Chapter 2) (c–e): Stability diagrams, respectively, for σ_1, σ_2 and σ_3 axes after rotational. (f): Stability diagram for the stress ratio R (after Macheyeki et al., 2008b).

Table 6.2a - Earthquake focal-mechanism data, Kebede: Kebede and Kulhanek (1991); Harvard: Harvard Centröid Moment Tensor catalogue (CMT); Brazier: Brazier et al. (2005). (Mb): magnitude, (Strike Dip, Slip): parameters of one of the focal planes, the second one being orthogonal, (S_{Hmax}, S_{hmin}): maximum and minimum horizontal principal stress directions, (Reg): stress regime according to the World Stress Map. The S_{Hmax}, S_{hmin} and Regime (Reg) are obtained according to the World Stress Map standard.

	Date	Time	Lat (°)	Long (°)	Mb	Source	Strike	Dip	Slip	S_{Hmax}	S_{hmin}	Reg.
1	19720213	10:02:00	-4.50	34.10	5.0	Kebede	340	62	-061	146	56	NF
2	19771215	23:20:04	-4.80	34.92	5.6	Harvard	151	31	-064	128	38	NF
3	19771215	23:20:04	-4.80	34.90	5.7	Kebede	348	56	-129	12	102	NF
4	19900405	19:20:48	-3.05	36.05	5.1	Harvard	352	45	-090	172	82	NF
5	19900515	15:21:28	-3.43	35.77	4.7	Harvard	332	29	-106	166	76	NF
6	19900515	16:24:25	-3.12	35.40	5.2	Harvard	059	43	-136	96	6	NF
7	19910222	22:06:01	-3.94	35.94	4.4	Harvard	182	45	-104	12	102	NF
8	19940129	00:23:33	-5.03	35.92	4.1	Brazier	162	43	-71	148	58	NF
9	19940212	16:37:33	-3.88	35.67	4.5	Brazier	316	68	-77	131	41	NF
10	19940720	11:32:03	-4.25	35.58	4.5	Brazier	301	64	-11	76	166	SS
11	19941127	04:20:53	-4.08	35.83	4.0	Brazier	93	69	-22	52	142	SS
12	19961220	03:53:02	-5.18	35.96	4.6	Harvard	229	57	-010	2	92	SS
13	20030614	03:10:02	-5.71	35.97	4.6	Harvard	340	26	-112	180	90	NF

Table 6.2b - Parameters of the present-day stress tensor inverted from the focal-mechanism data of Table 6.3a (n): number of data used in the inversion, (nt): total number of data in the database, (σ_1, σ_2, σ_3): orientation of the three principal stress axes in plunge/azimuth format, (R): stress ratio, (SD): average slip deviation in degrees, (F5): misfit function, (QR): quality rank, (R0): stress regime index, (Reg): stress regime according to the World Stress Map, (S_{Hmax}, S_{hmin}): respectively, maximum and minimum horizontal principal stress directions.

N	nt	σ_1	σ_2	σ_3	R	S.D.	F5	Q.R.	R'	Reg	S_{Hmax}	S_{hmin}
10	13	83/248	02/352	06/083	0.50	7.15	7.89	C	0.50	NF	172	82

Table 6.3 - Resolved stress on the regional faults by the application of the present-day regional stress tensor determined from the inversion of earthquake focal mechanisms. Parameters of the regional stress tensor are from Table 6.2a, b. The orientations of the fault planes are in dip/dip direction format, and those of the shear direction in plunge/azimuth format. Shear sense: NS - normal with a sinistral component, ND-normal with a dextral component. (Nmag and Tmag): normal and shear stress magnitudes within an arbitrary scale where the magnitude of σ_1=100 and the magnitude of σ_3=0, (Φ): Friction angle, (Ts): Slip tendency according to Morris et al. (1996). The reactivation likelihood is proportional to Ts (after Macheyeki et al., 2008b).

Fault		Computed shear stress					Slip Tendency	
Name	Orientation	Shear direction	Shear sense	N_{mag}	T_{mag}	Φ	Ts	Likelihood
Mponde	60/087	60/083	NS	35.2	47.6	53.5	1.35	Highest
Saranda	60/129	51/085	NS	50.1	38.4	37.5	0.77	Medium
Bubu (Gonga)	60/150	54/112	NS	59	27.6	25.1	0.47	Low
Bubu (Makutupora)	60/136	51/091	NS	53.5	35.1	33.3	0.66	Medium
Bubu (Nkambala)	60/125	52/082	NS	48.1	40.1	39.8	0.83	Medium
Makanda	60/096	59/079	NS	36.4	46.9	52.2	1.29	Highest
Hombolo	60/304	41/244	NS	34.9	38.8	48	1.11	High
Bahi	60/038	51/083	ND	51.8	40.2	37.8	0.78	Medium
Fufu Main	60/134	51/089	NS	52.5	36.1	34.5	0.69	Medium
Fufu North	60/105	57/077	NS	39	45.7	49.5	1.17	High
Sanzawa	60/215	39/277	ND	38.6	35.9	43	0.93	Medium
Balangida South	*60/154*	*56/122*	*NS*	*60.1*	*25.6*	*23.1*	*0.43*	*Low*
Balangida North	*60/144*	*51/096*	*NS*	*55.3*	*33*	*30.8*	*0.6*	*Medium*

6.2.3 Slip-tendency analysis

Using the principles stated in section 2.3 and the methods explained in section 4.4, the normal stress (σ_n) and shear stress (τ), the friction angle ϕ = arctan τ/σ_n and the slip tendency Ts = τ/σ_n are given for each fault under the modeled stress tensors. The results show that in the Dodoma area, the lozenge-shaped fault pattern, defined by the orientation of the basement shear zones, dolerite dykes and associated fractures (NE- and NW-trends), presents the lowest reactivation likelihood, while the newly formed N-S and still weakly expressed N-S faults present the highest likelihood (Fig. 6.15).

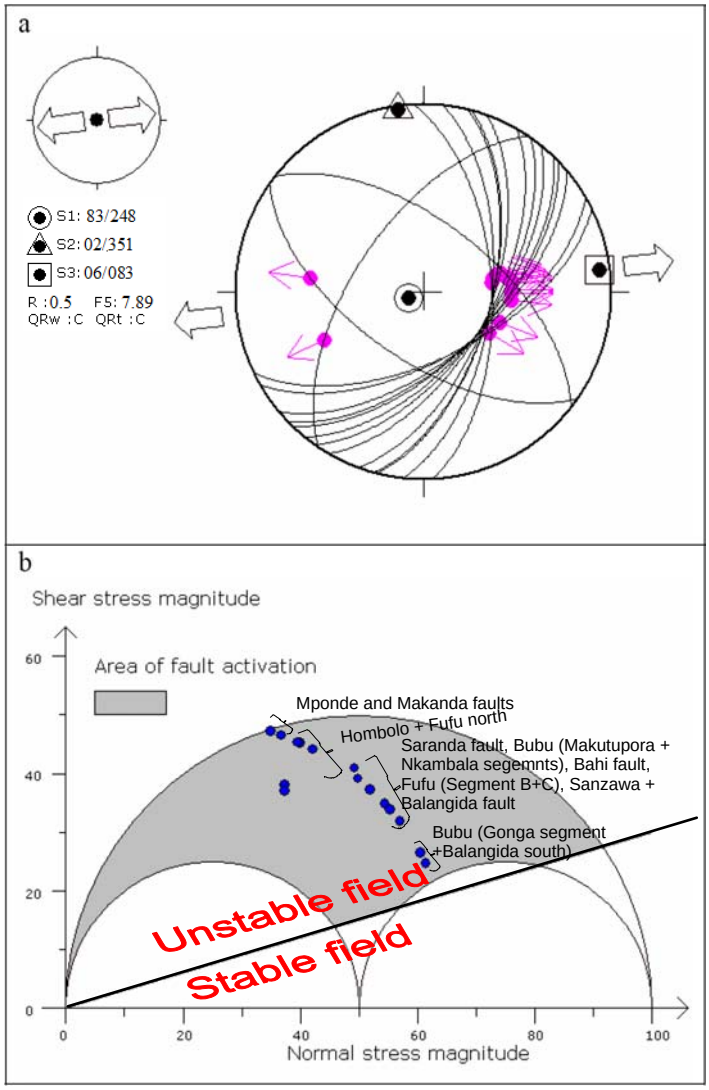

Fig. 6.15 - Application of stress tensor to selected faults in the Dodoma area. Data are from Table 6.3. (a) Stereoplot of the faults with their modeled slip. (b) Corresponding Mohr diagram. All faults plot above the line of initial friction (16.7°), between the σ_3-σ_1 circle and the σ_2-σ_1 circle. The faults with the highest reactivation likelihood are closer to the external circle (σ_3-σ_1) and those with the lowest reactivation likelihood are closer to the internal (σ_2-σ_1) circle. On the normal stress magnitude scale, σ_1= 100, σ_3 = 0 and σ_2 = R * 100 where R = σ_2-σ_3/σ_1- 3.

The input data for these calculations are those presented in Table 6.3 and correspond to Fig. 6.15a. The corresponding Mohr diagram is presented in Fig. 6.15b. The latter shows that all faults plot above the line of initial friction (i.e., the line that separates between the stable and unstable fields of the Mohr diagram). Furthermore, Fig. 6.15b shows that the faults display a linear trend between the stable and unstable field (i.e., between the $\sigma 3$-$\sigma 1$ circle and the $\sigma 2$-$\sigma 1$ circle). It follows therefore that the closer to the external circle a fault plots, the higher its likelihood of being reactivated and vice versa (see also Table 6.3 for other related parameters).

The main conclusions drawn from the slip-tendency analysis are:
1. the faults reactivating the NE-trend of basement dolerite dykes and associated fractures represent the lowest reactivation likelihood (Balangida South and northern part of the Gonga segment (called "Bubu North" in Macheyeki et al. (2008b));
2. medium reactivation likelihood is obtained for the NW-trending faults, like the Bahi and Sanzawa faults, and the NNE-trending Balangida North, Saranda, Nkambala and Makutupora segments (called "Bubu South" in Macheyeki et al. (2008b));
3. high slip tendency is given to the almost N-trending northern extremity of the Fufu fault, and to the NNW-trending Makanda fault (called "Dodoma-Kigwe" in Macheyeki et al. (2008b) and Hombolo fault (Table 6.3);
4. the NNW-trending Mponde fault has the highest slip tendency of all faults analyzed as it trends almost orthogonal to the S_{hmin} direction.

6.3. Summary and conclusions

The above paleostress data on active faults show different recent extensional directions at different locations (Fig. 6.16). Although these data are still rather limited in number and quality, they do reveal the present direction of extension to range between WSW-ENE to WNW-ESE and NW-SE to NE-SW. Where faults that trend in different directions interact, such as is the case for Segment 2 of the Mponde fault and the Balangida South segment, the S_{hmin} tend to be complicated. For instance, S_{hmin}, computed from fault-slip data from the Mponde fault, seems to be more in agreement with the extension direction across the Balangida fault than it is for the Mponde fault. Interestingly, however, the focal mechanisms taken within the study area show very similar results of extension directions as those obtained from fault-slip data. For instance, based on Fig. 6.13, focal mechanisms 1 and 2 show an extensional regime with a NE-SW to NNE-SSW extension direction, similar to that obtained from fault-slip data in the same area (Mponde, Segment 1 and 2; Figs. 6.2a; 6.3a), also summarized in Fig. 6.17. In addition, focal mechanism 13 (Fig. 6.13) obtained for an area near Hombolo fault, between sites 5 and 9 in Fig. 6.1, is similar in terms of extension direction (nearly E-W) to that obtained from recent fault-slip data on the Hombolo fault (Fig. 6.9i).

When geological fault-slip data are complemented with present-day stress regimes computed from earthquake focal-mechanism data that were obtained from an area that is

larger than the study area, a WSW-ENE (nearly E-W) extensional direction is confirmed (Fig. 6.16).

Reduced stress tensors related to old tectonic activities show two principal directions of compression: NW-SE and E-W. An area that comprises traces of both directions is the Makutupora segment of the Bubu fault. The E-W direction of compression is more prominent than the NW-SE direction. Based on the analysis of fault data from the Hombolo fault, the NW-SE direction of compression, characterized by both low-angle and high-angle faults, can be shown to represent the oldest tectonic activity, while the E-W direction of compression appears to be associated with a younger compressional event (not yet identified). This means that the oldest NW-SE compressive regime affected both the Hombolo area and the Makutupora area.

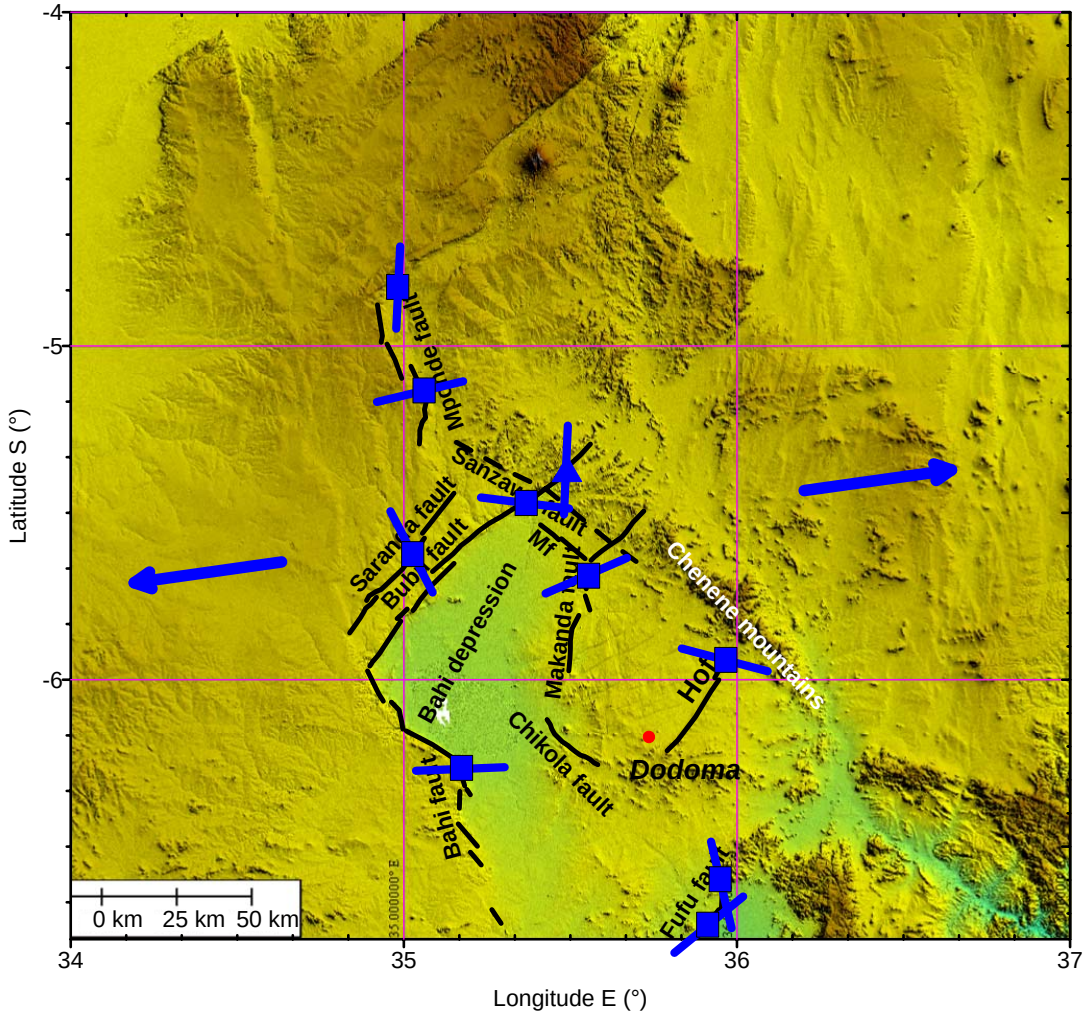

Fig. 6.16 - Extensional directions as S_{hmin} (square boxes representing normal stress regime according to the principle of the World Stress Map) for recent stress field of the Dodoma area, obtained from geological fault-slip data are plotted on the SRTM topography. The overall extensional direction shown by arrows (N082°E) is taken from Macheyeki et al. (2008b).

6.4. Assessment of accuracy and limitations of used methods

- During fault-slip data collection in the field, two types of 'pseudo slip lines' were observed that could be mistakenly interpreted as real fault-slip indications. 'Pseudo slip lines' can be created by water moving down slope (Fig. 6.16), but also by rock blasts during road constructions. When the rock is blasted, part of the rock slips away leaving behind some lines that define the mechanical movement(s) imposed by the blasting process, very similar to tectonic slip lines (Fig. 6.16).

Fig. 6.16 - 'Pseudo slip lines': (left) on granite due to moving water at Saranda mid (05°40.7'S/34°59.2'E); (right) on gneisses due to rock blasting at Fufu (06°39'S/35°58'E).

- The main challenge with the use of focal-mechanism data for computing stress tensors is the decision on or choice of which of the two potential focal planes to use in the stress inversion. Focal mechanisms always comprise two possible fault-plane solutions: i.e. the real fault plane and the auxiliary plane. The choice can usually be made quite easily if knowledge is available about the strikes and dips of the faults in region. In this study, the choice of the fault plane was made mainly based on the regional mapping of the main fault structures and on field observations.

Chapter 7

Paleoseismic Investigations

A summarized version of this chapter is being prepared for publication as:
Macheyeki, A.S., Delvaux, D., De Batist, M. & Mruma, M., (in prep.) Paleoseimic Investigations along the Bubu fault, Dodoma-Tanzania. *J. Geodynamics*.

7. Paleoseismic investigations

Based on the morphometric analyses, field observations and paleostress analysis, a site (i.e., near Magungu village, on the 42 km long Gonga segment of the Bubu fault was chosen for paleoseismic investigation. A trench was established across the Bubu fault and studied in detail.

In this chapter, the description of the trench is given, followed by the tectono-chronostratigraphic interpretation and a summary.

7.1. Location and characteristics of the trench

The Magungu trench is/was located at 35º20'36"E, 5º28'51"S (Fig. 7.1) or 0759563E, 9393998N (UTM 36 M, Arc 1960), at 960 m above mean sea level.

The trench is within the Gonga segment of the Bubu fault (Fig. 7.2). The position of the trench is marked by a white filled square toward the right end of area '3b' on Fig. 7.2.

The detailed topographic map of the Gonga segment at Magungu trench is shown in Fig. 7.3a. In this figure (a 90 m resolution SRTM-DEM with contours at 50 m intervals), the location of the trench is shown by a black filled rectangle at an elevation of ~ 960 m. Bubu river tributaries, indicated by letters P, Q and R, are shown in blue. The 2.6 km long topographic profile (indicated by a trace in black dotted line) (Fig. 7.3a), is shown in Fig. 7.4. The panoramic view of the trench area, marked by a rectangle in Fig. 7.3a, is shown in Fig. 7.3b. In Fig. 4.5, the depression that is seen on the NE of the picture represents a river channel which is marked as Q in Fig. 7.3a.

As shown in Fig. 7.3a, the trench was established about 350 m SW of channel Q and about 1.2 km NE of channel P. The river channels, which are tributaries of the Bubu River, are V-shaped and seem to be actively eroding the hanging wall in the Bubu River.

Close to the fault scarp, the red soil is pronounced owing to weathering of ferromagnesian minerals. The latter are believed to originate from both Precambrian mafic rocks and dolerites of unknown ages. The latter are found outcropping on the footwall of the Bubu fault. Field relationships show that they intrude Precambrian rocks, which are mainly composed of gneisses.

Away from the fault scarp towards the eastern side, the soil color changes. It becomes more greyish. Towards the Bubu river dark grey soil, mainly silt-sand dominates: this is thought to be a result of pronounced reworking of the soil with other deposits by river channels (both the tributaries and the main Bubu River). The detail of the local geology of this area is not presented here.

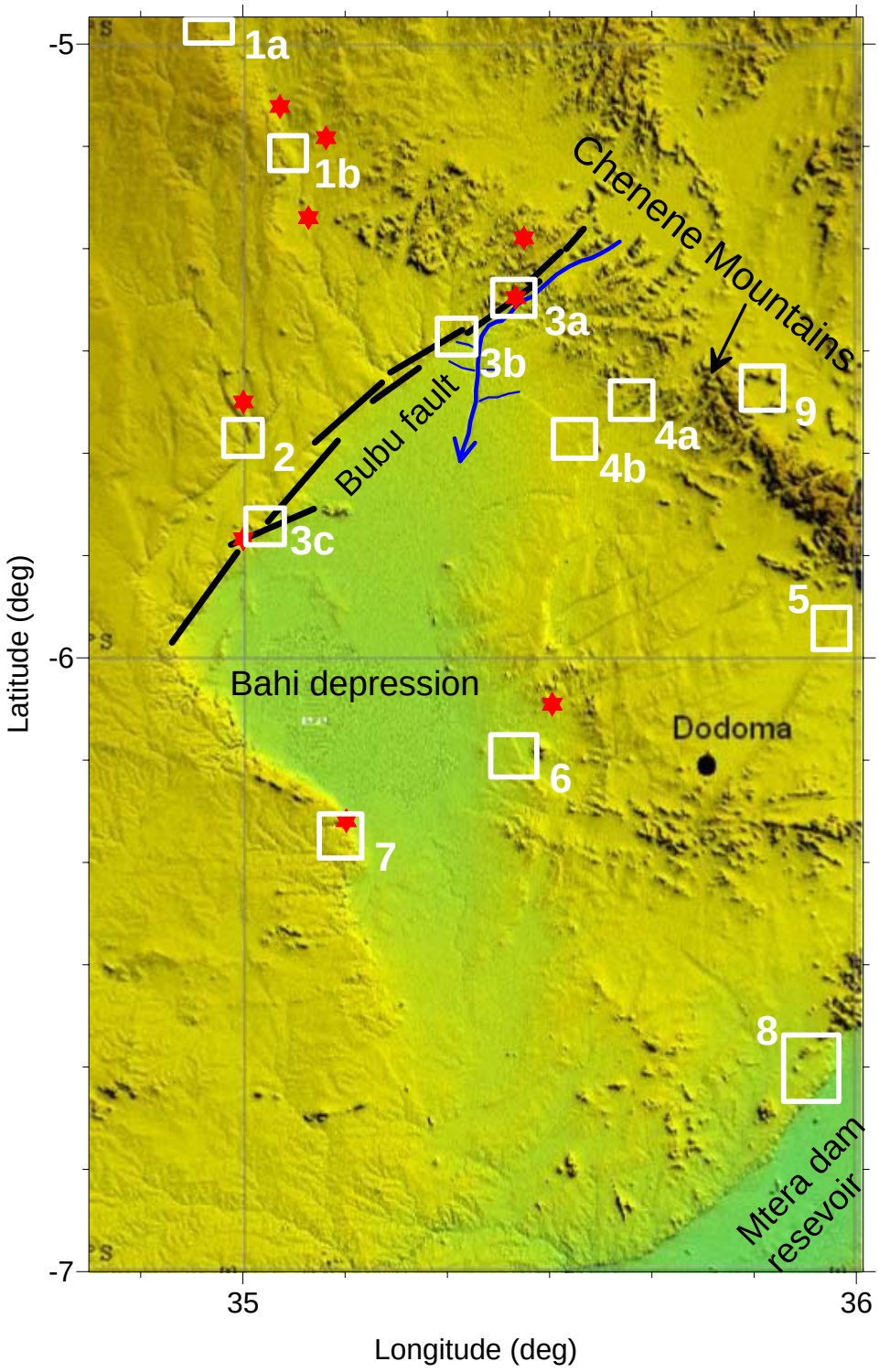

Fig. 7.1 - The 90 m resolution SRTM-DEM of the Dodoma area showing the sample points for paleostress analysis. The Magungu trench is located on the Bubu fault within sample point area marked by '3b'. See also Fig. 7.2.

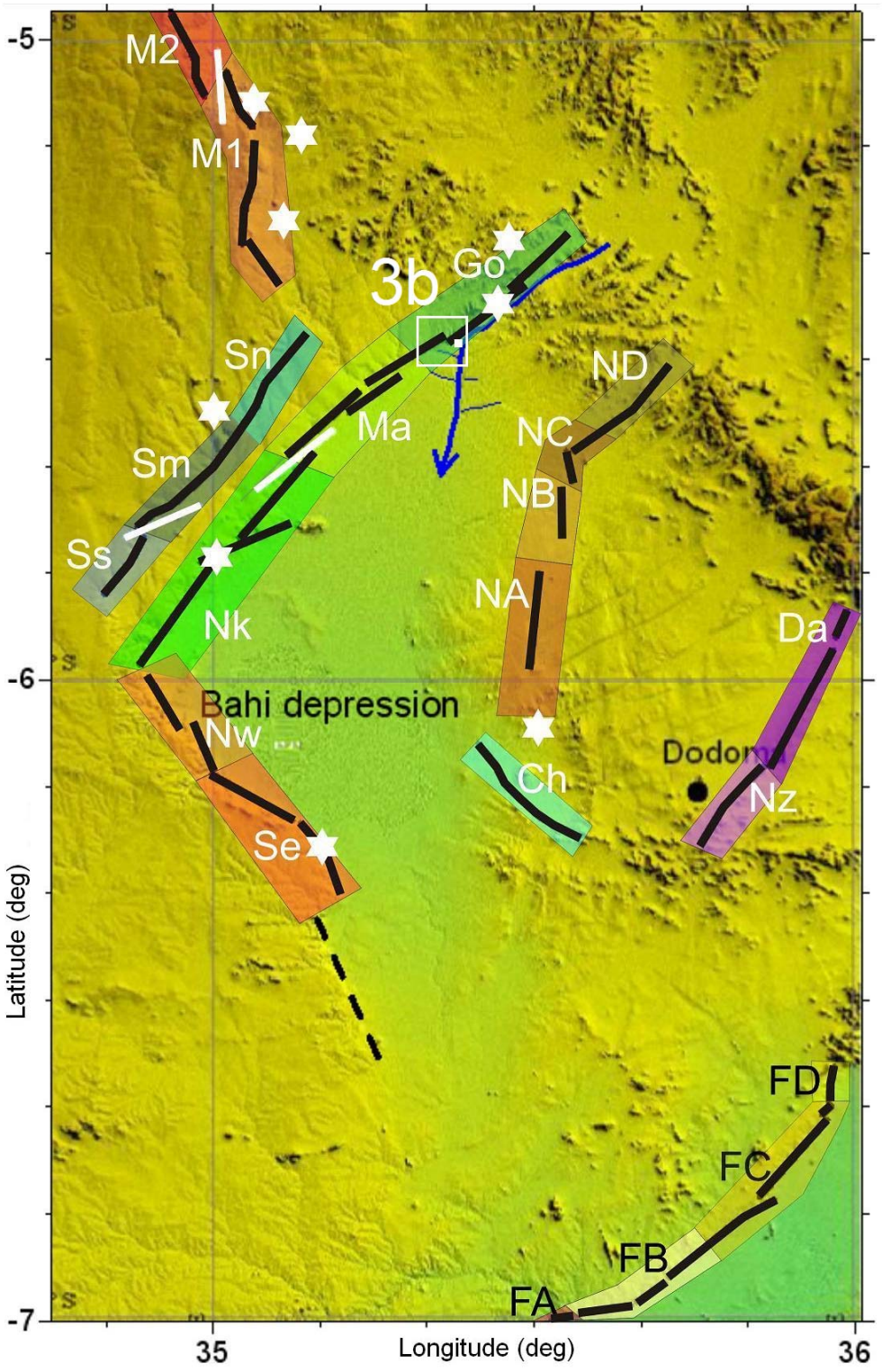

Fig. 7.2 - The 90 m resolution SRTM-DEM of the study area showing the fault segments and the location of the Magungu trench. The Magungu trench, located within an area marked by '3b' within the Gonga segment 'Go' is indicated by a white filled square. The blue line represents the Bubu River as seen from 90 m SRTM-DEM. Note that the Gonga segment 'Go' is part of the Bubu fault.

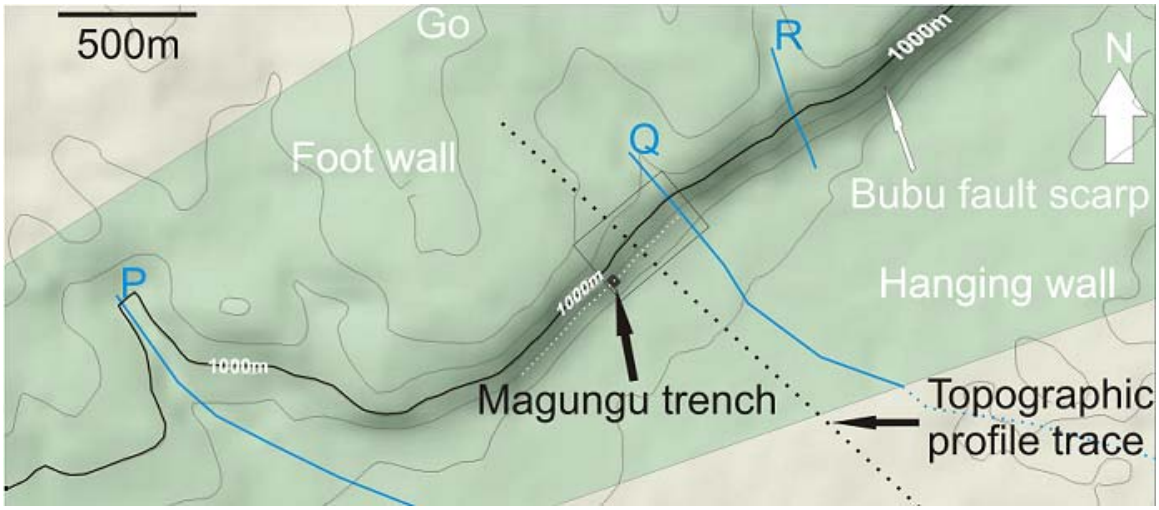

Fig. 7.3a - The detailed topographic map of the Gonga segment (Go) at Magungu trench within the 90 m resolution SRTM-DEM with 50 m contour lines. The labeled contour line is 1000 m above mean sea level. Blue lines are tributaries P, Q and R of the Bubu River that is found on the eastern side of this map. Blue dotted lines are inferred trace of the tributary 'Q'. Black dotted line represent a ~ 2.6 km long topographic profile across the Bubu fault at Magungu area, just about 100 m NE of (but parallel to) the Magungu trench. The latter is shown by a black filled square. The white dotted line parallel to the fault represents approximate inflexion (turning) points of the Bubu fault scarp (see also Fig. 4.7). The trench was established around 960 m above the mean sea level. The rectangle in thin black outline represents the area where a picture was taken. This picture is shown in Fig. 7.3b.

Fig. 7.3b - Panoramic view of the trench site at Magungu village.
Arrow points at the point on which the Magungu trench was established. Picture taken facing NW.

Figure 7.4 shows the topographic profile of the Magungu area. This profile was established about 100 m NE of the Magungu trench because it was not possible to establish a topographic profile that runs within the trench trace due to thick tree cover as seen in Fig. 7.3b and Fig. 4.7. Fig. 7.4 is similar to Fig. 4.6, but the trace of the trench

(slightly exaggerated) has also been projected on Fig. 7.4 in order to show the relationship between the topography and the trench location. As explained in Chapter 4, the trench was established in such a way that it was centered on the scarp inflection point (Fig. 7.3a). The trench was 10 m long, 1.5 m wide and 4 m deep, and had a N140°E orientation, i.e. NW-SE.

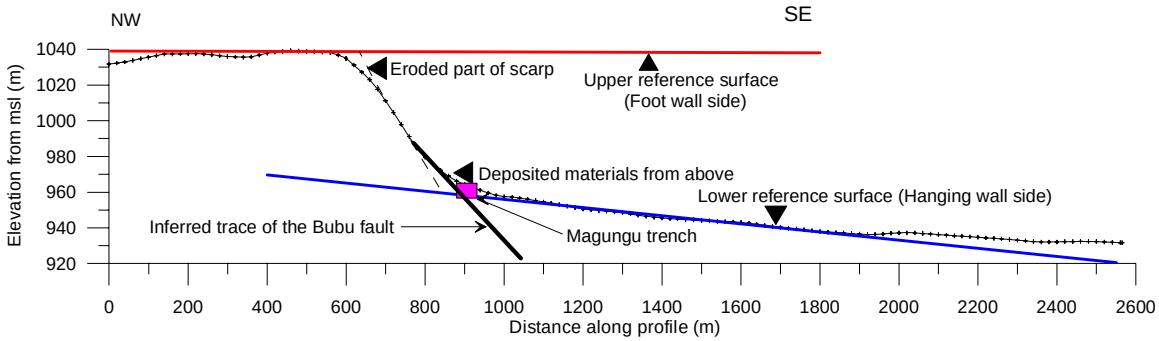

Fig. 7.4 - The topographic profile of the Bubu fault at Magungu showing the approximate location of the Magungu trench. Compare the location and elevation of the trench from Fig. 7.3a. In Fig. 7.3a, the trace of this topography is shown by a dashed black line drawn perpendicular to the fault. Note also that the trench location is projected about 100 m NE from its location.

7.2. Observations

Figure 7.5a shows a mosaic of pictures that were taken facing the southwestern wall. The corresponding interpretation is shown in Fig. 7.5b. The pictures were somewhat distorted during mosaicking due to the fact that the pictures had to be taken from outside (and inclined to) the trench and somewhat at slightly different orientations. This wall provided a better picture of the stratigraphic units and the corresponding faulting event(s). In Fig. 7.5b, selected areas marked by two rectangles ‘a’ and ‘b’ are zoomed in and interpreted in Fig. 7.6 and Fig. 7.7, respectively. The zoom of the area marked by rectangle ‘a’ was taken from the opposite wall of the trench (i.e. the northeastern wall) and mirrored in a vertical axis.

At least 5 lithologic units and four normal faults (f0, f1, F1 and F2) were revealed (Fig. 7.5-8) in the trench. They are described as follows:

1. Basement
   The basement (Base) is exposed over 2 m in the hanging wall side. It consists of highly to moderately weathered gneiss with intercalations of mafic rocks. The mafic rocks are probably delivered from dolerite dikes in the vicinity. It is cut by a normal fault (f0), at an angle of ≤ 40°SE. The fault, f0 is considered to be an inferred fault because there is not clear stratigraphic offset associated with it. Furthermore, there are no slip-lines associated with the fault. Its approximate position is established based on the fact that it is at this place where the basement outcrops as a highly

weathered unit. At this place, the basement is also in contact with a highly weathered unit 'KC'.

2. Unit KC
This unit, which is mainly a hard substance, is coherently calcrete-rich with reddish cemented silt-sand matrix. Close to the contact with the basement, KC grades into Kcw, a highly weathered calcrete-rich subunit that is intercalated with weathered basement fragments. It has a thickness of over 100 cm and it is cut by two normal faults F1 (45°SE) and F2 (54°SE) towards the foot of scarp and partly by f0. Faults, F1 and F2 are not associated with slip lines. Unit KC overlies the basement unconformably. It is considered that KC was deposited in a shallow-water or semi-arid environment. In addition, the water table was probably fluctuating (capillary rise and fall), allowing the deposition of Ca-rich (± Si-rich) materials with time, indicating that KC was close to the surface for an extended period of time.

3. Unit C1
Like Unit KC, Unit C1 is also in contact with the basement. It consists of loose conglomeratic materials that are characterized by rounded to sub-rounded basement gneiss pebbles of up to 15 cm in diameter. It has a thickness of up to 80 cm and thins away towards both the hanging wall and footwall. The unit tapers off progressively on the hanging wall side and appears to be truncated by F1 as it comes in contact with KC and C3b. It appears to be offset by f1. Like f0, F1 and F2, no fault slip indicators were observed on or associated with f1.

4. Unit C2
This unit has a thickness of up to 60 cm. It is a clast-supported deposit and consists of unsorted angular pebbles and boulders that are randomly deposited. It also has significant amount of pisoliths (Fe-rich). It unconformably overlies C1 and appears to be affected by f1.

5. Unit C3a
This unit consists of reddish brown colluvium characterized by matrix-supported materials consisting of unsorted angular pebbles and boulders with pisoliths. Compared to C2, angular pebbles and boulders in C3a are fewer and more weathered. It is up to 70 cm thick. It overlies C2 unconformably. Its upper contact with C3b is relatively diffuse and its texture and extent are not so distinct.

6. Unit C3b
This unit consists of reddish brown colluvium with unsorted sub-angular gravel, pebbles and soil. Unit C3b is massive in appearance. Occassionaly, angular boulders are found within C3b, implying a proximal source (by gravity reworking?). Roots from dead trees and grasses are common. It is over 100 cm thick and extends on both the hanging wall and footwall sides outside the trench limits. It covers unconformably all units C2, C1 and KC. It is cut by both F1 and F2. F1 has a displacement of about 35 cm and F2 has a displacement 30 cm. These displacements are along the fault planes.

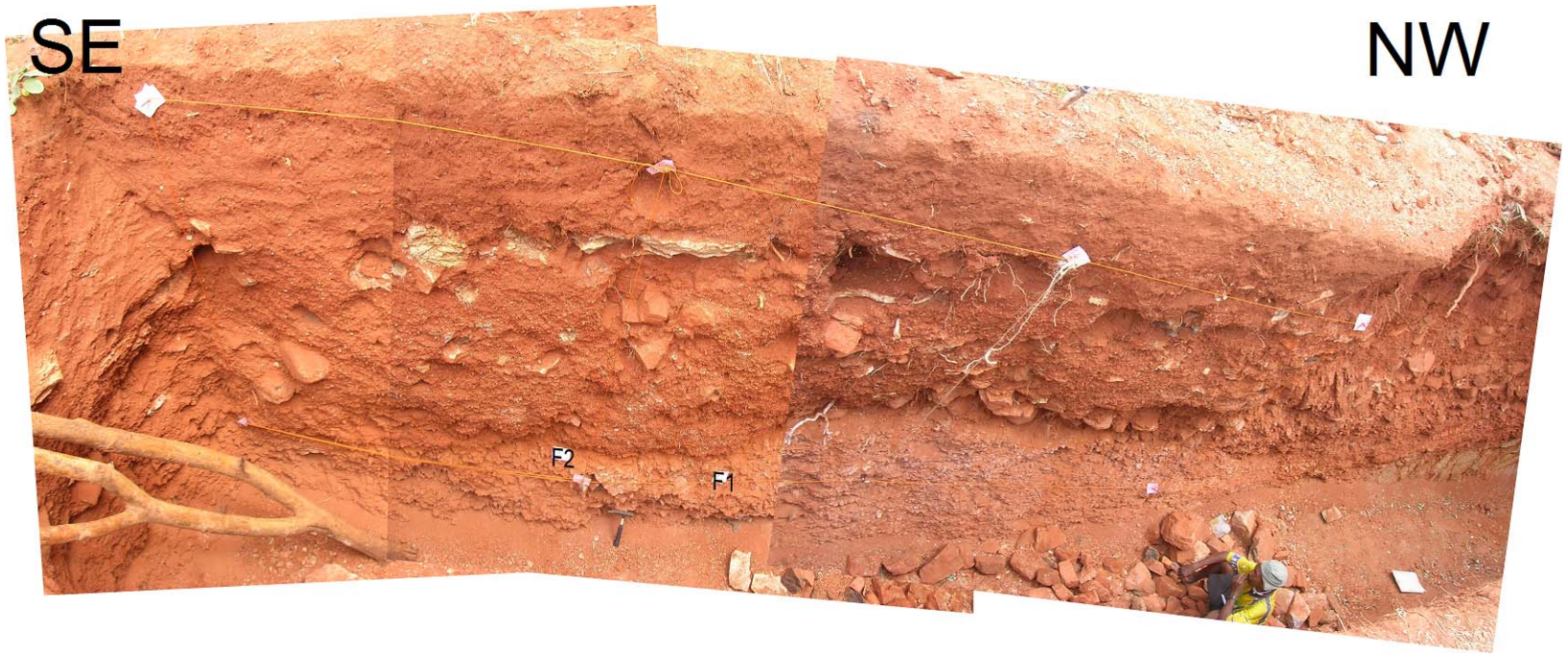

Fig. 7.5a - Photograph mosaics of the SW wall of the Magungu trench. The pictures are a little bit distorted because they were taken at different positions and at slightly different orientations. The trench is about 10 m long, 1.5 m wide and 4 m deep (Fig. 7.5b). For scale see the geological hammer at the bottom of the trench.

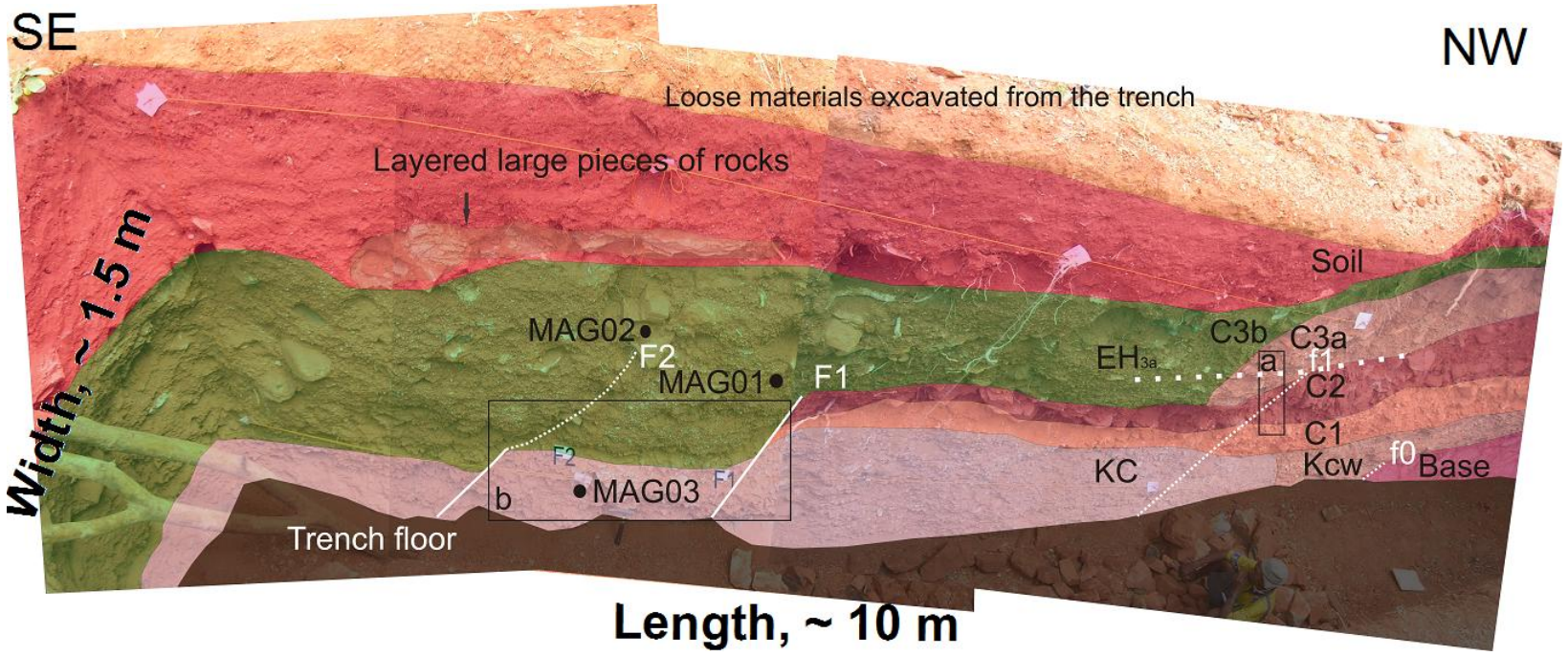

Fig. 7.5b - Photograph mosaics of the SW wall of the Magungu trench with interpretation. 'Base' = basement. Rectangle 'a' is represented by a corresponding zoom (Fig. 7.6) of the same stratigraphic unit on the opposite wall (i.e., mirrored in a vertical axis). The area defined by rectangle 'b' is magnified in Fig. 7.7. Sample points are marked as black dots and sample numbers MAG01; MAG02 and MAG03 are also shown. EH3a represents an infered event horizon at the base of unit C3a. Fig. 7.8 carries the similar information at scale. Units KC, Kcw, C1, C2, C3a and C3b are detailed in section 7.2.

7. Soil

The soil cover is characterized by reddish brown, silt/sand. It is up to 80 cm thick and covers Unit C3. It is not affected by any fault. Locally, its base is marked by a line of layered large piece of rocks (about 10 cm in diameter).

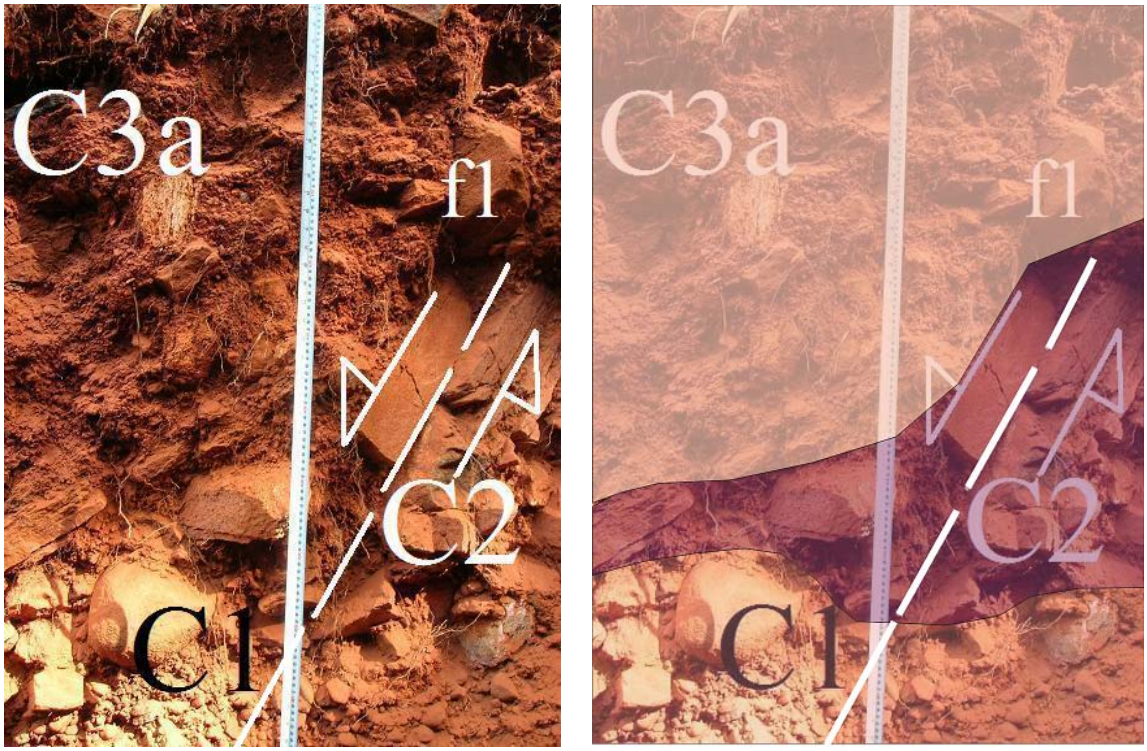

Fig. 7.6 - Normal faulting in the Magungu trench as revealed from the northeastern wall. This fault corresponds to f1 in Fig. 7.5a,b. Left: without interpretation of layers. Right: with interpretation of layers.

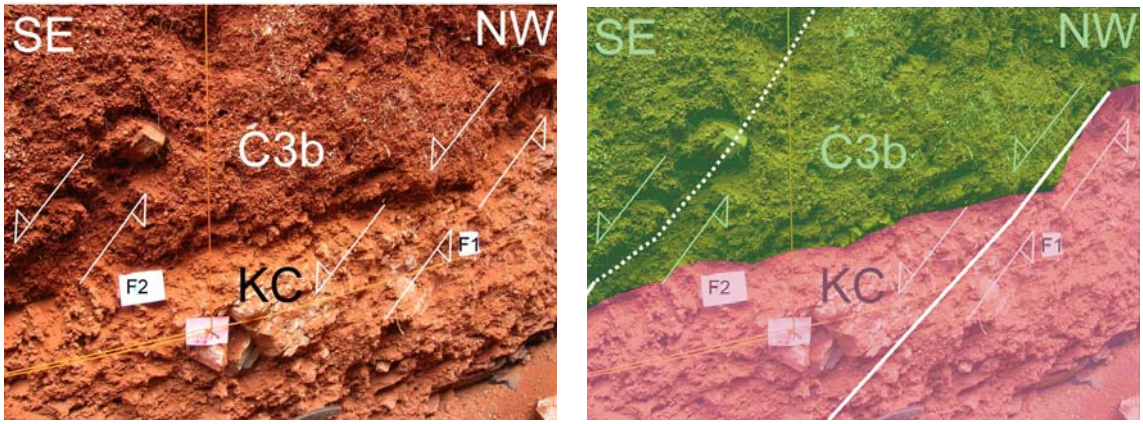

Fig. 7.7 - A zoom of the rectangle 'b' in Fig. 7.6b. In this picture, the most recent faults, F1 and F2 and their associated senses of displacement are shown. Left: without interpretation of layers. Right: with interpretation of layers. Locations of faults F1 and F2 are also shown by white lines. The dashed line part of F2 implies that part of F2 is not very certain (compare with Figs. 7.5; 7.8).

7.3. Dating samples

Several samples were taken for dating. MAG01 was taken in order to constrain the age limit of F1 and the minimum age of C3b. Similarly, MAG02 was taken in order to constrain the lower limit ages of both C3b and F2. For determination of minimum age of unit KC, MAG03 was taken.

As detailed in Chapter 4, we took three samples for ^{14}C - Accelerator Mass Spectrometry (AMS) dating and three samples for thermal luminescence (TL) dating technique. Time was not enough to analyze the samples by both techniques. We only managed to analyze the samples by ^{14}C. Due to the absence of any visible samples of charcoal, the ^{14}C dating was done on organic carbon residues. The results are presented in ^{14}C age (BP), i.e. ^{14}C age before Present (BP). The results are therefore given along with the degree of uncertainity (i.e. ± 50 years), as shown in Table 7.1. The results are also presented as calendar ages, calibrated at intervals which are equivalent to 1σ probability (~ 68 % confidence level). Both ways of presentation are shown in Fig. 7.8.

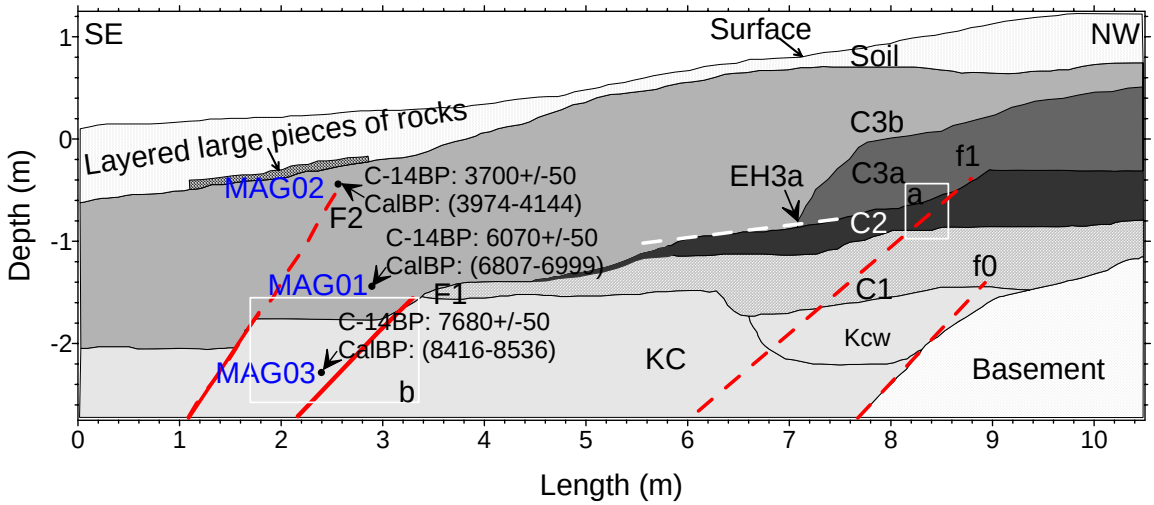

Fig. 7.8 - Interpretation of the Magungu trench (into scale) showing various deposits which are displaced in parts by normal faults, f0, f1, F1 and F2. The white rectangles 'a' and 'b' are the same as in Fig. 7.5b. We add the calibrated ^{14}C - ages of MAG01, MAG02 and MAG03 as well. The coordinates of the samples (x, y) are: MAG01 = (2.89, -1.45), MAG02 = (2.55, -0.45) and MAG03 = (2.38, -2.24); all coordinates in meters as shown in the figure. EH_{3a} represents an infered event horizon at the base of unit C3a.

Table 7.1 - ^{14}C AMS results for the Magugu trench samples at Magungu, Bubu fault.

Sample ID	Analyzed fraction	^{14}C age (BP)	Calendar age (cal BP)
MAG01	Organic carbon residure	6070 ± 50	6807-6811 6857-6999
MAG02	Organic carbon residure	3700 ± 50	3974-4094 4123-4144
MAG03	Organic carbon residure	7680 ± 50	8416-8482 8491-8518 8532-8536

7.4. Tectono-chronostratigraphy

7.4.1 Identification of paleoearthquakes

In this subsection, we interprete the faulting events based on stratigraphy, stratigraphic offsets and upward termination of faults. The oldest faulting phase, f0, seems to affect both the basement and KC, but the amount of displacement is not evident (Figs. 7.5b; 7.6; 7.8). Fault f1 affects Units C2 and C1.

The deposition of the conglomeratic unit C1 above KC is interpreted as reflecting the onset of a high energy environment as a consequence of vertical differential movement, but with a distal source. Unit C2 with angular blocks is most likely from the proximity. Emplacement of C2 on top of C1 with a sharp contact could have been triggered by an unknown faulting event not visible here. However, the disappearance of C1 and C2 immediately after F1 indicates that both units were later on eroded and deposited elsewhere outside the trench.

Unit C3a deposited on top of C2 contains finer but still angular rock fragments. In addition, the fragments in unit C3a are not as randomly deposited as the fragments from unit C2. Unit C3a truncates fault f1. We interpret C3a to be a colluvial wedge derived from a fault scarp, and hence that the base of unit C3a is the event horizon. Fault f1 is also inferred to continue downwards into KC/Kcw (Figs. 7.5b; 7.6; 7.8).

Geometric relationships show that Unit C3b was unconformably deposited on top of C3a. The texture of this unit (unsorted sub-angular gravel, pebbles and soil) indicate that it was deposited as a colluvial wedge. However, the presence of soil may indicate that C3b resided close to the surface for some time. Alternatively, the soil could have been mixed with gravel and pebbles and deposited together as one unit (C3b). Both faults F1 and F2 were active during the deposition of C3b, F1 earlier than F2. F1 is displacing the basal contact of Unit C3b in a sharp way. Termination of F1 is relatively sharp. F2 is also displacing the basal contact of Unit C3b but fades rapidly upwards (after 50 cm) (Fig. 7.5b; 7.7; 7.8). However, it is seen to affect most of the thickness of C3b. It does not displace the upper limit of C3b. This means that there is an event horizon situated between the event horizon related to F1 and the top of unit C3b.

The youngest deposit in the sequence is soil (Figs. 7.5b; 7.7; 7.8). Therefore, the whole relative age of faults and stratigraphic or lithologic units relationship can be summarized as; Basement → KC → f0→ regional easterly tilt + erosion → C1 → C2 → f1 → C3a → F1 → Erosion → C3b → F2 (+F1) → Soil.

7.4.2 Absolute tectono-chronostratigraphy

The ^{14}C-ages obtained are as follows: for Unit C3b, samples MAG01 and MAG02 were taken. MAG01, which was taken close to the bottom of Unit C3b, but just above the

horizon truncating F1, yielded an age of 6807-6999 cal. yr BP, while MAG02, from close to the summit of Unit C3b, supposedly above the event horizon related to F2, yielded an age of 3974-4144 cal. yr BP. Thus, event 3 (Table 7.2) is bracketed between MAG02 (minimum) and MAG01 (maximum), and events 2 and 1 are bracketed between MAG01 (minimum) and MAG03 (maximum).

For unit KC, sample MAG03 was taken and yielded an age of 8416-8536 cal. yr BP. Thus unit KC is much younger than it was thought before. Previously, we considered KC to be the Kilimatinde Cement, i.e. of Miocene to Early Pliocene age. Our assumption was based on the texture of the deposit, the composition of the deposit (calcrete-rich) and its relationship with the basement, i.e. it overlies the basement (e.g. Fozzard, 1961). Therefore, we then take this age interval, i.e. 8416-8536 cal. yr BP to be the minimum age of unit KC and maximum age of F1 and f1 (Table 7.2).

Table 7.2 - Age constraints of f1, F1 and F2 (from Table 7.1 and Fig. 7.8)

Faulting event	**Minimum age (cal. yr. BP)**	**Maximum age (cal. yr. BP)**
Event 3 (on splay F2)	3974 - 4144	6807 - 6999
Event 2 (on splay F1)	6807 - 6999	8416 - 8536
Event 1 (on splay f1)	6807 - 6999	8416 - 8536

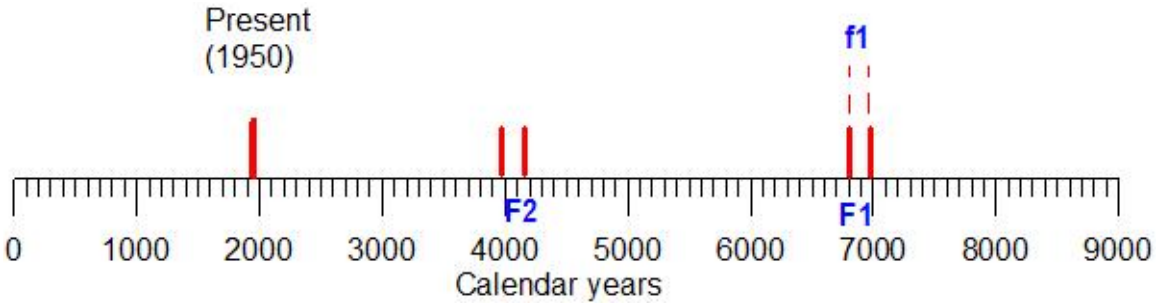

Fig. 7.9 - Calibrated ^{14}C ages BP and minimum ages of observed faulting events; Event 1 = f1 (not dated, hence shown by dotted lines), event 2 = F1 (6807-6999yr BP), event 3 = F2 (3974-4144yr BP). These are 1-sigma ranges. Considering maximum ages of the events, then event 3 (F2) occurred between 3974 and 6999 cal. yr. BP, and the other two events between 6807 and 8536 cal. yr. BP (Table 7.2).

The absolute dating does not allow separating events 1 and 2, although they appear to be stratigraphically separated. To calculate the interval between events 2 and 3, the full age brackets for both events have to be considered, yielding a minimum age of 0 yr (6807-6999), which is negative (-192 yr) and thus becomes 0, and a maximum of 4562 yr (8536-3974) (Fig. 7.9).

Using the full probability density function, instead of just the 1-sigma age values as in Fig. 7.9, we obtain 2-sigma age values as shown in Fig. 7.10. The top plot shows the calibrated ages of the three samples (i.e., MAG01, MAG02 and MAG03). The middle

plot shows the probability density functions for events 3 and 2 (and for event 1 as well, since event 1 has the same bounds as event 2). The lower plot shows the probability density function for the interval between events 3 and 2.

From Fig. 7.10 follows that the probability density function for the interval between event 3 and 2 ranges between 0 and more than 4000 yr, although the probability that it is 0 is less than that it is along the horizontal axis (time span in years).

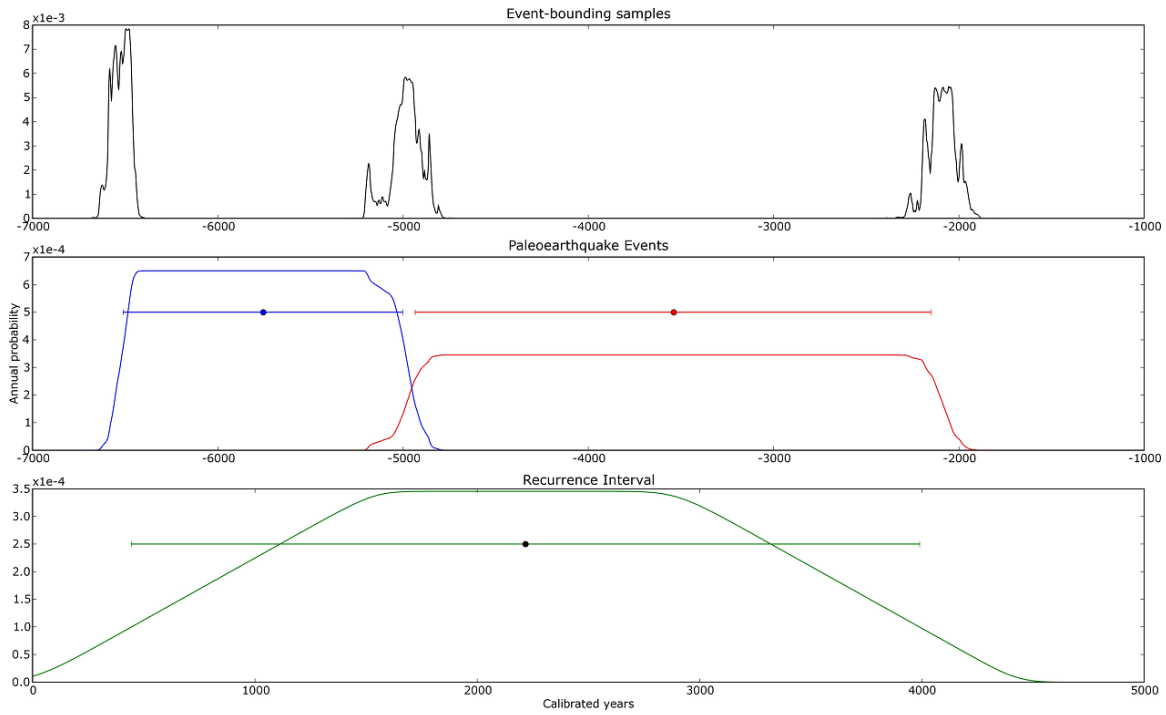

Fig. 7.10 – The 2-sigma value plots for the three samples MAG01, MAG02 and MAG03 using the full probability density function. Note that the scale for the two upper plots is absolute age (in calibrated years BP), whereas the scale for the lower plot is time span (in years).

Thus we obtain the following 2-sigma ranges:
- Event 3: -4926.9 to -2143.6 (Mean: -3539.7)
- Event 2: -6505.8 to -4998.8 (Mean: -5754.7)

In other words, the interval 1 (i.e., the range between event 3 and event 2) corresponds to the whole range from 444.6 yr to 3989.4 yr (Mean: 2216.9 yr). Thus, the recurrence interval corresponding to 2-sigma probability is 2216.9 yr.

These results also show that the most recent tectonic activity (F2) took place in the Middle Holocene (more recently than 6807-6999 cal. yr BP; Fig.7.8). This age interval also corresponds to the maximum ages of soil. It also corresponds to the minimum age of Unit C3b. The maximum age of Unit C3b corresponds to the minimum age of F1 dated at 6807-6999 cal. yr BP.

Using equation (1), discussed in section 2.5.5, the corresponding average coseismic slip rate between the two discrete events F1 and F2 is:

(35 + 30) / 2 cm / 2216.9 yr = 0.014660 cm / yr or 0.15 mm/yr.

However, this slip rate is just tentative as three age data points cannot provide a statistically sound recurrence interval (or slip rate).

7.5. Summary

The Magungu trench, located on the 42 km long Gonga segment of the Bubu fault, shows two types of faults: old faults and young faults.

Faults f0 and f1 represent older faults, with f0 being older than f1. Fault f0 affects the basement and is considered to have been reactivated several times. Fault f1 affects mainly the unconsolidated materials but its extension into the basement or older deposits such as KC is not clear. Both faults are inferred as no clear displacement parameters (such as slip lines, displacement) were found in the trench.

Faults F1 and F2 represent the younger faults. Fault F1 is much more evident than fault F2. Both faults have comparable displacements: 35 cm for fault F1 and 30 cm for fault F2. This corresponds to an average displacement of 32.5cm. The two younger faults affect much more recent deposits. Using the full probability density function, the average recurrence interval is estimated to be 2216.9 yr, giving an average coseismic slip rate of about 0.15 mm/yr.

7.6. Assessment of accuracy and limitations of used methods

The main limitations considered during logging and sampling was the fact that similar-appearing landforms can be produced by different, unrelated geomorphic processes (e.g., Chorley et al., 1984; Bolt, 1993; Solonenko, 1977a). Bolt (1993) identifies several types of pseudotectonic features that mimic fault ruptures of surfaces (case study in central Asia); (1) fissures associated with volcanic doming (and collapse), (2) linear grooves and troughs related to glaciations and ice-marginal drainage, (3) linear canyons excavated along zones of weak rock, and (4) selective erosion along fault-line scarps.

An additional limitation is imposed by the absence of clear, macroscopic charcoal samples for ^{14}C-dating. As a consequence, bulk samples of Unit C3b had to be taken and dated, with the risk for obtaining mixed ages by contamination with older carbon (reworked material) or younger carbon (leaching of soil material).

Chapter 8

Chenene Surface Fractures

8. Chenene surface fractures

In February 2004 surface fractures were reported at about 2 km east of Chenene village, 50-60 km north of Dodoma. The fractures were wide and deep enough for domestic animals to get stuck into them. The "Chenene fractures" appeared after a minor earthquake shook the area, although the exact date and magnitude of the quake responsible for these surface fractures are uncertain.

As it was not clear what the exact cause of the fractures was, they were investigated in detail during three field campaigns in February, June and November 2007. The field work involved reconnaissance work, tracing and mapping of the fractures, and trenching across some of them. In this chapter, the results of these field investigations will be presented.

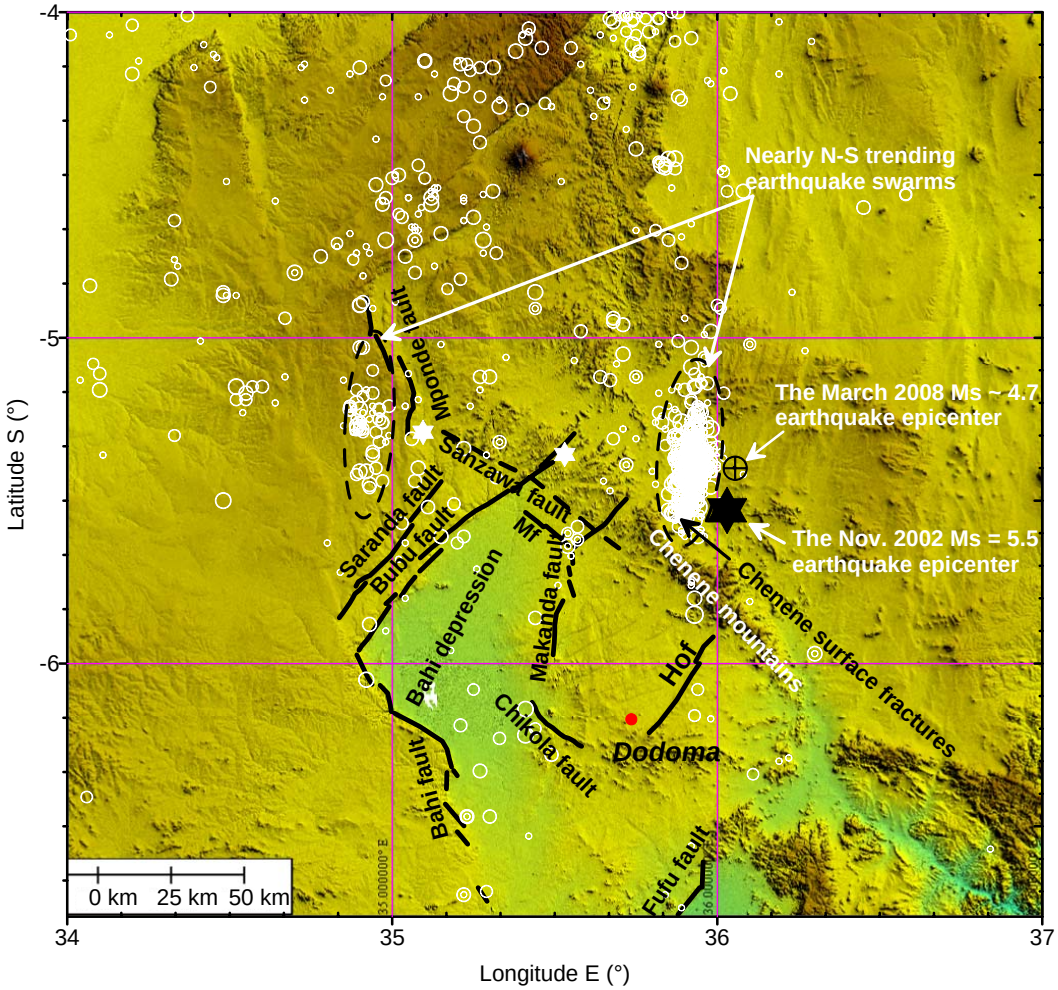

Fig. 8.1a - Location of the Chenene surface fractures in relation to the earthquake epicenters as recorded during 1994-1995 by the Tanzania Broadband Seismic Experiment. The white circles are earthquake epicentres ranging from m_b = 0.5 (smallest circles) to m_b = 5.9 (largest circles). Small white stars show locations of hot spring fields associated with the Gonga segment (Bubu fault) and the Mponde fault. Note the strong N–S clustering of the epicentres north of Dodoma as indicated by the two N-S trending eliptical regions (dashed lines). The one to the west, the Mponde fault earthquake cluster, is not dealt with here.

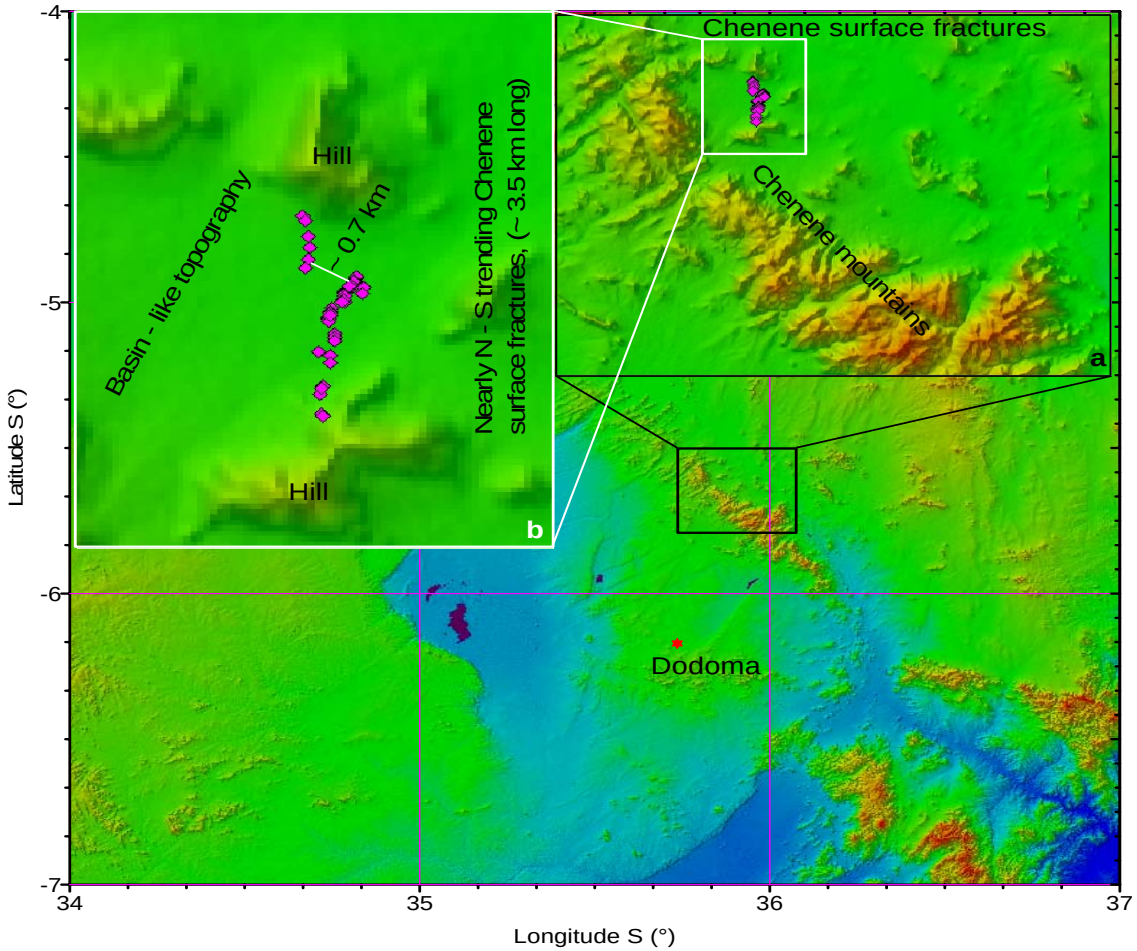

Fig. 8.1b - Surface fractures, represented by magenta cubic points, at Chenene in detail. Zoom in 'a' shows the position of the surface fractures against the NW-SE trending Chenene Mountains. Zoom in 'b' gives the details of the surface fractures in relation to the basin-like topography in which they are located.

8.1. Occurrence of surface fractures in the region

Surface fractures at Chenene village are located in a sub-planar surface that is flanked by hills to the northern, southern and southeastern parts (Fig. 8.1a,b). The hills are part of the NW-SE trending Chenene Mountains.

In plan-view, the fractures are oriented nearly N-S and occur in *en échelon* pattern. Some of the fractures occur as left-stepping fractures, while others occur as right-stepping fractures. The left-stepping fractures are more prominent than the right-stepping fractures.

The surface fractures at Chenene can be subdivided into three main parts: i.e., a northern part (Fracture set A), a middle part (Fracture set B) and a southern part (Fracture set C). The three fracture sets are about 750 m, 1030 m and 1490 m long, respectively, with a

total measured length in the order of 3.5 km. Each of these fracture sets is generally made up of even smaller fractures (Fig. 8.2).

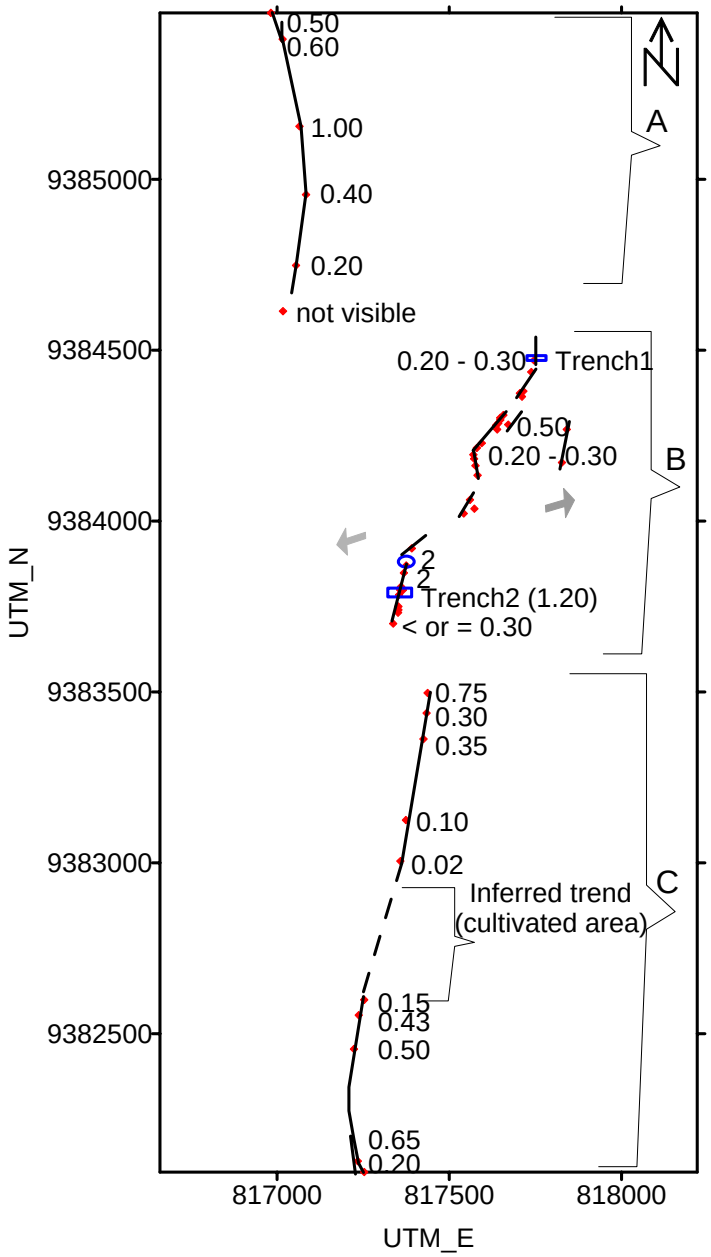

Fig. 8.2 - Plot of all Chenene fractures (about 3.5 km total rupture length). They occur as three main left-stepping sets of fractures: i.e., Fracture set A to the north (750 m long), fracture set B in the middle part (1030 m long) and fracture set C to the south (1490 m long). The general trend of the fractures is ~ N-S. The two trenches in the middle fracture set are marked by open rectangular blue boxes. A blue open sphere represents one of the widest cracks in fracture set B, where a cow fell in the fracture and died a short while after the rupture event in February 2004. Numbers refer to the horizontal displacement/width of fracture/rupture at a given point in meters. No vertical or lateral displacement was evident in the field. Thick lines represent an observed surface rupture (fault strands) whereas dotted lines are inferred surface fracture(s). Filled red boxes represent the areas visited during fieldwork. Grey thick arrows point to the current S_{hmin} direction (i.e., N082°E) as determined by Macheyeki et al. (2008b).

In plan view, fracture set A is transversely separated from fracture set B by a distance of about 700 m. Fracture set B is about 250 m from fracture set C (Fig. 8.2).

8.2. Morphology of the Chenene surface fractures

The fractures, in plan view, occur in an *en échelon* pattern, characterized by both left and right steps (Figs. 8.1a; 8.2). They occupy a zone, about 700 m wide. The fractures vary in width from a few millimeters on their tips up to over 2 m at the middle (Fig. 8.3a-e).

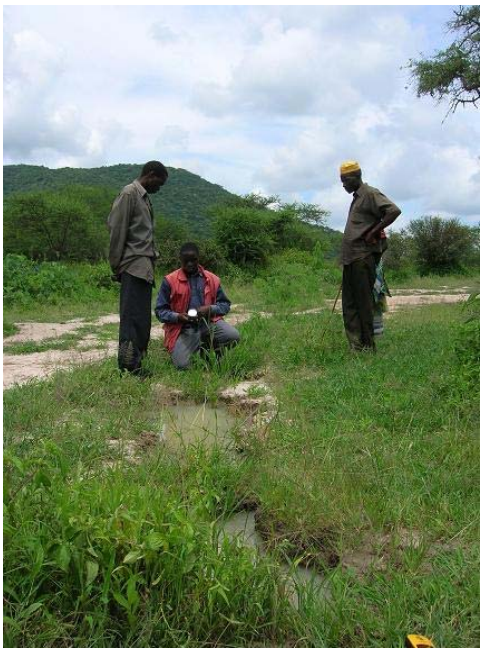
a


b


c

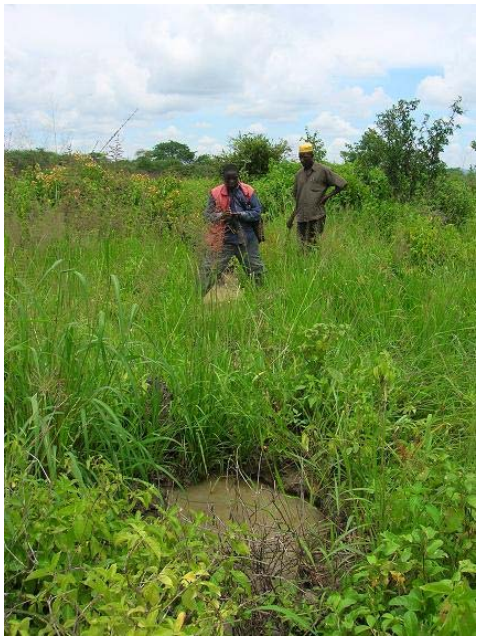

d

e

Fig. 8.3 - (a) Chenene fractures (northern part of fracture set B, about 50 m south of Trench1) as observed in February 2007. Horizontal (dilatational) movement was estimated to be 20-30 cm with no visible component of vertical offset. The hill on the background is indicated in Fig. 8.1b. Picture taken facing north (b) A relatively fresh-looking surface fracture at Chenene as observed in February 2007, about 200 m south of Trench 1. Horizontal movement was estimated to be 45-50 cm with no visible component of vertical offset. Picture taken facing north. (d) Chenene fracture (Fracture set B) as observed in May 2007. The fracture has a width of about 50 cm. Picture taken facing north. (d) A relatively fresh-looking surface fractures at Chenene as observed in February 2007, about 250 m south of Trench 1. Dilational opening was also estimated to be 20-30 cm with no visible component of vertical offset. Picture taken facing south. (e) Chenene fracture (Fracture set B) as observed in May 2007. The fracture is about 200 cm wide. This fracture is about 200 m north of Trench 2. Picture taken facing south.

8.3. Stratigraphy of surface fractures

8.3.1 Northern trench (Trench 1)

A first trench was established in fracture set B, at 05°33.7'S, 35°52'E (817997E, 9384440N, UTM36M, ARC 1960). There are two sets of fractures that occur in the trench: i) a set of relatively old (primary) and unsorted sand-filled fractures, and ii) a set of relatively young (secondary) open fractures.

8.3.1.1 Primary fractures

The old, primary fractures cut through the entire depth of trench. They are filled with loose but sorted brownish sand. The fractures are, however, discontinuous, with variable width that generally decreases downwards. For instance, on and near the surface, the fractures are > 6 cm wide, whereas at 2 m deep their width decreases to ~2 cm (Figs. 8.4; 8.7).

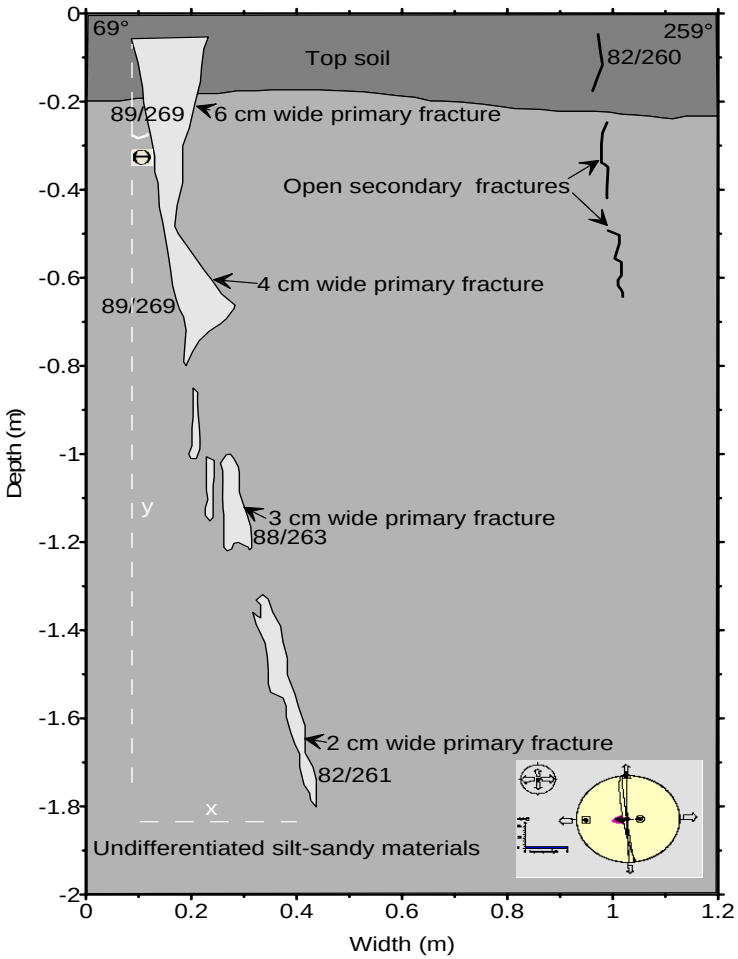

Fig. 8.4 - Trench 1 showing both primary and secondary fractures. Primary fractures are filled with sandy deposits. Both types of fractures dip to the west (compare with Fig. 8.5). Insert is a reduced stress tensor that shows both high-angle planes and extension direction.

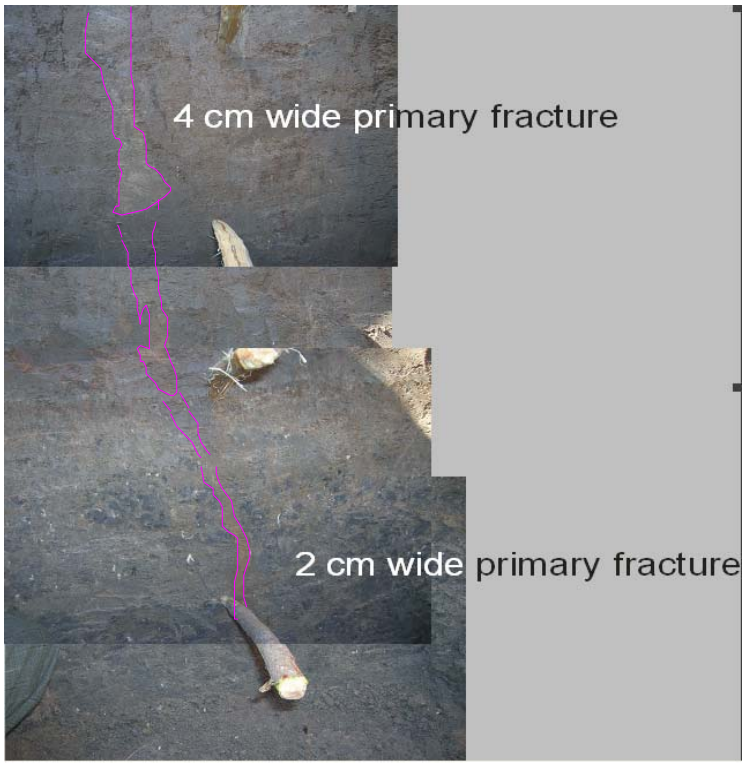

Fig. 8.5 - Secondary fractures in Trench 1 (Mosaic of pictures, compare with Fig. 8.4). The primary fractures (as traced by lines) appear as sub-vertical strips. Note the pegs hammered in the trench wall as markers. Photos taken facing the southern wall.

The dips and strikes of these fractures are not the same (Table 8.1). However, the average dip/dip direction is 80/260 (Fig. 8.4). This was obtained by first measuring the vertical height y = 1.7 m of primary fractures and the corresponding horizontal distance x = 0.3 m (Fig. 8.4). The dip angle $\Theta = \arctan(x/y) = \sim 10°$. Then from 90° - Θ, the dip is obtained. This shows that the fracture is dipping to the west and opens in a N082°E direction.

Table 8.1 - The dip / dip directions and thickness of the surface fracture near Chenene as revealed in the northern and the southern trenches.

SNo	Dip/Dip direction	Depth (cm)	Fracture type	Fracture thickness (cm)	Trench Location
1	89/269	30	Primary	6	Northern (Trench 1)
2	89/269	60		4	
3	88/263	120		3	
4	82/261	150		2	
5	82/260	30	Secondary	< 2	
6	70/091	60	Secondary	< 2	Southern (Trench 2)
7	76/295	60		< 2	

8.3.1.2 Secondary fractures

The secondary fractures tend to be much thinner than the primary ones, with uniform thickness, which is generally < 2 cm. A large number of secondary fractures is restricted to the uppermost part of the trench, ca. the first 1 m.

8.3.2 Southern trench (Trench 2)

The second trench was also established in fracture set B, at 05°34.1'S, 35°51.9'E (817439E, 9383779N). Like in the northern trench, there are also two sets of fractures: i) primary and ii) secondary fractures. However, there is only one primary fracture in the trench that is filled by soil and other superficial materials. The trench exposed two types of deposits: i.e., silt-sandy material (layered but significantly contorted) at the bottom and clayey soil material on top (Fig. 8.6a). A much closer view of these fractures is provided in Fig. 8.6b.

8.3.2.1 Primary fractures

The primary fracture is as wide as 1 m. It is filled by, from top to bottom, sand soil (50 cm), relatively thin alternating dark-whitish silt soil and alternating dark soil that assumes layers that are deformed (Fig. 8.6a,b). Presence of deformed superficial materials implies that deposition took place relatively abruptly and in wet conditions.

8.3.2.2 Secondary fractures

Secondary fractures roughly occur as sigmoid, *en échelon* joints on either end of the primary fracture (Figs. 8.6a,b; 8.7). Like in the northern trench, these fractures are open and fade away at depth.

Fig. 8.6a - Primary and secondary fractures in Trench 2.
Photo taken facing southern wall.

Fig. 8.6b - Zoom of Figure 8.6a. The *en échelon* pattern of secondary fractures clearly demarcates the margin of the primary fracture (the equivalent figure is Fig. 8.7). Note the contorted layers within the primary fracture in this photograph and Fig. 8.6a.

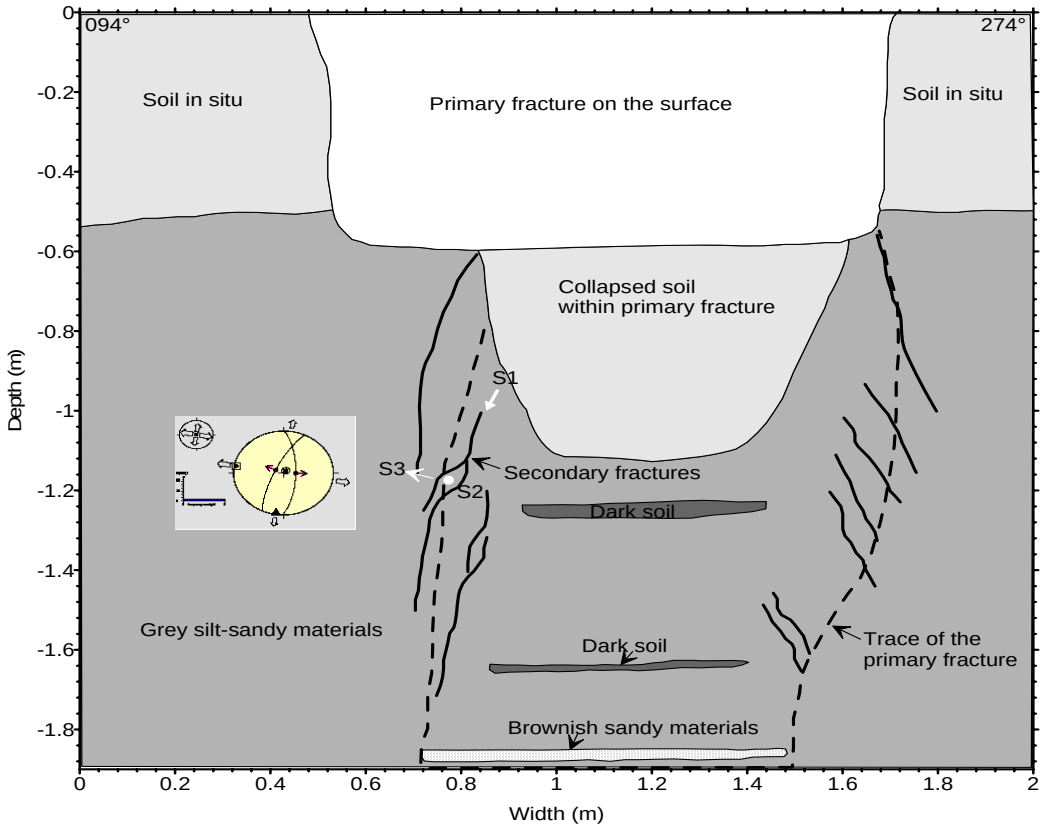

Fig. 8.7 - Primary and secondary fractures in Trench 2. The primary fracture is filled by soil and other superficial materials (Fig. 8.6a,b). Secondary fractures are open. S1 = σ_1 = maximum principal stress; S2 = σ_2 = intermediate principal stress; S3 = σ_3 = minimum principal stress.

As can be observed in Table 8.1, only the dip and dip direction of the primary and secondary fractures could be documented in the northern trench, whereas in the southern trench only dip and dip direction of secondary fractures were observed. Data show that the primary fractures dip westerly towards the northern end of the fractured zone (as revealed in Trench 1), whereas towards the south it was not clear whether the primary fractures also dip westerly or not. Secondary fractures clearly show both westerly and easterly dip directions in either trench. The amount of dip increases towards the surface for both types of fractures: i.e., they tend to be subvertical at or near the surface.

8.4. Displacement parameters

The following displacement parameters are indicated in Table 8.2: horizontal displacement (or dilational opening), elevation or altitude versus distance along the fracture, etc. The corresponding plots are presented in Figs. 8.8; 8.9; 8.10.

Table 8.2 - Displacement parameters. nd = no data; Alt = altitude; Δh = width of crack/fracture; R.Elv = relative elevation; L = distance and FR = Fracture set.

Point ID	UTME	UTMN	E (°)	E (min)	N (°)	N (min)	Alt (m)	Δh (cm)	R.Elv (m)	L (m)	FR
p10	817253	9382095	35	51.8490	-5	35.1534	1220	20	70	0	C
p9	817234	9382127	35	51.8376	-5	35.1366	1211	65	61	37	C
p8	817223	9382455	35	51.8316	-5	34.9614	1195	50	45	361	C
p7	817237	9382554	35	51.8394	-5	34.9074	1205	43	55	459	C
p6	817253	9382599	35	51.8472	-5	34.8828	1192	15	42	504	C
p5	817358	9383005	35	51.9024	-5	34.6596	1182	1	32	916	C
p4	817374	9383125	35	51.9107	-5	34.5961	1174	8	24	1037	C
wpt106	817206	9383174	35	51.7722	-5	34.4394	1165	0	15	1080	C
p3	817425	9383362	35	51.9336	-5	34.4616	1183	35	33	1279	C
p2	817434	9383438	35	51.9432	-5	34.4250	1182	3	32	1355	C
p1	817437	9383497	35	51.9432	-5	34.3944	1176	75	26	1414	C
wpt134	817337	9383700	35	51.8418	-5	34.1544	1166		16	1607	B
wpt133	817351	9383732	35	51.8490	-5	34.1370	1168		18	1640	B
wpt132	817352	9383740	35	51.8502	-5	34.1316	1169		19	1648	B
wpt131	817352	9383750	35	51.8496	-5	34.1262	1168		18	1658	B
wpt130	817354	9383784	35	51.8508	-5	34.1082	1165		15	1692	B
wpt138	817358	9383798	35	51.8532	-5	34.1004	1166		16	1706	B
wpt140	817365	9383798	35	51.8568	-5	34.1004	1170		20	1707	B
wpt139	817358	9383799	35	51.8532	-5	34.1004	1166	120	16	1707	B
wpt129	817360	9383808	35	51.8538	-5	34.0956	1167	200	17	1716	B
wpt128	817368	9383848	35	51.8586	-5	34.0728	1166		16	1757	B
wpt127	817375	9383870	35	51.8616	-5	34.0620	1163	200	13	1779	B
wpt126	817391	9383920	35	51.8706	-5	34.0344	1167		17	1830	B
wpt105	817542	9384022	35	51.9516	-5	33.9786	1159		9	1949	B

wpt103	817573	9384036	35	51.9690	-5	33.9438	1158		8	1967	B
wpt104	817560	9384062	35	51.9618	-5	33.9576	1157		7	1991	B
wpt102	817582	9384134	35	51.9738	-5	33.9174	1156		6	2065	B
wpt101	817576	9384162	35	51.9702	-5	33.9030	1158		8	2092	B
wpt100	817572	9384182	35	51.9678	-5	33.8922	1159	25	9	2111	B
wpt99	817570	9384194	35	51.9666	-5	33.8856	1159		9	2123	B
wpt98	817580	9384214	35	51.9720	-5	33.8742	1157		7	2144	B
p_2	817827	9384171	35	52.1533	-5	34.0280	1169	10	19	2154	B
wpt97	817594	9384228	35	51.9798	-5	33.8670	1159	50	9	2160	B
wpt124	817639	9384268	35	52.0056	-5	33.8448	1167	50	17	2207	B
wpt123	817636	9384280	35	52.0026	-5	33.8382	1163		13	2218	B
wpt125	817642	9384286	35	52.0056	-5	33.8358	1162	50	12	2225	B
wpt96	817671	9384282	35	52.0212	-5	33.8376	1161		11	2227	B
wpt122	817648	9384296	35	52.0086	-5	33.8304	1162		12	2236	B
wpt121	817648	9384302	35	52.0098	-5	33.8268	1164		14	2242	B
p_1	817841	9384268	35	52.1605	-5	33.9760	1170	3	20	2251	B
wpt120	817657	9384310	35	52.0134	-5	33.8226	1165		15	2252	B
wpt95	817711	9384364	35	52.0428	-5	33.7926	1159		9	2315	B
wpt119	817705	9384374	35	52.0392	-5	33.7878	1165		15	2323	B
wpt118	817715	9384380	35	52.0446	-5	33.7842	1174		24	2331	B
wpt94	817738	9384436	35	52.0572	-5	33.7542	1157		7	2391	B
wpt117	817746	9384470	35	52.0614	-5	33.7350	1160	25	10	2426	B
p19	817017	9384614	35	51.7128	-5	33.7914	1172	0	22	2530	A
p18	817055	9384748	35	51.7356	-5	33.7182	1174	20	24	2660	A
p17	817084	9384955	35	51.7494	-5	33.6048	1184	40	34	2865	A
p16	817065	9385155	35	51.7356	-5	33.4896	1196	100	46	3066	A
p15	817016	9385410	35	51.7128	-5	33.3570	1211	60	61	3323	A
p14	816982	9385487	35	51.6918	-5	33.3162	1239	50	89	3403	A

The plot of horizontal (dilational) displacement versus distance along the fractured zone, (measured from south; fracture set C) shows that maximum opening occurs in the middle part (Fig. 8.8). There exists an inverse relationship between elevation versus distance along the fractured zone (measured from south; fracture set C; Fig. 8.9). The relationship between the two plots can be seen more closely when both plots are put together as in Fig. 8.10.

8.5. Discussion

The newly formed, N-S trending isolated faults (or fractures), found at Chenene village, just north of NW-SE trending Chenene Mountains display variable dilational openings that attain maximum values towards the center of the deformed zone (up to 2 m) and minimum values at the tips, few cm (Fig. 8.8). The current direction of extension in the region (i.e., the current S_{hmin}) is interpreted to be nearly E-W (N080°E) (Macheyeki et al., 2008b). No vertical or lateral offsets were recognized in the field. These results would

imply that these features are actually not faults but fractures. Hereafter, the three possibilities are discussed.

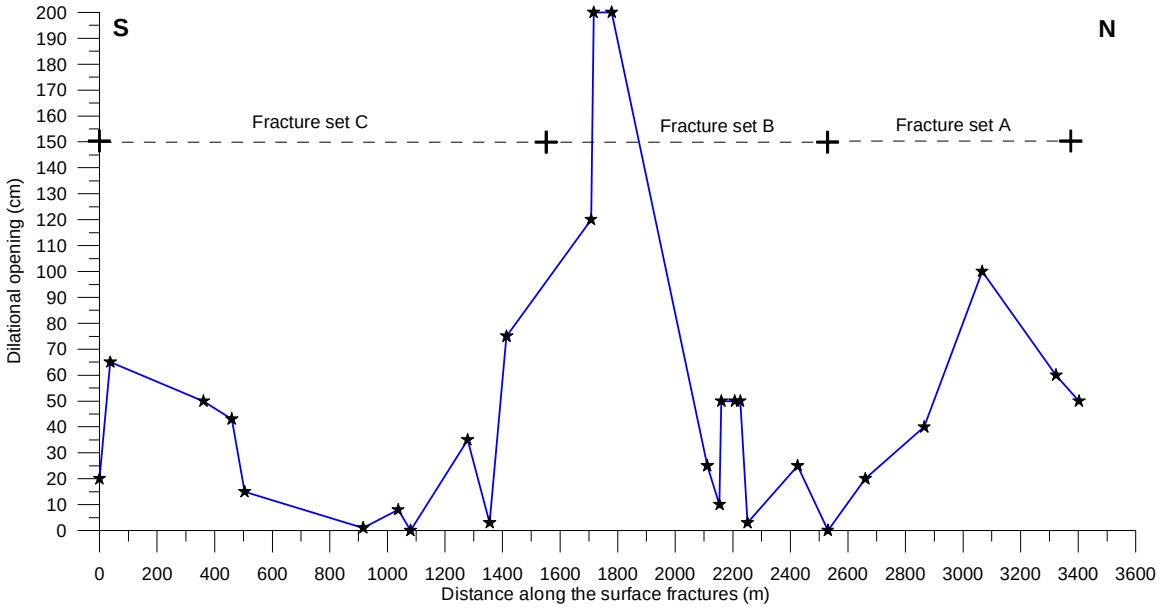

Fig. 8.8 - Plot of horizontal (dilatational) displacement (cm) versus distance along the fractured zone (m), measured from south (Fracture set C). Maximum horizontal displacement occurs on the middle part (Fracture set B).

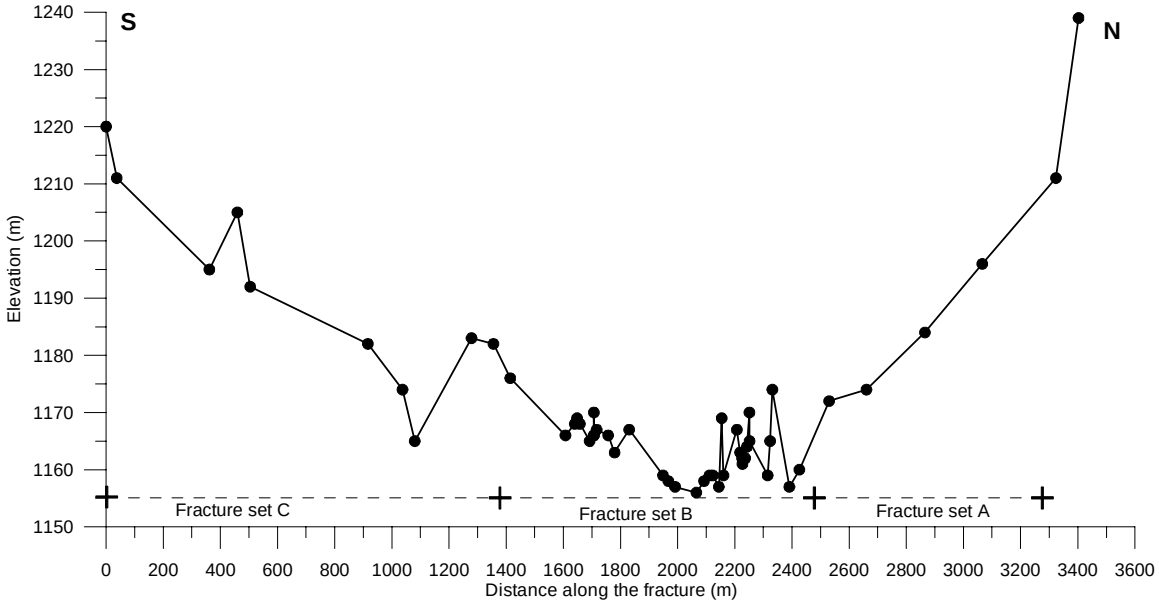

Fig. 8.9 - Plot of Elevation (m) versus distance along the Chenene fractured zone (m), measured from south (Fracture set C). The plot shows that fracture set B is located within sub-basin topography.

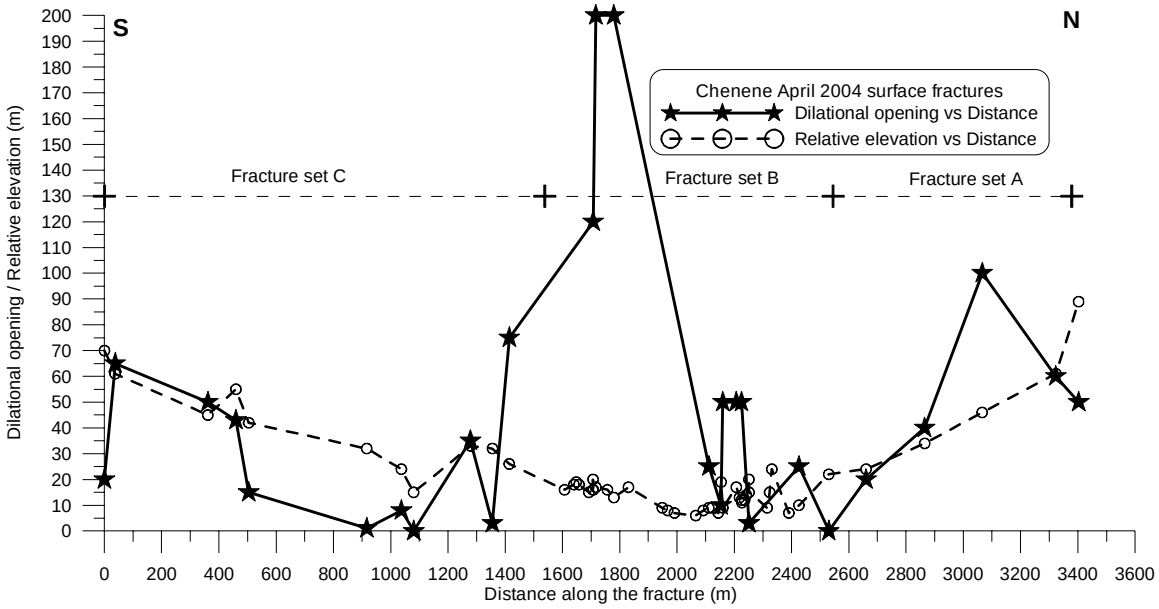

Fig. 8.10 - Plot of both horizontal and relative elevation (m) versus distance along the Chenene surface fractures (m). Please not the inverse relationship between elevation and dilational opening.

1. Surface fractures near Chenene village highlight an interesting phenomenon. They were reported to have occurred in February 2004 following a relatively weak earthquake. That earthquake is not recorded in the international catalogues, which means that its magnitude was $M_w \leq 4.5$ (e.g., Wells and Coppersmith, 1994). However, such a relatively weak earthquake is not likely to cause any surface rupture (Wells and Coppersmith, 1994; McCalpin, 1996; Keller and Pinter, 2002; Piccardi, 2005). Under normal circumstances, surface ruptures occur only with earthquakes of magnitude $M_w \geq 5\text{-}6$ (Wells and Coppersmith, 1994; Keller and Pinter 2002). It is therefore possible that these surface fractures were instead –in part, or totally– associated with the shallow-seated, $M_w = 5.5$ earthquake of 4 November 2002, reported in Macheyeki et al. (2008a; 2008b). The epicenter of this earthquake was within 25 km east of the Chenene surface fractures (Fig. 8.1a). The fractures may not have reached the surface in 2002, but the deformation may have been brought to the surface during a series of successive, relatively weak earthquakes (including tectonic ones, i.e. deeper than 10 km). Two factors could have facilitated this. Firstly, the direction of extension of the fractures is oriented according to the current extensional stress field, i.e. nearly E-W (e.g. Macheyeki et al., 2008b). Secondly, the fractures occur within old, weak zones; thus their formation requires relatively small extensional stresses (e.g., Angelier, 1989).

2. An alternative hypothesis is that these surface fractures were caused by dike injection from a magma reservoir along self-generated fractures at depth (e.g., McCalpin, 1996). In this case, the Chenene village surface fractures could be reflecting the southernmost part of a relatively large dike that continues further north of this area in a N-S trend, as defined by the relatively narrow N-S seismicity pattern (Fig. 8.2a,b; Macheyeki et al., 2008b). The opening of the fractures, if magma-driven, would thus

have been largely aseismic. This could also explain why their formation does not appear to be related to an important seismic event.

3. A third possibility would be liquefaction of a deposit in the subsurface due to seismic shaking. In favourable conditions, liquefaction can occur at relatively low magnitudes ($M < 5.0$). Liquefaction can result in sand dikes and sand volcanoes, but also in lateral spreading (e.g., Vanneste et al., 1999).

Similar surface fractures have been reported elsewhere in Tanzania by the Ministry of Energy and Minerals (e.g. in the 10 pages internal report of January 1993 on *Preliminary report on the assessment of the reported fault in the lakes Manyara-Natron area*). The authors conclude that the fractures, which they refer to as "cracks", could have been the rejuvenation of a pre-existing fault within the Gregory Rift Valley. They further state that "…similar phenomena have occurred in Kahama in 1983 and Nzega in 1990".

Chapter 9

Discussion

9. Discussion

9.1. Tectonic activity in the Dodoma area

This work has documented and demonstrated that the Dodoma area is tectonically active. The main evidences are i) the occurrence of earthquake swarms, ii) thermal springs, iii) neotectonic fault scarps, iv) displaced middle Holocene layers in a paleoseismic trench, and v) open tension cracks in a cultivated field.

Rift-related tectonic activity of this area can be traced back as far as Late-Miocene (~12-10 Ma), at the time when rifting reached and started to affect the Tanzanian craton from the northern part of the eastern branch (e.g., Ebinger, 1989b; Nyblade and Brazier, 2002).

Regionally, the Dodoma area and the surroundings, from about 80 km south of Dodoma to the North Tanzania Divergence, accounting for an area of about ≥ 250 km x 400 km (defining the Manyara-Dodoma rift segment), are participating in rifting as a single unit (Macheyeki et al., 2008b). Most volcanoes of the Manyara-Dodoma rift segment lie at the intersection of N-S to NNW-SSE and NE-SW trending faults. The Late-Pleistocene Hanang volcano lies at the intersection of the ~ N-S trending Manyara rift border fault and the NE-SW trending Balangida North fault. Similarly, the Ngorongoro volcano is located between the NE-SW trending Eyasi bordering fault and the ~ N-S trending Manyara bordering fault.

Although the location of these volcanoes demonstrate that there is a clear structural control, the rigidity of the thick Archean Tanzanian craton, characterized by a 170-250 km-thick lithospheric keel (e.g., Nyblade and Brazier, 2002; Weeraratne et al., 2003), seems to limit their extent in the interior of the craton, since Cenozoic times. This accounts for the absence of such volcanoes in the Dodoma area.

The presence of thermal springs, thought to originate from deep sources (James, 1957; 1958; 1967a; Harris, 1958; 1959; Walker, 1967), suggests that even the Dodoma area is tectonically active. The presence of strong seismicity as well as active faults in the Dodoma region (Macheyeki et al., 2008b) shows that the area is not only tectonically but also seismically active. Preliminary trenching investigations along the Bubu fault evidences signs of mid-Holocene paleoseismic activity. The thermal springs are generally located in the hanging wall of the active faults (Figs. 3.12; 5.19), which trend NE-SW, NW-SE and NNW-SSE to N-S. Regionally, these thermal springs seem to be aligned in a ~ N-S direction, in the alignment of the Hanang and Ngorongoro volcanoes. Such a pattern could imply that the locus of active deformation is along a N-S trend and could explain why focal-mechanism data coupled with fault-slip data indicate a nearly E-W extension of the Manyara-Dodoma rift segment. In addition, south of the Manyara-

Dodoma rift segment (within the Dodoma area), especially due north from the Chenene mountains, epicentres defined by the 1994-1995 Tanzania Broadband Seismic Experiment Project (Nyblade et al., 1996) reveal two clear N-S trends: (a) along the bordering N-S trending Mponde fault, and (b) just north of the antithetic NE-trending Hombolo fault (Fig. 8.1a,b). All these evidences indicate that the Manyara-Dodoma rift segment area is currently opening in an E-W direction and that it is seismically active.

9.2. Tectonic evolution of the Dodoma area

Based on the results obtained, the evolution of the Dodoma area in both regional and local tectonic framework can be summarized as follows (Table 9.1).

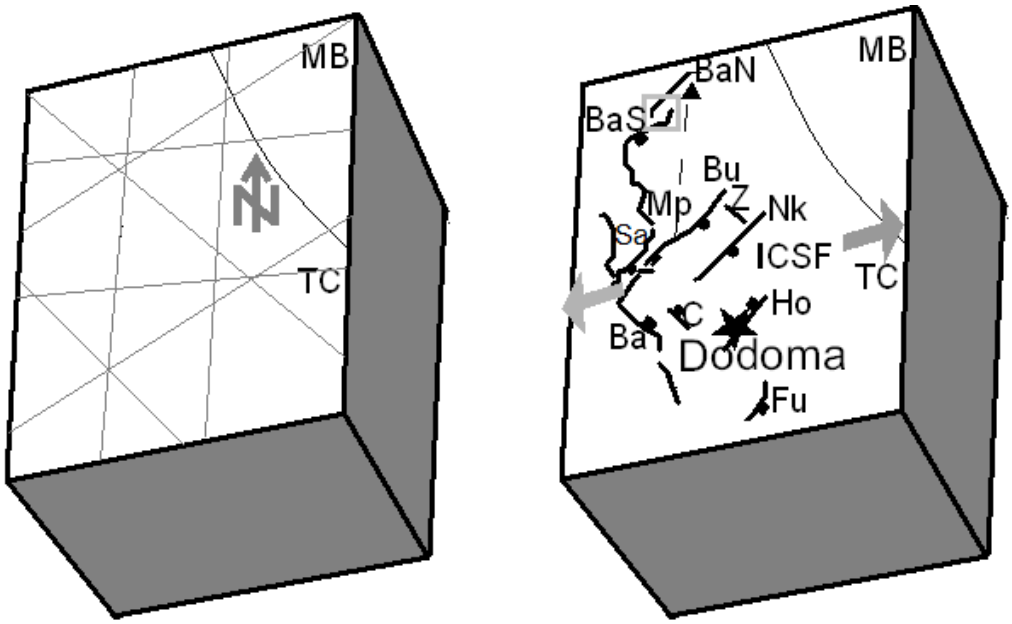

Fig. 9.1 - Cartoon of the Tanzanian craton. Left: before 12-10 Ma. The grey straight lines in various directions represent various structural directions of weakness. Right: the Dodoma area, after 12-10 Ma. The Hombolo (Ho), Nkambala (Nk); Bubu (Bu), Saranda (Sa), Balangida south and north (BaN and BaS), Fufu (Fu), Maziwa (Z), Chikola (C), Bahi (Ba) and Mponde (Mp) normal faults were formed. The grey arrows show the current direction of extension. The grey box represents a Stage 3 to 4 relay ramp (see also Section 2.2.4; Fig. 2.14) between the Balangida south and north around the Hanang volcano. The dashed lines represent N-S alignment of the thermal springs. Note that the faults trending in a N-S direction are very irregular, most likely due to the fact that new fault segments are still in their early stages of growth and interactions in a current ~ E-W extension direction by exploiting existing zones of weakness (e.g., Shudofsky, 1985). CSF = Chenene surface fractures, which trend nearly N-S. The curved dark grey line represents the boundary between the Tanzanian craton and the diffuse zone between the craton and mobile belts (MB).

Rifting started after volcanism. Oldest volcanism (45-36 Ma) is reported on the eastern branch of the EARS (e.g., Foster and Jackson, 1998; Ghebreab, 1998; Ebinger et al., 1993; Nyblade and Brazier, 2002). By Mid-Miocene (13-12 Ma), volcanism was initiated on the

western branch (Ebinger, 1989b; Foster and Jackson, 1998; Kampunzu et al., 1998; Table 9.1). In Tanzania, volcanism continues north of the country (Oldoinyo Lengai). The processes of volcanism seem to have continued southwards with time, every time followed by rifting (Ebinger et al., 1993).

Rifting started during the Early Oligocene (33-30 Ma) (Zeyen et al., 1997) in the eastern branch (Lake Turkana) (Table 9.1). By 12-10 Ma, the rifting reached the northern part of the Tanzanian craton (e.g., Nyblade and Brazier, 2002; Weeraratne et al., 2003; Vogt et al., 2006) whereby it failed to penetrate the craton by spreading into eastern and western branches. Note that the Tanzanian craton already contained Precambrian structures trending in various directions (N-S, E-W, NE-SW, and NW-SE), as shown in the cartoon (Fig. 9.1). Rifting has continued since 12-10 Ma to date. However, two main rift phases have been documented (e.g., Dawson, 1992): i.e., a 12-10 Ma rifting stage, characterized by normal faulting followed by volcanism, and a 1.3-1.2 and 0.9 Ma rifting stage, also characterized by normal faulting but with relatively minor but predominantly explosive volcanic activity, involving nephelinite, phonolite and carbonatite (Table 9.1).

Table 9.1 - Summary of current and paleo-tectono-chronology of the East African Rift, with emphasis on the Dodoma area.

Time	Event(s)	Reference(s)
Mid-Late Eocene (~ 45-36 Ma)	Volcanism initiation on the eastern branch	(Foster and Jackson, 1998; Ghebreab, 1998)
Early-Oligocene (33-30 Ma)	Rift development around Lake Turkana	Zeyen et al. (1997)
Late-Oligocene (~ 25 Ma)	Opening of the Nubian-Arabian plates by faulting	(Ghebreab, 1998)
Mid-Miocene (~ 13-12 Ma)	Volcanism initiation in the western branch	(Ebinger, 1989b; Foster and Jackson, 1998; Kampunzu et al., 1998)
Late-Miocene (~ 12- 10 Ma)	Southern rift propagation that reached the Tanzanian craton where it tried to escape it by spreading into eastern and western branches. Note that the Tanzanian craton had already Precambrian structures trending in various directions (N-S, E-W, NE-SW, and NW-SE) as shown in Fig. 9.1.	(Nyblade and Brazier, 2002; Weeraratne et al., 2003; Vogt et al., 2006)
Late-Miocene (~ 8.1 Ma)	First-stage rifting; followed by volcanism Wide tectonic depressions developed and large amounts of basic magma formed large shield volcanoes	(Dawson, 1992)
Late-Pliocene	A last episode of pronounced graben	(Dawson, 1992)

to Early-Pleistocene (??)	faulting and associated uplift of the graben flanks	
Mid-Late Pleistocene (~ 1.3-1.2 and 0.9 Ma)	Second-rifting stage; a small-scale rifting stage but an extensive one Appearance of silicic caldera volcanoes	(Fairhead et al., 1972; MacIntyre et al., 1974)
Late-Pleistocene (~ < 1.3-1.2 Ma)	Volcanism (relatively minor) characterized by explosive nephelinites (e.g. the Hanang volcano), phonolite and carbonatite within the rift basin	(Fairhead et al., 1972; MacIntyre et al., 1974 ; Corti et al., 2003 ; Macheyeki et al., 2008b)
Today	Volcanism continues north of the Dodoma area (Oldoinyo Lengai) About N080°E stress field dominates Entire Dodoma area seismically active; characterized by ~ N-S trending earthquake swarms in places such as north of Chenene and west of the Mponde fault, Focal-mechanism solutions, essentially normal Faulting continuous to exploit the existing zones of weakness on the Tanzanian craton; see cartoon (Fig. 9.1). Scarp heights increase northerly.	

9.3. Rifting the cratonic lithosphere along the Tanzanian craton margin

As shown in Chapter 3, the eastern branch of the EARS in South Kenya and Central Tanzania generally follows the diffuse contact between the Tanzanian craton and the Neoproterozoic Mozambique belt (which itself remobilizes the Paleoproterozoic Usagaran belt). It has also been shown that the Manyara-Dodoma rift segment in Central Tanzania does not follow a straight N-S line as idealized in Fig. 9.2, but rather is composed of a jagged system of major (border) faults of different orientations (e.g., Fig. 9.1). In particular, the NE-SW trend is represented by the Eyasi rift faults, the Balangida faults, the Saranda-Bubu faults, and the Dodoma faults (Macheyeki et al., 2008b). The southwestern extremities of all these fault systems are directed towards the centre of the Tanzanian craton. They appear to reactivate pre-existing structures (of possible late Pan-African age) that mark the marginal zone of the Tanzanian craton at its contact with the Mozambique belt. These seem to mark attempts of rifting penetrating into the Tanzanian craton, benefiting from the presence of older zones of weaknesses. However, as these rift faults reached the intact core of the Tanzanian craton, they did not succeed to progress

further and rifting failed. The Eyasi rift branch is the best known example of such a failed rift (Ebinger et al., 1997), but also the Speke and Winam Gulfs along the eastern side of Lake Victoria (Rach and Rosendahl, 1989).

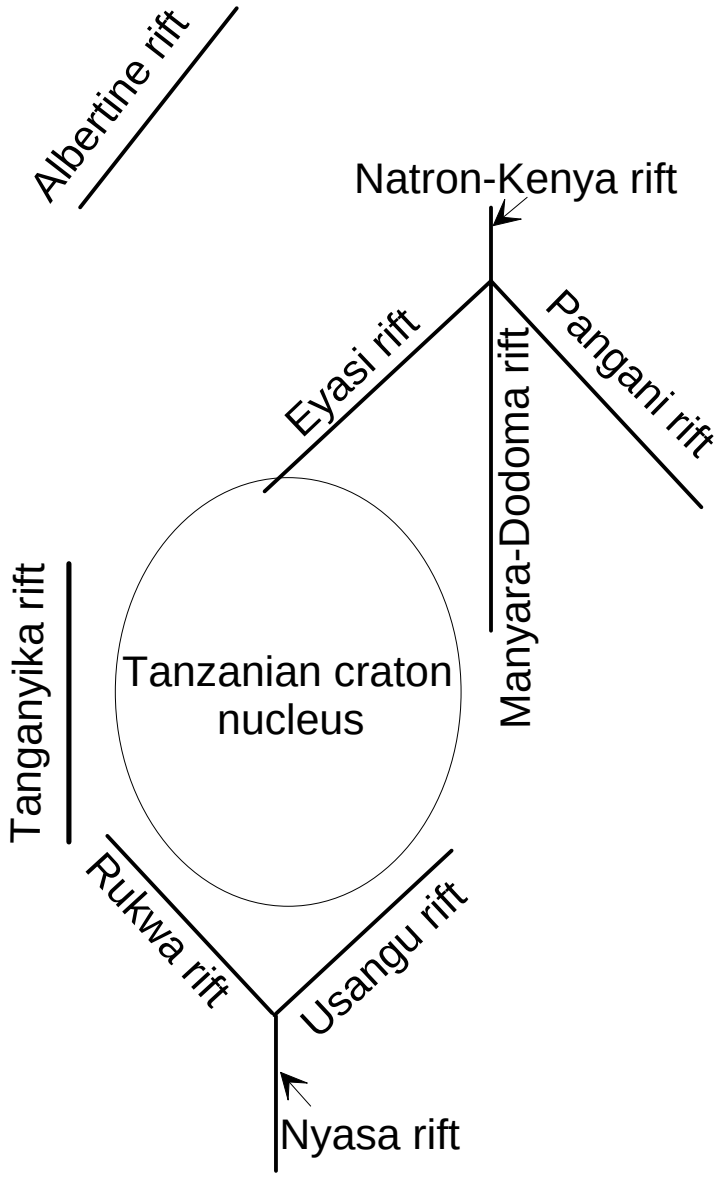

Fig. 9.2 - Simplified conceptual model for the EARS in and across the Tanzanian craton nucleus in relation to the Rukwa-Nyasa-Usangu rifts, the Eyasi-Natron (Natron-Kenya)-Pangani rifts, the Tanganyika rift, Albertine rift and the Manyara-Dodoma rift. This figure demonstrates that the rigidity of Tanzanian craton increases towards its nucleus.

This confirms the view of Ebinger et al. (1997) that the Archean Tanzanian craton is mechanically stronger than the Neoproterozoic lithosphere and has still a deep cratonic root despite the possible presence of a mantle plume underneath. Strictly speaking, the Tanzanian craton can be defined as restricted to the Archean crust. However, poor geochronological constraints during the initial periods of geological mapping led to the

confusion of the Archean crust with its surrounding Proterozoic crystalline rim. When considered together, they form a cratonic crust of a larger extent than the deeply rooted Archean craton. It seems that it is only the cratonic margins that can be deformed (e.g., Ebinger, 1989a; Nyblade and Brazier, 2002; Weeraratne et al., 2003); thus the stability and rigidity of the craton increases towards its nucleus (Fig. 9.2), most likely located at the centre. The nucleus of the Tanzanian craton is much thicker, with a lithospheric keel reaching 170-250 km (e.g., Nyblade and Brazier, 2002); the crust and upper part of the mantle being brittle and the other part of the upper mantle being ductile (Fig. 9.3). Precambrian structures within the craton (e.g., Fairhead and Stuart, 1982; Lenoir et al., 1994; Theunissen et al., 1996) and outside the craton (e.g., Ebinger, 1989a; 1989b) are causing the formation of zones of structural weaknesses of various orientations (e.g., Macheyeki et al., 2008b).

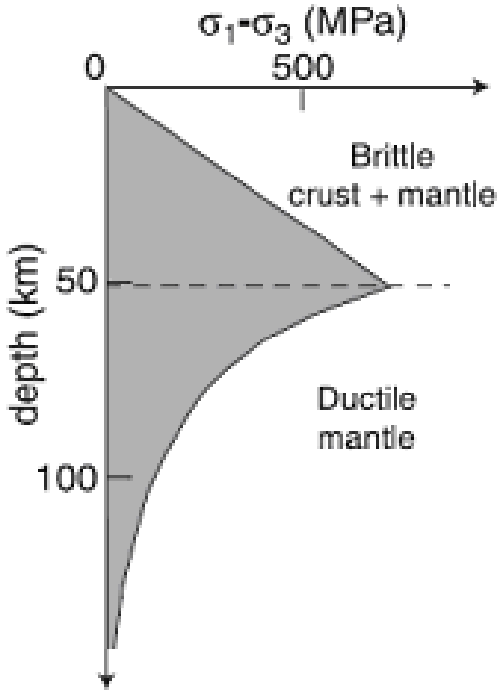

Fig. 9.3 - Examples of strength profiles for an old stable two-layer lithosphere (Brun, 1999), similar to that of the Tanzanian craton.

9.4. Stress transmission and rift propagation

A large mantle plume seems to rise below the Tanzanian craton lithosphere (e.g., Ebinger et al., 1993; Tesha et al., 1997; Zeyen et al., 1997), elevating its surface to an altitude of ~ 1000 m high and generating extensional stresses due to gravity spreading. Compressional far-field stresses generated at plate boundaries, mainly by the Indian and Antlantic ridges (Heidbach et al., 2007) and from South Africa (Chapola, 2005), tend to counter-balance the opening due to the underlying mantle plume. These two types of stresses strongly influence the evolution of the EARS (e.g., Dawson, 1992). It can be

considered that the mantle plume stresses outweigh the far-field stresses from the Indian and Antlantic ridges. The far-field stresses, especially from southern Africa could be responsible for the local stress perturbations as reported in many parts of the EARS (e.g., Dawson, 1992).

It is well accepted that rifting along the eastern branch of the EARS propagates from north to south (e.g., Ebinger et al., 1989; 1997; Le Gall et al., 2008). Generally, all of the Cenozoic structures observed in the Tanzanian craton are reactivated Precambrian structures (shear zones and faults). The EARS reactivates mainly the NW-SE, N-S and NE-SW trending Precambrian structures because they are oriented suitably with regard to the current stresses. The proposed scenario is as follows. During the first rifting stage, the north-south propagation of the rift into North Tanzania resulted in the development of three isolated rift basins, trending NW-SE (Pangani), NE-SW (Eyasi) and N-S (Natron and Manyara). The orientation of these basins was controlled by the reactivation of existing structures, which also imposed the associated local direction of opening at a high angle to its trend. Altogether, the overall direction of extension was probably in a E-W direction.

With successful rifting, these three rift segments further evolved during the second rifting phase, but to different degrees depending on the new stress-field conditions. Rifting was favoured due south, with accentuation of the Natron and Manyara rifts and further propagation of crustal extension as far as towards the Dodoma region. In the Manyara-Dodoma area, three sets of faults (NE-SW, NW-SE and N-S), initially formed by reactivation of pre-existing weaknesses, continued to grow.

9.5. Relationship between volcanism, earthquakes and faults

Magmatism (volcanism) seems to pre-date faulting (rifting) in many parts of the EARS (e.g., Foster and Jackson, 1998; Ghebreab, 1998). This is based on the fact that old volcanoes such as the Kilimanjaro, Meru and Ngorongoro are located on the shoulders of the EARS or away from its main depression (e.g., Ebinger, 1989b; Foster and Jackson, 1998; Fig. 3.11). The biggest volcanoes seem to be on the extreme west or east of the EARS main depression.

In Tanzania and Kenya, a temporal and spatial relationship exists. Large volcanoes (mainly shield volcanoes) formed in Late-Miocene and they were characterized by predominantly basic magmatism (Dawson, 1992). Subsequent volcanoes, such as the Late-Pleistocene nephelinitic Hanang volcano, were relatively small in size and their locations seem to be towards the centre of the rift axis (e.g., Ebinger, 2005; Fig. 3.11). This is based on the fact that as the continental lithosphere undergoes extension, major magma intrusions concentrate in a relatively narrow area (e.g., Mohr, 1987; Morley, 1994; 1999a; 1999b; Ebinger and Casey, 2001). It is possible that this process is associated with the modification of thermal and mechanical properties of the lithosphere by weakening it

and enhancing deformation and strain localization (e.g., Lynch and Morgan, 1987; Chèry et al., 1989; Geoffroy, 1998; Morley, 1999a).

Although the Hanang volcano in the Manyara-Dodoma area is considered inactive, there is no evidence to show that its magma reservoir is completely inactive as well. If it is, then it could account for the earthquake swarms that have affected the Manyara-Dodoma area. Otherwise, these earthquake swarms could be associated with small magma intrusions in shallow crustal levels, i.e. dikes. Dikes can form normal faults and fissures resulting in swarms of small shallow earthquakes that rarely exceed $M_w = 5.5$, while most have $M_w = 4.5$ (McCalpin, 1996). The shallow earthquakes are mainly a function of upward migration of magma at typical rates in the order of 0.1 to 6 km/hr (e.g., Klein et al., 1987). In the Manyara-Dodoma rift segment, there is an intensive seismicity generally characterized by earthquakes of less than $M_w = 6.0$ (Macheyeki et al., 2008a, b). In some places, such as the Chenene area, both the observed surface fractures and the earthquake swarms are oriented ~ N-S. The N-S trending Chenene surface fractures are an example of manifestation of the current strain or deformation consistent with the ~ E-W extension. Ebinger (2005) and Corti (2008) show that within the eastern branch of the EARS, a clear rift-ward migration of strain exists away from the border faults (located on the west) and towards the central rift located eastward. But the earthquake swarms and the associated surface deformation (e.g., surface fractures) in the Dodoma area do not reveal a clear shift of deformation towards the central rift. Surface deformation has been reported elsewhere (e.g., Kahama, Nzenga) in recent years (i.e., Tanzanian Government internal reports, 1983; Appendix 4) but the deformation pattern is not yet established. This could be partly due to the young rift age in the Manyara-Dodoma rift segment and partly due to lack of seismic data over a sufficiently long time span. Seismic data are only available for less than 100 years, which is not sufficient to establish whether the rift is shifting towards the east or not.

9.6. Possible extension of the 2-phase rifting model southwards to the Dodoma region

In the recent models of rift evolution developed for the Ethiopian and Kenya-North Tanzania rift segments in the eastern branch of the EARS, continental break-up evolves with time from an early stage of fault-controlled extension with diffuse volcanism towards a late (and active) stage of magma-assisted stretching with focused magmatism and faulting in the rift floor (Ebinger and Casey, 2001; Ebinger, 2005; Buck, 2006; Casey et al., 2006; Corti, 2008; Ibs-Von Seth et al., 2008).

During the initial stage of extension, the lithosphere is still strong and strain is accommodated by large faults in brittle layers and ductile deformation in the weaker layers. Strain localizes along a single, large but narrow deformation zone. The latter is commonly along a high-angle fault system, localizing earliest volcanic centres. On one side, it flanks a broad uplift and on the other, it bounds an asymmetric rift basin. It is

commonly described as a large offset "border fault system" that is seismically active down to the base of the crust. This stage should correspond to the first phase of rifting defined by Dawson (1992).

During the second phase of rifting, which started 1.3-1.2 Ma ago in South-Kenya and North Tanzania (Fairhead et al., 1972; MacIntyre et al., 1974), deformation migrated towards the centre of the rift basin into a narrow zone marked by magmatic injections in the crust, through a large number of small faults and cracks. It forms a "magmatic segment" marked by aligned eruptive centres, fissures and short faults displacing < 2 Ma sediments in the centre of the basin and localizing relatively superficial earthquake swarms.

The transition from the fault-controlled extension towards the magma-assisted stretching results from a marked reduction of the lithospheric strength. In both the brittle and ductile layers, strain localized along a narrow zone is marked by magma intrusion. The injection of magma diminishes markedly the level of plate-driving stress necessary for the break-up (Buck, 2006). As a result, the former border fault system becomes less active, although seismic activity might still occur (Ibs-von-Seth, 2001), and active deformation concentrates in the new narrow magmatic zone, away from the former border fault, on the basin side.

This model characterizes both the Ethiopian rift system (Ebinger and Casey, 2001; Ebinger, 2005; Buck, 2006; Casey et al., 2006) and the Kenya rift, up to at least Lake Natron (Ibs-Von Seth et al., 2001; 2008; Ebinger, 2007). In the light of the present work, the question on whether this model might be extended to the Manyara-Dodoma rift segment might be raised.

Several lines of evidence suggest that the Manyara-Dodoma segment of the western branch of the EARS could be presently in a transitional stage towards the development of a narrow zone of focused faulting in the rift floor, away (eastwards) from the main border fault system. The main elements are i) the development of elongated earthquake swarms along a line from Lake Manyara to the Chenene Mountains, ii) the apparition of open cracks in the ground, and iii) the presence of helium-bearing springs (Macheyeki et al., 2008b). It is not clear if this process could be assisted by magmatic dyke injection at depth, but as shown by Ibs-von-Seth et al. (2008), the development of focused earthquake swarms are often related to magma injection at depth. The development of open cracks in the soil, apparently not related to major seismogenic events, also indicates that a significant part of the extension process could occur aseismically as it would be the case with magmatic dyke injection at depth. However, no subsurface manifestations of volcanism are known along that new tectonic line. Further geophysical and geochemical investigations would be necessary to clarify this.

9.7. Seismic-hazard assessment

As stated in section 2.5.5, earthquake slip rates and recurrence intervals are two critical components of any seismic-hazard assessment. For a sound seismic-hazard assessment we need to integrate seismic, historic, paleoseismological and even archeological data (e.g., Pavlides et al., 1999). Unfortunately, for the Dodoma area, we lack paleoseismological and archeological data. Even the seismic data available is not homogeneous (or continuous), thus assessment of the seismic hazard with the aim of constructing a reliable probabilistic seismic-hazard map for the Dodoma area is far from completion.

As the Dodoma area is within the active East African Rift System, efforts have to be made to collect enough scientific data (i.e., seismological, historic, archeological, paleoseismological and geophysical) and to regularly integrate all of these data in order to keep the seismic map of the country up-to-date.

Data from seismology show that the Dodoma area has experienced earthquakes of up to M_w = 6.2 (e.g., Macheyeki et al., 2008a; 2008b). Analysis of the trenching data has shown that the area can indeed be affected by large earthquake, potentially of magnitude M_w = 6.3-6.4. Average slip rates are in the order of 0.15 mm/yr. This amount of slip rate is, however, an order of magnitude smaller than slip rates obtained elsewhere within the EARS in Tanzania. For example, Baer et al. (2008) report slip rates of about 2-4 mm/yr in northern Tanzania. Calais et al. (submitted), also report far-field extension of the EARS of about 3-4 mm/yr.

In our opinion, this area deserves to be further investigated in more detail. Since this work identifies faults that have the potential of being reactivated and since preliminary fault slip rates and recurrence intervals have been determined for the Dodoma area, then, a base for further paleoseimological studies is established.

Chapter 10

Conclusions and Recommendations

10. Conclusions and recommendations

Using various approaches, such as i) analysis of 90 m resolution SRTM-DEM data, ii) determination of present-day and paleo-tectonic stresses from focal mechanisms and from geological data, and iii) trenching, it is possible to conclude that the Dodoma area is indeed seismically and tectonically active. By the use of empirical relationships between fault length and vertical displacement on faults that are considered to be active, it has been established that earthquakes of magnitudes of $0 < M_w \leq 6.4$ can occur in the area. A preliminary paleoseismic investigation suggests that at least one earthquake capable of generating surface fractures probably occurred during the Middle Holocene along the Bubu fault.

The present tectonic structure of the Dodoma area is the result of a long geological evolution that started with the formation of the Archean nucleus of the Tanzanian craton. The deformations related to the Pan-African orogeny reworked deeply the rim of the Tanzanian craton and defined marked weakness zones that would later focus and guide the rifting processes linked to the southwards propagation of the eastern branch of the EARS. Late Cenozoic rifting itself occurred in two successive phases. The earlier structures formed during the initial rift stage are progressively abandoned to the benefit of younger structures that reflect the current state of crustal stress field.

This work allowed defining the Manyara-Dodoma rift segment as the presently active southwards continuation of the rift, south of the North Tanzania Divergence. The importance of the current tectonic activity in this area has been previously underestimated. In consequence, it is hereby recommended that within the Dodoma area – or even within the whole Manyara-Dodoma rift segment – the civil-engineering building codes have to be taken seriously, bearing in mind that indeed the area is seismically active and can be hit by earthquakes of up to M_w = 6.3-6.4, which are potentially destructive. Future studies focused on seismic-hazard evaluation should give more emphasis on active ~ N-S trending faults because these are structures that stand high to highest likelihood of being reactivated, and hence causing large and destructive earthquakes. NE-SW trending faults that dip NW could be given priority as well.

It is hereby recommended to establish at least 4 more trenches: i.e., two across Segment 1 of the Mponde fault and two across the Dam segment of the Hombolo fault. Each of these trenches has to be established on suitable locations, and has to be deep enough (ca. 6-10 m), long enough (ca. 15-20 m), wide enough (ca. 2-4 m) and parallel to the others in order to test the lateral continuation of stratigraphic units and active faults. Of these four trenches, the best ones can be protected for further paleoseismological studies. The criteria for site location should be those stated in Chapter 4, but for smaller fault scarps, particularly those which are eroded, such as the Hombolo Dam segment, geophysical techniques have to be employed in order to increase the likelihood of intersecting active faults in the trenches. Detailed topographic surveys of the trenches

have to be conducted, in order to aid geomorphologic indicator analysis and to have precise fault offset calculations.

References

References

Abdallah, A., Courtillot, V., Kasser, M., Le Dain, A.Y., Lepine, J.C., Robineau, B., Ruegg, J.C., Tapponnier, P., Tarantola, A., 1979. Relevance of Afar seismicity and volcanism to the mechanics of accreting plate boundaries. *Nature* 282, 17-23.

Aitken, M.J., 1998. An introduction to optical dating. *Oxford University Press*: Oxford, 267 pp.

Allen, P.A., Allen, J.R., 2005. Basin analysis. Principles and applications. 2d ed. *Blackwell*: UK, 549 pp.

Anderson, E.M., 1951. The Dynamics of Faulting and dyke formation with applications to Britain. 2d ed. *Oliver and Boyd*: Edinburgh, 206 pp.

Angelier, J., 1979a. Néotectonique de l'arc égéen. *Soc. géol. Nord. pub*. 3, 418.

Angelier, J., 1989. From orientation to magnitudes in paleostress determinations using fault slip data. *J. Struct. Geol.* 11, 37-50.

Angelier, J., 1994. Fault slip analysis and paleostress reconstruction. *In*: Hancock, P.L. (Ed.) Continental Deformation. *Pergamon*: Oxford.

Angelier, J., Bergerat, F., 1983. Syste`me de contrainte en extension intracontinentale. *Bull. Cent. Rech. Expl. Prod. Elf Aquitaine* 7, 137-147.

Anhaeusser, C.R., Mason, R., Viljoen, M.J., Viljoen, R.P., 1969. A reapraisal of some aspects of Precambrian shield geology. *Geol. Soc. Amer. Bul.* 80, 2175-2200.

Arad, A., Morton, W.H., 1969. Mineral springs and saline lakes of the Western Rift Valley, Uganda. *Geoch. et Cosmoch. Acta* 33, 1169-1181.

Arnold, J.R., Libby, W.F., 1949. Age determinations by radiocarbon content: Checks with samples with known age. *Science* 110, 678-680.

Atmaoui, N., Hollnack, N., 2003. Neotectonics and extension direction of the Southern Kenya Rift, Lake Magadi area. *Tectonophysics* 364, 71-83.

Bada, J.L., Luyendyk, B.P., Maynard, J.B., 1970. Marine sediments: Dating by the racemization of amino acids. *Science* 170, 730-732.

Baer, G., Hamiel., Y., Shamir, G., Nof., 2008. Evolution of a magma-driven earthquake swarm and triggering of nearby Oldoinyo Lengai eruption, as resolved by InSAR, ground observations and elastic modeling, East African Rift, 2007. *Earth and Plan. Sci. Letters* 272, 339-352.

Bahat, D., Mohr, P., 1987. Horst faulting in continental rifts. *Tectonophysics* 141 (1-3), 61-73.

Baljinnyam, I., Bayasgalan, A., Borisov, B.A., Cisternas, A., Dem'yanovich, M.G., Ganbaatar, L., Kochetkov, V.M., Kurushin, R.A., Molnar, P., Philip, H., and Vashchilov, Y.Y., 1993. Ruptures of major earthquakes and active deformation in Mongolia and its surroundings. *Geol. Soc. Amer. Mem.* 181, 1-62.

Barth, H., 1996. Gold in the Dodoman basement of Tanzania. Hanover, 53 pp.

Barth, A., 2007. Frequency sensitive moment tensor inversion for light to moderate magnitude earthquakes in eastern Africa and derivation of the regional stress _field. *PhD thesis*: University at Karlsruhe (TH).

Bates, R.L., Jackson, J.A., 1987. Glossary of Geology. 3d ed., *Amer. Geol. Inst*: Alexandria, VA, USA.

Bell, K., Dodson, H.S., 1981. The Geochronology of the Tanzania Shield. *J. Geol*. 89(1), 109-128.

Beloussov, V.V., 1962. Basic Problems in Geotectonics. *McGray-Hill Book Co*: USA.

Berger, G.W., 1987. Thermoluminescence dating of the Pleistocene Old Crow tephra and adjacent loess, near Fairbanks, Alska. *Can. J. Earth Sci*. 24, 1975-1984.

Biasi, G.P., Weldon, R.J., Fumal, T.E., Seitz, G.G., 2002. Paleoseismic event dating and conditional probability of large earthquakes on the southern San Andreas Fault, California: *Bul. Seismo. Soci. Amer.* 92, 2761-2781.

Bjornsson, A., Saemundsson, K, Einarsson, P., Tryggvason, E., Gronvavald, K., 1977. Current rifting episode in north Ireland. *Nature* 266, 318-323.

Björck, S., Wohlfarth, B., 2004. 14C Chronostratigraphic techniques in Paleoseismology. *In*: Last, W.M. and Smol J.P., (Editors). Tracking environmental change using lake sediments (vol. 1)-Basin analysis, Coring, and chronological techniques. *Kluwer Academic Publishers*: Dordrech/Boston/London, 205-245 pp.

Blés, J.L., Feuga, B., 1986. The fracture of rocks (studies in geology series). *North Oxford Acad. Pub. Ltd*: Great Britain.

Block, L., Royden, L.H., 1990. Core complex geometries and regional scale flow in the lower crust. *Tectonics* 9, 557-567.

Bolt, B.A. 1993. Earthquakes and Geological Discovery. *Scientific Amer. Lib.:* New York.

Bonaccorso, A., Davis, P.M., 1993. Dislocation modeling of the 1989 dike intrusion into the flank of Mount Etna, Sicily. *J. Geophys. Res*. 98, 4261-4268.

Bonavia, F.F., Chorowicz, J., Knackstedt, M.A., 1995. Have wet and dry Precambrian crust largely governed Cenozoic intraplate magmatism from Arabia to East Africa? *Geophys. Res. Letters* 22, 2337-2340.

Bosher, R., Duennebier, F.K., 1985. Seismicity associated with the Christmas 1965 event at Kilauea Volcano. *J. Geophys. Res*. 90, 4529-4536.

Bosworth, W., 1985. Geometry of propagating rifts. *Nature* 316, 625-627.

Bosworth, W., Strecker, M.R., Blisniuk, P.M., 1992. Integration of East African paleostress and present-day stress data: implications for continental stress field dynamics. *J. Geophys. Res*. 97, 11851-11865.

Bott, M.H.P., 1959. The Mechanism of oblique-slip faulting. *Geol. Magaz*. 96, 109-117.

Bott, M.H.P., 1995. Mechanisms of rifting: geodynamic modeling of continental rift systems. *In*: Olsen, K.H. (Ed.), Continental Rifts: Evolution, Structure, Tectonics. *Elsevier Series*: Amsterdam, 409-436p.

Bucknam, R.C., Anderson, R.E., 1979. Estimation of fault-scarp ages from a scarp-height-slope-angle relationship. *Geology*, 7 (1), 11-14.

Burbank, D.W., Anderson, R.S., 2001. Tectonic Geomorphology. *Blackwell Science* 33 (43), 105-129.

Braile, L.W., Keller, G.R., Wendlandt, P., Khan, M.A., 1995. The East African Rift. *In:* K. H. Olsen: Continental Rifts: Evolution, Structure, Tectonics. *Elsevier Series*: Amsterdam, 213-231 pp.

Brandsdottir, B., Einarson, P., 1979. Seismic activity associated with the September 1977 deflation of the Krafla central volcano in northeastern Iceland. *J. Volc. Geotherm. Res.* 6, 197-212.

Brazier, R.A., Nyblade, A.A., Florentin, J., 2005. Focal mechanisms and stress regime in NE and SW Tanzania, East Africa. *Geophys. Res. Letters* 32(14), 1-4.

Brewer, M.S., Haslam, H.W, Darbyshire, P.F.P., Davis, A.E., 1979. Rb/Sr age determinations in the Bangweulu Block, Luapula Province, Zambia: *Inst. Geol. Sci. London* 79, 11.

Brun, J.P., 1999. Narrow rifts versus wide rifts: inferences for the mechanics of rifting from laboratory experiments. *Philos. Transact. Roy. Soci. London, Series* A357, 695-712.

Brun, J.P., Sokoutis, D., Van Den Driessche, J., 1994. Analogue modeling of detachment fault systems and core complexes. *Geology* 22, 319-322.

Buck, W.R., 1991. Modes of continental lithospheric extension. *J. Geophys. Res*. 96, 20161-20178.

Buck, W.R., 1998. Flexural rotation of normal faults: *Tectonics* 7, 956-973.

Buck, W.R., 2006. The role of magma in the development of the Afro-Arabian System. *In:* Yirgu, G., Ebinger, C.J., Maguire, P.K.H. (eds), The Afar Volcanic Province within the East African Rift System. *Geol. Soci. London, Spec. Pub*. 259, 43-54.

Bürgmann, R., Pollard, D., Martel, S.J., 1994. Slip distributions on faults: Effects of stress gradients, inelastic deformation, heterogeneous host-rock stiffness, and fault interaction. *J. Struc. Geol.* 16, 1675-1690.

Bullen, K.E., Bolt, B.A., 1985. An introduction to the theory of seismology. *Camridge University Press*: Cambridge.

Burbank, D.W., Anderson, R.S., 2001. Tectonic Geomorphology. *Blackwell Science*: 33 (43), 105-129.

Bursik, M., 1992. How to predict an eruption at Long Valley calderas. EOS. *Trans. Am. Gephys. Union* 73, 343.

Busby, C.J., Ingersoll, R.V., 1995. Tectonics of Sedimentary Basins. *Blackwell Sciences, Inc.*: USA, 579 pp.

Byerlee, J.D., 1978. Friction of rocks. *Pure App. Geophys*. 116, 615-626.

Calais, E., Hartnady, C., Ebinger, C., Nocquet, J.M., 2006. Kinematics of the East African Rift from GPS and earthquake slip vector data. *Geol. Soci. Spec. Pub*. 259, 9-22.

Calais, E., d'Oreye, N., Albaric, J., Deschamps, A., Delvaux, D., Déverchère, J., Ebinger, C., Ferdinand, R.W., Kervyn, F., Macheyeki, A.S., Oyen, A., Perrot, J., Saria, E., Smets, B., Stamps, D.S., Wauthier, C., (submitted). Aseismic strain accommodation by dyking in a youthful continental rift, East Africa. *Nature.*

Camelbeeck, T., Iranga, M.D. 1996. Deep crustal earthquakes and active faults along the Rukwa trough, Eastern Africa. *Geophys. J. Intern*. 124, 612-630.

Cartwright, J.A., Trudgill, B.D., Mansfield, C.S., 1995. Fault growth by segment linkage: an explanation for scatter in maximum displacement and trace length data from the Canyonlands grabens of SE Utah. *J. Struct. Geol.* 17, 1319-1326.

Catuneanu, O., Wopfner, H., Eriksson, P.G., Cairncross, B., Rubidge, B.S., Smith, R.M.H., Hancox, P.J., 2005. The Karoo basins of south-central Africa. *J. Afr. Earth Sci.* 43, 211-253.

Casey, M., Ebinger, C., Keir, D., Gloaguen, R., Mohamed, F., 2006. Strain accommodation in transitional rifts: extension by magma intrusion and faulting in Ethiopian rift magmatic segments. *In*: Yirgu, G., Ebinger, C.J., Maguire, P.K.H., (eds) 2006. The Afar Volcanic province within the East African Rift System. *Geol. Soc. London Spec. Pub.* 259, 143-163.

Cerling, T.E., Craig, H., 1994, Cosmogenic production rates of ^{3}He from 39 to 46 °N latitude, western USA and France. *Geoch. et Cosmoch. Acta* 58, 249-255.

Chapola, L.S., 2005. Stress regimes in Eastern and Southern Africa. East African Rift System Conference (16-18 August 2005, Mbeya-Tanzania). *Special Abstract Vol. Issue*.

Chèry, J., Daignie`res, M., Lucazeau, F., Vilotte, J.-P., 1989. Strain localization in rift zones (case of thermally softened lithosphere): a finite element approach. *Bulletin de la Soci. Ge´ol. de France* 8, 437-443.

Chorley, R.J., Schumm, S.C., Sugden, D.E., 1984. Geomorphology. *Methuen*: London, 605 pp.

Chesley, J.T., Rudnick, R.L., Lee, C.-T., 1999. Re-Os systematics of mantle xenoliths from the East African rift: Age, structure and history of the Tanzanian craton. *Geoch. et Cosmoch. Acta* 63, 1203-1217.

Chorowicz, J., 1989. Transfer and Transform Fault Zones in Continental Rifts: Examples in the Afro-Arabian Rift System. Implications of Crust Breaking. *J. Afr. Earth Sci.* 8 (2/3/4), 203-214.

Chorowicz, J., 2005. The East African rift system. *J. Afr. Earth Sci*. 43, 379-410

Chorowicz, J., Sorlien, C., 1992. Oblique extensional tectonics in the Malawi Rift, Africa. *Geol. Soci. Amer. Bull*. 104, 1015-1023.

Coney, P.J., 1980. Cordilleran metamorphic core complexes: an overview. *In*: Crittenden, M.D., Coney, P.J., Davis, G.H. (Eds.), Cordilleran Metamorphic Core Complexes. *Geol. Soci. Amer. Memoir* 153, 7-31.

Corti, A., Bonini, M., Conticelli, S., Innocenti, F., Manetti, P., Sokoutis, D., 2003. Analogue modeling of continental extension: a review focused on the relations between the patterns of deformation and the presence of magma. *Earth Sci. Rev.* 63, 169-247.

Corti, G., 2008. Control of rift obliquity on the evolution and segmentation of the main Ethiopian rift. *Letters*. Doi:10.1038/ngeo160 (Nature publishing group).

Cowie, P.A. Scholz, C.H., 1992a. Growth of faults by accumulation of seismic slip. *J. Geophy. Res.* 97(B7), 11085-11095.

Cowie, P.A. Scholz, C.H., 1992b. Physical explanation for the displacement-length relationships of faults using a post-yield fracture mechanics model. *J.Struc. Geol.* 14(10), 1133-1148.

Coolen, J.J.M.M.M., 1980. Chemical petrology of the Furua granulite complex, southern Tanzania. *GUA Papers of Geology* 13: Free University of Amsterdam, pp 258.

Cox, A., Doell, R.R., Dalrymple, G.B., 1964. Reversals of the earth's magnetic field. *Science* 144, 1537-43.

Creer, K.M., 1962. The dispersion of the geomagnetic field due to secular variation and its determination for remote times from paleomagnetic data, *J. Geophys. Res. 67*, 3461-3476.

Crone, A.J. Haller, K.M., 1991. Segmentation and the coseismic behaviour of Basin and Range normal faults: examples from east-central Idaho and southwest Montana, U.S.A. *J. Struct. Geol*. 13, 151-164.

Crone, A.J., Machette, M.N., Bowman, J.R., 1992. Geologic investigations of the 1988. Tennant Creek, Australia, earthquake-implications for paleoseismicity in stable continental regions. *U.S.Geol. Surv. Bull*. 2032A, 1-51.

Daly, M.C., 1998. Crustal Shear Zones in Central Africa: A Kinematic Approach to Proterozoic Tectonics. *Episodes*, 11(1).

Das, S., Boartwrit, J., Scholz, C.H. (eds), 1986. Earthquake Source Mechanisms, *Amer. Geophys. Union Mon*. 37, Maurice Ewing Series 6.

Dawson, J.B., 1992. Neogene tectonics and volcanicity in the North Tanzania sector of the Gregory Rift Valley: contrasts with the Kenya sector, *Tectonophysics* 204, 81-92.

Deino, A. L., Tauxe, L., Monaghan, M., Drake, R., 1990. $^{40}Ar/^{39}Ar$ age calibration of the litho- and paleomagnetic stratigraphies of the Ngorora Formation, Kenya. *J. Geol.* 98, 567-587.

Delvaux, D., 1991. The Karoo to Recent rifting in the western branch of the East-African Rift System: A bibliographical synthesis. *Musee Roy. Afr. Central Tervuren* (*Dép. Géol. Min., Rap. Ann.)* 1989-1990, 63-83.

Delvaux, D., Moeys, R., Stapel, G., Petit, C., Levi, K., Miroshnichenko, A., Ruzhich, V., Sankov, V., 1997. Paleostress reconstructions and geodynamics of the Baikal region, Central Asia. Part II: Cenozoic rifting. *In:* Cloetingh, S., Fernandez, M., Munoz, J.A., Sassi, W., Horvath, F. (editors), Structural controls on sedimentary basin formation. *Tectonics* 282, 1-38.

Delvaux, D., Sperner, B., 2003. Stress tensor inversion from fault kinematic indicators and focal mechanism data: the TENSOR program. *In*: Nieuwland, D. (Ed.) New Insights into Structural Interpretation and Modelling. *Geol. Soci. London, Spec. Pub* 212, 75-100.

Destro, N., Alkimin, F.F., Magnavita, L.P., Szatmari, P., 2002. The jeremoabo transpressional transfer fault, recˆoncavo-tucano rift, ne Brazil. *J. Struct. Geol.* 25, 1263-1279.

Dost, B., Evers, L., 2000. Site selection and interpretation of trenching results along the Peel boundary fault, Workshop proceedings: HAN2000-Evaluation of the potential for large earthquakes in regions of present day low seismic activity in Europe. *Han-sur-Lesse, Belgium*, 53-56.

Doyle, H., 1995. Seismology. *John Willey & Sons*: England, 218p.

Dunne, W.M., Hancock, P.L., 1994. Paleostress analysis of small-scale brittle structures, *In*: Hancocock, P.L. (ed) Continental deformation. *Pergamon*: Oxford, 101-120 pp.

Dzurisin, D., Anderson, L.A., Eaton, G.P., Koyanagi, Y.P., Lipman, P.W., Lockwood, J.P., Okamura, R.T., Puniwai, G.S., Sato, M.K., Yamashika, K.M., 1980. Geophysical observations of Kilauea volcano, Hawaii. Constraints on the magma supply during the November 1975-September 1977. *J. Volcanol. Geotherm. Res.* 7, 241-269.

Ebinger, C.J., 1989a. Tectonic development of the western branch of the East African Rift System. *Geol. Soci. Amer. Bull*. 101, 885-903.

Ebinger, C.J., 1989b. Geometric and kinematic development of border faults and accommodation zones, Kivu-Rusizi rift, Africa. *Tectonics* 8, 117-133.

Ebinger, C.J., Casey, M., 2001. Continental breakup in magmatic provinces: an Ethiopian example. *Geology* 29, 527-530.

Ebinger, C.J., Bechtel, T.D., Forsyth, D.W., Bowin, C.O., 1989. Effective elastic plate thicknesses beneath the East African and Afar dommes. *J. Geophys. Res*. 94, 2883-290.

Ebinger, C.J., Poudjom Djomai, Y., Mbede, E., Foster, A.N., Dawson, J.B., 1997. Rifting Archean lithosphere: Eyasi-Manyara-Natron rifts, East Africa. *J. Geol. Soci. London* 154, 947-960.

Ebinger, C., 2005. Continental break-up: the East African perspective. *A&G* 46, 2.16-2.21.

Ebinger, C.J., Deino, A.L., Tesha, A.L., Becker, T., Ring, U., 1993. Tectonic controls on rift basin morphology: Evolution of the Northern Malawi (Nyasa) rift. *J. Geophys. Res.* 98 (B10), 17,821-17,836.

Ebinger, C.J., Ibrahim, A., 1994. Mutiple episodes of rifting in Central and East Africa: A re-evaluation of gravity data. *Geol. Rundschau* 83, 689-702.

Einarsson, P., 1991. Earthquakes and present-day tectonism in Iceland. *Tectonophysics* 189, 261-279.

Einarson, P., BBjornsson, A., 1979. Earthquakes in Ireland. *Jokull* 29, 37-43.

Einarson, P., Brandsdottir, B., 1980. Seismological evidence for magma lateral magma intrusion during the July 1978 deflation of the Krafla volcano in NE-Iceland. *J. Geophys*. 47, 160-165.

Eldeen, U.Z., Delvaux, D., Jacobs, P., 2002. Tectonic evolution in the Wadi Araba Segment of the Dead Sea Rift, South-West Jordan. *EGU Stephan Mueller Spec. Pub Series* 2, 1-19.

England, P.C., 1983. Constraints on extension of continental lithosphere. *J. Geophys. Res*. 88, 1145-1152.

Fairbanks, R.G., Mortlock, R.A., Chiu, T.C., Cao, L., et al., 2005. Radiocarbon calibration curve spanning 0 to 50,000 years BP based on paired $^{230}Th/^{234}U/^{238}U$ and ^{14}C dates on pristine corals. *Quat. Sci. Rev*. 25, 21-22; 3084-3087.

Fairhead, J.D., Girdler, R.W., 1971. The Seismicity of Africa. *Geophys, J.R. astr. Soc*., 271-301.

Fairhead, J.D., Mitchell, J.G., Williams, L.A.J., 1972. New K/Ar determinations on Rift volcanics of South Kenya and their bearing on the age of Rift faulting. *Nature* 238, 66-69.

Fairhead, J.D., Stuart, G.W., 1982. The seismicity of the East-African rift system and comparison with other continental rifts. *In*: Palmason, G. (ed.): Continental and Oceanic Rifts. *Geod. Series* 8, 41-61.

Farr, T.G., Kobrick, M., 2000. Shuttle Radar Topography Mission produces a wealth of data. Amer. Geophys. Union Eos. 81, 583-585.

Ferrill, D, Morris, A.P., 2001. Displacement gradient and deformation in normal fault systems. *J. Struct. Geol.* 23, 619-638.

Ferrucci, F., Patané, D., 1993. Seismic activity accompanying the outbreak of the 1991-1993 eruption of Mt. Etna (Italy). *J. Volcanol. Geotherm. Res*. 57, 125-135.

Foster, A.N, Jackson, J.A., Eminger, C.J., 1995. Source mechanisms and centroid depths of recent African earthquakes (abstract). *Terra Nova* 7, 35.

Foster, A.N, Jackson, J.A., 1998. Source parameters of large African earthquakes: implications for crustal rheology and regional kinematics. *Geophys. J. Intern*. 134, 422-448.

Fozzard, P.M.H., 1959. The Geology of the Mpondi river area: Quarter Degree Sheet 123 (41 NW.). Kwa Mtoro. *Records of the Geological Survey of Tanganyika* 9, 10-12.

Fozzard, P.M.H., 1961. Geological Survey of Tanzania. 1:125.000 Geological map Quarter Degree Sheet 123 Kwa Mtoro. *Geological Survey Division*: Dodoma-Tanzania.

Fozzard, P.M.H., 1962. Brief explanation of the Geology of QDS177 Manzoka-Geological Survey of Tanganyika (*Unpublished Report): Dodoma*-Tanzania. 1-7p.

Fritts, H.C., 1976. Tree Rings and Climate. *Academic Press*: New York.

Fritz, H., Tenczer, V., Hauzenberger, C.A., Wallbrecher, E., Hoinkes, G., Muhongo, S., Mogessie, A., 2005. Central Tanzanian tectonic map: A step forward to decipher Proterozoic structural events in the East African Orogen. *Tectonics* 24(6), doi: 10.1029/2005TC001796. issn: 0278-7407.

Gabert, G., 1973. Uber praambrische Olivinmonzoite (Kentallenite) in Zentral-Tanzania. *Geol. Jahrbuch* B6, 51-79.

Gabert, G., Wendt, I., 1974. Datierungen von granitischen Gesteinen im Dodoman und Usagaran System und in der Ndembera Serie (Tanzania). *Geol. Jahrbuch* 11, 3-55.

Geoffroy, L., 1998. Diapirism and intraplate extension-cause or consequence. Comptes Rendus de l'Academie des Sciences, Serie II: *Sci. de la Terre et des Planets* 326, 267-273.

Ghebreab, W., 1998. Tectonics of the Red Sea region reassessed. *Earth-Sci. Rev*. 45, 1-44

Gibbs, A.D., 1984. Structural evolution of extensional basin margins. *J. Geol. Soci. London* 141, 609-620.

Girdler, R.W., 1983. Processes of planetary rifting as seen in the rifting and break up of Africa. *Tectonopysics* 94, 241-252.

Goes, S.D.B., 1996. Irregular recurrence of large earthquakes: An analysis of historic and paleoseismic catalogs. *J. Geoph. Research*.101B3, 5739-5749.

Grindley, G.W., Hull, A.G., 1986. Historical Taupo earthquakes and earth deformation. *Bull. R. Soc. N.Z*. 24, 173-186.

Groshong, R. H. Jr., 2006. 3-D Structural Geology: A Practical Guide to Quantitative Surface and Subsurface Map Interpretation, 2d ed. *Springer*: The Netherlands.

Gürpinar, A., 2005. The importance of paleoseismology in seismic hazard studies for critical facilities. *Tectonophys*ics 408, 23-28. doi:10.1016/j.tecto.2005.05.042.

Hackett, W.R., Smith, R.P., 1992. Quaternary volcanism, tectonics, and sedimentation in the Idaho National Engineering Laboratory area. 1-18 pp. *In:* J.R. Wilson (ed.). Field guide to geologic excursions in Utah and adjacent areas of Nevada, Idaho and Wyoming. Geological Society of America Rocky Mountain Section Guidebook. *Utah Geol. Surv. Misc. Pub*., 92-3.

Hancock, P.L., 1985. Brittle microtectonics: principles and practice. *J. Struc. Geol*. 7 (3/4), 437-457.

Harris, J.F., 1958. Geological investigations, sampling and diamond-drilling at Manyeghi Helium-bearing hot springs, Singida districts. *Records of the Geological Survey of Tanganyika* 8, 86-98.

Harris, J.F., 1959. Analysis of Natural Gases and Accompanying Spring Waters. *Records of the Geological Survey of Tanganyika* 9, 94.

Harris, R.A., 1998. Introduction to a special section: Stress triggers, stress shadows, and implications for seismic hazards J. *Geophys. Res*. 103(24), 347-358.

Hartley, R., Watts, A.B., Fairhead, J.D., 1996. Isostasy of Africa. *Earth and Plan. Sci. Letters* 137, 1-18.

Heidbach, O., Fuchs, K., Müller, B., Reinecker, J., Sperner, B., Tingay, M., Wenzel, F., 2007. The World Stress Map-Release 2005, 1:46,000,000, *Comm. of the Geolog. Map of the World*, Paris.

Herrmann, R.B., 1975. A student's guide to the use of P and S wave data for focal mechanism determination. *Earthquake Notes* 46, 21-36.

Holmes, A., 1952. The sequence of Precambrian orogenic belts in south and central Africa: *18th Intern. Geol. Gongr. London* (1984) 14, 254-269.

Hopper, J.R., Buck, R.W., 1996. The effect of lower crust flow on continental extension and passive margin formation. *J. Geophys. Res.* 101, 20175-20194.

http://www.seamless.usgs.gov

http://geology.er.usgs.gov/eastern/plates.html

http://geology.cr.usgs.gov/capabilities/gronemtrac/geochron/thermo/tech.html

Hu, J.C., Angelier, J., 2004. Stress permutations: Three-dimensional distinct element analysis accounts for a common phenomenon in brittle tectonics. *J. Geophys. Res.* 109, B09403, doi:10.1029/2003JB002616.

Hus, R., 2004. Structure and evolution of transfer zones in extensional tectonic basins-A study based on examples from Lake Baikal and analogue sandbox models. PhD Thesis-*University of Gent*: Belgium.

IAEA, 2002. Evaluation of Seismic Hazards for Nuclear Power Plants. *IAEA Safety Standard Series* (NS-G-3.3): Vienna, 31p.

Ibs-von Seht, M., Blumenstein, S., Wagner, R., Hollnack, D., Wohlenberg, J., 2001. Seismicity, seismotectonics and crustal structure of the southern Kenya Rift-new data from the Lake Magadi area. *Geophys. J. Intern*. 146, 439-453.

Ibs-Von Seth, M., Plenefish, T., Klinge, K., 2008. Earthquake swarms in continental rifts - A comparison of selected cases in America, Africa and Europe. *Tectonophysics* (in press).

Imber, J., Tuckwell, G.W., Childs, C., Walsh, J.J., Manzocchi, T., Heath, A.E., Bonson, C.G., Strand, J., 2004. Three-dimensional distinct element modeling of relay growth and breaching along normal faults. *J. Struc. Geol*. 26, 1897-1911.

Iranga, M.D., 1992. Seismicity of Tanzania: Distribution in time, space, magnitude, and strain release. *Tectonophysics* 209, 313-320.

Jackson, D.M., Swanson, D.A., Koyanagi, R.Y., Wright, T.L., 1975. The August and October 1968 East Rift eruptions of Kilauea volcano, Hawaii. *U.S. Geol. Surv. Prof. Paper* 890, 1-33.

Jackson, J.A., White, N.J., 1989. Normal faulting in the upper continental crust: observations from regions of active extension. *J. Struct. Geol.* 11 (1-2), 15-36.

James, J.F., 1957. Analysis of Natural Gases and Accompanying Spring Waters. *Records of the Geological Survey of Tanganyika* 7, 104-106.

James, J.F., 1958. Analysis of Natural Gases and Accompanying Spring Waters. *Records of the Geological Survey of Tanganyika* 8, 112-113.

James, T.C., 1967a. Thermal springs in Tanzania. Institution of Mining and Metallurgy. *Transactions/Section B (Applied Earth Science)*. 76, B1-B18.

James, T.C., 1967b. Thermal springs in Tanzania-Discussions and Conclusions. Institution of Mining and Metallurgy, *Transactions/Section B (Applied earth science)* 76, B168-174.

Johnson, M.R., Van Vuuren, C.J., Hegenberger, W.F., Key, R., Shoko, U., 1996. Stratigraphy of the Karoo Supergroup in southern Africa: an overview. *J. Afr. Earth Sci.* 23 (1), 3-15.

Kampunzu, A.B., Bonhomme, M.G., Kanika, M., 1998. Geochronology of volcanic rocks and evolution of Cenozoic Western Branch of the East African Rift System. *J. Afr. Earth Sci.* 26 (3), 441-461.

Kampunzu, A.B., Popoff, M., 1991. Distribution of the main Phanerozoic African Rifts and associated magmatism. Introductory notes, in Kampunzu, A.B., Lubala, R.T., (eds.). Magmatism in extensional structural settings: *Springer-Verlag*: Berlin, 2-10 pp.

Karpin, T.L., Thurber, C.H., 1987. The relationship between earthquake swarms and magma transport. Klauea volcano, Hawaii. *Pure Appl. Geophys*. 125, 971-991.

Kebede, F., 1989. Seismotectonics studies of the East African Rift System North of 12°S to southern Red Sea. Ph.D. Thesis. *Uppsala Univ*: Sweden.

Kebede, F., Kulhanek, O., 1991. Recent seismicity of the East African Rift system and its implications. *Phys. Earth and Plan. Interiors* 68, 259-273.

Kelleher, J.A., Sykes, L.R., Oliver, J., 1973. Possible criteria for predicting earthquake locations to major plate boundaries of Pacific and Caribbean. *J. Geophys. Res.* 78, 2547-2585.

Keller, A., Pinter, N., 2002. Active tectonics. Earthquakes, Uplift and Landscape. 2d ed. *Prentice Hall Earth Sciences Series*: New Jersey, 362 pp.

Keraren, K., Klemperer, S.L., 2008. Discontinuous and dichronous evolution of the Main Ethiopian Rift: Implications for development of continental rifts. *Earth and Plan. Sci. Letters* 265, 96-111.

Kilembe, E.A., Rosendahl, B.R., 1992. Structure and stratigraphy of the Rukwa rift. *Tectonophysics* 209 (1-4), 143-158.

Klein, F.W., Koyanagi, R.Y., Nakata, J.S., and Tanigawa, W.R., 1987. The seismicity of Kilauea's magma system. *In:* Volcanism in Hawaii (R.W.Decker, T.L. Wright, and P.H. Stauffer, eds.). *U.S. Geol. Surv. Prof. Pap*.1350, 1019-1185.

Koehn, D., Aanyu, K., Haines, S., Sachau, T., 2007. Rift nucleation, rift propagation and the creation of basement micro-plates within active rifts. *Tectonophysics* doi: 10.1016/j.tecto.2007.10.003.

Kroner, A., 1977. The Precambrian geotectonic evolution of Africa: plate accretion vs. plate destruction: *Prec. Res.* 4, 163-213.

Ku, T.L., 1976. The uranium-series methods of age determination. *Annu. Rev. Earth Planet. Sci. 4,* 347-379.

Kutschera, W., 1999. Accelerator mass spectrometry: analyzing our world atom by atom. *Amer. Inst. Phys. (AIP) Conf. Proceedings* 495, 407-428.

Kusznir, N.J., Marsden, G., Egan, S.S., 1991. A flexural-cantilever simple-shear / pure-shear model of continental lithosphere extension: applications to the Jeanne d'Arc Basin, Grand Banks and Viking graben, *North Sea: Geol. Soci. London Spec. Pub*. 56, 41-60.

Lal, D., 1991, Cosmic ray labeling of erosion surfaces: In-situ nuclide production rates and erosion models. *Earth and Plan. Sci. Letters* 104, 424-439.

Langston, C.A., Brazier, R., Nyblade, A.A., Owens, T.J., 1998. Local 318 magnitude scale and seismicity rate for Tanzania, East Africa. *Bull. Seism- 319 mol. Soc. Am.* 88, 712-721.

Larsen, P.H., 1988. Relay structures in a Lower Permian basement-involved extensional system. East Greenland. *J. Struct. Geol.* 10, 3-8.

Leeder, M.R., 1995. Continental rifts and proto-oceanic rift troughs. *In*: C. Busby and R. Ingersoll (Editors). Tectonics of the Sedimentary Basins. *Blackwell Science*: Boston, 119-148 pp.

Le Gall, B., Gerigon, L., Rolet, J., Ebinger, C., Gloaguen, R., Nilsen, O., Dypvik, H., Deffontaines, B., Mruma, A., 2004. Neogene-Holocene rift propagation in central Tanzania: Morphostructural and aeromagnetic evidence from the Kilombero area. *Geol. Soci. Amer. Bull.* 116 (3/4), 490-510.

Le Gall, B., Nonnotte, P., Rolet, J., Benoit, M., Guillou, H., Mousseau-Nonnotte, M., Albaric, J., Deverchère, J., 2008. Rift propagation at craton margin. Distribution of faulting and volcanism in the North Tanzanian Divergence (East Africa) during Neogene times. *Tectonophysics* 448, 1-19.

Lenoir, J.L., Liégeois, J-P., Theunissen, K., Klerkx, J., 1994. The Paleoproterozoic Ubendian shear belt in Tanzania: geochronology and structure. *J. Afr. Earth Sci.* 19(3), 169-184.

Libby, W.F., 1955. Radiocarbon Dating. *University of Chicago Press*: Chicago, 175p.

Lister, G.S., Etheridge, M.A., Symonds, P.A., 1986. Detachment faulting and the evolution of passive continental margins. *Geology* 14, 246-250.

Lynch, H.D., Morgan, P., 1987. The tensile strength of the lithosphere and the localization of extension. *In*: Coward, M.P., Dewey, J.F., Hancock, P.L. (Eds.), Continental Extensional Tectonics. *Geol. Soc. Spec. Pub*. 28, 53-65.

Machette, M.N., Personius, S.F., Nelson, A.R., Schwartz, D.P., Lund, W.R., 1991. The Wasatch fault zone, Utah; segmentation and history of Holocene earthquakes. *J. Struct. Geol.* 13, 137-149.

Macheyeki, A.S., Delvaux, D., De Batist, M., Mruma, A., 2008a. Active faults and fault segmentation in the Dodoma area, Tanzania: A first assessment of the seismic hazard in the area, *J. Tanz. Earth Sci*. (In press).

Macheyeki, A.S., Delvaux, D., De Batist, M., Mruma, A., 2008b. Fault kinematics and tectonic stress in the seismically active Manyara-Dodoma rift branch in Central Tanzania - Implications for the East African Rift. *J. Afr. Earth Sci*. 51, 163-188.

MacIntyre, R.M., Mitchell, J.G, Dawson, J.B., 1974. Age of the fault movements in the Tanzanian sector of the East African rift system. *Nature* 247, 354-356.

Makris, J., Ginzburg, A., 1987. The Afar depression: transition between continental rifting and seafloor spreading, *Tectonophysics* 141, 199-214.

Marco, S., Stein, M., Agnon, A., Ron, H., 1996. Long term earthquake clustering: a 50,000 year paleoseismic record in the Dead Sea Graben, *J. Geophys. Res*. 101 (B3), 6179-6192.

Marco, S., Agnon, A., 2005. High-resolution stratigraphy reveals repeated earthquake faulting in the Masada Fault Zone, Dead Sea Transform. *Tectonophysics* 408 (1-4), 101-112.

Mariita, N.O., Keller, G.R., 2007. An integrated geophysical study of the northern Kenya rift. *J. Afr. Earth Sci*. 48, 80-94.

Mart, Y., Dauteuil, O., 2000. Analogue experiments of propagation of oblique rifts. *Tectonophysics* 316, 121-132.

McCalpin, J.P. (Ed.), 1996. Paleoseismology. *Academic Press*: New York, 583 pp.

McCalpin, J.P., 1987. Recommended setbacks from active normal faults, *In:* McCalpin, James, editor, *Proceedings of the 23rd Annual Symposium on Engineering Geology and Soils Engineering*: Logan, Utah State University, April 6- 8, 1987, 35-56p.

McClay, K.R., 1987. The mapping of geological structures: *Open University press & Halseted press*: New York.

McClay, K.R., Dooley, T., Whithouse, P., Mills, M., 2002. 4-D evolution of rift systems: Insight from scaled physical models. *Bull. Amer. Assoc. Petrol. Geologists* 86 (6), 935-959.

McClay, K.R., White, M.J., 1995. Analogue modeling of orthogonal and oblique rifting. *Marine and Petrol. Geol.* 12, 137-151.

McConnell, R.B., 1972. Geological development of the rift system of eastern Africa. *Geol. Soc. Amer. Bull*. 83, 2549-2572.

Michetti, A.M., Audemard, M., Frank, A., Marco, S., 2005. Future trends in paleoseismology: Integrated study of the seismic landscape as a vital tool in seismic hazard analyses. *Tectonophysics* 408, 3-21.

Minakami, T., 1974. Seismology of volcanoes in Japan. *In*: Civetta, L., Gasparini, P., Luongo, G., Rapolla, A. (Eds.), *Phys. Volcanol.:* Elsevier, Amsterdam.

Minissale, A., 1991. Thermal springs in Italy: their relation to recent tectonics. *Applied Geoch*. 6 (2), 201-212.

Minster, J.B., Jordan, T.H., 1978. Present-day plate motion. *J. Geophys. Res*. 83 (NB11), 5331-5354.

Modisi, M.P., Atekwana, E.A., Kampunzu, A.B., Ngwisanyi, T.H., 2000. Rift kinematics during the incipient stages of continental extension: Evidence from the nascent Okavango rift basin, Northwest Botswana. *Geology* 28 (10), 939-942.

Mohr, P., 1987. Patterns of faulting in the Ethiopian Rift Valley. *Tectonophysics* 143, 169-179.

Morley, C.K., Wescott, W.A., Stone, D.M., Harper, R.M., Wigger, S.T., Karanja, F.M., 1992. Tectonic evolution of the northern Kenya Rift. *J. Geol. Soc. London* 149, 333-348.

Morley, C.K., 1994. Interaction of deep and shallow processes in the evolution of the Kenya Rift. *Tectonophysics* 236, 81-91.

Morley, C.K., 1998. Variable extension in Lake Tanganyika. *Tectonics* 7, 785-801.

Morley, C.K., 1999. Geoscience of Rift Systems-Evolution of East Africa. *Amer. Assoc. Petrol. Geologists Studies in Geol.* 44*,* 242.

Morley, C.K., 1999a. Aspects of transfer zone geometry and evolution in East African Rifts. *In*: Morley, C.K. (Ed.), Geoscience of Rift Systems-Evolution of East Africa. *Amer. Assoc. Petrol. Geologists Studies in Geol.* 44, 161-171.

Morley, C.K., 1999b. Marked along-strike variations in dip of normal faults-the Lokichar fault, N. Kenya rift: a possible cause for metamorphic core complexes. *J. Struct. Geol.* 21, 479-492.

Morley, C.K., Ngenoh, D.K., Ego, J.K., 1999. Introduction to the East African Rift System. *In:* C.K.Morley ed., Geoscience of Rift Systems -Evolution of East Africa. *Amer. Assoc. Petrol. Geologists Studies in Geol.* 44, 1-18.

Morley, C.K., Vanhauwaert, P., De Batist, M., 2000. Evidence for high frequency cyclic fault activity from high resolution seismic reflection survey, Rukwa Rift, Tanzania. *J. Geol. Soc.* 157, 983-994.

Morris, A., Ferrill, D.A., Henderson, D.B., 1996. Slip-tendency analysis and fault reactivation. *Geology* 24(3), 275-278.

Mugisha, E., Ebinger, C.J., Strecker, M., Pope, D., 1997. Two-stage rifting in the Kenya rift: implications for half-graben models. *Tectonocphysics* 278, 63-81.

Mulugeta, G., 1985. Dynamic models of continental rift valley systems. *Tectonophysics* 113, 49-73.

Mulugeta, G., Ghebreab, W., 2001. Modeling heterogeneous stretching during episodic or steady rifting of the continental lithosphere. *Geology* 29, 895-898.

Mruma, A.H., 1995. Stratigraphy and palaeodepositional environment of the Palaoproterozoic volcano-sedimentary Konse Group in Tanzania. *J. Afr. Earth Sci.* 21(2), 281-290.

Nishiizumi, K., Kohl, C.P., Shoemaker J.R., Arnold, J.R., Klein, J., Fink, D., Middleton, R., 1991. In situ ^{10}Be and ^{26}Al exposure ages at Meteor Crater, Arizona. *Geoch. et Cosmoch. Acta* 55, 2699-2703.

Nolet, G., Mueller, S., 1982. A model for the deep structure of the East African rift system from the simultaneous inversion of teleseismic data. *Tectonophysics* 4, 151-178.

Noller, J.S., Sower, J.M., Lettis, W.R., (2000). Quaternary geochronology: methods and applications. American Geophysical Union: Washington. 1-61 pp.

Nusbaum, R.L., Girgler, R.W., Heirtzler, J.R., Hutt, D.J., Green, D., Millings, V.E., Schmoll, B.S., Shapiro, J., 1993. The distribution of earthquakes and volcanoes along the East African Rift System. *Episode* 16, 427-432.

Nyambe, I.A., 1999. Tectonic and climatic controls on sedimentation during deposition of the Sinakumbe Group and Karoo Supergroup, in the mid-Zambezi Valley Basin, southern Zambia. *J. Afr. Earth Sci*. 28 (2), 443-463.

Nyblade, A.A., Brazier, R.A., 2002. Precambrian lithospheric controls on the development of the East African Rift System. *Geology* 30, 755-758.

Nyblade, A.A., Birt, C., Langston, C.A., Owens, T.J., Last, R.J., 1996. Seismic experiment reveals rifting of craton in Tanzania. *Eos Transactions AGU* 77, 517-521.

Nyblade, A.A., Pollack, H.N., 1992. A gravity model for the lithosphere in western Kenya and northeastern Tanzania. *Tectonophysics 212*, 257-267.

Okada, Y., Yomamato, E., 1991. Dyke intrusion model for the 1989 seismovolcanic activity off Ito, central Japan. *J. Geophys. Res.* 96, 10361-10376.

Olsen, K.H. (Ed.), 1995. Continental Rifts: Evolution, Structure, Tectonics. *Elsevier Sci. B.V*: Amsterdam, 466p.

Olsen, K.H., Morgan, P., 1995. Progress in understanding continental rifts. *In*: Olsen, K.H. (Ed.), 1995. Continental Rifts: Evolution, Structure, Tectonics. *Elsevier Sci. B.V*: Amsterdam, 1-26 pp

Ota, Y., Chappell, J., Kelley, R., Yonekura, N., Matsumoto, E., Nishimura, T., 1992. Holocene coral reef terraces and coseismic uplift of HuonPenisula, Papua New Guinea. *Quat. Res.* 40, 177-188.

Park, R.G., 1997. Foundations of Structural Geology, 3d ed. *Chapman & Hall*: London.

Parsons, T., Thompson, G.A., 1991. The role of magma overpressure in suppressing earthquakes and topography: worldwide examples. *Science* 253**,** 1399-1402.

Parsons, T., Thompson, G.A., 1993. Does magmatism influence low-angle normal faulting? *Geology* 21**,** 247-250.

Pavlides, B.S., Zhang, P., Pantosti, D., 1999. Earthquakes, active faulting, and paleo-seismological studies for the reconstruction of seismic history of faults. *Tectonophysics* 308, 7-10.

Peacock, D.C.P., Sanderson, D.J., 1991. Displacements, segment linkage and relay ramps in normal fault zones. *J. Struct. Geol.* 13 (6), 721-733.

Peacock, D.C.P., Sanderson, D.J., 1994. Geometry and development of relay ramps in normal fault systems. *Bull. Amer. Assoc. Petrol. Geologists* 78, 147-165.

Peacock, D.C. P., Sanderson, D.J., 1996. Effects of propagation rate on displacement variations along faults. *J. Struct. Geol.* 18 (2/3), 311-320.

Peacock, D.C.P., 2001. The temporal relationship between joints and faults. *J. Struct. Geol.* 23, 329-341.

Peacock, D.C.P., Parfitt, E.A., 2001. Active relay ramps and normal fault propagation on Kilauea Volcano, Hawaii. *J. Struct. Geol.* 24, 729-742.

Peacock, D.C.P., Knipe, R.J., Sanderson, D.J., 2000a. Glossary of normal faults. *J. Struct. Geol.* 22:291-305.

Petit, J.P., 1987. Criteria for the sense of movement on fault surfaces in brittle rocks. *J. Struct. Geol.* 9, 597-608.

Petit, C., Ebinger, C., 2000. Flexure and mechanical behavior of cratonic lithosphere: Gravity models of the East African and Baikal rifts. *J. Geophy. Res*. 105 (B8), 19,151-19,162.

Philip, H., Avagyan, A., Karakhanian, A., Ritz, J., Rebai, S., 2001. Estimating slip rates and recurrence intervals for strong earthquakes along an intracontinental fault: example of the Pambak-Sevan-Sunik fault (Armenia). *Tectonophysics* 343, 205-232.

Piccardi, L., 2005. Paleoseismic evidence of legendary earthquakes: The apparition of Archangel Michael at Monte Sant'Angelo (Italy). *Tectonophysics* 408, 113-128

Pik, R., Marty, B., Carignan, J., Yirgu, G., Ayalew, T., 2008. Timing of East African Rift development in southern Ethiopia: Implication for mantle plume activity and evolution of topography. *Geology* 36 (2), 167-170.

Pinna, P., Muhongo, S., Mcharo, A., Le Goff, E., Deschamps, Y., Ralay, F., Milesi, J.P., 2004. 1:2,000,000 Geology and mineral map of Tanzania. *BRGM*: Orléans, France.

Pollard, D.D., Segall, P., 1987. Theoretical displacements and stresses near fractures in rock: with applications to faults, joints, veins, dikes and solution surfaces. In Atkinson, B.K., editor, Fracture Mechanics of Rocks. *Academic Press*: London, 277-349p

Pollard, D.D.P., Aydin, A., 1988. Progress in understanding jointing over the past century. *Bull. Geol. Soc. Am*er. 100, 1181-1204.

Prodehl, C., Fuchs, K., Mechie, J., 1997. Seismic-refraction studies of the Afro-Arabian Rift System-a brief review. *Tectonophysics* 278, 1-13

Rach, N.M., Rosendahl, B.R., 1989. Tectonic controls on the Speke Gulf. *J .Afr. Earth Sci*., 8, 471-488.

Ragan, D.M., 1973. Structural Geology. An Introduction to Geometrical Techniques. 2d ed. *John Wiles & Sons, Inc.*: Canada, 141-157p.

Rabus, B., Eineder, M., Roth, A., Bamler, B., 2003. The shuttle radar topography mission-a new class of digital elevation models acquired by space borne radar. ISPRS *J. Photog. and Rem. Sens*. 57, 241-262.

Reid, H.F., 1910. The elastic rebounce theory of earthquakes. *Bull. Dept. Geol. Unv. Cal.* 6, 413-444.

Ring, U., Betzler, C. Delvaux, D. 1992. Normal vs. strike-slip faulting during rift development in East Africa: the Malawi rift. *Geology* 20, 1015-1018.

Roberts, A. Yielding, G., 1994. Continental extensional tectonics. *In:* Hancock, P.L., editor, Continental deformation. *Pergamon Press*: UK, 223-250p

Roberts, G.P., Cowie, P., Papanikolaou, I., Michetti, A.M., 2004. Fault scaling relationships, deformation rates and seismic hazards: an example from the Lazio-Abruzzo Apennines, Central Italy. *J. Struct. Geol.* 26, 377-398.

Rogers, N., Mcdonald, R., Fitton, J.G., George, R., Smith, M., Barreiro, B., 2000. Two mantle plumes beneath the East African Rift system: Sr, Nd and Pb isotope evidence from Kenyan Rift basalts. *Earth and Plan. Sci. Letters* 176, 387-400.

Rosen, P.A., Hensley, S., Joughin, I.R., Li, F.K., Madsen, S.N., Rodriguez, E., Goldstein, R.M., 2000. Synthetic aperture radar interferometry. *Proc. IEEE*, *88,* 333-382.

Rosendahl, R.B., 1987. Architecture of continental rifts with special reference to East Africa. *Ann. Rev. Earth &Plan. Sci.* 15, 445-503.

Royden, L.H., Keen, C.E., VonHerzen, R.P., 1980. Continental margin subsidence and heat flow, important parameters in formation of petroleum hydrocarbon: *Amer. Ass. Petrol. Geologists Bull.* 64**,** 173-187.

Salah, M.G., Alsharhan, A.S., 1996. Structural influence on hydrocarbon entrapment in the Northwestern North Sea, Egypt. *Amer. Ass. Petrol. Geologists Bull.* 80**,** 101-118.

Sarna-Wojcicki, A.M., Meyer, C.E., Woodward, M.J., Lamothe, P.L., 1981. Composition of air-fall ash erupted on May 18, May 25, June 12, July 22, and August 17. In Lipman, P. W. & D. R. Mullineaux (eds), The 1980 Eruption of Mt. St. Helens. *U.S. Geol. Surv. Profess. Paper* 1250, 667-681.

Şengör, A.M.C., 1987a. Aulacogen, in Seyfert, C.K (ed.), the encyclopedia of structural geology and plate tectonics: *Van Nostrand Reinhold*: New York, 18-25p.

Shackleton, R.M., 1986. Precambrian collision tectonics in Africa. In: Coward, M.P. & Ries, A.C. (eds.) Collision Tectonics. *Geol. Soc. Spec. Publ.*, 19, 329-349.

Shah, E., 1986. Seismicity of Kenya (Ph.D. Thesis). *Univ. of Nairobi*: Kenya.

Shearer, P.M., 1999. Introduction to seismology. *Cambridge University Press*: UK, 260p.

Schwartz, D.P., Coppersmith, K.J., 1984. Fault behavior and characteristic earthquakes: Examples from Wasatch and San Andreas Fault zone. J. *Geophys. Res.* 89, 5681-5698.

Scholz, C.A., Rosendahl, B.R., Scott, D.L., 1990. Development of course-grained facies in lacustrine rift basins: examples from East Africa. *Geology* 18, 140-144.

Scholz, C.A., Moore Jr, T.C., Hutchinson, D.R., Golmshtok, A.Ja, Klitgord, K.D., Kurotchkin, A.G., 1998. Comparative sequence stratigraphy of low-latitude versus high-latitude lacustrine rift basins: seismic data examples from the East African and Baikal rifts. *Paleogeography, Paleoclimatology, Paleoecology* 140 (1-4), 401-420.

Sharav, A., 2003. Differential SAR Interferometry for crustal deformation study. MSc-thesis: *ITC*-The Netherlands, 66p.

Shimazaki K., Nakata, T., 1980. Time-predictable recurrence model for large earthquakes. *Geophys. Res. Lett.* 7, 279-282.

Shudofsky, G.N., 1985. Source mechanisms and focal depths of East African earthquakes using Raleigh-wave and body wave modeling. *Geophys. J. Roy. Astron. Soc.* 83, 563-614.

Sibson, R.H., 1986b. Earthquakes and lineament infrastructure. *Phil. Trans. Roy. Soc. London* A317, 63-79.

Sieh, K. Bursik, M., 1986. Most recent eruption of Mono Craters, Eastern Central California. *J. Geophys. Res.* 91, 12539-12571.

Sieh, K.E., Stuiver, M., Brillinger, D., 1989. A more precise chronology of earthquakes produced by the San Andreas Fault in Southern California: *J. Geophys. Res.* 94 (B1), 603-623.

Simiyu, S.M., Keller, G.R., 1997. An integrated analysis of lithospheric structure across the East African Plateau based on gravity anomalies and recent seismic studies. *Tectonophysics* 278, 191-313.

Skobelev, S.F., Hanon, M., Klerkx, J., Govorova, N.N., Lukina, N.V., Kazmin, V.G., 2004. Active faults of Africa: a review. *Tectonophysics* 380 (3), 131-137

Smith, M., 1994. Stratigraphic and structural constraints on mechanisms of active rifting in the Gregory rift, Kenya. *In*: Prodehl, C., Keller, G.R., Khan, M.A. (Eds.), Crustal and upper mantle structure of the Kenya rift. *Tectonopysics* 236, 3-22.

Smith, M., Mosley, P., 1993. Crustal heterogeneity and basement influence on the development of the Kenya Rift, East Africa. *Tectonics* 12, 591-606.

Sokoutis, D., Brun, J-P., Van Den Driessche, J., Pavlides, S., 1993. A major Oligo-Miocene detachment in southern Rhodope controlling north Aegean extension. J. Geol. Soc. London 150, 243-246.

Solonenko, V.P. 1977a. Seismogenic deformations and paleoseismological method, *In* Solonenko, V.P. (ed.) Seismic zonation of eastern Siberia and its geological and geophysical basis. *Nauka Pub. House*: Novosibirsk.

Sperner, B., Müller, B., Heidbach, O., Delvaux, D., Reinecker, J., Fuchs, K., 2003. Tectonic stress in the Earth's crust: advances in the World Stress Map project. *In*: Nieuwland, D. (Ed.) New Insights into Structural Interpretation and Modeling. *Geol. Soc. London Spec. Pub.* 212, 101-116.

Spooner, C.M., Hepworth, J.V., Fairbairn, H.W., 1970. Whole-rock Rb-Sr isotopic investigation of some East African granulites. *Geol. Mag.* 107, 511-522.

Steier, P., Rom, W., Puchegger, S., 2001. New methods and critical aspects in Bayesian mathematics for ^{14}C calibration. *Radiocarbon* 43, 373-380.

Strecker, M.R., Blisniuk, P.M., Eisbacher, G.H., 1990. Rotation of extension direction in the central Kenya rift. *Geology* 18, 299-302.

Stuiver, M., 1970. Oxygen and carbon isotope ratios of fresh-water carbonates as climatic indicators. *J. Geophys. Res.* 75, 5247-5257.

Stuiver, M., Reimer, P., 1993. Extended ^{14}C data base and revised CALIB 3.0 ^{14}C age calibration program 1993. *Radiocarbon* 35, 215-230.

Swanson, D.A., Jackson, D.B., Koyanagi, R.Y., Wright, T.L., 1976a. The February 1969 East Rift eruption of Kilauea volcano, Hawaii. *U. S. Geol. Surv. Prof. Paper* 891, 1-30.

Sykes, L.R., 1970. Focal mechanism solutions for earthquakes along the world rift system. *Bull. Seismol. Sot. Am.* 60, 1749-1752.

Tanz. Gov. Internal reports, 1983. Preliminary report on the assessment of the reported fault in the Lakes Manyara-Natron area, 10p.

Tentler, T., Mazzoli, S., 2005. Architecture of normal faults in the rift zone of central north Iceland. *J. Struct. Geol.* 27, 1721-1739.

Tessema, A., Antoine, L.A.G., 2004. Processing and interpretation of the gravity field of the East African Rift: implication for crustal extension. *Tectonopysics* 394, 87-110.

Tesha, A.L., Nyblade, A.A., Keller, G.R., Doser, D.I., 1997. Rift localization in suture-thickened crust: evidence from Bouguer gravity anomalies in northeastern Tanzanian, East Africa. *In*: K. Fuchs, R. Altherr, B. Muller and C. Prodehl, Editors; Stress and Stress Release in the Lithosphere, *Tectonophysics* 278, 315-328.

Theunissen, K., Klerkx, J., Melnikov, A., Mruma, A., 1996. Mechanisms of Inheritance of rift faulting in the western branch of East African Rift, Tanzania. *Tectonics* 15 (4), 776-790.

Tongue, J., Maguire, P., Burton, P., 1994. An earthquake study in the Lake Baringo basin of the Central Kenya Rift. *Tectonophysics* 236, 151-164.

Vanneste, K., Meghraoui, M., Camelbeeck, T., 1999. Late Quaternary earthquake-related soft-sediment deformation along the Belgian portion of the Feldbiss Fault, Lower Rhine Graben system. *Tectonophysics* 309, 57-79.

Vermilye, J.M, Scholz, C.H., 1999. Fault propagation and segmentation: insight from the microstructural examination of a small fault. *J. Struct. Geol.* 21, 1623-1636.

Vink, G.E., Morgan, W.J.S., Zhao, W., 1984. Preferential rifting of continents: a source of displaced terranes. *J. Geophys. Res.* 89**,** 10072-10076.

Vogt, M., Kröner, A., Poller, U., Sommer, H., Muhongo, S. and Wingate, M. T. D., 2006. Archaean and Palaeoproterozoic gneisses reworked during a Neoproterozoic (Pan-African high-grade event in the Mozambique belt of East Africa: Structural relationships and zircon ages from Kidatu area, central Tanzania. *J. Afr. Earth Sci.* 45(2), 139-155.

Wades, F.B., Oates, F., 1938. An explanation of degree sheet no. 52. *Dodoma-Geological Survey of Tanganyika* 17, 1-60.

Wagner, G.S. Langston, C.H., 1988. East African earthquake body wave inversion with implications for continental structure and deformation. *J. Geophys*. 94, 503-518.

Walker, B.G., 1967. Springs of deep -seated origin in Tanzania. *Mineral Res. Div. Tanz. Rep. BGW*/4.

Walker, B.G., 1969. Springs of deep seated origin in Tanzania. *Proc. XXIII Intern. Geol. Cong.* 19, 171-180.

Wallace, R.E., 1951. Geometry of shearing stress and relation to faulting, *J. Geol.* 59, 118-130.

Wallace, R.E., 1970. Earthquake recurrence intervals on the San Andreas Fault. *Geol. Soc. Amer. Bull.* 81, 2875-2890.

Wallace, R.E., 1977. Profiles and ages of young fault scarps, north-central Nevada, *Geol. Soc. Amer. Bull.* 88, 1267-1281.

Walsh, J.J., Bailey, W.R., Childs, C., Nicol, A., Bonson, C.G., 2003. Formation of segmented normal faults: a 3-D perspective. *J. Struct. Geol.* 25, 1251-1262.

Walsh, J.J., Watterson, J., 1987. Distributions of cumulative displacement and seismic slip on a single normal fault surface. *J. Struct. Geol.* 9, 1039-1046.

Weeraratne, D.S., Forsyth, D.W., Fischer, K.M., Nyblade, A.A, 2003. Evidence for an upper mantle plume beneath the Tanzanian craton from Rayleigh wave tomography. *J. Geophysical Res.* 108 (B9), 2427 doi:10.1029/2002JB002273.

Wehmiller, J.F., Belknap, D.F., Boutin, B.S., Mirecki, J.E., Rahaim, S.D. York, L.L. 1988. A review of the aminostratigraphy of Quaternary mollusks from United States Atlantic Coastal Plain sites; in Easterbrook, D.J., ed., Dating Quaternary Sediments. *Geol. Soc. Amer. Spec. Paper* 227, 69-110.

Wells, D.L., Coppersmith, K.J., 1994. New empirical relations among magnitude, rupture length, rupture width, rupture area and surface displacement. *Bull. Geol. Seism. Soc. Am*. 84, 974-1002.

Wendt, I., Besang, C., Hare, W., Kreuzer, H., Lend, H., Müller, P., 1972. Age determinations of granitic intrusions and metamorphic events in the early Precambrian of Tanzania, *Proceedings of the 24th Intern. Geol. Cong. Montreal I,* 295-314.

Wernicke, B.P., 1991. The fluid crustal layer and its implications for continental dynamics, in Salisbury, M.H., Fountain, D.M. (eds). Exposed cross-section of the continental crust. *Kluwer*: Dordrecht, 509-544p.

Wernicke, B., 1981. Low-angle normal faults in the Basin and Range province: nappe tectonics in a extending orogen. *Nature* 291, 645-647.

Wernicke, B., 1985. Uniform-sense normal simple shear of the continental lithosphere. *Can. J. Earth Sci.* 22 (1), 108-125.

Wescott, W.A., Diggens, J.N., 1998. Depositional history and stratigraphic evolution of the Sakamena Group (Middle Karoo Supergroup) in the southern Morondava Basin, Madagascar. *J. Afr. Earth Sci*. 27 (3/4), 461-479.

Westgate, J.A., Gorton, M.P., 1981. Correlation techniques in tephra studies. *In*: S. Self and R.S.J. Sparks, Editors, *Tephra studies*: Reidel, Dordrecht, 73-94 pp.

Yamaguchi, D.K., Hoblitt, R.P., 1995. Tree-ring dating of pre-1980 volcanic flowage deposits at Mount St. Helens, Washington. *Geol. Soc. Am. Bull* 107, 1077-1093.

Yin, A., 1989. Origin of regional rooted low-angle normal faults: A mechanical model and its tectonic implications. *Tectonics* 8, 469-482.

Young, M.J., Gawthorpe, R. L., Hardy, S., 2001. Growth and Linkage of a segment normal fault zone; the Late Jurassic Murchison-Statfjord North Fault, northern North Sea. *J. Struct. Geol.* 23, 1993-1952.

Zhang, P., Mao, F., Slemmons, D.B., 1998. Rupture terminations and size of segment boundaries from historical earthquake ruptures in the Basin and Range Province. *Tectonopysics* 308, 37-52.

Zeyen, H., Volker, F., Wehrle, V., Fuchs, K., Sobolev, S.V., 1997. Styles of Continental rifting: Crust-mantle detachment and mantle plumes. *Tectonopysics* 278, 329-352

Ziegler, P., 1992. Plate tectonics, plate moving mechanisms and rifting. *Tectonics* 215, 9-34.

Zoback, M.L., 1992. First- and second-order patterns of stress in the lithosphere: the World Stress Map project. *J. Geophys. Res.* 97, 11703-11728.

Appendix 1

The SRTM-derived profiles in the Dodoma area

The SRTM-derived profiles in the Dodoma area

All profiles established from SRTM-data in the Dodoma area are enclosed on a separate data disk provided with this thesis.

Each profile has four (4) columns:
- column 1 = distance (m);
- column 2 = northings (in UTM 36, ARC1960 projection);
- column 3 = eastings (in UTM 36, ARC1960 projection);
- column 4 = elevation (m).

The nomenclature of the profiles is as in Table 5.1. It should be noted that few profiles which do not appear in Table 5.1 do appear here because they were not conclusive enough to be presented in Table 5.1.

Appendix 2

Thermal springs in the Dodoma area

Thermal springs in the Dodoma area

A2.1 Spatial relationship

A2.1.1 The Mponde hot springs

The Mponde hot springs are located within the Mponde Segment 1. Approximate location of the springs is about 5°18'S, 35°05'E. Average temperature is 42°C. Nitrogen/helium gas flows at a rate of about 200 l/h. Total salinity is about 2000 ppm, NaCl being the major salt.

The springs are controlled by recent block faulting in the area. The gas emitted from the vents contains 10.2 % helium (Fawley, 1957; Walker, 1967; Macheyeki et al., 2008b).

A2.1.2 The Hika (Saranda) hot springs

The Hika (Saranda) hot springs are located at Saranda mid fault segment. The approximate location of these springs is 5°35'S, 35°00'E. Average rate of flow of the water (which is rich in $NaHCO_3$) is about 1100 g/h. The temperature is 28°C. Nitrogen/helium gas flows at the rate of about 5 l/h. Total salinity is 320 ppm.

The regional location of these springs might be related to recent block faulting in the area, although it is also thought that these springs are controlled by the intersection of basic dykes and the foliation in the underlying gneisses (Walker, 1967).

A2.1.3 The Nkambala (Kilimatinde) saline/hot springs

Two saline/hot springs are located on the fault scarp at the Nkambala segment at about 5°50'S, 35°00'E. NaCl is the dominant solute.

A2.1.4 The Gonga hot springs

The Gonga hot springs are located within the Bubu river. They are located at about 5°20'S, 35°28'E. Average temperature is 45°C. The rate of flow is about 1000 g/h and characterized by slightly acid sulphate-chloride water. Gas flow (nitrogen/helium gas) is about 15 l/h.

The setting of the springs is probably controlled by the intersection of a basic dyke with the foliation of the underlying migmatite gneisses. A recent rift fault passes within a

kilometer of the springs. The rates of flow of water and gas from the springs are estimated to be not less than 500 g/h. The gas contains about 8 % helium (Walker, 1967; Macheyeki et al., 2008a; 2008b).

A2.1.5 Hot springs at Makanda fault (Segment A)

The hot springs at Makanda fault (Segment A) are located at about 6°05'S, 35°30'E, close to the Kigwe railway station. Several saline springs occur near Kigwe to the east of the Bahi depression. The concentration of NaCl in some of the waters is suggestive of deep-seated origin.

A2.1.6 The Southwestern segment (Ikasi) hot springs

The saline/hot water spring field along the Bahi fault is located at the southernmost part of the fault, at about 6°15'S, 35°10'E. A number of natural and artificial brine springs occur near this place (famously known as Ikasi). The salinity is variable but approaches 100,000 ppm, in some occurrences, NaCl being the dominant salt. Although the temperature of the brines at the surface is normal, rapid increases with depth were noted in boreholes in the area (Lambert, 1954; Fawley, 1957; Walker, 1967).

A2.2 Compositional data

Table A2.1 - Compositional data for some hot/saline springs in the Dodoma area (After Walker, 1967). KMT stands for Kilimatinde.

Spring Name	Gonga	Mponde		Saranda (Hika)	Kondoa	Kigwe	Ikasi	KMT
Location	Latitude	5°20'S	5°18'S	5°35'S	4°55'S	6°05'S	6°15'S	5°50'S
	Longitude	35°28'E	35°05'E	35°00'E	35°48'E	35°30'E	35°10'E	35°00'E
Temperature °C	45		42	28	25			
Water flow (g/h)	1000	***		1,100	3,000			
Gas flow (l/h)	15		200	5	100			
Water composition (ppm)								
NaCl		211	1,189	89	193			
Na_2CO_3			48					
$NaHCO_3$		160	264	150				
Na_2SO_4		220	530	49	58			
NaF		11	24	11	2			
KCl			11					
K_2SO_4								
$CaCl_2$								
$CaCO_3$								

$Ca(HOO_3)_2$	218	20	52	246			
$CaSO_4$							
$MgCO_3$							
$Mg(HOO_3)_2$	24		5	185			
SiO_2	50		50	60			
P^H	6.9	9.5	8.1	7.5			
Gas composition (vol. %)							
CO_2	1.2	0.2	0.6	3.9			
H_2S	0.5	trace	trace				
CO	0.4		0.2				
O_2		0.2		2.7			
H_2							
CH_4, etc	2.4	0.4	2.9				
He	8.9	10.2	7.1	0.3			
Ar (Kr, Ne,							
Xe)		0.5		1			
N_2	86.6	87.5	89.2	91.6			
Prob. Related geol. features	Block faulting						

Appendix 3

Fault-slip data in the Dodoma area

05.06535°S
Mponde fault_Segment _1 035.03392°E

Fault-slip data		Input row data (User format)											
			Plane		Line		Slip	Conf.	Weight	Activ.	Striae	Subset	Comments
Id	Format	Type	Ori1A	Ori1B	Ori2A	Ori2B	Sense	Level	Factor	Type	Intens.	Index	
A070507-3-001	11	4	73	278			M	P	1,0	2	0	1,0	Pegmatictic GNT rock, in a river trench
A070507-3-002	11	4	87	253			M	P	1,0	2	0	1,0	Pegmatictic GNT rock, in a river trench
A070507-3-003	11	4	53	320			M	P	1,0	2	0	1,0	Pegmatictic GNT rock, in a river trench
A070507-3-004	11	4	76	243			M	P	1,0	1	0	1,0	Pegmatictic GNT rock, in a river trench
A070507-3-005	11	1	61	166	5	253	D	P	2,0	2	2	2,0	sliken sides?
A070507-3-006	11	4	47	329			M	P	1,0	2	0	1,0	
A070507-3-007	11	4	87	34			M	P	2,0	2	0	1,0	
A070507-3-008	11	4	57	283			M	P	1,0	2	0	1,0	
A070507-3-009	11	4	72	165			M	P	1,0	2	0	1,0	
A070507-3-010	11	4	82	169			M	P	1,0	2	0	3,0	Epidotized, old surface
A070507-3-011	11	4	70	190			M	P	1,0	2	0	1,0	Hw pegmatitic rock
A070507-3-012	11	4	80	258			M	P	1,0	2	0	1,0	Hw pegmatoc rock
A070507-3-013	11	4	68	165			M	P	1,0	2	0	1,0	
A070507-3-014	11	4	46	186			M	P	1,0	1	0	1,0	
A070507-3-015	11	4	57	181			M	P	1,0	1	0	1,0	
A070507-3-016	11	4	80	334			M	P	1,0	2	0	1,0	
A070507-3-017	11	4	60	231			M	P	1,0	1	0	1,0	
A070507-3-018	11	4	50	340			M	P	1,0	1	0	1,0	Small fracture
A070507-3-019	11	4	63	194			M	P	1,0	1	0	1,0	Large fracture
A070507-3-020	11	4	53	248			M	P	1,0	1	0	1,0	Large fracture
A070507-3-021	11	4	40	252			M	P	1,0	1	0	1,0	Large fracture
A070507-3-022	11	4	80	87			M	P	1,0	1	0	1,0	Large fracture
A070507-3-023	11	4	82	256			M	P	2,0	1	0	1,0	Large fracture
A070507-3-024	11	4	70	177			M	P	2,0	2	0	1,0	Large fracture
A070507-3-025	11	4	32	197			M	P	2,0	2	0	1,0	Large fracture
A070507-3-026	11	4	82	170			M	P	2,0	2	0	1,0	Large fracture
A070507-3-027	11	4	52	198			M	P	2,0	2	0	1,0	fracture, small
A070507-3-028	11	4	64	187			M	P	2,0	2	0	1,0	small fracture
A070507-3-029	11	4	45	214			M	P	2,0	2	0	1,0	
A070507-3-030	11	4	70	82			M	P	3,0	2	0	1,0	large surface, fault zone?
A070507-3-031	11	4	63	185			M	P	2,0	2	0	1,0	large surface, fault zone?, conjugate system
A070507-3-032	11	4	44	174			M	P	2,0	2	0	1,0	
A070507-3-033	11	4	87	289			M	P	2,0	2	0	2,0	
A070507-3-034	11	4	60	199			M	P	2,0	2	0	2,0	
A100507-05-001	11	4	74	351			M	X	1,0	2	0	1,0	Silicified fracture (vein on granite)
A100507-05-002	11	4	53	227			M	X	1,0	2	0	1,0	not real same fracture
A100507-05-003	11	4	65	341			M	X	1,0	2	0	1,0	
A100507-05-004	11	4	89	113			M	X	1,0	2	0	1,0	Recent fracture/fracture plane
A100507-05-005	11	4	84	272			M	X	1,0	2	0	1,0	Recent fracture/fracture plane
A100507-05-006	11	4	86	165			M	X	1,0	2	0	1,0	Prominent fault/fracture (recent)
A100507-05-007	11	4	52	329			M	X	1,0	2	0	1,0	Non mineralized plane-boulder/insitu?
A100507-05-008	11	4	72	182			M	X	1,0	2	0	1,0	Non mineralized plane-boulder/insitu?
A100507-05-009	11	4	70	191			M	X	1,0	2	0	1,0	Non mineralized plane-boulder/insitu?

Mponde fault_Segment 2 **05.15173°S 035.05631°E**

Fault-slip data		Input row data (User format)											
			Plane		Line		Slip	Conf.	Weight	Activ.	Striae	Subset	Comments
Id	Format	Type	Ori1A	Ori1B	Ori2A	Ori2B	Sense	Level	Factor	Type	Intens.	Index	
A100507-05-001	11	4	74	351			X	X	1,0	2	0		Silicified fracture (vein on granite)
A100507-05-002	11	4	53	227			X	X	1,0	2	0		not real same fracture
A100507-05-003	11	4	65	341			X	X	1,0	2	0		
A100507-05-004	11	4	89	113			X	X	1,0	2	0		Recent fracture/fracture plane
A100507-05-005	11	4	84	272			X	X	1,0	2	0		Recent fracture/fracture plane
A100507-05-006	11	4	86	165			X	X	1,0	2	0		Prominent fault/fracture (recent)
A100507-05-007	11	4	52	329			X	X	1,0	2	0		Non mineralized plane-boulder/insitu?
A100507-05-008	11	4	72	182			X	X	1,0	2	0		Non mineralized plane-boulder/insitu?
A100507-05-009	11	4	70	191			X	X	1,0	2	0		Non mineralized plane-boulder/insitu?

Saranda_Mid Segment **05.67984°S 034.98660°E**

Fault-slip data		Input row data (User format)											
			Plane		Line		Slip	Conf.	Weight	Activ.	Striae	Subset	Comments
Id	Format	Type	Ori1A	Ori1B	Ori2A	Ori2B	Sense	Level	Factor	Type	Intens.	Index	
ND04-001	11	4	50	162			S	P	3,0	0	0		Smoothed fracture planes
ND04-002	11	4	38	292			S	P	3,0	0	0		
ND04-003	11	4	42	29			S	P	3,0	0	0		
ND04-004	11	4	55	156			S	P	3,0	0	0		
ND04-005	11	4	59	148			S	P	3,0	0	0		
ND04-006	11	4	70	159			S	P	3,0	0	0		
ND04-007	11	4	45	157			S	P	3,0	0	0		
ND04-008	11	4	53	147			S	P	3,0	0	0		
ND04-009	11	4	81	160			S	P	3,0	0	0		
ND04-010	11	4	80	178			S	P	3,0	0	0		
ND04-011	11	4	58	145			S	P	3,0	0	0		
ND04-012	11	4	76	144			S	P	3,0	0	0		
ND04-013	11	4	81	63			S	P	3,0	0	0		
ND04-014	11	4	70	282			S	P	3,0	0	0		
ND04-015	11	4	60	128			S	P	3,0	0	0		
A070507-2-001	11	4	64	331			M	X	1,0	1	0		joints
A070507-2-002	11	4	88	269			M	X	1,0	1	0		joints
A080507-1-003	11	4	50	167			M	X	3,0	1	0		Fault plane
A080507-1-004	11	4	87	249			M	X	3,0	1	0		
A080507-1-005	11	4	81	73			M	X	2,0	1	0		joints
A080507-1-006	11	4	69	69			M	X	2,0	1	0		joint
A080507-1-007	11	4	88	211			M	X	2,0	1	0		joint
A080507-1-008	11	4	74	228			M	X	2,0	1	0		prominent joint
A080507-1-009	11	4	88	169			M	X	2,0	1	0		joint
A080507-1-010	11	1	40	142	34	104	N	C	3,0	1	3		mostlikely by WATER,
A080507-1-011	11	4	54	132			M	X	2,0	1	0		
A080507-1-012	11	2	76	226	46	102		P	1,0	1	0		
A080507-1-013	11	4	74	113			M	X	1,0	1	0		

Bubu fault_Gonga segment at Gonga hot spring field

Fault-slip data		Input row data (User format)											
			Plane		Line		Slip	Conf.	Weight	Activ.	Striae	Subset	Comments
Id	Format	Type	Ori1A	Ori1B	Ori2A	Ori2B	Sense	Level	Factor	Type	Intens.	Index	
ND06-001	11	1	59	147	32	215	N	C	3	0	0		Curved fracture with slip lines and clear sense of movement
ND06-002	11	1	60	155	39	217	N	C	3	1	2		
ND06-003	11	1	66	148	34	220	N	C	3	1	2		
ND06-004	11	1	86	111	6	21	D	P	6	1	2		Planar fracture controlling spring outflow
ND06-005	11	1	85	117	6	28	D	P	6	1	2		
ND06-006	11	1	13	245	12	262	I	S	4	1	2		Striae on flat surface reactivating quartz vein
ND06-007	11	1	9	247	8	247	I	S	4	1	2		
ND06-008	11	4	89	60			S	P	4	1	0		Planar fractures
ND06-009	11	4	80	175			S	P	4	1	0		
ND06-010	11	4	70	22			S	P	4	1	0		
ND06-011	11	4	86	88			S	P	4	1	0		
ND06-012	11	4	85	40			S	P	4	1	0		
ND06-013	11	4	85	38			S	P	4	1	0		
ND06-014	11	4	87	34			S	P	4	1	0		
ND06-015	11	4	88	56			S	P	4	1	0		
ND06-016	11	4	80	40			S	P	6	1	0		Major join set
ND06-017	11	4	78	286			S	P	3	1	0		minor joints associated
ND06-018	11	4	88	254			S	P	3	1	0		
ND06-019	11	4	85	99			S	P	4	1	0		ND06-019 -> 023: Same block
ND06-020	11	4	84	64			S	P	4	1	0		ND06-019 -> 023: Same block
ND06-021	11	4	89	236			S	P	4	1	0		ND06-019 -> 023: Same block
ND06-022	11	4	88	96			S	P	4	1	0		ND06-019 -> 023: Same block
ND06-023	11	4	85	212			S	P	4	1	0		ND06-019 -> 023: Same block
ND06-024	11	4	73	53			S	P	4	1	0		With greenish filling
ND06-025	11	4	80	83			S	P	7	1	0		
ND06-026	11	4	87	123			S	P	4	1	0		
ND06-027	11	4	84	76			S	P	7	1	0		
ND06-028	11	4	85	74			S	P	7	1	0		
ND06-029	11	4	89	74			S	P	7	1	0		
ND06-030	11	4	80	132			S	P	4	1	0		
ND06-031	11	4	80	265			S	P	4	1	0		
ND06-032	11	4	85	88			S	P	7	1	0		Dominant fracture (longest)

Bubu fault_Gonga segment at Gonga hot spring field

Fault-slip data		Input row data (User format)											
			Plane		Line		Slip	Conf.	Weight	Activ.	Striae	Subset	Comments
Id	Format	Type	Ori1A	Ori1B	Ori2A	Ori2B	Sense	Level	Factor	Type	Intens.	Index	
ND06-033	11	4	85	74			S	P	7	1	0		
ND06-034	11	4	80	42			S	P	3	1	0		minor fracture
ND06-035	11	4	83	83			S	P	7	1	0		
ND06-036	11	4	85	6			S	P	8	1	0		Large transverse fracture
ND06-037	11	4	76	153			S	P	5	1	0		
ND06-038	11	4	88	163			S	P	5	1	0		
ND06-039	11	4	87	340			S	P	8	1	0		Large fracture parallel to river
ND06-040	11	4	89	55			S	P	4	1	0		
ND06-041	11	4	85	43			S	P	4	1	0		
ND06-042	11	4	89	56			S	P	4	1	0		
ND06-043	11	1	86	52	1	142	D	P	4	1	0		
ND06-044	11	1	86	273	54	358	D	P	4	1	0		
ND06-045	11	4	86	235			S	P	4	1	0		
ND06-046	11	4	85	54			S	P	4	1	0		
ND06-047	11	4	80	310			S	P	4	1	0		
ND06-048	11	4	82	91			S	P	4	1	0		
ND06-049	11	4	80	244			S	P	4	1	0		
ND06-050	11	4	76	68			S	P	4	1	0		
ND06-051	11	4	80	80			S	P	4	1	0		
ND06-052	11	1	84	55	11	326	D	P	4	1	0		
ND06-053	11	4	82	68			S	P	4	1	0		
ND06-054	11	4	85	68			S	P	4	1	0		
ND06-055	11	4	83	70			S	P	4	1	0		
ND06-056	11	4	85	73			S	P	4	1	0		
ND06-057	11	4	86	73			S	P	4	1	0		
ND06-058	11	4	85	246			S	P	4	1	0		

Bubu fault_Gonga segment at Magungu

Fault-slip data		Input row data (User format)											
			Plane		Line		Slip	Conf.	Weight	Activ.	Striae	Subset	Comments
Id	Format	Type	Ori1A	Ori1B	Ori2A	Ori2B	Sense	Level	Factor	Type	Intens.	Index	
BMAG01	11	4	65	44			X	X	2,0	0	0		Fracture on GNT gneisse
BMAG02	11	4	66	127			X	X	2,0	0	0		Fracture on GNT gneisse
BMAG03	11	4	83	310			X	X	2,0	0	0		Fracture on GNT gneisse
BMAG04	11	4	86	132			X	X	2,0	0	0		Fracture on GNT gneisse
BMAG05	11	4	70	149			X	X	2,0	0	0		
BMAG06	11	4	75	141			X	X	2,0	0	0		
BMAG07	11	4	79	44			X	X	2,0	0	0		
BMAG08	11	4	70	127			X	X	2,0	0	0		

Bubu fault_Gonga segment at Magungu

Fault-slip data	Input row data (User format)												
			Plane		Line		Slip	Conf.	Weight	Activ.	Striae	Subset	Comments
Id	Format	Type	Ori1A	Ori1B	Ori2A	Ori2B	Sense	Level	Factor	Type	Intens.	Index	
BMAG09	11	4	60	25			X	X	2,0	0	0		
BMAG10	11	4	62	148			X	X	2,0	0	0		
BMAG12	11	4	89	233			X	X	2,0	0	0		
BMAG13	11	4	66	47			X	X	2,0	0	0		
BMAG14	11	4	86	301			X	X	2,0	0	0		

Bubu fault at Makutupora segment

Fault-slip data		Input row data (User format)											
			Plane		Line		Slip	Conf.	Weight	Activ.	Striae	Subset	Comments
Id	Format	Type	Ori1A	Ori1B	Ori2A	Ori2B	Sense	Level	Factor	Type	Intens.	Index	
A080507-1-001	11	4	22	77			M	X	3,0	3	0		K-feldspar gneiss
A080507-1-002	11	4	57	30			M	X	3,0	3	0		
A080507-1-003	11	4	63	28			M	X	3,0	3	0		
A080507-1-004	11	4	62	185			M	X	3,0	3	0		
A080507-1-005	11	4	54	238			M	X	3,0	3	0		
A080507-1-006	11	4	65	178			M	X	3,0	3	0		
A080507-1-007	11	1	60	223	30	152	X	X	2,0	2	0		Hw, basement, K-feld
A080507-1-008	11	4	79	138			M	X	3,0	3	0		
A080507-1-009	11	4	82	58			M	X	3,0	3	0		
A080507-1-010	11	4	39	292			M	X	3,0	3	0		
A080507-1-011	11	4	80	218			M	X	3,0	3	0		
A080507-1-012	11	1	86	130	22	218	D	C	3,0	2	2		deep seated, FeO
A080507-1-013	11	1	83	263	1	173	D	P	3,0	2	1		
A080507-1-014	11	1	88	206	8	296	D	P	3,0	2	1		On basement and on soild, reactivated in the same trend
A080507-1-015	11	1	60	211	15	293	D	P	3,0	2	1		
A080507-1-016	11	4	65	154			M	X	3,0	2	0		
A080507-1-017	11	4	84	164			M	X	3,0	2	0		
A080507-1-018	11	1	88	210	2	120	D	P	1,0	2	1		
A080507-1-019	11	1	88	38	45	126	X	X	1,0	2	1		old fault plane
A080507-1-020	11	4	86	164			M	X	1,0	2	0		sub-orthogonal to prev. plane,
A080507-1-021	11	1	88	28	14	117	D	P	1,0	2	2		As above
A080507-1-022	11	4	82	44			M	X	2,0	2	0		
A080507-1-023	11	4	50	256			M	X	2,0	2	0		
A080507-1-024	11	4	49	244			M	X	2,0	2	0		
A080507-1-025	11	4	3	192			M	X	2,0	3	0		
A080507-1-026	11	4	73	238			M	X	2,0	2	0		
A080507-1-027	11	4	80	234			M	X	3,0	2	0		Kaolinize surface
A080507-1-028	11	1	69	191	7	104	D	P	2,0	2	2		EARS related
ND03-001	11	4	25	98			S	C	4,0	0	0		A/ Lowest excavation: shear joints (smooth surfaces)
ND03-002	11	4	30	96			S	C	4,0	0	0		
ND03-003	11	4	25	111			S	C	4,0	0	0		
ND03-004	11	4	28	114			S	C	4,0	0	0		
ND03-005	11	4	35	49			S	C	4,0	0	0		
ND03-006	11	4	28	88			S	C	4,0	0	0		
ND03-007	11	1	39	231	9	152	S	P	3,0	0	0		Surfaces with reddish coating and slip lines
ND03-008	11	1	56	202	28	133	D	P	3,0	0	0		
ND03-009	11	1	70	210	25	290	S	P	3,0	0	0		

Continued on next page

Continued from previous page

ND03-010	11	1	59	254	13	336	S	P	3,0	0	0	
ND03-011	11	1	55	217	3	129	S	P	3,0	0	0	
ND03-012	11	1	58	170	45	118	X	X	3,0	0	0	iron + chlorite
ND03-013	11	1	22	219	22	218	X	X	3,0	0	0	
ND03-014	11	4	78	253			S	C	3,0	0	0	
ND03-015	11	4	53	130			S	C	3,0	0	0	epidotized + iron oxyde
ND03-016	11	4	72	236			S	C	3,0	0	0	
ND03-017	11	4	69	292			S	C	3,0	0	0	
ND03-018	11	1	39	292	28	242	X	X	6,0	0	0	2m straight & smoothed plane, well exp. slip lines, traces of Chl
ND03-019	11	2	71	169	78	236		P	4,0	1	0	B/ 2nd excav. major fracture systems in weathered GNT
ND03-020	11	2	83	166	72	43		P	4,0	1	0	Smooth surfaces with Chl
ND03-021	11	2	82	167	64	232		P	4,0	1	0	
ND03-022	11	4	64	260			S	C	3,0	0	0	
ND03-023	11	4	73	208			S	C	3,0	0	0	
ND03-024	11	4	79	178			S	C	3,0	0	0	
ND03-025	11	1	46	216	15	292	S	S	3,0	0	0	
ND03-026	11	1	50	161	13	82	X	X	3,0	0	0	
ND03-027	11	1	88	22	8	112	X	X	5,0	0	0	C/ 3rd excavation: also fractures in weathered GNT
ND03-028	11	4	85	8			S	C	3,0	0	0	
ND03-029	11	4	85	278			S	C	3,0	0	0	
ND03-030	11	1	35	30	22	83	I	C	4,0	0	0	Reverse certain
ND03-031	11	1	39	31	25	86	I	C	4,0	0	0	ND02_30 -> 35: all from same plane system
ND03-032	11	1	50	62	34	117	I	C	4,0	0	0	
ND03-033	11	1	36	30	30	68	I	C	4,0	0	0	
ND03-034	11	1	42	22	26	79	I	C	4,0	0	0	
ND03-035	11	1	53	26	22	98	I	C	4,0	0	0	
ND03-036	11	4	64	104			S	C	2,0	0	0	
ND03-037	11	1	55	16	40	322	X	X	2,0	0	0	Strie ??
ND03-038	11	1	89	8	54	279	X	X	2,0	0	0	Strie ??
ND03-039	11	1	89	236	13	326	S	P	5,0	0	0	
ND03-040	11	4	85	103			S	P	5,0	0	0	

Makanda fault_Segment D **5.58893°S 35.63585°E**

Fault-slip data		Input row data (User format)											
			Plane		Line		Slip	Conf.	Weight	Activ.	Striae	Subset	Comments
Id	Format	Type	Ori1A	Ori1B	Ori2A	Ori2B	Sense	Level	Factor	Type	Intens.	Index	
A110507-6-001	11	4	85	256			M	X	2	2	0		Hw gneisse, sericitized, prominent joint set
A110507-6-002	11	4	83	218			M	X	2	2	0		Hw gneisse, sericitized, prominent joint set
A110507-6-003	11	4	70	62			M	X	2	2	0		Coated with Fe-oxide
A110507-6-004	11	4	43	31			M	X	2	2	0		Coated with Fe-oxide
A110507-6-005	11	1	85	323	36	237	S	X	3	2	0		Recent, on GNT, prominent fracture
A110507-6-006	11	4	89	240			M	X	3	2	0		Recent, on GNT, prominent fracture
A110507-6-007	11	4	86	94			M	X	3	2	0		asa, rel.small fracture
A110507-6-008	11	4	87	242			M	X	3	2	0		
A110507-6-009	11	4	88	169			M	X	3	2	0		
A110507-6-010	11	4	89	150			M	X	3	2	0		
A110507-6-011	11	4	87	154			M	X	3	2	0		
A110507-6-012	11	4	63	221			M	X	3	2	0		Reactivated, silicified vein

Hombolo fault_Dam segment

Fault-slip data		Input row data (User format)											
			Plane		Line		Slip	Conf.	Weight	Activ.	Striae	Subset	Comments
Id	Format	Type	Ori1A	Ori1B	Ori2A	Ori2B	Sense	Level	Factor	Type	Intens.	Index	
HOMB01	11	4	88	55			F	C	4	0	0		Foliation in amphibolite schist
HOMB02	11	4	84	27			F	C	4	0	0		Amphibolite - granite contact
HOMB03	11	4	85	22			F	C	4	0	0		
HOMB04	11	4	89	15			F	C	4	0	0		Foliation
HOMB05	11	4	78	75			F	X	4	0	0		
HOMB06	11	4	85	110			X	X	4	0	0		Large fracture system ("dry" fractures)
HOMB07	11	4	82	112			X	X	4	0	0		
HOMB08	11	4	72	105			X	X	4	0	0		Smaller fractures
HOMB09	11	4	88	104			X	X	4	0	0		
HOMB10	11	4	88	122			X	X	4	0	0		
HOMB11	11	1	10	264	9	294	I	S	4	0	0		Qz-Chlorite deep slickensides
HOMB12	11	1	5	199	1	111	I	S	4	0	0		
HOMB13	11	1	6	278	5	309	I	C	5	0	0		Riedels, lunate fractures, with striae
HOMB14	11	1	18	283	15	312	I	C	5	0	0		
HOMB15	11	1	15	298	15	307	I	C	5	0	0		
HOMB16	11	1	18	308	18	317	I	C	5	0	0		
HOMB17	11	1	20	300	20	312	I	C	5	0	0		Qz accretion steps
HOMB18	11	1	5	286	5	303	I	X	5	0	0		
HOMB19	11	1	2	355	1	304	I	C	5	0	0		
HOMB20	11	1	18	289	17	311	I	C	5	0	0		
HOMB21	11	4	84	30			S	C	5	0	0		Shear joint with chlorite
HOMB22	11	1	75	210	61	271	N	P	3	0	0		With iron coating

Hombolo fault_Dam segment

Fault-slip data		Input row data (User format)											
			Plane		Line		Slip	Conf.	Weight	Activ.	Striae	Subset	Comments
Id	Format	Type	Ori1A	Ori1B	Ori2A	Ori2B	Sense	Level	Factor	Type	Intens.	Index	
HOMB23	11	4	85	25			M	P	3	0	0		fractures
HOMB24	11	4	70	78			M	P	3	0	0		Dry fractures
HOMB25	11	4	45	230			M	P	3	0	0		Dry fractures
HOMB26	11	4	60	72			M	P	3	0	0		Dry fractures
HOMB27	11	4	89	115			M	P	3	0	0		Brittle fractures in GNT injected by carbonaceous veins
HOMB28	11	4	85	314			M	P	3	0	0		
HOMB29	11	4	85	100			M	P	3	0	0		
HOMB30	11	4	88	289			M	P	3	0	0		
HOMB31	11	4	52	78			M	P	3	0	0		
HOMB32	11	4	50	65			M	P	3	0	0		
HOMB33	11	4	89	306			M	P	3	0	0		
HOMB34	11	4	45	48			M	P	3	0	0		
HOMB35	11	4	89	110			M	P	3	0	0		
HOMB36	11	4	52	78			M	P	3	0	0		
HOMB37	11	4	50	67			M	P	3	0	0		
HOMB38	11	4	89	306			M	P	3	0	0		
HOMB39	11	1	72	275	71	290	N	P	2	0	0		Conjugated fractures in pegmatitic granite
HOMB40	11	1	69	274	67	297	N	P	4	0	0		
HOMB41	11	2	78	84	64	262		P	4	1	0		
HOMB42	11	2	58	80	60	307		P	4	1	0		
HOMB43	11	1	60	307	53	267	N	P	4	0	0		Striae ?
HOMB44	11	2	62	89	62	306		P	4	1	0		
HOMB45	11	1	62	306	46	250	N	P	4	0	0		
HOMB46	11	2	68	78	45	252		P	4	1	0		
HOMB47	11	2	65	80	67	292		P	4	1	0		
HOMB48	11	2	68	72	72	303		P	4	1	0		
HOMB49	11	4	65	80			N	P	3	0	0		
HOMB50	11	4	73	306			N	P	3	0	0		
HOMB51	11	4	71	307			N	P	3	0	0		
HOMB52	11	4	68	305			N	P	3	0	0		
HOMB53	11	4	68	88			N	P	3	0	0		
HOMB54	11	1	76	268	75	285	N	P	3	0	0		
HOMB55	11	4	55	300			N	P	3	0	0		
HOMB56	11	4	80	290			N	P	3	0	0		
HOMB57	11	4	70	66			N	P	3	0	0		
HOMB58	11	4	70	314			N	P	3	0	0		

Hombolo fault_Dam segment

Fault-slip data		Input row data (User format)											
			Plane		Line		Slip	Conf.	Weight	Activ.	Striae	Subset	Comments
Id	Format	Type	Ori1A	Ori1B	Ori2A	Ori2B	Sense	Level	Factor	Type	Intens.	Index	
HOMB59	11	2	55	84	62	300		P	3	1	0		
HOMB60	11	2	65	85	70	310		P	3	1	0		
HOMB61	11	2	63	83	69	304		P	3	1	0		
HOMB62	11	4	68	312			M	X	3	0	0		Along lake shore in granite-gneiss
HOMB63	11	4	62	318			M	X	3	0	0		Along lake shore in granite-gneiss
HOMB64	11	4	72	299			M	X	3	0	0		Along lake shore in granite-gneiss
HOMB65	11	4	60	319			M	X	3	0	0		Along lake shore in granite-gneiss
HOMB66	11	4	68	313			M	X	3	0	0		Along lake shore in granite-gneiss
HOMB67	11	4	56	293			M	X	3	0	0		Along lake shore in granite-gneiss
HOMB68	11	4	68	296			M	X	3	0	0		Along lake shore in granite-gneiss
HOMB69	11	4	64	315			M	X	3	0	0		Along lake shore in granite-gneiss
HOMB70	11	4	70	310			M	X	3	0	0		Along lake shore in granite-gneiss
HOMB71	11	4	75	110			M	X	3	0	0		Along lake shore in granite-gneiss

Bahi fault, Southeastern segment **06°14'49.4"S/93090 35°09'35.8"E/0738989**

Fault-slip data		Input row data (User format)											
			Plane		Line		Slip	Conf.	Weight	Activ.	Striae	Subset	Comments
Id	Format	Type	Ori1A	Ori1B	Ori2A	Ori2B	Sense	Level	Factor	Type	Intens.	Index	
IKA-001	11	4	82	68			T	P	2	2	0		Fresh joint/fracture, on big high angle NE dipping scarp
IKA-002	11	1	72	348	34	65	S	P	2	2	0		On fresh, pellitic rock (Riedel shears?)
IKA-003	11	4	65	275			T	P	2	2	0		
IKA-004	11	4	85	18			T	P	2	2	0		Prominent plane
IKA-005	11	4	85	270			T	P	2	2	0		NOT ptominent
IKA-006	11	4	84	28			T	P	2	2	0		Prominent
IKA-007	11	4	70	82			T	P	2	2	0		Prominent
IKA-008	11	4	71	39			M	P	2	2	0		Epidotized surface
IKA-009	11	4	74	24			M	P	2	2	0		Fresh
IKA-010	11	4	76	248			M	P	2	2	0		Fresh
IKA-011	11	4	49	176			M	P	2	2	0		Dips almost opposite
IKA-012	11	4	89	251			M	P	2	2	0		On schist
IKA-013	11	4	88	64			M	P	2	2	0		On schist
IKA-014	11	1	85	245	46	160	D	P	2	2	0		
IKA-015	11	4	86	73			M	P	2	2	0		On qurtzite/gneisse
IKA-016	11	4	80	68			M	P	2	2	0		On qurtzite/gneisse
IKA-017	11	4	83	237			M	P	2	2	0		General dipping of gneissic rocks (prominent)
IKA-018	11	4	84	244			M	P	2	2	0		Fresh

Fufu fault, Main part **06°40'52.8"**
35°57'31.0"

Fault-slip data		Input row data (User format)											
			Plane		Line		Slip	Conf.	Weight	Activ.	Striae	Subset	Comments
Id	Format	Type	Ori1A	Ori1B	Ori2A	Ori2B	Sense	Level	Factor	Type	Intens.	Index	
FF01-001	11	4	76	350			X	X	2,0	0	0		unmineralized, recent?
FF01-002	11	4	75	312			X	X	2,0	0	0		unmineralized, recent?
FF01-003	11	4	70	310			X	X	2,0	0	0		
FF01-004	11	4	85	48			X	X	2,0	0	0		
FF01-005	11	2	80	312	66	283		X	2,0	1	0		
FF01-006	11	4	70	310			X	X	2	0	0		faulted fold, fold=PHASE I
FF01-007	11	4	74	329			X	X	3	0	0		prominent plane or fracture
FF01-008	11	4	82	347			X	X	2,0	0	0		
FF01-009	11	2	80	314	89	203		X	2,0	1	0		
FF01-010	11	2	78	318	63	168		X	2,0	1	0		
FF02-001	11	2	78	310	88	108		X	2,0	1	0		unmineralized, recent?
FF02-002	11	2	79	135	71	312		X	2,0	1	0		
FF02-003	11	4	47	269			X	X	2,0	0	0		
FF02-004	11	4	87	238			X	X	2,0	0	0		
FF02-005	11	4	87	342			X	X	2,0	0	0		
FF02-006	11	4	76	305			X	X	2,0	0	0		
FF02-007	11	4	89	18			X	X	2,0	0	0		
FF02-008	11	2	89	125	89	231		X	2,0	1	0		conjugates at 35°57'29.4"/06°40'49.9"/775m
FF02-009	11	1	84	209	26	296	D	X	2,0	0	0		Associated with epidot., older plane than others-phase-II
FF02-010	11	4	89	134			X	X	2,0	0	0		
FF04-001	11	4	75	350			X	X	2,0	0	0		
FF04-002	11	4	86	20			X	X	2,0	0	0		
FF04-003	11	4	72	342			X	X	2	0	0		
FF04-004	11	2	60	154	76	311		X	2,0	1	0		
FF04-005	11	4	87	345			X	X	2,0	0	0		
FF04-006	11	4	74	306			X	X	2,0	0	0		
FF04-007	11	4	36	171			X	X	2,0	0	0		Listric fault
FF04-008	11	4	49	171			X	X	2,0	0	0		Listric fault
FF04-009	11	4	34	162			X	X	2,0	0	0		Parallel to the lower surface of the listric fault
FF04-010	11	4	85	272			X	X	2,0	0	0		Perpendicular to 36/171, joint?
FF04-011	11	4	37	174			X	X	2,0	0	0		Low angle faults, barren,

Fufu fault, Main part

Fault-slip data		Input row data (User format)											
			Plane		Line		Slip	Conf.	Weight	Activ.	Striae	Subset	Comments
Id	Format	Type	Ori1A	Ori1B	Ori2A	Ori2B	Sense	Level	Factor	Type	Intens.	Index	
FF04-012	11	4	76	130			X	X	2,0	0	0		No mineralization
FF04-013	11	4	87	18			X	X	2,0	0	0		No mineralization
FF04-014	11	4	80	49			X	X	2,0	0	0		No mineralization
FF04-015	11	4	75	174			X	X	2,0	0	0		No mineralization
FF05-001	11	1	87	93	4	183	D	X	0,5	0	0		Silicified
FF05-002	11	1	82	194	43	276	N	X	0,5	0	0		Qrtz& sericite on fault plane
FF05-003	11	4	89	80			X	X	0,5	0	0		
FF05-004	11	4	89	84			X	X	0,5	0	0		
FF05-005	11	4	86	114			X	X	0,5	0	0		
FF05-006	11	4	85	255			X	X	0,5	0	0		Quartzitic rx, which is intruded by mafic (upper)
FF05-007	11	4	77	312			X	X	0,5	0	0		Quartzitic rx, which is intruded by mafic (upper)
FF05-008	11	4	78	159			X	X	0,5	0	0		Quartzitic rx, which is intruded by mafic (upper)
FF05-009	11	1	88	336	86	273	X	X	0,5	0	0		Quartzitic rx, which is intruded by mafic (upper)
FF05-010	11	1	89	162	8	72	S	X	0,5	0	0		Lunate sctructures, PHASE II
FF05-011	11	1	76	321	18	236	D	X	0,5	0	0		Qtz sheared, PHASE II
FF06-001	11	4	68	152			X	X	0,5	0	0		Barren quartzite, located south, away from the scarp
FF06-002	11	4	72	47			X	X	0,5	0	0		Barren quartzite, located south, away from the scarp
FF06-003	11	4	65	58			X	X	0,5	0	0		Barren quartzite, located south, away from the scarp
FF06-004	11	4	30	298			X	X	0,5	0	0		Barren quartzite, located south, away from the scarp
FF06-005	11	4	60	145			X	X	0,5	0	0		Barren quartzite, located south, away from the scarp
FF07-001	11	4	70	125			X	X	0,5	0	0		Faultzone (crushed zone).
FF07-002	11	4	70	150			X	X	0,5	0	0		Gneissic rock
FF07-003	11	4	82	154			X	X	0,5	0	0		Plus down dip sliken sides? Reverse fault?
FF07-004	11	4	88	244			X	X	0,5	0	0		small listric faults, antithetic to FUFU04 listric faults
FF08-001	11	1	78	331	65	34	N	X	0,5	0	0		sericite (mica) grooves, tectonized
FF08-002	11	4	88	58			X	X	0,5	0	0		On quartzite
FF08-003	11	4	65	64			X	X	0,5	0	0		sericite (mica) grooves, tectonized
FF08-004	11	4	74	27			X	X	0,5	0	0		Ferruginized surface
FF08-005	11	1	69	226	23	146	S	X	0,5	0	0		Recent
FF09-001	11	4	50	319			N	X	0,5	0	0		
FF09-002	11	4	84	74			X	X	0,5	0	0		
FF09-003	11	4	39	317			X	X	0,5	0	0		
FF09-004	11	1	74	281	20	5	S	X	0,5	0	0		Kaolinized surface, 15cm2
FF09-005	11	4	63	128			X	X	0,5	0	0		Kaolinized surface
FF09-006	11	4	34	311			X	X	0,5	0	0		Kaolinized surface
FF09-007	11	2	78	251	82	128		X	0,5	1	0		Trace of mineralization
FF09-008	11	4	56	293			X	X	0,5	0	0		

Fufu fault, Main part

Fault-slip data		Input row data (User format)											
			Plane		Line		Slip	Conf.	Weight	Activ.	Striae	Subset	Comments
Id	Format	Type	Ori1A	Ori1B	Ori2A	Ori2B	Sense	Level	Factor	Type	Intens.	Index	
FF09-009	11	2	87	325	85	254		X	0,5	1	0		Fresh, unmineralized, RECENT
FF09-010	11	1	84	318	31	232	S	X	0,5	0	0		S. sides change from steps to lunate, slip angle of sliken sides, on fold
FF09-011	11	1	84	318	5	229	S	X	0,5	0	0		S. sides change from steps to lunate, slip angle of sliken sides, on fold
FF09-012	11	2	78	219	67	91		X	0,5	1	0		Fresh unmineralized quartzite
FF10-001	11	1	81	127	68	60	S	X	0,5	0	0		Grooves of serpentine
FF10-002	11	4	62	156			X	X	0,5	0	0		
FF10-003	11	4	83	82			X	X	0,5	0	0		
FF10-004	11	1	88	214	32	125	S	X	0,5	0	0		Some soils also seem to have been reactivated, RECENT FAULT
FF10-005	11	1	83	169	31	83	S	X	0,5	0	0		Some soils also seem to have been reactivated, RECENT FAULT
FF10-006	11	2	79	326	51	154		X	0,5	1	0		Quartzite
FF10-007	11	1	51	154	27	89	S	X	0,5	0	0		Quartzite
FF10-008	11	1	82	228	21	141	S	X	2,0	0	0		Quartz-grooves
FF10-009	11	4	74	74			X	X	2,0	0	0		Unmineralized
FF10-010	11	4	72	199			X	X	2,0	0	0		Unmineralized
FF13-001	11	4	77	304			S	X	0,5	0	0		Grooves of serpentine
FF13-002	11	4	71	199			X	X	0,5	0	0		
FF13-003	11	4	55	124			X	X	0,5	0	0		
FF13-004	11	4	80	148			X	X	0,5	0	0		
FF13-005	11	4	70	22			X	X	0,5	0	0		
FF13-006	11	4	84	341			X	X	0,5	0	0		
FF13-007	11	4	75	178			X	X	0,5	0	0		Recent fault
FF13-008	11	4	75	164			X	X	0,5	0	0		Recent fault
FF13-009	11	1	75	324	66	16	N	X	0,5	0	0		Recent fault
FF14-001	11	4	73	43			X	X	0,5	0	0		
FF14-002	11	4	77	319			X	X	0,5	0	0		
FF14-003	11	4	73	134			X	X	0,5	0	0		
FF14-004	11	4	59	274			X	X	0,5	0	0		
FF15-001	11	4	71	137			X	X	0,5	0	0		
FF15-002	11	4	85	232			X	X	0,5	0	0		
FF15-003	11	4	65	52			X	X	0,5	0	0		
FF15-004	11	4	71	40			X	X	0,5	0	0		
FF15-005	11	4	64	51			X	X	0,5	0	0		
FF15-006	11	4	77	122			X	X	0,5	0	0		
FF15-007	11	1	56	177	55	159	N	X	0,5	0	0		Recent fault
FF15-008	11	4	78	31			X	X	0,5	0	0		Rec. fault, cold water spring 100m north . Calcrete developing

Fufu fault, Northern part **06°38'37.3"**
35°57'40.5"

Fault-slip data		Input row data (User format)											
			Plane		Line		Slip	Conf.	Weight	Activ.	Striae	Subset	Comments
Id	Format	Type	Ori1A	Ori1B	Ori2A	Ori2B	Sense	Level	Factor	Type	Intens.	Index	
FF16-001	11	1	78	118	77	95	N	C	1	0	0		Qtz grooves
FF16-002	11	1	67	146	66	165	N	C	1	2	2		Qtz grooves
FF16-003	11	1	89	11	89	337	N	C	1	2	2		Qtz grooves
FF16-004	11	4	70	335			X	X	1	0	0		Fracture plane
FF16-005	11	4	89	190			X	X	1	0	0		Fracture plane
FF16-006	11	1	77	97	76	88	N	P	1	0	0		
FF16-007	11	1	81	148	71	213	N	P	1	2	2		
FF16-008	11	1	40	45	14	332	S	P	1	2	2		
FF16-009	11	1	49	228	42	267	D	P	1	1	1		No mineral alteration, Younger event
FF16-010	11	1	83	3	1	273	S	C	1	2	1		No mineral alteration, Younger event
FF16-011	11	2	83	3	74	183		X	1	1	0		No mineral alteration, Younger event
FF16-012	11	4	64	116			X	X	0	0	0		
FF16-013	11	4	74	40			X	X	0	0	0		
FF16-014	11	4	78	165			X	X	0	0	0		
FF16-015	11	4	71	43			X	X	0	0	0		
FF16-016	11	4	87	5			X	X	0	0	0		
FF16-017	11	1	44	39	42	16	S	C	0	0	1		Epidot. surface, Recent, but older than FF16-009, 49/228.
FF16-018	11	4	49	46			X	X	0	0	0		Fracture/joint
FF16-019	11	4	73	4			X	X	0	0	0		Assoc. with soils grooves-shaped, (hard to deter. sense of mov.)
FF16-020	11	1	81	281	59	356	S	P	1	0	1		

Appendix 4

Reports on earthquakes/tremors in the area of Dodoma

Reports on earthquakes/tremors in the area of Dodoma

Appendix 4 contains three archived miscellaneous reports:

- Report 1 is about earthquake tremors in Tanzania on 7 May 1964,
- Report 2 is about phenomena related to earthquake tremors, which occurred between April and July 1965 in Singida (Tanzania),
- Report 3 is about possible recent faulting in Tanzania.

WHITTINGHAM, 1964

REPORT ON THE EARTH TREMOR OF 7th MAY 1964

On 7th May 1964 at about 08.46 hrs. (East African Time), an earth tremor lasting 30 to 60 seconds was felt over a wide area of northern, central and western Tanganyika, Kenya and Uganda, at places as far a part as Bukoba, Kampala, Nairobi, Tanga, Morogoro, Iringa, Tukuyu and Kigoma.

Although the earth tremor was of mild intensity compared with earthquakes experienced in major seismic areas in other parts of the world, this is the strongest tremor within living memory of the inhabitants of Mbulu, Kondoa and Masai Districts of Tanganyika where the effects were most strongly felt. Since the seismic effects were widespread, the earth tremor was probably of deep-seated origin. The earth tremor was not felt in Mtwara or Ruvuma Regions or Mahenge Districts and only a few people noticed the tremor in Dar es Salaam and Coast Region.

Early reports showed that the shock was most intense in Mbulu District and that tremors of unusual strength had been experienced at places situated near to the Gregory Rift in Tanganyika and in Kenya. A visit was accordingly made to Kondoa, Mbulu and Masai Districts from 13th to 18th May 1964 to examine the effects in those areas and to collect information from eye-witnesses.

In many places no note of the exact time of the shock was made and where the time was recorded synchronization of the time is doubtful. Hence only approximate times can be given in most cases. Unfortunately the seismograph at Dodoma was not operating.

The Main Earth Tremor

At all the stations visited the main earth tremor occured between 08.45 and 09.00 hrs. on 7th May 1964. At places where the tremor was most intense about 5 consecutive shocks were felt, the 3rd and 4th shocks being strongest.

The direction of the shocks in places of greatest intensity is somewhat confused, although near Babati many people experienced a "swing" in the direction, first from the north-west, then from the east. At the stations west of the Rift wall the main shocks appeared to come from the east, which would suggest that movement took place along the Rift wall itself.

Between Kondoa and Babati, however, people living on Pienaar's Heights also experienced shocks coming from the east. At Galappo and Gidas some people heard sounds immediately preceding the tremor resembling "wind and rain" or "the noise of a jet aircraft". The significance of these sounds is uncertain unless they represent the sound of actual movement along a fault.

Slight fore-shocks were experienced about 5 to 10 minutes before the main tremor at places on or near the Rift wall.

From the evidence summarized above it would appear that while the initial movement took place along the Rift wall, movement of a more violent nature took place along the faults east of Pienaar's Heights passing through Kolo and Galappo. Violent movement may also have continued along the Rift wall. It is possible that movement also took place along major faults to the east, such as those which follow the western edge of the Makami depression in south Masailand. Until reports from that area are received, however, this cannot be verified.

Whittingham, J.K., 1964. Report on the earth tremor of 7th may 1964. Ministry of Water, Energy and Minerals, Mineral Ressources Division, Dodoma, Tanzania, Unpublished report.

The Belt of greatest Shook Intensity

The belt of greatest intensity of the shock, determined by the amount of damage caused, appears to run west of north from Kondoa to Oldeani and probably beyond on to the Serengeti Plains. This belt is 30 to 40 miles wide at Oldeani and about 10 miles wide near Bereku. At places visited within this belt the intensity of the shock was VII (Modified Mercalli Scale of 1931—Ref. Byerly, 1942, pp. 57-58). Oldeani, Mbulu, Dareda, and Gidas lie in the middle of this belt while Babati lies on the eastern edge. Past experience has shown that this belt is especially prone to earth tremors and many houses at Mbulu and Oldeani have built-on buttresses. In 1960 when a seismograph was operating at Dodoma, many small tremors were recorded at 200 to 400 kms. from Dodoma. The origin of these tremors remained in doubt, since the distance from a second seismographic station was not available. The tremors were provisionally considered to have come from the Wembere and Lake Eyasi areas, but it is possible that some may in fact have originated from the belt described here.

The belt of greatest intensity of the earth tremor lies in the vicinity of the Rift wall and the Kolo-Galappo faults, but does not follow the trend of the faults. The belt runs west of north in the terrain of Usagaran rocks 10 to 40 miles east of a shear zone of Archaean age which forms the boundary between the central granite area and the Usagaran metamorphic terrain of eastern Tanganyika and Kenya. In this zone sheared metamorphic rocks dip to the east. The significance of this relationship remains uncertain. The Rift faults which cross the belt of greatest intensity may have had some further localizing effect on the intensity of the shock within the belt.

The shock reached a moderately high intensity in the Singida-Iramba Districts (V), near Musoma (V) and along the eastern foot of the Ukaguru and Nguru Mountains between Kilosa and Turiani (VI). The tremor reached an intensity of IV in the Tukuyu-Mbeya area.

Damage to Buildings

In the Mbulu and Kondoa Districts many brick buildings were damaged, walls, chimney stacks and tiled roofs were seriously cracked and many collapsedd. Old brick buildings were the most seriously damaged while newly built brick houses were sometimes slightly cracked but remained safe. The stone an cement German-built boma at Mbulu suffered extensive damage by the cracking of walls. Many brick-built Government quarters in Mbulu were still standing but badly cracked and unsafe. Most of the older brick buildings at Dareda Mission were badly cracked, ceilings collapsed and interior walls fell down. Damage to farm buildings at Oldeani was similar to that at Dareda, but more widespread. The farms high on the slopes of Oldeani Mountain appear to have suffered most, and some farmers noticed that the houses which were most seriously damaged were those elongated N-S.

At all these places, plaster on walls was cracked and often fell down. In general, interior walls appear to have suffered more than external walls. Many buildings which appear undamaged from the outside can be seen inside to be unsafe. There is no known instance of a window having been broken as a result of the earth tremor. Mud-walled houses were damaged over a wide area. Mud walls fell down in houses at Mbulu, Oldeani, Manghola, Dareda, Babati, Galappo, Bereku, Gidas, and Kondoa.

Disturbances in Nature caused by the Earth Tremor

Falls of rock occured at many places along the Rift wall and on the precipitous southern slopes of Kwaraha Mountain. These falls do not necessarily indicate a high intensity of shock since such falls may occur on these escarpments in the rainy season without any earth disturbances. The dislodgement of a large boulder from a tor near Gidas must, however, have resulted from a considerable shock since the boulder was formerly in a moderately stable position.

Washways near springs occured with small scale landslipping near Mbulu and near Gidas. Saline springs in Kondoa township increased their flow. At Duguloi north-west of Babati, springs turned milky and were contaminated for several days.

A feature of special interest is an earthquake fountain (Richter, 1958, pp. 106-109) at Swera, about 12 miles south of Bereku, in a small valley about 2 miles west of the Arusha-Dodoma road where a maize shamba had been cultivated. According to villagers, at the time of the main shock, water and sand shot up vertically into the air to a height of about 20-30 feet. After the tremor, the fountain subsided but water continued to gush out for a whole day, eroding away the maize shamba and carrying the sediment away down the valley. At the time of visit, water was only trickling out from near the surface but it was seen that an area of maize shamba about 100 yards square had been affected and a small crater-like depression 2 to 3 yards in diameter was still visible in the centre of the area affected. The earthquake fountain was probably caused by sudden expulsion of confined ground-water from joints and cracks in the rocks below which were being compressed during the earth tremor.

An observer flying over Ol Doinyo Lengai volcano after the earth tremor reported that the volcano was erupting. The Masai living at the eastern foot of the mountain had noticed the earth tremor but stated that they had not seen any eruption. There was no sign of outpouring smoke from the crater at the time of the visit.

References

BYERLY, P. 1942. Seismology. Prentice-Hall Inc. New York.

RICHTER, C.F. 1958. Elementary Seismology. Freeman, San Francisco.

DUNDAS, D.L., 1965

PHENOMENA RELATED TO EARTH-TREMORS
WHICH OCCURRED BETWEEN APRIL AND JULY
1965 AT NGIMU, SINGIDA DISTRICT

1. Introduction. As a result of a request by the Regional Executive Officer, Singida, the author visited Ngimu (about 24 miles ENE. of Singida) on 9th July 1965 to examine damage to Ngimu Primary School and a reported crack in the ground "eight miles long and six feet deep."

2. According to the local inhabitants at Ngimu, a series of minor preliminary shocks, beginning on the 24th of April, 1965, preceded the main earth-tremor which is said to have occurred at about 5 pm. (14.00 G.M.T.) on the 18th of May, 1965. This main shock, which caused the damage to Ngimu Primary School, was followed by a further series of minor shocks, which occurred intermittently with gradually diminishing intensity until the time of the author's visit.

3. The intensity of the main shock (of 18th May, 1965) at Ngimu was probably V-VI on the Modified Mercalli (M-M) Earthquake Intensity Scale, and some of the later shocks were probably of intensity IV or V. (Intensities are defined by the Modified Mercalli scale as follows:-

IV. During the day felt indoors by many, outdoors by few. At night some awakened. Dishes, windows, doors disturbed.

V. Felt by nearly everyone, many awakened. Some dishes, windows, etc. broken; unstable objects overturned.

VI. Felt by all; many frightened and run outdoors.)

4. The damage to Ngimu Primary School was slight. A few cracks (not more than ¼" wide) were seen in some of the internal walls and a more serious crack, see Plate I, affected the outside wall on the NE. corner of the building. However, this damage could easily and cheaply be repaired, and, meanwhile, unless further more serious earthquake damage occurs, the building is perfectly safe. No other noteworthy damage to buildings appears to have occurred in connection with these earth-tremors at Ngimu.

Dundas, D.L., 1965. Phenomena related to earth-tremors which occurred between April and July 1965 at Ngimu, Singida. Ministry of Water, Energy and Minerals, Mineral Ressources Division, Dodoma, Tanzania, Unpublished report

300 yards NW. of the trig. point at the summit of Buhama Hill (about 5 miles E. of Ngimu). This fault, which is one of a series of faults with a similar north-easterly or east-north-easterly trend in this area, forms the south-eastern boundary of the Balangida Lelu "rift-valley", which has been dropped down relative to the higher ground to the north-west and south-east.

6. The reported crack "eight miles long and six feet deep" follows along the line of the Buhama fault. It would more accurately be described as a discontinuous series of cracks. The cracks were usually 1" to 2" wide, but were sometimes up to 6" wide and at least 6 feet deep see Plate II. They were only seen to affect the soil; in no case was any recent cracking observed in any outcrops of the underlying granitic rocks. The author followed the line of cracks for about two miles between the Tolongonyi and Lamba stream-beds (See map accompanying this report). The line of cracks was reported to continue for about three miles north-eastwards from the Tolongonyi stream-bed, and for about the same distance south-westwards from the Lamba stream-bed.

7. The line of cracks described above is said to have opened up simultaneously with the earth-tremor of the 18th of May, 1965. At the same time, a boulder of granite about 4 feet in diameter was dislodged and rolled down the fault-scarp one mile due south of Itaho rock.

8. Conclusions.

(a) The damage to property at Ngimu caused by the earth-tremors of April-July, 1965, was slight.

(b) There is no known way of predicting individual earthquakes. However, by examining records of past seismic activity, and the distribution of recent geological faults, certain areas may be designated seismically active areas. Ngimu lies within such a seismically active area. Hence it is to be expected that further earth tremors, some possibly more severe than those which occurred there this year, may occur from time to time.

- 3 -

In view of the possibility of earth-tremors in the Balangida Lelu valley area, the following recommendations are made:-

1) If possible, buildings in the area should not be more than one storey high. If it is essential to erect buildings of two or more storeys, they should be of strong construction and should be designed with the possibility of earth-tremors in mind.

2) The people in this area should if necessary be dissuaded from building on, or close beneath, steep, rocky ground where their houses might be damaged by rock-falls which may occur as a result of earth-tremors.

3) Permanent buildings should, if possible, be sited away from the lines of known geological faults.

Ministry of Water, Energy and Minerals

MINERAL RESOURCES DIVISION, Dodoma
TANZANIA

POSSIBLE RECENT FAULTING IN TANZANIA

by

B.G. WALKER, Geologist

Unpublished report

DODOMA
20.4.1967.

References:

Degree Square 10.
Records File 3088
Map GS 2035, 1872
Plates I, II & III

Possible Recent faulting in Tanzania

Earthquakes are relatively common phenomena in Tanzania particularly in the region of the Central Africa Rift and the Lake Tanganyika and Nyasa rift valleys where on up to 25 days a year tremors are experienced. The frequency of earthquakes diminishes towards the coast so that Dar es Salaam only experiences one perceptible tremor during two or three years.

Although the tremors are undoubtedly associated with movements on the faults of the rift systems, never in Tanzania have any actual displacements in these faults, been measured following a tremor.

Relevant accounts of earthquake effects in the records of this Division only cover tremors which occured during the past few years and these reports only postulate movement on certain named faults as the cause of the tremors, actual displacements on these faults were not observed.

The Earth tremor of 7th May 1964

This was the most severe tremor to have occurred in living memory of the inhabitants of Mbulu, Kondoa and Masai Districts where the effects were most strongly felt. Rock falls occured at many places along the rift wall and sounds which may have been caused by fault movements were heard near the Rift wall and near the Gallapo and Kolo faults (see Map: Earth Tremor of 7th May 1964, area of greatest intensity).

The North Tremors which occurred between April and July 1965.

The main shock in a series of tremors occurred on 18th May 1965. The tremors appear to have been connected with movement along the Buhoma faults. A series of cracks opened following the line of the fault for a distance of eight miles. The cracks were usually 1" to 2" wide but were sometimes up to 6" wide and at least 6 feet deep (see photograph 1). They were only seen to affect the soil.

BUHAMA

Seismic Activity near Lake Jipe North Pare

Minor earth tremors have been recorded close to fault planes in the Lake Jipe area. Cracks in the soils of the area are reported to have occurred in 1948, 1952 and 1965 and have been attributed to movements on faults in the area. (see photographs 2 and 3 and Map North Pare (Lake Jipe).

References

CHAIMA, D.S. 1966. Seismic activity near Lake Jipo. Unpub. Rep. Min. Eng. Div. Tanzania.

DUNDAS, D.L. 1965. Phenomena related to earth-tremors which occurred between April and July 1965 at Ngimu, Singida. Unpub. Rep. Min. Eng. Div. Tanganyika.

EAST AFRICA METEOROLOGICAL DEPT. 1964. Earth tremors in E. Africa. Unpub. Rep. Geol. Surv. Tanganyika.

KING, A.J. 1961. Seismology in E. Africa. Unpub. Rep. Geol. Surv. Tanganyika.

SEISMOGRAPHICAL RECORDS. Records Office Rep. 1757.

WHITTINGHAM, J.K. 1964. Report on the earth-tremor of 7th May 1964. Unpub. Rep. Geol. Surv. Tanganyika.

DODOMA.

20th April, 1967.

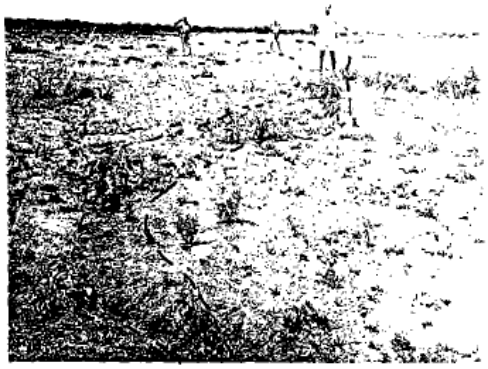

Plate 5 :

Plate 6 :

Discontinuous, loop shaped cracks at Tarolia. Almost filled up

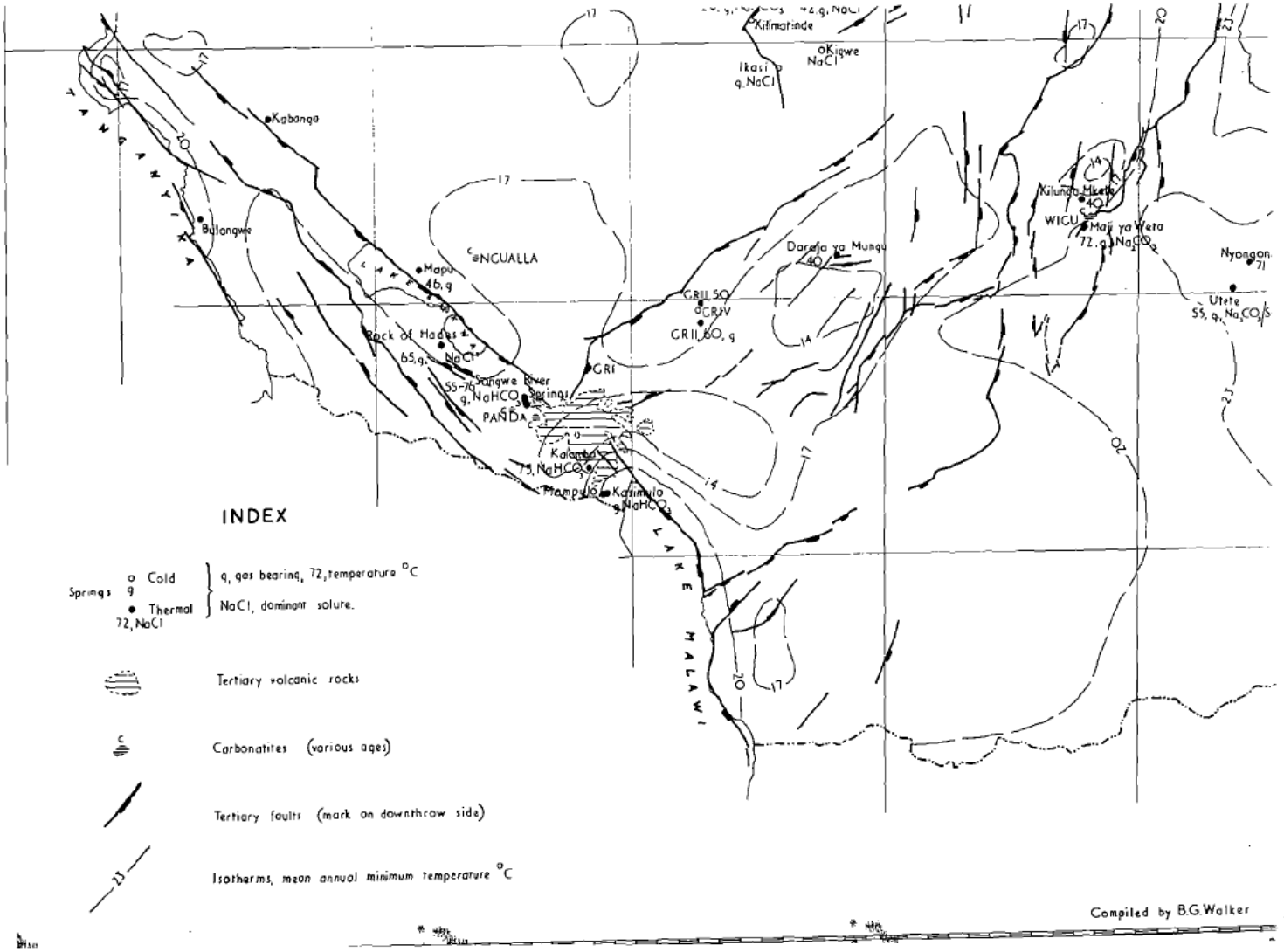
Kabanga
Bulongwa
Mapu
46, g
NCUALLA
Rock of Hades
65, g, NaCl
Songwe River Springs
55–70 g, NaHCO3
PANDA
Kalambo
75, NaHCO3
Mpimbwe
Katumbila
NaHCO3
GRI
GRII SO
GRIV
GRII SO, g
Daraja ya Mungu
40
Kilungo Mkeka
40
WIGU
Maji ya Weta
72, g, Na2CO3
Nyongon
71
Utete
55, g, Na2CO3
Kifimatinde
Ikasi
g, NaCl
Kigwe
NaCl
TANZANIA
LAKE MALAWI
INDEX
Springs
Cold
g
Thermal
72, NaCl
g, gas bearing, 72, temperature °C
NaCl, dominant solute.
Tertiary volcanic rocks
Carbonatites (various ages)
Tertiary faults (mark on downthrow side)
Isotherms, mean annual minimum temperature °C
Compiled by B.G. Walker

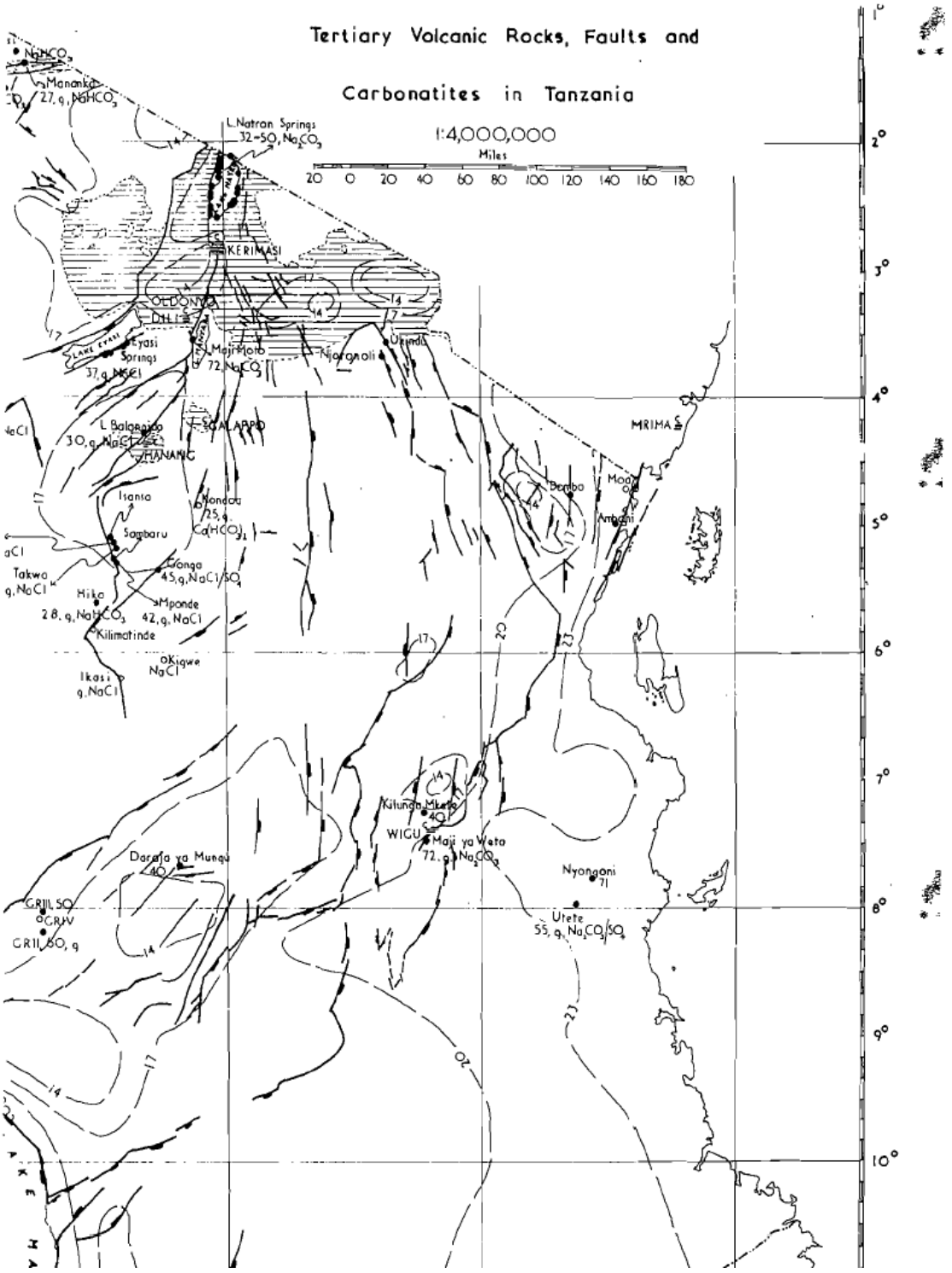
Tertiary Volcanic Rocks, Faults and
Carbonatites in Tanzania
1:4,000,000
Miles
20 0 20 40 60 80 100 120 140 160 180
KERIMASI
OLDONYO
DILLI
Mananka
27, q, NaHCO3
L.Natron Springs
32-SO, Na2CO3
Eyasi
Springs
37, q, NaCl
L Balangida
30, q, NaCl
MANANG
SCALAPPO
Mondoa
25, q
Ca(HCO3)2
Sagbaru
Itanta
Takwa
q, NaCl
Hiko
28, q, NaHCO3
Mponde
42, q, NaCl
Kilimatinde
Kigwe
NaCl
Ikasi
q, NaCl
Gonga
45, q, NaCl/SO4
Maji Moto
72, Na2CO3
Ngorongoli
Usandi
MRIMA
Bombo
Moa
Antioni
Kilunga Mkalo
40
WIGU
Maji ya Wata
72, q, Na2CO3
Darafa ya Munqa
40
Nyongoni
71
Utete
55, q, Na2CO3/SO4
GRIII SO
GRIV
GRII SO, q
1°
2°
3°
4°
5°
6°
7°
8°
9°
10°

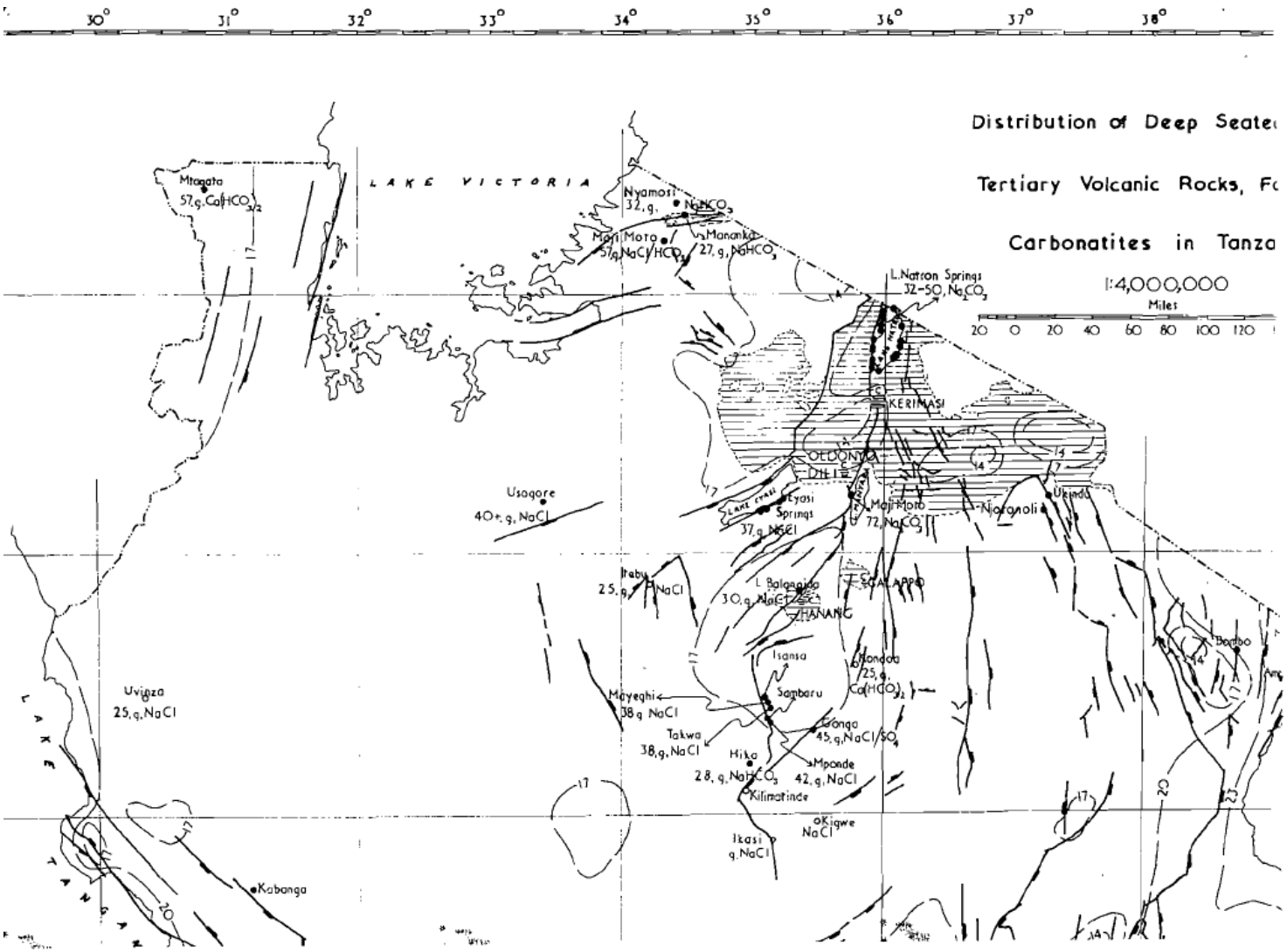
30° 31° 32° 33° 34° 35° 36° 37° 38°
Distribution of Deep Seate
Tertiary Volcanic Rocks, Fc
Carbonatites in Tanza
1:4,000,000
Miles
20 0 20 40 60 80 100 120
LAKE VICTORIA
Mtagata
57, g, CaHCO3/2
Nyamosi
32, g,
Maji Moto
57, g, NaCl/HCO3
Manonko
27, g, NaHCO3
L. Natron Springs
32-50, Na2CO3
KERIMASI
OLDONYO
DILI
Usagore
40+, g, NaCl
Eyasi
Springs
37, g, NaCl
Maji Moto
72, NaCO3
Ukinda
Nioronoli
Itaba
25, g, NaCl
L. Balangida
30, g, NaCl
SADIMAN
HANANG
Bombo
Isansa
Mondoa
25, g,
Ca(HCO3)2
Sambaru
Mayeghi
38 g NaCl
Takwa
38, g, NaCl
Hika
28, g, NaHCO3
Mponde
42, g, NaCl
Kilimatinde
Kigwe
NaCl
Ikasi
g, NaCl
Uvinza
25, g, NaCl
LAKE TANGANYIKA
Kabanga

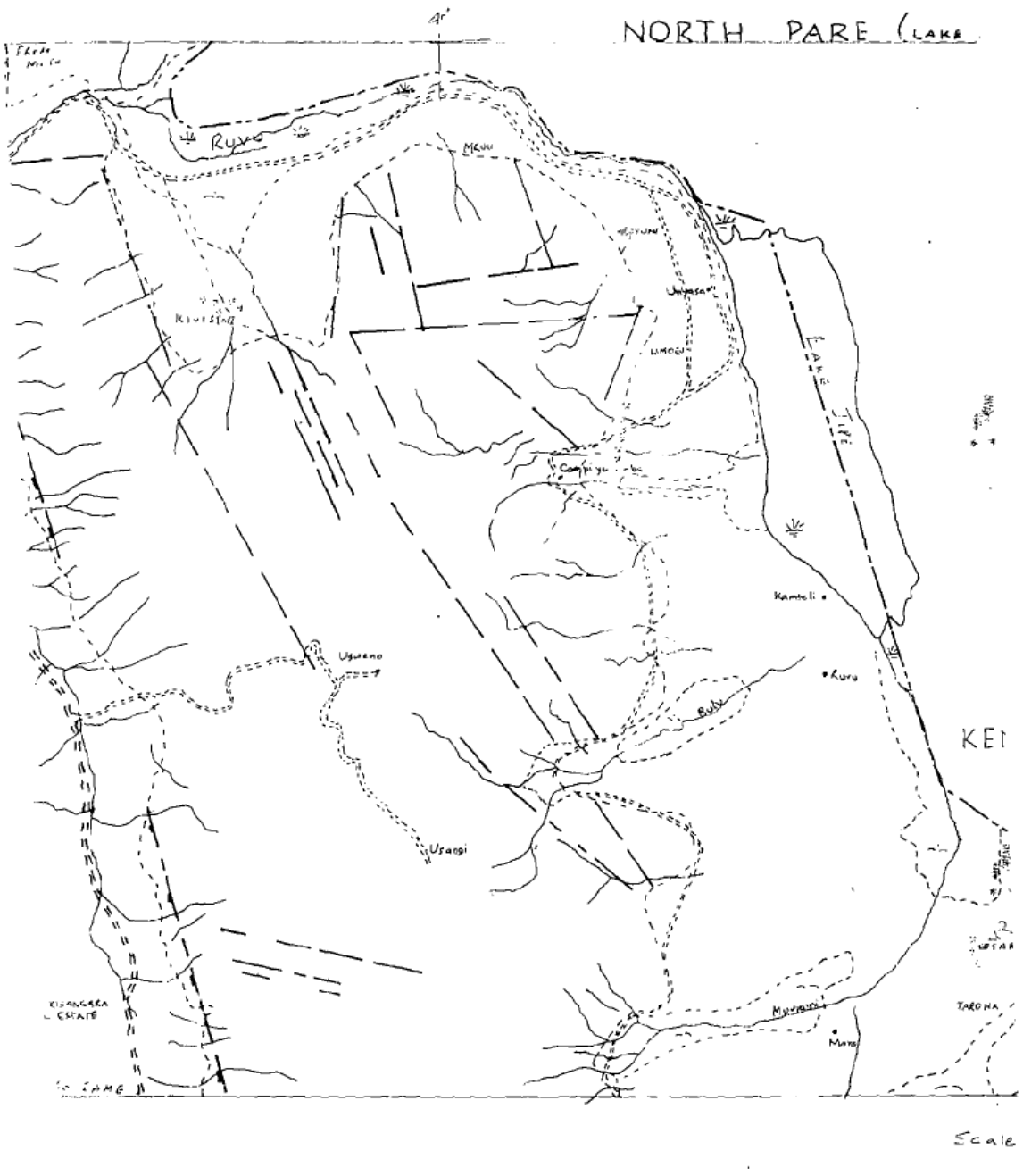
NORTH PARE (LAKE
RUVU
MKUU
KIVUSINI
Ugweno
Usangi
Kamoli
Kuru
Bubu
KEI
Mang'
TARORA
KISANGARA ESTATE
Scale

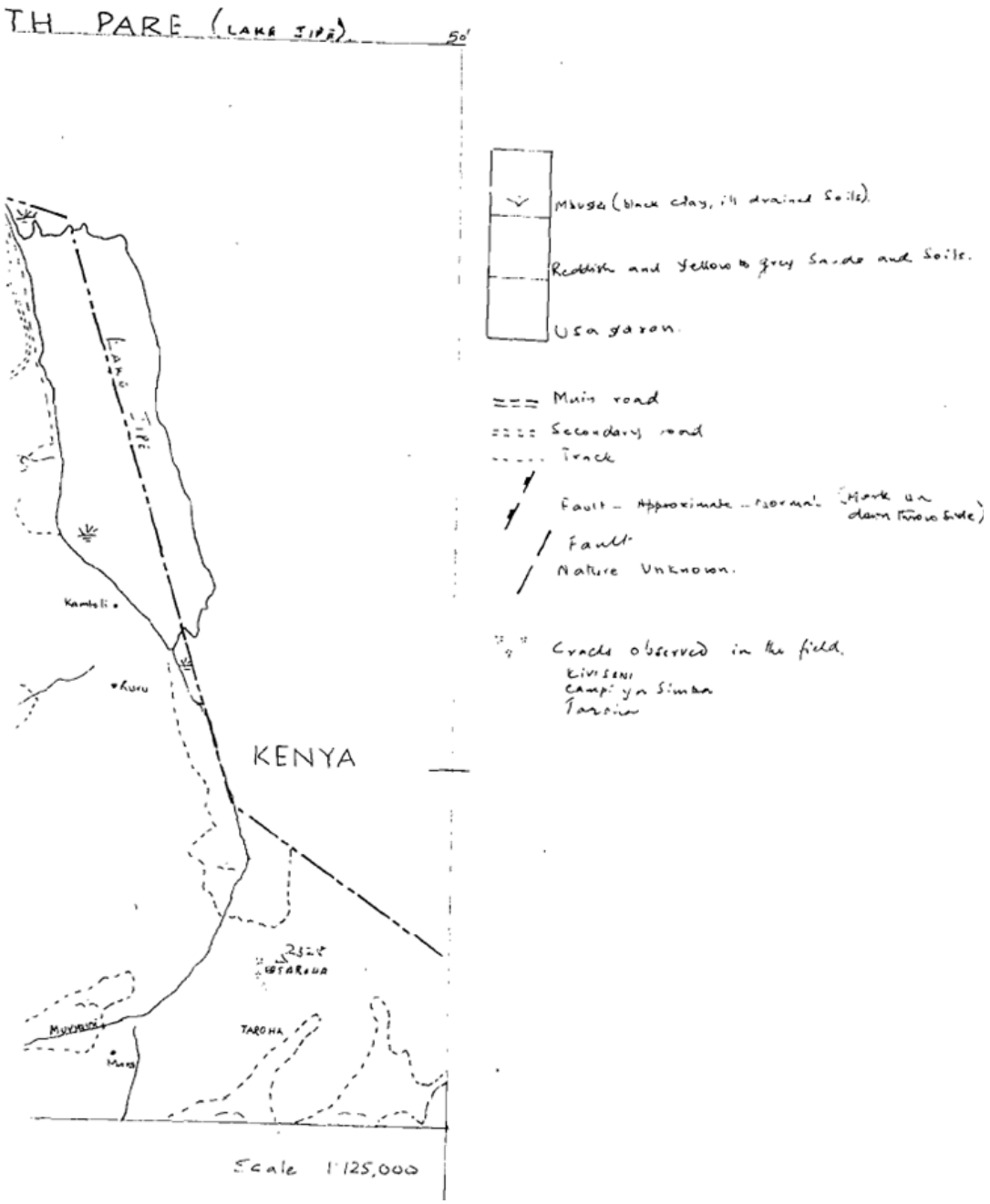
TH PARE (LAKE JIPE)
50'
LAKE JIPE
Kamteli
Kuru
KENYA
2522
TAROHA
Scale 1:125,000
Mbuga (black clay, ill drained Soils).
Reddish and Yellow to grey Sands and Soils.
Usa garon.
Main road
Secondary road
Track
Fault - Approximate - normal (Mark on down throw side)
Fault
Nature Unknown.
Cracks observed in the field.
Kivi seni
Kampi ya Simba
Taroha

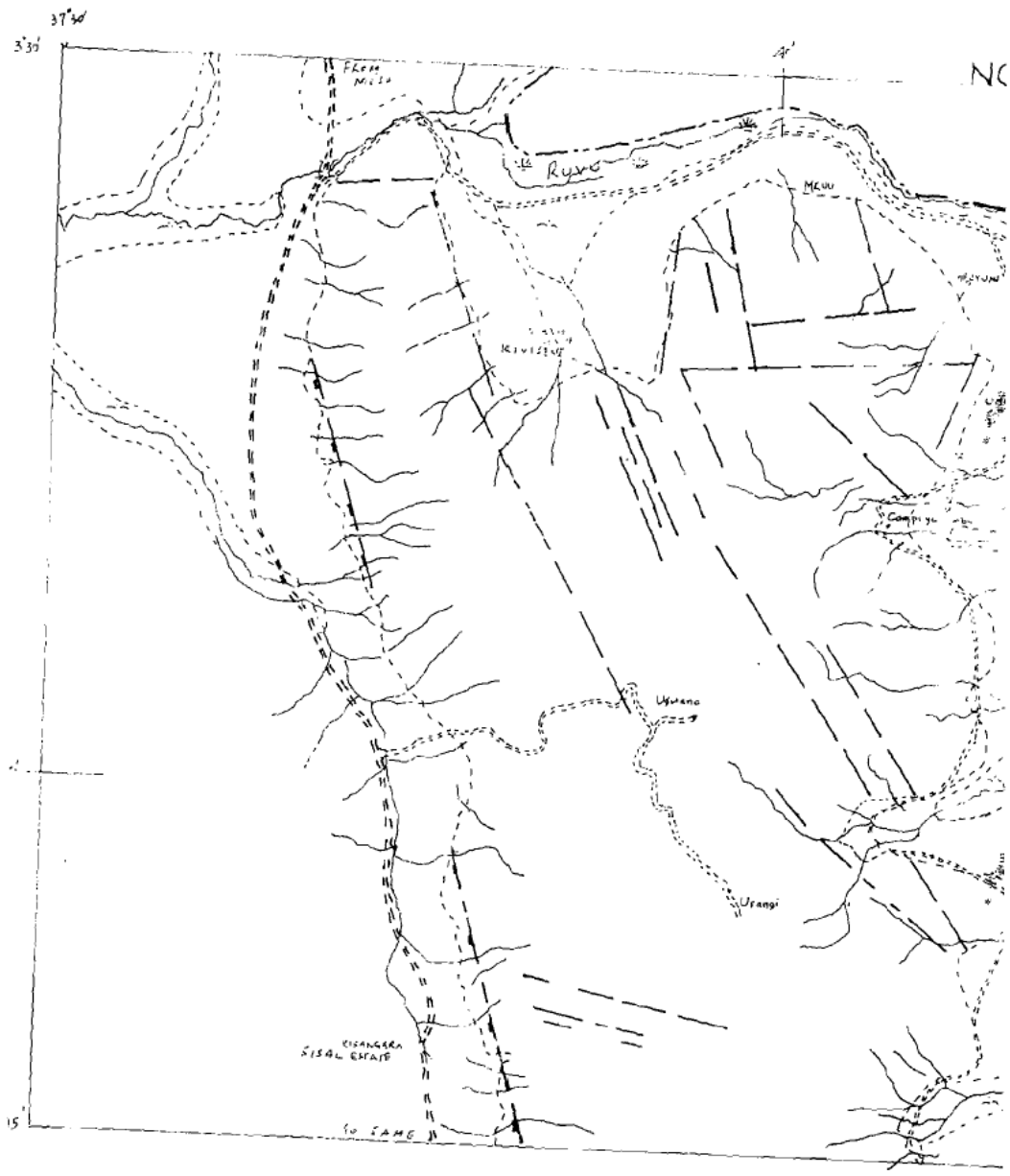
Ruvu
Mkuu
Ukwere
Urangi
KISANGARA
SISAL ESTATE
TO SAME

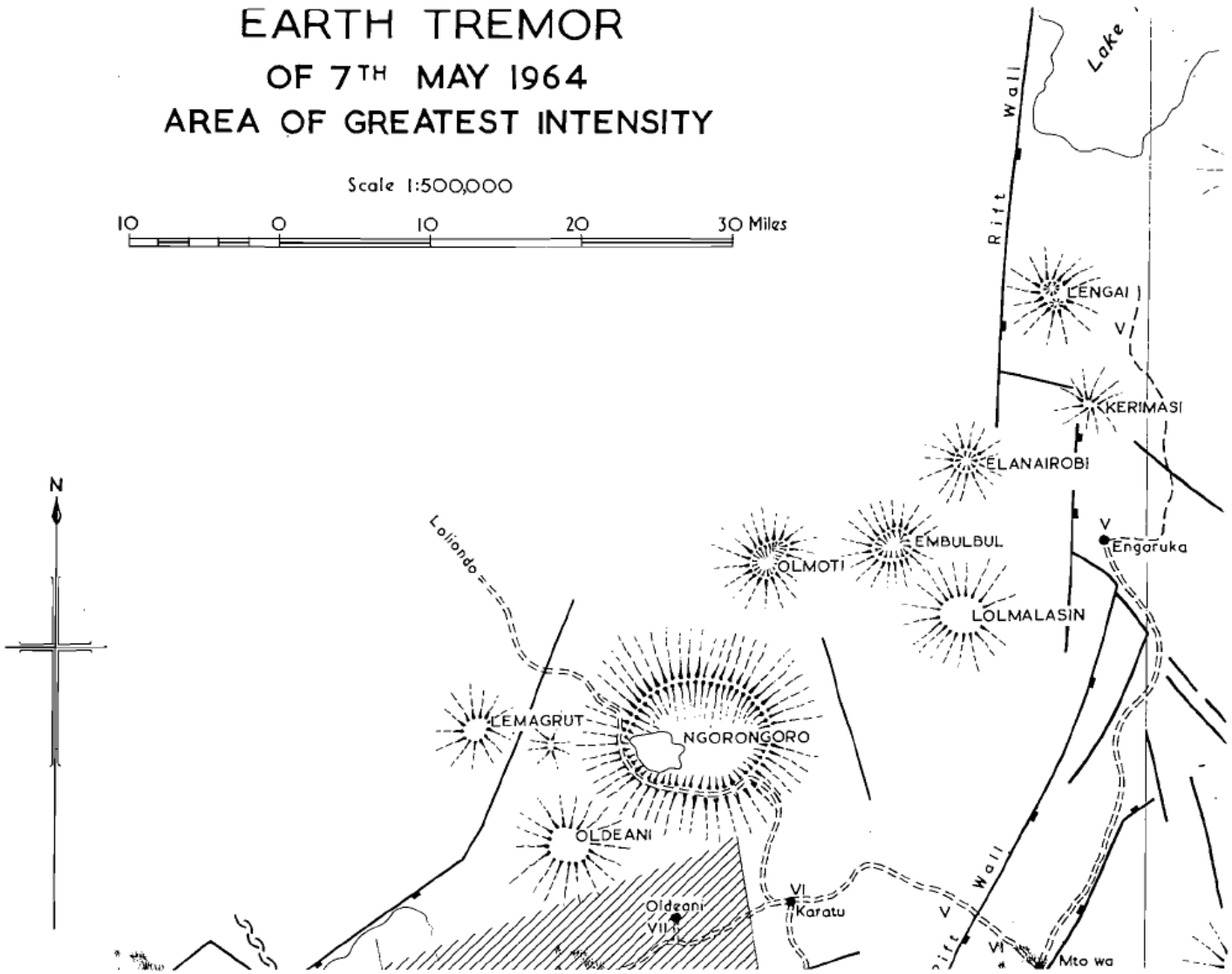
EARTH TREMOR
OF 7TH MAY 1964
AREA OF GREATEST INTENSITY
Scale 1:500,000
10 0 10 20 30 Miles
N
Lake
Wall
Rift
LENGAI
V
KERIMASI
ELANAIROBI
V
Engaruka
EMBULBUL
OLMOTI
LOLMALASIN
Loliondo
LEMAGRUT
NGORONGORO
OLDEANI
Oldeani
VIII
VI
Karatu
V
Wall
Rift
VI
Mto wa

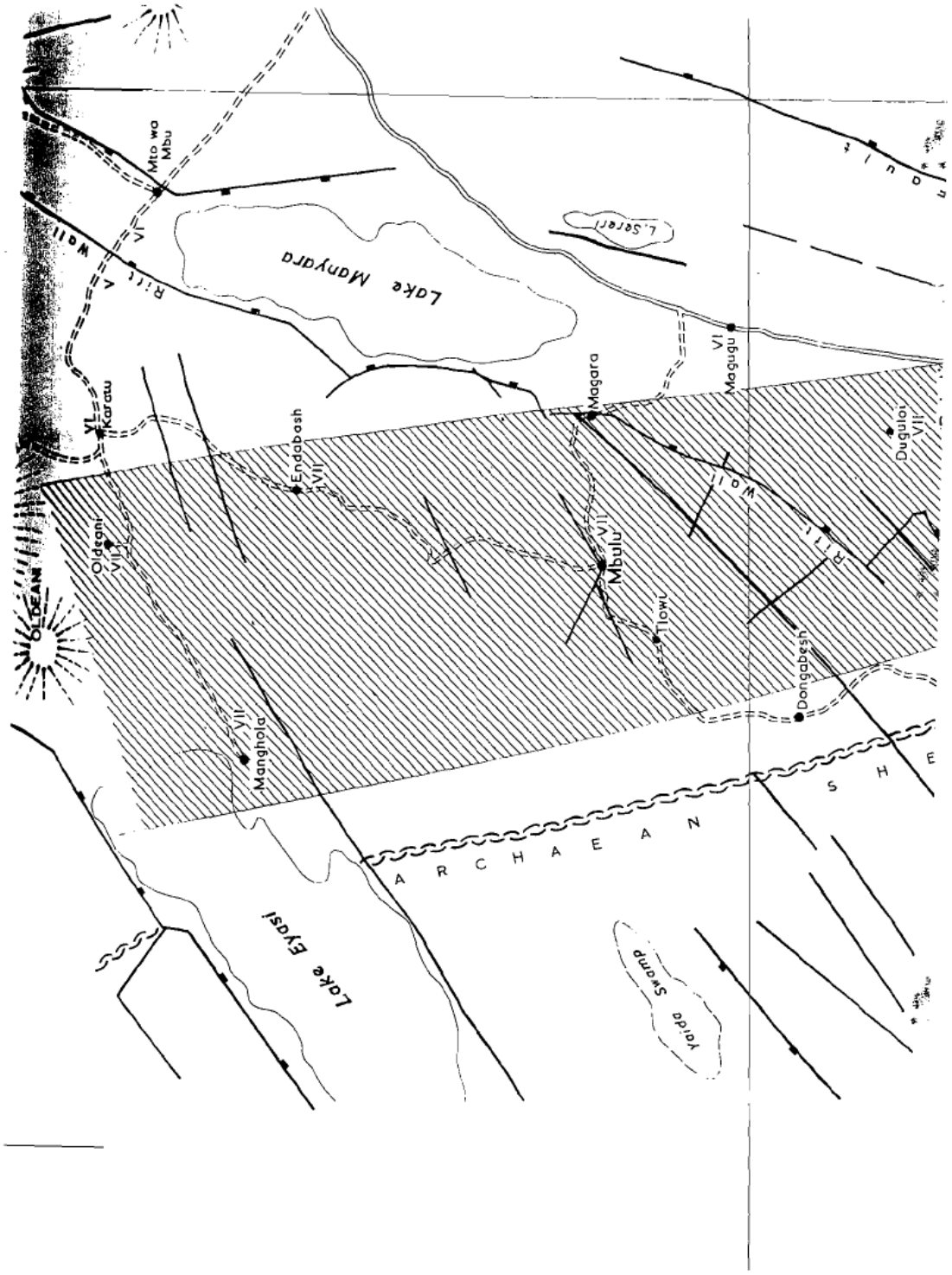
Mto wa Mbu
Lake Manyara
L. Sorei
Magara
Magugu
VI
Endabash
VII
Mbulu
Dongabesh
Duguloi
VII
Olgoni
VII
Manghola
VII
Tlowi
Lake Eyasi
Yaida Swamp
ARCHAEAN
SHE

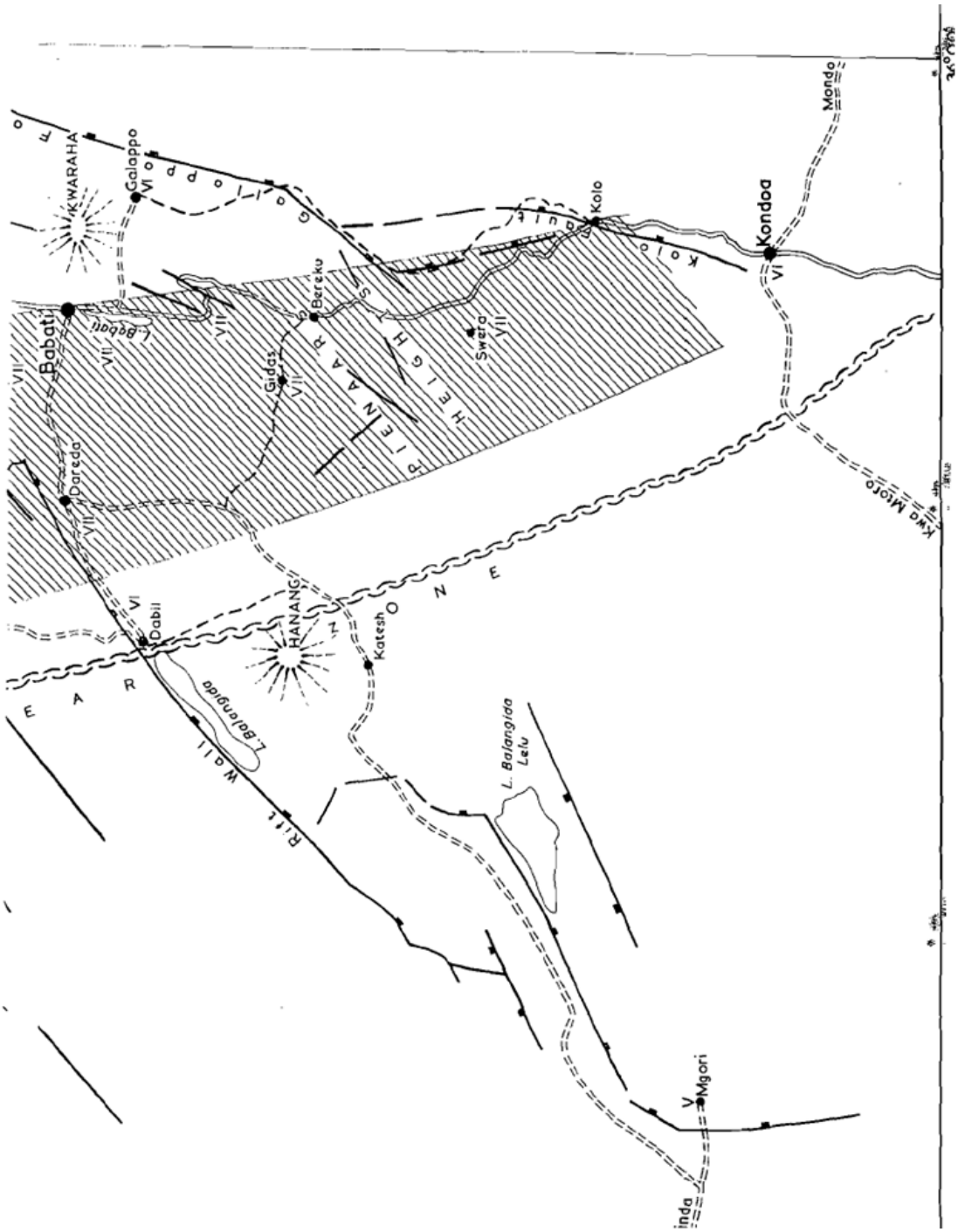
Galappo
KWARAHA
Babati
Dareda
Dabil
Bereku
Gidas
Swera
Kolo
Kondoa
Monda
HANANG
Kattesh
L. Balangida
Lelu
L. Balangida
L. Babati
MGORI
Mgori
RIFT
WALI
EAR
ONE
Kwa Mtoto